



VNIVERSITAT DE VALÈNCIA

DEPARTAMENT DE FÍSICA APLICADA I ELECTROMAGNETISME
PROGRAMA DE DOCTORADO EN FÍSICA

Yodatos bajo condiciones extremas: Transiciones de fase
inducidas por la presión, propiedades estructurales,
vibracionales y electrónicas

PhD candidate:

Akun Liang

Supervisor:

Prof. Daniel Errandonea Ponce

Valencia, Spain; July 2022


Don Daniel Errandonea Ponce, Profesor Titular de la Universidad de Valencia

INFORMA:

Que la presente memoria "Yodatos bajo condiciones extremas: Transiciones de fase inducidas por la presión, propiedades estructurales, vibracionales y electrónicas" se ha realizado bajo su dirección en el Departamento de Física Aplicada de la Universidad de Valencia por el licenciado en Física Don Akun Liang, y que constituye su Tesis para optar al grado de Doctor en Física.

Y para que aquí conste, en cumplimiento de la legislación vigente, presenta en la Universidad de Valencia la referida Tesis Doctoral.

Burjassot, a 12 de Julio 2022

A handwritten signature in black ink, consisting of several overlapping, fluid strokes that form a complex, cursive shape.

Fdo.: Daniel Errandonea Ponce

Director de Tesis y Tutor

Contents

Acknowledgements	vi
List of publications	viii
Resumen en castellano	xii
1. Introducción	xii
2. Objetivos	xiii
3. Resultados y conclusiones	xiv
1. Introduction	1
1.1 Nonlinear optical materials	1
1.2 Metal iodates	2
1.3 The bandgap of metal iodates at ambient conditions	4
1.4 High pressure science	8
1.5 Aims of the thesis	11
1.6 Organization of the thesis	12
2. Theoretical background and experimental techniques	13
2.1 Membrane-type diamond anvil cell	13
2.2 X-ray diffraction	15
2.3 Raman scattering	19
2.4 Infrared spectroscopy	22
2.5 Optical absorption	26
3. Crystal structure, atomic vibrations, and electronic band structure of Fe(IO₃)₃ under pressure	31
3.1 Introduction	31
3.2 Experiment and Calculation details	33
3.3 Results and Discussion	36
3.4 Conclusions	49
3.5 Author Contribution	50
4. Crystal structure, atomic vibrations and electronic band structure of Co(IO₃)₂ under pressure	83
4.1 Introduction	84
4.2 Experiments and Calculations details	85
4.3 Results and Discussion	88
4.4 Conclusions	98

4.5 Author Contribution	100
5. Crystal structure and atomic vibration of Zn(IO₃)₂ under pressure	123
5.1 Introduction	123
5.2 Experiment and calculation details	125
5.3 Results and Discussion	127
5.4 Conclusions	134
5.5 Author contribution	135
6. Crystal structure and atomic vibrations of Mg(IO₃)₂, electronic band structure of Mg(IO₃)₂ and Zn(IO₃)₂ under pressure	159
6.1 Introduction	160
6.2 Experiment and calculation details	162
6.3 Results and Discussion	165
6.4 Conclusions	176
6.5 Author contribution	177
7. Conclusions	203
7.1 Crystal structure at ambient pressure	203
7.2 Crystal structure and compressibility at high pressure	205
7.3 Oxygen coordination increase of iodine	208
7.4 Raman spectra at ambient pressure	208
7.5 Raman spectra at high pressure	210
7.6 Infrared spectra	210
7.7 Electronic band structure	211
Bibliography	213

Acknowledgements

The three years were short, as if I had just arrived in Valencia yesterday. But the experience of studying and researching here is indelible and eternal for me. First of all, I would like to thank my supervisor and tutor Prof. Daniel Errandonea, for choosing me as his PhD student from many candidates three years ago, for his guidance in research and study, for his respect for my opinions, for the support he gave me in realizing my research ideas, and for his concern for my life. In China, we say “It is important to have a good teacher and a good friend to learn from”. I am happy I found both of them here.

I would like to thank Dr. Robin Turnbull. We have collaborated on nine papers so far and we have helped each other with the experiments and discussed the data analysis with each other. I would like to thank Dr. Abraham de Jesús Loredó Trejo, Dr. Pablo Botella Vives, Dr. Alberto Rodríguez, and María Santos for the many happy moments we have had together in and out of the office. I would like to thank Dr. Tomas Marqueño, Dr. Enrico Bandiello and Daniel Diaz Anichtchenko for their help in studying and personal living.

I would like to thank Prof. Francisco Javier Manjón Herrera for allowing me to conduct my Raman experiments in his laboratory and his valuable discussions and suggestions on our research. I would like to thank Samuel Gallego Parra for his help in the Raman experiments. I would like to thank Dr. Catalin Popescu for his many useful help in the high-pressure X-ray diffraction experiments in ALBA synchrotron, and Dr. Ibraheem Yousef for his useful help in the high-pressure Infrared spectroscopy experiments.

I would like to thank Prof. Alfonso Muñoz González and Prof. Placida Rodríguez Hernández for providing all the theoretical calculations for this study.

I would like to thank Prof. Alfredo Segura García del Río for his help to explain some fundamental physics and discussion in some parts of this research. I would like to thank Prof. Fernando Rodríguez for his discussion on the multi-band absorption of $\text{Co}(\text{IO}_3)_2$.

I would like to thank Prof. Julio Pellicer Porres, Prof. David Santamaria Perez, and Prof. Domingo Martínez García for their discussion in the group meeting.

I would like to thank all the colleagues and friends at the department of applied physics and ICMUV at University of Valencia, for their help and the moment we shared

together.

At the end, I would like to thank my parents, for their unconditional support and understanding, I am very sorry that I could not be with them and take care of them during my three-years studies in Spain. I would also like to thank my girlfriend Dr. Lan-Ting Shi, my soul mate and scientific collaborator. It's my family that gives me the motivation to keep going.

List of publications

Thesis work:

1. **A. Liang**, S. Rahman, H. Saqib, P. Rodriguez-Hernandez, A. Munoz, G. Nenert, I. Yousef, C. Popescu, and D. Errandonea, First-Order Isostructural Phase Transition Induced by High Pressure in $\text{Fe}(\text{IO}_3)_3$, *J. Phys. Chem. C* **124**, 8669 (2020).

2. **A. Liang**, S. Rahman, P. Rodriguez-Hernandez, A. Muñoz, F. J. Manjón, G. Nenert, and D. Errandonea, High-Pressure Raman Study of $\text{Fe}(\text{IO}_3)_3$: Soft-Mode Behavior Driven by Coordination Changes of Iodine Atoms, *J. Phys. Chem. C* **124**, 21329 (2020).

3. **A. Liang**, P. Rodríguez-Hernandez, A. Munoz, S. Raman, A. Segura, and D. Errandonea, Pressure-Dependent Modifications in the Optical and Electronic Properties of $\text{Fe}(\text{IO}_3)_3$: The Role of Fe 3d and I 5p Lone-Pair Electrons, *Inorg. Chem. Front.* **8**, 4780 (2021).

4. **A. Liang**, C. Popescu, F. J. Manjon, R. Turnbull, E. Bandiello, P. Rodriguez-Hernandez, A. Muñoz, I. Yousef, Z. Hebboul, and D. Errandonea, Pressure-Driven Symmetry-Preserving Phase Transitions in $\text{Co}(\text{IO}_3)_2$, *J. Phys. Chem. C* **125**, 17448 (2021).

5. **A. Liang**, F. Rodríguez, Rodríguez-Hernandez, P, A. Muñoz, R. Turnbull, and D. Errandonea, High-Pressure Tuning of $d-d$ Crystal-Field Electronic Transitions and Electronic Band Gap in $\text{Co}(\text{IO}_3)_2$, *Phys. Rev. B* **105**, 115204 (2022)

6. **A. Liang**, C. Popescu, F. J. Manjon, A. Muñoz, Z. Hebboul, and D. Errandonea, Structural and Vibrational Study of $\text{Zn}(\text{IO}_3)_2$ Combining High-Pressure Experiments and Density-Functional Theory, *Phys. Rev. B* **103**, 054102 (2021).

7. **A. Liang**, R. Turnbull, E. Bandiello, I. Yousef, C. Popescu, Z. Hebboul, and D. Errandonea, High-Pressure Spectroscopy Study of $\text{Zn}(\text{IO}_3)_2$ Using Far-Infrared Synchrotron Radiation, *Crystals* **11**, 34 (2021).

8. **A. Liang**, R. Turnbull, C. Popescu, F. J. Manjón, E. Bandiello, A. Muñoz, I. Yousef, Z. Hebboul, and D. Errandonea, Pressure-Induced Phase Transition and Increase of Oxygen-Iodine Coordination in Magnesium Iodate, *Phys. Rev. B* **105**, 054105 (2022).

9. **A. Liang**, R. Turnbull, P. Rodríguez-hernandez, A. Muñoz, M. Jasmin, L. Shi,

and D. Errandonea, General Relationship between the Band-Gap Energy and Iodine-Oxygen Bond Distance in Metal Iodates, *Phys. Rev. Mater.* 6, 044603 (2022)

Other works:

1. **A. Liang**, L. T. Shi, S. Gallego-Parra, O. Gomis, D. Errandonea, and I. M. Tiginyanu, Pressure-Induced Band Anticrossing in Two Adamantine Ordered-Vacancy Compounds: CdGa₂S₄ and HgGa₂S₄, *J. Alloys Compd.* 886, 161226 (2021).

2. L. T. Shi, Y. K. Wei, **A. K. Liang**, R. Turnbull, C. Cheng, X. R. Chen, and G. F. Ji, Prediction of Pressure-Induced Superconductivity in the Novel Ternary System ScCaH_{2n} (N= 1-6), *J. Mater. Chem. C* 9, 7284 (2021).

3. Y. Zhou, **A. Liang**, Z.-Y. Zeng, X.-R. Chen, and H. Geng, Anisotropic Lattice Thermal Conductivity in Topological Semimetal ZrGeX (X=S, Se, Te): A First-Principles Study, *J. Phys. Condens. Matter.* 33, 135401 (2021).

4. V. Bilovol, M. Fontana, J. A. Rocca, H. H. M. Chanduví, A. M. M. Navarro, A. V. G. Rebaza, L. A. Errico, **A. Liang**, D. Errandonea, and A. M. Ureña, Structural, Vibrational and Electronic Properties in the Glass-Crystal Transition of Thin Films Sb₇₀Te₃₀ Doped with Sn, *J. Alloys Compd.* 845, 156307 (2020).

5. T. Ouahrani, F. Medjdoub, S. Gueddida, A. L. Fernandez, R. Franco, N. Benkhattou, M. Badawi, **A. Liang**, J. Gonzalez, and D. Errandonea, Understanding the Pressure Effect on the Elastic, Electronic, Vibrational, and Bonding Properties of the CeScO₃ Perovskite, *J. Phys. Chem. C* 107 (2020).

6. Z. Hebboul, A. Ghozlane, R. Turnbull, A. Benghia, S. Allaoui, **A. Liang**, D. Errandonea, A. Touhami, A. Rahmani, and I. K. Lefkaier, Simple New Method for the Preparation of La(IO₃)₃ Nanoparticles, *Nanomaterials* 10, 2400 (2020).

7. Y. Zhou, L.-T. Shi, **A. Liang**, Z.-Y. Zeng, X.-R. Chen, and H.-Y. Geng, Novel Structural Phases and the Properties of LaX (X = P, As) under High Pressure: First-Principles Study, *RSC Adv.* 11, 3058 (2021).

8. R. Chikhaoui, Z. Hebboul, M. A. Fadla, K. Bredillet, **A. Liang**, D. Errandonea, S. Beauquis, A. Benghia, J. C. Marty, R. Le Dantec, Y. Mugnier, and E. Bandiello, Synthesis and Characterization of Novel Nanoparticles of Lithium Aluminum Iodate LiAl(IO₃)₄, and DFT Calculations of the Crystal Structure and Physical Properties, *Nanomaterials* 11, 3289 (2021).

9. A. B. Garg, **A. Liang**, D. Errandonea, P. Rodríguez-Hernández, and A. Muñoz,

Monoclinic–Triclinic Phase Transition Induced by Pressure in Fergusonite-Type YbNbO_4 , *J. Phys. Condens. Matter* 34, 174007 (2022).

10. R. Turnbull, J. González-Platas, F. Rodríguez, **A. Liang**, C. Popescu, Z. He, D. Santamaría-Pérez, P. Rodríguez-Hernández, A. Muñoz, and D. Errandonea, Pressure-Induced Phase Transition and Band Gap Decrease in Semiconducting $\beta\text{-Cu}_2\text{V}_2\text{O}_7$, *Inorg. Chem.* 61, 3697 (2022).

11. L.-T. Shi, R. Turnbull, **A. Liang**, X.-R. Chen, and G.-F. Ji, Metallization and Superconductivity of NBH_{12} Compounds Stabilized by Dihydrogen Bonds, *J. Mater. Chem. C* 10, 3081 (2022).

Resumen en castellano

1. Introducción

Recientemente se han sintetizado un gran número de nuevos yodatos metálicos [1–7]. También se han realizado múltiples estudios sobre sus propiedades. En particular, la estructura cristalina, la generación del segundo armónico, la energía de la banda prohibida electrónica (band gap) y la estructura de las bandas electrónicas se han estudiado en condiciones ambientales. La síntesis y caracterización de numerosos yodatos metálicos nuevos ha sido impulsada por la búsqueda de materiales ópticos no lineales (NLO) con aplicaciones tanto en comunicaciones, en sensores ópticos, como dispositivos de almacenamiento óptico. Debido a la existencia de un par de electrones solitarios (LEP) en el yodo, los yodatos metálicos suelen formar una diversa gama de estructuras cristalinas no centrosimétricas sujetas a una distorsión Jahn-Teller de segundo orden. Por lo tanto, los yodatos metálicos suelen tener una alta eficiencia de generación de segundos armónicos (SHG). Por ejemplo, el $\text{BaNbO}(\text{IO}_3)_5$ [1], en el que los poliedros NbO_6 , IO_3 y BaO forman un entorno distorsionado y la polarización de los mismos está en la misma dirección, presenta una excelente respuesta SHG, unas 14 veces mayor que la de los materiales NLO comerciales más utilizados, el KH_2PO_4 (KDP). Por otro lado, la respuesta SHG del $\text{Bi}(\text{IO}_3)_2$ [8] es aproximadamente 11.5 veces mayor que la del KDP bajo radiación láser de 1064 nm; la respuesta SHG del $\text{LiZn}(\text{IO}_3)_3$ y del $\text{LiCd}(\text{IO}_3)_3$ [6] es aproximadamente 14 y 12 veces mayor que la del KDP bajo radiación láser de 1064 nm; además, el efecto SHG del $\text{LiMg}(\text{IO}_3)_3$ [9] es aproximadamente 24 veces mayor que el del KDP bajo radiación láser de 1024 nm.

Un buen candidato para el desarrollo de materiales NLO debe tener las siguientes propiedades [10–12]: (i). Es necesaria una gran respuesta SHG para la alta eficiencia de conversión del láser. (ii). Una amplia región de transparencia, lo que significa un gran bandgap para convertir la frecuencia del láser en una región amplia y aplicable. Esto es razonable porque, si la energía del bandgap de los materiales NLO es estrecha, y menor que la energía del láser de entrada o de salida, entonces los materiales NLO absorberán el láser de entrada y activarán los electrones de la banda de valencia a la banda de conducción. (iii). Un alto umbral de daño del láser (LDT). Este requisito también está relacionado con el bandgap de los materiales NLO, si los materiales NLO

tienen un bandgap amplio, la transferencia de energía del láser a los materiales NLO es despreciable. (iv). Buena estabilidad química para la aplicación práctica y (v). Una birrefringencia moderada.

La estructura cristalina de los yodatos metálicos juega un papel importante en la respuesta SHG, así como también lo hacen la estructura de bandas electrónica y la energía de bandgap de la misma. Por ello, en esta tesis doctoral se estudia en profundidad y se presentan y analizan resultados de la estructura cristalina a alta presión, las vibraciones atómicas y la estructura de bandas electrónica de cuatro yodatos metálicos. Estos son el yodato de hierro, $\text{Fe}(\text{IO}_3)_3$, el yodato de cobalto, $\text{Co}(\text{IO}_3)_2$, el yodato de zinc, $\text{Zn}(\text{IO}_3)_2$, y yodato de magnesio $\text{Mg}(\text{IO}_3)_2$. Estos materiales han sido estudiados por medio de difracción de rayos X a alta presión (HPXRD), dispersión Raman a alta presión (HPRS), espectroscopia infrarroja por transformada de Fourier a alta presión (HPFTIR), absorción óptica a alta presión (HPOA) y cálculos de primeros principios empleando la teoría del funcional de la densidad. En el trabajo se presentan resultados sobre los efectos de la presión sobre el LEP estereoquímicamente activo en el yodo y la estructura cristalina, observándose fenómenos como el aumento de la coordinación del yodo con el oxígeno inducida por la presión, las transiciones de fase isoestructurales inducidas por la presión y la expansión de la distancia de enlace yodo-oxígeno inducida por la presión. Diversas características comunes de los espectros Raman de los compuestos estudiados también se observan a presión ambiente y a alta presión. Algunos modos Raman-activos muestran un comportamiento de ablandamiento (softening) bajo presión que está íntimamente relacionado con el cambio de la estructura cristalina bajo presión. Los cambios en la estructura de bandas electrónica, combinados con los cambios de la estructura cristalina bajo compresión, nos llevan a establecer dos reglas fenomenológicas útiles para el diseño de yodatos metálicos de energía de banda prohibida ancha.

2. Objetivos

1). Investigar en detalle la estructura cristalina, las vibraciones atómicas, y el par de electrones solitarios estereoquímicamente activo de los compuestos $\text{Fe}(\text{IO}_3)_3$, $\text{Zn}(\text{IO}_3)_2$, $\text{Co}(\text{IO}_3)_2$, y $\text{Mg}(\text{IO}_3)_2$ bajo condiciones estáticas de alta presión, a temperatura ambiente, utilizando celdas de yunques de diamante.

- 2). Investigar los cambios inducidos por la presión en la energía del bandgap de los compuestos $\text{Fe}(\text{IO}_3)_3$, $\text{Zn}(\text{IO}_3)_2$, $\text{Co}(\text{IO}_3)_2$ y $\text{Mg}(\text{IO}_3)_2$.
- 3). Adicionalmente, combinado los resultados y conclusiones de los dos puntos anteriores, tratar de encontrar la relación entre la energía del bandgap y la estructura cristalina.
- 4). Encontrar una regla práctica para diseñar yodatos metálicos de banda prohibida ancha.

3. Resultados y conclusiones

3.1 Estructura cristalina a presión ambiente

Las estructuras cristalinas a presión ambiental de los cuatro yodatos metálicos se muestran esquemáticamente en la **Figura 1**. La información de la estructura cristalina y los detalles de refinamiento de la estructura de los mismos se resumen en la **Tabla 1**. Excepto el $\text{Fe}(\text{IO}_3)_3$, que cristaliza en una estructura hexagonal descrita por el grupo espacial $P6_3$ (Nº 173), el resto de los yodatos metálicos aquí estudiados cristalizan en una estructura monoclinica, descrita por el grupo espacial $P2_1$ (Nº 4). La estructura cristalina de los mismos está formada por unidades poliédricas IO_3 y AO_6 ($A=\text{metal}$) y comparten algunas características comunes. El poliedro IO_3 tiene una geometría molecular piramidal trigonal, con tres átomos de oxígeno en la base y un átomo de yodo en el vértice. Los átomos metálicos tienen una coordinación octaédrica. Cuando la estructura cristalina se observa a lo largo del eje c de los yodatos de Fe y Zn (equivalente al eje b de los yodatos de Co y Mg), cada átomo de yodo está enlazado con tres átomos de oxígeno y la distancia de enlace oscila entre 1,8 Å y 2,0 Å. Cada catión metálico está rodeado por seis pirámides IO_3 que comparten un átomo de oxígeno con los octaedros por los vértices. Si las estructuras de la **Figura 1** se observan perpendicularmente al eje c de los yodatos de Fe y Zn (que es el eje b de los yodatos de Co y Mg), se puede ver que la estructura cristalina de los cuatro yodatos metálicos muestra una estructura tipo laminar, formada por capas de IO_3 que están conectadas por los octaedros de AO_6 . Según los parámetros de red de los yodatos de Co, Zn y Mg resumidos en la **Tabla 1**, el parámetro de red a y c de los mismos tienen un valor muy similar entre ellos y el ángulo monoclinico es cercano a los 120 grados, por lo que la estructura cristalina de

estos tres yodatos metálicos se puede describir como pseudohexagonal. El volumen de la celda unidad por unidad de fórmula de los yodatos de Co, Zn y Mg es similar (**Tabla 1**), es alrededor de 1/3 de la del $\text{Fe}(\text{IO}_3)_3$. El parámetro de red *a* en el $\text{Zn}(\text{IO}_3)_2$ es casi la mitad del mismo parámetro de la estructura de los yodatos de Co y Mg.

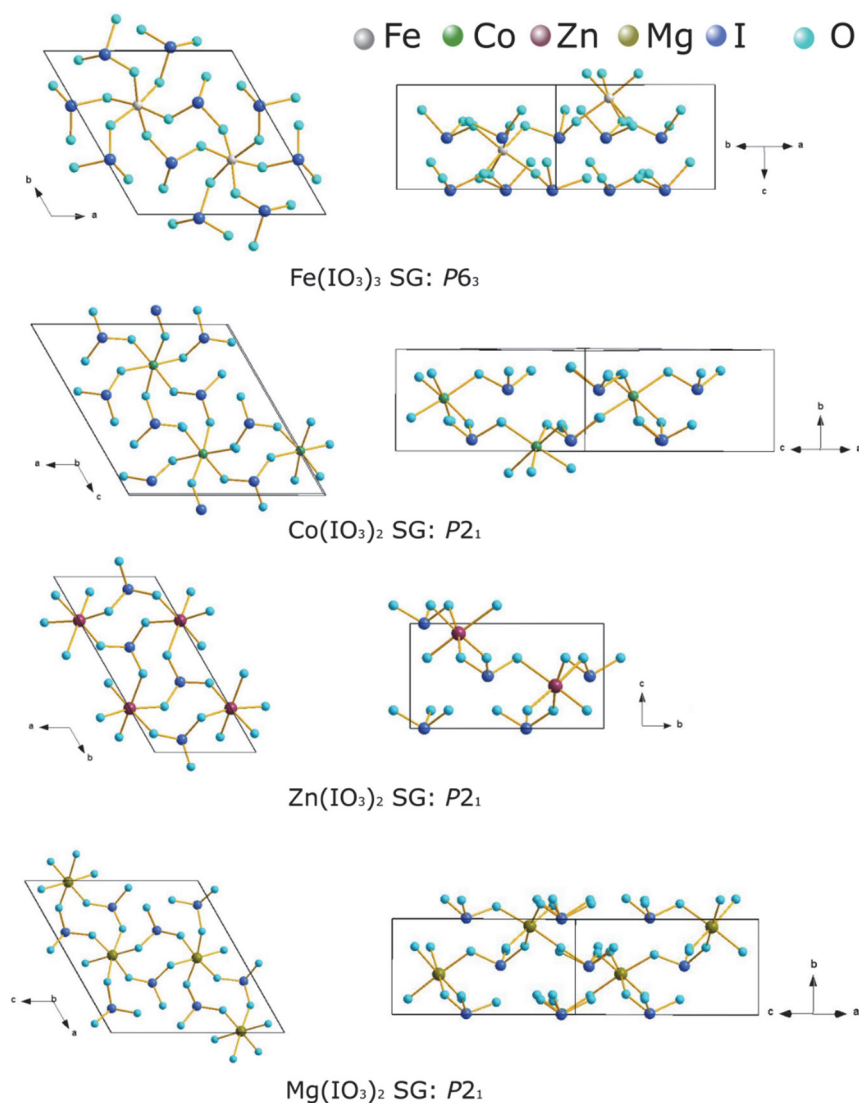


Figura 1. Estructura cristalina de $\text{Fe}(\text{IO}_3)_3$, $\text{Co}(\text{IO}_3)_2$, $\text{Zn}(\text{IO}_3)_2$ y $\text{Mg}(\text{IO}_3)_2$ a presión ambiente. Para cada estructura se enseñan dos proyecciones distintas. Los átomos de hierro, cobalto, zinc, magnesio, yodo y oxígeno se muestran en color gris, verde, marrón, amarillo pálido, azul y azul cian, respectivamente. "SG" significa grupo espacial.

Formula	Fe(IO ₃) ₃	Co(IO ₃) ₂	Zn(IO ₃) ₂	Mg(IO ₃) ₂
Crystal system	hexagonal	monoclinic	monoclinic	monoclinic
Space group	<i>P</i> 6 ₃	<i>P</i> 2 ₁	<i>P</i> 2 ₁	<i>P</i> 2 ₁
a (Å)	9.2476(4)	10.943(6)	5.465(4)	11.2563
b (Å)	9.2476(4)	5.078(1)	10.952(8)	5.0497
c (Å)	5.2326(2)	10.925(4)	5.129(4)	11.2128
β (°)	120	119.814(3)	120.37(8)	119.8256
Z	2	4	2	4
V(Å ³)/Z	193.00	131.67	132.4	138.23
Refinement method	Rietveld	Rietveld	Rietveld	Rietveld
<i>R</i> _p	3.83%	9.60%	7.22%	9.23%
<i>R</i> _{wp}	13.42%	13.30%	9.91%	8.85%

Tabla 1. Datos de la estructura cristalina de los distintos compuestos y detalle del refinamiento de la estructura de los cuatro yodatos metálicos estudiados en esta tesis. Los parámetros de red se obtienen a partir del refinamiento de Rietveld de los patrones XRD recogidos a presión ambiente. *R*_p y *R*_{wp} reflejan la calidad del refinamiento de Rietveld.

3.2 Estructura cristalina y compresibilidad a alta presión

En el rango de presiones cubierto por nuestro estudio, el Fe(IO₃)₃ experimenta tres transiciones de fase isoestructurales (IPT). Las mismas ocurren a 1.5-2.0 GPa, 5.7-6.0 GPa y 22.2 GPa, respectivamente (ver **Figura 2**). Las dos primeras IPTs se evidenciaron por la dependencia no lineal de la presión de los modos vibracionales activos Raman, por la discontinuidad de las constantes elásticas calculadas y por la inestabilidad dinámica evidenciada en la dispersión de fonones calculada bajo alta presión. La tercera IPT se puso de manifiesto por la aparición de nuevos picos en el patrón de XRD a 22.2 GPa. La estructura cristalina de la tercera fase de alta presión (HP) se resolvió por el método de Rietveld. Los patrones XRD de esta fase pueden ser refinados empleando el mismo grupo espacial que describe la fase de LP, pero con diferentes parámetros de red. La tercera IPT estuvo acompañada de un colapso del 5% en el volumen de la celda unitaria, lo que indica que es una transición de fase de primer orden.

El $\text{Co}(\text{IO}_3)_2$ experimenta dos IPTs. La primera a 3 GPa y la segunda en el rango de presión de 9-11 GPa (ver **Figura 2**). Las transiciones de fase se evidenciaron por el comportamiento no lineal de los parámetros de red, la evolución en presión de la distancia de enlace Co-O calculada, los cambios de la intensidad relativa de dos modos Raman y variación con la presión de los modos Raman e infrarrojos activos. No se encontró ninguna discontinuidad en el volumen de la celda unitaria alrededor de la presión de transición de fase.

El $\text{Zn}(\text{IO}_3)_2$ experimenta dos IPTs. Las transiciones de fase tienen lugar en el rango de presión de 2.5-3.4 GPa y 8-9 GPa, respectivamente (ver **Figura 2**). Las transiciones de fase se pusieron de manifiesto por el comportamiento no lineal de la dependencia de la presión de los parámetros de red, el comportamiento de la distancia de enlace Zn-O calculada y la dependencia de la presión de los modos Raman e infrarrojos activos. Al igual que en el $\text{Co}(\text{IO}_3)_2$, no se encontró ninguna discontinuidad en el volumen de la celda unitaria alrededor de la presión de transición de fase.

El $\text{Mg}(\text{IO}_3)_2$ tiene un comportamiento diferente. Este compuesto experimenta una transición de fase de la estructura monoclinica de LP (grupo espacial: $P2_1$) a una estructura trigonal (grupo espacial: $P3$). La transición de fase ocurre en el rango de presión de 7.7-9.6 GPa (ver **Figura 2**). La transición de fase se evidenció mediante el refinamiento Rietveld de los patrones XRD y la aparición de nuevos picos en los espectros Raman e infrarrojo a alta presión. No se encontró ninguna discontinuidad en el volumen de la celda unitaria alrededor de la presión de transición de fase. En este material no se observó las IPTs encontradas en los otros tres yodatos metálicos.

El módulo de compresibilidad (módulo de bulk) de los cuatro yodatos metálicos estudiados en las diferentes fases se resume en la **Tabla 2**. Para las fases de baja presiones (fase de presión ambiental, fase I1 y fase I2), el módulo de compresibilidad del $\text{Fe}(\text{IO}_3)_3$ es el más grande. Por otro lado, el $\text{Zn}(\text{IO}_3)_2$ tiene el módulo de compresibilidad más pequeño. Nótese que esta magnitud física aumenta drásticamente en la fase de alta presión (fase I2 del $\text{Co}(\text{IO}_3)_2$ o HP de otros compuestos). La razón de este fenómeno es el aumento gradual de la coordinación del yodo con átomos de oxígeno. Los nuevos enlaces formados entre el yodo y los oxígenos pertenecientes a la capa vecina IO_3 fortalecen la resistencia del material a la presión externa. Los cuatro yodatos metálicos muestran un notable comportamiento anisotrópico, el eje c en el $\text{Fe}(\text{IO}_3)_3$ y el $\text{Zn}(\text{IO}_3)_2$ y el eje b en el $\text{Co}(\text{IO}_3)_2$ y el $\text{Mg}(\text{IO}_3)_2$ son los ejes más

compresibles. Esto se debe a la estructura de capas ordenadas perpendicularmente a esas direcciones.

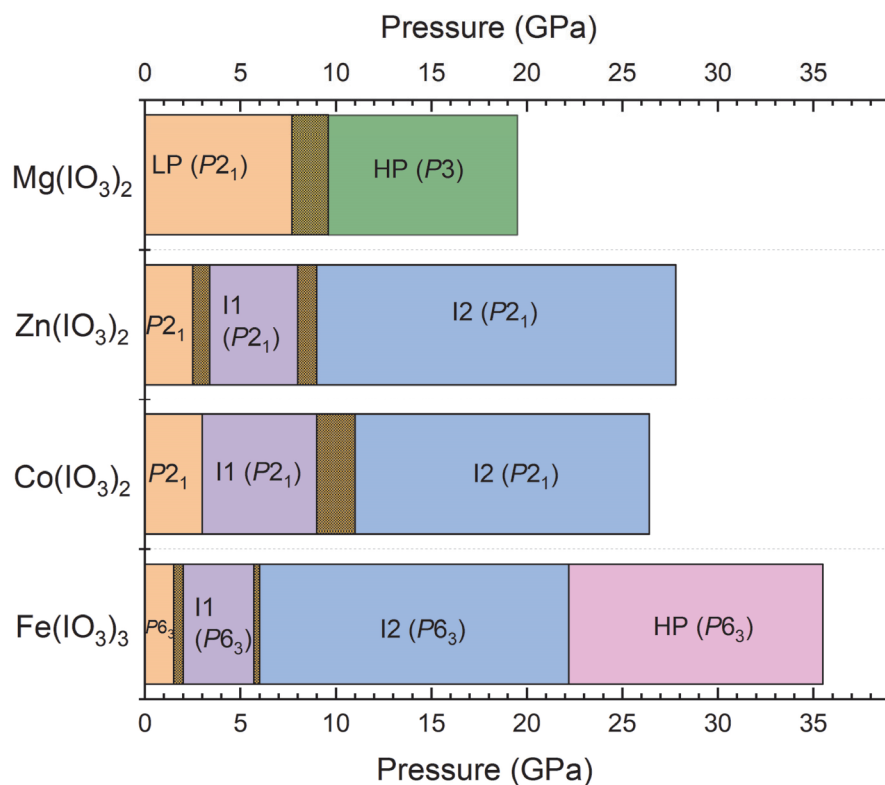


Figura 2. Resumen de la estructura cristalina y el grupo espacial adoptado a los cuatro yodatos metálicos estudiados en esta tesis en función de la presión. El área rellena con el patrón de rejilla indica el intervalo de presión en el que se produce la transición de fase.

Compuestos	Fase	BM-EOS	V_0 (Å ³)	B_0 (GPa)	B_0'
Fe(IO ₃) ₃	Ambient+I1+I2	3 rd -order	385	55(2)	4.3(0.3)
	HP	2 nd -order	353(9)	73(9)	4.0
Co(IO ₃) ₂	Ambient+I1	3 rd -order	529	29.8(1)	3.5(0.3)
	I2	3 rd -order	462.9(5.6)	70.8(3.6)	5.2(0.6)
Zn(IO ₃) ₂	Ambient+I1+I2	3 rd -order	264.8(4)	21.6(0.7)	7.0(0.3)
Mg(IO ₃) ₂	LP	3 rd -order	552.8	22.2(0.8)	4.2(0.4)
	HP	3 rd -order	369.6(0.3)	63.6(0.4)	3.3(0.1)

Tabla 2. Volumen determinado experimentalmente, módulo de masa y la derivada de presión correspondiente para los cuatro yodatos metálicos en diferentes fases. El módulo de masa se obtuvo a partir del ajuste del volumen de la celda unitaria adoptando la ecuación de estado de Birch-Murnaghan (BM-EOS)

3.3 Aumento de la coordinación del oxígeno del yodo

Para todos los yodatos metálicos estudiados en esta tesis, hay dos tipos de enlaces I-O. Ambos enlaces son diferentes entre sí en cuanto a la distancia de enlace. El primer tipo de enlaces I-O, es entre el yodo y los átomos de oxígeno de la capa interna, como por ejemplo O7, O8 y O9 en la **Figura 3**. En esta figura utilizamos la distancia de enlace I-O calculada de Mg(IO₃)₂ como ejemplo. Las distancias de enlace oscilan entre 1.8 y 2.0 Å, a presión ambiente. Interesantemente, la distancia de enlace aumenta ligeramente bajo presión. El otro tipo de enlaces I-O, corresponde a un rango de distancias de enlace de 2.5 a 3.2 Å. Estos enlaces están ilustrados por la distancia con los átomos O10, O5 y O8' en la **Figura 3**. Los mismos corresponden a enlaces entre el yodo y los átomos de oxígeno en la capa vecina de IO₃. Este tipo de enlace sólo se forma bajo alta presión, como consecuencia de dos efectos; (i). El acortamiento de la distancia de enlace inducido por la presión (debido a la reducción de la distancia entre capas) y (ii). La existencia de un LEP en el yodo. El segundo tipo de enlaces I-O se acortan bajo presión. El acercamiento de los átomos de oxígeno de la capa intermedia al yodo favorece el alejamiento del yodo de los átomos de oxígeno de la capa interna y provoca el alargamiento bajo presión del primer tipo de distancia de enlace I-O.

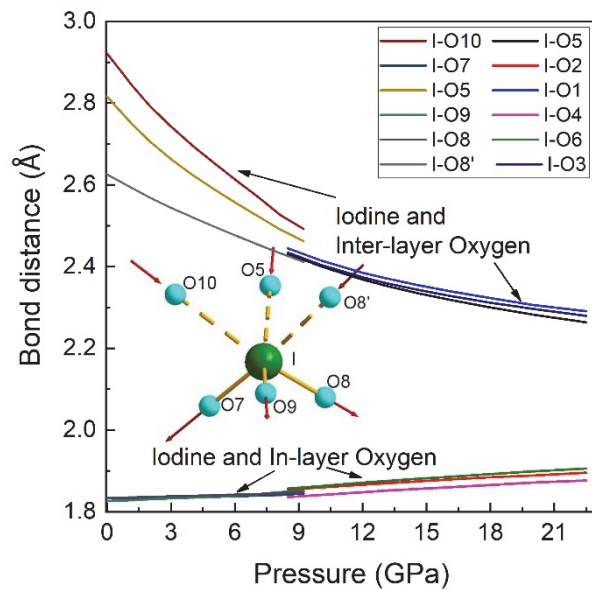


Figura 3. Distancia de enlace calculada entre el yodo y el oxígeno en función de la presión en el $\text{Mg}(\text{IO}_3)_2$. La discontinuidad en torno a 9 GPa es una razón de la sutil transición de fase inducida por la presión.

3.4 Espectros Raman a presión ambiente

La **Figura 4** muestra los espectros Raman de los cuatro yodatos metálicos medidos en condiciones ambientales. Los espectros Raman pueden dividirse en tres regiones bien diferenciadas: (i). La región de alta frecuencia, la cual está situada en el intervalo de números de onda de $600\text{-}900\text{ cm}^{-1}$. Los fonones de esta región están relacionados con vibraciones de estiramiento de los enlaces I-O (modos stretching), los modos más fuertes se encuentran en esta región y se han marcado en la **Figura 4** indicándose su número de onda. (ii). La región de frecuencia media, la cual se encuentra en el intervalo de números de onda de $300\text{-}500\text{ cm}^{-1}$. Esta región está principalmente dominada por modos de flexión de los enlaces I-O. (iii). La región de baja frecuencia, que involucra modos con números de onda inferiores a 300 cm^{-1} . Estos modos están generalmente asociados a los movimientos de traslación y rotación de los iones yodato como unidades rígidas, por lo cual se conocen como modos externos.

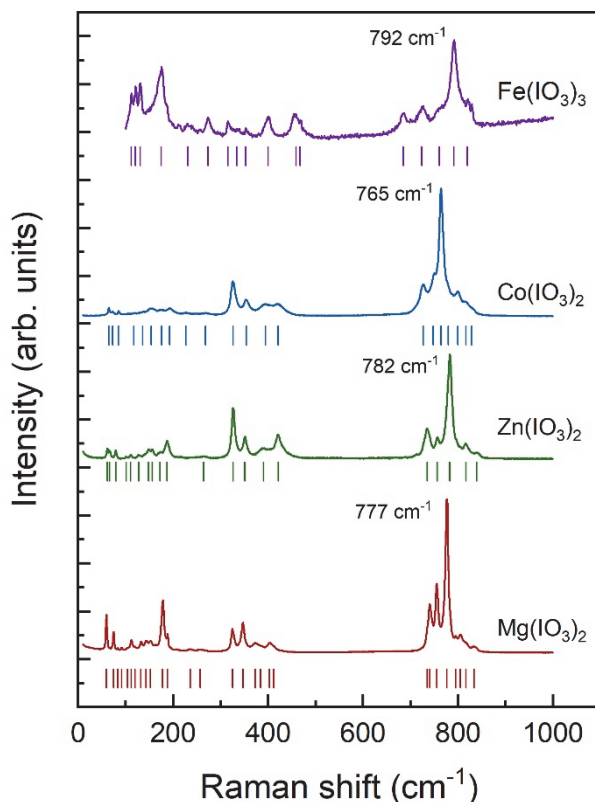


Figura 4. Espectros Raman de los cuatro yodatos metálicos en condiciones ambientales. El número de onda de los modos más fuertes en cada espectro Raman se ha marcado al lado. Las cortas barras verticales debajo de cada espectro Raman son una indicación de la posición del pico determinado.

3.5 Espectros Raman a alta presión

La mayoría de los modos Raman en la región de alta frecuencia muestran un ablandamiento bajo compresión (disminución de la frecuencia con la presión). Este es un comportamiento no habitual y es el resultado de la ampliación de las distancias de enlace I-O inducida por la presión. Todos los modos en la región de media y baja frecuencia se endurecen bajo compresión (aumento de la frecuencia con la presión), la combinación de ambos fenómenos causa una reducción de la brecha existente entre los fonones de las regiones de media y alta frecuencia. Además, algunos modos Raman en los yodatos de Fe, Co y Zn muestran un comportamiento altamente no lineal bajo presión. En particular, la pendiente de la curva frecuencia-presión de estos modos cambia en la presión donde se producen las IPTs. Por otro lado, en el espectro Raman del $\text{Mg}(\text{IO}_3)_2$ aparecen algunos picos nuevos en torno a 7.7 GPa. Este hecho apoya la

transición de fase monoclinica a trigonal detectada en XRD.

3.6 Espectros infrarrojos

Los espectros infrarrojos se midieron para números de onda inferiores a 700 cm^{-1} . Para el caso del $\text{Fe}(\text{IO}_3)_3$, se detectaron 12 modos infrarrojos-activos a presión ambiente, 8 de ellos fueron seguidos bajo alta presión hasta la presión donde ocurre la tercer IPT. Además, se observó que hay un cambio repentino de la frecuencia de los modos a 15.3 GPa. Estos cambios en los espectros infrarrojos se han asignado a la tercera IPT. Sólo se han podido seguir con precisión cinco modos infrarrojos activos bajo presión en la fase HP.

Se han detectado un total de 9 modos infrarrojos activos en el $\text{Co}(\text{IO}_3)_2$ a la presión más baja (0.2 GPa) y todos ellos se han seguido bajo alta presión. La mayoría de los modos muestra un comportamiento no lineal bajo presión. El signo de su pendiente (curva frecuencia versus presión) cambia a la presión donde se producen las IPTs. No se observaron nuevos picos bajo presión.

En el $\text{Zn}(\text{IO}_3)_2$ se detectaron un total de 25 modos infrarrojos activos a la presión más baja (0.9 GPa), y 18 de ellos se han seguido bajo presión. La mayoría de los modos infrarrojos activos muestran un comportamiento no lineal bajo presión. Como en los otros compuestos, el signo de la pendiente cambia a la presión en la que se produce la IPT. En este compuesto además se produce un cambio inesperado en el coeficiente de presión a 13 GPa. Esto podría ser un indicio de la ocurrencia de una tercera transición de fase, pero dicha transición no se observó en los otros métodos de diagnóstico empleados.

Se han detectado un total de 14 modos infrarrojos activos en la fase LP y 9 en la fase HP del $\text{Mg}(\text{IO}_3)_2$, observándose dos nuevos picos a 9.6 GPa. Los cambios en el espectro infrarrojo están relacionados con la transición de fase monoclinica a trigonal inducida por la presión y detectada en los estudios Raman y XRD.

3.7 Estructura de banda electrónica

Según la estructura de bandas electrónica calculada por el método de la teoría del funcional de la densidad, los cuatro yodatos metálicos estudiados presentan un gap indirecto. Para el $\text{Fe}(\text{IO}_3)_3$, el mínimo de la estructura de valencia (VBM) en la

estructura electrónica está dominado por el estado $O-2p$, mientras que el máximo de la banda de conducción (CBM) está dominado por estados $Fe-3d$ y el $I-5p$. El bandgap del $Fe(IO_3)_3$ muestra un comportamiento no lineal con la presión antes de la tercera transición de fase. El comportamiento no lineal puede explicarse por dos efectos que compiten bajo presión. Uno es el acortamiento inducido por la presión de la distancia de enlace Fe-O que hace que aumente el solapamiento entre los orbitales del Fe y los orbitales del O. Este hecho favorece el estrechamiento del bandgap. Por otro lado, el ligero aumento de la distancia de enlace I-O reduce la hibridación entre los átomos de yodo y oxígeno. Este hecho favorece la apertura de la energía del bandgap. La competencia entre ambos fenómenos causa el comportamiento no lineal observado. También hemos observado que existe un salto (discontinuidad) del bandgap a 23.5 GPa, que está acompañado de una transición indirecta a indirecta en la estructura de banda electrónica. El cambio abrupto del bandgap está relacionado con el colapso de volumen de la celda unidad encontrado en HPXRD. La resistividad también exhibe un comportamiento no lineal antes de la tercera IPT y muestra una rápida disminución después de la tercera transición, alrededor de 20 GPa. Los cambios son un resultado del aumento exponencial de la concentración de portadores libres intrínsecos.

En el caso del $Co(IO_3)_2$, el bandgap muestra una rápida disminución desde la presión ambiente hasta alrededor de 8 GPa, y luego muestra una pequeña dependencia de la presión. El VBM en la estructura de banda electrónica está dominado por los estados $O-2p$ y $Co-3d$, y el CBM está dominado por los estados $I-5p$, con una pequeña contribución de los estados $O-2p$. El comportamiento del bandgap puede explicarse por la competencia de dos efectos bajo presión. El aumento de la hibridación entre los estados del Co y el O causada por el acortamiento de la distancia de enlace Co-O. Este hecho favorece el estrechamiento de la energía del bandgap. Por otro lado, la ampliación de la distancia de enlace I-O bajo presión, que disminuye la hibridación entre los átomos de yodo y oxígeno, este hecho favorece la apertura de la energía del bandgap. En los espectros de absorción óptica, también encontramos la banda de absorción múltiple causada por la transición interna entre los niveles $d-d$ en el Co^{2+} . Estas tres bandas de absorción observadas se han asignado a la transición del estado básico ${}^4T_{1g}(F)$ al estado de espín permitido ${}^4T_{1g}(P)$, al estado de espín prohibido ${}^2A_{1g}(G)$ y al estado ${}^2T_{1g}(H)$. Hay un estrechamiento inducido por la presión de la banda de absorción, resultado de la supresión inducida por la presión de la distorsión Jahn-Teller.

La transición de alto espín a bajo espín se ha predicho que debe ocurrir a 110 GPa.

Para el $\text{Zn}(\text{IO}_3)_2$ y el $\text{Mg}(\text{IO}_3)_2$, el VBM está dominado por los estados O-2*p*, y el CBM está dominado por los estados O-2*p* e I-5*p*. El bandgap muestra un comportamiento no lineal bajo presión. Según el diagrama molecular establecido para estos compuestos mediante el uso de las DOS, PDOS y COOP calculadas entre el yodo y el oxígeno, el bandgap para los dos compuestos está determinado por la diferencia de energía entre (i). El estado antienlace de la interacción *p-p* entre el oxígeno y el yodo (ii). El estado de no unión del O-2*p*. Hay dos efectos que compiten bajo presión, el aumento de la distancia de enlace entre el yodo y el oxígeno de la capa interna favorece la reducción de la hibridación entre ellos, y estrecha la separación entre el estado de enlace y el de antienlace, estrechando así la energía del bandgap. El acortamiento de la distancia de enlace entre el yodo y el oxígeno intercalado favorece el aumento de la interacción entre ellos, y aumenta la separación entre los estados de enlace y antienlace, abriendo así la energía de bandgap.

El estado 3*d* parcialmente relleno en el metal de transición contribuye al VBM o al CBM, estrechando así la energía del bandgap de los yodatos metálicos. Por lo tanto, la primera regla propuesta para diseñar yodatos metálicos de energía de banda ancha es evitar el uso de metales de transición con llenado parcial en los niveles *d*. De acuerdo con los estudios de la estructura de banda electrónica de los yodatos de Mg y Zn, junto con los estudios de la estructura cristalina a alta presión de los mismos, podemos observar que existe una relación negativa entre la energía de bandgap y la distancia de enlace media entre los átomos de yodo y de oxígeno de la capa interna en los yodatos de metales de transición sin electrones tipo *d* o con una capa *d* cerrada. Además, esta relación inversa se ha confirmado cotejando usando la energía del bandgap y la distancia media de los enlaces I-O (oxígeno de la capa interna) de 71 yodatos metálicos diferentes en condiciones ambientales, según la bibliografía (ver **Figura 5**). Cuanto más corta es la distancia de enlace I-O, más amplia es la energía del bandgap. Por lo tanto, la segunda regla propuesta para diseñar yodatos metálicos de banda ancha es acortar la distancia de enlace I-O.

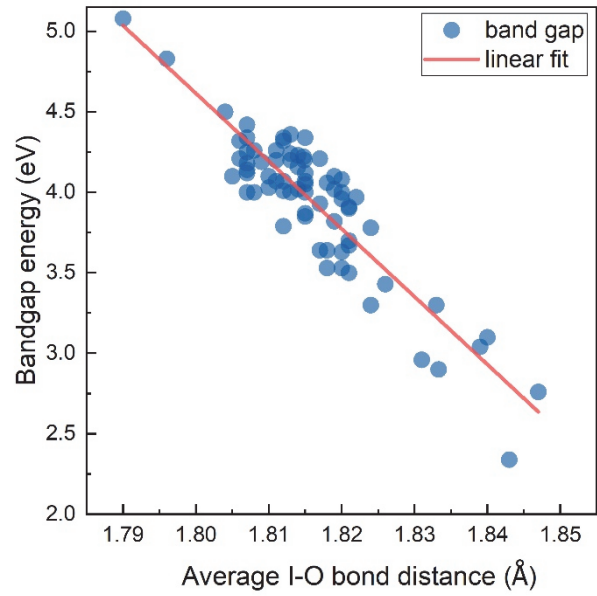


Figura 5. Energía del bandgap colado y distancia media de los enlaces I-O reportados en la literatura. Sólo se incluyen aquí los yodatos metálicos sin metales de transición o con configuración electrónica de capa cerrada.

1. Introduction

1.1 Nonlinear optical materials

Nonlinear optical (NLO) materials can modify the output wavelengths of lasers, thus playing a key role in laser science and technology. The second-order nonlinear optical process, including second harmonic generation (SHG), different frequency generation (DFG) and Sum frequency generation (SFG), are the most utilized processes for laser frequency conversion [13], when two intense laser beams with frequencies ω_1 and ω_2 are introduced into an NLO crystal, the output laser has the following four frequencies by different process: $2\omega_1$ and $2\omega_2$ by the SHG effect, $\omega_1+\omega_2$ by SFG effect and $\omega_1-\omega_2$ by the DFG effect. Thus, the output wavelength of lasers can be dramatically expanded to the region where the original laser could not cover or poorly operated. Since the first observation of SHG in a α -SiO₂ crystal [14], and with the developments of more than half a century, now the most widely used second-order NLO materials are inorganic crystals including: KH₂PO₄ (KDP) [15], KTiOPO₄ (KTP) [16], KBe₂BO₃F₂ (KBBF) [17], β -BaB₂O₄ (β -BBO) [18], LiB₃O₅ (LBO) [19] and LiNbO₃ (LN) [20]. Most of those materials satisfy the need for NLO materials in the ultraviolet, visible and near infrared regions, however, the demand for the NLO materials used for the deep-UV ($\lambda < 0.2 \mu\text{m}$) and mid-IR ($2.5 \mu\text{m} < \lambda < 25\mu\text{m}$) regions, with excellent performance in SHG efficiency and stability is still urgent.

A good candidate for NLO materials should have the following character [10–12]: (i). Large SHG response is necessary for the high laser conversion efficiency. (ii). A wide transparency region, which means a large bandgap in order to convert the laser frequency in a wide and applicable region. This is reasonable because, if the bandgap energy of the NLO materials is narrow, and smaller than the energy of the input or output laser, then the NLO materials will absorb the input laser and active the electrons from the valence band to the conduction band. (iii). High laser damage threshold (LDT). This requirement is also related to the bandgap of the NLO materials, if the NLO materials have a wide bandgap, the energy transfer from the laser to the NLO materials is negligible. (iv). Good chemical stability for practical application and (v). Moderate birefringence.

1.2 Metal iodates

Numerous novel metal iodates have been synthesized and characterized as the next generation of nonlinear optical (NLO) materials, with the metal cation species covering: alkali metal [21,22], alkaline-earth metals [23,24], transition metals [25], post-transition metals [26], and lanthanide elements [27], while the iodates include $[\text{IO}_3]^-$ trigonal pyramids [28,29], or dimeric chains like $[\text{I}_2\text{O}_5]$ [30], $[\text{I}_3\text{O}_8]^-$ [25] and $[\text{I}_4\text{O}_{11}]^{2-}$ [30]. It is known that only crystals with non-centrosymmetric structure (NCS) can be SHG-active. Because of the existence of the stereochemically active lone electron pair (LEP) in I^{5+} [29], the iodate, like IO_3 and IO_4 group, favors the formation of asymmetric polyhedra, therefore metal iodates usually crystallize with the a NCS and exhibit promising SHG responses. For instance, the most studied metal iodate as a NLO material is $\alpha\text{-LiIO}_3$ [31]. Due to the presence of a LEP in I^{5+} cation, IO_3 forms a distorted pyramid. It has been reported to show a wide transparency region, large SHG coefficient, high LDT and good thermal stability. Another case is the successful synthesis of $\text{BaNbO}(\text{IO}_3)_5$ [1], by introducing the Nb^{5+} cations in the metal iodates, both the Nb^{5+} , Ba^{2+} , I^{5+} cations are in asymmetric coordination environment attributed to the second-order Jahn-Teller effect, and by manipulating the polarization of the NbO_6 , IO_3 and BaO to the same direction, $\text{BaNbO}(\text{IO}_3)_5$ exhibits an excellent SHG response, about 14 times large than that of KDP and around 660 times large than that of $\alpha\text{-SiO}_2$ [1]. More examples of the metal iodates with a very strong SHG effect can be found in $\text{Bi}(\text{IO}_3)_2\text{F}_2$ (about 11.5 times larger than that of KDP under 1064 nm laser radiation) [8], $\text{Be}(\text{BO}_3)(\text{IO}_3)$ which exhibit a SHG response of about 7.2 times larger than that of KDP under 1064 nm laser [7], for $\text{LiZn}(\text{IO}_3)_3$ and $\text{LiCd}(\text{IO}_3)_3$ is about 14 and 12 time larger than that of KDP [6], respectively. Furthermore, the SHG effect of $\text{LiMg}(\text{IO}_3)_3$ is about 24 times larger than that of KDP under 1064 nm laser radiation [9].

It is worth explaining the LEP in I^{5+} in more depth because it has significant effect on the crystal structure of metal iodates not only at ambient pressure, but also under high pressure as discussed later in this doctoral thesis. Here we use $\text{Na}_2\text{Ti}(\text{IO}_3)_6$ as an example, the crystal structure of $\text{Na}_2\text{Ti}(\text{IO}_3)_6$ has been shown in **Figure 1a** [29], every Ti atoms is surrounded by six oxygen atoms, and every iodine is bonded with three oxygen atoms, each TiO_6 octahedral unit is surround by six IO_3 pyramids by sharing one oxygen. The Na^+ ions fill in the empty space of the structure. The theoretically

calculated electron localization functions (ELFs) are shown in **Figure 1b**, the purple area shows the LEP. We find that all the LEPs on I^{5+} are aligned in a parallel manner, generating a macroscopic dipole moment and thereby making $Na_2Ti(IO_3)_6$ a strong polar material. We can understand the LEP in I^{5+} here in a simple way, the electron configuration of iodine is $5s^25p^5$, and that for oxygen is $2s^22p^4$. Each covalent bond between iodine and oxygen needs 2 electrons, so iodine will donate two p electrons to each of the two oxygen which did not bond with Ti (double bond) and one p electron to the oxygen which shared with Ti (single bond), thus leaving the two s electrons free as LEP. The LEP in iodine will not always results in polarization in materials, it also depends on the orientation of the LEP for each iodine, like in metal iodates $A_2Ti(IO_3)_6$ where A represent K, Rb, Cs or Tl (see the calculated ELFs of them in **Figure 2**) [29], the LEP on each IO_3 polyhedral located in the converse directions from the one in the opposite location, results in mutual of the local dipole moment and make the materials nonpolar.

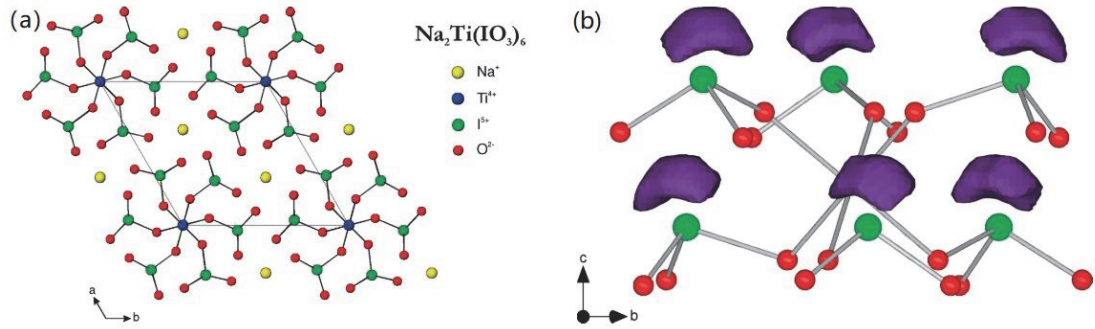


Figure 1. (a) Crystal structure of $Na_2Ti(IO_3)_6$ shown in ball-and-stick [29]. (b) Theoretically calculated ELFs of $Na_2Ti(IO_3)_6$ with $\eta=0.9$. Here the red and green balls represent oxygen and iodine atoms, respectively. The LEPs are shown by the purple areas. All the subfigures of this figure are reproduced from Ref. [29].

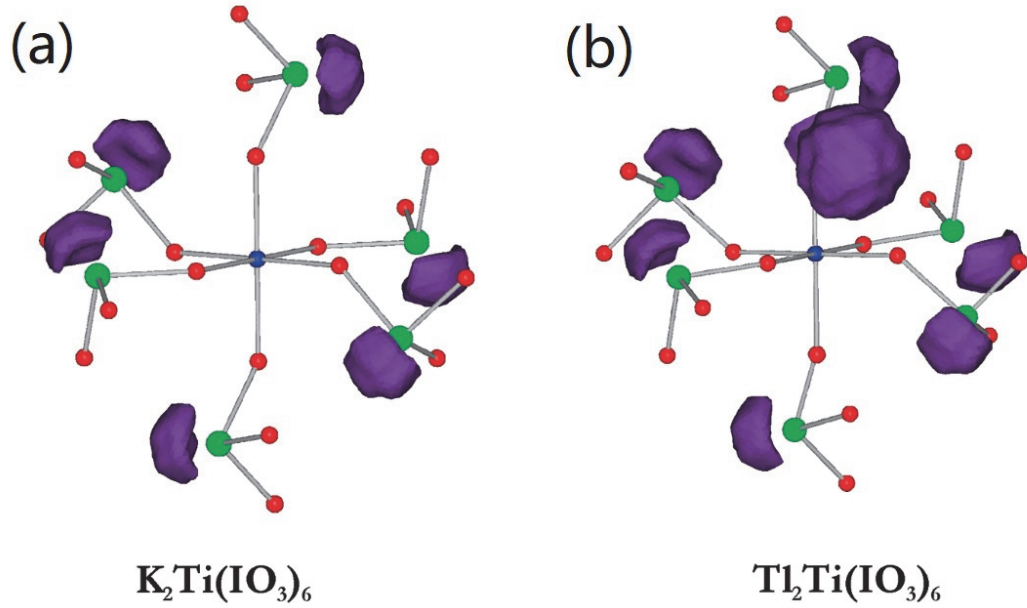


Figure 2. Theoretically calculated ELF structures for (a) $\text{K}_2\text{Ti}(\text{IO}_3)_6$ and (b) $\text{Tl}_2\text{Ti}(\text{IO}_3)_6$ with $\eta=0.9$. The blue, green and red ball are titanium, iodine and oxygen atom, respectively. The LEFs are shown in purple. The figures are reproduced from Ref [29].

1.3 The bandgap of metal iodates at ambient conditions

As per the requirements of an ideal NLO materials described in the **Chapter 1.1** of this thesis, a wide bandgap energy for NLO materials is essential since it directly affects the transparency and has a significant influence on the LDT [32] and SHG responses [33]. Therefore, in this chapter we want to investigate the bandgaps of the reported metal iodates in the literature, we have summarized most of the reported metal iodates in **Table 1**, with the experimental and theoretically calculated bandgap energy, as well as the bandgap nature (direct or indirect), dominated orbital of the VBM and CBM in the calculated electronic band structure. Notice, the information about the dominated feature in the VBM and CBM is obtained from the theoretically calculated density of state (DOS) and projected density of state (PDOS) of the metal iodates.

Some common feature can be drawn here from **Table 1**: (i). $\text{Fe}(\text{IO}_3)_3$ is the metal iodate with the lowest bandgap energy, 2.1 eV, found in the literature [34], while $\text{Rb}_3(\text{IO}_3)_3(\text{I}_2\text{O}_5)(\text{HIO}_3)_4(\text{H}_2\text{O})$ have the highest bandgap, 5.1 eV, reported in the literature up to data [35]. Metal iodates exhibits a wide bandgap range from around 2 eV to 5 eV. The bandgap of metal iodates reported in the literature are mainly located

in the energy range from 3.5 eV to 4.5 eV [36]. (ii). According to the theoretically calculated electronic band structure, most of the metal iodates show an indirect bandgap nature, which may be related to the common NCS for metal iodates as we discussed in **Chapter 1.2** in this thesis. (iii) For most of the metal iodates in **Table 1**, the theoretically calculated bandgap for the metal iodates underestimate the bandgap energy compared with that obtained from optical absorption experiment, like $\text{Zn}(\text{IO}_3)_2$ [37], $\alpha\text{-AgI}_3\text{O}_8$ [25] and so on. This is related to the generalized gradient approximation (GGA) with the Perdew-Burke-Ernzerhof (PBE) for solids prescription (PBEsol) approximations used in the theoretical calculation to describe the exchange and correlation energies [38]. On the other hand, there are also a few case that the theoretically calculated bandgap of metal iodates overestimate the bandgap compared with the data obtained from experiment, such as $\text{Fe}(\text{IO}_3)_3$ [34], RbIO_3F [32] and so on. The reasons related to the overestimations of the bandgap are still under debate [39] and out of the scope of this doctoral thesis, so it will not be discussed here. (iv). According to the theoretically calculated DOS and PDOS for metal iodates, when metal iodates only contain non-transition or closed-shelled transition metal, the VBM is dominated by the O-2*p* orbital, meanwhile, the CBM is dominated by the I-5*p* and O-2*p*, like what have been found in most of the non-transition metal iodates (like $\text{Mg}(\text{IO}_3)_2$ [36], $\text{LiMg}(\text{IO}_3)_3$ [9] and so on) and closed-shelled transition metal iodates (such as $\text{Zn}(\text{IO}_3)_2$ [36]). So for these kinds of metal iodates, the bandgap is determined by the interaction between iodine and oxygen. (iv). For the metal iodates contain open-shelled transition metal, the partial filled *d* orbital will contribute to either the VBM or CBM, thus result in the narrowing of the bandgap, such as the 5*d* orbital dominate the CBM in $M\text{Au}(\text{IO}_3)_4$ where $M=\text{Na, Rb or Cs}$ [40]. These feature can be used to explain the fact that the bandgap of the non-transition metal iodates always smaller than that of the metal iodates only have non-transition or closed-shelled metal when they have similar chemical formula. For example, the bandgap for $\text{Li}_2\text{Sn}(\text{IO}_3)_6$ is 3.9 eV [41], but that for $\text{Li}_2\text{Ti}(\text{IO}_3)_6$ is only 3.0 eV [2] because the partial filled 3*d* orbital of Ti contribute to the CBM of its electronic band structure.

Compounds	Band gap type	Band-gap energy (eV)		Valence band maxima (VBM)		Conduction band minima (CBM)		Ref.
		exp	cal	dominated	other	dominated	other	
Fe(IO ₃) ₃	In	2.1	2.50	O(2p)	I(5s,5p)	Fe(3d), I(5p)	O(2p)	[34]
Zn(IO ₃) ₂	In	3.9	2.96	O(2p)	I(5p)	I(5p), O(2p)	O(2s)	[36]
Mg(IO ₃) ₂	In	3.0	3.40	O(2p)	I(5p)	I(5p), O(2p)	×	
CsIO ₃	D	4.2	3.25	O(2p)	I(5s)	I(5p)	O(2p)	[42]
CsIO ₂ F ₂	In	4.5	4.15	O(2p)	F(2p)	I(5p)	O(2p)	[42]
Ce ₂ I ₆ O ₁₈	×	2.5	×	O(2p)	×	I(5p)	Ce(5d)	[27]
Sn(IO ₃) ₄	In	4.0	2.75	O(2p)	I(5s,5p)	I(5p)	Sn(5s)	[43]
RbIO ₃	×	4.0	2.79	O(2p)	×	I(5p), O(2p)	×	[32]
RbIO ₃ F	×	4.2	4.3	O(2p)	F(2p)	I(5p)	O(2p)	
α-AgI ₃ O ₈	In	3.8	2.43	O(2p)	Ag(4d)	I(5p)	O(2p)	[25]
β-AgI ₃ O ₈	In	3.6	2.46	O(2p)	Ag(4d)	I(5p)	O(2p)	
NaI ₃ O ₈	In	3.9	3.11	O(2p)	I(5s,5p)	I(5p)	O(2p)	
α-LiIO ₃	In	4.0	2.81	O(2p)	×	I(5p) O(2p)	×	[44, 45]
Tl(IO ₃) ₃	×	3.4	2.20	O(2s,2p)	Tl(6s)	O(2s,2p), I(5s,5p)	×	[28]
Tl ₄ (IO ₃) ₆	×	2.9	1.80	O(2s,2p)	I(5s,5p)	O(2s,2p), Tl(6s)	×	[28]
YI ₅ O ₁₄	D	3.8	×	O(2p)	I(5s,5p)	I(5p)	O(2p)	[5]
GdI ₅ O ₁₄	D	4.1	×	O(2p)	I(5s,5p)	I(5p)	O(2p)	[5]
Na ₃ Bi(IO ₃) ₆	In	3.2	3.34	O(2p)	I(5s,5p), Bi(6s)	I(5p), O(2p)	I(5s), Bi(6p)	[46]
NaBi(IO ₃) ₄	In	3.5	3.0	O(2p)	I(5s,5p), Bi(6s)	I(5p)	O(2p)	[47]
K ₂ Bi ₅ O ₁₅	In	3.5	2.51	O(2p)	×	I(5p)	O(2p)	[48]
Rb ₂ Bi ₅ O ₁₅	In	3.5	2.47	O(2p)	×	I(5p)	O(2p)	
K ₈ Ce ₂ I ₁₈ O ₅₃	In	2.3	1.13	O(2p)	I(5s,5p)	I(5p)	O(2p)	[49]
α-NaAu(IO ₃) ₄	In	2.6	2.14	O(2p)	Au(5d), I(5s,5p)	Au(5d)	O(2p), I(5p)	[40]
RbAu(IO ₃) ₄	In	2.5	2.31	O(2p)	Au(5d), I(5s,5p)	Au(5d)	O(2p), I(5p)	
α-CsAu(IO ₃) ₄	In	2.6	2.30	O(2p)	Au(5d), I(5s,5p)	Au(5d)	O(2p), I(5p)	

$\text{Cs}_2\text{Sn}(\text{IO}_3)_6$	×	4.1	×	×	×	×	×	
$\text{Li}_2\text{Sn}(\text{IO}_3)_6$	×	3.9	×	×	×	×	×	
$\text{K}_2\text{Sn}(\text{IO}_3)_6$	×	4.0	×	×	×	×	×	[41]
$\text{Na}_2\text{Sn}(\text{IO}_3)_6$	×	4.0	×	×	×	×	×	
$\text{Rb}_2\text{Sn}(\text{IO}_3)_6$	×	4.1	×	×	×	×	×	
$\text{LiMg}(\text{IO}_3)_3$	In	4.3	3.35	$\text{O}(2p)$	$\text{I}(5s, 5p)$	$\text{I}(5p)$	$\text{O}(2p)$	[9]
$\text{Li}_2\text{Ti}(\text{IO}_3)_6$	×	3.0	1.60	$\text{O}(2p)$	$\text{I}(5s, 5p)$	$\text{Ti}(3d)$	$\text{O}(2s, 2p)$	[2]
$\text{Na}_2\text{Ti}(\text{IO}_3)_6$	×	3.3	2.95	$\text{O}(2p)$	×	$\text{Ti}(3d), \text{I}(5p)$	$\text{O}(2s, 2p)$	
$\text{Rb}_2\text{Ti}(\text{IO}_3)_6$	×	3.3	×	×	×	×	×	
$\text{Cs}_2\text{Ti}(\text{IO}_3)_6$	×	3.2	×	×	×	×	×	[29]
$\text{Tl}_2\text{Ti}(\text{IO}_3)_6$	×	3.2	2.88	$\text{O}(2p)$	×	$\text{Ti}(3d), \text{I}(5p)$	$\text{O}(2s, 2p)$	
$\text{K}_2\text{Ti}(\text{IO}_3)_6$	×	3.3	3.14	$\text{O}(2p)$	×	$\text{Ti}(3d), \text{I}(5p)$	$\text{O}(2s, 2p)$	
$\text{KLi}_2(\text{IO}_3)_3$	×	4.3	×	×	×	×	×	[22]
$\text{Li}_2\text{Ge}(\text{IO}_3)_6$	In	3.9	3.18	$\text{O}(2p)$	$\text{I}(5s, 5p)$	$\text{I}(5p)$	$\text{O}(2p), \text{Ge}(4s)$	
$\text{Na}_2\text{Ge}(\text{IO}_3)_6$	In	4.6	3.31	×	×	×	×	[50]
$\text{Rb}_2\text{Ge}(\text{IO}_3)_6$	×	4.1	×	×	×	×	×	
$\text{Cs}_2\text{Ge}(\text{IO}_3)_6$	×	4.1	×	×	×	×	×	
$\text{Ba}_3\text{Ga}_2(\text{IO}_3)_{12}$	In	3.1	3.09	$\text{O}(2p)$	×	$\text{I}(5p), \text{O}(2p)$	×	[51]
$\text{Bi}(\text{IO}_3)\text{F}_2$	In	4.0	3.26	$\text{O}(2p)$	$\text{Bi}(6s), \text{I}(5s, 5p)$	$\text{I}(5p), \text{Bi}(6p)$	$\text{O}(2p)$	[8]
$\text{KBi}_2(\text{IO}_3)_2\text{F}_5$	In	3.8	2.89	$\text{O}(2p)$	$\text{F}(2p), \text{I}(5s, 5p)$	$\text{I}(5p)$	$\text{O}(2p)$	
$\text{RbBi}_2(\text{IO}_3)_2\text{F}_5$	In	3.8	2.97	$\text{O}(2p)$	$\text{F}(2p), \text{I}(5s, 5p)$	$\text{I}(5p)$	$\text{O}(2p)$	[4]
$\text{CsBi}_2(\text{IO}_3)_2\text{F}_5$	In	3.8	2.99	$\text{O}(2p)$	$\text{F}(2p), \text{I}(5s, 5p)$	$\text{I}(5p)$	$\text{O}(2p)$	
$\text{LiZn}(\text{IO}_3)_3$	D	4.2	4.4	$\text{O}(2p)$	$\text{I}(5p)$	$\text{I}(5p), \text{O}(2p)$	×	
$\text{LiCd}(\text{IO}_3)_3$	D	4.2	4.3	$\text{O}(2p)$	$\text{I}(5p)$	$\text{I}(5p), \text{O}(2p)$	×	[6]
$\text{SrSn}(\text{IO}_3)_6$	In	4.1	3.19	$\text{O}(2p)$	$\text{I}(5p)$	$\text{I}(5p)$	$\text{O}(2p)$	[26]
$\text{Ag}_2\text{Zr}(\text{IO}_3)_6$	In	3.8	2.64	$\text{O}(2p), \text{Ag}(4d)$	$\text{I}(5s, 5p)$	$\text{I}(5p), \text{O}(2p)$	×	
$\text{LaZr}(\text{IO}_3)_5\text{F}_2$	In	4.1	3.29	$\text{O}(2p)$	$\text{I}(5s, 5p)$	$\text{I}(5p), \text{Zr}(4d)$	$\text{O}(2p)$	[52]
$\text{BiO}(\text{IO}_3)$	×	3.3	2.0	$\text{O}(2p)$	$\text{I}(5s, 5p)$	$\text{I}(5p), \text{O}(2p)$	×	[3]
$\text{BaNbO}(\text{IO}_3)_5$	D	3.6	2.55	$\text{O}(2p)$	$\text{I}(5p)$	$\text{Nb}(4d), \text{I}(5p)$	×	[1]
$\text{Zn}_2(\text{VO}_4)(\text{IO}_3)$	In	3.3	2.7	$\text{O}(2p)$	$\text{V}(3d), \text{Zn}(3d)$	$\text{V}(3d), \text{I}(5p), \text{O}(2p)$	×	[53]
$\text{LaVO}(\text{IO}_3)_5$	In	3.6	1.7	$\text{O}(2p)$	$\text{I}(5s, 5p)$	$\text{V}(3d), \text{La}(5d), \text{I}(5p)$	×	[54]

LaV ₂ O ₆ (IO ₃)	In	3.6	2.54	O(2 <i>p</i>)	I(5 <i>s</i> , 5 <i>p</i>)	V(3 <i>d</i>), I(5 <i>p</i>)	O(2 <i>p</i>)	
Rb ₃ (IO ₃) ₃ (I ₂ O ₅) (HIO ₃) ₄ (H ₂ O)	×	5.1	×	×	×	×	×	[35]

Table 1. A summary of the band-gap energy of part of the reported metal iodates in literature (all the experimental value have been rounded to one decimal place), as well as the bandgap nature, the atomic orbital which dominated the valance band maxima (VBM) and conduction band minima (CBM) based on the results from the theoretically calculated density of state (DOS) and projected density of state (PDOS), “exp” means data determined in experiments and “cal” means data predicted by theoretical calculations, respectively. For the bandgap type, “In” and “D” represent the indirect and direct bandgap, respectively. The blank where filled with “×” means no available data was found.

1.4 High pressure science

Pressure, as a fundamental thermodynamic variable, is an efficient external parameter for manipulating the interatomic distance within materials, in turn modifying the chemical bonding. For example, high pressure has been demonstrated to be able to convert weak π , van der Waals and hydrogen bond into a strong covalent or ionic bond [55,56], and also efficiently increase the coordination number by transforming the crystal structure to a higher symmetry one in IIB–VIA compounds [57]. By altering interatomic distance pressure also can drive crystal structure phase transition in materials. Almost all the materials will undergo several phase transitions under compression. In this way it is possible to generate new polymorphs and materials with promising properties. The classic example is the synthesis of diamond from graphite at high pressure and high temperature [58]. Other examples include the synthesis of ultrahard nanotwinned cubic boron nitride with a hardness compared with the optimal hardness of diamond [59], the synthesis of high-energy high-density polymeric nitrogen [60], and the long-sought metallic hydrogen [61].

Pressure can modify the conventional valence state of an element predicted by the periodic table at ambient conditions. Under pressure, Cs can show a high oxidation beyond +1 by sharing their 5*p* electrons, CsF_{*n*} (*n*>1) compounds found to be stable at a range of 5 to 200 GPa under compression [62]. Hg can transfer charge from the *d* orbitals to the orbitals of F and behave as a transition metal, forming HgF₄ and HgF₃ which have been found to be thermodynamically stable at 38 and 73 GPa, respectively.

More interestingly, HgF_4 is found to be unstable under further compression, decomposing into HgF_3 and F_2 at a pressure higher than 200 GPa [63]. Pressure also can drive chemical reactions by influencing the electronic orbitals and their occupancy. Even the chemically inert noble gas can react with Mg and form thermodynamically stable compounds as MgXe and Mg_2Xe at 125 GPa. The Mg-Kr and Mg-Ar systems are stable at a pressure around 250 GPa [64]. Pressure also can stabilize new stoichiometries of some elements that are not be expected at ambient conditions. Such as the synthesis of hydrogen-rich metal hydrides including LiH_x [65], FeH_2/H_3 [66], RhH_2 [67], IrH_3 [68], and sodium chloride with unusual stoichiometries like Na_3Cl [69], NaCl_3 [69] etc.

Pressure provides also a new route for the searching of the high-temperature or even room-temperature superconductors. Metallic hydrogen has been theoretically predicted to be a room-temperature superconductor since 1960 [70] due to the very high vibrational frequencies in the light hydrogen atom, which can provide a strong electron-phonon interaction. The required pressure used to synthesize metallic hydrogen has been predicted between 400 to 500 GPa [71–73]. This has driven numerous efforts to synthesize metallic hydrogen under high pressure, but since reaching the extreme condition sufficient for the synthesis of metallic hydrogen in laboratory is challenging, the focus has recently move to hydrogen-dominated covalent hydrides, where the target pressure is lowered. In 2015, H_3S was synthesized at high pressure and high temperature with an alleged superconducting transition temperature of 203 K at around 150 GPa [74]. In 2019, the same group successfully synthesized LaH_{10} with a critical temperature of 250 K at 151 GPa [75]. In 2021, YH_6 and YH_{10} have been successfully synthesized with a critical temperature of around 220 K at 183 GPa, and around 243 K at 201 GPa, respectively [76]. Furthermore, high pressures have also been found to be an efficient tool to increase the superconducting transition temperature of the superconducting materials which have been well investigated at ambient pressure. For example, at ambient conditions, the highest critical temperature (133 K) [77] has been achieved in the copper oxide system up to date. The application of around 45 GPa of pressure can upshift the critical temperature to 164 K [78].

Pressure can cause the electron delocalization in the materials by increasing the electron density and the kinetic energy of the electrons, when the kinetic energy surpasses the potential energy, therefore, the electron will favor delocalization. The

pressure-induced electron delocalization can cause energy-band broadening, bandgap closure and metallization, it has been proven that sufficient pressure, in principle, turns many insulators into conductors [61,79–82]. Furthermore, the insulators found at ambient pressure can become superconductors after metallization [83]. Pressure can also regulate the spin state of materials. For example, in the high-pressure study of $\text{Co}_2\text{Te}_3\text{O}_8$, the spin state of Co has been found to transform from the high-spin state to the low-spin state at around 7.6 GPa [84], the high-spin to low-spin state transition also have been found in CoCl_2 at around 70 GPa [85].

High pressure studies, in general, involve two steps: the generation of high pressure and the modern diagnostics to measure multiple properties of the studied sample. Pressure can be generated in two different ways; static pressure and dynamic compression. The most commonly used static pressure apparatuses are diamond anvil cells (DAC), and large volume presses (LVP) (like piston-cylinder devices, multi-anvil apparatuses, etc). DACs are capable of generating static pressures up to several megabars, the highest recorded pressure is over 1000 GPa. this was achieved by using synthesized optically transparent microballs of bulk nanocrystalline diamond as the second stage anvils in conventional diamond anvil cells [86]. Diamond is the hardest material found in nature and are transparent for infrared, visible, and ultraviolet radiation, which allows the use of various diagnostics. The disadvantage for DACs is that the sample chamber is tiny as a sacrifice of the ultrahigh pressure. It is unlikely to synthesis the commercial used novel materials nor be used for the diagnostics that require a large amount of samples, such as neutron diffraction. The highest pressure achieved in LVP is 109 GPa in a Kawai-type apparatus equipped with sintered diamond anvils [87], and the sample size in LVP usually can excess 1mm^3 (In comparison, the sample cavity of a DAC is typically less than 0.001mm^3). The techniques used to generate dynamic compression are two-stage gas gun, laser-driven compression and explosion. Under shock compression, the sample is subjected to transient high pressure and high temperature, the pressure can easily excess megabar in a short time scale in a time range from nano- to femto-seconds [88].

The high pressure *in situ* characterization techniques include: (i). High-pressure optical absorption, which can measure the bandgap and *d-d* internal transitions of materials. (ii). High-pressure inelastic optical scattering which are high-pressure Raman scattering, high-pressure Brillouin spectroscopy, high-pressure infrared spectroscopy

and high pressure optical fluorescence spectroscopy. They are capable of providing important information about the atomic vibration, acoustic velocities, and electronic structure of studied materials. (iii). High-pressure X-ray techniques, including high-pressure x-ray emission spectroscopy, high pressure electronic inelastic x-ray scattering, high-pressure resonant inelastic x-ray scattering spectroscopy, high-pressure nuclear resonant X-ray spectroscopy, high-pressure X-ray imaging, high-pressure x-ray diffraction and high-pressure radial X-ray diffraction. These tools can investigate the structural, vibrational, electronic, and magnetic properties of materials under pressure. (iv). high-pressure neutron diffraction. As neutrons have their own spin and the scattering intensity only depended on the scattering factor but not the atomic number, this diagnostic has the unique advantage on measuring the crystal structures and magnetic ordering of crystalline and amorphous materials with light elements. (v). Neutron inelastic scattering technique can provide the spin resonance and phonon dispersion. (vi). High-pressure ultrasonic probes enable us to measure the compressional and shear elastic-wave velocity in crystal under pressure. (vii). High pressure resistivity measurement and magnetic susceptibility measurements, which are useful in the investigation of superconductivity.

1.5 Aims of the thesis

A wide bandgap is one of the most important requirement for the metal iodates used as NLO, and the existence of the LEP in iodine is responsible for the NCS of metal iodates and shows a polarized feature, which in turn is related to another most important requirement for NLO: SHG efficiency. Therefore, the objectives of our research are:

- i). Investigate the crystal structure, atomic vibration, the stereochemically active LEP of $\text{Fe}(\text{IO}_3)_3$, $\text{Zn}(\text{IO}_3)_2$, $\text{Co}(\text{IO}_3)_2$, and $\text{Mg}(\text{IO}_3)_2$ under static high pressure conditions by using diamond anvil cells.
- ii). Investigate the bandgap energy change of $\text{Fe}(\text{IO}_3)_3$, $\text{Zn}(\text{IO}_3)_2$, $\text{Co}(\text{IO}_3)_2$ and $\text{Mg}(\text{IO}_3)_2$ under pressure.
- iii). Try to find the relationship between the bandgap energy and the crystal structure.
- iv). Find a rule for designing wide bandgap metal iodates.

1.6 Organization of the thesis

The thesis has been structured into 7 chapters as following:

-Chapter 1: The present introductory chapter.

-Chapter 2: Experimental and calculated methods. In this chapter a brief introduction of the experimental methods is given, including the combination of DAC techniques, with synchrotron based polycrystalline X-ray diffraction and Fourier-transform infrared spectroscopy, Raman scattering, optical absorption spectra.

-Chapter 3: $\text{Fe}(\text{IO}_3)_3$ under pressure. In this chapter, the results of the crystal structure, atomic vibration, and electronic band structure study on $\text{Fe}(\text{IO}_3)_3$ from both experiment and theoretical calculation are reported. Here I will propose a first empirical rule for designing wide bandgap metal iodates.

-Chapter 4: $\text{Co}(\text{IO}_3)_2$ under pressure. In this chapter, the investigation on the crystal structure, atomic vibration, and electronic band structure of $\text{Co}(\text{IO}_3)_2$ are reported. The results will be compared with those from Fe iodate. Specially, I will show the study on the multi-band absorption spectra of Co iodates, which is a unique feature among the studied metal iodates in this thesis.

-Chapter 5: $\text{Zn}(\text{IO}_3)_2$ under pressure. In this chapter, the investigation on the crystal structure and atomic vibrations on $\text{Zn}(\text{IO}_3)_2$ from experiments and calculations are reported, and the results are compared with those of $\text{Co}(\text{IO}_3)_2$ and $\text{Fe}(\text{IO}_3)_3$. The electronic band structure of Zn iodates is reported in chapter 6 together with that of $\text{Mg}(\text{IO}_3)_2$.

-Chapter 6: $\text{Mg}(\text{IO}_3)_2$ under pressure. In this chapter, firstly, the crystal structure and atomic vibration study on $\text{Mg}(\text{IO}_3)_2$ are reported. Secondly, the electronic band structure study on both Mg and Zn iodates are presented, as well as the second rule for designing wide bandgap energy metal iodates.

-Chapter 7: This is the last chapter. This chapter gives a compressive summary and present the conclusions on this doctoral thesis.

2. Theoretical background and experimental techniques

In this chapter, the fundamental principle and experimental techniques of several diagnostics used in our studies are introduced, including diamond anvil cell (DAC), X-ray diffraction (XRD), Raman scattering (RS), infrared spectroscopy (IR) and optical absorption (OA).

2.1 Membrane-type diamond anvil cell

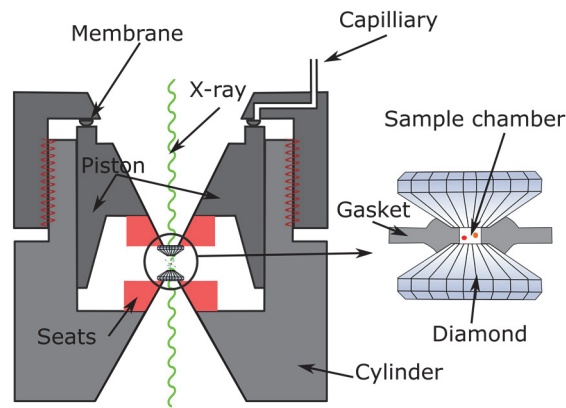


Figure 3. Illustration of membrane-type diamond anvil cell used in the contributing work.

Figure 3 is a cross-section illustration of the membrane-type diamond anvil cell (DAC) used in our studies to generate the high pressure environment. The piston was driven by the membrane, which will be expanded outward when inflated. The most important component of DAC is a pair of opposed single-crystal diamond anvils, the chosen of single-crystal diamond as the anvil is beneficial, as diamond has some outstanding properties; including (i). The extreme high hardness and fracture toughness, diamond is the hardness materials found in the nature, the Vickers hardness is range from 60 GPa to 120 GPa according to the different crystal plane [89]. (ii). Diamond is transparent over a wide range of wavelengths so that the properties changes of the sample at high pressure can be probed with a series of modern probing technique, like X-rays, Raman, infrared and optical absorption. (iii). Ultrahigh high melting temperature, which make

it possible to heat the sample up to a few thousands Kelvin. (iv). Diamond is insulator and high magnetic compatibility, which make the electrical and magnetic measurement possible. (v). Diamond is chemical inertness, and it hard to react with sample. The diamond used here is around 0.5 carats, with a culet of a few hundred micrometers in diameter, preferably parallel to the (100) plane.

Between the two diamond, a gasket was used to support the diamond and encapsulating the sample, as well as the pressure transmitting medium (PTM) and pressure gauge. Hardness steel, high strength tungsten and rhenium are commonly used gasket depending on different experiment goal. The gasket must possess a certain level of ductility to allow the volume reduction with increasing pressure. By squeezing the gasket, it forms a thick ring around the culet of diamond, which could support the diamond and enables pressure generation of several megabars. The gasket need to be pre-indented to fit the shape of the diamond culets, and a hole need to be drilled in the center and serve as the sample chamber before conducting the high-pressure experiments.

The use of PTM in the sample chamber ensure the sample subjected to a hydrostatic pressure within a certain pressure range depending on the type of PTM. The hydrostatic limits of 11 commonly used PTM have been studied and reported by Klotz *et al* [90]. For example, the most commonly used liquid PTM, a mixture of methanol and ethanol in a ratio of 4:1, could provide hydrostatic environment up to around 10 GPa at ambient temperature. The same limit also has been founded in another liquid PTM, a mixture of methanol, ethanol and water in ratio of 16:3:1. Silicone oil, used in some of our high-pressure experiment, can provide the hydrostatic environment up to 3 GPa, above which its strength rises with pressure. Among the common used gas PTM like argon, nitrogen, helium and neon. At ambient temperature, helium has the best performance and can provide the quasi-hydrostatic condition over 100 GPa, that is 15 GPa for neon and 10 GPa for nitrogen. In our high-pressure infrared spectroscopy experiment and some of the high-pressure optical absorption experiment, solid PTM were chosen, the hydrostatic limit of several solid PTM have been studied and reported by Celeste *et al* [91]. For example, Potassium bromide (KBr) can provide hydrostatic environment up to 2 GPa, and quasi-hydrostatic environment up to 11 GPa, and CsI can provide hydrostatic condition up to 3 GPa and quasi-hydrostatic condition up to 18 GPa.

To measure the pressure inside the sample chamber, the equation of state (EOS)

of some materials, like NaCl, at isothermal conditions was used, which have been established from the shock-wave measurement of particle velocity (U_p) and wave velocity (U_s). By using the X-ray from synchrotron light source, the unit-cell volume of the pressure standard can be obtained, thus the pressure can be calculated from the P - V relation. Once we have the primary pressure standard, the EOS of some other materials can be established [92], like Au, Pt, Ta, Cu, W and Al, the EOS of them can be used as a second standard for the measurement of pressure in the sample chamber. However, not all the high-pressure experiment need the use of X-ray, so second pressure standard can be measured in the laboratory by spectroscopic methods are urgently needed. By using the Ruby fluorescence shift, accuracy of pressure measurement can be controlled to 2% [93] at pressure up to 55 GPa. Furthermore, the fluorescence of ruby can be easily measured by using a lasers beam through the ruby grains loaded in the sample chamber.

2.2 X-ray diffraction

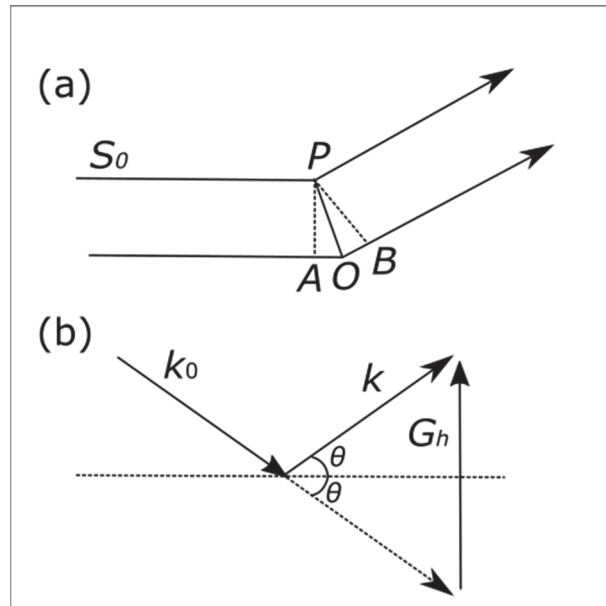


Figure 4. (a) Schematic diagram of X-ray diffraction in crystal. (b). Schematic diagram of Bragg reflection.

In **Figure 4a**, S_0 and S are unit vectors of incident and diffracted lines, the potential vector of an arbitrary lattice cite P is $R_i=l_1a_1+l_2a_2+l_3a_3$, so the optical path difference of the incident light pass through P and O is

$$\vec{OA} + \vec{OB} = -\mathbf{R}_l \cdot \mathbf{n}_0 + \mathbf{R}_l \cdot \mathbf{n} = \mathbf{R}_l \cdot (\mathbf{S} - \mathbf{S}_0) \quad (2.1)$$

the diffraction theory shows that the conditions for diffraction to be extremely large is

$$\mathbf{R}_l \cdot (\mathbf{n} - \mathbf{n}_0) = \mu\lambda \quad (2.2)$$

Where λ is the wavelength of the incident light and μ is integer. Make

$$\mathbf{k} - \mathbf{k}_0 = \frac{2\pi}{\lambda} (\mathbf{n} - \mathbf{n}_0)$$

So **equation 2.2** could be written as

$$\mathbf{R}_l \cdot (\mathbf{k} - \mathbf{k}_0) = 2\pi\mu \quad (2.3)$$

Where the \mathbf{k} and \mathbf{k}_0 are the wave vector of the incident and diffraction light as **Figure 4b** shown. Make

$$\mathbf{k} - \mathbf{k}_0 = \mathbf{G}_{h'}$$

So **equation 2.3** can be written as

$$\mathbf{R}_l \cdot \mathbf{G}_{h'} = 2\pi\mu \quad (2.4)$$

The dimension of \mathbf{R}_l and $\mathbf{G}_{h'}$ are inverse, and \mathbf{R}_l is the lattice vector of lattice site, $\mathbf{G}_{h'}$ is the reciprocal lattice vector.

Actually, $\mathbf{k} - \mathbf{k}_0$ and \mathbf{G}_h is equivalent, so we can make

$$\mathbf{k} - \mathbf{k}_0 = n\mathbf{G}_h \quad (2.5)$$

Where n is integer, **equation 2.5** means when the diffracted wave vector and the incident wave vector differ by one or several reciprocal lattice vectors, the diffraction enhancement condition is satisfied.

When $n=1$, \mathbf{k} , \mathbf{k}_0 and \mathbf{G}_h form a triangle (**Figure 4b** shown), If the Compton effect is ignored, then we have $|\mathbf{k}| = |\mathbf{k}_0| = 2\pi/\lambda$, So the vertical bisector of \mathbf{G}_h bisects the angle between \mathbf{k} and \mathbf{k}_0 (as the dash line in **Figure 4b** shown). So when the diffraction line is exactly the direction of light reflection for a certain crystal plane family, this diffraction direction is the direction of diffraction enhancement.

$$|\mathbf{k} - \mathbf{k}_0| = |n\mathbf{G}_h| = 2|\mathbf{k}| \sin \theta = \frac{4\pi \sin \theta}{\lambda} \quad (2.6)$$

According to **equation 2.5**, we got

$$|\mathbf{k} - \mathbf{k}_0| = |n\mathbf{G}_h| = \frac{2\pi n}{d_{h_1, h_2, h_3}} \quad (2.7)$$

From the **equation 2.6** and **2.7**, we got the **Bragg law** as

$$2d_{h_1, h_2, h_3} \sin \theta = n\lambda \quad (2.8)$$

Where d_{h_1, h_2, h_3} is the spacing of crystal plane ($h_1 h_2 h_3$) family, and n is the diffraction level.

The intensity of the XRD diffraction peaks depend on the atoms in the crystal structure. Different atoms have different scattering abilities for X-ray. The scattering of X-rays by atoms depends on the scattering of X-rays by each electron within the atom. The electrons of an atom are distributed in a certain area, so there is a certain phase difference between the scattered waves of X-ray electron emission caused by different parts of the atom. The intensity of the total scattered wave of an atom is related to the phase difference of each scattered wave, and the scattering ability of an atom varies depending on the distribution of electrons outside its nucleus.

Make the nucleus as the origin, the phase difference of the scattering of the wave vector \mathbf{k} between an electron located at \mathbf{r} and by an electron at the origin O is

$$\delta = (\mathbf{k} - \mathbf{k}_0) \cdot \mathbf{r}$$

the atomic shape factor f is

$$f = \frac{\sum_j \alpha \exp[i(\mathbf{k} - \mathbf{k}_0) \cdot \mathbf{r}_j]}{\alpha} = \sum_j \exp[i(\mathbf{k} - \mathbf{k}_0) \cdot \mathbf{r}_j] \quad (2.9)$$

where α is the scattering amplitude of electrons to the incident wave.

According to quantum theory, the distribution of electrons outside the nucleus should be viewed as a cloud of electrons with a certain density distribution, let the probability of distribution of electrons be $\rho(\mathbf{r})$, so the atomic shape factor is

$$f = \int \rho(\mathbf{r}) \exp[i(\mathbf{k} - \mathbf{k}_0) \cdot \mathbf{r}_j] d\tau = \int \rho(\mathbf{r}) \exp[i\mathbf{G}_h \cdot \mathbf{r}_j] d\tau \quad (2.10)$$

Where $\mathbf{k} - \mathbf{k}_0 = \mathbf{G}_h$ is the reciprocal lattice vector.

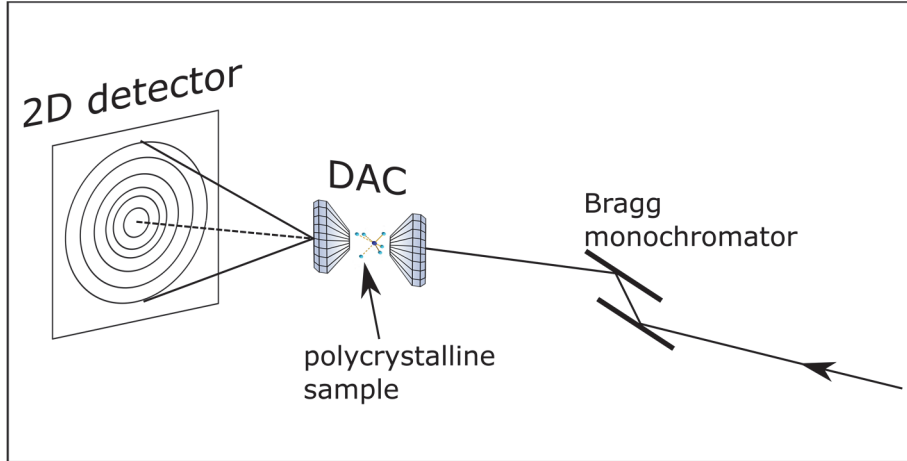


Figure 5. Schematic diagram of angle-dispersive X-ray diffraction by using a synchrotron light source.

The powder diffraction, also called the Debye-Scherrer method, is the most common used technique in high pressure research. The samples are usually polycrystalline, so they contain a very large number of fine single crystals with various orientations. **Figure 5** is the schematic diagram of the angle dispersive X-ray diffraction by using a monochromatic X-ray beam in a synchrotron light source. When the incident X-rays meet the sample, for each group of crystal plane families, there are always many small single crystals in positions suitable for reflection and satisfy the **Bragg law**, so that the diffraction lines form a series of conical surfaces with the incident direction as the central axis. When these conical surfaces meet the cylindrical detector, it forms a series of diffraction rings (like **Figure 5** shown). From the size of the circle, the angle between the crystal plane producing this diffraction ring and the incident X-rays can be obtained, and thus the spacing d of the crystal plane can be calculated. The 2-dimensional diffraction image collected in the detector can be transformed to a plot of 2θ vs intensity spectra. The detail information of the crystal structure, including lattice parameter, space group, atomic position, can be obtained from the Rietveld refinement of the X-ray patterns.

2.3 Raman scattering

There are three cases of interaction between light and medium:

- (i). If the medium is homogeneous and thermal undulations are neglected. The light does not change after passing through the medium and continues to propagate in the original direction of propagation, without any interaction with the medium.
- (ii). If the medium is not homogeneous, the light wave is scattered to other directions after interacted with medium, as long as this process is independent of time, the frequency of the scattered light will not undergo any change, only the direction of the wave vector is deflected, which is what we called elastic scattering.
- (iii). If the inhomogeneity of the medium changes with time, the light waves exchange energy with the medium, causing the frequency of the scattered light to be different with that of incident light, which is what we call inelastic scattering.

The first case barley found in nature, the second case including Rayleigh scattering, Tyndall effect and Mie scattering, the third case including Raman and Brillouin scattering.

When the monochromatic light with electric vector \mathbf{E} is incident on the substance, the distribution of the positive and negative charges of the molecules or atoms of the substance will change and form electric dipole moment, and the induced dipole moment \mathbf{M} per unit volume is proportional to the incident electric vector \mathbf{E} as

$$\mathbf{M} = \alpha \cdot \mathbf{E} \quad (2.11)$$

Where α is polarizability tensor, the vibrating electric dipole will then radiate electromagnetic waves and become scattered light.

In the aspect of classical electromagnetic theory, the electric field component \mathbf{E} in the electromagnetic field varies following the equation:

$$\mathbf{E} = \mathbf{E}_0 \cos \omega_L t \quad (2.12)$$

Here ω_L is so much bigger than the vibration frequency of atoms, but similar to that of electrons, so the induced dipole moment \mathbf{M} can be written as the series of electric vector \mathbf{E} as

$$M = \alpha E + \frac{1}{2!} \beta E^2 + \frac{1}{3!} \gamma E^3 + \dots + \frac{1}{n!} \varepsilon E^n \quad (2.13)$$

Where α is polarizability tensor of electrons, the order of magnitude is $10^{-40} \text{ C}\cdot\text{V}^{-1}\cdot\text{m}^2$, β is supper polarizability, and γ, ε are high-order tensor. Below we only discuss the linear part.

The polarizability tensor α dependent on the distribution $\alpha(\rho)$ of the electrons in the system, in the case of diatomic molecules, α and normal coordination have a linear relationship when the nuclear displacement is small enough. Expand α to normal coordinates by **Taylor series**.

$$\alpha = \alpha_0 + \left(\frac{\partial \alpha}{\partial Q}\right)_0 Q + \frac{1}{2!} \left(\frac{\partial^2 \alpha}{\partial Q^2}\right)_0 Q^2 + \frac{1}{3!} \left(\frac{\partial^3 \alpha}{\partial Q^3}\right)_0 Q^3 + \dots \quad (2.14)$$

If the atom vibrates at frequency of ω_q , thus $Q=Q_0 \cos \omega_q t$, then the variation of electron polarizability with time in the first-level Raman effect is

$$\alpha(t) = \alpha_0 + \left(\frac{\partial \alpha}{\partial Q}\right)_0 Q_0 \cos \omega_q t \quad (2.15)$$

by combining **equations 2.15** and **2.11**, we have

$$M(t) = \alpha_0 E_0 \cos \omega_L t + \left(\frac{\partial \alpha}{\partial Q}\right)_0 Q_0 \cos \omega_L t \cos \omega_q t$$

$$M(t) = \alpha_0 E_0 \cos \omega_L t + \frac{1}{2} \left(\frac{\partial \alpha}{\partial Q}\right)_0 Q_0 E_0 [\cos(\omega_L - \omega_q)t + \cos(\omega_L + \omega_q)t] \quad (2.16)$$

The first part of **equation 2.16** is elastic scattering, because the frequency is unchanged compared with that for the incident light, the second part where contain two new kind of frequency, $\omega_L \pm \omega_q$, is the inelastic Raman scattering, the one with the reduced frequency $\omega_L - \omega_q$ is called Stoke, and the one with increased frequency, $\omega_L + \omega_q$, is called anti-Stoke.

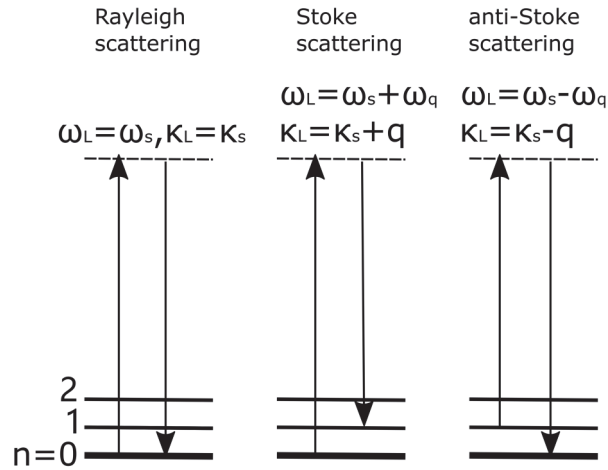


Figure 6. Schematic diagram of Raman and Rayleigh scattering process. The vibrational energy state was shown in solid line at the bottom and the virtual energy state have been shown in dash line at the top.

In the aspect of quantum mechanics (**Figure 6**), make the frequency and wave vector of the incident light as (ω_L, k_L) , outgoing light as (ω_s, k_s) . When the light hit the substance, it active the electrons or the vibration of lattice from the ground state to a virtual energy state, and then back to the ground state, and emit a light with the same frequency and wave vector as the incident light, this process is Rayleigh scattering. If the electron or lattice didn't go back to the ground state after be active, but jump to the $n=1$ state, then the frequency of the outgoing light smaller than that for incident light, $\omega_s = \omega_L - \omega_q$, it is Stoke scattering. If the electron or lattice in the $n=1$ state have been active by the incident light, and then jump to the ground state, the outgoing frequency is higher than that for incident light, $\omega_s = \omega_L + \omega_q$, then it is anti-Stoke scattering. Both the Stoke and anti-Stoke provide the same information of the atomic vibration. According to the Maxwell-Boltzmann distribution law, the population of molecules at the ground state ($n=0$) is much larger than that at the excited state ($n=1$) when the molecule is in thermal equilibrium. Therefore, the Stoke line is much stronger in intensity compared with that of anti-Stoke line, so usually, we only measure the Stoke part of the spectrum.

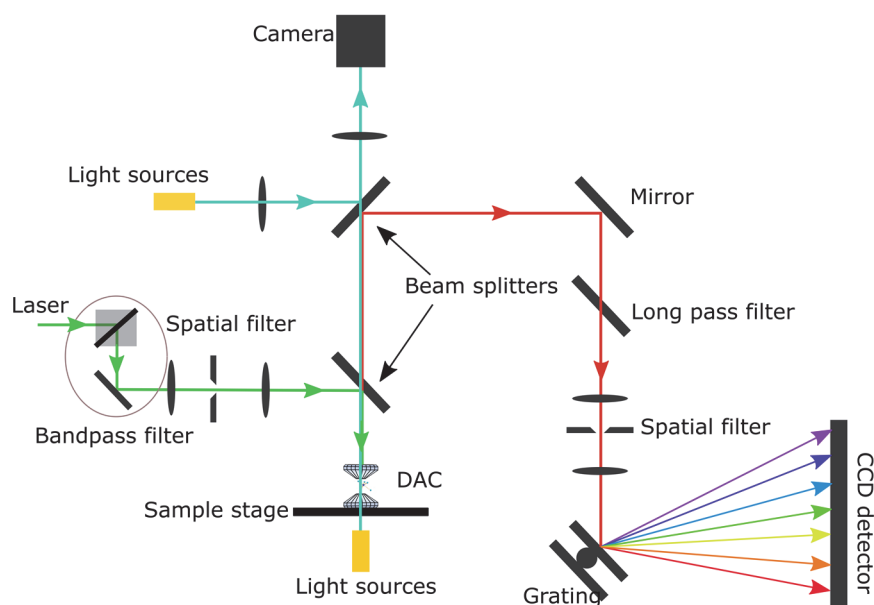


Figure 7. Illustration of the beam path of Raman set-up used in our studies. The incoming lasers beam are shown in green and the Raman scattering lights are shown in red.

Figure 7 is the schematics of Horiba Jobin Yvon LabRAM Raman setup used in our experiment, the laser was guided by the spectrometer through the bandpass filter and beam splitters into the DAC and sample, five different laser source with different wavelength can be chosen, UV-325 nm, Violet-442 nm, Green-532 nm, Red-632 nm and NIR-785nm. The sample was firstly focused by the 50 \times objective in the white light modes and then the Red laser with suitable filter was introduced into the sample, the Raman scattered light was guided by several beam splitters, mirror, long pass filter and spatial filter to the grating, where it could be dispersed by wavelength. A liquid nitrogen cooled charge coupled device (CCD) will recorded the intensity of the laser in wavelength. The resolution of the CCD is better than 2 cm^{-1} , and the signal can down to 10 cm^{-1} .

2.4 Infrared spectroscopy

The wavenumber ranges for near-infrared, mid-infrared and far-infrared is 12500-4000 cm^{-1} , 4000-400 cm^{-1} , and 400-10 cm^{-1} , respectively. When a continuous wavelength infrared light source irradiates the sample, it causes a jump between molecular vibrational energy states, but because the energy difference between molecular vibrational energy states (around 0.05-1.0 eV) is larger than that between rotational

energy state (0.0001-0.05 eV), it is inevitably accompanied by a jump between rotational energies. Therefore, the incident light source will be absorbed at certain wavelengths, which is the infrared absorption spectrum. Since the infrared light is directed to the sample through the interferometer, we first obtain an interferogram that needs to be converted, and the light intensity expressed not as a function of wavelength, but as a function of mirror position within the interferometer, and the Fourier transform will be used to convert the infrared intensity to a function of wavenumber. So the infrared spectroscopy we used in the experiment is also called Fourier Transformed Infrared Spectroscopy (FTIR).

The absorption of infrared light by matter requires the following two conditions: (i). The radiation photon has an energy equal to the energy required for the jump between vibrational energy states. (ii). There is a coupling between the radiation and the matter. Now we will explain them separately.

According to the quantum theory, the vibrational energy E_v for simple harmonic oscillator can be expressed as

$$E_v = \left(v + \frac{1}{2}\right) hf = \left(v + \frac{1}{2}\right) a \quad (2.17)$$

Where f is the frequency of the vibration, and it can be expressed as

$$f = \frac{1}{2\pi} \sqrt{\frac{k}{m}}$$

Where k is the chemical bonding force constant, m is the reduced mass for those two atoms with a mass of m_1 and m_2 . The relationship between them are

$$m = \frac{m_1 \cdot m_2}{m_1 + m_2}$$

v in **equation 2.17** is the quantum number, and $v=0, 1, 2, 3, \dots$.

In practice, diatomic molecules are not simple harmonic oscillators, and a more accurate expression for the vibrational energy would be

$$E_v = \left(v + \frac{1}{2}\right) a - \left(v + \frac{1}{2}\right)^2 b, a > b \quad (2.18)$$

Where a and b is constants, the diagram of the energy state for both a harmonic oscillators and diatomic molecules are illustrated in **Figure 8**.

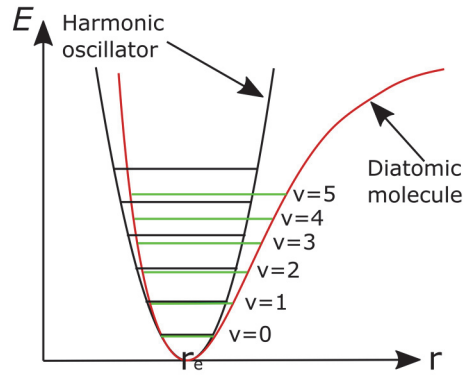


Figure 8. Illustration of vibrational energy state for harmonic oscillators and diatomic molecules.

According to the **equation 2.18**, the jump between two vibrational energy state is

$$h\nu = E_2 - E_1$$

$$\tilde{\nu} = \frac{1}{\lambda} = \frac{E_2 - E_1}{hc} = \frac{1}{hc} \left\{ \left[\left(v' + \frac{1}{2} \right) a - \left(v' + \frac{1}{2} \right)^2 b \right] - \left[\left(v + \frac{1}{2} \right) a - \left(v + \frac{1}{2} \right)^2 b \right] \right\}$$

$$\tilde{\nu} = (v' - v)\omega - (v' - v)(v' + v + 1)x\omega \quad (2.19)$$

Here $\omega = a/hc = f/c$, and $x = b/a$. If we ignore the second part of **equation 2.19**, then

$$\tilde{\nu} = (v' - v)\omega = \Delta v \cdot \omega, \Delta v = 1, 2, 3, \dots$$

$$\tilde{\nu} = \omega, 2\omega, 3\omega, \dots$$

For example, the infrared spectrum of CO molecular have absorption peak located at 4.67, 2.35 and 1.58 μm , the ratio of the countdown for this three wavelength is approximate 1:2:3. Corresponding to the jump between the ground state and the three lowest excited energy state. Another relationship we can obtained from **equation 2.19** is that the vibrational frequency for diatomic molecular depends on the atomic masses and the force constants between them.

Another condition that needs to be fulfilled is the coupling between radiation and matter. In order to satisfy this condition, the molecular vibrations must be accompanied by a change in the dipole moment. The infrared jump is dipole moment induced, i.e., the energy transfer mechanism occurs through the interaction of the dipole moment change caused by the vibrational process and the alternating electromagnetic field. A molecule also shows different polarities, called dipoles, due to the difference in the electronegativity of the atoms that make it up. The dipole moment (μ) of a molecule is usually used to describe the magnitude of the polarity of the molecule. When a dipole

is in an electromagnetic radiation field, the field reverses periodically and the dipole will experience alternating forces that increase or decrease the dipole moment. Because the dipole has a certain original vibration frequency, obviously, only when the radiation frequency and dipole frequency match, the molecule and radiation interaction (vibration coupling) and increase its vibration energy, so that the amplitude increases, that is, the molecule from the original ground vibrational state jump to a higher vibration energy state. Therefore, not all vibrations will produce infrared absorption, only the vibration of the dipole moment change ($\Delta\mu\neq 0$) can cause observable infrared absorption spectrum, the molecule is called infrared active. On the other hand, the molecular where $\Delta\mu=0$ cannot produce infrared vibrational absorption, called infrared inactive.

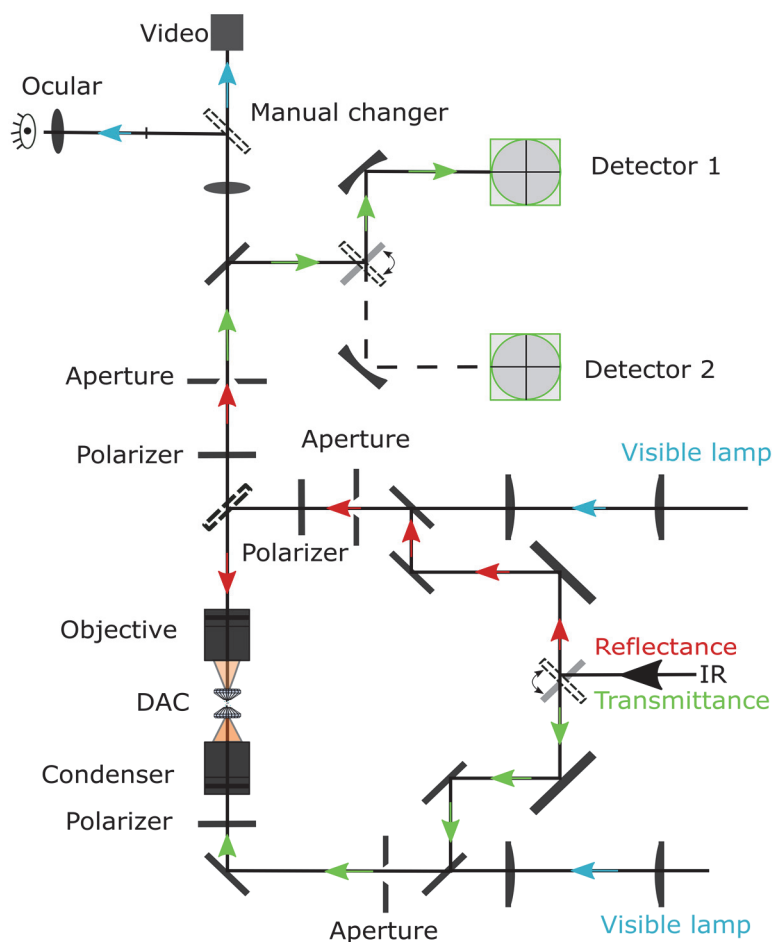


Figure 9. Optical beam path of the microscope used in MIRAS beamline in ALBA synchrotron.

Figure 9 is the beam path of the microscope used in MIRAS beamline in ALBA synchrotron, the DAC is fixed in the sample stage, between the objective and condenser, the sample can be focused to the right position by using the white light from the visible lamp both from the bottom and top of DAC. After the alignment of the DAC and sample, the visible lamp can be turned off, and the infrared light from the synchrotron light source will be input to the microscope. There are two modes for the measurement of infrared microspectroscopy: reflection and transmission. There are two different beam path for reflection and transmission, the infrared light from the bottom of the DAC, and transmitted from the bottom of the sample to the top and then to the detector 1. All the infrared microspectroscopy we measured in this doctoral thesis is in this mode. The infrared light will firstly pass through an empty space in the sample chamber, the spectra of the empty space will be recorded as reference, to eliminate the effect of instrument and DAC on the IR spectra of sample. When using the reflection modes, the infrared light passes through from the top of the DAC and reach to the top of the sample, the infrared light reflected by the top surface of the sample and then to the detector. The infrared microspectroscopy can covering a wavelength ranges from 25000 cm^{-1} to 100 cm^{-1} and the resolution is better than 4 cm^{-1} .

2.5 Optical absorption

According to the energy band theory, the energy band structure usually includes the energy band, the band gap and the case of electron-filled energy band. Among them, the energy band and the band gap depend on the atomic structure and crystal structure of the crystal, and the electron filling is subject to the **least-energy principle** and the **Pauli exclusion principle**. For a semiconductor, the electrons fill exactly some of the lowest energy bands, called the full band, and the topmost full band is called the valence band ($E_V(\mathbf{k})$). The series of energy bands above the valence band is called the empty band, and the lowest energy one is called the conduction band ($E_C(\mathbf{k})$). The energy difference between valence band and conduction band is the band gap (E_g).

$$E_C(\mathbf{k}) = E_C + \frac{\hbar^2 \mathbf{k}^2}{2m_e^*}$$

$$E_V(\mathbf{k}) = E_V - \frac{\hbar^2 \mathbf{k}^2}{2m_h^*}$$

$$E_g = E_C - E_V$$

Where m_e^* , m_h^* are the effective mass of electrons and electron hole.

If the minima of conduction band and the maxima of valence band is at the same point of k -space, then the bandgap is direct. When the electron jump from the valence band to the conduction band, the wave vector k stays unchanged. The energy around Fermi level (E_{CV}) can be expressed as

$$E_{CV} = E_g + \left(\frac{\hbar^2}{2\mu}\right)k^2$$

Where $\mu^{-1} = m_c^{-1} + m_v^{-1}$ is the effective mass, the joint density of state D_j is

$$D_j = \begin{cases} \left[\frac{2^{1/2}\mu^{3/2}}{\pi^2\hbar^3} \right] (E_{CV} - E_g)^{1/2} & \text{when } E_{CV} > E_g \\ 0 & \text{when } E_{CV} < E_g \end{cases}$$

And the dielectric function around bandgap can be expressed as

$$\epsilon_i(\omega) = \begin{cases} Ax^{-2}(x-1)^{1/2} & \text{when } x > 1 \\ 0 & \text{when } x < 1 \end{cases}$$

$$A = \frac{2e^2(2\mu)^{3/2}}{m^2\omega^2\hbar^3} |P_{CV}|^2 E_g^{-3/2}, x = \frac{\hbar\omega}{E_g} \quad (2.20)$$

According to **equation 2.20**, when white light pass through the materials, only the photon with an energy higher than the bandgap energy (E_g) will be adsorbed. The electrons in the valence band maxima will be active to the conduction band minima. ϵ_i^2 , or we could say the square of the absorbance coefficient, have a linear relationship with the energy of the photon. So if we plot the α^2 vs energy (photon) for direct bandgap materials, and fit the absorption part by a linear function, then the intercept of the linear fitting with x -axis is the bandgap energy of the materials.

When the valence band maxima and the conduction band minima are not at the same point in the k -space, when the electrons jump between them, the wave vector will change and the bandgap is indirect. This process is necessarily accompanied by the absorption or emission of phonons through interaction with the lattice.

$$\hbar\omega = E_{CV} \pm E_p$$

where E_p is the energy of phonon.

Around the fermi level of indirect bandgap, the dielectric function has a relationship with the energy of photon as

$$\varepsilon_i(\omega) \propto \begin{cases} (\hbar\omega \mp E_p - E_g)^{1/2} & \text{when } \hbar\omega \geq E_g \pm E_p \\ 0 & \text{when } \hbar\omega \leq E_g \pm E_p \end{cases} \quad (2.21)$$

The jump of the electron in the indirect bandgap is a two-stage process. The first step is that the electron at the top of the valence band absorbs photon energy and jump to a virtual state, and the second part is that the electron moves from the virtual state to the bottom of the conduction band by absorbing or emitting a phonon. As we explained in the direct bandgap, the photon only with an energy higher than the indirect bandgap will be absorbed by the materials when a white light passed through the materials. The square root of the absorbance coefficient has a linear relationship with the energy, and if we plot the square root of the absorbance coefficient vs energy of the light, fitting the absorption part with a linear equation, the intercept of the linear fitting with x -axis is the indirect bandgap of the studied materials.

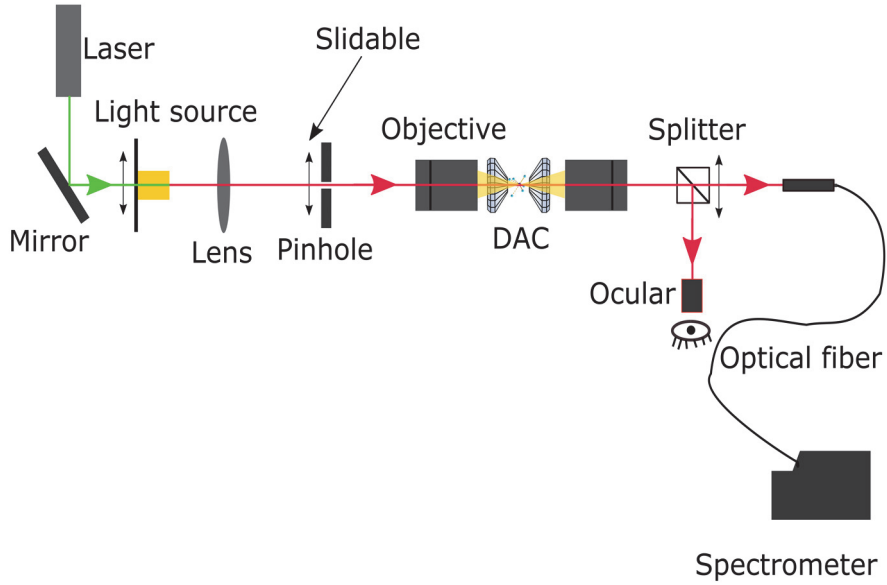


Figure 10. Illustration of the optical absorption experiments set-up.

The optical absorption experiments in this doctoral thesis were conducted in a home-built set-up in University of Valencia. It consisting of a tungsten lamp, fused silica lenses, pinhole, reflecting optics objective (15 \times), and a visible-near IR

spectrometer (Ocean Optics Maya2000 Pro). The loaded DAC was fixed between the two optics objectives, the sample was focused by using the white light and Ocular. The white light was focused on a spot of around 40 μm in diameter. The laser was used to measure the fluorescence of ruby. The sample-in and sample-out method was used to measure the optical absorption spectra of sample under pressure [94]. The intensity transmitted through the sample is normalized to the intensity transmitted through a clear area of the PTM.

3. Crystal structure, atomic vibrations, and electronic band structure of $\text{Fe}(\text{IO}_3)_3$ under pressure

We will start our high pressure study with iron iodates. This study is relevant to investigate the role of the LEP in the crystal structure of metal iodates, how the LEP react to the external pressure and the way it affects the crystal structure of metal iodates. The chemical formula of iron iodate is simple and iron could be a representation of the $3d$ transition metals. In this chapter, the results of the high-pressure X-ray diffraction (HPXRD), High-pressure Raman scattering (HPRS), high-pressure synchrotron based Fourier transform infrared microspectroscopy (HPFTIR), and first-principle calculations on $\text{Fe}(\text{IO}_3)_3$ are reported. From those four diagnostics, we found that $\text{Fe}(\text{IO}_3)_3$ undergoes three isostructural phase transitions (IPTs) at the pressure range of 1.5-2.0, 5.7-6.0, and 15-22 GPa, respectively. The equation of state (EOS) and pressure dependence of the lattice parameter are reported, as well as the pressure dependence of the Raman and infrared phonon frequencies. The reported experimental results will be compared with the value obtained from the theoretical calculations. Meanwhile, the vibration symmetry has been tentatively assigned to the experimentally observed Raman and infrared modes with the help of the theoretical calculations.

In this chapter, the electronic band structure of $\text{Fe}(\text{IO}_3)_3$ was investigated by using the high-pressure optical absorption (HPOA) experiments, high pressure resistivity measurement and first-principle calculations. The bandgap energy of $\text{Fe}(\text{IO}_3)_3$ exhibits a nonlinear reduction, and a bandgap collapse happened at around 24 GPa. The bandgap behavior under pressure have been explained combining theoretical calculations and the resistivity change of $\text{Fe}(\text{IO}_3)_3$ under pressure. Furthermore, by comparing the bandgap energy and the calculated electronic band structure of $\text{Fe}(\text{IO}_3)_3$ with other metal iodates reported in the literature, the first rule for designing wide bandgap metal iodates is established.

3.1 Introduction

By introducing the pressure in the study of the metal iodates, we expected to clarify the

behavior of the crystal structure, LEP in iodine, the atomic vibration and the bandgap energy of $\text{Fe}(\text{IO}_3)_3$ under pressure, and most importantly, the relationship between all these changes. Before our study, only LiIO_3 [95–97], KIO_3 [98] and AgIO_3 [99] have been studied under compression. All of them exhibits totally different behavior under pressure. LiIO_3 was reported to undergo a phase transition at around 4 GPa at the first study [95], but the following research showed that LiIO_3 is stable up to 73 GPa and do not have any phase transition. On the other hand, KIO_3 undergoes two phase transitions at around 7 and 14 GPa, and AgIO_3 exhibits a phase transition at 2.7 GPa and 240 °C.

$\text{Fe}(\text{IO}_3)_3$ crystallizes in a hexagonal structure (space group: $P6_3$, No. 173) at ambient conditions. The crystal structure is shown in **Figure 11**. When view along the c -axis, each iodine is coordinated by three oxygen atoms and form a slightly distorted IO_3 pyramid polyhedron, each iron atom is surrounded by six IO_3 pyramids by sharing one oxygen. When view perpendicular to the c -axis, there is a layered structure formed by IO_3 units, the top of the IO_3 pyramids are aligned to the same direction, and the LEP of iodine are located at the opposite direction of the bottom of the pyramid. In the IO_3 layer, the bond distance between iodine and inlayer oxygen range from 1.8 to 2.0 Å (O1, O2 and O3 in **Figure 11c**), while the bond distance between the iodine and the interlayer oxygen in the neighboring IO_3 layer are range from 2.5 to 3.0 Å (O1', O2' and O3' in **Figure 11c**).

This chapter include three published first-author papers of the author on the study of $\text{Fe}(\text{IO}_3)_3$ [34,100,101]. The first paper was published in March 2020 [100], Wherein the HPXRD and HPFTIR results on $\text{Fe}(\text{IO}_3)_3$ up to 35 GPa were reported, combined with the theoretical calculations on the EOS and vibration modes under pressure. An IPT was found accompanied by a volume collapse, we also found the evidence of the IPT in HPFTIR and the theoretical calculations. The bulk modulus, IR modes assignment, Grüneisen parameter of the IR mode both from experiment and calculation were reported in this paper.

The second paper was published in September 2020 [101], we moved the study of $\text{Fe}(\text{IO}_3)_3$ to the HPRS, combined with the theoretical calculations on the high-pressure phonon dispersion and pressure dependence of elastic constants. We revealed two IPTs of $\text{Fe}(\text{IO}_3)_3$ at the pressure interval of 1.5-2.0 and 5.7-6.0 GPa, respectively. These transitions are extremely subtle and difficult to be detected by HPXRD and HPIR. In the manuscript, the mechanism driven those two IPTs was discussed.

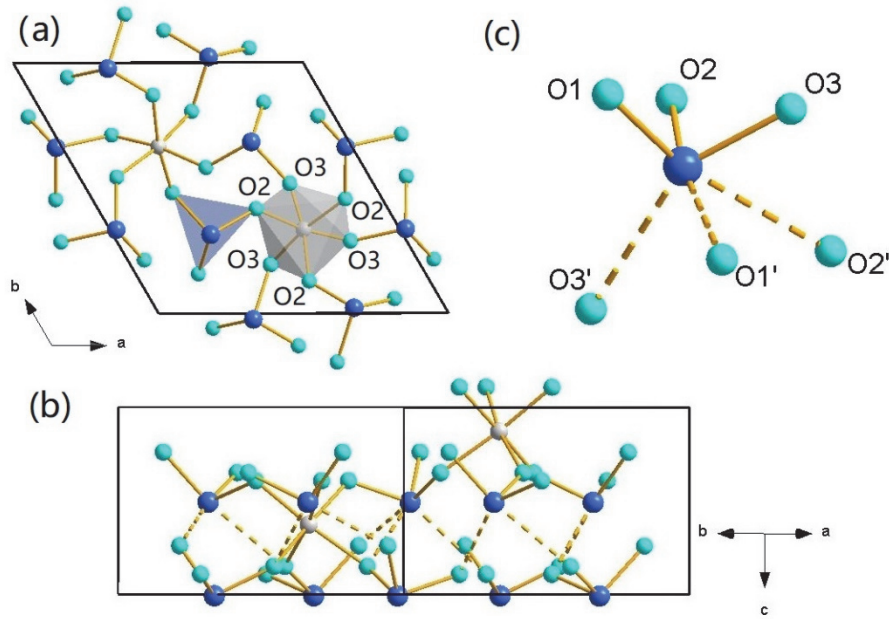


Figure 11. Crystal structure of $\text{Fe}(\text{IO}_3)_3$ at ambient pressure, (a) along the c -axis, (b) perpendicular to the c axis and (c) the detail of the IO_6 polyhedron. In this figure, the gray, blue, and cyan-blue ball represent iron, iodine, and oxygen, respectively. The solid yellow line is the bond formed at ambient pressure, while the dash yellow line is the bond which only formed under pressure. The name of the oxygen shown in (a) and (c) is the same as in Ref. [102]

In the third paper on $\text{Fe}(\text{IO}_3)_3$, which was published in September 2021 [34], reported the HPOA experiment on $\text{Fe}(\text{IO}_3)_3$ up to 25 GPa, and high pressure resistivity measurements up to 40 GPa. The bandgap and resistivity changes of $\text{Fe}(\text{IO}_3)_3$ under pressure have been explained with the help of the calculated electronic band structure and electron-localization function (ELF).

3.2 Experiment and Calculation details

3.2.1 Sample preparation

The sample used in all the studies was prepared with the same methods. $\text{Fe}(\text{IO}_3)_3$ was prepared by reacting $\text{Fe}(\text{NO}_3)_3 \cdot 9\text{H}_2\text{O}$ with NaIO_3 . The solution containing NaIO_3 was heated up to 60 °C, then the solution containing $\text{Fe}(\text{NO}_3)_3 \cdot 9\text{H}_2\text{O}$ was added step by step.

The solution was maintained at 60 °C for two days under vigorous stirring. Finally, the precipitate was recovered by filtration and was dried overnight at 120 °C. The structure and the purity of the synthesized sample was characterized by the powder XRD at ambient conditions, the Rietveld method was used to refine the XRD spectra by using FULLPROF program [103].

3.2.2 HP X-ray Diffraction

A diamond anvil cell (DAC) was used to generate the high pressure environment. Because $\text{Fe}(\text{IO}_3)_3$ have a zeolite structure, and the hole is around 5.0 Å. Therefore, silicone oil was selected as the pressure-transition medium (PTM) in order to avoid that the PTM penetrated into the holes of $\text{Fe}(\text{IO}_3)_3$. The ruby fluorescence method was used as the pressure calibration [93]. HPXRD was performed at the Shanghai Synchrotron Radiation Facility (SSRF, BL15U1 beamline) with a wavelength of 0.6199 Å, the two-dimensional (2D) XRD images were collected with MAR 165 detector, and the 2D images were integrated by using the Dioptas software [104]. The XRD spectra was refined by using the FULLPROF program [103].

3.2.3 HP Infrared spectroscopy

HPFTIR measurements were performed at MIRAS beamline of the ALBA synchrotron [105], a membrane-type of DAC have been used to generate the high pressure environment, and CsI was used as the PTM in this experiment [91]. HPFTIR was performed in the transmission mode by using a masking aperture with a size of 50 $\mu\text{m} \times 50 \mu\text{m}$. A 3000 Hyperion microscope coupled with a Vertex 70 spectrometer (Bruker Optik GmbH, Germany) and a helium-cooled bolometer detector was used to collect the spectra in the 660-100 cm^{-1} Far-IR range with a resolution of 4 cm^{-1} . The Peakfit software was used to analyze the FTIR spectra and the peaks was fitted by the Gaussian functions.

3.2.4 HP Raman scattering

A membrane-type DAC was used to generate the high pressure environment, and

silicone oil was used as the PTM to avoid the hydration of iron iodates. Ruby fluorescence scale was used as the pressure gauge [93]. The sample, PTM and ruby were loaded in the 200- μm hole drilled in the center of gasket, which was pre-indented to a thickness of 40 μm . HPRS measurement was performed in an inVia Renishaw Raman spectroscopy system with a 5 \times magnification objective. The wavelength of the laser used in the experiment is 532 nm and the grating is 2400 lines/mm. The resolution of the spectra is better than 2 cm^{-1} .

3.2.5 HP optical absorption

A membrane-type of DAC with a culet of 500 μm was used to provide the high pressure environment. Polycrystalline was first pressed into a 10 μm -thick platelets with the near-parallel faces by using a DAC. Then the sample, together with the solid PTM (KBr) and ruby pressure gauge [93] were loaded in a 250 μm hole drilled on a stainless-steel gasket, which have been pre-indented to a thickness of 40 μm . The sample-in and sample-out method was used to acquire the HPOA spectra of the sample on a home-built optical setup. It consists of consisting of a tungsten lamp, fused silica lenses, reflecting optics objectives (15 \times), and a visible-near IR spectrometer (Ocean Optics Maya2000 Pro). The intensity $I(\omega)$ transmitted through the sample was normalized to the intensity $I_0(\omega)$ transmitted through a clear area of PTM.

3.2.6 HP resistivity measurement

HP resistivity was performed with the standard four-probe technique by using four platinum leads, the gasket was insulated with a mixture of epoxy and cubic boron nitride, no PTM was used in this experiment and the ruby fluorescence was used to determine the pressure [93]. The resistance was determined by the Van der Pauw method [106].

3.2.7 Overview of calculation

Calculation of total-energy, phonon and electronic band structure were performed within the framework of the density of function (DFT) [107] and the projector-augmented wave method [108,109] as implemented in the Vienna an initio simulations

package (VASP) [110–113]. A plan-wave energy cutoff of 530 eV was used to ensure a high precision in the calculations. The exchange-correlation energy was described within the generalized-gradient approximation (GGA) in the GGA+ U method with the Perdew-Burke-Ernzerhof for solids (PBEsol) [114] due to the presence of Fe atoms on the basis of Dudarev’s method [115], for the calculation, the $U_{\text{eff}}=5.4$ eV. All the structure parameters were obtained at selected optimization volumes, for the calculation of the Raman and Infrared phonons, lattice-dynamic calculations were performed at the zone center of the Brillouin zone (BZ) (Γ point) [116]. The Monkhorst-Pack scheme [117] was employed to discretize the BZ integrations with suitable meshes. The phonon frequency and phonon dispersion curves were calculated by the direct force method and provided by the diagonalization of the dynamical matrix. The elastic constant was calculated by using density functional perturbation theory, and we also can obtain the symmetry and eigenvectors of the modes at Γ point in this calculation. The atomic movement associated with the phonons were visualized by using the J-ICE software [118].

3.3 Results and Discussion

3.4.1 Crystal structure under pressure

Selected XRD profiles of $\text{Fe}(\text{IO}_3)_3$ at different pressures are shown in **Figure 12**. At pressure below than 22.2 GPa, there are no new peaks appearing nor peak splitting. All the peaks shift to the high angle due to the contraction of the crystal structure under compression. The shift of different peaks has a very different rate, which means the crystal structure of $\text{Fe}(\text{IO}_3)_3$ is highly anisotropic. At the pressure of 22.2 GPa and above, some new peaks appear in the XRD spectra which have been indicated with black diamonds, and the new peaks grow in intensity under pressure. These changes in XRD indicate the occurrence of a phase transition. According to our Rietveld refinement reported in our published paper [100], we found that both the XRD before and after the

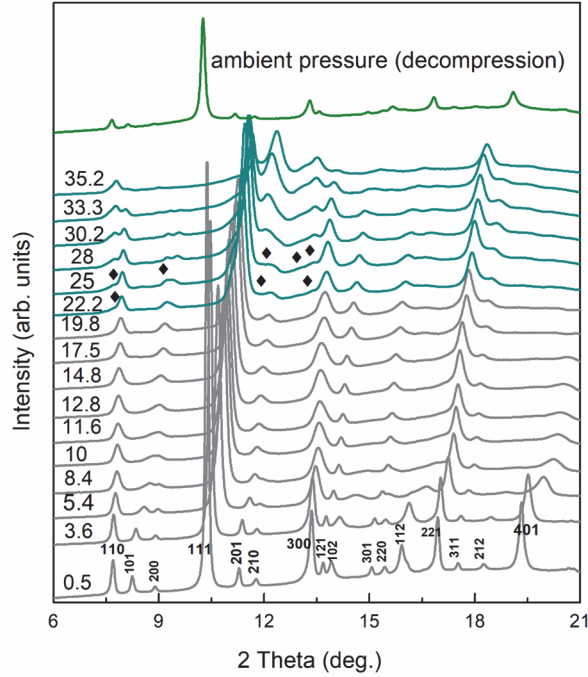


Figure 12. XRD spectra of $\text{Fe}(\text{IO}_3)_3$ at selected pressure. The pressure of each spectra was indicated in the left with the units of “GPa”. different phase was shown in different color and the black diamond indicated the appearance of the new peaks at high pressure.

phase transition can be refined by the same space group ($P6_3$) but with different lattice parameters, which means the phase transition happened at 22.2 GPa is IPT. Our refinement also shown that at pressures higher than 22.2 GPa, the low-pressure phase (LP) and high-pressure phase (HP) coexist until the highest pressure reached in our experiment. To sum up, $\text{Fe}(\text{IO}_3)_3$ undergoes a reversible first-order IPT at 22.2 GPa.

The lattice parameter and unit-cell volume of $\text{Fe}(\text{IO}_3)_3$ was derived from the Rietveld refinement at each pressure. Results are shown in ref. [100], together with that obtained from theoretical calculations. The HP phase exhibits a collapse on the lattice parameter c , and the unit-cell volume by nearly 5 % at 22.2 GPa. On the contrary, the lattice parameter a is enlarged under pressure. The theoretically calculated lattice parameters and unit-cell volume show a similar behavior and they are in a good agreement with the experiments, which supports the IPT we found in the experiment. Furthermore, we found that both from the experiment and calculation, the crystal structure is more compressible in c -axis than along the a - and b -axis, and show a huge anisotropic behavior, owing to the layer structure along c -axis formed by the IO_3 polyhedra. On the other hand, the mixed arrangement of the FeO_6 and IO_3 units along the a - and b -axis resisted more the external compression. By adopting the 3rd Birch-

Murnaghan [119] (BM) equation of state (EOS) for the LP phase and 2nd BMEOS for the HP phase, the bulk modulus of the LP phase is determined to be 55±2 GPa and 36±1 GPa in experiment and calculation, respectively. While the bulk modulus of the HP phase is 73±9 GPa (48±3 GPa) in experiment (calculation). The bulk modulus of LP phase is large than that of α -LiIO₃ (34±3 GPa) [96] and the ambient-pressure phase of KIO₃ (24.3±5 GPa) [98], similar to the bulk modulus of LiZn(IO₃)₃ (55 GPa) [120].

3.4.2 Coordination of iodine under pressure

Based on the fact that the lattice parameters and unit-cell volume of Fe(IO₃)₃ have been described very well by theoretical calculations under pressure, here we analyze the coordination behavior of IO₃ by using the theoretically calculated pressure dependence of the iodine-oxygen bond distances (**Figure 13**). There are two types of iodine-oxygen bond distances as we discussed in the Introduction. The bond between iodine and inlayer oxygen, this kind of bond will slightly expand under compression. Another kind of bond is between iodine and interlayer oxygen, which the bond distance decrease under compression. If we chose the 2.48 Å as the maximum distance for iodine-oxygen bond (25% larger than the shortest I-O bond distance [121]), then the oxygen coordination of iodine in Fe(IO₃)₃ will gradually increase from 3 to 6 under pressure. As the shortening of the bond distances between iodine and the interlayer oxygen, and the existence of the LEP at the top of the IO₃ pyramid which point toward to the neighboring IO₃ layer, iodine favors to form new bonds with the oxygen in the neighboring IO₃ layer (O₁' , O₂' or O₃' in **Figure 11** and **13**). As a consequence, the inlayer oxygen (O₁, O₂ and O₃ in **Figure 11** and **13**) will be pushed away from the iodine, and the bond distance between them becomes larger under compression.

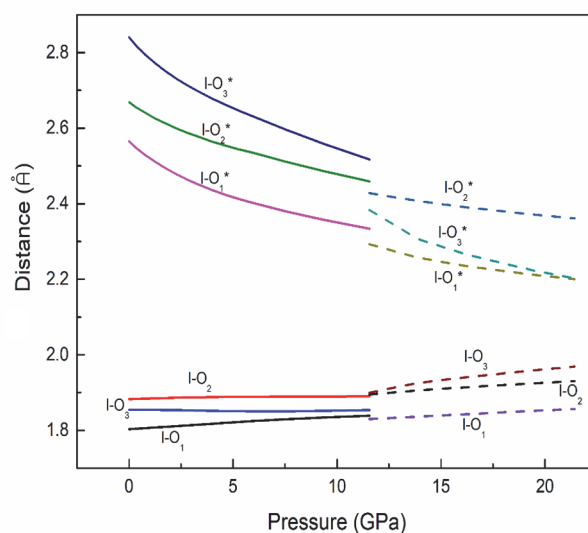


Figure 13. Theoretically calculated bond distance between iodine and oxygen as a function of pressure.

3.4.3 HP Raman spectra

According to the group theory, the structure of $\text{Fe}(\text{IO}_3)_3$ have 39 vibrational modes ($13A+13E_1+13E_2$), including three acoustic modes ($A+E_1+E_2$). Raman spectra of $\text{Fe}(\text{IO}_3)_3$ at selected pressure are shown in **Figure 14**. The Raman spectra at 0.5 GPa, it can be divided into three regions: The high-frequency region ($600\text{-}900\text{ cm}^{-1}$), which is mainly contributed by the stretching of I-O bond, the strongest peak was located in this region at 792 cm^{-1} ; the mid-frequency region, located in the wavenumber between 300 and 500 cm^{-1} , dominated by the bending of I-O bonds; the low-frequency region, which is the mode at the wavenumber below than 200 cm^{-1} . Under compression, the modes at the low- and mid-frequency regions shift to the higher wavenumber. However, most of the modes at high-frequency region soften under pressure, which is due to the enlargement of the I-O bond distance under compression. The pressure-induced mode softening in high-frequency region also results in the closing of the phonon gap between mid- and high-frequency region. No new Raman peaks was detected up to the highest pressure in the experiment and the changes in the Raman spectra under compression is reversible.

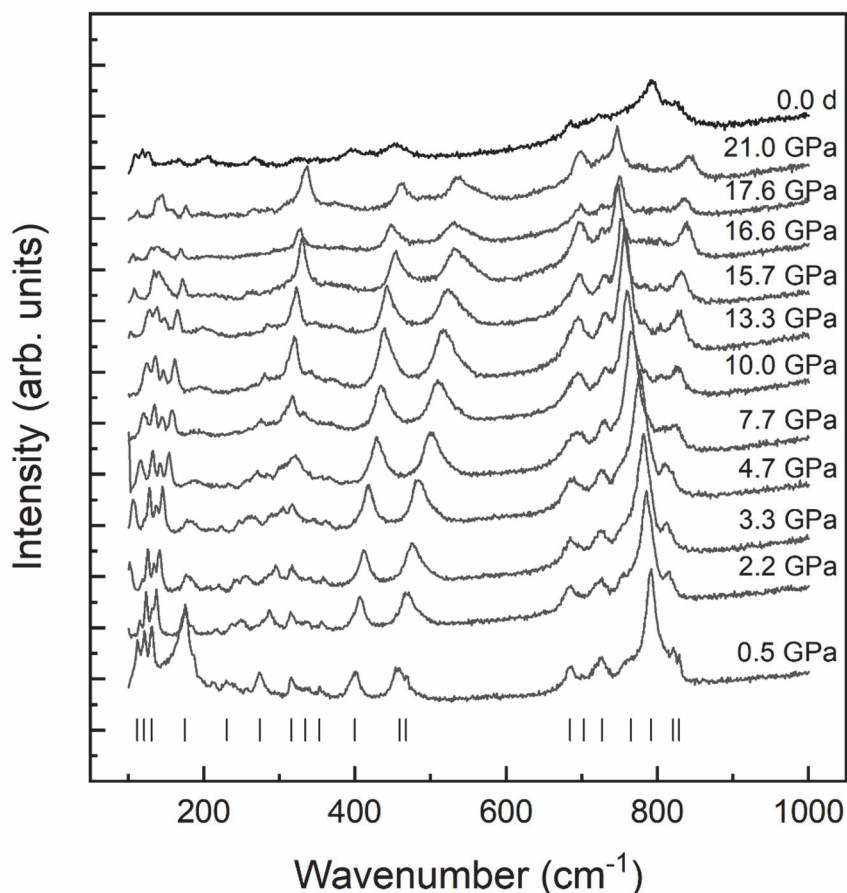


Figure 14. Raman spectra of $\text{Fe}(\text{IO}_3)_3$ at selected pressure, the vertical line at the bottom shows the Raman modes determined for the spectra at 0.5 GPa.

The pressure dependence of the Raman modes under pressure determined both from experiments and calculations is plotted in **Figure 15**. The vibration symmetry of the experimentally observed modes has been assigned, based on the comparison of the frequency at ambient pressure and their pressure coefficient at high pressure with those obtained from DFT calculations. We can find the nonlinear behavior of the modes under pressure both in experiments and calculations. The change of the pressure coefficient was located at around 1.7 and 5.8 GPa, respectively. Indicating the possibility of two subtle IPTs. In order to further confirm the existence of those two IPTs in $\text{Fe}(\text{IO}_3)_3$, we have carefully checked the calculated pressure dependence of the atomic I-O bond distances. Moreover, we have calculated the pressure dependence of the elastic constants and the phonon dispersion at 0, 1.5, 5.7 and 7.5 GPa (can be found in our published paper ref. [101]), the discontinuity found in the calculated pressure

dependence of the interatomic I-O bond distance and elastic constants supports the occurrence of IPTs in $\text{Fe}(\text{IO}_3)_3$. Furthermore, we also found a dynamic instability in the calculated phonon dispersion at 1.5 and 5.7 GPa, and a nonlinear behavior of the full width at half-maximum (FWHM) of phonon 400 and 792 cm^{-1} under high pressure. All these facts provide further evidence of the IPTs. The IPTs we found at 1.5 to 2.0 and 5.7 to 6.0 GPa are triggered by the increase of the oxygen coordination of iodine, which in turn is driven by the decrease of the stereoactivity of the LEP in iodine.

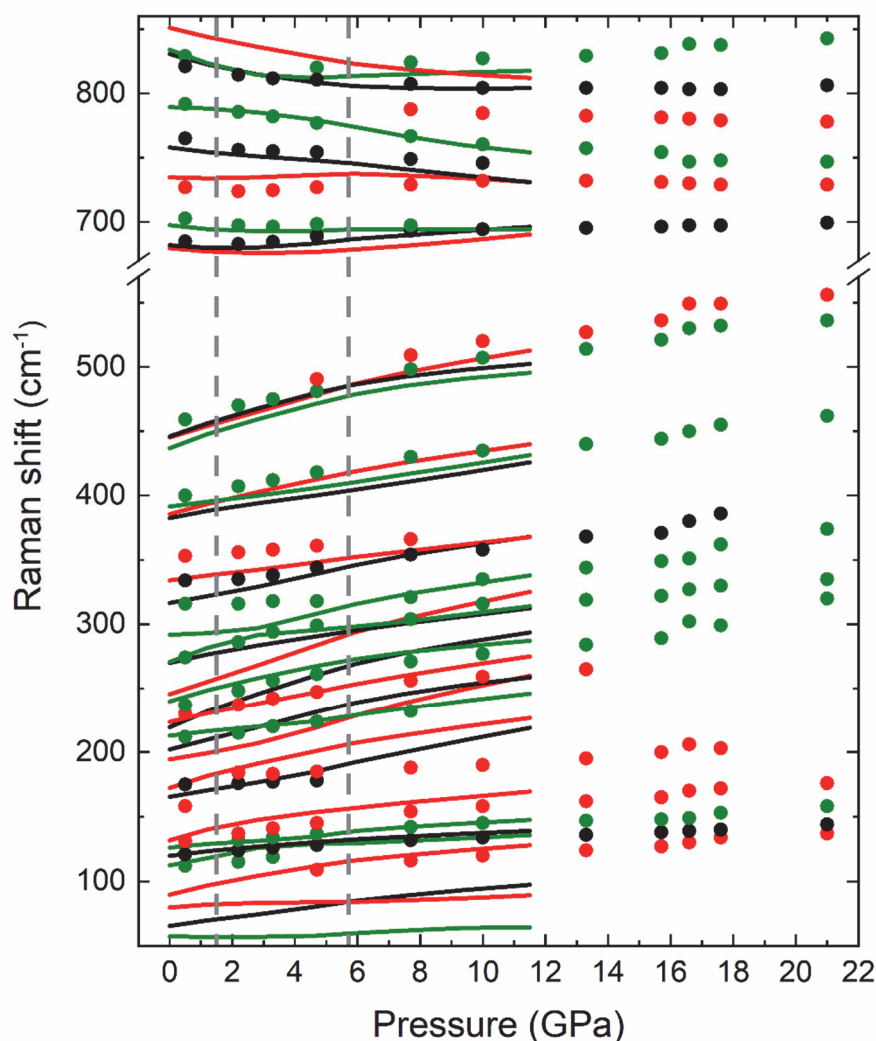


Figure 15. Pressure dependence of the Raman-active modes determined from experiment (symbols) and calculation (solid lines), A, E_1 and E_2 mode are shown in green, black and red, respectively. In order to compare the modes from calculation and experiment, the calculated modes in high-frequency region have been up-shifted by 60 cm^{-1} .

3.4.4 HP infrared spectra

The IR spectra of $\text{Fe}(\text{IO}_3)_3$ at selected pressures are shown in **Figure 16**. According to group theory, the $\text{Fe}(\text{IO}_3)_3$ has, $13A+13E_1$, in total 26 IR-active modes, including 2 acoustic modes ($A+E_1$). 12 IR modes have been detected at ambient pressure and 8 modes have been followed at the pressure below than 15.3 GPa.

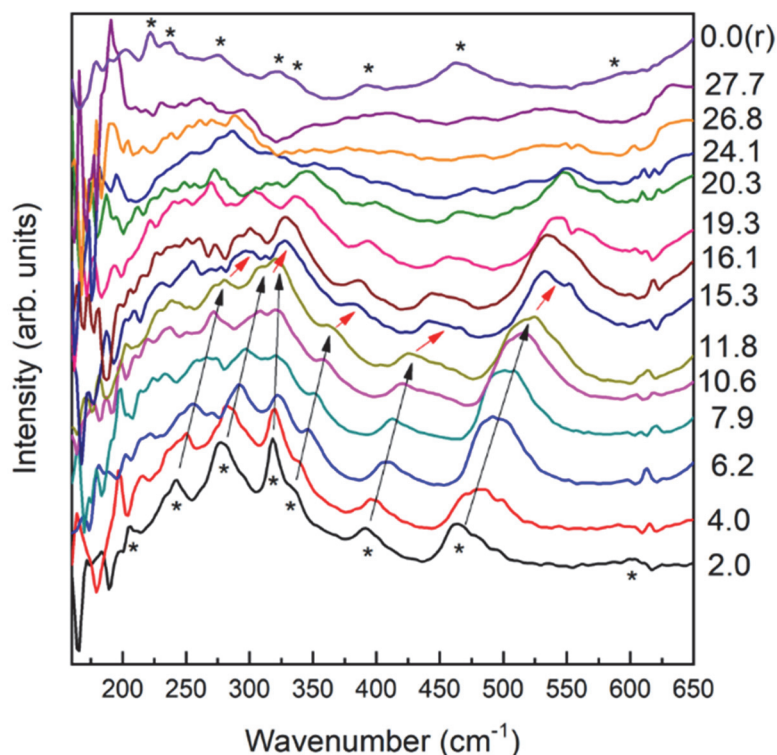


Figure 16. FTIR spectra of $\text{Fe}(\text{IO}_3)_3$ at selected pressure, the pressure of each spectrum were indicted on the right with the units in “GPa”. The top spectra were collected at ambient pressure after the pressure full release. The black arrows show the evolution of the detected IR modes and the red arrows show the abrupt change of the modes at 15.3 GPa.

Below 15.3 GPa, all the IR modes shift to the higher frequency, which is in agreement with Raman modes at the same frequency region. However, there is an abrupt shift of the modes at 15.3 GPa and only 5 modes can be followed at the pressure of 15.3 GPa and above, indicating the emergence of a phase transition. Furthermore, the IR modes also show a different pressure coefficient before and after the phase transition. The phase transition pressure found in the HPFTIR is different from that in

HPXRD (22.2 GPa), may arise from the fact that different PTM was used in those two experiments, silicone oil and CsI, respectively. The non-hydrostatic stresses is different in different PTM, and the non-hydrostaticity in solid CsI is large than that in the liquid silicone oil [122,123]. So here the HPFTIR supplement the vibration modes with the HPRS, also provide further evidence of the IPT we found in HPXRD.

3.4.5 HP electronic band structure

According to the calculated electronic band structure of $\text{Fe}(\text{IO}_3)_3$, the bandgap of $\text{Fe}(\text{IO}_3)_3$ at ambient pressure is indirect (see our published paper ref. [34]). The valence band maxima (VBM) is located at a point (-0.1939, 0.5000, 0.1939) along the Γ -E direction of the description while the conduction band minima (CBM) is located at the Γ high-symmetry point, the calculation predicted bandgap energy of $\text{Fe}(\text{IO}_3)_3$ is 2.5 eV. The calculated density of state (DOS) and projected density of state (PDOS) indicating that the VBM is dominated by O-2*p* orbital, with a small contribution from I-5*s*, 5*p* orbital. The CBM is dominated by the Fe-3*d* state and I-5*p* state, with a small contribution from O-2*p* orbital. We also reported the OA spectra of $\text{Fe}(\text{IO}_3)_3$ at ambient pressure in ref [34]. The experimental bandgap energy, 2.1 eV, was obtained by adopting a Tauc plot which for indirect bandgap energy on the OA spectra. By extrapolating the linear fit of the high-energy part of the $(\alpha h\nu)^{1/2}$ vs $h\nu$ plot to zero [124], where α is the absorption coefficient, h is the Planck constant, and ν is the photon frequency. Moreover, the OA spectra was well fitted by the Urbach empirical rule [125]. As we summarized in **Table 1** in **Chapter 1.3**, $\text{Fe}(\text{IO}_3)_3$ have the smallest bandgap energy reported in the literature for metal iodates, which is due to the fact that partial filled 3*d* state contribute to the CBM and thus narrow the bandgap energy compared with the non-transition or closed shelled transition metal iodates.

The OA spectra and the bandgap energy of $\text{Fe}(\text{IO}_3)_3$ at high pressure up to 25 GPa is shown in **Figure 17**. Here we can found that the calculation overestimated the bandgap energy by around 0.4 eV, but the calculation indeed described the same behavior of the bandgap under pressure when compared with that from the experiment. The OA spectra and the bandgap energy are divided into four regions: In region I and III, the bandgap of the $\text{Fe}(\text{IO}_3)_3$ decrease with the increasing pressure. In region II, the

bandgap of $\text{Fe}(\text{IO}_3)_3$ show an independent behavior with the pressure. There is a bandgap collapse at around 23 GPa in experiment and 13 GPa in theoretical calculation, which we believe is associated with the third IPT happened at 22.2 GPa in HPXRD, accompanied by a 5% collapse in the unit-cell volume. By comparing the OA spectra of $\text{Fe}(\text{IO}_3)_3$ in ref. [34] and the bandgap collecting in the decompression process, we can found that the change in the bandgap energy under pressure is totally reversible, in consistence with the reversibility we found in other diagnostics.

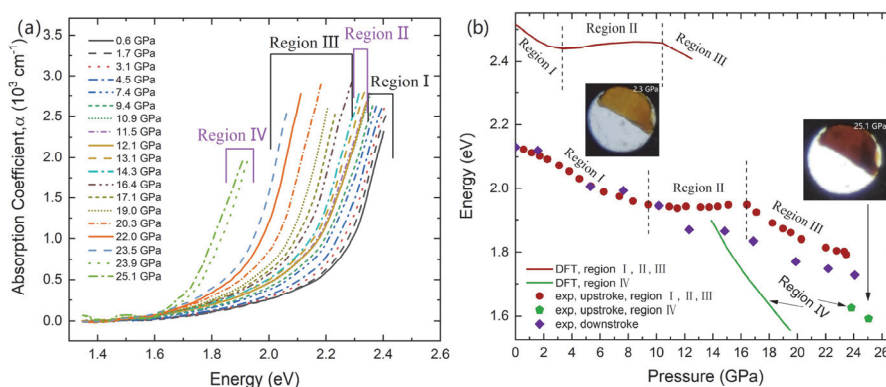


Figure 17. (a) OA spectra of $\text{Fe}(\text{IO}_3)_3$ at selected pressure. According to the shift rate of the absorption edge, the OA spectra can be divided into four regions (region I, II, III and IV). (b) Experimental (symbol) and theoretically calculated (solid lines) bandgap energy of $\text{Fe}(\text{IO}_3)_3$ as a function of pressure, the error of the experimental data is smaller than the symbol, the insert optical micrograph showing the loading of the sample at 2.3 and 25.1 GPa, respectively.

Given the good agreement between calculations and the experiments regarding the bandgap of $\text{Fe}(\text{IO}_3)_3$, we will explain the bandgap behavior of $\text{Fe}(\text{IO}_3)_3$ under pressure by taking advantage of the theoretical calculation. Here we have calculated the pressure dependence of the bond distance and electronic band structure of $\text{Fe}(\text{IO}_3)_3$ under pressure and plotted the atomic character in VBM and CBM in **Figure 18**. As what have been observed from the DOS and PDOS of $\text{Fe}(\text{IO}_3)_3$ at ambient pressure and high pressure, the bandgap energy was strongly affected by the interaction between Fe, I and O (**Figure 18b** and **18c**). So we plotted the calculated pressure dependence of the Fe-O and I-O bond distance in **Figure 18a**. Before the third IPT, the Fe-O bond distance decrease with the increasing pressure. On the contrary, the I-O bond distance (including I-O1 and I-O2) slightly increase with the increasing pressure. In region I, the interaction between Fe and O dominated the bandgap energy over the interaction between I and O

as the atomic character of Fe is much higher than that of I in CBM (**Figure 18b**), the shorten of the Fe-O bond distance increased the hybridization between Fe-3*d* and O-2*p* orbital, this fact favors the narrowing of bandgap, like what observed in other oxides: e. g. PbWO₄ [126] and PbCrO₄ [127]. In region II, according to the calculated atomic character in CBM (**Figure 18b**), the contribution from I-6*p* increase while the Fe-3*d* decrease, because the enlargement of the I-O bond distance. Therefore, the hybridization between iodine and oxygen reduced, so the enlargement of the I-O bond distance favors to open the bandgap, those two affects competed under compression to keep the bandgap energy constant in region II. In region III, once again the contribution from Fe-3*d* in CBM increase and from I-6*p* decrease, so the bandgap starts to decrease in region III. The O-2*p* orbital remains dominant in VBM throughout the pressure interval investigated in our experiment (**Figure 18c**).

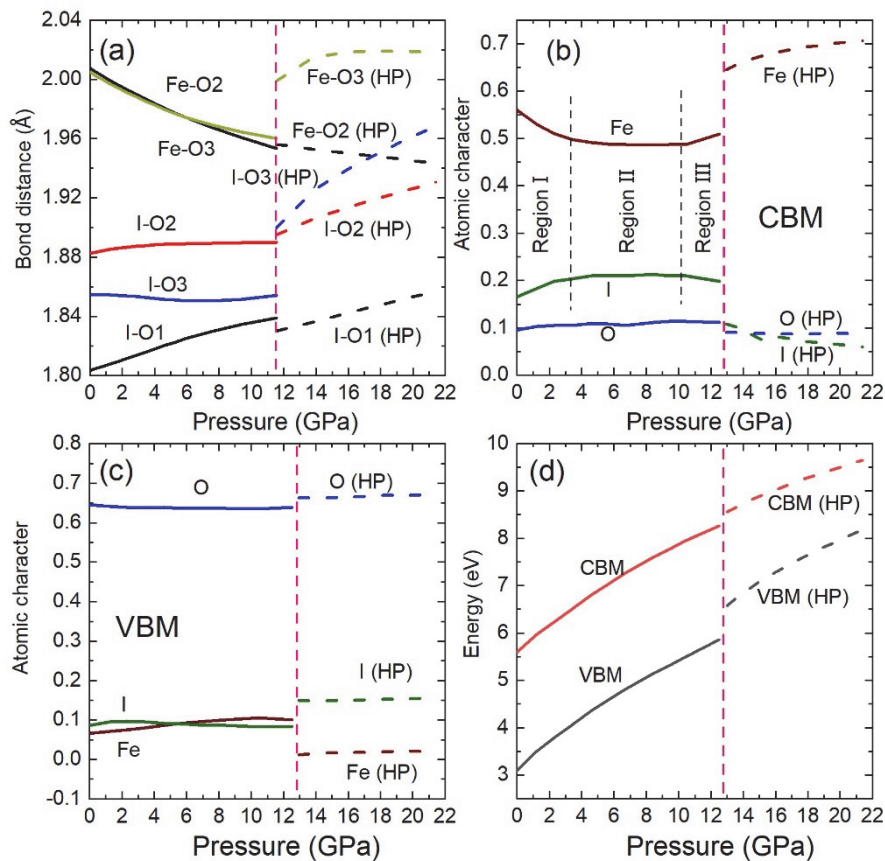


Figure 18. (a) Theoretically calculated pressure dependence of the Fe-O and I-O bond distance. (b) Theoretically calculated atomic character in CBM as a function of pressure. (c) Theoretically calculated atomic character in VBM as a function of pressure. (d) Theoretically calculated pressure dependence of the energy in VBM and CBM.

After the third transition, the unit-cell volume collapse by around 5%, caused the bandgap jump. The contribution from Fe-3d increase a lot in the CBM and that from I-6p decreased. Therefore, after the third IPT, the interaction between Fe and O once again dominated the band gap change, thus the bandgap of Fe(IO₃)₃ expected to decrease linearly under pressure, as what we observed both in experiment and calculation.

3.4.6 HP transport properties

The pressure dependence of the resistivity of Fe(IO₃)₃ is plotted in **Figure 19**. This figure exhibits the measurement results from two different experiment under compression and decompression, and they matched with each other very well. The missing of the resistivity data from both two experiments at the compression process below 3 GPa is probably due to the bad contact between the metal leads and the sample. The resistivity of Fe(IO₃)₃ is around 5 GΩ at low pressure, in consistent with its semiconductor nature [128]. Similar to the bandgap change under pressure, the resistivity of Fe(IO₃)₃ exhibits a nonlinear behavior, and the coefficient change happened at around 6 and 20 GPa, which could be related to the change from region I to region II, and region II to region III found in **Figure 18**. Notice, no PTM was used in the measurement of resistivity, and that for the OA experiment is CsI, the different hydrostatic environment maybe the reason of the different coefficient-change pressure [122]. At 23 GPa, there is an abrupt jump (five orders of magnitude) of the resistivity, which is a consequence of the third IPT found in HPXRD, HPFTIR, HPOA and the theoretical calculation. The resistivity change at the experiment which the highest pressure is up to 30 GPa is fully reversibly, but in the experiment up to 40 GPa, the resistivity change shows a hysteresis of around 10 GPa.

It is reasonable to assume that the decrease of the resistivity results from the exponential increase of the carrier concentration, with activation energy E_A . In the pressure range where the resistivity decrease, we have the following equation

$$\frac{\rho(p)}{\rho(p_0)} \approx \frac{n(p_0)}{n(p)} = e^{\frac{E_A(p) - E_A(p_0)}{KT}}$$

Then the logarithmic pressure coefficient of the resistivity is related to the pressure

coefficient of the activation energy of the carrier concentration. So

$$\frac{d}{dP} \left(\ln \frac{\rho(P)}{\rho(P_0)} \right) = \frac{1}{KT} \frac{dE_A}{dP}$$

By adopting a linear fitting of the resistivity at the pressure range from 22 to 27 GPa, we obtained the pressure coefficient is about -2 GPa^{-1} , then we can get

$$\frac{dE_A}{dP} = KT \frac{d}{dP} \left(\ln \frac{\rho(P)}{\rho(P_0)} \right) \cong -52 \text{ meV/GPa}$$

The pressure coefficient of the activation energy we obtained from this assumption is similar to that obtained from **Figure 17b** by adopting a linear fitting on the green line (-60 meV/GPa). The good agreement suggests that the observed decrease of the measured resistivity in the pressure range between 22 to 27 GPa can correspond to the intrinsic resistivity of the semiconducting high-pressure phase. Here we use a simple Drude model to estimate the pressure dependence of the intrinsic resistivity by

$$\rho(P) = [\sigma(P)]^{-1} = [e(n + p)\mu_{av}]^{-1} = [2en_i\mu_{av}]^{-1} = [2e\sqrt{N_c N_v}\mu_{av}]^{-1} e^{\frac{E_g(P)}{2KT}}$$

$$N_{c,v} = 2.51 \times 10^{19} \left(\frac{m_{c,v}^*}{m_0} \right) \left(\frac{T}{300K} \right)^{\frac{3}{2}} \text{ cm}^{-3}$$

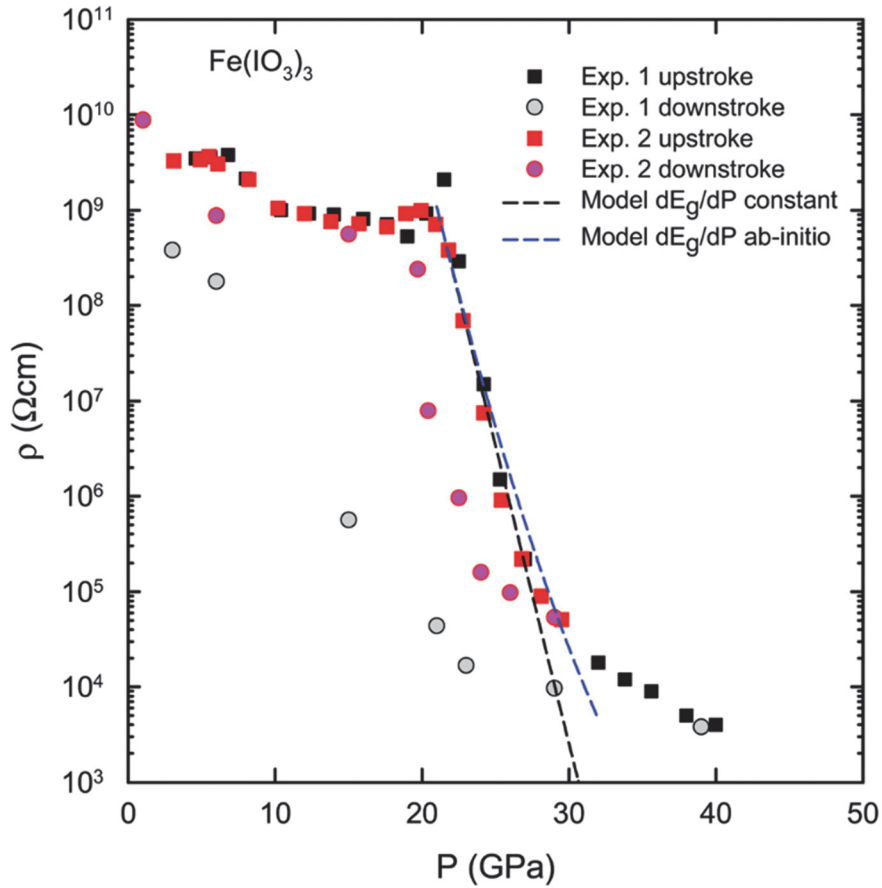


Figure 19. The resistivity of $\text{Fe}(\text{IO}_3)_3$ as a function of pressure acquired from two different experiments in the upstroke and downstroke process. The black and blue dash line are predicted by the model we discussed in the text.

Where e is the electron charge, $n=p=n_i$ is the intrinsic carrier concentration, μ_{av} is the average carrier mobility, N_c (N_v) is the effective density of states in the conduction (valence) band, $m^*_{c,v}$ is the density of states effective mass in the conduction (valence) band, m_0 is the electron mass, and $E_g(P)$ is the bandgap energy. It is reasonable to assume a high carrier mobility since the reproducibility of the resistivity measurement from the two different experiments (**Figure 19**). The black dash line in **Figure 19** have been calculated by assuming $\mu_{av} = 900 \text{ cm}^2\text{V}^{-1}\text{s}^{-1}$, $m^*_{c,v} = 2m_0$, $E_g = 1.6 \text{ eV}$ at the transition pressure, and the pressure coefficient is $dE_g/dP = -60 \text{ meV/GPa}$. The blue dash line has been calculated by using the same parameter as the black line but with a nonlinear pressure dependence of the bandgap calculated from the green line in **Figure 17b**. The experimental and Drude model predicted behavior of the resistivity after the third IPT is in a good agreement (**Figure 19**).

3.4 Conclusions

(1) $\text{Fe}(\text{IO}_3)_3$ undergoes a first-order phase transition at 22.2 GPa based on the HPXRD experiment, accompanied by a 5% collapse in the unit-cell volume. The transition has been further confirmed by the synchrotron based HPFTIR at 15.3 GPa and first-principle calculations at around 11 GPa. (See ref. [100])

(2) $\text{Fe}(\text{IO}_3)_3$ undergoes two IPTs at the pressure interval of 1.5-2.0 and 5.7-6.0 GPa, without any discontinuity on the unit-cell volume. Those two IPTs were characterized by the HPRS and theoretical calculation on the elastic constants and phonon dispersion. The nonlinear behavior of the pressure dependence of the Raman-active mode frequencies, the discontinuity of the theoretically calculated interatomic I-O bond distance and elastic constants, the dynamic instability of the calculated phonon dispersion at 1.5 and 5.7 GPa provide the evidence of the claimed two IPTs in $\text{Fe}(\text{IO}_3)_3$. The two IPTs were triggered by the oxygen coordination increase of iodine under compression. (See ref. [101])

(3) The bulk modulus of $\text{Fe}(\text{IO}_3)_3$ for the LP phase (low-pressure phase, from ambient pressure up to 22.2 GPa) is 55 ± 2 GPa (36 ± 1 GPa) in experiment (calculation), and that for the HP phase (high-pressure phase, from 22.2 GPa up to 35.2 GPa) is 73 ± 9 GPa (48 ± 3 GPa) in experiment (calculation). (See ref. [100])

(4) The crystal structure of $\text{Fe}(\text{IO}_3)_3$ show a huge anisotropic behavior under compression and the c -axis is the most compressible axis. This behavior is related to the layer structure along c -axis formed of IO_3 polyhedral, all the lattice parameters show a discontinuity at the pressure where the third IPT happened. The lattice parameter, unit-cell volume of $\text{Fe}(\text{IO}_3)_3$ determined from experiment and calculation show a good agreement. (See ref. [100])

(5) According to the theoretical calculations, the bond distance between the iodine and the inlayer oxygen slight increase under compression both for LP and HP phase. On the contrary, the bond distance between iodine and the interlayer oxygen decrease under compression. If we chose the 2.48 Å as the maximum bonding distance between iodine and oxygen, then the oxygen coordination of iodine will gradually increase from 3 to 6 fold. (See ref. [100])

(6) In the Raman spectra of $\text{Fe}(\text{IO}_3)_3$ at ambient pressure, the modes with the highest intensity, 792 cm^{-1} , was found in the high-frequency region. Under compression, most

of the Raman modes in the high-frequency region (600-900 cm^{-1}) show a softening behavior, which is due to the enlargement of the bond distance between iodine and inlayer oxygen. (See ref. [101])

(7) According to the calculated electronic band structure, the bandgap of $\text{Fe}(\text{IO}_3)_3$ is indirect, the bandgap of $\text{Fe}(\text{IO}_3)_3$ is 2.1 eV (2.5 eV) obtained from optical absorption experiment (theoretical calculation). $\text{Fe}(\text{IO}_3)_3$ is the metal iodate have the smallest bandgap reported in the literature until now. The VBM is dominated by the O-2*p* orbital, and the CBM is dominated by the Fe-3*d* and I-5*p* state. The first instruction for designing a wide-bandgap metal iodate is avoiding the use of partial filled transition metal. (See ref. [34])

(8) The bandgap energy of $\text{Fe}(\text{IO}_3)_3$ show a nonlinear behavior before the third transition, decrease from 2.1 eV to around 1.8 eV, and show a linear reduction after the third transition. The nonlinear behavior can be explained by the competition between two effects; The pressure-induced shortening of the bond distance between Fe and O will increase the overlap between them and it favors to narrow the bandgap energy. The pressure-induced slightly enlargement of the bond distance between iodine and the inlayer oxygen will decrease the hybridization between them, and it favors to open the bandgap. The bandgap collapse happened at around 23 GPa (13 GPa) in experiment (calculation) which is believed to be triggered by the unit-cell collapse at the third transition. (See ref. [34])

(9) The resistivity of $\text{Fe}(\text{IO}_3)_3$ first show a nonlinear behavior, corresponding to the nonlinear behavior of the bandgap, and then show a linear reduction at the pressure range from 20 GPa to 30 GPa by five orders of magnitude. By using a simple Drude model to reproduce the resistivity at the HP phase, we found the pressure dependence of the resistivity in the HP phase is due to the exponential increase of the intrinsic carrier concentration. (See ref. [34])

(10) The changes in the HPXRD, HPRS, HPFTIR, HPOA spectra and the resistivity of $\text{Fe}(\text{IO}_3)_3$ up to 35 GPa is reversible. (See ref. [34,100,101])

3.5 Author Contribution

The author of this doctoral thesis is the first author of all the three published papers, which are the main content of this chapter. The experiment including, HPFTIR, HPRS,

HPOA spectra were conducted by the author. Daniel Errandonea supervised the studied project. The author analyzed all the experiment data. The author and Daniel Errandonea wrote the manuscript which was revised by all the co-authors. HPXRD, HP resistivity measurements were conducted by Saqib Rahman and Hajra Saqib. The sample used in the experiment was synthesized by Gwilherm Nénert. The theoretical calculations were conducted by Placida Rodriguez-Hernandez and Alfonso Muñoz. Francisco Javier Manjón provide the help in the HPRS experiment and the discussion on the Raman results. Ibraheem Yousef and Catalin Popescu provide the help in the synchrotron-based HPFTIR experiment. Alfredo Segura provide support to the analysis on the resistivity behavior.

A. Liang, S. Rahman, H. Saqib, P. Rodriguez-Hernandez, A. Munoz, G. Nenert, I. Yousef, C. Popescu, and D. Errandonea, First-Order Isostructural Phase Transition Induced by High Pressure in $\text{Fe}(\text{IO}_3)_3$, *J. Phys. Chem. C* **124**, 8669 (2020).

A. Liang, S. Rahman, P. Rodriguez-Hernandez, A. Muñoz, F. J. Manjón, G. Nenert, and D. Errandonea, High-Pressure Raman Study of $\text{Fe}(\text{IO}_3)_3$: Soft-Mode Behavior Driven by Coordination Changes of Iodine Atoms, *J. Phys. Chem. C* **124**, 21329 (2020).

A. Liang, P. Rodríguez-Hernandez, A. Munoz, S. Raman, A. Segura, and D. Errandonea, Pressure-Dependent Modifications in the Optical and Electronic Properties of $\text{Fe}(\text{IO}_3)_3$: The Role of Fe 3d and I 5p Lone-Pair Electrons, *Inorg. Chem. Front.* **8**, 4780 (2021).

First-Order Isostructural Phase Transition Induced by High Pressure in $\text{Fe}(\text{IO}_3)_3$

Akun Liang, Saqib Rahman, Hajra Saqib, Placida Rodriguez-Hernandez, Alfonso Muñoz, Gwilherm Nénert, Ibraheem Yousef, Catalin Popescu, and Daniel Errandonea*

Cite This: *J. Phys. Chem. C* 2020, 124, 8669–8679

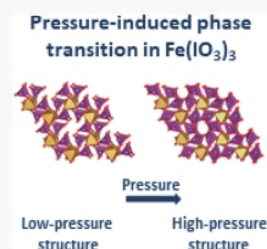
Read Online

ACCESS |

Metrics & More

Article Recommendations

ABSTRACT: The high-pressure (HP) behavior of $\text{Fe}(\text{IO}_3)_3$ was studied up to 35 GPa using powder X-ray diffraction, infrared micro-spectroscopy, and *ab initio* density-functional theory calculations. $\text{Fe}(\text{IO}_3)_3$ shows a pressure-induced structural phase transition at 15–22 GPa. Powder X-ray diffraction was employed to obtain the structure of the HP phase. This phase can be described by the same space group ($P6_3$) as the low-pressure phase but with a substantial different c/a ratio. This conclusion is supported by our computational simulations. The discovered phase transition involves a large volume collapse and a change in the coordination polyhedron of iodine, being a first-order transition. It also produces substantial changes in the infrared and Raman vibrational spectra. The pressure dependences of infrared and Raman phonon frequencies and unit-cell parameters have been obtained. A mode assignment is proposed for phonons based upon *ab initio* calculations. The bulk modulus of the two phases was obtained by fitting a Birch–Murnaghan equation of state to synchrotron X-ray powder diffraction data resulting in $B_0 = 55(2)$ GPa for the low-pressure phase and $B_0 = 73(9)$ GPa for the HP phase. Calculations gave $B_0 = 36(1)$ GPa and $B_0 = 48(3)$ GPa for the same phases, respectively. The results are compared with other iodates, in particular LiIO_3 , for which we have also performed density-functional theory calculations. A possible mechanism driving the observed phase transition will be discussed.



INTRODUCTION

The family of metal iodates has been extensively studied at ambient pressure because of their dielectric, magnetic, or nonlinear optical properties.¹ Many of them have been also studied for the reason that they are superionic conductors.² Such properties make them excellent barocaloric materials, very promising for the development of ecofriendly solid-state cooling technologies.³ On the other hand, numerous iodates are fascinating because they have IO_3 units with lone-pair orbitals,⁴ which give materials particular characteristics.⁵

High-pressure (HP) research is known to be an efficient tool to determine the characteristics of materials.⁶ In general, HP reduces the interatomic distances in materials in a controlled manner, which results in significant changes of the physical and chemical characteristics.⁶ The discoveries in HP research include multiple structural phase transitions which trigger interesting phenomena like metallization or superconductivity.^{6,7} Among iodates, only LiIO_3 ,^{8–10} KIO_3 ,¹¹ and AgIO_3 ¹² have been studied under compression. In a first study on LiIO_3 ,⁸ it was proposed that a HP phase would exist beyond 4 GPa. In a subsequent work, it has been found that no phase transition takes place up to 23 GPa.⁹ More recently, studies have been extended up to 73 GPa, but no new phase of LiIO_3 has been found.¹⁰ In contrast, KIO_3 shows a very different behavior, with phase transitions around 7 and 14 GPa.¹¹ On the other hand, in AgIO_3 ,¹² a new phase was obtained at 2.7 GPa by heating above 240 °C. These facts suggest that the HP

behavior of metal iodates can be extremely complex and should be further studied for a better understanding of the HP behavior of this family of compounds.

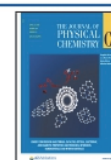
In this work, we will study $\text{Fe}(\text{IO}_3)_3$. The interest on this compound comes not only from the facts described above, but also from the circumstance that its crystal structure (shown in Figure 1) contains zeolitic-like channels, which could lead to an interesting HP behavior.¹³ The crystal structure of $\text{Fe}(\text{IO}_3)_3$ is described by space group $P6_3$.¹⁴ It consists of FeO_6 octahedral units connected by iodine atoms, each of which is coordinated by three oxygen atoms in a trigonal pyramidal geometry with nonbonding lone-pair orbitals (see Figure 1).¹⁴ Such a characteristic makes the HP behavior of compounds interesting and unpredictable.¹⁵ In addition, the crystal structure of $\text{Fe}(\text{IO}_3)_3$ is isomorphic to the structure of $\text{Cr}(\text{IO}_3)_3$, $\text{Sc}(\text{IO}_3)_3$, and other iodates.¹⁶ This makes the results obtained from $\text{Fe}(\text{IO}_3)_3$ useful to make predictions on the HP behavior of other iodates.

In order to characterize the HP behavior of $\text{Fe}(\text{IO}_3)_3$, we performed synchrotron powder X-ray diffraction (XRD) and

Received: March 9, 2020

Revised: March 28, 2020

Published: March 29, 2020



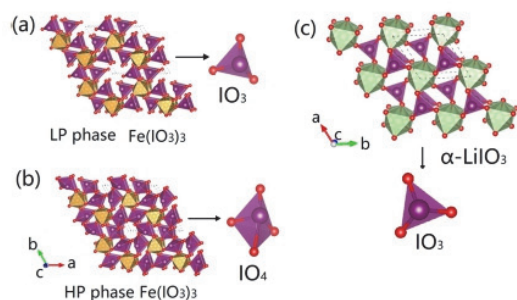


Figure 1. Crystal structure of low-pressure and HP structures of $\text{Fe}(\text{IO}_3)_3$. Both described by space group $P6_3$. FeO_6 octahedra are shown in yellow and the coordination polyhedra of I atoms in purple. There is a coordination change at the phase transition. The zeolitic channels along the c -axis can be identified in the figure. The crystal structure of LiIO_3 is also shown. In this case, LiO_6 octahedra are shown in green.

Fourier transform infrared (FTIR) microspectroscopy measurements, which have been combined with density-functional theory (DFT) calculations. This is the first time that these techniques are used combined to study the HP behavior of an iodate. In the next section, we will provide technical details of our studies and report evidence of the existence of a first-order isostructural phase transition, which triggers a coordination change of iodine atoms and substantial changes in phonons. The behavior of $\text{Fe}(\text{IO}_3)_3$ will be discussed in comparison with the behavior of other iodates under compression.

METHODS

Sample Preparation. The $\text{Fe}(\text{IO}_3)_3$ sample was prepared by reacting $\text{Fe}(\text{NO}_3)_3 \cdot 9\text{H}_2\text{O}$ with NaIO_3 . An excess of $\text{Fe}(\text{NO}_3)_3 \cdot 9\text{H}_2\text{O}$ was used to insure the displacement of the reaction equilibrium. A solution containing NaIO_3 was heated up at 60°C with stirring and a solution of $\text{Fe}(\text{NO}_3)_3 \cdot 9\text{H}_2\text{O}$ was added step by step. Then, the solution was allowed to mature for 2 days at 60°C still under vigorous stirring. The precipitate was recovered by filtration and was dried overnight at 120°C . Characterization of the as-prepared sample was done by powder XRD using an Empyrean diffractometer from Malvern Panalytical, equipped with a Bragg–Brentano^{HD} setting, using cobalt radiation ($\lambda = 1.789007 \text{ \AA}$), and a Bragg–Brentano geometry. A Rietveld refinement was carried

out using the HighScore suite.¹⁷ The XRD pattern of $\text{Fe}(\text{IO}_3)_3$ and final Rietveld refinement, assuming the crystal structure reported in the literature¹⁴ (space group c), are shown in Figure 2. The matching of the refinement to the experiment is very good. The derived unit-cell parameters are $a = 9.2476(4) \text{ \AA}$ and $c = 5.2326(2) \text{ \AA}$ and the atomic coordinates are reported in Table 1. They agree with the literature.¹⁴ No impurities or minor phases were detected by XRD.

Table 1. Comparison of the Calculated Crystal Structure (Space Group $P6_3$) at Ambient Pressure With Our and Previous Experiments^a

		$a = 9.2476(4) \text{ \AA}$	$c = 5.2326(2) \text{ \AA}$	
this work (exp)		$a = 9.19 \text{ \AA}$	$c = 5.22 \text{ \AA}$	
ref 14		$a = 9.2318(8) \text{ \AA}$	$c = 5.2297(5) \text{ \AA}$	
ref 1		$a = 9.18767 \text{ \AA}$	$c = 5.116 \text{ \AA}$	
this work (DFT)				
atom		x	y	z
Fe(2b)	this work (exp)	0.3333	0.6667	0.625(1)
	ref 14	0.3333	0.6667	0.6387(32)
	ref 1	0.3333	0.6667	0.628(3)
	this work (DFT)	0.3333	0.6667	0.61799
I (6c)	this work (exp)	0.3166(1)	0.9790(3)	0.008(1)
	ref 14	0.3128(3)	0.9779(3)	0
	ref 1	0.3151(2)	0.9782(2)	0.008(2)
	this work (DFT)	0.31703	0.97579	0.00755
O1(6c)	this work (exp)	0.833(2)	0.074(2)	0.223(3)
	ref 14	0.8240(35)	0.0435(34)	0.2414(81)
	ref 1	0.842(2)	0.057(2)	0.241(4)
	this work (DFT)	0.84206	0.07016	0.26332
O2(6c)	this work (exp)	0.589(2)	0.136(2)	0.348(3)
	ref 14	0.5785(39)	0.1266(36)	0.3444(85)
	ref 1	0.583(2)	0.128(2)	0.351(4)
	this work (DFT)	0.57323	0.1251	0.33887
O3(6c)	this work (exp)	0.199(2)	0.717(2)	0.386(2)
	ref 14	0.1967(36)	0.7156(38)	0.3994(64)
	ref 1	0.194(2)	0.712(2)	0.393(3)
	this work (DFT)	0.18927	0.71706	0.3866

^aThe table includes the unit-cell parameters and atomic coordinates of $\text{Fe}(\text{IO}_3)_3$ as derived from the Rietveld refinement.

HP X-ray Diffraction. HP angle-dispersive powder XRD experiments were performed at room-temperature (RT) employing a diamond-anvil cell (DAC). As metal iodates can

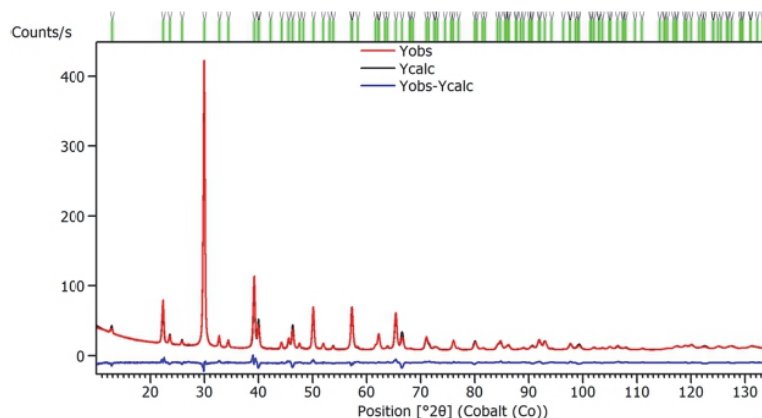


Figure 2. Rietveld refinement of $\text{Fe}(\text{IO}_3)_3$ corresponding to ambient pressure with statistics $R_{\text{wp}} = 4.1$ (space group $P6_3$, cell parameters $a = 9.2476(4) \text{ \AA}$ and $c = 5.2326(2) \text{ \AA}$). Ticks indicate the positions of reflections.

be hydrated, in order to avoid the influence of water absorption in the HP behavior,¹⁸ silicone oil was used as the pressure-transmitting medium (PTM),¹⁹ which is quasi-hydrostatic up to 12 GPa, but has been used previously as a pressure medium up to 64 GPa.²⁰ Beyond 20 GPa, silicone oil is in fact superior to other PTM-like alcohol mixtures.¹⁹ The ruby fluorescence method was employed for pressure calibration.²¹ The accuracy of pressure measurements was 0.05 GPa. The experiments were performed at the Shanghai Synchrotron Radiation Facility (SSRF, BL15U1 beamline) using an X-ray wavelength of 0.6199 Å. Two-dimensional (2D) XRD images were collected with a MAR 165 detector. The 2D images were integrated using the Dioptas software.²² The structural analysis was carried out using PowderCell²³ and FULLPROF.²⁴

HP Infrared Spectroscopy. HP FTIR microspectroscopy measurements were performed at MIRAS beamline of the ALBA synchrotron light source. The sample was loaded in a DAC equipped with IIAC-diamonds. In these experiments, CsI²⁵ was used as the PTM because of its transparency in the Far-IR frequency domain and the ruby scale was used for pressure determination (0.05 GPa accuracy).²¹ Synchrotron-based FTIR-microspectroscopy data were recorded in the transmission mode of operation using a masking aperture size of 50 $\mu\text{m} \times 50 \mu\text{m}$. The beam current inside the synchrotron ring was 250 mA. The measurements were performed using a 3000 Hyperion microscope coupled to a Vertex 70 spectrometer (Bruker Optik GmbH, Germ/any). The microscope was equipped with a helium-cooled bolometer detector optimized for operation in a range covering the far-infrared spectral region. A Mylar beam splitter was used in the spectrometer. Spectra were collected using a 15 \times Schwarzschild magnification objective coupled to a 15 \times Schwarzschild magnification condenser. Single-point measurements at each pressure value were collected using OPUS 7.5 (Bruker Optik GmbH, Germany) in the 660–100 cm^{-1} Far-IR range with a 4 cm^{-1} spectral resolution and 256 co-added scans per spectrum. The analysis of FTIR results was performed using PeakFit. The background was subtracted using the automatic baseline feature and the peaks were fitted using Gaussian functions. Within the experimental resolution, this treatment should not influence the peak positions.

DFT Calculations. Calculations of the total energy were performed within the framework of the DFT²⁶ and the projector-augmented wave^{27,28} method as implemented in the Vienna ab initio simulations package (VASP).^{29–32} A plane-wave energy cutoff of 530 eV was used to ensure a high precision in our calculations. The exchange–correlation energy was described within the generalized gradient approximation (GGA) in the GGA + U method with the Perdew–Burke–Erzerhof for solids (PBEsol).³³ The GGA + U was used to account for the strong correlation between the electrons in the d shell, on the basis of Dudarev’s method.³⁴ In this method, the Coulomb interaction U and the onsite exchange interaction J^{H} are treated together as an U_{eff} . For our calculations, we employed $U_{\text{eff}} = 5.4$ eV. Similar values were previously used with success in the study of other iron compounds.^{35–37} To ensure the quality of the chosen U_{eff} value, we calculated the dependence of the phase transition as a function of the U_{eff} in a range from 3 to 7 eV. The Monkhorst–Pack scheme³⁸ was employed to discretize the Brillouin zone (BZ) integrations with suitable meshes.

This procedure achieves very high convergences of 1 meV per formula unit in the total energy. In the optimized configurations, the forces are lower than 2 meV/Å per atom in each of the Cartesian directions and the deviation of the stress tensor from a diagonal hydrostatic form is less than 1 kbar. All the structural parameters were obtained at selected optimized volumes.

To study the Raman and infrared phonons, lattice-dynamics calculations were performed at the zone center (Γ point) of the BZ using the direct method.³⁹ The frequencies of the normal modes are provided by the diagonalization of the dynamical matrix. These calculations also allow us to identify the symmetry and eigenvectors of the phonon modes at the Γ point.

RESULTS AND DISCUSSION

HP Phase Transition. Before discussing the HP results, we will comment on the description of the crystal structure at

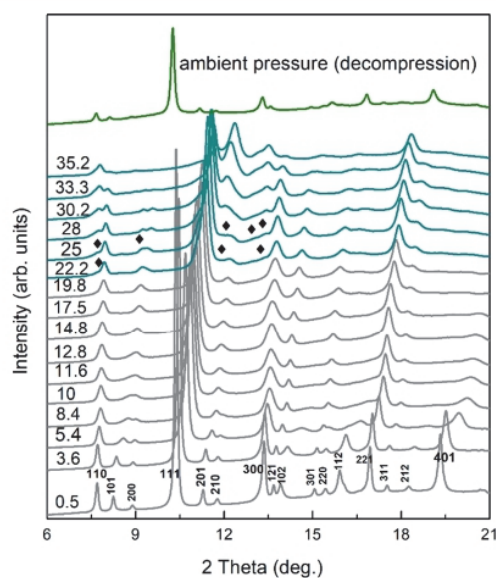


Figure 3. Selection of XRD patterns measured at different pressures, which are indicated in GPa in the figure. Black diamonds indicate the appearance of peaks of the HP phase.

ambient pressure (described by space group $P6_3$) obtained from our DFT calculations. The optimized unit-cell parameters are shown in Table 1 together with the calculated atomic positions. It can be seen that there is a close agreement of calculations with the experimental results, both for lattice parameters and atomic positions. The calculations give a good description of the crystal structure, underestimating the unit-cell volume by only 3%. Such a small difference is typical of DFT calculations being caused by an underestimation of the cohesion energy.^{40,41}

We will start now discussing the HP results. A selection of XRD patterns measured under pressure are summarized in Figure 3. At the lowest pressure measured in the DAC (0.5 GPa), the XRD pattern corresponds to the known-crystal structure of $\text{Fe}(\text{IO}_3)_3$ (space group $P6_3$). This is confirmed by structural refinements. The results of the refinements are shown in Figure 4. Under compression, up to 19.8 GPa, the changes in the XRD patterns are limited to the shift of peaks toward higher angles because of the contraction of the unit cell.

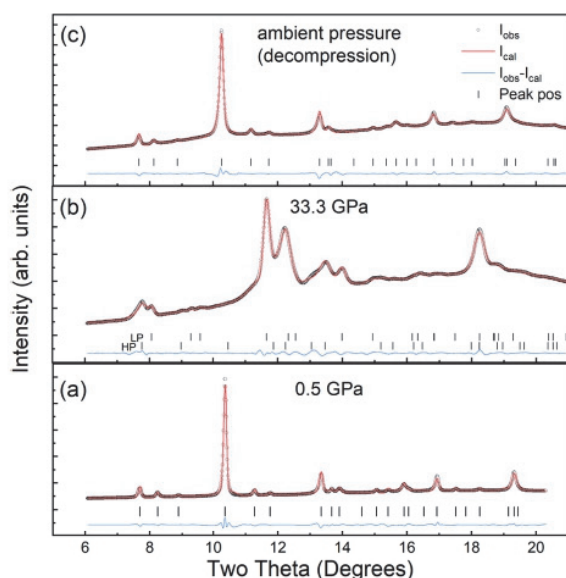


Figure 4. Typical refinements of XRD patterns measured for the low-pressure and HP phases (both described to space group $P6_3$) with the Rietveld method. The pressures are indicated in GPa in the figure. At 33 GPa, the phase coexistence can be seen.

Table 2. Calculated Crystal Structure of the LP Phase ($P6_3$) at 11.6 GPa and HP Phase ($P6_3$) at 22 GPa^a

low-pressure phase			
$a = 9.072 \text{ \AA}$, $c = 4.293 \text{ \AA}$ (DFT at 11.6 GPa)			
$a = 9.067(2) \text{ \AA}$, $c = 4.659(1) \text{ \AA}$ (XRD at 11.6 GPa)			
atom	x	y	z
Fe (2b)	0.3333	0.6667	0.6391
I (6c)	0.3148	0.9930	0.0484
O1 (6c)	0.8284	0.0433	0.2179
O2 (6c)	0.5779	0.1166	0.3583
O3 (6c)	0.1965	0.7240	0.3648
high-pressure phase			
$a = 9.276 \text{ \AA}$, $c = 3.570 \text{ \AA}$ (DFT at 22 GPa)			
$a = 9.159(2) \text{ \AA}$, $c = 3.959(1) \text{ \AA}$ (XRD at 22.2 GPa)			
atom	x	y	z
Fe (2b)	0.3333	0.6667	0.5702
I (6c)	0.3171	-0.0124	0.1335
O1 (6c)	0.8481	0.0658	0.2775
O2 (6c)	0.6012	0.1194	0.3004
O3 (6c)	0.1772	0.7239	0.3009

^aExperimental unit-cell parameters are also shown.

All the patterns up to 19.8 GPa can be explained by the ambient-pressure crystal structure with the corresponding change of unit-cell parameters. At 22.2 GPa, additional peaks (denoted by black diamonds in Figure 3) can be seen in the XRD patterns. These peaks gradually grow in intensity as the pressure increases at the same time that more additional peaks become evident. In parallel, the peaks assigned to the ambient-pressure phase become weaker. All these facts indicate the occurrence of a phase transition, which is also supported by our FTIR experiments, which detected the transition at 15 GPa and by DFT calculations. Our computing simulations found at 12 GPa, during the optimization of the crystal structure, that the structure of $\text{Fe}(\text{IO}_3)_3$ “spontaneously” suffers an abrupt change of the c/a axial ratio and a volume collapse of nearly

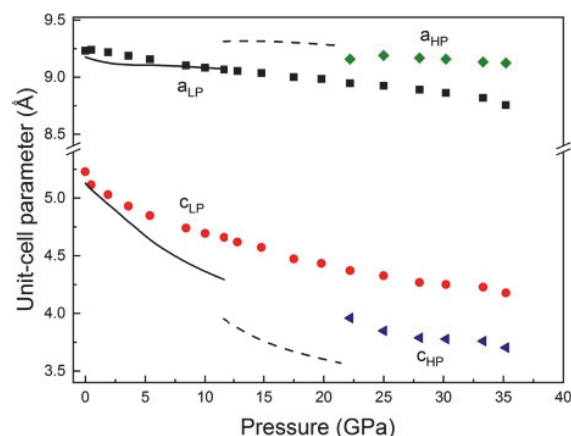


Figure 5. Pressure dependence of unit-cell parameters. Lines are from calculations and symbols from experiments. Experimental errors are smaller than the symbol size.

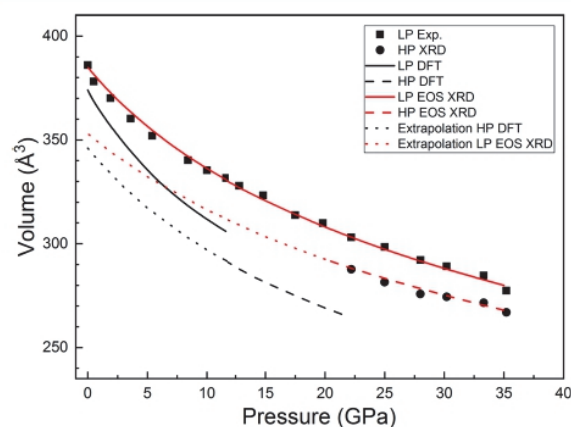


Figure 6. Pressure dependence of unit-cell volume. Black lines are from calculations and symbols from experiments. The red lines represent the EOS fits using the Birch–Murnaghan EOS described in the text. The dotted lines are the extrapolations to ambient pressure of the results of the HP phase. Experimental errors are smaller than the symbol size.

5% when compared with the low-pressure phase at the same pressure. This “spontaneous” evolution of the crystal structure could be interpreted as the occurrence of an isostructural phase transition to a HP phase, which is described by the same space group, $P6_3$, than the low-pressure phase. The new phase remains stable up to the highest pressure achieved in our studies. The structural information of the HP phase is given in Table 2. In this table, we also include structural information of the low-pressure phase at 11.6 GPa. Comparing the results at ambient pressure, with those of the low-pressure phase at 11.6 GPa and the HP phase at 22 GPa, it can be seen that pressure modifies not only the unit-cell parameters but also the atomic positions. All of them change gradually in the low-pressure phase, but the structural parameters undergo a discontinuous change at the phase transition.

The structural change found by calculations is related to the formation of a fourth I–O bond, modifying the iodine coordination polyhedron from the common trigonal pyramidal geometry to a tetrahedral-like geometry (see Figure 1). We made this conclusion based upon changes of bond distances. Such a coordination change could be triggered by pressure,

Table 3. Equation of State Parameters for Different Iodates

phase	BM-EOS	V_0 (\AA^3)	B_0 (GPa)	B'_0	reference	
$\text{Fe}(\text{IO}_3)_3$						
LP	Exp 3rd-order	385	55(2)	4.3(0.3)	this work	
LP	Theo 3rd-order	374	36(1)	4.6(0.1)		
HP	Exp 2nd-order	353(9)	73(9)	4.0		
HP	Theo 2nd-order	346(5)	48(3)	4.0		
phase	BM-EOS	V_0 (\AA^3)	B_0 (GPa)	B'_0	reference	
LiIO_3						
α	Theo 3rd-order	134.4	34(1)	4.2(0.2)	this work	
α	Exp 3rd-order	134.5	34(3)	5(0.8)	9	
α	Exp 3rd-order	134.5	55(3)	2.9(0.4)	10	
phase	BM-EOS	V_0 (\AA^3)	B_0 (GPa)	B'_0	reference	
KIO_3						
ambient pressure phase (triclinic phase III)	Exp 2nd-order		355.3	24.3(5)	4.0	11
high pressure phase I (HP I)	Exp 2nd-order		152.3(4)	67(3)	4.0	
HP I	DFT 2nd-order		150.81	70.9	4.0	
HP I	DFT 3rd-order		150.81	67.9	5.9	
phase	BM-EOS	V_0 (\AA^3)	B_0 (GPa)	B'_0	reference	
$\text{LiZn}(\text{IO}_3)_3$						
ambient pressure phase	estimated from empirical relations		527.04	55	52	

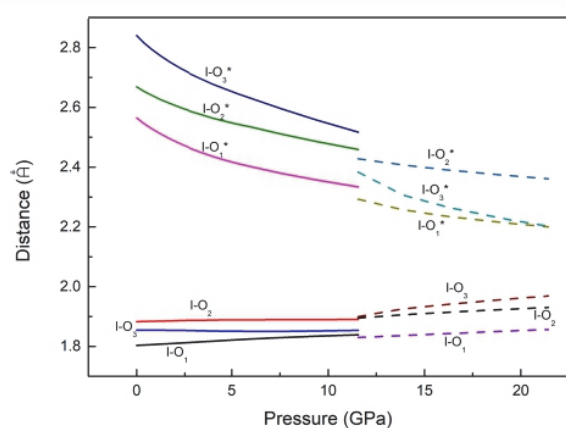


Figure 7. Pressure dependence of I–O bond distances obtained from calculations.

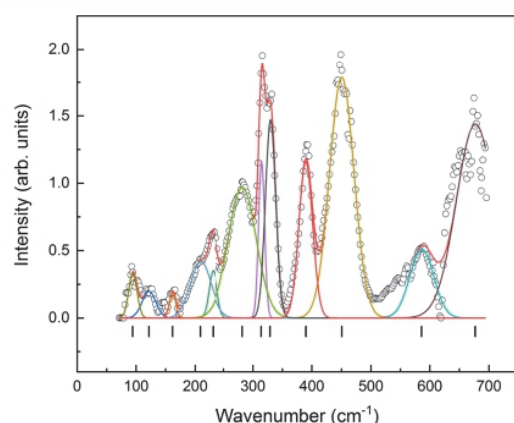


Figure 8. Background-subtracted IR spectrum at ambient conditions. The Gaussians used for the fits are also shown.

which favors the linking of the lone electron pair of iodine to one oxygen atom in the nearest IO_3 unit. A confirmation of it could come from future HP extended X-ray absorption fine-

structure measurements at the iodine K-edge. The proposed coordination change of iodine would cause a closure of the zeolitic channels of $\text{Fe}(\text{IO}_3)_3$, see Figure 1. The relative decrease of the empty volume is estimated to be 4%. As we will show below, this structural modification has consequences in the lattice vibrations of $\text{Fe}(\text{IO}_3)_3$.

A Rietveld analysis⁴² of the XRD patterns measured from 22.2 GPa up to 35.2 GPa confirms the theoretical predictions. These patterns can be explained by the coexistence of the low-pressure and HP phases, both phases described by space group $P6_3$. This can be seen in Figure 4 where we show the fitting of the XRD pattern measured at 33.3 GPa considering both phases. By comparing the intensities of the main peaks assigned to each phase, we quantified the fraction of each of them, increasing the fraction of the HP phase from 5% at 22.2 GPa to 66% at 35.2 GPa. We also observed that the phase transition is reversible as shown by the XRD patterns measured after decompression (see Figures 3 and 4). Upon decompression, we did not collect intermediate points from the highest pressure to ambient pressure; thus, we cannot discuss if there is hysteresis or not in the transition. Phase coexistence has been observed in many other oxides under HP.^{43,44} The reasons for it could be multiple. An argument recently proposed to explain it is the presence of kinetic barriers, which could be locally overcome by the presence of defects which provide a kinetic pathway of the phase transition.⁴⁵

The difference between the transition pressure predicted by DFT and the experimental onset of the phase transition can be because calculations have been performed at 0 K temperature.⁴⁶ However, it can be also related to the presence of kinetic barriers.⁴⁹ These facts, and the possible presence of radial pressure gradients,⁴⁷ can be the cause of the observed phase coexistence. On the other hand, the fact that the transition pressure is lower in FTIR experiments than in XRD experiments could be related to the influence in experiments of nonhydrostatic stresses in FTIR experiments because of the use of a solid pressure medium, where nonhydrostaticity is even larger than in silicone oil.^{48,49} A systematic analysis of the influence of nonhydrostaticity and kinetic barriers in the HP behavior of $\text{Fe}(\text{IO}_3)_3$ is beyond the scope of this work.

Table 4. Frequency of Phonons (ω), Pressure Coefficient ($d\omega/dP$), and Grüneisen Parameters for Different Modes (γ) of the Low-Pressure Phase^a

mode	theory (ambient pressure, $B_0 = 36$ GPa)			experiment (ambient pressure, $B_0 = 55$ GPa)				
	ω (cm ⁻¹)	$d\omega/dP$ (cm ⁻¹ /GPa)	γ	ω^{55} (cm ⁻¹)	ω^{56} (cm ⁻¹)	ω (cm ⁻¹) (this work)	$d\omega/dP$ (cm ⁻¹ /GPa)	γ
A	57.3	0.73	0.46		55(R)			
E1	65.6	2.07	1.13					
E2	79.8	1.46	0.66					
E2	89.6	3.30	1.32	86(R)	85(R)			
A	112.3	1.85	0.59		110(R)	94(2) (IR)		
E1	119.8	1.65	0.50					
A	126.1	1.92	0.55	127(IR), 125(R)	125(R)	122(2) (IR)		
E2	131.8	3.11	0.85					
E1	165.4	4.72	1.03	168(IR), 166(R)	165(R)	162(2) (IR)	5.25(1)	1.78(1)
E2	172.3	4.66	0.97					
E2	194.5	4.75	0.88					
E1	202.2	4.78	0.85		205(R)			
A	212.7	4.35	0.74			209(2) (IR)	2.80(1)	0.74(1)
E1	219.4	4.68	0.77					
E2	223.4	5.80	0.94	223(R)	225(R)			
A	239.8	4.56	0.69	228(IR)		231(2) (IR)	4.00(1)	0.95(1)
E2	245.3	6.02	0.88					
E1	269.8	3.82	0.51	266(R)	265(R)			
A	270.7	4.27	0.57					
A	291.7	4.35	0.54			282(2) (IR)	2.43(1)	0.47(1)
E1	316.5	4.60	0.52	314(IR), 320(R)	315(R)	314(2) (IR)	0.62(1)	0.11(1)
E2	334.2	2.95	0.32	350(R)	350(R)			
E1	382.5	3.68	0.35			329(2) (IR)	3.15(1)	0.53(1)
E2	385.5	3.82	0.36					
A	391.4	4.37	0.40	395(IR), 394(R)	395(R)	390(2) (IR)	3.64(1)	0.51(1)
A	436.9	5.12	0.42					
E2	445.1	5.10	0.41					
E1	445.9	5.79	0.47	451(IR), 450(R)	445(R)	451(2) (IR)	5.82(1)	0.71(1)
E2	619.8	1.02	0.06					
E1	622.1	1.36	0.08			586(2) (IR)	2.05(1)	0.19(1)
A	637.7	-0.01	0.00					
E2	674.7	-0.17	-0.01					
E1	697.9	-2.26	-0.12	699(IR), 685(R)	685(R)	677(2) (IR)		
A	729.2	-3.29	-0.16	726(R)	726(R)			
E1	770.7	-2.24	-0.10	764(IR), 755(R)	756(R)			
A	773.6	-1.37	-0.06					
E2	791.1	-3.08	-0.14		796(R)			

^aA and E₁ modes are Raman- and IR-active. E₂ modes are only Raman-active. In the results from the literature, R and IR means the experimental technique (Raman or IR).

Compressibility. From our XRD experiments and calculations, we have obtained the pressure dependence of the unit-cell parameters of both phases of Fe(IO₃)₃. The results are shown in Figure 5. Both methods agree in the fact that the crystal structure is significantly more compressible along the *c*-axis than along the *a*-axis. Such anisotropic behavior is similar to that of other members of this family of compounds.^{10,11} This is related to the fact that IO₃ units are oriented in such a way that the lone-pair electrons of iodine are basically aligned along the *c*-axis. In Figure 5, the abrupt change of the unit-cell parameters at the phase transition can be also seen.

In Figure 6, we present the pressure evolution of the unit-cell volume. We found that Fe(IO₃)₃ is highly compressible, with a 22% volume reduction from ambient pressure to the transition pressure (22 GPa). We also found that, the pressure dependence of the volume can be described using the 2nd and 3rd Birch–Murnaghan equations of state (EOS),⁵⁰ for the HP

and low-pressure phases, respectively. The fits have been carried out using the EOSFit programme.⁵¹ The values of the determined ambient pressure unit-cell volume (V_0), bulk modulus (B_0), and pressure derivative (B'_0) for the different phases are given in Table 3. These parameters are compared there with those previously reported for other iodates. The low-pressure phase has a bulk modulus of 55(2) and 36(1) GPa according to experiments and calculations, respectively. These values lie within the range of values reported in the literature for the bulk modulus of LiIO₃^{9,10} and LiZn(IO₃)₃,⁵² but are larger than the bulk modulus of KIO₃ (see Table 3).¹¹ Regarding the HP phase, it can be seen that after the phase transition the bulk modulus is considerably enlarged (i.e., compressibility is reduced) as reported also in KIO₃.¹¹ This is mainly due to the collapse of the volume at the phase transition (see Figure 6). The abrupt change of the volume ($\Delta V/V = -5.5\%$) and the axial ratio at the phase transition and the enhancement of the bulk modulus support that the phase

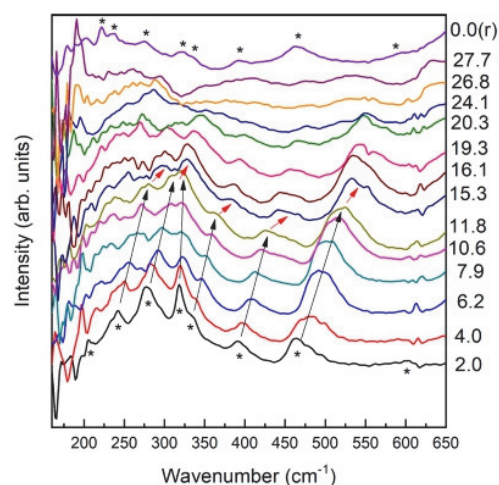


Figure 9. IR spectra at different pressures which are indicated in GPa in the figure. The asterisks indicate the different phonon. Black arrows show the pressure evolution in the low-pressure phase. Red arrows show the changes at the phase transition. The upper trace shows the spectrum measured at ambient pressure after pressure release, which is denoted by (r).

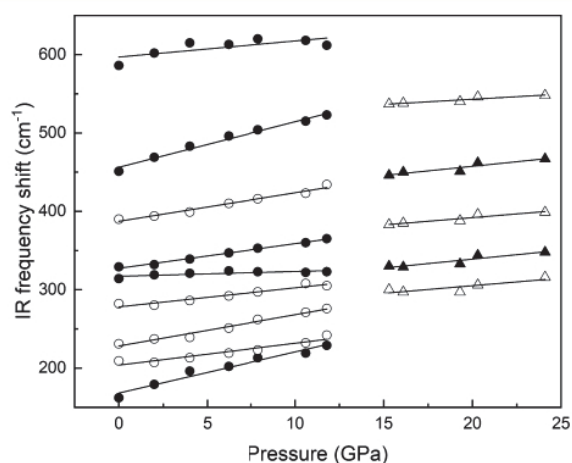


Figure 10. Pressure dependence of IR modes obtained from experiments. Circles: low-pressure phase. Triangles: HP phase. Black and white colors are used for E_1 and A modes, respectively. Experimental errors are smaller than the symbol size.

transition is of a first-order nature.⁵³ This is also supported by the sluggish character of the transition, the observed coexistence of phases, and the proposed existence of kinetic barriers, and formation of new I–O bonds. To conclude the discussion on the bulk modulus, we would like to mention that given the discrepancies found in the literature on the bulk modulus of LiIO_3 ,^{9,10} we have calculated the pressure dependence of the volume of this compound. The determined EOS is shown in Table 3. Our results agree better with the results reported by Hu⁹ as compared to the results reported by Zhang.¹⁰

Polyhedral Changes. A deeper understanding of the HP behavior can be obtained from the analysis of the polyhedral behavior.⁵⁴ As calculations and experiments give a similar description of the pressure evolution of unit-cell parameters, and oxygen positions cannot be accurately determined from our HP XRD experiments, we will base this part of the

discussion on the *ab initio* calculations. The first thing we have noticed is that in the low-pressure phase, the FeO_6 octahedron becomes gradually more symmetric under compression, being in fact a regular octahedron just before the phase transition. If the pressure dependence of the volume of this octahedron is described with a 2nd order Birch–Murnaghan EOS, a bulk modulus of 115(5) GPa is obtained for it. Thus, the volume reduction of FeO_6 cannot account for the volume decrease of the crystal, which is in part determined by the reduction of the “empty” space surrounding the IO_3 units. As a consequence, the second-coordination sphere of iodine atoms is reduced favoring the formation of new I–O bonds. This can be seen by looking at the pressure dependence of I–O bonds in Figure 7. In this figure, it can be observed that the I–O distances of the trigonal pyramidal IO_3 unit (lines without asterisks in the figure) are little affected by pressure, with a tendency to the increase of the average bond distances. In contrast, the next three nearest oxygen atoms get closer to iodine upon pressure increase (lines with asterisks in the figure). On the other hand, at the phase transition there is an abrupt change of the I–O distances. In particular, if distances below 2.4 Å are considered, the coordination number of iodine atoms becomes four as commented before (shown in Figure 1). In addition, there are two additional oxygen atoms, which were in the low-pressure phase on the side of the lone-pair electrons of iodine, which also get closer to the iodine atoms. This phenomenon is enhanced under further compression, the coordination becoming around iodine fivefold at the highest pressure, with the sixth nearest oxygen at a distance of 2.4 Å, which is shorter than the fourth I–O distance at ambient pressure.

IR and Raman Phonons. To conclude, we will discuss the vibrational properties of $\text{Fe}(\text{IO}_3)_3$. We will start this section commenting on the IR and Raman spectra at low pressure. Figure 8 shows the IR absorption spectrum measured at ambient conditions outside the DAC. We identified at least 12 absorption bands. Their frequencies have been determined making a Gaussian fit to the different bands (see Figure 8). The frequencies of six of the modes agree well with the IR modes reported in the literature.⁵⁵ In order to assign the modes and discuss the infrared results, we used our DFT calculations. According to group theory, $\text{Fe}(\text{IO}_3)_3$ has 24 IR-active modes ($12 A + 12 \times 10^1$). These modes are also Raman-active. There are, in addition, 12 extra Raman modes with symmetry E_2 , making a total of 37 Raman-active modes ($12 A + 12 \times 10^1 + 13 \times 10^2$). From our DFT simulations, we have calculated the frequencies of all the vibrational modes, which are shown in Table 4. The calculated frequencies agree reasonably well with the present and previous IR and Raman experiments.^{56,57} Differences between calculated and experimental mode frequencies are similar to the difference between different experimental studies (see Table 4). The mode assignment given by calculations is also reported in the table. It has been noticed that there is a group of phonons with frequencies lower than 330 cm^{-1} , another group with frequencies between 360 and 425 cm^{-1} , and a third group with frequencies higher than 590 cm^{-1} . The high-frequency modes correspond to stretching modes within the pyramidal IO_3 unit, the intermediate-frequency modes correspond to bending vibration of IO_3 , and the low-frequency modes can be basically associated to vibrations that involve the movement of Fe atoms and the IO_3 units as a rigid element.

The results of HP FTIR measurements are shown in Figure 9. The spectrum at 2 GPa resembles the ambient pressure

Table 5. Frequency of Phonons (ω), Pressure Coefficient ($d\omega/dP$), and Grüneisen Parameters for Different Modes (γ) of the HP Phase at 15.3 GPa^a

mode	theory (15 GPa, $B_0 = 48$ GPa)			experiment (15.3 GPa, $B_0 = 73$ GPa)		
	ω (cm^{-1})	$d\omega/dP$ ($\text{cm}^{-1}/\text{GPa}$)	γ	ω (cm^{-1}) (this work)	$d\omega/dP$ ($\text{cm}^{-1}/\text{GPa}$)	γ
A	87.8	0.19	0.10			
E2	99.3	0.83	0.40			
E1	127.0	0.20	0.08			
E2	138.0	0.28	0.10			
E1	144.8	0.07	0.02			
A	150.9	0.64	0.20			
A	186.2	1.71	0.44			
E2	199.9	1.95	0.47			
A	226.4	0.48	0.10			
E1	231.0	2.85	0.59			
E2	243.9	2.85	0.56			
E1	267.4	2.39	0.43			
E2	272.0	2.76	0.49			
A	280.9	2.87	0.49			
E2	295.2	2.43	0.40			
E1	311.5	2.12	0.33	300(2) (IR)	1.94(1)	0.47(1)
A	323.8	1.67	0.25			
E1	329.1	3.86	0.56	330(2) (IR)	2.27(1)	0.50(1)
E2	344.6	4.14	0.58			
A	348.7	4.23	0.58			
E1	358.3	4.49	0.60	383(2) (IR)	1.87(1)	0.35(1)
E	403.3	4.22	0.50			
A	432.4	2.76	0.31			
E2	436.6	3.40	0.37			
E1	455.2	3.04	0.32	446(2) (IR)	2.34(1)	0.38(1)
A	468.3	3.81	0.39			
E1	469.7	4.17	0.43			
E2	498.3	3.23	0.31			
A	558.5	0.09	0.01	537(2) (IR)	1.31(1)	0.17(1)
E1	564.2	-0.16	-0.01			
E2	602.9	-1.24	-0.10			
E2	625.9	-0.21	-0.02			
E1	651.8	-1.21	-0.09			
A	678.1	-2.39	-0.17			
A	728.2	-0.95	-0.06			
E1	738.4	-1.39	-0.09			
E2	750.2	-1.88	-0.12			

^aA and E₁ modes are Raman- and IR-active. E₂ modes are only Raman-active.

spectrum. In this case, only the modes between 200 and 650 cm^{-1} can be clearly identified. They are indicated by asterisks in Figure 9. In the figure, it can be seen that as pressure increases, up to 11.8 GPa, the only change in the IR spectrum is the gradual shift of the mode frequencies toward higher frequencies (see the black arrows in the figure). This is a consequence of the shortening of interatomic distances. However, at 15.3 GPa drastic changes occur in the IR spectrum, supporting the existence of the phase transition previously described. These changes involve the merging of several modes and an abrupt phonon shift, which is shown by red arrows in the figure. We consider this as an evidence of the phase transition. We will show below that such changes in phonon frequencies are in agreement with changes predicted by DFT calculations. Therefore, the phase transition detected by FTIR spectroscopy can be correlated to the one observed by XRD. In fact, the changes of IR phonons at 15.3 GPa are related to the changes in bond distances previously described.⁵⁸ Upon further compression, the modes again

gradually shift with pressure. In addition, there also a loss of intensity because of the decrease of the sample thickness. Under decompression, the changes are reversible as can be seen in the spectrum shown in the top of Figure 9. The pressure dependences of the identified IR modes are shown in Figure 10. There, not only the discontinuity in frequencies but also the changes in the pressure dependence can be seen. In both phases, the modes have a linear pressure dependence. In Tables 4 and 5, we summarize the theoretical and experimental pressure dependence of phonons (including also the Grüneisen parameter) for both the low-pressure phase (at ambient pressure) and the HP phase (at 15.3 GPa).

In Figures 11 and 12, we represent the calculated pressure dependence for IR modes and for the modes that are only Raman-active, respectively. There, it can be seen that the structural changes associated to the phase transition cause drastic changes in the frequencies of the modes. Indeed, they resemble the changes observed in FTIR experiments. This fact supports the assignment of changes in the IR spectrum at 15.3

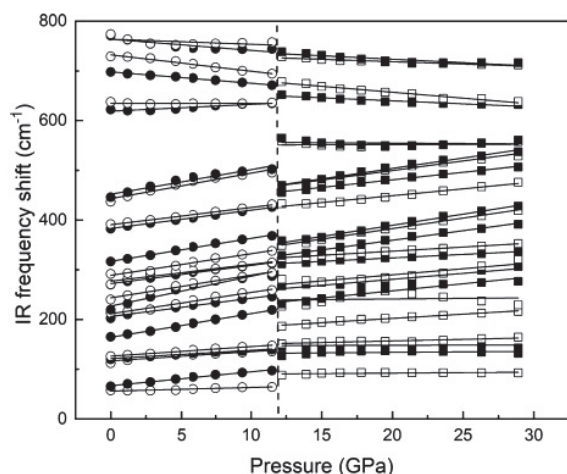


Figure 11. Pressure dependence of A and E_1 modes obtained from calculations. These modes are Raman- and IR-active. Circles: low-pressure phase. Squares: HP phase. Black and white colors are used for E_1 and A modes, respectively.

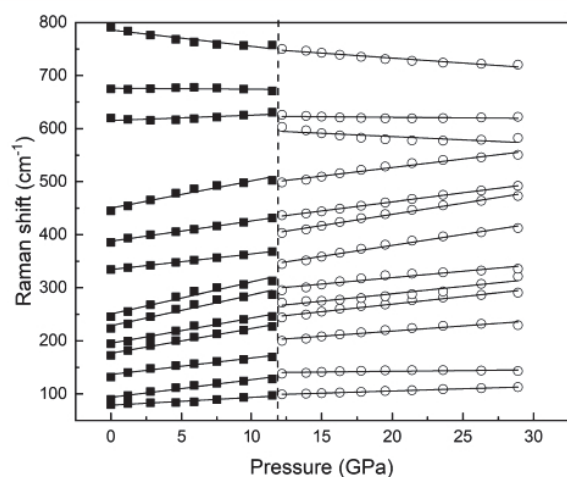


Figure 12. Pressure dependence of E_2 modes obtained from calculations. These modes are only Raman-active. Squares: low-pressure phase. Circles: HP phase.

GPa because of the phase transition predicted by DFT and observed in XRD experiments. Another interesting feature that can be observed in Figures 11 and 12 (and in Tables 4 and 5) is the existence of modes, which are gradually softened under compression. These modes belong to those assigned to the internal vibrations of the iodate molecule. The presence of such soft modes in the low-pressure phase is consistent with the occurrence of a phase transition, as “weak soft-modes” (they are not classical soft-modes because the frequency never reaches zero and therefore their existence does not contradict the first-order nature of the transition) could be related to a collective instability, which tend to make the crystal structure unstable.⁵⁸ The presence of similar modes in the HP phase suggests the existence of a second phase transition at pressure beyond those pressures covered by the present study.

CONCLUSIONS

We have studied the HP behavior of $\text{Fe}(\text{IO}_3)_3$ by means of XRD, infrared micro-spectroscopy, and DFT calculations. This

is the first time an iodate is studied by HP FTIR spectroscopy. We have found evidence of the existence of a pressure-driven phase transition. The HP phase can be described by the same space group as the low-pressure phase; however, the transition is a first-order transformation involving a volume collapse larger than 5%. The phase transition is related to the change of the activity of iodine lone-pair electrons, which under compression prefer to link to oxygen atoms. The pressure dependence of unit-cell parameters for the two phases has been determined. The fit of the pressure–volume results with a Birch–Mumaghan equation of state indicate that $\text{Fe}(\text{IO}_3)_3$ is highly compressible with a bulk modulus $B_0 = 55(2)$ GPa. The HP phase is less compressible with $B_0 = 73(9)$ GPa. Finally, detailed information is provided on infrared- and Raman-active modes, being the pressure dependence of phonon frequencies determined. Based upon calculations, we have assigned the symmetry of different modes.

AUTHOR INFORMATION

Corresponding Author

Daniel Errandonea – Departamento de Física Aplicada—ICMUV—MALTA Consolider Team, Universitat de València, 46100 Burjassot (Valencia), Spain; orcid.org/0000-0003-0189-4221; Email: daniel.errandonea@uv.es

Authors

Akun Liang – Departamento de Física Aplicada—ICMUV—MALTA Consolider Team, Universitat de València, 46100 Burjassot (Valencia), Spain

Saqib Rahman – Center for High Pressure Science and Technology Advanced Research Shanghai, 201203 Shanghai, China

Hajra Saqib – Shanghai Institute of Technical Physics, Chinese Academy of Science, 200083 Shanghai, China

Placida Rodríguez-Hernández – Departamento Física, Malta Consolider Team, and Instituto de Materiales y Nanotecnología, Universidad de La Laguna, 38206 La Laguna, Spain; orcid.org/0000-0002-4148-6516

Alfonso Muñoz – Departamento Física, Malta Consolider Team, and Instituto de Materiales y Nanotecnología, Universidad de La Laguna, 38206 La Laguna, Spain; orcid.org/0000-0003-3347-6518

Gwilherm Nénert – Malvern Panalytical B.V., 7602 EA Almelo, The Netherlands

Ibraheem Yousef – CELLS-ALBA Synchrotron Light Facility, 08290 Barcelona, Spain

Catalin Popescu – CELLS-ALBA Synchrotron Light Facility, 08290 Barcelona, Spain

Complete contact information is available at: <https://pubs.acs.org/10.1021/acs.jpcc.0c02080>

Notes

The authors declare no competing financial interest.

ACKNOWLEDGMENTS

This work was supported by the Spanish Ministry of Science, Innovation and Universities under grants MAT2016-75586-C4-1/3-P and RED2018-102612-T (MALTA Consolider-Team network) and by Generalitat Valenciana under grant Prometeo/2018/123 (EFIMAT). A.L. and D.E. would like to thank the Generalitat Valenciana for the Ph.D. fellowship GRISOLIAP/2019/025. C.P. acknowledges the financial support from the Spanish Ministerio de Economía y

Competividad through the FIS2017-83295 project. The FTIR experiments were performed at MIRAS beamline at the ALBA Synchrotron with the collaboration of ALBA staff.

REFERENCES

- (1) Galez, C.; Mugnier, Y.; Bouillot, J.; Lambert, Y.; Le Dantec, R. Synthesis and Characterisation of Fe(IO₃)₃ Nanosized Powder. *J. Alloys Compd.* **2006**, *416*, 261–264.
- (2) Sorokin, N. I.; Shaldin, Y. V. Thermally Induced Charge Relaxation in α -LiIO₃ Superionic Conductor. *Phys. Solid State* **2017**, *59*, 1713–1716.
- (3) Sagotra, A. K.; Errandonea, D.; Cazorla, C. Mechanocaloric Effects in Superionic Thin Films from Atomistic Simulations. *Nat. Commun.* **2017**, *8*, 963.
- (4) Hermet, P. First-Principles Based Analysis of the Piezoelectric Response in α -LiIO₃. *Comput. Mater. Sci.* **2017**, *138*, 199–203.
- (5) Gonzalez-Platas, J.; Rodriguez-Hernandez, P.; Muñoz, A.; Rodriguez-Mendoza, U. R.; Nénert, G.; Errandonea, D. A High-Pressure Investigation of the Synthetic Analogue of Chalcocite, CuSeO₃·2H₂O. *Crystals* **2019**, *9*, 643.
- (6) Mao, H.-K.; Chen, B.; Chen, J.; Li, K.; Lin, J.-F.; Yang, W.; Zheng, H. Recent Advances in High-Pressure Science and Technology. *Matter Radiat. Extremes* **2016**, *1*, 59–75.
- (7) Errandonea, D.; Garg, A. B. Recent Progress on the Characterization of the High-Pressure Behaviour of AVO₄ Orthovanadates. *Prog. Mater. Sci.* **2018**, *97*, 123–169.
- (8) Liu, J.; Shen, Z.; Zhang, Y.; Yin, X.; He, S. The P-T Phase Diagram of Lithium Iodate (LiIO₃) up to 40 Kbars. *Acta Phys. Sin.* **1983**, *32*, 118–123.
- (9) Hu, J.; Chen, L.; Wang, L.; Tang, R.; Che, R. Isothermal Compression of α -LiIO₃ and Its Phase Transition under High Pressure and High Temperature. *Acta Phys. Sin.* **1987**, *36*, 1099–1104.
- (10) Zhang, W. W.; Cui, Q. L.; Pan, Y. W.; Dong, S. S.; Liu, J.; Zou, G. T. High-Pressure x-Ray Diffraction Study of LiIO₃ to 75 GPa. *J. Phys.: Condens. Matter* **2002**, *14*, 10579–10582.
- (11) Bayarjargal, L.; Wiehl, L.; Friedrich, A.; Winkler, B.; Juarez-Arellano, E. A.; Morgenroth, W.; Haussühl, E. Phase Transitions in KIO₃. *J. Phys.: Condens. Matter* **2012**, *24*, 325401.
- (12) Suffren, Y.; Gautier-Luneau, I.; Darie, C.; Goujon, C.; Legendre, M.; Leynaud, O. First Evidence of a Phase Transition in a High-Pressure Metal Iodate: Structural and Thermal Studies of AgIO₃ Polymorphs. *Eur. J. Inorg. Chem.* **2013**, *2013*, 3526–3532.
- (13) Jordá, J. L.; Rey, F.; Sastre, G.; Valencia, S.; Palomino, M.; Corma, A.; Segura, A.; Errandonea, D.; Lacomba, R.; Manjón, F. J.; et al. Synthesis of a Novel Zeolite through a Pressure-Induced Reconstructive Phase Transition Process. *Angew. Chem., Int. Ed.* **2013**, *125*, 10652–10656.
- (14) Jansen, M. Zur Kristallstruktur von Fe₃O₉. *J. Solid State Chem.* **1976**, *17*, 1–6.
- (15) Pereira, A. L. D. J.; Santamaría-Pérez, D.; Vilaplana, R.; Errandonea, D.; Popescu, C.; Da Silva, E. L.; Sans, J. A.; Rodríguez-Carvajal, J.; Muñoz, A.; Rodríguez-Hernández, P.; et al. Experimental and Theoretical Study of SbPO₄ under Compression. *Inorg. Chem.* **2020**, *59*, 287–307.
- (16) Phanon, D.; Mosset, A.; Gautier-Luneau, I. New Materials for Infrared Non-Linear Optics. Syntheses, Structural Characterisations, Second Harmonic Generation and Optical Transparency of M(IO₃)₃ Metallic Iodates. *J. Mater. Chem.* **2007**, *17*, 1123–1130.
- (17) Degen, T.; Sadki, M.; Bron, E.; König, U.; Nénert, G. The HighScore suite. *Powder Diffr.* **2014**, *29*, S13–S18.
- (18) Bandiello, E.; Errandonea, D.; Ferrari, S.; Pellicer-Porres, J.; Martínez-García, D.; Achary, S. N.; Tyagi, A. K.; Popescu, C. Pressure-Induced Hexagonal to Monoclinic Phase Transition of Partially Hydrated CePO₄. *Inorg. Chem.* **2019**, *58*, 4480–4490.
- (19) Klotz, S.; Chervin, J.-C.; Munsch, P.; Le Marchand, G. Hydrostatic Limits of 11 Pressure Transmitting Media. *J. Phys. D: Appl. Phys.* **2009**, *42*, 075413.
- (20) Shen, Y.; Kumar, R. S.; Pravica, M.; Nicol, M. F. Characteristics of Silicone Fluid as a Pressure Transmitting Medium in Diamond Anvil Cells. *Rev. Sci. Instrum.* **2004**, *75*, 4450–4454.
- (21) Mao, H. K.; Xu, J.; Bell, P. M. Calibration of the Ruby Pressure Gauge to 800 Kbar under Quasi-Hydrostatic Conditions. *J. Geophys. Res.* **1986**, *91*, 4673–4676.
- (22) Prescher, C.; Prakapenka, V. B. DIOPTAS: A Program for Reduction of Two-Dimensional X-Ray Diffraction Data and Data Exploration. *High Pressure Res.* **2015**, *35*, 223–230.
- (23) Kraus, W.; Nolze, G. POWDER CELL - A Program for the Representation and Manipulation of Crystal Structures and Calculation of the Resulting X-Ray Powder Patterns. *J. Appl. Crystallogr.* **1996**, *29*, 301–303.
- (24) Rodríguez-Carvajal, J. Recent Advances in Magnetic Structure Determination by Neutron Powder Diffraction. *Phys. B Condens. Matter* **1993**, *192*, 55–69.
- (25) Asaumi, K.; Kondo, Y. Effect of Very High Pressure on the Optical Absorption Spectra in CsI. *Solid State Commun.* **1981**, *40*, 715–718.
- (26) Hohenberg, P.; Kohn, W. Inhomogeneous Electron Gas. *Phys. Rev.* **1964**, *136*, B864–B871.
- (27) Kresse, G.; Joubert, D. From Ultrasoft Pseudopotentials to the Projector Augmented-Wave Method. *Phys. Rev. B: Condens. Matter Mater. Phys.* **1999**, *59*, 1758–1775.
- (28) Blöchl, P. E. Projector Augmented-Wave Method. *Phys. Rev. B: Condens. Matter Mater. Phys.* **1994**, *50*, 17953–17979.
- (29) Kresse, G.; Hafner, J. Ab initio molecular dynamics for liquid metals. *Phys. Rev. B: Condens. Matter Mater. Phys.* **1993**, *47*, S58–S61.
- (30) Kresse, G.; Hafner, J. Ab initio molecular-dynamics simulation of the liquid-metal-amorphous-semiconductor transition in germanium. *Phys. Rev. B: Condens. Matter Mater. Phys.* **1994**, *49*, 14251–14269.
- (31) Kresse, G.; Furthmüller, J. Efficiency of Ab-Initio Total Energy Calculations for Metals and Semiconductors Using a Plane-Wave Basis Set. *Comput. Mater. Sci.* **1996**, *6*, 15–50.
- (32) Kresse, G.; Furthmüller, J. Efficient iterative schemes for ab initio total-energy calculations using a plane-wave basis set. *Phys. Rev. B: Condens. Matter Mater. Phys.* **1996**, *54*, 11169–11186.
- (33) Perdew, J. P.; Ruzsinszky, A.; Csonka, G. I.; Vydrov, O. A.; Scuseria, G. E.; Constantin, L. A.; Zhou, X.; Burke, K. Restoring the Density-Gradient Expansion for Exchange in Solids and Surfaces. *Phys. Rev. Lett.* **2008**, *100*, 136406.
- (34) Dudarev, S. L.; Botton, G. A.; Savrasov, S. Y.; Humphreys, C. J.; Sutton, A. P. Electron-energy-loss spectra and the structural stability of nickel oxide: An LSDA+U study. *Phys. Rev. B: Condens. Matter Mater. Phys.* **1998**, *57*, 1505.
- (35) López, S.; Romero, A. H.; Mejía-López, J.; Mazo-Zuluaga, J.; Restrepo, J. Structure and Electronic Properties of Iron Oxide Clusters: A First-Principles Study. *Phys. Rev. B: Condens. Matter Mater. Phys.* **2009**, *80*, 085107.
- (36) López-Moreno, S.; Romero, A. H.; Mejía-López, J.; Muñoz, A.; Roshchin, I. V. First-Principles Study of Electronic, Vibrational, Elastic, and Magnetic Properties of FeF₂ as a Function of Pressure. *Phys. Rev. B: Condens. Matter Mater. Phys.* **2012**, *85*, 134110.
- (37) Mejía-López, J.; Mazo-Zuluaga, J.; López-Moreno, S.; Muñoz, F.; Duque, L. F.; Romero, A. H. Physical Properties of Quasi-One-Dimensional MgO and Fe₃O₄-Based Nanostructures. *Phys. Rev. B: Condens. Matter Mater. Phys.* **2014**, *90*, 035411.
- (38) Monkhorst, H. J.; Pack, J. D. Special Points for Brillouin-Zone Integrations. *Phys. Rev. B: Condens. Matter Mater. Phys.* **1976**, *13*, 5188–5192.
- (39) Parlinski, K. *Computer Code PHONON*: Krakow, Poland, 2010.
- (40) Achary, S. N.; Errandonea, D.; Muñoz, A.; Rodríguez-Hernández, P.; Manjón, F. J.; Krishna, P. S. R.; Patwe, S. J.; Grover, V.; Tyagi, A. K. Experimental and Theoretical Investigations on the Polymorphism and Metastability of BiPO₄. *Dalton Trans.* **2013**, *42*, 14999–15015.

(41) Mujica, A.; Rubio, A.; Muñoz, A.; Needs, R. J. High-Pressure Phases of Group-IV, III-V, and II-VI Compounds. *Rev. Mod. Phys.* **2003**, *75*, 863.

(42) Rietveld, H. M. A Profile Refinement Method for Nuclear and Magnetic Structures. *J. Appl. Crystallogr.* **1969**, *2*, 65–71.

(43) Errandonea, D.; Manjón, F. J.; Garro, N.; Rodríguez-Hernández, P.; Radescu, S.; Mujica, A.; Muñoz, A.; Tu, C. Y. Combined Raman Scattering and Ab Initio Investigation of Pressure-Induced Structural Phase Transitions in the Scintillator ZnWO₄. *Phys. Rev. B: Condens. Matter Mater. Phys.* **2008**, *78*, 054116.

(44) Samanta, S.; Li, Q.; Cheng, B.; Huang, Y.; Pei, C.; Wang, Q.; Ma, Y.; Wang, L. Phase Coexistence and Pressure-Temperature Phase Evolution of VO₂(A) Nanorods Near the Semiconductor-Semiconductor Transition. *Phys. Rev. B: Condens. Matter Mater. Phys.* **2017**, *95*, 045135.

(45) Akahane, K.; Russo, J.; Tanakab, H. A Possible Four-Phase Coexistence in a Single-Component System. *Nat. Commun.* **2016**, *7*, 12599.

(46) Winkler, B.; Milman, V. Density Functional Theory Based Calculations for High Pressure Research. *Z. Kristallogr.* **2014**, *229*, 112–122.

(47) Bandiello, E.; Errandonea, D.; Pellicer-Porres, J.; Garg, A. B.; Rodríguez-Hernández, P.; Muñoz, A.; Martínez-García, D.; Rao, R.; Popescu, C. Effect of High Pressure on the Crystal Structure and Vibrational Properties of Olivine-Type LiNiPO₄. *Inorg. Chem.* **2018**, *57*, 10265–10276.

(48) Errandonea, D.; Meng, Y.; Somayazulu, M.; Häusermann, D. Pressure-induced transition in titanium metal: a systematic study of the effects of uniaxial stress. *Phys. B Condens. Matter* **2005**, *355*, 116–125.

(49) Errandonea, D.; Muñoz, A.; Gonzalez-Platas, J. Comment on “High-Pressure x-Ray Diffraction Study of YBO₃/Eu³⁺, GdBO₃, and EuBO₃: Pressure-Induced Amorphization in GdBO₃”. *J. Appl. Phys.* **2014**, *115*, 216101.

(50) Birch, F. Finite strain isotherm and velocities for single-crystal and polycrystalline NaCl at high pressures and 300°K. *J. Geophys. Res.* **1978**, *83*, 1257–1268.

(51) Angel, R. J.; Gonzalez-Platas, J.; Alvaro, M. EosFit7c and a Fortran Module (Library) for Equation of State Calculations. *Z. Kristallogr.* **2014**, *229*, 405–419.

(52) Hebboul, Z.; Galez, C.; Benbental, D.; Beauquis, S.; Mugnier, Y.; Benmakhlof, A.; Bouchenafa, M.; Errandonea, D. Synthesis, Characterization, and Crystal Structure Determination of a New Lithium Zinc Iodate Polymorph LiZn(IO₃)₃. *Crystals* **2019**, *9*, 464.

(53) Dove, M. T. Theory of Displacive Phase Transitions in Minerals. *Am. Mineral.* **1997**, *82*, 213–244.

(54) Errandonea, D.; Muñoz, A.; Rodríguez-Hernández, P.; Gomis, O.; Achary, S. N.; Popescu, C.; Patwe, S. J.; Tyagi, A. K. High-Pressure Crystal Structure, Lattice Vibrations, and Band Structure of BiSbO₄. *Inorg. Chem.* **2016**, *55*, 4958–4969.

(55) Junaid Bushiri, M.; Kochuthresia, T. C.; Vaidyan, V. K.; Gautier-Luneau, I. Raman Scattering Structural Studies of Nonlinear Optical M(IO₃)₃ (M=Fe, Ga, α-In) and Linear Optical β-In(IO₃)₃. *J. Nonlinear Opt. Phys. Mater.* **2014**, *23*, 1450039.

(56) Ristić, M.; Musić, S.; Ivanda, M. A Study of the Thermal Stability of Fe(IO₃)₃ by ⁵⁷Fe Mossbauer, FT-IR and Raman Spectroscopies. *J. Mol. Struct.* **1999**, *480–481*, 637–640.

(57) Sun, B.; Dreger, Z. A.; Gupta, Y. M. High-Pressure Effects in Pyrene Crystals: Vibrational Spectroscopy. *J. Phys. Chem. A* **2008**, *112*, 10546–10551.

(58) Errandonea, D.; Pellicer-Porres, J.; Pujol, M. C.; Carvajal, J. J.; Aguiló, M. Room-temperature vibrational properties of potassium gadolinium double tungstate under compression up to 32GPa. *J. Alloys Compd.* **2015**, *638*, 14–20.

High-Pressure Raman Study of $\text{Fe}(\text{IO}_3)_3$: Soft-Mode Behavior Driven by Coordination Changes of Iodine Atoms

Akun Liang, Saqib Rahman, Placida Rodriguez-Hernandez, Alfonso Muñoz, Francisco Javier Manjón, Gwilherm Nenert, and Daniel Errandonea*

Cite This: *J. Phys. Chem. C* 2020, 124, 21329–21337

Read Online

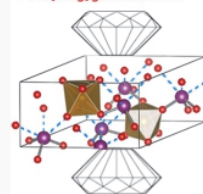
ACCESS |

Metrics & More

Article Recommendations

Supporting Information

ABSTRACT: We report high-pressure Raman spectroscopy studies of $\text{Fe}(\text{IO}_3)_3$ up to nearly 21 GPa that have been interpreted with the help of density functional theory calculations, which include the calculation of phonon dispersion curves and elastic constants at different pressures. Zero-pressure Raman-active mode frequencies and their pressure dependences have been determined. Modes have been assigned and correlated to atomic movements with the help of calculations. Interestingly, in the high-frequency region, there are several modes that soften under compression. These modes have been identified as internal vibrations of the IO_3 coordination polyhedron. Their unusual behavior is a consequence of the changes induced by pressure in the coordination sphere of iodine, which gradually change from a threefold coordination to an almost sixfold coordination under compression. The coordination change is favored by the decrease of the stereoactivity of the iodine lone electron pair so that likely a real sixfold coordination is attained after a first-order phase transition previously reported to occur above 21 GPa. The strong nonlinear behavior found in Raman-active modes as well as in theoretically calculated elastic constants has been discovered to be related to the occurrence of two previously unreported isostructural phase transitions at 1.5–2.0 and 5.7–6.0 GPa as shown by dynamic instabilities close to the Brillouin zone center.

 $\text{Fe}(\text{IO}_3)_3$ under HP

Metal iodates usually show an asymmetric coordination geometry because of the presence of lone electron pairs (LEPs) in the iodine atom. Consequently, they can form a diversity of unusual structures and many of them have multiple promising properties or applications, such as large second-harmonic generation coefficient materials,^{1–4} chiral materials with second-order nonlinear optical activity in the visible and near- and mid-IR ranges,⁵ and barocaloric materials.⁶

Of particular interest are compounds with the composition $\text{M}(\text{IO}_3)_3$, with M being a trivalent metal atom and iodine (I) being a pentavalent atom. These metal iodates show a diversity of unusual crystalline structures because of the asymmetric coordination geometry produced by the iodine LEP. A feature of these compounds is that IO_3 units do not form planar triangles, such as in borate (BO_3) or carbon trioxide (CO_3) units. Instead, IO_3 units are not planar and have a pyramidal form with three O atoms in the corners of the base and the iodine atom in the top corner of the pyramid. This unit can be seen in Figure 1, where the crystal structure of $\text{Fe}(\text{IO}_3)_3$ is schematically represented. In fact, the polyhedron around I could be described as an IO_3E tetrahedron, where E is the iodine LEP. Therefore, iodine can be considered as fourfold coordinated if we take into account the LEP, with iodine sitting in the center of a distorted tetrahedron where the oxygen atoms are occupying three corners and the fourth one is occupied by the lone pair of electrons of the iodine atom. It should be noted that the I–O bond distance in the IO_3E unit is of the order of 1.9 Å, while the I–O distances to the three second-next oxygen neighbors are between 2.55 and 2.95 Å (see Figure 1). We show that these atoms become relevant at

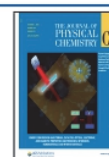
high pressure (HP) to increase the coordination of I atoms and explain the changes observed in the vibrational properties of $\text{Fe}(\text{IO}_3)_3$.

It is well known that HP modifies interatomic distances, leading to changes in the physical properties of materials. This has contributed to improve the properties of materials and to several discoveries that have impacted physics, chemistry, and materials sciences. Among transition-metal iodates, such studies have been carried out only in $\text{Fe}(\text{IO}_3)_3$.⁷ This material was studied by powder X-ray diffraction (XRD), IR spectroscopy, and density functional theory (DFT) simulations. It undergoes a first-order phase transition at 22 GPa, with a volume change and an abrupt change of the c/a axial ratio. The phase transition is triggered by changes in the coordination of iodine atoms, which is driven by the decrease of the stereoactivity of the iodine LEP. DFT calculations have proposed the occurrence of unusual softening of vibrational modes associated with internal vibrations of the IO_3 molecule. However, this hypothesis has not been confirmed by Raman experiments yet, which have been only reported at ambient conditions.^{8,9}

Received: July 17, 2020

Revised: September 2, 2020

Published: September 11, 2020



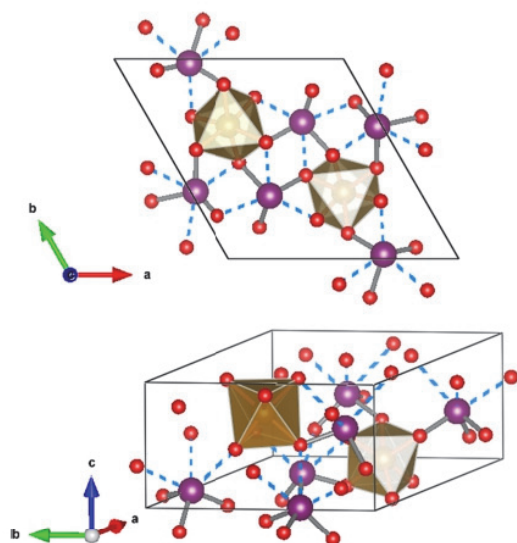


Figure 1. Schematic representation of the crystal structure of $\text{Fe}(\text{IO}_3)_3$ at room pressure. Two different perspectives are shown. FeO_6 octahedral units are shown in brown. I and O atoms are represented in purple and red, respectively. Short I–O bonds are shown with gray solid lines, while long I–O bonds that do not result in an increased coordination are shown with blue dashed lines. Fe atoms are sixfold coordinated, whereas I atoms are threefold coordinated.

In this work, we explore the proposed phonon-softening phenomenon by HP Raman spectroscopy (RS), which will be analyzed with the help of *ab initio* DFT calculations. We have performed HP RS experiments up to 21 GPa to minimize the influence of precursor effects of the first-order phase transition that has been reported to occur at 22 GPa. Combining experimental and theoretical results, we propose for the first time a tentative symmetry assignment for Raman modes of $\text{Fe}(\text{IO}_3)_3$ and discuss the nature of the soft phonons. In particular, we have found evidence of the occurrence of two subtle isostructural phase transitions (IPTs), which were not detected by previous studies.

Before presenting and discussing our results, we briefly describe the crystal structure of $\text{Fe}(\text{IO}_3)_3$, which is shown in Figure 1. The description of the structure is relevant for the discussion of the results reported here. In Figure 1, it can be seen that the structure is formed by FeO_6 octahedral units connected by isolated IO_3 trigonal pyramids which deviate from the ideal $3m$ point symmetry because the lone pair takes up a larger region of space than do the single I–O bonds. In the figure, we have included the bonds corresponding to the IO_3 coordination polyhedron and dashed lines indicating the three second-neighbor O atoms, which become relevant under compression.

We start discussing the Raman spectra under ambient conditions which are shown in Figure 2. The spectrum is very similar to those reported in the literature.^{8,9} As can be observed, the Raman-active modes are distributed in two isolated regions. One region is for wavenumbers smaller than 500 cm^{-1} and the other is for wavenumbers larger than 650 cm^{-1} , with a phonon gap between the two regions. The strongest mode is located at 792 cm^{-1} . Along the paper, we show that the high-frequency modes are linked to I–O vibrations. In particular, they are internal modes of IO_3 units.

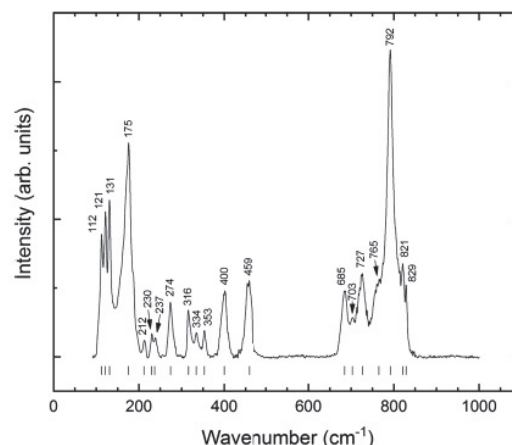


Figure 2. Ambient-pressure Raman spectrum of $\text{Fe}(\text{IO}_3)_3$ recorded outside the DAC. Ticks show the position of the identified modes. Their wavenumbers are also given.

For $\text{Fe}(\text{IO}_3)_3$, group theory predicts 37 Raman-active modes ($12A_1 + 12E_1 + 13E_2$). In previous studies,^{8,9} Ristic et al. measured 17 modes and Bushiri et al. measured 14 modes. In our experiments, we have measured 20 modes. The Raman-active modes are summarized in Table 1, where they have been given a superindex to number them in the order of increasing frequency. It can be seen that there is good agreement between the frequencies reported in different experiments.

DFT-calculated frequencies of $\text{Fe}(\text{IO}_3)_3$ are also listed in Table 1. DFT calculations give a good description of experimentally observed Raman-active mode frequencies, with the differences being smaller than 10%, which is typical for most oxides.¹⁰ In particular, the mode frequencies of $\text{Fe}(\text{IO}_3)_3$ in the low-frequency region are slightly underestimated by our PBEsol + *U* calculations, as happens in many other oxides.¹⁰ On the other hand, the calculated high-frequency modes have an offset of nearly 60 cm^{-1} with respect to experiments. The comparison of frequencies and their pressure dependences (to be discussed) allowed us to propose a tentative assignment of the experimentally observed Raman-active modes. The symmetry of the different modes is included in Table 1.

According to our mode assignment, the strongest Raman-active mode, located at a wavenumber of 792 cm^{-1} (A^{11} mode in Table 1), can be identified as an internal symmetric stretching vibration of O atoms against the I atom inside IO_3 units (see Figure S1 in the Supporting Information) and calculated to be at 729.2 cm^{-1} in Table 1. Notice that DFT describes properly not only Raman-active modes but also IR-active modes, which are already reported,⁷ and their pressure dependence.

Interestingly, in many metal iodates with different compositions, the strongest Raman-active mode is always located in the $730\text{--}800\text{ cm}^{-1}$ region. In $\text{Ni}(\text{IO}_3)_2$, $\text{Mn}(\text{IO}_3)_2$, $\text{Co}(\text{IO}_3)_2$, and $\text{Zn}(\text{IO}_3)_2$, the strongest Raman-active mode is in the $763\text{--}782\text{ cm}^{-1}$ range.¹¹ In $\text{Al}(\text{IO}_3)_3$, $\text{Ga}(\text{IO}_3)_3$, and $\text{In}(\text{IO}_3)_3$, it is in the $730\text{--}800\text{ cm}^{-1}$ range.¹² Finally, in KIO_3 , the strongest mode¹³ is at 748 cm^{-1} . All these iodates have in common that in their structure, iodine atoms form IO_3 trigonal pyramids with very short I–O bond distances. Based on this fact, it has been generally assumed that the strongest Raman-active mode of each compound is an internal symmetric stretching I–O vibration inside the IO_3 unit. In the case of

Table 1. Theoretical and Experimental Zero-Pressure Frequencies, ω , Pressure Coefficients, $d\omega/dP$, and Grüneisen Parameters, γ , of Raman-Active Modes of $\text{Fe}(\text{IO}_3)_3$ ^a

mode	theory			experiment				
	ω_0^b (cm ⁻¹)	$d\omega/dP^b$ (cm ⁻¹ /GPa)	γ^b	ω_0^b (cm ⁻¹)	$d\omega/dP^b$ (cm ⁻¹ /GPa)	γ^b	ω_0^c (cm ⁻¹)	ω_0^d (cm ⁻¹)
A ¹ (RI)	57.3	-0.08	-0.05					55
E ₁ ¹ (RI)	65.6	3.10	1.70					
E ₂ ¹ (R)	79.8	1.24	0.56					
E ₂ ² (R)	89.6	5.21	2.09				86	85
A ² (RI)	112.3	4.88	1.56	112	2.44	1.20		110
E ₁ ² (RI)	119.8	2.48	0.75	121	1.78	0.81	125	125
A ³ (RI)	126.1	1.85	0.53					
E ₂ ³ (R)	131.8	5.57	1.52	131	3.57	1.50		
E ₁ ³ (RI)	165.4	3.96	0.86	175	0.70	0.22	166	165
E ₂ ⁴ (R)	172.3	6.65	1.39					
E ₂ ⁵ (R)	194.5	4.49	0.83					
E ₁ ⁴ (RI)	202.2	6.16	1.10					
A ⁴ (RI)	212.7	2.53	0.43	212	2.76	0.72		205
E ₁ ⁵ (RI)	219.4	9.30	1.53					
E ₂ ⁶ (R)	223.5	5.17	0.83	230	4.27	1.02	223	225
A ⁵ (RI)	239.8	6.48	0.97	237	6.76	1.57		
E ₂ ⁷ (R)	245.3	7.99	1.17					
E ₁ ⁶ (RI)	269.8	4.83	0.64					
A ⁶ (RI)	270.7	7.35	0.98	274	7.14	1.43	266	265
A ⁷ (RI)	291.7	1.88	0.23	316	0.65	0.11	320	315
E ₁ ⁷ (RI)	316.5	4.51	0.51	334	1.36	0.22		
E ₂ ⁸ (R)	334.2	2.90	0.31	353	1.78	0.28	350	350
E ₁ ⁸ (RI)	382.5	4.06	0.38					
E ₂ ⁹ (R)	385.5	6.06	0.57					
A ⁸ (RI)	391.4	3.02	0.28	400	4.27	0.59	394	395
A ⁹ (RI)	436.9	7.89	0.65	459	5.78	0.69	450	445
E ₁ ¹⁰ (R)	445.1	7.15	0.58					
E ₁ ⁹ (RI)	445.9	7.74	0.62					
E ₂ ¹¹ (R)	619.8	-1.40	-0.08					
E ₁ ¹⁰ (RI)	622.1	-0.65	-0.04	685	-0.20	-0.02	685	685
A ¹⁰ (RI)	637.7	-1.68	-0.09	703	-2.32	-0.18		
E ₂ ¹² (R)	674.7	0.07	0.00	727	-0.87	-0.07	726	726
E ₁ ¹¹ (RI)	697.9	-2.38	-0.12	765	-3.72	-0.27	755	756
A ¹¹ (RI)	729.2	-1.45	-0.07	792	-3.51	-0.24	795	796
E ₁ ¹² (RI)	770.7	-5.59	-0.26	821	-3.40	-0.23		826
A ¹² (RI)	774.0	-6.95	-0.32	829	-6.41	-0.43	831	
E ₂ ¹³ (R)	791.1	-5.25	-0.24					

^aIn fact, our experimental frequencies correspond to 0.5 GPa. Raman-active (R) or both Raman- and IR-active (RI) are indicated. Results of previous experiments^{8,9} have also been included for comparison. To calculate the Grüneisen parameters, we have used the theoretical bulk modulus (36 GPa) for calculations and the experimental bulk modulus (55 GPa) for experiments.^{7 b}This work. ^cRef.⁹ ^dRef.⁸

$\text{Fe}(\text{IO}_3)_3$, we support this conclusion by calculating the atomic motions associated with these modes (see Figure S1). This fact will be discussed in more detail when presenting the HP results. The three Raman-active modes (E_1^{12} , A^{12} , and E_2^{13}) with higher frequencies than the symmetric stretching mode correspond to asymmetric stretching I–O vibrations inside the IO_3 unit (see Figures S2–S4 in the Supporting Information).

We now start discussing the HP behavior of the Raman spectra in $\text{Fe}(\text{IO}_3)_3$. In Figure 3, we show Raman spectra at different pressures. In Figure 4, we show the pressure dependence of phonon wavenumbers. The spectrum measured at 0.5 GPa is very similar to the ambient-pressure spectrum shown in Figure 2. The Raman spectra under compression show a monotonous behavior with no abrupt frequency changes up to 21 GPa, indicating that a first-order transition does not happen in this pressure range. The intensity changes

observed beyond 15 GPa for the modes around 150 and 320 cm^{-1} are related to phonon merging or splitting due to the different pressure dependences of modes (see Figure 4). The nonoccurrence of a first-order transition in the pressure range of the present study is in good agreement with the results from previous XRD measurements.⁷ Previous IR spectroscopy studies located the transition at 15 GPa.⁷ The lower transition pressure observed in these experiments is due to the use of a less hydrostatic medium in IR experiments (CsI) than in present Raman and previous XRD experiments (silicone oil).^{7,10,14,15} However, when analyzing the pressure dependence of modes with the help of DFT calculations, we have found that there are modes showing strong nonlinear pressure dependences and soft-mode behaviors (see Figure 4) that suggest possible continuous transitions as discussed next. All changes observed in the RS spectrum under compression are reversible, as can be seen in Figure 3 in the top RS spectrum

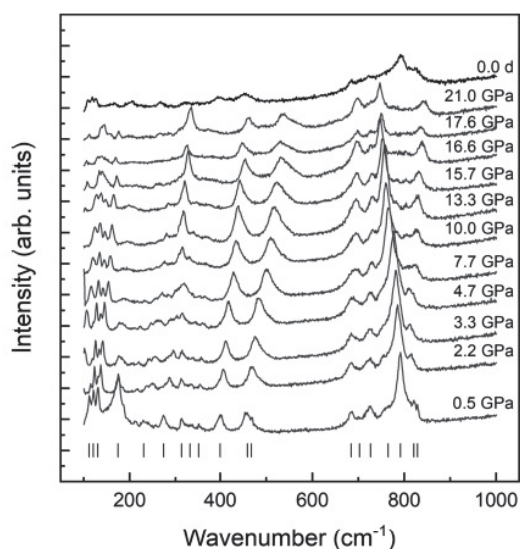


Figure 3. Selection of Raman spectra recorded in $\text{Fe}(\text{IO}_3)_3$ at different pressures. The top Raman spectrum was taken upon decompression “d” to show the reversibility of the process. Bottom marks indicate the frequencies of the experimental modes at the smallest pressure.

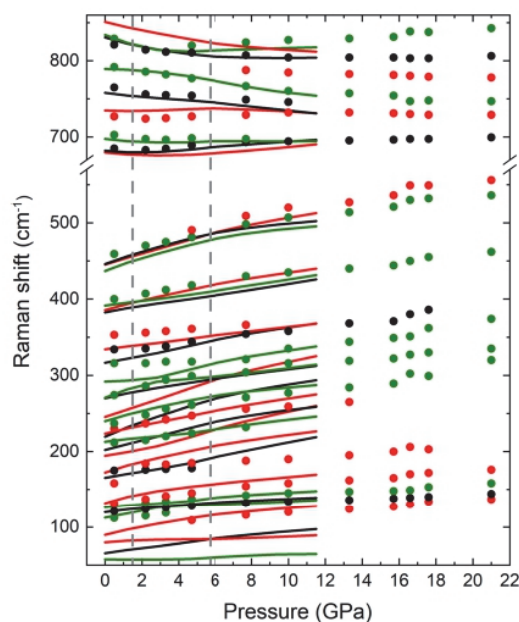


Figure 4. Experimental (symbols) and theoretical (solid lines) pressure dependence of Raman-active mode frequencies in $\text{Fe}(\text{IO}_3)_3$. The green, black, and red colors correspond to the A_1 , E_1 , and E_2 modes, respectively. In the high-frequency region (top panel), calculated modes have been shifted 60 cm^{-1} to higher frequencies to facilitate comparison with experiments. The vertical dashed lines indicate the pressures where changes associated to the two IPTs can be observed.

recorded after decompression. Note that at 10 GPa, there are two peaks near 300 cm^{-1} that overlap. This causes an apparent increase in intensity at this frequency. In Figure 3, a pressure-induced closing of the phonon gap can be also noticed. This fact is mainly caused by the hardening of modes below 450 cm^{-1} and the softening of all the measured high-frequency

modes. Therefore, the closing of the phonon gap, more evident in Figure 4, where we have plotted the pressure dependence of the experimental and theoretical Raman-active modes, also suggests an increase of I coordination.

Experimental and theoretical zero-pressure frequencies, pressure coefficients, and Grüneisen parameters show relatively good agreement, as can be seen in Figure 4 and in Table 1. In the figure, DFT results are shown only up to 12 GPa because they underestimate the transition pressure of the first-order transition, as discussed in ref 7. Therefore, for consistency, DFT results are compared with experiments only for the pressures below the theoretical first-order phase transition. As observed in Figure 4, many Raman-active modes show anomalous pressure dependences. Not only there are high-frequency soft modes but also there are many modes in the low- and high-frequency regions that show an S-like nonlinear pressure dependence that will be commented later. Consequently, the zero-pressure coefficients in Table 1 have been obtained using the pressure range where the frequency dependence is linear with pressure, near 0 GPa, and the Grüneisen parameters have been calculated using the bulk moduli given in the caption of Table 1. In Figures 3 and 4, it can be seen that there is a progressive closing of the phonon gap with increasing pressure, which suggests the existence of a close first-order phase transition above 21 GPa, that is, consistent with XRD measurements.⁷ Additionally, in the high-frequency region, all the modes of $\text{Fe}(\text{IO}_3)_3$ have a soft-mode behavior, at least between 0 and 2 GPa. Using J-ICE, we have identified that the high-frequency modes mainly correspond to symmetric and asymmetric I–O stretching vibrations inside the IO_3 units (see Figures S1–S4 for examples). As shown in Figure 4, DFT not only supports the existence of soft modes but also provides a qualitatively good description for the pressure dependence of most observed modes. Note that for high-frequency modes, theoretical calculations describe nicely the pressure dependence of experimental mode frequencies when an upward shift of 60 cm^{-1} is applied to calculated frequencies.

Interestingly, we have found that one of the experimental soft modes of $\text{Fe}(\text{IO}_3)_3$ is the strongest mode at 792 cm^{-1} that we have tentatively attributed to the A_1^{11} mode (with a calculated frequency of 729.2 cm^{-1}). The observed mode softening of the high-frequency modes can be correlated to the pressure-induced increase of two of the short I–O bond distances (see Figure 5), which is expected to reduce the restoring force of stretching vibrations. According to our calculations, iodine atoms are threefold coordinated at room pressure. However, by considering as coordinated to iodine all those oxygen atoms with an I–O bond length up to 33% larger than the maximum distance among the three short I–O bonds, it can be concluded that the coordination number of iodine increases as pressure increases. In particular, the iodine coordination first becomes fourfold (at least above 5.7 GPa) and then gradually approaches a sixfold coordination (see Figure 5), becoming six at the phase transition at 22 GPa.⁷ This can be explained by the progressive reduction of the iodine LEP stereoactivity with increasing pressure, as found in a number of heavy pnictogen (As, Sb, and Bi) compounds with a strong LEP stereoactivity at room pressure, such as $\alpha\text{-Sb}_2\text{O}_3$,^{16–18} $\beta\text{-Bi}_2\text{O}_3$,^{19,20} isostructural Sb_2S_3 , Sb_2Se_3 , and Bi_2S_3 compounds,²¹ $\alpha\text{-As}_2\text{Te}_3$,²² SbPO_4 ,^{2,3} and As_2S_3 .²⁴

Under a harmonic approximation, it can be assumed as a first approximation that the force constant, k , of the internal

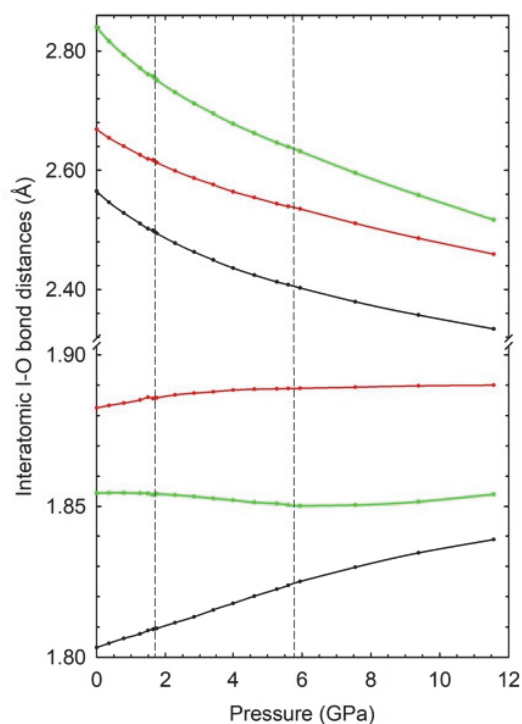


Figure 5. Calculated pressure dependence of I–O bond distances. The vertical dashed lines indicate the pressures where changes associated to the two IPTs can be observed. A gradual increase of I coordination can be inferred from this figure.

phonons of IO_3 is a function of $(d_{\text{I-O}})^{-3}$, where $d_{\text{I-O}}$ is the average I–O bond distance.²⁵ Because the frequency of a stretching mode is proportional to the square root of the force constant and inversely proportional to the square root of the reduced mass, μ , of the bond, $\omega = (k/\mu)^{1/2}$, we have that $\omega^{-2/3}$ should have a linear dependence on the average I–O bond distance. Using the results of our calculations, we have correlated the theoretical frequencies of the soft modes with the theoretical average I–O bond distance in IO_3 units (see Figure 6). Here, it can be seen that indeed there is a clear

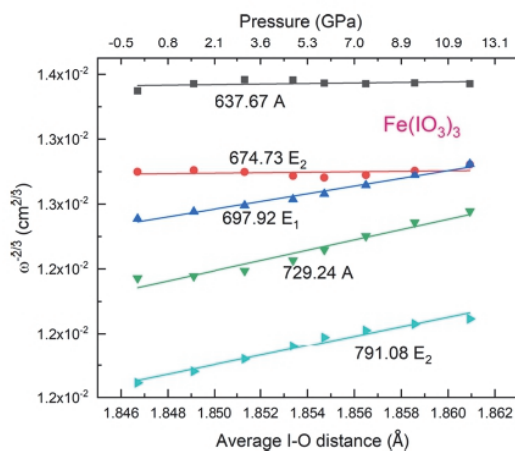


Figure 6. Theoretical $\omega^{-2/3}$ vs average theoretical I–O bond distances in IO_3 units of $\text{Fe}(\text{IO}_3)_3$. In the upper axis, the pressure of each average bond distance is indicated. It can be seen that the average I–O bond distance increases under compression.

linear relationship between the $\omega^{-2/3}$ and the calculated average I–O bond distance for the soft high-frequency modes. Thus, the decrease of the phonon frequencies is a consequence of the slight enlargement of the three shortest I–O distances in order to accommodate additional O atoms around iodine as pressure increases.

It is noteworthy that the average distance of the three short I–O bonds of the IO_3 unit increases slightly under compression because of the changes induced by pressure in the crystal structure of $\text{Fe}(\text{IO}_3)_3$.⁷ Simultaneously, second-neighbor I–O distances above 2.5 Å show a notable decrease at HP (see Figure 5). Therefore, these O atoms enter progressively into the coordination sphere of iodine atoms and induce changes in the coordination of I atoms. We believe that the enlargement of the short I–O bonds under compression is responsible for the softening of most high-frequency modes and is a consequence of a charge transfer from the short I–O bonds to the large I–O bonds in order to increase the iodine coordination. Such an increase of the bond distance and decrease of the bond charge has been recently observed in As_2S_3 ²⁴ and has been related to the novel phenomena of “metavalent” bonding, that is, the observation of a new type of chemical bonding intermediate between covalent and metallic bonding and characterized by bonds with less than two electrons per bond.^{26,27} In some oxides with strong LEP stereoactivity at room pressure, this behavior has been related to the existence of unusual IPTs, such as in $\alpha\text{-Sb}_2\text{O}_3$ ^{16–18} and $\beta\text{-Bi}_2\text{O}_3$.^{19,20}

We now present evidence supporting the existence of subtle IPTs in $\text{Fe}(\text{IO}_3)_3$. Such transitions were not detected by previous XRD studies because these subtle phase transitions involve only continuous changes in the crystal structure, with no discontinuities in the unit-cell parameters or atomic positions. In contrast, RS experiments, sensing local properties, as the vibrations are, are more sensitive for detecting such subtle transitions. We have found evidence for the two IPTs not only from the pressure dependence of phonons and bond distances but also from the analysis of atomic positions and elastic constants that correlate with changes in lattice parameters at HP. A detailed analysis of all this information places the transitions, near 1.5–2.0 and 5.7–6.0 GPa. For the sake of brevity, we present the evidence for the two IPTs in Figures S5–S10 of the Supporting Information. These figures show the theoretical pressure dependence of the unit-cell parameters and free atomic parameters of $\text{Fe}(\text{IO}_3)_3$. In particular, the two IPTs, marked by the vertical dashed lines in these figures, can explain the strong nonlinear S-like behavior of a number of parameters of $\text{Fe}(\text{IO}_3)_3$; for instance, the z-coordinate of the Fe atom. Additional support for the two IPTs near 1.5 and 5.7 GPa comes from the pressure dependence of the elastic constants, which is shown in Figure 7. In particular, at 1.7 GPa, there is a clear jump of C_{33} , C_{66} , C_{12} , and C_{13} . Such changes are indicative of the occurrence of phase transitions.^{28–30} At 5.7 GPa, there are also changes in the elastic constant, and they are less evident than at 1.7 GPa; however, there are detectable changes in the pressure dependence of C_{13} and C_{33} , as can be seen in Figure 7.

In order to understand the nature of the two IPTs without change of volume, we have calculated the phonon dispersion curves of $\text{Fe}(\text{IO}_3)_3$ at 0, 1.5, 5.7, and 7.5 GPa, which are shown in Figure 8. As observed, the phonon dispersion curves show small dynamic instabilities (negative frequencies) near the Γ -point at 1.5 and 5.7 GPa that are not observed either at 0 GPa

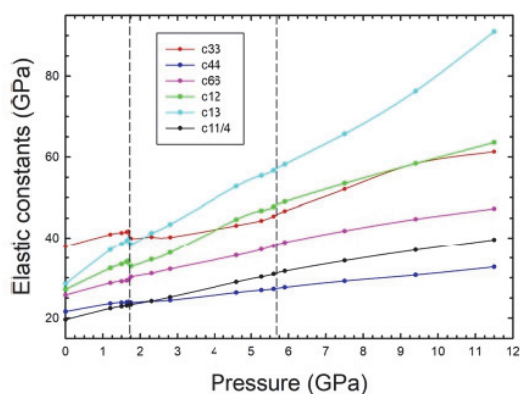


Figure 7. Calculated pressure dependence of elastic constants in $\text{Fe}(\text{IO}_3)_3$. The vertical dashed lines indicate the pressures where changes due to the two IPTs can be observed. Note the changes of the elastic constants especially around 1.5 GPa.

or at 7.5 GPa. Consequently, we can conclude that the two IPTs observed in $\text{Fe}(\text{IO}_3)_3$ are of similar nature to the one of tetragonal $\beta\text{-Bi}_2\text{O}_3$ ^{19,20} and perhaps also in $\alpha\text{-Sb}_2\text{O}_3$.^{16–18}

Additional support to the existence of two IPTs in $\text{Fe}(\text{IO}_3)_3$ comes from the study of phonon lifetime change with pressure. In the case of RS, the full width at half-maximum (fwhm) is related inversely to the phonon lifetime. The pressure dependence of the fwhm of two modes of $\text{Fe}(\text{IO}_3)_3$, which do not overlap with other modes, is shown in Figure 9. It is evident from the figure that the line width of the mode with a wavenumber of 400 cm^{-1} increases substantially with pressure beyond 2 GPa. On the other hand, the mode with a wavenumber of 792 cm^{-1} has a sharp change in the pressure evolution of the line width at 6 GPa. Such changes are typical

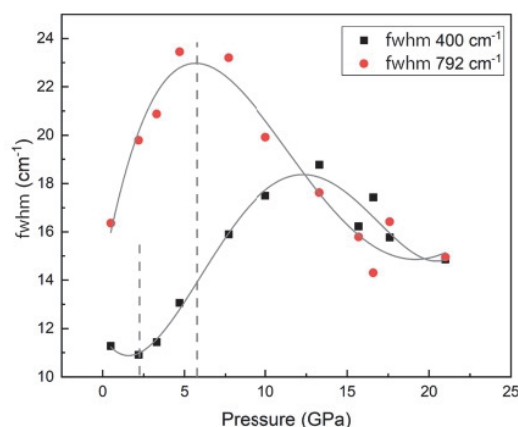


Figure 9. Pressure dependence of the fwhm of phonons with wavenumbers of 400 and 792 cm^{-1} .

of IPT transitions.^{18–22} We think that the fact that they take place at the same pressure that changes in pressure dependence of phonons, bond distances, and elastic constants is not a mere coincidence but another evidence of the occurrence of IPTs in $\text{Fe}(\text{IO}_3)_3$. Additional changes are observed in the behavior of phonon fwhm around 15–20 GPa, but they are related to precursor effects of the first-order transition previously reported at 22 GPa.

Summing up, both Raman experiments and DFT calculations support that there are soft modes in $\text{Fe}(\text{IO}_3)_3$ which are related to the increase of the three short I–O bonds with pressure. The short I–O bonds increase, while the second-neighbor I–O bonds decrease with pressure. Moreover, the nonlinear S-like behavior of several Raman-active modes (also of several IR-active modes)⁷ as well as of some elastic

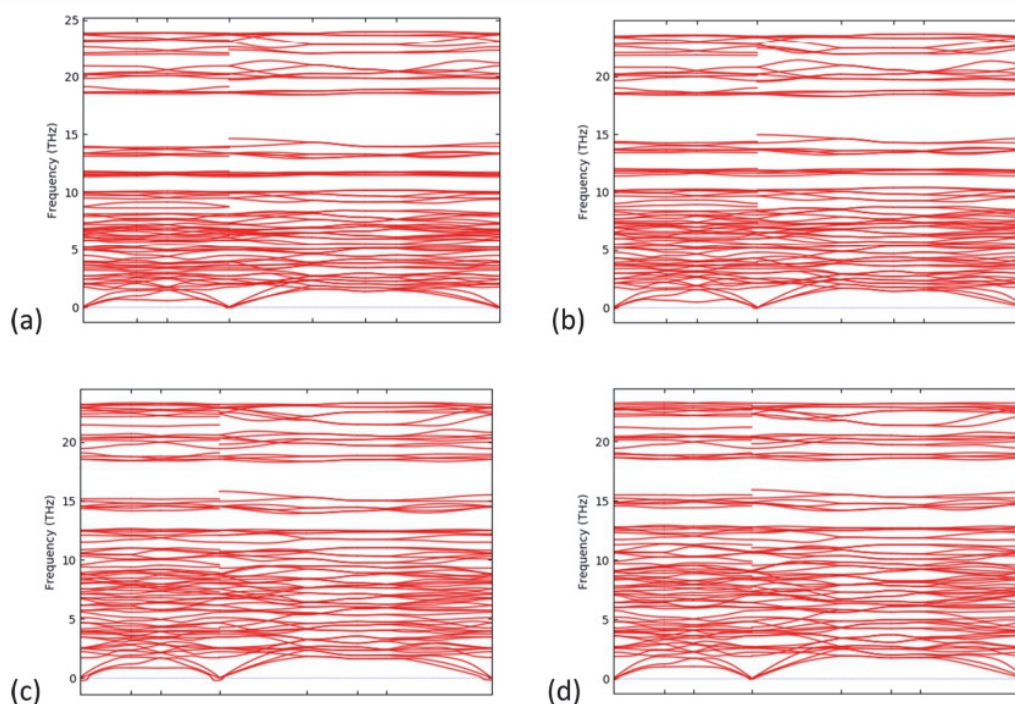


Figure 8. Calculated phonon dispersion curves along the $\Gamma\text{-M-K-}\Gamma\text{-A-L-H-}\Gamma$ direction at 0 (a), 1.5 (b), 5.7 (c), and 7.5 GPa (d). At 1.5 and 5.7 GPa, small dynamic instabilities (smaller at 1.5 GPa) are observed near the Γ -point which are not observed at 0 and 7.5 GPa.

constants can be explained by the occurrence of two IPTs around 1.5–2.0 and 5.7–6.0 GPa. The two IPTs are clearly related to changes in the behavior of lattice parameters and free atomic positions.

The formation of additional I–O bonds at HP in metal iodates has important consequences of the behavior of phonons under compression.³¹ Therefore, the present discovery of continuous IPTs in a metal iodate, such as $\text{Fe}(\text{IO}_3)_3$, opens the door to interesting findings in this family of compounds at HP. In particular, we have noticed that in KIO_3 also, two internal stretching modes of the IO_3 unit are soft modes.¹³ This compound undergoes a phase transition at 5 GPa. It would be not surprising that the observed soft modes in KIO_3 could be related to a collective instability which makes the crystal structure unstable, thus triggering a phase transition.^{32,33} This suggests that the triggering of phase transitions by soft modes could be a common feature of metal iodates.

In conclusion, the lattice dynamics of $\text{Fe}(\text{IO}_3)_3$ has been studied up to 21 GPa, within the range of stability of the low-pressure hexagonal phase, by means of RS measurements, which have been interpreted using DFT calculations. Our measurements and calculations evidence a progressive decrease of the phonon gap and the softening of most high-frequency vibrational modes at least up to 2 GPa. The frequency, pressure dependence, and symmetry of the different modes have been determined. The soft modes in the high-frequency region are related to internal I–O vibrations of IO_3 units. Among them, we include the symmetric stretching I–O vibration of IO_3 units, which is the strongest Raman-active mode. The soft mode behavior is proposed to be connected with the increase of the shortest I–O bond distances because of a gradual increase of the iodine coordination that leads to a decrease of the short I–O bond forces due to a charge transfer to long I–O distances. The nonlinear S-like behavior of a number of experimental and theoretical Raman-active modes, as well as other physical properties, can be explained by the existence of two IPTs at 1.5–2.0 and 5.7–6.0 GPa which occur without a volume change and only a change in volume compressibility. Our results have been compared with the results from other metal iodates in order to try to find general features in the iodate family. The present discovery of unusual IPTs in a metal iodate, such as $\text{Fe}(\text{IO}_3)_3$, and their relationship to soft modes open the door to interesting findings in the iodate family of compounds under compression and invite to revisit the HP behavior of iodine-based compounds, such as KIO_3 .

METHODS

Samples. For the study of $\text{Fe}(\text{IO}_3)_3$, we used the same sample used in our previous XRD and IR studies⁷ that was prepared by a coprecipitation technique. A description of the sample preparation method can be found in ref 7. The purity of the sample and crystal structure were confirmed by XRD measurements.⁷

HP Generation. We performed HP RS measurements at room temperature up to 21 GPa using silicone oil as a pressure-transmitting medium (PTM)^{14,15} to avoid the hydration of the metal iodates¹ and the ruby fluorescence scale as our pressure gauge.³⁴ The silicone fluid is as good a PTM as a 4:1 methanol/ethanol mixture up to a pressure of about 20 GPa.³⁵ For these studies, samples, ruby chips, and the PTM were loaded in the 200 μm diameter hole of a

preindented steel gasket inside a diamond-anvil cell (DAC). We made a careful loading of materials inside the DAC to avoid both sample hydration and sample bridging between diamond anvils.³⁶ Because of the size of the ruby pressure gauge and the distance between ruby chips and the measuring point (sample position), there is a radial pressure inhomogeneity in the DAC. We estimate the pressure difference between ruby and the sample to be smaller than 3% of the ruby pressure.³⁷

Raman Spectroscopy. HP RS measurements, with a fixed time of 20 s, were performed using an inVia Renishaw Raman spectrometer system with a 5 \times magnification objective. A laser wavelength of 532 nm and a grating of 2400 lines-mm⁻¹ provided a spectral resolution better than 2 cm⁻¹. A laser power inferior to 10 mW before the DAC was used to avoid sample heating.

Overview of the Calculations. DFT calculations were used for the interpretation of experiments and mode assignment. Total-energy and phonon calculations as a function of pressure for $\text{Fe}(\text{IO}_3)_3$ were previously published by a part of the coauthors of this work.⁷ Such calculations were performed using the Vienna Ab initio Simulation Package (VASP) within the generalized gradient approximation with the Perdew–Burke–Ernzerhof (PBE) for solids (PBEsol) functionals. The Hubbard potential, U , was also used ($U_{\text{eff}} = 5.4$ eV) to account for the strong correlation between the electrons in the d shell, as previously performed to explain XRD and IR results.⁷ After optimizing the crystal structure at different pressures, the phonon frequencies and phonon dispersion curves were calculated using the direct force method. The elastic constants were calculated using density functional perturbation theory. Thanks to DFT calculations, we have been able to identify atomic motions associated with phonons using the J-ICE software.³⁸

ASSOCIATED CONTENT

Supporting Information

The Supporting Information is available free of charge at <https://pubs.acs.org/doi/10.1021/acs.jpcc.0c06541>.

Atomic vibrations of Raman modes and calculated pressure dependence of unit-cell parameters and atomic positions (PDF)

AUTHOR INFORMATION

Corresponding Author

Daniel Errandonea – Departamento de Física Aplicada—ICMUV—MALTA Consolider Team, Universitat de Valencia, 46100 Burjassot, Valencia, Spain; orcid.org/0000-0003-0189-4221; Email: daniel.errandonea@uv.es

Authors

Akun Liang – Departamento de Física Aplicada—ICMUV—MALTA Consolider Team, Universitat de Valencia, 46100 Burjassot, Valencia, Spain

Saqib Rahman – Center for High Pressure Science and Technology Advanced Research, 201203 Shanghai, China

Placida Rodríguez-Hernández – Departamento Física, Malta Consolider Team, and Instituto de Materiales y Nanotecnología, Universidad de La Laguna, 38206 La Laguna, Tenerife, Spain; orcid.org/0000-0002-4148-6516

Alfonso Muñoz – Departamento Física, Malta Consolider Team, and Instituto de Materiales y Nanotecnología,

Universidad de La Laguna, 38206 La Laguna, Tenerife, Spain;
● orcid.org/0000-0003-3347-6518

Francisco Javier Manjón – Instituto de Diseño para la Fabricación y Producción Automatizada, MALTA-Consolider Team, Universitat Politècnica de València, 46022 Valencia, Spain; ● orcid.org/0000-0002-3926-1705

Gwilherm Nenert – Malvern Panalytical B.V., 7602 EA Almelo, The Netherlands

Complete contact information is available at:
<https://pubs.acs.org/10.1021/acs.jpcc.0c06541>

Author Contributions

The manuscript was written through contributions of all authors. All authors have given approval to the final version of the manuscript.

Notes

The authors declare no competing financial interest.

ACKNOWLEDGMENTS

This work was supported by the Spanish Ministry of Science, Innovation and Universities, the Spanish Research Agency (AEI), the European Fund for Regional Development (ERDF, FEDER) under grants MAT2016-75586-C4-1/2/3-P, PID2019-106383GB-C41/42/43, and RED2018-102612-T (MALTA Consolider-Team Network), and the Generalitat Valenciana under grant Prometeo/2018/123 (EFIMAT). A.L. and D.E. would like to thank the Generalitat Valenciana for the Ph.D. fellowship GRISOLIAP/2019/025).

REFERENCES

- (1) Nassau, K.; Shiever, J. W.; Prescott, B. E. Transition Metal Iodates. I. Preparation and Characterization of the 3d Iodates. *J. Solid State Chem.* **1973**, *7*, 186–204.
- (2) Jansen, M. Zur Kristallstruktur von Fe_3O_9 . *J. Solid State Chem.* **1976**, *17*, 1–6.
- (3) Hu, C.-L.; Mao, J.-G. Recent Advances on Second-Order NLO Materials Based on Metal Iodates. *Coord. Chem. Rev.* **2015**, *288*, 1–17.
- (4) Hebboul, Z.; Galez, C.; Benbental, D.; Beauquis, S.; Mugnier, Y.; Benmakhlof, A.; Bouchenafa, M.; Errandonea, D. Synthesis, Characterization, and Crystal Structure Determination of a New Lithium Zinc Iodate Polymorph $\text{LiZn}(\text{IO}_3)_3$. *Crystals* **2019**, *9*, 464.
- (5) Bergman, J. G.; Boyd, G. D.; Ashkin, A.; Kurtz, S. K. New Nonlinear Optical Materials: Metal Oxides with Nonbonded Electrons. *J. Appl. Phys.* **1969**, *40*, 2860–2863.
- (6) Sagotra, A. K.; Errandonea, D.; Cazorla, C. Mechanocaloric Effects in Superionic Thin Films from Atomistic Simulations. *Nat. Commun.* **2017**, *8*, 963.
- (7) Liang, A.; Rahman, S.; Saqib, H.; Rodriguez-Hernandez, P.; Muñoz, A.; Nenert, G.; Yousef, I.; Popescu, C.; Errandonea, D. First-Order Isostructural Phase Transition Induced by High-Pressure in $\text{Fe}(\text{IO}_3)_3$. *J. Phys. Chem. C* **2020**, *124*, 8669–8679.
- (8) Ristić, M.; Musić, S.; Ivanda, M. A Study of the Thermal Stability of $\text{Fe}(\text{IO}_3)_3$ by ^{57}Fe Mossbauer, FT-IR and Raman Spectroscopies. *J. Mol. Struct.* **1999**, *480–481*, 637–640.
- (9) Bushiri, M. J.; Kochuthresia, T. C.; Vaidyan, V. K.; Gautier-Luneau, I. Raman Scattering Structural Studies of Nonlinear Optical $\text{M}(\text{IO}_3)_3$ ($\text{M}=\text{Fe}$, Ga , $\alpha\text{-In}$) and Linear Optical $\beta\text{-In}(\text{IO}_3)_3$. *J. Nonlinear Opt. Phys. Mater.* **2014**, *23*, 1450039.
- (10) Errandonea, D.; Muñoz, A.; Rodríguez-Hernández, P.; Gomis, O.; Achary, S. N.; Popescu, C.; Patwe, S. J.; Tyagi, A. K. High-Pressure Crystal Structure, Lattice Vibrations, and Band Structure of BiSbO_4 . *Inorg. Chem.* **2016**, *55*, 4958–4969.
- (11) Kochuthresia, T. C.; Gautier-Luneau, I.; Vaidyan, V. K.; Bushiri, M. J. Raman and Ftir Spectral Investigations of Twinned

$\text{M}(\text{IO}_3)_2$ ($\text{M} = \text{Mn}$, Ni , Co , AND Zn) Crystals. *J. Appl. Spectrosc.* **2016**, *82*, 941–946.

(12) Ngo, N.; Kalachnikova, K.; Assefa, Z.; Haire, R. G.; Sykora, R. E. Synthesis and Structure of $\text{In}(\text{IO}_3)_3$ and Vibrational Spectroscopy of $\text{M}(\text{IO}_3)_3$ ($\text{M}=\text{Al}$, Ga , In). *J. Solid State Chem.* **2006**, *179*, 3824–3830.

(13) Shen, Z. X.; Wang, X. B.; Li, H. P.; Tang, S. H.; Zhou, F. High Pressure Raman Study and Phase Transitions of KIO_3 Non-Linear Optical Single Crystals. *Rev. High Pressure Sci. Technol.* **1998**, *7*, 751–753.

(14) Klotz, S.; Chervin, J.-C.; Munsch, P.; Le Marchand, G. Hydrostatic Limits of 11 Pressure Transmitting Media. *J. Phys. D: Appl. Phys.* **2009**, *42*, 075413.

(15) Errandonea, D.; Meng, Y.; Somayazulu, M.; Häusermann, D. Pressure-Induced $\rightarrow \omega$ Transition in Titanium Metal: A Systematic Study of the Effects of Uniaxial Stress. *Phys. B* **2005**, *355*, 116–125.

(16) Sui, Z.; Hu, S.; Chen, H.; Gao, C.; Su, H.; Rahman, A.; Dai, R.; Wang, Z.; Zheng, X.; Zhang, Z. Laser Effects on Phase Transition for Cubic Sb_2O_3 Microcrystals under High Pressure. *J. Mater. Chem. C* **2017**, *5*, 5451–5457.

(17) Zhao, Z.; Zeng, Q.; Zhang, H.; Wang, S.; Hirai, S.; Zeng, Z.; Mao, W. L. Structural Transition and Amorphization in Compressed $\alpha\text{-Sb}_2\text{O}_3$. *Phys. Rev. B: Condens. Matter Mater. Phys.* **2015**, *91*, 184112.

(18) Pereira, A. L. J.; Gracia, L.; Santamaría-Pérez, D.; Vilaplana, R.; Manjón, F. J.; Errandonea, D.; Nalin, M.; Beltrán, A. Structural and Vibrational Study of Cubic Sb_2O_3 under High Pressure. *Phys. Rev. B: Condens. Matter Mater. Phys.* **2012**, *85*, 174108.

(19) Pereira, A. L. J.; Gomis, O.; Sans, J. A.; Contreras-García, J.; Manjón, F. J.; Rodríguez-Hernández, P.; Muñoz, A.; Beltrán, A. $\beta\text{-Bi}_2\text{O}_3$ under Compression: Optical and Elastic Properties and Electron Density Topology Analysis. *Phys. Rev. B* **2016**, *93*, 224111.

(20) Pereira, A. L. J.; Sans, J. A.; Vilaplana, R.; Gomis, O.; Manjón, F. J.; Rodríguez-Hernández, P.; Muñoz, A.; Popescu, C.; Beltrán, A. Isostructural Second-Order Phase Transition of $\beta\text{-Bi}_2\text{O}_3$ at High Pressures: An Experimental and Theoretical Study. *J. Phys. Chem. C* **2014**, *118*, 23189–23201.

(21) Ibáñez, J.; Sans, J. A.; Popescu, C.; López-Vidrier, J.; Elvira-Betanzos, J. J.; Cuenca-Gotor, V. P.; Gomis, O.; Manjón, F. J.; Rodríguez-Hernández, P.; Muñoz, A. Structural, Vibrational, and Electronic Study of Sb_2S_3 at High Pressure. *J. Phys. Chem. C* **2016**, *120*, 10547–10558.

(22) Cuenca-Gotor, V. P.; Sans, J. A.; Ibáñez, J.; Popescu, C.; Gomis, O.; Vilaplana, R.; Manjón, F. J.; Leonardo, A.; Sagasta, E.; Suárez-Alcubilla, A.; et al. Structural, Vibrational, and Electronic Study of $\alpha\text{-As}_2\text{Te}_3$ under Compression. *J. Phys. Chem. C* **2016**, *120*, 19340–19352.

(23) Pereira, A. L. D. J.; Santamaría-Pérez, D.; Vilaplana, R.; Errandonea, D.; Popescu, C.; Da Silva, E. L.; Sans, J. A.; Rodríguez-Carvajal, J.; Muñoz, A.; Rodríguez-Hernández, P.; et al. Experimental and Theoretical Study of SbPO_4 under Compression. *Inorg. Chem.* **2020**, *59*, 287–307.

(24) Cuenca-Gotor, V. P.; Sans, J. A.; Gomis, O.; Mujica, A.; Radescu, S.; Muñoz, A.; Rodríguez-Hernández, P.; Da Silva, E. L.; Popescu, C.; Ibáñez, J.; et al. Orpiment under Compression: Metavalent Bonding at High Pressure. *Phys. Chem. Chem. Phys.* **2020**, *22*, 3352–3369.

(25) Bucknum, M. J. Chemical Physics of Phonons and Superconductivity: A Heuristic Approach. *Nat. Preced.* **2008**, *1586*, 2.

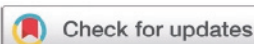
(26) Wuttig, M.; Deringer, V. L.; Gonze, X.; Bichara, C.; Raty, J.-Y. Incipient Metals: Functional Materials with a Unique Bonding Mechanism. *Adv. Mater.* **2018**, *30*, 1803777.

(27) Raty, J. Y.; Schumacher, M.; Golub, P.; Deringer, V. L.; Gatti, C.; Wuttig, M. A Quantum-Mechanical Map for Bonding and Properties in Solids. *Adv. Mater.* **2019**, *31*, 1806280.

(28) Boccara, N. Second-Order Phase Transitions Characterized by a Deformation of the Unit Cell. *Ann. Phys.* **1968**, *47*, 40–64.

(29) Errandonea, D. Landau Theory Applied to Phase Transitions in Calcium Orthotungstate and Isostructural Compounds. *Europhys. Lett.* **2007**, *77*, 56001.

- (30) Tröster, A.; Schranz, W.; Ehsan, S.; Belbase, K.; Blaha, P. Symmetry-Adapted Finite Strain Landau Theory Applied to KMnF_3 . *Crystals* **2020**, *10*, 124.
- (31) Monteseuro, V.; Errandonea, D.; Achary, S. N.; Sans, J. A.; Manjón, F. J.; Gallego-Parra, S.; Popescu, C. Structural Characterization of Aurophilic Gold(I) Iodide under High Pressure. *Inorg. Chem.* **2019**, *58*, 10665–10670.
- (32) Errandonea, D.; Pellicer-Porres, J.; Pujol, M. C.; Carvajal, J. J.; Aguiló, M. Room-Temperature Vibrational Properties of Potassium Gadolinium Double Tungstate under Compression up to 32 GPa. *J. Alloys Compd.* **2015**, *638*, 14–20.
- (33) Liu, J.; Shen, Z.; Zhang, Y.; Yin, X.; He, S. The P-T Phase Diagram of Lithium Iodate (LiIO_3) up to 40 Kbars. *Acta Phys. Sin.* **1983**, *32*, 118–123.
- (34) Mao, H. K.; Xu, J.; Bell, P. M. Calibration of the Ruby Pressure Gauge to 800 Kbar under Quasi-Hydrostatic Conditions. *J. Geophys. Res.* **1986**, *91*, 4673–4676.
- (35) Shen, Y.; Kumar, R. S.; Pravica, M.; Nicol, M. F. Characteristics of silicone fluid as a pressure transmitting medium in diamond anvil cells. *Rev. Sci. Instrum.* **2004**, *75*, 4450–4454.
- (36) Errandonea, D.; Muñoz, A.; Gonzalez-Platas, J. Comment on High-Pressure x-Ray Diffraction Study of $\text{YBO}_3/\text{Eu}^{3+}$, GdBO_3 , and EuBO_3 : Pressure-Induced Amorphization in GdBO_3 . *J. Appl. Phys.* **2014**, *115*, 216101.
- (37) Jayaraman, A. Diamond anvil cell and high-pressure physical investigations. *Rev. Mod. Phys.* **1983**, *55*, 65–108.
- (38) Canepa, P.; Hanson, R. M.; Ugliengo, P.; Alfredsson, M. J-ICE: A New Jmol Interface for Handling and Visualizing Crystallographic and Electronic Properties. *J. Appl. Crystallogr.* **2011**, *44*, 225–229.



Cite this: *Inorg. Chem. Front.*, 2021, **8**, 4780

Pressure-dependent modifications in the optical and electronic properties of $\text{Fe}(\text{IO}_3)_3$: the role of Fe 3d and I 5p lone-pair electrons

Akun Liang,^a Placida Rodriguez-Hernandez,^b Alfonso Muñoz,^b Saqib Rahman,^{c,d} Alfredo Segura^a and Daniel Errandonea^{b,*a}

We have determined by means of optical-absorption experiments that $\text{Fe}(\text{IO}_3)_3$ is an indirect band-gap material with a band-gap energy of 2.1 eV. This makes this compound the iodate with the smallest band gap. We also found that under compression the band-gap energy has an unusual non-linear pressure dependence, which is followed by an abrupt and discontinuous decrease of the band gap at 24 GPa. The observed behavior is explained by means of density-functional calculations, which show that the behavior of the band gap is governed by the combined influence of Fe 4d and I 5p lone pair electrons. In addition, the abrupt decrease of the band-gap energy at 24 GPa is a consequence of a first-order structural phase transition. These conclusions are confirmed by resistivity measurements, which show that intrinsic carriers dominate the transport properties of $\text{Fe}(\text{IO}_3)_3$.

Received 13th July 2021,
Accepted 14th September 2021
DOI: 10.1039/d1qi00870f

rsc.li/frontiers-inorganic

1. Introduction

Many transition-metal iodates crystallize in non-centrosymmetric structures (NCS) containing polyhedral units formed by transition-metal cations (such as Fe^{3+} , Zn^{2+} , or Co^{2+}), coordinated by oxygen atoms, and lone electron pair (LEP) iodine cations (I^{5+}).^{1–13} These iodates became the focus of attention in recent years.^{1–13} The research into this family of compounds is mainly motivated by the search for high-performance nonlinear-optical materials (NLO), which play a significant role in photoelectric and laser technology.^{14–16} The ideal NLO materials in turn should have a large second-harmonic generation (SHG) efficiency, a high laser-damage threshold (LDT), a wide transparency window, and good thermal stability.¹⁷ In particular, the band gaps of metal iodates will directly determine their transparency and have a significant effect on the SHG efficiency.¹⁷ Thus, it is necessary to understand how the transition metal and iodine with LEP could affect the band-gap value of metal iodates. Such characterization can

accurately be performed by combining optical-absorption experiments and band-structure calculations.¹⁸ A deeper understanding can be achieved if ambient-pressure studies are combined with high-pressure studies.¹⁸ High-pressure (HP) is an efficient tool for manipulating interatomic distances and the stereo-chemical activity of LEP in iodine. This will result in important modifications of the physical properties, including the optical and electronic properties.¹⁹ In the case of metal iodates it has been shown that compression induces fascinating and unusual phenomena, including non-linear compressibilities, phonon softening, and the occurrence of symmetry preserving phase transitions.^{20,21} However, the influence of these transitions on the electronic band gap remains unknown.

Here we chose $\text{Fe}(\text{IO}_3)_3$ as a research object since we have accurately determined its structural and vibrational behavior under pressure in our previous work.^{20,22} However, until now, the band-gap energy of $\text{Fe}(\text{IO}_3)_3$ and its pressure dependence are unknown. At room pressure, $\text{Fe}(\text{IO}_3)_3$ crystallizes in a hexagonal structure (space group: $P6_3$, no. 173),²³ which is shown in Fig. 1. In this crystal structure, every iron atom is surrounded by six IO_3 trigonal pyramids by sharing one oxygen atom (see Fig. 1a). In addition, different FeO_6 octahedral units are bridged by two IO_3 units. When observed from the direction perpendicular to the c -axis, the IO_3 units form a layered structure along the c -axis, and the “empty” space between the IO_3 layers favors a highly anisotropic behavior of $\text{Fe}(\text{IO}_3)_3$ under compression. This makes the c -axis the most compressible direction according to HP X-ray diffraction (HPXRD) experi-

^aDepartamento de Física Aplicada-ICMUV-MALTA Consolider Team, Universitat de València, c/Dr. Moliner 50, 46100 Burjassot, Valencia, Spain.

E-mail: daniel.errandonea@uv.es

^bDepartamento de Física and Instituto de Materiales y Nanotecnología, MALTA Consolider Team, Universidad de La Laguna, 38206 La Laguna, Tenerife, Spain

^cCenter for High Pressure Science (CHiPS), State Key Laboratory of Metastable Materials Science and Technology, Yanshan University, Qinhuangdao, Hebei 066004, China

^dCenter for High Pressure Science and Technology Advanced Research, Shanghai 201203, China

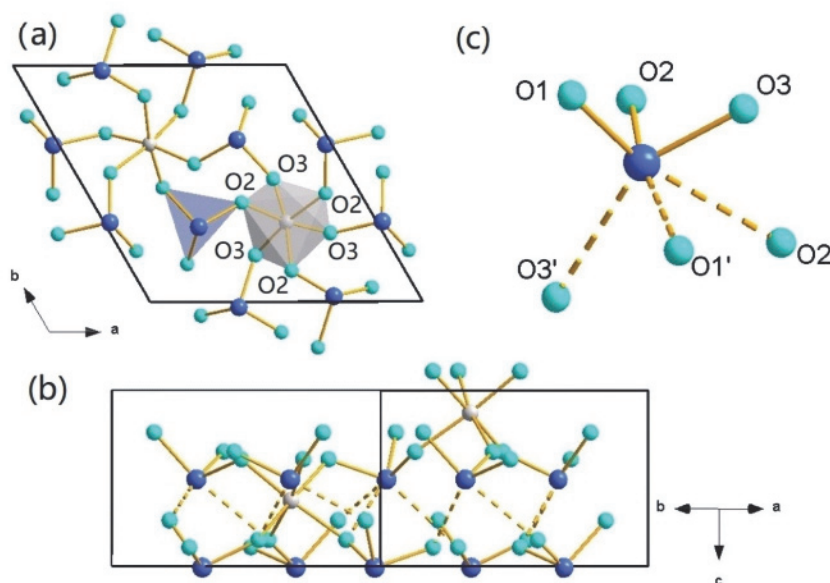


Fig. 1 Crystal structure of $\text{Fe}(\text{IO}_3)_3$ at ambient pressure derived from the Rietveld refinement results of the XRD spectra reported before.²⁰ (a) Along the c -axis, (b) perpendicular to the c -axis, (c) the detail of IO_6 polyhedral in (b). Iron, iodine, and oxygen are shown in gray, blue, and light blue, respectively. Solid yellow lines are interatomic bonds at ambient pressure while the dashed yellow lines are the bonds which are gradually formed under pressure. The labels of the oxygen atoms in (a) and (c) correspond to the labels used in ref. 20 and will be used in the discussion.

ments.²⁰ By combining HPXRD, HP Raman scattering (HP-RS), HP infrared spectroscopy experiments, and first-principle calculations, we have previously found that $\text{Fe}(\text{IO}_3)_3$ undergoes a series of isosymmetric phase transitions (IPTs) at 1.5, 5.7, and 22 GPa. The pressure of the last transition is strongly dependent on deviatoric stress. The first two IPTs are subtle and are caused by a gradual modification of the iodine coordination from 3- to 6-fold and a decrease of the stereo-chemical activity of LEP in iodine. This is a result of the decrease of the bond distance between iodine and the oxygen atoms in the neighboring IO_3 units. The new bonds between iodine and oxygen formed under pressure are shown in dashed lines in Fig. 1b and c. The third transition involves a unit-cell volume collapse of around 5%. The HP behavior of $\text{Fe}(\text{IO}_3)_3$ is qualitatively similar to that of $\text{Zn}(\text{IO}_3)_2$ and $\text{Co}(\text{IO}_3)_2$, even though the crystal structure of them are different.^{21,24} Therefore, a HP study on electronic and optical properties of $\text{Fe}(\text{IO}_3)_3$ will contribute not only to the better understanding of this material, but may also be of great help to make predictions on the HP band-gap behavior on other metal iodates.

In this paper, we report a joint experimental and theoretical study of the electronic band structure of $\text{Fe}(\text{IO}_3)_3$ under pressure up to 40 GPa. The band-gap energy of $\text{Fe}(\text{IO}_3)_3$ at ambient and high pressure are derived from optical-absorption experiments and first-principle band-structure calculations. These studies are complemented with HP resistivity measurements. The ambient-pressure results are compared with other metal iodates. At high pressure, the band-gap energy obtained from both experiments and calculations shows a strong non-linear behavior before the third phase transition, as well as a large band-gap energy collapse after it. We also report the cal-

culated electronic density of state (DOS) and projected density of state (PDOS), combined with the calculated atomic characters around the Fermi level. These results, along with the previous knowledge on the HP structure are used to explain the HP behavior of the band-gap energy of $\text{Fe}(\text{IO}_3)_3$.

II. Experimental details

For the experiments, we used the same polycrystalline $\text{Fe}(\text{IO}_3)_3$ sample used in our previous HP experiments.^{20,22} Details of the sample preparation method can be found in ref. 20. According to our previous XRD measurements, there are no detectable impurities, and the crystal structure agrees with the literature.²⁵ HP optical-absorption experiments were conducted by employing a membrane diamond-anvil cell (DAC) with diamond culets of 500 μm . Polycrystalline $\text{Fe}(\text{IO}_3)_3$ was first pressed into compact orange transparent 10 μm -thick platelets with near-parallel faces by using a DAC. Then the platelet was loaded in a 250 μm -diameter hole drilled on a stainless-steel gasket which had been pre-indented to a thickness of 40 μm . Potassium bromide (KBr) was used as a pressure-transmitting medium (PTM) because of its excellent optical properties²⁶ and to provide a similar environment in optical and transport measurements. The transmission range of KBr is 0.23 to 25 μm (ref. 26) and it can provide hydrostatic conditions up to 2 GPa and quasi-hydrostatic environment up to 11 GPa.²⁷ The ruby fluorescence method was employed for pressure calibration.²⁸ The sample-in sample-out method^{29,30} was used to acquire the optical-absorption spectra of the sample under pressure, on a home-built optical setup consist-

Research Article

ing of a tungsten lamp, fused silica lenses, reflecting optics objectives (15 \times), and a visible-near IR spectrometer (Ocean Optics Maya2000 Pro). With this method, the intensity $I(\omega)$ transmitted through the sample is normalized to the intensity $I_0(\omega)$ transmitted through a clear area of KBr. More details about the data acquisition and treatment process can be found elsewhere.³¹ HP electrical resistivity measurements were performed with the standard four-probe technique in a DAC up to 40 GPa.³² The gasket was insulated with a mixture of epoxy and cubic boron nitride. Four platinum leads were arranged to contact the sample in the chamber. No pressure medium was used for the resistivity measurement, and the ruby scale²⁸ was employed to determine pressure. The resistance was determined by the Van der Pauw method.³²

III. Calculation details

Band-structure calculations were conducted within the framework of the density-functional theory (DFT). We have used the projector-augmented wave method as implemented in the Vienna *ab initio* simulations package (VASP). A plane-wave energy cutoff of 530 eV was used, and the exchange–correlation energy was described within the generalized-gradient approximation (GGA) with the GGA + U method due to the presence of Fe atoms. We have employed the Perdew–Burke–Ernzerhof for solids (PBEsol) functionals. The Monkhorst–Pack scheme was applied to discretize the Brillouin zone (BZ) integrations with suitable meshes. This calculation method gives an accurate description of the structural and vibrational properties of Fe(IO_3)₃.^{20,22}

IV. Results and discussion

A. Electronic and optical properties at room pressure

The optical-absorption spectrum of Fe(IO_3)₃ at ambient pressure is shown in Fig. 2. The shape of the absorption spectrum supports that the band gap is indirect, having, in addition, a low-energy absorption tail that follows an exponential dependence with energy. This absorption tail is typical of polycrystalline samples being related to disorder.³³ Fig. 2 also shows as an inset a Tauc plot³⁴ supporting the indirect nature of the bandgap with an estimated bandgap energy of 2.08(5) eV. A more precise determination of the bandgap energy can be achieved by using a model assuming an indirect band gap plus a low-energy tail described by the Urbach empirical rule.³³ Details of the fitting procedure can be found in ref. 33. The fit at ambient pressure is shown in Fig. 2. The band-gap energy obtained at ambient pressure is 2.10(5) eV, which agrees with the value obtained from the Tauc plot. The indirect band-gap character is in accordance with the calculated electronic band structure, which is shown in Fig. 3. The conduction band minimum (CBM) is located at the Γ high-symmetry point, and the valence band maximum (VBM) is at $(-0.1939, 0.5000, 0.1939)$ k -point, a point along the Γ –E direction of the

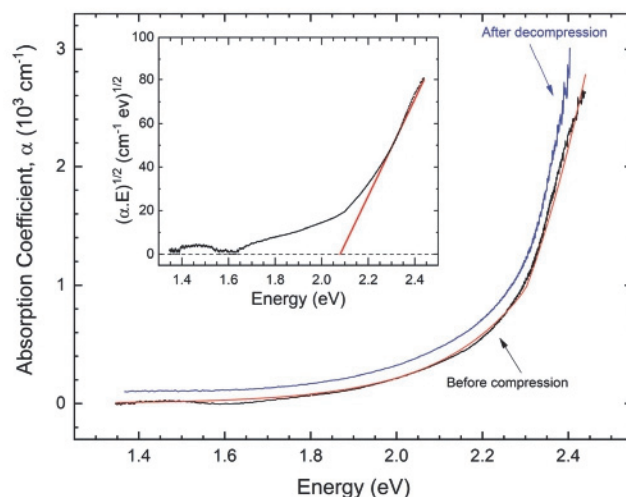


Fig. 2 Optical-absorption spectra of Fe(IO_3)₃ at room pressure. The black (blue) line is the spectrum measured before (after) compression. The decompression spectrum is shifted vertically for the sake of clarity. The red line is the result of the fit assuming an indirect band gap plus a low-energy Urbach absorption tail. The inset shows the Tauc plot. The red line shows the extrapolation of the linear region to the abscissa (dashed line).

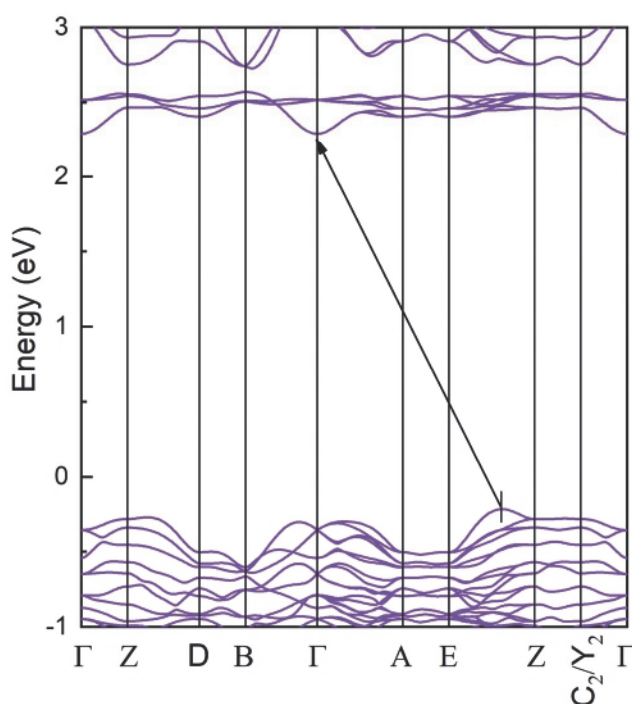


Fig. 3 Calculated electronic band structure of Fe(IO_3)₃ at ambient pressure. The fundamental band gap is shown by the arrow.

Brillouin zone. The ambient-pressure band-gap energy of Fe(IO_3)₃ was calculated as 2.50 eV, which is 19% larger than the experimental value. This difference is typical of DFT calculations³⁵ being related to the approximations used to describe the exchange and correlation energies in the GGA-PBEsol

description. Despite it, DFT calculations give an accurate description of the HP behavior of band-gap energy, being crucial for understanding the experimental phenomena. Since the ambient-pressure band gap energy of $\text{Fe}(\text{IO}_3)_3$ was not determined before, in order to discuss present results, we compare our results with other metal iodates. In Table 1, we list the band gap value of $\text{Fe}(\text{IO}_3)_3$ and of metal iodates found in the literature.^{1,3,6,9,10,13,36–46}

Common features we can draw here from Table 1. (i) Most metal iodates have an indirect band gap, which is related to their common low-symmetry non-centrosymmetric crystal structure. (ii) They also exhibit a wide band gap, with a band-gap energy ranging from 2.1 eV, in $\text{Fe}(\text{IO}_3)_3$ as determined in this work, to 4.3 eV, in $\text{LiMg}(\text{IO}_3)_3$.⁴³ (iii) In most iodates, the upper region of the valence band and lower region of the conduction band are mainly composed of oxygen 2p and iodine 5p states. Thus, the bonding interactions of IO_3 groups determine their band gap. Consequently, iodates, where the cation is not a transition metal, have a wide band gap. See for instance, NaI_3O_8 (3.9 eV),¹⁰ $\text{Na}_2\text{Sn}(\text{IO}_3)_6$ (4.0 eV),^{9,13,37} and $\text{Rb}_2\text{Sn}(\text{IO}_3)_6$ (4.1 eV).^{9,13} (iv) In transition-metal (TM) iodates, the contribution of TM d states to the CBM induces a decrease of the band-gap energy (E_{gap}). However, their contribution to the VBM does not influence the band-gap energy, as can be seen by comparing, for instance α - and β - AgI_3O_8 (3.8 and 3.6 eV)¹⁰ with α - $\text{NaAu}(\text{IO}_3)_4$ (2.6 eV) and $\text{RbAu}(\text{IO}_3)_4$ (2.5 eV).⁹ While in α - and β - AgI_3O_8 , 4d orbitals of Ag partially contribute

to the VBM,¹⁰ in α - $\text{NaAu}(\text{IO}_3)_4$ and $\text{RbAu}(\text{IO}_3)_4$ the 5d orbitals of Au dominate the CBM.⁹ These features can be used to explain the value of the band-gap energy of the metal iodates and for interpreting its HP behavior. In particular, it provides a nice correlation of band gaps to orbital configuration and a qualitative explanation for the 2.1 eV bandgap energy of $\text{Fe}(\text{IO}_3)_3$. In this compound, the band-gap energy is more than 1 eV lower than transition-metal iodates with closed-shell d electrons, e.g. $\text{Zn}(\text{IO}_3)_2$ and $\text{Tl}(\text{IO}_3)_3$,^{41,44} and almost half of that of non-transitions metal iodates, e.g. CsIO_3 , RbIO_3 , and α - LiIO_3 .^{3,38–41,44} This phenomenon is analogous to what happens in MnWO_4 and CuWO_4 . Owing to the contribution d orbitals to states near the Fermi level, these tungstates have a band gap of more than 1 eV smaller than isostructural tungstates, like MgWO_4 , CdWO_4 .^{47,48} An analogous situation happens when comparing FeVO_4 with other non-TM vanadates.⁴⁹

The above given discussion is supported by our DFT calculations in $\text{Fe}(\text{IO}_3)_3$. The electronic density of state (DOS) and projected density of state (PDOS) are shown in Fig. 4. Below the Fermi level, the valence band can be divided into three energy regions (low energy region: -25 to -10 eV, middle energy region: -10 to -4 eV, and the high energy region: -4 to 0 eV). The region immediately below -25 eV, not shown in the figure, is only contributed by the 4s orbitals of Fe. The lower energy region has significant O-2s and I-5sp contributions. The middle region is mainly contributed by Fe-3d, I-5p, and

Table 1 Summary of the band-gap energy of part of the reported metal iodates in the literature (all the experimental values have been rounded to one decimal place), as well as the band-gap type, and the atomic orbital which dominate the valence band maxima (VBM), and conduction band minima (CBM). Orbital contributions are based on the results from the theoretical calculated density of state and projected density of state. "Exp" means data determined in experiments and "Cal" means data predicted by theoretical calculation, respectively

Compounds	Bandgap type	Band-gap energy (eV)		Valence band maxima (VBM)		Conduction band minima (CBM)		Ref.
		Exp	Cal	Dominated	Other	Dominated	Other	
$\text{Zn}(\text{IO}_3)_2$	Indirect	3.5	2.58	O(2p)	I(5p), Zn(3d)	I(5p)	O(2p)	44
CsIO_3	Direct	4.2	3.25	O(2p)	I(5s)	I(5p)	O(2p)	38
$\text{Ce}_2\text{I}_6\text{O}_{18}$		2.5		O(2p)		I(5p)	Ce(5d)	45
$\text{Sn}(\text{IO}_3)_4$	Indirect	4.0	2.75	O(2p)	I(5p), I(5s)	I(5p)	Sn(5s)	46
RbIO_3		4.0	2.79	O(2p)		I(5p)		39
α - AgI_3O_8	Indirect	3.8	2.43	O(2p)	Ag(4d)	I(5p)	O(2p)	10
β - AgI_3O_8	Indirect	3.6	2.46	O(2p)	Ag(4d)	I(5p)	O(2p)	10
NaI_3O_8	Indirect	3.9	3.11	O(2p)	I(5p), I(5s)	I(5p)	O(2p)	10
α - LiIO_3	Indirect	4.0	2.81	O(2p)		I(5p), O(2p)		40 and 42
$\text{Tl}(\text{IO}_3)_3$		3.4	2.20	O(2s,2p)	Tl(6s)	O(2s,2p), I(5s,5p)		41
$\text{Tl}_4(\text{IO}_3)_6$		2.9	1.80	O(2s,2p)	I(5s,5p)	O(2s,2p), Tl(6s)		41
YI_5O_{14}	Direct	3.8		O(2p)	I(5s,5p)	I(5p)	O(2p)	3
$\text{GdI}_5\text{O}_{14}$	Direct	4.1		O(2p)	I(5s,5p)	I(5p)	O(2p)	3
α - $\text{NaAu}(\text{IO}_3)_4$	Indirect	2.6	2.14	O(2p)	Au(5d), I(5s,5p)	Au(5d)	O(2p), I(5p)	9
$\text{Na}_3\text{Bi}(\text{IO}_3)_6$	Indirect	3.2	3.34	O(2p)	I(5s,5p), Bi(6s)	I(5p), O(2p)	I(5s), Bi(6p)	37
$\text{Na}_2\text{Sn}(\text{IO}_3)_6$		4.0						13
$\text{RbAu}(\text{IO}_3)_4$	Indirect	2.5	2.31	O(2p)	Au(5d), I(5s,5p)	Au(5d)	O(2p), I(5p)	9
$\text{Rb}_2\text{Sn}(\text{IO}_3)_6$		4.1						13
α - $\text{CsAu}(\text{IO}_3)_4$	Indirect	2.6	2.30	O(2p)	Au(5d), I(5s,5p)	Au(5d)	O(2p), I(5p)	9
$\text{Cs}_2\text{Sn}(\text{IO}_3)_6$		4.1						13
$\text{LiMg}(\text{IO}_3)_3$	Indirect	4.3	3.35	O(2p)	I(5s, 5p)	I(5p)	O(2p)	43
$\text{Li}_2\text{Ti}(\text{IO}_3)_6$		3.0	1.60	O(2p)	I(5s,5p)	Ti(3d)	O(2s,2p)	6
$\text{KLi}_2(\text{IO}_3)_3$		4.3						36
$\text{K}_2\text{Ti}(\text{IO}_3)_6$		3.3	3.14	O(2p)		Ti(3d), I(5p)	O(2s,2p)	1
$\text{Fe}(\text{IO}_3)_3$	Indirect	2.1	2.50	O(2p)	I(5s,5p)	Fe(3d), I(5p)	O(2p)	This work

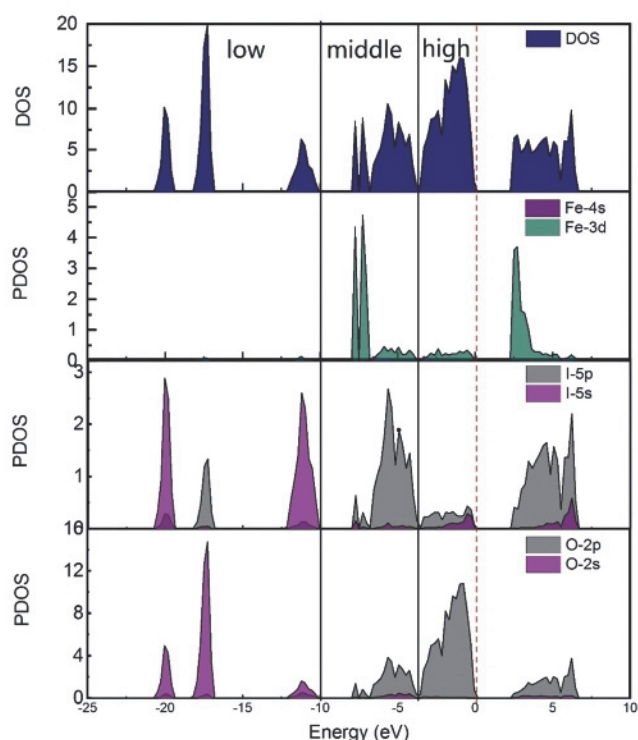


Fig. 4 Calculated total (DOS) and projected density of state (PDOS) of $\text{Fe}(\text{IO}_3)_3$ at ambient pressure, the Fermi level is shown in vertical dash line, the solid black line divides the valence band into three regions.

O-2p, indicating strong I–O covalent interactions. The sharp peak of Fe-3d orbitals around -8 eV is associated with the bonding part of the d-subshell, whose anti-bonding part is located at the bottom of the conduction band. In the high energy region of the valence band the main contribution comes from O-2p, with a small contribution of I-5sp, which form the bonding iodates $[\text{IO}_3^-]$ states. The CBM is dominated by the narrow Fe-3d band, already described, and a broad band of I-5p states. The dominant contribution of Fe 3d states to the CBM is what makes $\text{Fe}(\text{IO}_3)_3$ to have the smallest band gap among metal iodates studied until today.

B. Electronic and transport properties at high pressure

Effects of pressure in the electronic. The optical-absorption spectra of $\text{Fe}(\text{IO}_3)_3$ at selected pressures are shown in Fig. 5. The absorption edge exhibits an overall redshift in the explored pressure range while showing four regions with different behaviors. The four pressure intervals can be better identified in Fig. 6 where we plot the pressure dependence of the band-gap energy together with the theoretical predictions. A Tauc plot analysis was used to obtain the experimental band-gap energy at each pressure. The most noticeable change is the abrupt collapse of E_{gap} from 23.5 to 23.9 GPa (between regions III and IV) can be correlated with the first-order phase transition detected by XRD experiments.²⁰

When comparing the experimental results with theoretical predictions, we should first stress that calculations largely

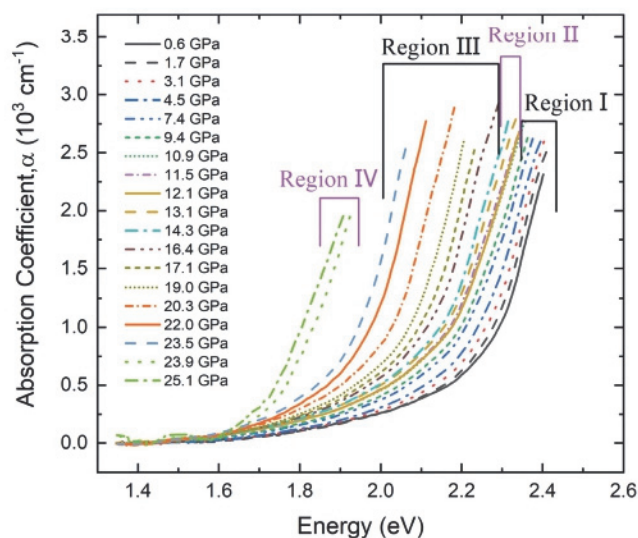


Fig. 5 Optical-absorption spectra of $\text{Fe}(\text{IO}_3)_3$ at selected pressures. The optical-absorption spectra are divided into different regions due to the different pressure coefficients of the band gap.

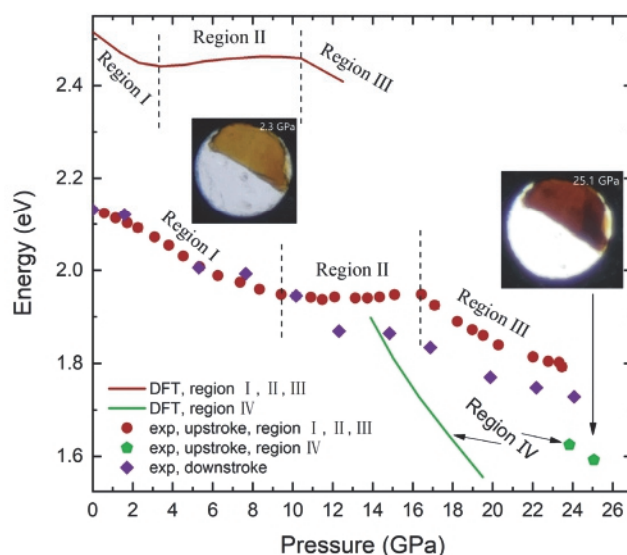


Fig. 6 Pressure dependence of band gap of $\text{Fe}(\text{IO}_3)_3$, experimental data were shown with dots while theoretical calculated data were shown with a solid line, the errors of the experimental data were smaller than the symbol. Region IV corresponds to the new phase we found in HPXRD in ref. 20. The inserted optical micrographs showing the loaded sample and the color change of $\text{Fe}(\text{IO}_3)_3$ in region IV.

underestimate the transition pressure of the first-order transition by 9 GPa (14 GPa instead of 23 GPa). This fact, known from our previous works, was discussed in ref. 20. Nevertheless, the theoretical calculations correctly predict the general trend of the pressure dependence of the band gap, the existence of three pressure intervals with different behavior, and the abrupt collapse of the band gap at the first-order transition. If we assume an approximately linear behavior in each

of the three pressure ranges, linear fittings to the experimental pressure dependence of the band gap in regions I, II, and III, yield pressure coefficient (dE_{gap}/dP) values of -22.7 ± 0.7 meV GPa $^{-1}$, 0.5 ± 0.7 meV GPa $^{-1}$ and -20.9 ± 0.7 meV GPa $^{-1}$ respectively, that quite consistently agree with the theoretical predictions (-29.3 ± 2 meV GPa $^{-1}$, 2.9 ± 0.6 meV GPa $^{-1}$ and -24.1 ± 2 meV GPa $^{-1}$).

The first-order phase transition at 23 GPa is accompanied by a color change from light yellow to brown in the sample, as can be observed in the insert optical micrographs of the sample in Fig. 6. The band-gap energy at the phase transitions is consistent with the collapse observed in the band-gap energy of multiple oxides (for instance, vanadates, wolfrates, molybdates, and chromates) when the first-order transition takes place.^{30,48,50,51} In region IV, above the phase transition, calculations predict a negative pressure coefficient but with a much larger absolute value (-60 ± 2 meV GPa $^{-1}$) than

the experimental one (-27 ± 2 meV GPa $^{-1}$). The difference can be most likely related to the insufficient number of points in region IV in the experiment. Unfortunately, due to limitations of the optical-absorption measurements, experiments could not be performed beyond 25.1 GPa.

An absorption spectrum collected after decompression is shown in Fig. 2. It shows that changed induced by pressure are reversible. The reversibility of the change of the band-gap energy under decompression can be also seen in Fig. 6. However, a 5 GPa hysteresis is observed, which is expected from the first-order nature of the transition from region III to region IV and consistently with the reversibility found in HPXRD²⁰ and HP-RS²² experiments.

We will now discuss in more detail the pressure behavior of E_{gap} on the basis of the calculated pressure dependence of the Fe–O and I–O bond distance shown in Fig. 7a, where oxygen atoms are named using the same nomenclature as in previous

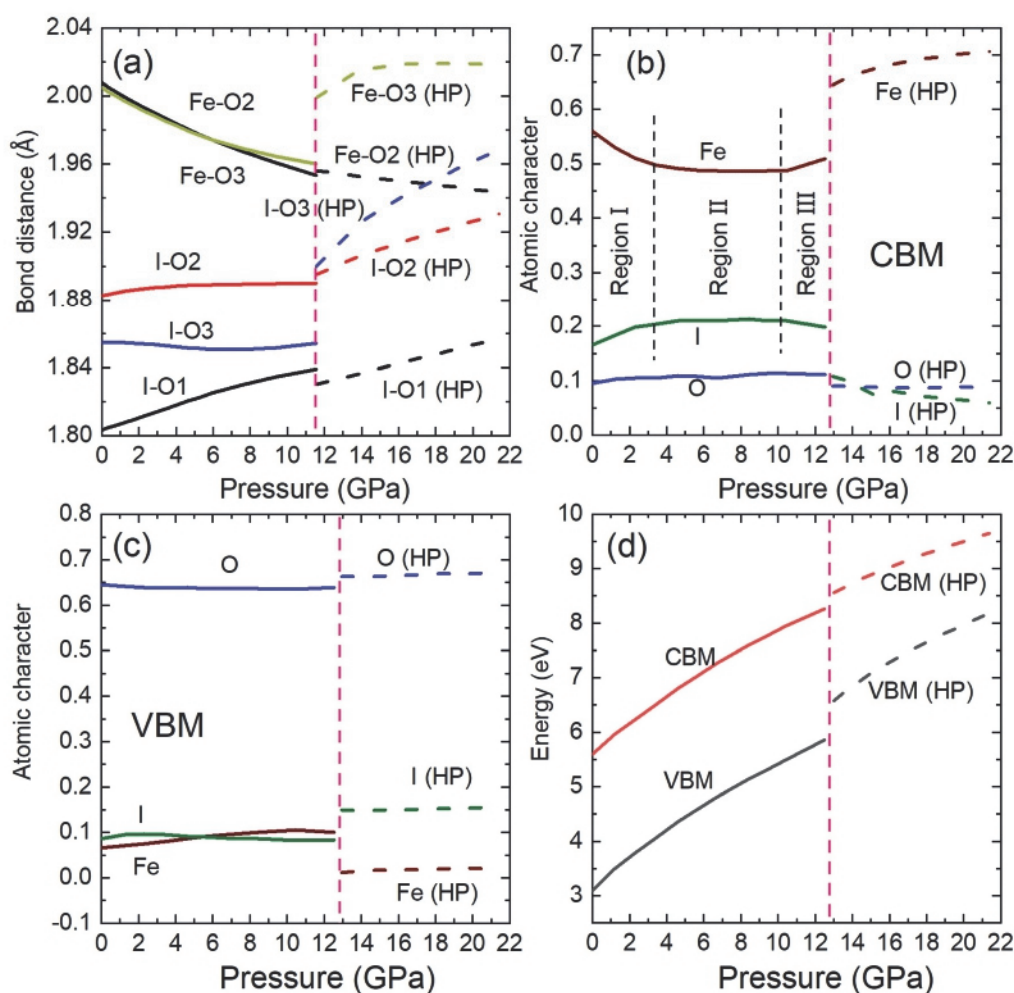


Fig. 7 Summary of the theoretical calculation results on electronic band structure and crystal structure. (a) Theoretically calculated pressure dependence of the Fe–O and I–O bond distance, the position of the O1, O2 and O3 can be found in Fig. 1. (b) Atomic character at CBM in the band structure as a function of pressure, here we also marked the different regions we determined in Fig. 6. (c) Atomic character at VBM in the band structure as a function of pressure. (d) Theoretically calculated pressure dependence of the energy of VBM and CBM in the electronic band structure. The solid line represents the phase before the third IPTs, and the dashed line depicts the results after third IPTs, the pink dash line indicating the calculation of the predicted phase transition pressure of the third IPTs. “HP” means the high-pressure phase which is in region IV.

Research Article

works^{20,22} and in Fig. 1. Under compression, before the first-order transition, the Fe-O2 and Fe-O3 distance continuously decrease from 2.01 Å to 1.96 Å, thus increasing the overlap between Fe and O orbitals. This fact favors the narrowing the band-gap energy as it happens in other oxides: *e.g.* PbWO₄ and PbCrO₄.^{30,50} In contrast, the bond distance of the three shorter I-O bonds (I-O1, I-O2, and I-O3) increases under pressure in order to accommodate additional oxygen atoms due to a pressure-driven gradual coordination increase.²² For instance, the bond distance of I-O1 increases from 1.80 Å at 0 GPa to 1.84 Å at 11.6 GPa, according to the calculations. Therefore, the hybridization between iodine and oxygen atoms is reduced, which favors the opening of the band-gap energy. The competitions of the two effects under compression can account for the s-shaped nonlinear pressure dependence of the band gap in Fe(IO₃)₃.^{30,50}

In region I, the effect of the Fe-O bond distance decrease dominates the band gap pressure behavior because of the large contribution of iron 3-d states to the CBM (see Fig. 7b). As the Fe-O distance decreases, Fe-3d/O 2p hybridization increases, and p-d repulsion^{52,53} causes the VBM to move to higher energy faster than the CBM, favoring thus the narrowing of E_{gap} . In region II, the contribution from iodine 6p states to the CBM increases, and the contribution from iron 3d states decreases. Thus, the influence on the band-gap energy of pressure effects on I-O bonds is enhanced. Consequently, the two contributions affecting E_{gap} are compensated, causing it to remain nearly constant. In region III, after additional I-O bonds are formed,²² the I-O distances show a very small pressure dependence, and the change of Fe-O bond distances with pressure again becomes dominant, favoring a decrease of E_{gap} , as observed. On the other hand, the atomic character at the VBM exhibits a negligible pressure dependence before the first-order phase transition (Fig. 7c), being dominated by the p orbitals of iodine up to the highest pressure. This indicates that changes in the conduction band are those governing the behavior of the band-gap energy.

We will now discuss the abrupt change of the band gap at the first-order transition. This change is caused by the unit-cell volume collapse (more than 5%) associated with the phase transition,²⁰ and the associated important changes in the coordination environment of Fe and I. See changes in Fe-O and I-O distances in Fig. 7a. The structural changes affect the valence band considerably, moving the VBM to higher energies more than CBM, as shown in Fig. 7d, and causing the abrupt decrease of the band-gap energy. Notice that the position of the VBM changes the position in the Brillouin zone from the (-0.2653, 0.5000, 0.2653) *k*-point to the (0, 0, 0.4796) *k*-point (Fig. 8). The transition also causes a decrease of the iodine contribution to the CBM and an increase from the contribution of iron. Thus, the band gap is expected to decrease with pressure after the transition, as observed.

In order to better illustrate the change in the iodine bonding at the phase transition, we have calculated the electron localization function (ELF) of Fe(IO₃)₃ at four different pressures corresponding to regions I, II, III, and IV as shown

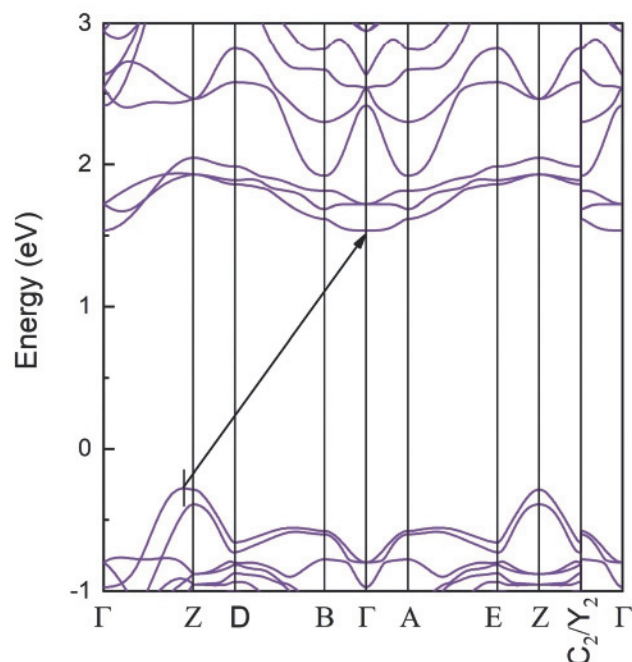


Fig. 8 Calculated electronic band structure of Fe(IO₃)₃ at 15 GPa. The fundamental band gap is shown by the arrow.

in Fig. 9. In the three first regions, there are only gradual changes in the ELF and overlay of the electron cloud between the iodine and oxygen as shown in the bottom left in Fig. 9b and the bottom right in Fig. 9c, which correspond to the gradual approximation of second-neighbor oxygen atoms to the LEP of iodine. However, when changing from region III to IV (first-order transition), there is a significant change in the bonding of iodine (Fig. 9d). This causes an enhancement of the contribution of oxygen and iodine atoms to the valence band and the observed changes of its topology.

Effects of pressure in transport properties. To complete the study, we have also performed resistivity measurements under high pressure. The results are shown in Fig. 10. Below 3 GPa, the resistivity was too high to be measured probably because of a bad contact between the sample and metallic leads used for measurements.⁵⁴ At low-pressure Fe(IO₃)₃ shows a resistivity of the order of 5 GΩ cm, which is consistent with its behavior as an intrinsic semiconductor.⁵⁴ Changes in the resistivity behavior with pressure are found at 6 and 20 GPa. This changes can be correlated to structural changes from region I to II and to III.²⁰ The difference of the pressures at which changes happen (as compared to optical experiments) are probably caused by the absence of any PTM in the resistivity measurements.^{55,56} At 20 GPa there is a slight increase of resistivity with pressure, which could be related to the formation of precursor defects of the first-order transition.⁵⁷ Such defects will lower the carrier mobility causing the resistivity to increase.⁵⁷ Finally, at 23 GPa, there is an abrupt decrease of the resistivity, confirming the occurrence of the first-order transition detected also by the present optical studies and pre-

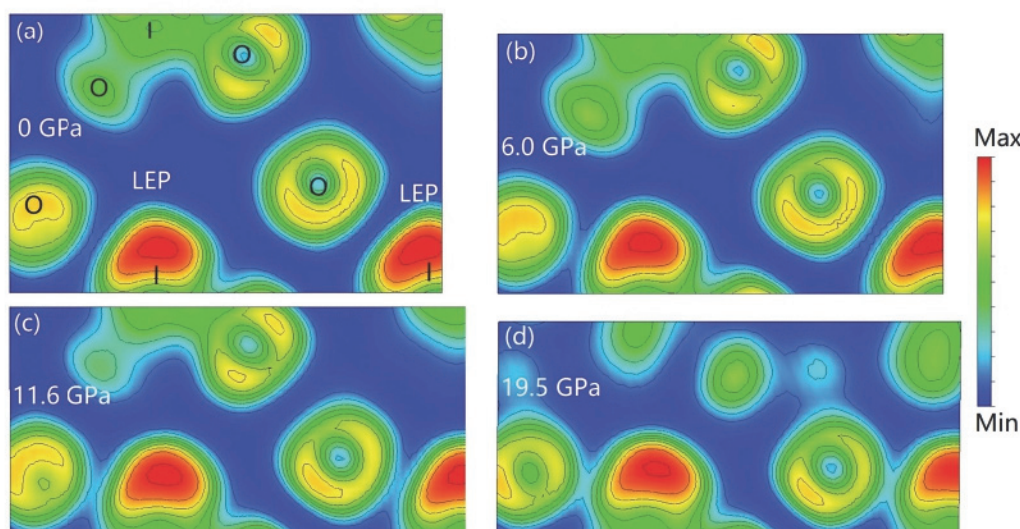


Fig. 9 2D contour plots of the electron-localization function of $\text{Fe}(\text{IO}_3)_3$ at selected pressures. The atoms are identified at the 0 GPa. We selected the plane $(-1, 2, 0)$, 3 Å away from the origin, to illustrate changes in the I–O bonds. Changes in the size of boxes correspond to changes of unit-cell parameters as a function of pressure.

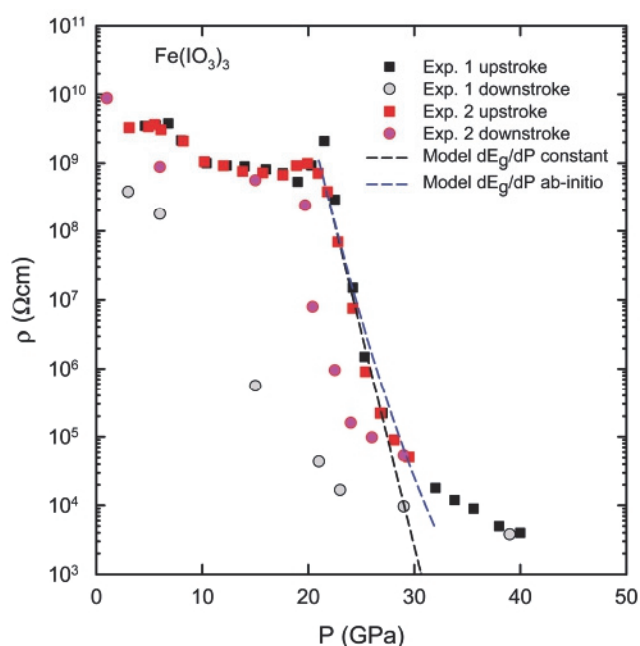


Fig. 10 Results of the resistivity measurements of $\text{Fe}(\text{IO}_3)_3$ at high pressure. Different symbols are from the two different experiments under compression and decompression (see inset). The lines are the results from the models discussed in the text.

vious XRD experiments.²⁰ Notice that the decrease of resistivity is of five orders of magnitude. This occurs in the two experiments we performed. In the experiment performed up to 30 GPa, the results are fully reversible. In the experiment performed up to 40 GPa they are reversible but with a hysteresis of 10 GPa, which is larger than in optical experiments. This could be related to the influence of precursor effects of a

transition happening at higher pressure than covered by this study.⁵⁷

We discuss now the resistivity result in more detail. It seems reasonable to assume that the decrease of the resistivity results from the exponential increase of the carrier concentration, with activation energy E_A . In that case, in the pressure interval through which the sample resistivity exponentially decreases, the following equation holds

$$\frac{\rho(P)}{\rho(P_0)} \approx \frac{n(P_0)}{n(P)} = e^{\frac{E_A(P) - E_A(P_0)}{kT}}$$

Then the logarithmic pressure coefficient of the resistivity is related to the pressure coefficient of the activation energy of the carrier concentration.

$$\frac{d}{dP} \left(\ln \frac{\rho(P)}{\rho(P_0)} \right) = \frac{1}{kT} \frac{dE_A}{dP}$$

From the experimental slope in the interval between 22 and 27 GPa (about -2 GPa^{-1}) we can then determine

$$\frac{dE_A}{dP} = kT \frac{d}{dP} \left(\ln \frac{\rho(P)}{\rho(P_0)} \right) \simeq -52 \text{ meV GPa}^{-1}$$

This value is smaller (in absolute value) than the average pressure coefficient of the high-pressure phase band gap (-60 meV GPa^{-1}), as calculated from the green line in Fig. 6. Nevertheless, given that the activation energy of the carrier concentration in the intrinsic regime of a semiconductor is $E_A = E_g/2$, the experimental pressure coefficient of the activation energy turns out to be within the expected order of magnitude.

This result suggests that the observed decrease of the measured resistivity in the high-pressure phase can correspond to the intrinsic resistivity of the semiconducting high-pressure

phase. We can then use a simple Drude model to estimate the pressure dependence of the intrinsic resistivity through⁵⁸

$$\begin{aligned}\rho(P) &= [\sigma(P)]^{-1} = [e(n+p)\mu_{\text{av}}]^{-1} = [2en_i\mu_{\text{av}}]^{-1} \\ &= [2e\sqrt{N_C N_V}\mu_{\text{av}}]^{-1} e^{\frac{E_g(P)}{2kT}} \\ N_{C,V} &= 2.51 \times 10^{19} \left(\frac{m_{C,V}^*}{m_0}\right)^{\frac{3}{2}} \left(\frac{T}{300 \text{ K}}\right)^{\frac{3}{2}} \text{ cm}^{-3}\end{aligned}$$

where e is the electron charge, $n = p = n_i$ is the intrinsic carrier concentration, μ_{av} is the average carrier mobility, N_C (N_V) is the effective density of states in the conduction (valence) band, $m_{C,V}^*$ is the density of states effective mass in the conduction (valence) band, m_0 is the electron mass, and $E_g(P)$ is the semiconductor band gap. Given the low noise and good reproducibility of the resistivity measurements, it seems reasonable to assume a relatively high carrier mobility. The black dashed line has been calculated by assuming $\mu_{\text{av}} = 900 \text{ cm}^2 \text{ V}^{-1} \text{ s}^{-1}$, $m_{C,V}^* = 2m_0$, $E_g = 1.6 \text{ eV}$ at the transition pressure, and a constant pressure coefficient $dE_g/dP = -60 \text{ meV GPa}^{-1}$. The blue dashed line has been calculated with the same parameters but assuming the nonlinear pressure dependence predicted by the *ab initio* calculations (green line in Fig. 6). This simple model predicts the observed lower logarithmic slope of the resistivity because of the nonlinear pressure dependence of the band gap.

V. Conclusions

Combining optical-absorption and resistivity measurements with density-functional calculations, we have characterized the electronic properties of $\text{Fe}(\text{IO}_3)_3$ and its behavior under high pressure. At ambient pressure, $\text{Fe}(\text{IO}_3)_3$ has a band-gap energy of 2.1 eV (2.5 eV in calculations). This makes this compound the metal iodate with the smallest band gap. The reason for this fact is discussed based on a systematic comparison with other iodates and the calculated electronic density of states. We concluded that the significant contribution of Fe-3d orbitals to the bottom of the conduction band is what makes $\text{Fe}(\text{IO}_3)_3$ have a band gap smaller than any other iodates.

At high pressure, the band gap of $\text{Fe}(\text{IO}_3)_3$ exhibits a nonlinear behavior which is followed by an abrupt decrease at 24 GPa. The nonlinear behavior below 24 GPa is caused by the competition of two effects: (i) the shortening of the Fe–O bond distance under compression which favors the closing of the bandgap and (ii) the slight enlargement of the I–O bond distance under pressure, which favors the opening of the bandgap. The abrupt decrease of the band-gap energy at 24 GPa is a consequence of a first-order phase transition which induces an important atomic reorganization. The observed changes in optical properties are correlated with changes in resistivity, which decreases by four orders of magnitude at the same pressure. The pressure dependence of the resistivity in the high-pressure phase is shown to be consistent with the exponential increase of the intrinsic carrier concentration. The observed changes are reversible when the sample is decompressed to ambient pressure.

Author contributions

The manuscript was written through the contributions of all authors. All authors have given approval to the final version of the manuscript.

Conflicts of interest

There are no conflicts to declare.

Acknowledgements

This work was supported by the Spanish Ministry of Science, Innovation and Universities under Grants PID2019-106383GB-C41-3 and RED2018-102612-T (MALTA Consolider-Team network) and by Generalitat Valenciana under Grant Prometeo/2018/123 (EFIMAT). A. L. and D. E. would like to thank the Generalitat Valenciana for the Ph.D. fellowship (GRISOLIAP/2019/025).

References

- H. Y. Chang, S. H. Kim, M. O. Kang and P. S. Halasyamani, Polar or Nonpolar? A + Cation Polarity Control in $\text{A}_2\text{Ti}(\text{IO}_3)_6$ (A = Li, Na, K, Rb, Cs, Tl), *J. Am. Chem. Soc.*, 2009, **131**, 6865–6873.
- C. F. Sun, C. L. Hu, X. Xu, J. B. Ling, T. Hu, F. Kong, X. F. Long and J. G. Mao, $\text{BaNbO}(\text{IO}_3)_5$: A New Polar Material with a Very Large SHG Response, *J. Am. Chem. Soc.*, 2009, **131**, 9486–9487.
- J. Chen, C. L. Hu, F. F. Mao, B. P. Yang, X. H. Zhang and J. G. Mao, $\text{REI}_5\text{O}_{14}$ (RE=Y and Gd): Promising SHG Materials Featuring the Semicircle-Shaped I_5O_{14} –Polyiodate Anion, *Angew. Chem., Int. Ed.*, 2019, **58**, 11666–11669.
- M. Gai, Y. Wang, T. Tong, Z. Yang and S. Pan, ZnIO_3F : Zinc Iodate Fluoride with Large Birefringence and Wide Band Gap, *Inorg. Chem.*, 2020, **59**, 4172–4175.
- K. Liu, J. Han, J. Huang, Z. Wei, Z. Yang and S. Pan, $\text{SrTi}(\text{IO}_3)_6 \cdot 2\text{H}_2\text{O}$ and $\text{SrSn}(\text{IO}_3)_6$: Distinct Arrangements of Lone Pair Electrons Leading to Large Birefringences, *RSC Adv.*, 2021, **11**, 10309–10315.
- H. Y. Chang, S. H. Kim, P. S. Halasyamani and K. M. Ok, Alignment of Lone Pairs in a New Polar Material: Synthesis, Characterization, and Functional Properties of $\text{Li}_2\text{Ti}(\text{IO}_3)_6$, *J. Am. Chem. Soc.*, 2009, **131**, 2426–2427.
- C. F. Sun, T. Hu, X. Xu and J. G. Mao, Syntheses, Crystal Structures, and Properties of Three New Lanthanum(III) Vanadium Iodates, *Dalton Trans.*, 2010, **39**, 7960–7967.
- L. A. Olsen, J. Lopez-Solano, A. Garca, T. Balić-Unić and E. Makovicky, Dependence of the Lone Pair of Bismuth on Coordination Environment and Pressure: An *Ab Initio* Study on $\text{Cu}_4\text{Bi}_5\text{S}_{10}$ and Bi_2S_3 , *J. Solid State Chem.*, 2010, **183**, 2133–2143.

- 9 C. Huang, C. L. Hu, X. Xu, B. P. Yang and J. G. Mao, Explorations of a Series of Second Order Nonlinear Optical Materials Based on Monovalent Metal Gold(III) Iodates, *Inorg. Chem.*, 2013, **52**, 11551–11562.
- 10 X. Xu, C. Hu, B. Li, B. Yang and J. Mao, α -AgI₃O₈ and β -AgI₃O₈ with Large SHG Responses: Polymerization of IO₃ Groups into the I₃O₈ Polyiodate Anion, *Chem. Mater.*, 2014, **26**, 3219–3230.
- 11 C. L. Hu and J. G. Mao, Recent Advances on Second-Order NLO Materials Based on Metal Iodates, *Coord. Chem. Rev.*, 2015, **288**, 1–144.
- 12 H. Liu, X. Jiang, X. Wang, L. Yang, Z. Lin, Z. Hu, X. Meng, X. Chen and J. Qin, Influence of A-Site Cations on Germanium Iodates as Mid-IR Nonlinear Optical Materials: A₂Ge(IO₃)₆ (A = Li, K, Rb and Cs) and BaGe(IO₃)₆·H₂O, *J. Mater. Chem. C*, 2018, **6**, 4698–4705.
- 13 Y. J. Jia, Y. G. Chen, Y. Guo, X. F. Guan, C. Li, B. Li, M. M. Liu and X. M. Zhang, LiMII(IO₃)₃ (MII=Zn and Cd): Two Promising Nonlinear Optical Crystals Derived from a Tunable Structure Model of α -LiIO₃, *Angew. Chem., Int. Ed.*, 2019, **58**, 17194–17198.
- 14 W. Yao, R. He, X. Wang, Z. Lin and C. Chen, Analysis of Deep-UV Nonlinear Optical Borates: Approaching the End, *Adv. Opt. Mater.*, 2014, **2**, 411–417.
- 15 K. M. Ok, Toward the Rational Design of Novel Noncentrosymmetric Materials: Factors Influencing the Framework Structures, *Acc. Chem. Res.*, 2016, **49**, 2774–2785.
- 16 P. S. Halasyamani and K. R. Poeppelmeier, Noncentrosymmetric Oxides, *Chem. Mater.*, 1998, **10**, 2753–2769.
- 17 F. F. Mao, C. L. Hu, J. Chen and J. G. Mao, A Series of Mixed-Metal Germanium Iodates as Second-Order Nonlinear Optical Materials, *Chem. Mater.*, 2018, **30**, 2443–2449.
- 18 A. Segura, F. J. Manjón, D. Errandonea, J. Pellicer-Porres, V. Muñoz, G. Tobias, P. Ordejón, E. Canadell, A. San Miguel and D. Sánchez-Portal, Specific Features of the Electronic Structure of III-VI Layered Semiconductors: Recent Results on Structural and Optical Measurements under Pressure and Electronic Structure Calculations, *Phys. Status Solidi B*, 2003, **235**, 267–276.
- 19 D. Errandonea, D. Martínez-García, A. Segura, J. Haines, E. Machado-Charry, E. Canadell, J. C. Chervin and A. Chevy, High-Pressure Electronic Structure and Phase Transitions in Monoclinic InSe: X-Ray Diffraction, Raman Spectroscopy, and Density Functional Theory, *Phys. Rev. B*, 2008, **77**, 045208.
- 20 A. Liang, S. Rahman, H. Saqib, P. Rodriguez-Hernandez, A. Munoz, G. Nenert, I. Yousef, C. Popescu and D. Errandonea, First-Order Isostructural Phase Transition Induced by High-Pressure in Fe(IO₃)₃, *J. Phys. Chem. C*, 2020, **124**, 8669–8679.
- 21 A. Liang, C. Popescu, F. J. Manjon, A. Muñoz, Z. Hebboul and D. Errandonea, Structural and Vibrational Study of Zn(IO₃)₂ Combining High-Pressure Experiments and Density-Functional Theory, *Phys. Rev. B*, 2021, **103**, 054102.
- 22 A. Liang, S. Rahman, P. Rodriguez-Hernandez, A. Muñoz, F. J. Manjón, G. Nenert and D. Errandonea, High-Pressure Raman Study of Fe(IO₃)₃: Soft-Mode Behavior Driven by Coordination Changes of Iodine Atoms, *J. Phys. Chem. C*, 2020, **124**, 21329–21337.
- 23 M. Jansen, Zur Kristallstruktur von FeJ₃O₉, *J. Solid State Chem.*, 1976, **17**, 1–6.
- 24 A. Liang, R. Turnbull, E. Bandiello, I. Yousef, C. Popescu, Z. Hebboul and D. Errandonea, High-Pressure Spectroscopy Study of Zn(IO₃)₂ Using Far-Infrared Synchrotron Radiation, *Crystals*, 2021, **11**, 34.
- 25 C. Galez, Y. Mugnier, J. Bouillot, Y. Lambert and R. Le Dantec, Synthesis and Characterisation of Fe(IO₃)₃ Nanosized Powder, *J. Alloys Compd.*, 2006, **416**, 261–264.
- 26 E. D. Palik, Potassium Bromide (KBr), in *Handbook of Optical Constants of Solid*, Academic Press, Maryland, 1997, pp. 989–1004.
- 27 A. Celeste, F. Borondics and F. Capitani, Hydrostaticity of Pressure-Transmitting Media for High Pressure Infrared Spectroscopy, *High Pressure Res.*, 2019, **39**, 608–618.
- 28 H. K. Mao, J. Xu and P. M. Bell, Calibration of the Ruby Pressure Gauge to 800 Kbar under Quasi-Hydrostatic Conditions, *J. Geophys. Res.*, 1986, **91**, 4673–4676.
- 29 D. Errandonea, C. Popescu, A. B. Garg, P. Botella, D. Martínez-García, J. Pellicer-Porres, P. Rodríguez-Hernández, A. Muñoz, V. Cuenca-Gotor and J. A. Sans, Pressure-Induced Phase Transition and Band-Gap Collapse in the Wide-Band-Gap Semiconductor InTaO₄, *Phys. Rev. B*, 2016, **93**, 035204.
- 30 D. Errandonea, D. Martínez-García, R. Lacomba-Perales, J. Ruiz-Fuertes and A. Segura, Effects of High Pressure on the Optical Absorption Spectrum of Scintillating PbWO₄ Crystals, *Appl. Phys. Lett.*, 2006, **89**, 091913.
- 31 O. Gomis, R. Vilaplana, F. J. Manjón, J. Ruiz-Fuertes, E. Pérez-González, J. López-Solano, E. Bandiello, D. Errandonea, A. Segura, P. Rodríguez-Hernández, A. Muñoz, V. V. Ursaki and I. M. Tiginyanu, HgGa₂Se₄ under High Pressure: An Optical Absorption Study, *Phys. Status Solidi B*, 2015, **252**, 2043–2051.
- 32 D. Errandonea, A. Segura, D. Martínez-García and V. Muñoz-San Jose, Hall-Effect and Resistivity Measurements in CdTe and ZnTe at High Pressure: Electronic Structure of Impurities in the Zinc-Blende Phase and the Semimetallic or Metallic Character of the High-Pressure Phases, *Phys. Rev. B*, 2009, **79**, 125203.
- 33 P. Botella, D. Errandonea, A. B. Garg, P. Rodriguez-Hernandez, A. Muñoz, S. N. Achary and A. Vomiero, High-Pressure Characterization of the Optical and Electronic Properties of InVO₄, InNbO₄, and InTaO₄, *SN Appl. Sci.*, 2019, **1**, 389.
- 34 J. Tauc, Optical Properties and Electronic Structure of Amorphous Ge and Si, *Mater. Res. Bull.*, 1968, **3**, 37–46.
- 35 M. K. Y. Chan and G. Ceder, Efficient Band Gap Prediction for Solids, *Phys. Rev. Lett.*, 2010, **105**, 196403.
- 36 H. Jo, H. G. Kim, H. R. Byun, J. I. Jang and K. M. Ok, Synthesis, Structure, and Third-Harmonic Generation

- Measurements of a Mixed Alkali Metal Iodate, $\text{KLi}_2(\text{IO}_3)_3$, *J. Solid State Chem.*, 2020, **282**, 452–460.
- 37 H. Song, D. Jiang, N. Wang, W. Xing, R. Guo, Z. Lin, J. Yao, Y. Wang, H. Tu and G. Zhang, $\text{Na}_3\text{Bi}(\text{IO}_3)_6$: An Alkali-Metal Bismuth Iodate with Intriguing One-Dimensional $[\text{BiI}_6\text{O}_{18}]$ Chains and Pressure-Induced Structural Transition, *Inorg. Chem.*, 2021, **60**, 2893–2898.
- 38 M. Zhang, C. Hu, T. Abudouwufu, Z. Yang and S. Pan, Functional Materials Design via Structural Regulation Originated from Ions Introduction: A Study Case in Cesium Iodate System, *Chem. Mater.*, 2018, **30**, 1136–1145.
- 39 Q. Wu, H. Liu, F. Jiang, L. Kang, L. Yang, Z. Lin, Z. Hu, X. Chen, X. Meng and J. Qin, RbIO_3 and RbIO_2F_2 : Two Promising Nonlinear Optical Materials in Mid-IR Region and Influence of Partially Replacing Oxygen with Fluorine for Improving Laser Damage Threshold, *Chem. Mater.*, 2016, **28**, 1413–1418.
- 40 D. N. Nikogosyan, Rarely Used and Archive Crystals, in *Nonlinear Optical Crystals: A Complete Survey*, Springer, New York, 2005, pp. 319–398.
- 41 J. Yeon, S. H. Kim and P. S. Halasyamani, New Thallium Iodates-Synthesis, Characterization, and Calculations of $\text{Tl}(\text{IO}_3)_3$ and $\text{Tl}_2(\text{IO}_3)_6$, $[\text{Tl}^{3+}\text{Tl}^{3+}(\text{IO}_3)_6]$, *J. Solid State Chem.*, 2009, **182**, 3269–3274.
- 42 G. Yao, Y. Chen, X. Y. An, Z. Q. Jiang, L. H. Cao, W. D. Wu and Y. Zhao, First-Principles Study of the Structural, Electronic and Optical Properties of Hexagonal LiIO_3 , *Chin. Phys. Lett.*, 2013, **30**, 067101.
- 43 J. Chen, C. L. Hu, F. F. Mao, X. H. Zhang, B. P. Yang and J. G. Mao, $\text{LiMg}(\text{IO}_3)_3$: An Excellent SHG Material Designed by Single-Site Aliovalent Substitution, *Chem. Sci.*, 2019, **10**, 10870–10875.
- 44 A. Benghia, Z. Hebboul, R. Chikhaoui, I. Khaldoun Lefkaier, A. Chouireb and S. Goumri-Said, Effect of Iodic Acid Concentration in Preparation of Zinc Iodate: Experimental Characterization of $\text{Zn}(\text{IO}_3)_2$, and Its Physical Properties from Density Functional Theory, *Vacuum*, 2020, **181**, 109660.
- 45 L. Xiao, Z. Cao, J. Yao, Z. Lin and Z. Hu, A New Cerium Iodate Infrared Nonlinear Optical Material with a Large Second-Harmonic Generation Response, *J. Mater. Chem. C*, 2017, **5**, 2130–2134.
- 46 M. Luo, F. Liang, X. Hao, D. Lin, B. Li, Z. Lin and N. Ye, Rational Design of the Nonlinear Optical Response in a Tin Iodate Fluoride $\text{Sn}(\text{IO}_3)_2\text{F}_2$, *Chem. Mater.*, 2020, **32**, 2615–2620.
- 47 J. Ruiz-Fuertes, D. Errandonea, A. Segura, F. J. Manjon, Z. Zhu and C. Y. Tu, Growth, Characterization, and High-Pressure Optical Studies of CuWO_4 , *High Pressure Res.*, 2008, **28**, 565–570.
- 48 J. Ruiz-Fuertes, S. López-Moreno, J. López-Solano, D. Errandonea, A. Segura, R. Lacomba-Perales, A. Muñoz, S. Radescu, P. Rodríguez-Hernández, M. Gospodinov, L. L. Nagornaya and C. Y. Tu, Pressure Effects on the Electronic and Optical Properties of AWO_4 Wolframites (A = Cd, Mg, Mn, and Zn): The Distinctive Behavior of Multiferroic MnWO_4 , *Phys. Rev. B*, 2012, **86**, 125202.
- 49 D. Errandonea, High Pressure Crystal Structures of Orthovanadates and Their Properties, *J. Appl. Phys.*, 2020, **128**, 040903.
- 50 D. Errandonea, E. Bandiello, A. Segura, J. J. Hamlin, M. B. Maple, P. Rodriguez-Hernandez and A. Muñoz, Tuning the Band Gap of PbCrO_4 through High-Pressure: Evidence of Wide-to-Narrow Semiconductor Transitions, *J. Alloys Compd.*, 2014, **587**, 14–20.
- 51 R. Lacomba-Perales, D. Errandonea, A. Segura, J. Ruiz-Fuertes, P. Rodríguez-Hernández, S. Radescu, J. López-Solano, A. Mujica and A. Muñoz, A Combined High-Pressure Experimental and Theoretical Study of the Electronic Band-Structure of Scheelite-Type AWO_4 (A = Ca, Sr, Ba, Pb) Compounds, *J. Appl. Phys.*, 2011, **110**, 043703.
- 52 S. H. Wei and A. Zunger, Role of Metal d States in II-VI Semiconductors, *Phys. Rev. B*, 1988, **37**, 8958–8981.
- 53 S. H. Wei and A. Zunger, Predicted Band-Gap Pressure Coefficients of All Diamond and Zinc-Blende Semiconductors: Chemical Trends, *Phys. Rev. B: Condens. Matter Mater. Phys.*, 1999, **60**, 5404–5411.
- 54 C. R. Rotundu, T. Čuk, R. L. Greene, Z. X. Shen, R. J. Hemley and V. V. Struzhkin, High-Pressure Resistivity Technique for Quasi-Hydrostatic Compression Experiments, *Rev. Sci. Instrum.*, 2013, **84**, 063903.
- 55 D. Errandonea, Y. Meng, M. Somayazulu and D. Hausermann, Pressure-induced alpha-to-omega transition in titanium metal: A systematic study of the effects of uniaxial stress, *Phys. B*, 2005, **355**, 116–125.
- 56 D. Errandonea, A. Muñoz and J. Gonzalez-Platas, Comment on “High-pressure X-ray diffraction study of $\text{YBO}_3/\text{Eu}^{3+}$, GdBO_3 , and EuBO_3 : Pressure-induced amorphization in GdBO_3 ”, *J. Appl. Phys.*, 2014, **115**, 216101.
- 57 F. J. Manjón, D. Errandonea, A. Segura, J. C. Chervin and V. Muñoz, Precursor Effects of the Rhombohedral-to-Cubic Phase Transition in Indium Selenide, *High Pressure Res.*, 2002, **22**, 261–266.
- 58 K. Seeger, *Semiconductor Physics*, Springer, Berlin, 1982.

4. Crystal structure, atomic vibrations and electronic band structure of $\text{Co}(\text{IO}_3)_2$ under pressure

Following the high-pressure study on $\text{Fe}(\text{IO}_3)_3$, we will now move the study to another $3d$ transition metal iodate, $\text{Co}(\text{IO}_3)_2$. $\text{Co}(\text{IO}_3)_2$ was studied by means of the high-pressure X-ray diffraction (HPXRD), high-pressure Raman scattering (HPRS), High-pressure synchrotron based Fourier transform infrared microspectroscopy (HPFTIR), high-pressure optical absorption (HPOA), and density function theory (DFT) calculations. Two pressure-induced monoclinic to monoclinic isostructural phase transitions (IPTs) were observed at around 3.0 and 9.0 GPa, respectively. The two IPTs were characterized by the pressure-induced nonlinear behavior of the lattice parameter, the Raman- and infrared-active modes, relative Raman intensity and the discontinuity of the unit-cell volume under pressure. Conclusion are supported by both in experiments and calculations. We have also revealed that the crystal structure of $\text{Co}(\text{IO}_3)_2$ show a pressure-induced expansion along certain crystallographic directions and a pressure-induced oxygen coordination increase of iodine. The bulk modulus, tentative symmetry assignment of the experiment observed Raman- and infrared-active modes and the corresponding Grüneisen parameters are reported in this chapter. All the results are compared with results from $\text{Fe}(\text{IO}_3)_3$.

The OA spectra of $\text{Co}(\text{IO}_3)_2$ show an electronic $d-d$ transition associated with Co^{2+} and the fundamental bandgap. The pressure dependence of the $d-d$ transition energy has been explained by the semiempirical Tanabe-Sugano (TS) diagram. The pressure-induced suppression of the Jahn-teller (JT) distortion in the CoO_6 polyhedral was observed and the high-spin ground state in $\text{Co}(\text{IO}_3)_2$ have been proven to be stable up to 110 GPa. The bandgap energy of $\text{Co}(\text{IO}_3)_2$ shows a linear reduction at the pressure below 8 GPa and become less pressure dependent above 8 GPa. The high-pressure behavior of the bandgap has been explained with the help of theoretically calculated electronic band structure under pressure.

4.1 Introduction

$\text{Co}(\text{IO}_3)_2$ crystallizes in a monoclinic crystal structure (space group: $P2_1$, No. 4) [129]. The space group is different from that of $\text{Fe}(\text{IO}_3)_3$, but as we will see later, it is the same as the space group of Zn and Mg iodates. The crystal structure of $\text{Co}(\text{IO}_3)_2$ is shown in **Figure 20**. When view along the b -axis, each iodine is bonded with three oxygen atoms, and the bond distance range from 1.8-1.9 Å. On the other hand, each Co atom is surrounded by six slightly distorted IO_3 pyramids by sharing one oxygen. When view perpendicular to b -axis, there is a layer structure formed by the IO_3 polyhedra. The crystal structure of $\text{Co}(\text{IO}_3)_2$ is similar to that of $\text{Fe}(\text{IO}_3)_3$, and both of them exhibits a huge anisotropic behavior under pressure owing to the layered structure. A representation of the IO_6 “polyhedral units” is shown in **Figure 20c**. Here we consider a 3+3 coordination of iodine, there are two types of iodine and oxygen bond: The first one is the short one, normally range from 1.8 to 2.0 Å and existed at ambient pressure (O1, O2 and O3 in **Figure 20c**). Another type of iodine and oxygen bond with the length range from 2.6 to 3.2 Å, and are gradually formed under high pressure, due to pressure-induced shortening of the bond distance and the existence of the stereochemical-active LEP in iodine (O3, O5 and O12 in **Figure 20c**), the same phenomenon as what we have described in $\text{Fe}(\text{IO}_3)_3$ (**Chapter 3.1** in this doctoral thesis).

The content of this chapter come from two published papers [130,131], the first paper, published in July 2021 [130]. It contains the HPXRD, HPRS, HPFTIR and the DFT calculations on the equation of state (EOS) of $\text{Co}(\text{IO}_3)_2$ up to 26 GPa. The pressure-induced IPTs, evidenced by all the four diagnostics used in this paper, are reported at 3 GPa and in the pressure range of 9.0-11.0 GPa, respectively. The pressure dependence of the lattice parameter obtained both from experiments and calculations reveals a counterintuitive expansion along the a and c axis at a pressure lower than the second IPT, but shortening along those two axis after the second IPT. The theoretically calculated pressure dependence of the Co-O and I-O bond distance was reported, indicating the increase in oxygen coordination of iodine under pressure. The pressure dependence of the Raman- and Infrared-active modes, their pressure coefficients and the Grüneisen parameters at zero pressure are reported in this paper too.

The second paper was published in March 2022 [131]. This paper mainly focused on the study of the HPOA spectra of $\text{Co}(\text{IO}_3)_2$, combined the DFT calculations on the

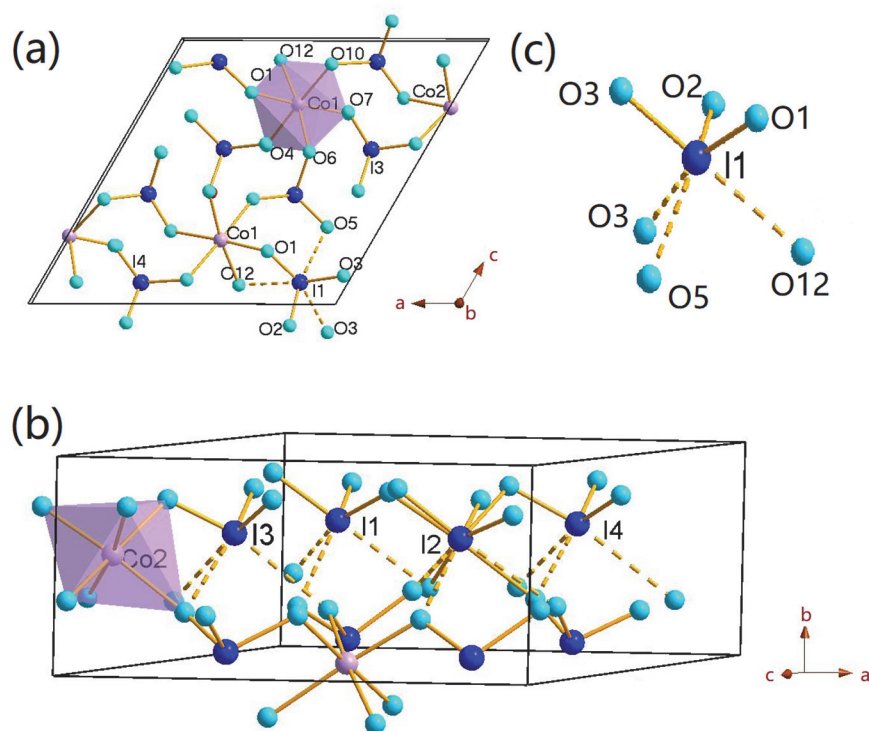


Figure 20. Crystal structure of $\text{Co}(\text{IO}_3)_2$ at ambient condition [129] (a). Along b-axis and (b) perpendicular to the b-axis. (c) Detail of the IO_6 polyhedral in (a) and (b). Purple, blue and cyan-blue balls represent Co, I and O atom. The solid yellow line are the bonds existed at ambient pressure and the dash yellow line are the bond that will formed at high pressure.

electronic band structure. There are two parts of the OA spectra, one is related to the internal $d-d$ transition of Co^{2+} , the change of the $d-d$ transition energy is related to the crystal structure change of CoO_6 octahedral under pressure. The second part is the absorption of the fundamental bandgap. The pressure dependence of the bandgap is reported, as well as the explanation of the bandgap behavior by analyzing the theoretically calculated electronic band structure.

4.2 Experiments and Calculations details

4.2.1 Sample preparation

Needle-like polycrystalline $\text{Co}(\text{IO}_3)_2$ were synthesized from an aqueous solution of

sodium iodate NaIO_3 (2 mmol, 98% purity, Fluka) and cobalt chloride CoCl_2 (1 mmol, 97% purity, Sigma-Aldrich) by the following reaction: $2\text{NaIO}_3 + \text{CoCl}_2 \rightarrow \text{Co}(\text{IO}_3)_2 + 2\text{NaCl}$. The reaction mixtures were slowly evaporated at 60 °C for 4 days. Finally, the synthesized sample were filtrated and washed with de-ionized water and characterized by the Scanning electrons microscope (SEM) and Energy-dispersive X-ray (EDX) [130]. The XRD of the sample was collected at ambient pressure by using an X'Pert Pro diffractometer from Panalytical ($\text{Cu } K_\alpha$ radiation) and it have been refined by a Rietveld method [132] with the reported crystal structure of $\text{Co}(\text{IO}_3)_2$ [129], no X-ray detectable impurity have been founded.

4.2.2 HP XRD

High pressure angle-dispersive powder X-ray diffraction was conducted at the BL04-MSPD beamline of ALBA synchrotron [133]. A membrane type DAC with diamond culets of 400 μm have been used to generate the high pressure environment. The sample, together with PTM and gold, was loaded in the 180- μm diameter hole drilled in the center of a stainless-steel gasket, which have been pre-indented to a thickness of 40 μm . A mixture of methanol: ethanol: water in a ratio of 16:3:1 was used as the PTM, the equation of state of gold was used as the pressure gauge [92]. An incident monochromatic X-ray beam with a wavelength of 0.4246 Å was used in the experiment and the spot size of the X-ray is 20 $\mu\text{m} \times 20 \mu\text{m}$. A Rayonix SX165 CCD detector was used to record the diffraction data; the sample-to-doctor distance was obtained by refining the diffraction data from LaB_6 . The method for the data analysis can be found in 3.2.2.

4.2.3 HPFTIR

HPFTIR was measured at the BL01-MIRAS beamline of ALBA synchrotron [105]. $\text{Co}(\text{IO}_3)_2$ was loaded in a DAC designed for IR microspectroscopy equipped with IIAC-diamonds with culets of 300 μm . A stainless-steel, which have been pre-indented to a thickness of 40 μm was used as the gasket, a 150- μm hole was drilled in the center and used as the sample chamber. Solid PTM CsI was used as the PTM. Ruby fluorescence scale was used as the pressure gauge [93]. More information about the data collection

and analysis can be found in 3.2.3 in this thesis.

4.2.4 HPRS

A membrane type DAC was used to generate the high pressure environment, stainless-steel was first pre-indented to a thickness of 45 μm , and then a 250- μm hole was drilled in the center and served as the sample chamber. A mixture of methanol: ethanol in a ratio of 4:1 was used as PTM. Ruby fluorescence scale was used as the pressure gauge [93]. The information of the experiment set-up and data analysis can be found in 3.2.4 in this thesis.

4.2.5 HPOA

A membrane type of DAC equipped with IIA-type diamond with culets diameters of 480 μm was used to generate the high pressure environment. A stainless-steel have been pre-indented to a thickness of 40 μm , a 200 μm hole was drilled in the center and served as the sample chamber. Polycrystalline $\text{Co}(\text{IO}_3)_2$ was first compressed to a 3- μm -thick platelet, then loaded in the sample chamber together with solid PTM (KBr) [134] and pressure gauge (ruby) [93]. The experimental setup can be found in 3.2.5 in this thesis. Due to the difference in the intensity about the spectra where related to the $d-d$ internal transition and the bandgap, so the spectra was collected by using two different light source.

4.2.6 Overview of calculations

As the calculation for $\text{Fe}(\text{IO}_3)_3$, VASP was used to do the DFT calculation on $\text{Co}(\text{IO}_3)_2$. Pseudopotentials were generated with the projector-augmented wave method [21] with a 540-eV plane-wave cutoff. The Brillouin-zone k -point integration was carried out using a significant sampling of a $4 \times 6 \times 4$ grid for the primitive unit cell. Instead of PBEsol we used in $\text{Fe}(\text{IO}_3)_3$ for exchange-correlation energy, we used PBEsol and the Armiento and Mattsson (AM05) prescription [135] in $\text{Co}(\text{IO}_3)_2$. The DFT+U scheme of Duradev *et al* [115] was used to treat the strongly correlated $3d$ state of the Co atom through effective parameter, $U_{\text{eff}}=U-J$, where U and J are the screened Coulomb and

exchange parameters, respectively. U_{eff} is 3.32 eV for Co atom [136]. The cell parameter and atomic position were fully relaxed to obtain the optimized configurations for a given volume. Then the pressure was obtained by fitting the equation of state to the volume. To perform the lattice-dynamic calculation, the phonopy package [137] was used to obtain the wavenumbers and the eigenvectors of the normal vibrational modes at Γ point and its irreducible representations.

4.3 Results and Discussion

XRD patterns of $\text{Co}(\text{IO}_3)_2$ at selected pressures are shown in **Figure 21**. There are no new peaks appearing up to the highest pressure in the experiment, nor do any of the peak split or disappear. Actually, all the XRD patterns at high pressure can be refined by the crystal structure at ambient pressure with different lattice parameters (space group: $P2_1$, No. 4), and the representative Rietveld refinement of the XRD can be found in the Supporting Information of ref [130]. Similar to the case of $\text{Fe}(\text{IO}_3)_3$, different XRD peaks indeed show a different shifting rate under compression, for example, peak (002) stay unchanged under pressure, while peak (-212) is much sensitive to pressure, indicating that the crystal structure of $\text{Co}(\text{IO}_3)_2$ will exhibit a huge anisotropic behavior. The pressure-induced change in the XRD patterns is reversible as the XRD collected from the released sample shows.

The pressure dependence of the lattice parameters determined both from experiments and calculations is plotted in **Figure 22**. Results were extracted from experiment by means of a Le Bail fit [138] of the XRD patterns. These results and the theoretically calculated lattice parameters show a good agreement, not only in the value but also in the evolution under pressure. Lattice parameter a and c show a nonlinear expansion with increasing pressure up to 9 GPa, after that both of them show a linear shortening up to the highest pressure. Lattice parameter b exhibits a reduction under pressure but with different pressure dependence before and after 9 GPa. Compared with the pressure dependence of lattice parameter a and c , b -axis is the most compressible axis, like what we found in $\text{Fe}(\text{IO}_3)_3$. The layered structure of the materials in b axis is responsible for this huge anisotropic behavior. The monoclinic angle, β , increase from 119.8 degree to 120 degrees at 3 GPa, after that it fluctuates in a very small range around 120 degrees. The nonlinear behavior of the lattice parameter evidences two IPTs. The

onset of the pressure-induced IPTs are located at 3 GPa and the pressure interval 9-11 GPa. Here we named the high pressure phases as I1 and I2 phase.

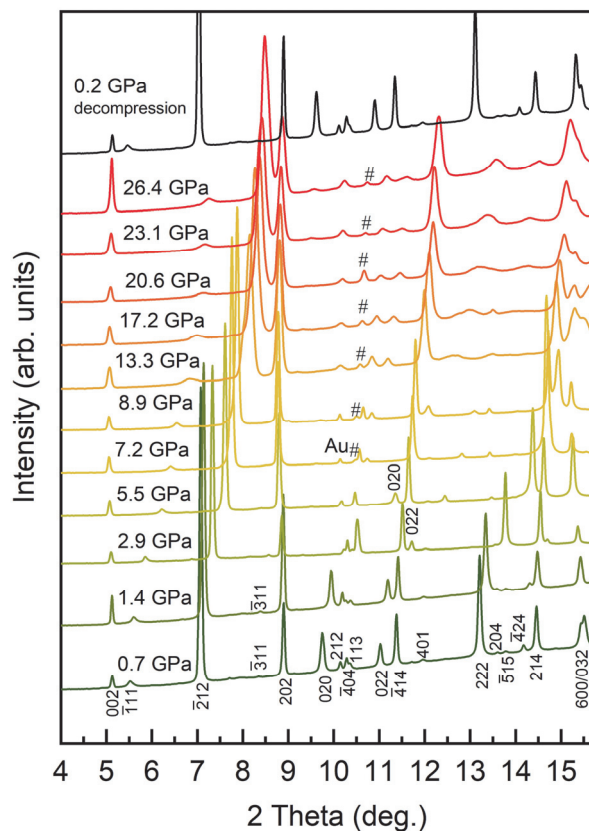


Figure 21. XRD spectra of $\text{Co}(\text{IO}_3)_2$ at selected pressure. Miller index for the observed reflection have been marked at 0.7 GPa.

A 3rd-order Birch-Murnaghan (BM) [139,140] EOS was used to fit the unit-cell volume at ambient+I1 and I2 phase separately (see ref [130]). We fitted the results from the ambient phase and I1 together due to the fact that there are no enough data in ambient-pressure phase to do the BM fitting and there is no discontinuity in the volume between those two phases. The bulk modulus for ambient+I1 phase is 29.8 GPa in experiments, 32.1 GPa and 30.7 GPa in the calculations with PBEsol and AM05 prescription, respectively. The bulk modulus determined for the I2 phase is 70.8 GPa in experiments, 50.7 GPa and 38.3 GPa from calculation with PBEsol and AM05. In experiments, the bulk modulus of $\text{Co}(\text{IO}_3)_2$ in ambient+I1 phase is almost half of that of the LP phase of $\text{Fe}(\text{IO}_3)_3$, and the calculations with PBEsol prescription agree better with the results obtained from experiments, so below we will only focus on the calculation results from PBEsol prescription. Additionally, by fitting the theoretically

calculated volume of IO_6 and CoO_6 polyhedral with a 3rd-order BM EOS, the bulk modulus of them at ambient+I1 phase are 22 and 102 GPa, respectively. Therefore, the bulk modulus of $\text{Co}(\text{IO}_3)_2$ is dominated by the compressibility of IO_6 polyhedra rather than that of CoO_6 octahedra.

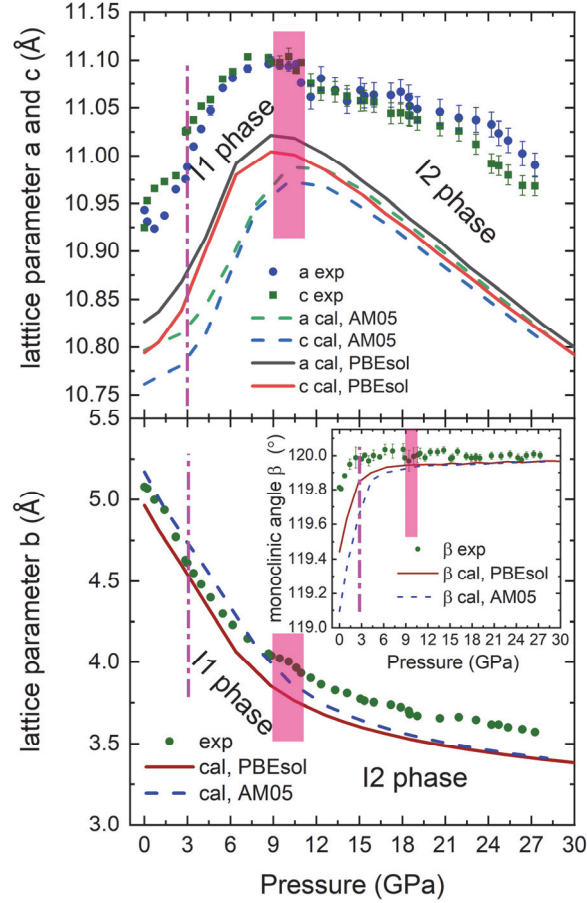


Figure 22. Pressure dependence of the lattice parameter obtained from experiment (symbol) and theoretical calculation (solid and dash line represent the calculation results with PBEsol and AM05 prescription for the exchange-correlation energy, respectively).

The theoretically calculated pressure dependence of I-O and Co-O bond distance can be found in ref [130], the Co-O bond shows a nonlinear reduction under pressure and a pressure-induced coefficient change happens at 3 and 9-11 GPa, respectively, providing further evidence of the two IPTs. The change of the six Co-O bond distances also indicates that the CoO octahedral units become less distorted under pressure. The three short I-O bonds show a slightly increase under pressure, while the three long I-O distances shorten under compression, which is a result of the gradual increase of the

oxygen coordination of iodine. To accommodate to the three new oxyanions, the three first-neighbor oxygen atoms will be pushed away from iodine. The same behavior was also observed in $\text{Fe}(\text{IO}_3)_3$.

The Raman (**Figure 23**) and FTIR spectra of $\text{Co}(\text{IO}_3)_2$ both at ambient and high pressure can be found in ref [130]. In the same work, there are tables providing the experimental and theoretical frequency of Raman- and infrared-active modes, as well as the pressure coefficient and Grüneisen parameters. The Raman and infrared spectra of $\text{Co}(\text{IO}_3)_2$ show some common features with those of $\text{Fe}(\text{IO}_3)_3$. (i). The Raman spectra can be divided into three regions, the high-frequency region ($600\text{-}900\text{ cm}^{-1}$), mid-frequency region ($300\text{-}500\text{ cm}^{-1}$), and low-frequency region ($10\text{-}300\text{ cm}^{-1}$). (ii). The high-frequency region is mainly contributed by the stretching of I-O bonds, and the strongest peaks (765 cm^{-1}) is found in this region. (iii). The modes at high-frequency region show a soft behavior under compression. We have demonstrated that the mode softening [101,141] is related to the expansion of the three short I-O bonds under pressure.

The mid-frequency region is dominated by I-O bending. We also collected the FTIR spectra in this wavenumber region, both of them can provide the vibration behavior for the I-O bending. According to crystal structure, $\text{Co}(\text{IO}_3)_2$ has 54A+54B, in total 108 vibrational modes, and all of them are both Raman- and Infrared-active. So in the mid-frequency, the modes we found in Raman spectra, are expected to be found in the infrared experiment as well. Indeed. Raman and infrared spectra show that both techniques detected the same vibration. They are similar in the frequency and show a similar evolution under pressure. There are also some modes that are not detected in Raman but found in Infrared spectra, which is useful as they can complement to each other.

There are no new peaks appearing in the complete pressure range in Raman and infrared spectra. The changes in the intensity of the modes 136 and 193 cm^{-1} reflects the two IPTs we found before. This can be seen by comparing the relative intensity of those two modes shown in ref. [130]. Furthermore, both the Raman (**Figure 24**) and infrared modes (**Figure 25**) evolved in a nonlinear way under pressure (**Figure 25**), and a pressure coefficient change happened at the phase transition pressure of those two IPTs. So all the diagnostics we used here supported the existence of those two IPTs. As we found in $\text{Fe}(\text{IO}_3)_3$, there is also a phonon gap closing in Raman spectra of $\text{Co}(\text{IO}_3)_2$,

this is a consequence of the hardening of the modes in mid-frequency region and softening of the modes in high-frequency region.

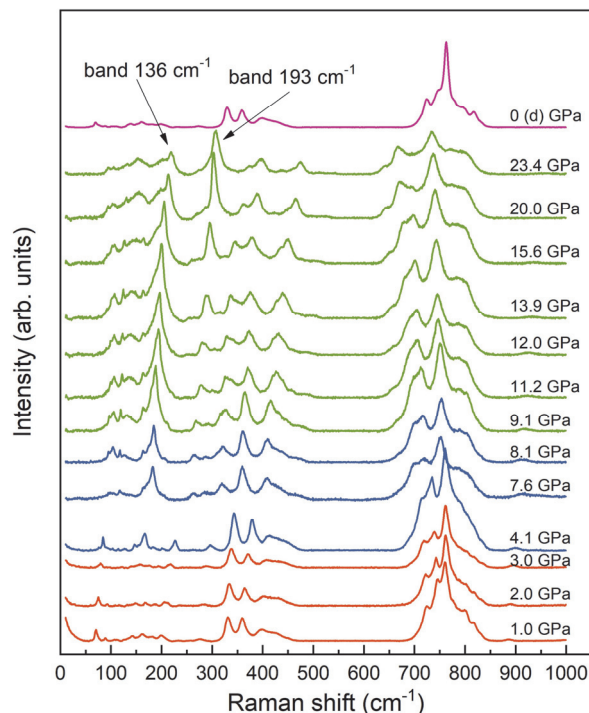


Figure 23. Raman spectra of $\text{Co}(\text{IO}_3)_2$ at selected pressure. Ambient, I1 and I2 phase are shown in different color.

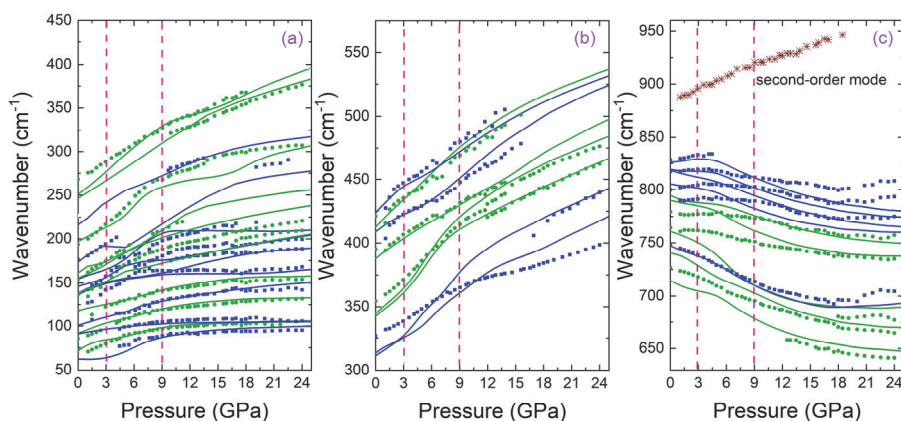


Figure 24. Pressure dependence of the experiment (dots) and calculation (solid line) determined Raman-active modes showing in three different frequency regions. The vertical dash line indicated the pressure coefficient changes, corresponding to the pressure where the IPT happened. For the sake of clarity, here we show the theoretical modes tentatively attributed to the experimentally observed modes. In the high-frequency region, we upshift the theoretically calculated modes by 70 cm^{-1} to better compared them with the experimental modes. A- and B-symmetry modes are shown in green and blue, respectively.

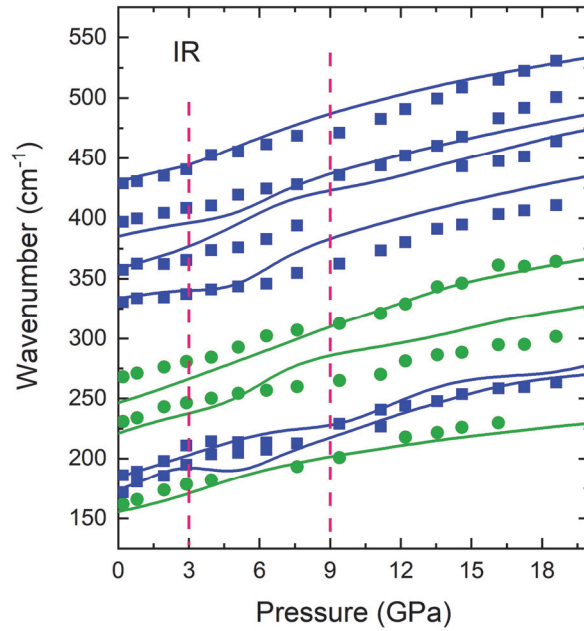


Figure 25. Pressure dependence of experiment (symbol) and theoretical calculation (solid lines) determined Infrared-active modes. The vertical dash line indicates the pressure where the two IPTs takes place. A- and B-symmetry modes are shown in green and blue, respectively.

Now we start to analyze the OA spectra of $\text{Co}(\text{IO}_3)_2$ at ambient and high pressure. The OA spectra can be divided into two parts: The part at the energy range from 2.0 to 2.6 eV shows the $d-d$ internal transition energy of Co^{2+} . Another part is located at the energy range from 2.6 to 3.6 eV, this part shows the absorption associate with the fundamental bandgap. In order to exhibit those two parts more clear, two light sources were used to collect the absorption spectra and the spectra was plotted in two separated figures (**Figure 26a** and **b**). Firstly, we will analyze the OA spectra related to the $d-d$ internal transition (**Figure 26a**). At the pressure below, we can fit the spectra with two absorption band located at around 2.15 and 2.46 eV. One of them stay unchanged and another one shows a slight blue shift under compression. At the pressure of 7.3 GPa and above, the second energy band starts to shift to higher energy with a totally different pressure coefficient, and a minor absorption band occurred between the two absorption bands. The OA spectra among all the pressure have been fitted by a Gaussian profile and the energy have been plotted in **Figure 27c**. Notably, the pressure coefficient of the absorption band changes in close proximity to the pressure of the second IPT we found

in other diagnostics.

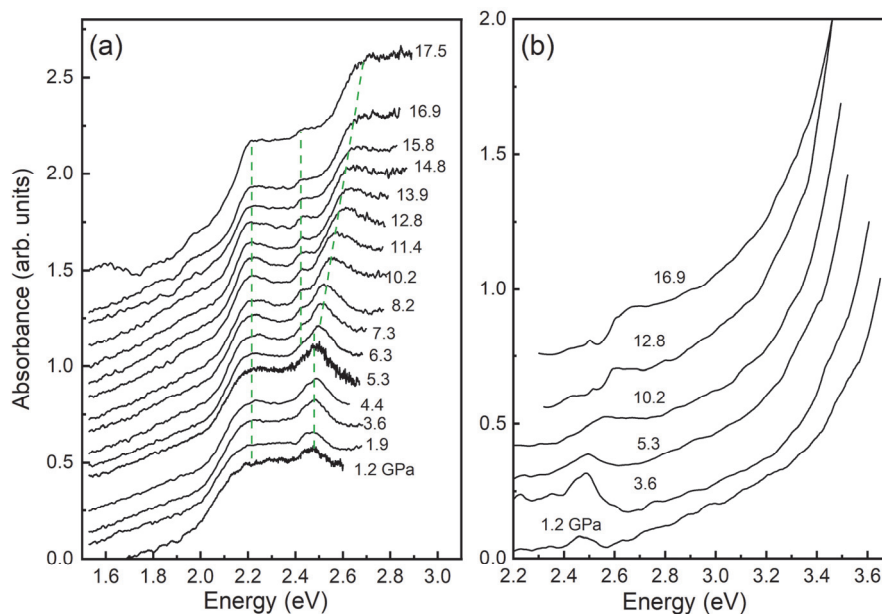


Figure 26. (a) OA spectra of Co(IO₃)₂ at the low-energy region, 1.5 to 3.1 eV, show the absorption band associated to the *d-d* internal transition of Co²⁺. (b) OA spectra at the high-energy region, 2.2 to 3.6 eV, where show the absorption band related to the fundamental bandgap.

In the crystal structure of Co(IO₃)₂, Co atoms occupy two nonequivalent crystallographic positions, we named it as Co1 and Co2. As we can observe in **Figure 27d**, the theoretically calculated distortion of Co1O₆ and Co2O₆ are almost identical, so here we can treat them as the same for the following analysis (a representative CoO₆ have been shown in **Figure 27a**). At ambient pressure, the average Co-O bond distance is 2.067 Å with a distortion index of $\sigma=0.06$ Å. The distortion of CoO₆ decrease very rapidly to 0.02 Å at 7.3 GPa, after that, the distortion index is independent of the pressure change. As we observed in the pressure dependence of Co-O bond distance, the CoO₆ octahedra become more symmetrical under pressure.

The electronic configuration of Co²⁺ in Co(IO₃)₂ is $3d^7$, the seven electrons occupy the d_{xy} , d_{xz} , d_{yz} , $d_{x^2-y^2}$ and d_{z^2} orbitals, the first three orbitals is in triply degenerate t_{2g} level and the last two are in doubly degenerate e_g level (**Figure 27b**). By subject to a weak Jahn-Teller effect, the Co²⁺ is in a slightly distortion coordination, causing a slight splitting of the t_{2g} and e_g level. According to the relationship between the local structure and the splitting Δ_t and Δ_e established in ref. [85,142,143] for halides and

oxides. The Δ_t and Δ_e in the d level of Co^{2+} were estimated to be 0.2-0.3 eV and 0.05 eV at ambient pressure, both of them decrease by a factor of 6 at 17.5 GPa (**Figure 27b**). Furthermore, the reduction of the crystal-field splitting with increase pressure caused the narrowing of the $d-d$ absorption band at 2.15 eV (**Figure 26a**).

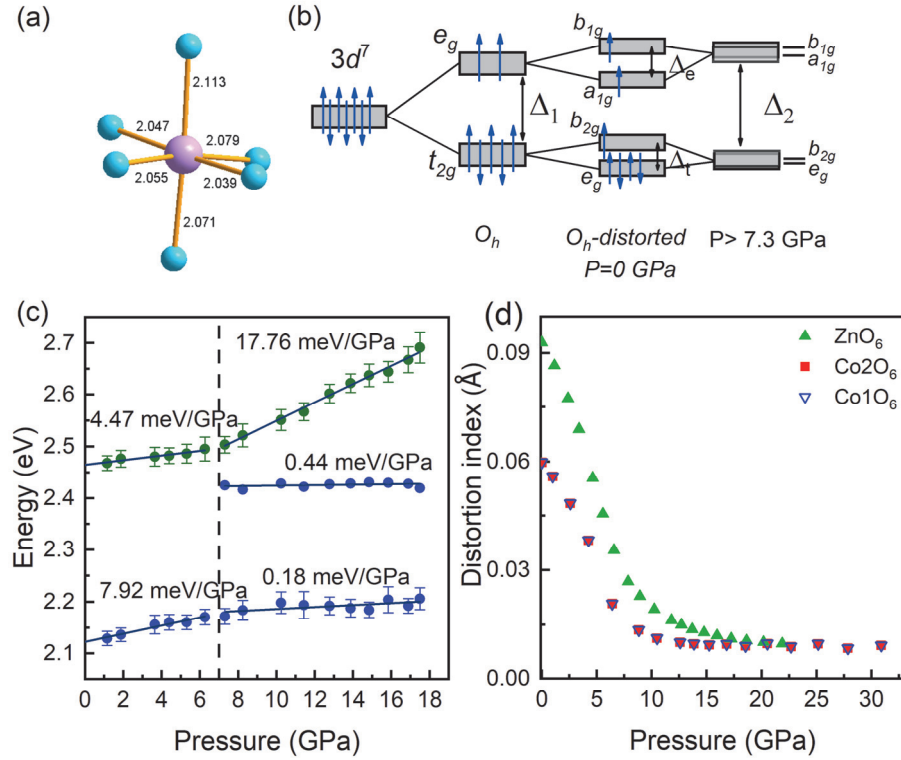


Figure 27. (a) Representative of the CoO_6 polyhedral in $\text{Co}(\text{IO}_3)_2$. (b) Diagram of Co^{2+} d levels in $\text{Co}(\text{IO}_3)_2$ below and above 7.3 GPa. (c) Pressure dependence of the $d-d$ transition energy. Solid lines are linear fit. (d) Theoretically calculated distortion index of Co_1O_6 , Co_2O_6 in $\text{Co}(\text{IO}_3)_2$ and ZnO_6 in $\text{Zn}(\text{IO}_3)_2$ as a function of pressure.

The absorption band we observed in the low energy region can be explained by using the Tanabe-Sugano (TS) diagram established for $3d^7$ state as shown in **Figure 28** [144], more description on the TS diagram can be found in ref [131]. In the high spin state of Co^{2+} , the ground state is $4T_{1g}(F)$ and the spin allowed transition are: $4T_{1g}(F) \rightarrow 4T_{2g}(F)$, $4T_{1g}(F) \rightarrow 4A_{2g}(F)$, $4T_{1g}(F) \rightarrow 4T_{1g}(P)$. Among them, the $4T_{1g}(F) \rightarrow 4T_{1g}(P)$ is the major feature for the OA spectra, since the $4T_{1g}(F) \rightarrow 4T_{2g}(F)$ transition is around 0.7 eV, below the explored energy region, for the transition $4T_{1g}(F) \rightarrow 4A_{2g}(F)$, involving two electrons jumping from t_{2g} to e_g , is proportional to 2Δ , caused a broadening of the peaks thus is difficult to be detected at ambient pressure. Therefore,

the band at 2.13 eV at 1.2 GPa is assigned to the spin-allowed $4T_{1g}(F) \rightarrow 4T_{1g}(P)$ transition. Another absorption band observed at the pressure lower than 7.3 GPa have been assigned to the transition $4T_{1g}(F) \rightarrow 2A_{1g}(G)$ as shown in **Figure 28**, based on the similar pressure coefficient between them. Although this transition is spin forbidden,

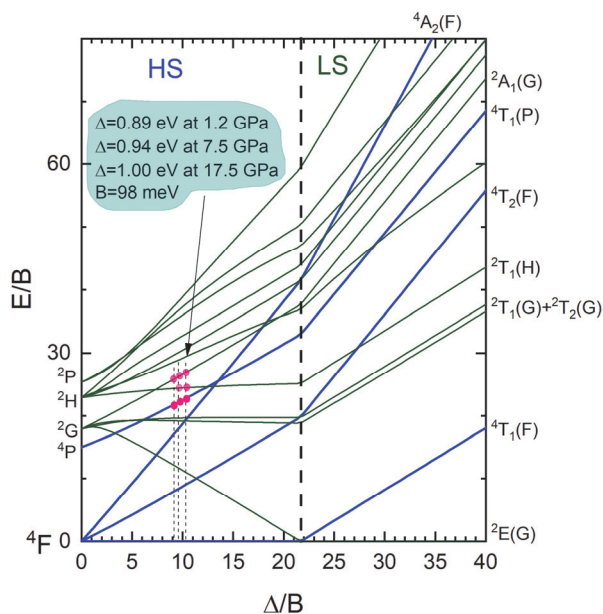


Figure 28. TS diagram for $3d^7$ ions calculated with $C/B = 4.62$. The state energy E is a function of the crystal-field energy Δ in terms of the Racah parameter B . The spin allowed transition were shown in blue. The vertical dash line indicated where the high spin (HS, $S=3/2$) to low spin (LS, $S=1/2$) happened.

the spin-orbit interaction and proximity of charge-transfer state makes it allowed. At pressure higher than 7.3 GPa, because of the narrowing of the $d-d$ transition band, there is a new weak peak emerging (**Figure 26a**) and the pressure dependence of the energy have been plotted in **Figure 27c**. The energy of this band is between those two absorption bands we found below 7.3 GPa and the pressure coefficient is similar to the transition $4T_{1g}(F) \rightarrow 2T_{1g}(H)$. So it is reasonable that we assigned this new peak to the spin-fliplike $4T_{1g}(F) \rightarrow 2T_{1g}(H)$ transition in the TS diagram.

As we have assigned all the observed absorption band in the low-energy region to the state in TS diagram, now by comparing the energy ratio between the experiment observed absorption band and the related state in TS diagram, we are able to solve the Racah parameter B for Co^{2+} in $\text{Co}(\text{IO}_3)_2$, as well as the crystal field energy Δ in different pressure. For example, the energy ratio between the experiment observed $d-d$ transition band at 1.2 GPa is $2.47 \text{ eV}/2.13 \text{ eV}=1.16$, the same ratio between state $2A_{1g}(G)$ and

${}^4T_{1g}(P)$ in the TS diagram is $\Delta/B = 9.08$ in x axis and $E/B = 21.7$ in y axis when E is 2.13 eV. So here we got the Racah parameters $B=0.098$ eV, $C=0.453$ eV and $\Delta=0.89$ eV. the value of the Racah parameter B in $\text{Co}(\text{IO}_3)_2$ is similar to the value in KCoF_3 ($B=0.105$ eV) [145], CoCl_2 ($B=0.097$ eV) [85] and CoO ($B=0.105$ eV) [146]. By the same method, we solved the crystal field energy Δ in $\text{Co}(\text{IO}_3)_2$ is 0.94 at 7.5 GPa and 1 eV at 17.5 GPa as we shown in **Figure 28**. The crystal field energy increases with the increasing pressure, according to the TS diagram in **Figure 28**, the high-spin to low-spin transition happened at $\Delta/B=22$ and the corresponding volume reduction needs to reach $\Delta=2.2$ eV would be 60%. Therefore. the spin transition pressure is predicted to be 110 GPa in $\text{Co}(\text{IO}_3)_2$, higher than the transition crossover found in CoCl_2 (70 GPa) [85].

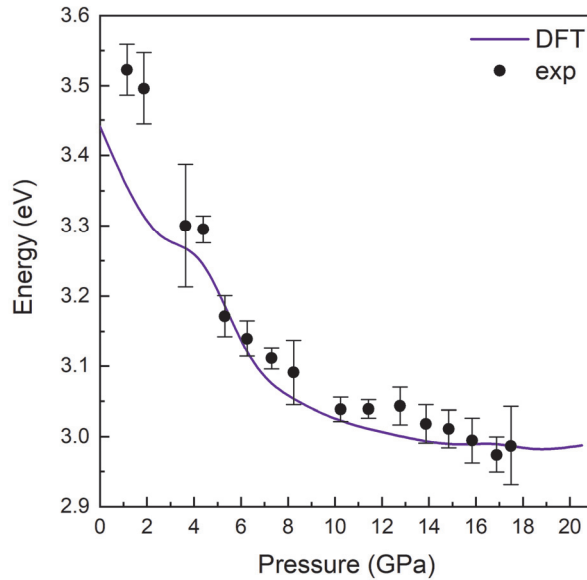


Figure 29. Pressure dependence of bandgap energy for $\text{Co}(\text{IO}_3)_2$ determined from experiment (dots) and theoretical calculation (solid line).

Figure 29 provides the pressure dependence of the bandgap energy of $\text{Co}(\text{IO}_3)_2$. The experimental bandgap was obtained by adopting the Tauc plot for indirect bandgap materials in the OA spectra we shown in **Figure 26b**. Similar to the behavior of the distortion index of CoO_6 under pressure, the bandgap energy first shows a negative relationship with pressure and then at pressure higher than 8 GPa, it is less pressure sensitive. As the DOS and PDOS of $\text{Co}(\text{IO}_3)_2$ shown in ref. [131], the VBM is dominated by $\text{Co-}3d$ and $\text{O-}2p$ state, while the CBM is dominated by the $\text{I-}5p$ state,

similar to that of $\text{Fe}(\text{IO}_3)_3$, the partial filled $3d$ state contribute to the energy near to Fermi level, which is a common feature for the partial filled transition metal iodates (see **Table 1** in **Chapter 1.3** of this thesis). So the bandgap of $\text{Co}(\text{IO}_3)_2$ will be dominated by the change of Co-O and I-O bond distance. Notice, the pressure dependence of the Co-O and I-O bond distance have been reported in ref. [130]. The Co-O bond distance shows a nonlinear reduction under compression, while the I-O bond distance (the three short bonds) will slightly increase under compression, in accommodate to the three additional oxygen in the next IO_3 layer. So there are two effects compete under pressure, the decrease of the Co-O bond distance increases the overlap between the Co and O orbital and favors narrow the bandgap energy. On the other hand, the enlargement of the I-O bonds reduces the hybridization between I and O atom, favoring open the bandgap energy. At the pressure lower than 7.3 GPa, Co contributes the most to the VBM, so the first effect dominated the bandgap energy at lower pressure, when pressure higher than 7.3 GPa, the contribution of Co decrease to the same level as O, those two effects neutralize each other and result in the less dependence on pressure. The atomic character at VBM and CBM can be found in ref. [131].

4.4 Conclusions

(1) $\text{Co}(\text{IO}_3)_2$ undergoes two IPTs at 3.0 GPa and in the pressure interval of 9.0-11.0 GPa, the phase transitions have been characterized by HPXRD, HPRS, HPFTIR, and DFT calculations, only the second phase transition have been found in HPOA. The lattice parameters a and c expand before the second IPT and shorten after the second IPT. The Raman- and infrared-active modes exhibits a nonlinear behavior under pressure. In HPOA, the bandgap energy also shows different pressure coefficients before and after 7.5 GPa, a pressure corresponding to the second IPTs. The driven mechanism of those two IPTs is the increase of the oxygen coordination of iodine under pressure, which is a consequence of the decrease of the stereoactivity of the LEP in iodine under pressure.

(2) The bulk modulus for the ambient+I1 phase and I2 phase were determined to be 29.8 and 70.8 GPa in experiment (32.1 and 50.7 GPa in theoretical calculation). The bulk modulus of $\text{Co}(\text{IO}_3)_2$ have been demonstrated to be dominated by IO_6 polyhedral, rather than CoO_6 octahedral.

- (3) The crystal structure of $\text{Co}(\text{IO}_3)_2$ show a huge anisotropic behavior, and b -axis is the most compressible axis, the reason is the layered structure along this axis formed by IO_3 pyramid.
- (4) The theoretically calculated pressure dependence of Co-O bond distance shows a nonlinear reduction under pressure, and the bond distance between iodine and inlayer oxygen slightly increases under compression, while the bond distance between iodine and inter-layer oxygen decreases under compression.
- (5) The Raman spectra of $\text{Co}(\text{IO}_3)_2$ can be divided into three regions according to the mode of atomic vibration. The strongest mode (765 cm^{-1}) is located in the high-frequency region. Furthermore, most of the modes in the high-frequency region soften under pressure, which is a result of the slightly enlargement of the bond distance between iodine and inlayer oxygen. The modes in mid- and low-frequency region harden under pressure and show a nonlinear behavior, supports the two IPTs found in other diagnostics.
- (6) The infrared spectrum shows the information at the mid-frequency region and part of the low-frequency region. The pressure dependence of the infrared-active modes shows a nonlinear behavior, support the two IPTs we found in other diagnostics.
- (7) The OA spectra of $\text{Co}(\text{IO}_3)_2$ can be divided into two regions, the low-energy region (2.0 eV to 2.8 eV) and high-energy region (2.6 eV to 3.6 eV). The low-energy region is related to the $d-d$ internal transition of Co^{2+} , and the high-energy region related to the fundamental bandgap. At the pressure below than 7.3 GPa, the $d-d$ transition spectra are broad, due to the slightly distorted CoO_6 octahedral. The distortion of CoO_6 decrease from 0.06 at ambient pressure to 0.01 at the pressure higher than 7.3 GPa, causes narrowing of the spectra.
- (8) The $d-d$ transition band have been well explained by the T-S diagram for $3d^7$. The Racah parameter for Co^{2+} in $\text{Co}(\text{IO}_3)_2$ is 0.098 eV and the crystal field splitting energy is 0.453 eV at 1.2 GPa, the crystal field splitting energy increased to 1.00 eV at 17.5 GPa. The predicted high-spin to low-spin transition is 110 GPa.
- (9) According to the theoretically calculated band structure of $\text{Co}(\text{IO}_3)_2$, it is an indirect bandgap material. The VBM is dominated by Co- $3d$ and O- $2p$ orbital, while the CBM is dominated by the I- $5p$ state. Therefore, the bandgap of $\text{Co}(\text{IO}_3)_2$ was dominated by the change of the Co-O and I-O bond distance.
- (10) The bandgap of $\text{Co}(\text{IO}_3)_2$ decrease sharply with pressure up to 7.3 GPa, and then

show an independent behavior of pressure. The shortening of the Co-O bond distance favors the narrowing of the bandgap energy, while the slightly enlargement of the I-O bond distance favors the opening of the bandgap energy. The competition of those two effects under pressure results in the non-linear bandgap change under pressure.

(11) The changes we observed in HPXRD, HPRS, HPFTIR and HPOA are reversible.

4.5 Author Contribution

The author of this doctoral thesis is the first author of all the two published papers, which are the main content of this chapter. HPRS and HPOA were conducted by the author. HPFTIR were conducted by the author, Robin Turnbull, and Enrico Bandiello. HPXRD was conducted by Catalin Popescu. The theoretical calculations were performed by Placida Rodriguez-Hernandez and Alfonso Muñoz. Francisco Javier Manjón provides help in the HPRS experiment and the discussion on the results. The sample used in those studies was synthesized by Zoulikha Hebboul. Ibraheem Yousef helped the HPFTIR experiment and Fernando Rodríguez helped in the analysis of the HPOA spectra. Daniel Errandonea supervised the studied project. All the data were analyzed by author. The author and Daniel Errandonea wrote the first draft of those two papers, those two papers were revised by all authors.

A. Liang, C. Popescu, F. J. Manjon, R. Turnbull, E. Bandiello, P. Rodriguez-Hernandez, A. Muñoz, I. Yousef, Z. Hebboul, and D. Errandonea, Pressure-Driven Symmetry-Preserving Phase Transitions in $\text{Co}(\text{IO}_3)_2$, *J. Phys. Chem. C* **125**, 17448 (2021).

A. Liang, F. Rodríguez, Rodríguez-Hernandez, P, A. Muñoz, R. Turnbull, and D. Errandonea, High-Pressure Tuning of $d-d$ Crystal-Field Electronic Transitions and Electronic Band Gap in $\text{Co}(\text{IO}_3)_2$, *Phys. Rev. B* **105**, 115204 (2022).

Pressure-Driven Symmetry-Preserving Phase Transitions in $\text{Co}(\text{IO}_3)_2$

A. Liang,* C. Popescu, F. J. Manjon, R. Turnbull, E. Bandiello, P. Rodriguez-Hernandez, A. Muñoz, I. Yousef, Z. Hebboul, and D. Errandonea

 Cite This: *J. Phys. Chem. C* 2021, 125, 17448–17461

 Read Online

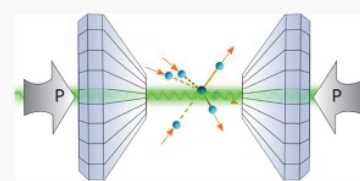
ACCESS |

 Metrics & More

 Article Recommendations

 Supporting Information

ABSTRACT: High-pressure synchrotron X-ray diffraction studies of cobalt iodate, $\text{Co}(\text{IO}_3)_2$, reveal a counterintuitive pressure-induced expansion along certain crystallographic directions. High-pressure Raman and infrared spectroscopy, combined with density-functional theory calculations, reveal that with increasing pressure, it becomes energetically favorable for certain I–O bonds to increase in length over the full range of pressure studied up to 28 GPa. This phenomenon is driven by the high-pressure behavior of iodate ion lone electron pairs. Two pressure-induced isosymmetric monoclinic–monoclinic phase transitions are observed at around 3.0 and 9.0 GPa, which are characterized by increasing oxygen coordination of the iodine atoms and the probable formation of pressure-induced metavalent bonds. Pressure–volume equations of state are presented, as well as a detailed discussion of the pressure dependences of the observed Raman- and infrared-active modes, which clarifies previous inconsistencies in the literature.



INTRODUCTION

Metal iodates, $\text{M}[\text{IO}_3]^-$, form a diverse range of non-centrosymmetric (NCS) materials, which exhibit useful and interesting properties such as non-linear optics;^{1–3} visible to far-IR transparency (12.5 μm);^{4,5} large second-harmonic generation coefficients;^{5–8} a high optical damage threshold; and good thermal stability (up to 400 °C).^{9,10} Consequently, the synthesis and behavior of metal iodates have been intensely studied under ambient conditions. In contrast, there remains a large deficit of studies of metal iodates under high-pressure (HP) conditions despite the clear possibility for new insights into pressure-induced effects,¹¹ in particular changes regarding the stereochemically active lone electron pair (LEP) of the iodate ion, $[\text{IO}_3]^-$.

Despite the scarcity of studies on iodates at HP in the literature, these have shown the potential for interesting physics of such compounds. For example, pressure-induced structural phase transitions have been observed in KIO_3 and AgIO_3 ,^{12,13} and we recently reported HP studies on the structural and vibrational properties of transition-metal iodates $\text{Fe}(\text{IO}_3)_3$ and $\text{Zn}(\text{IO}_3)_2$,^{14–16} in which we observed both first- and second-order phase transitions driven by increasing atomic coordination of the iodine atoms. Even though $\text{Fe}(\text{IO}_3)_3$ and $\text{Zn}(\text{IO}_3)_2$ are not isostructural, they exhibit similar HP phenomena, thus providing motivation to explore the HP behavior of other metal iodates. Cobalt iodate, $\text{Co}(\text{IO}_3)_2$, is a noteworthy candidate because cobalt is the next element in the periodic table after iron, and, until the present study, no HP data on the structural or vibrational properties of $\text{Co}(\text{IO}_3)_2$ were available.

The LEP of the iodate ion plays an important role in the HP phenomena reported herein. In the $[\text{IO}_3]^-$ ion, the iodine atom (electronic configuration $5s^25p^5$) shares its p-electrons

with the oxygen atoms, thus leaving the pair of 5s electrons stereochemically active. In particular, they are oriented along the *b*-axis in the $\text{Co}(\text{IO}_3)_2$ crystal structure.¹⁷ The $\text{Co}(\text{IO}_3)_2$ crystal structure is shown in Figure 1. Under ambient conditions, $\text{Co}(\text{IO}_3)_2$ crystallizes in the monoclinic space group $P2_1$ (S.G. no. 4) with the following unit-cell parameters: $a = 10.939(1)$ Å, $b = 5.071(1)$ Å, $c = 10.936(1)$ Å, and $\beta = 119.95(1)^\circ$.¹⁷ The $[\text{Co}]^{2+}$ cations are coordinated to six O atoms and form slightly distorted octahedral CoO_6 units, which are connected by IO_3 triangular pyramids. Each CoO_6 unit is surrounded by six IO_3 groups. When viewed perpendicular to the *b*-axis, the crystal structure of $\text{Co}(\text{IO}_3)_2$ is constituted by layers of IO_3 units parallel to the *ac*-plane (Figure 1b). The crystal structure of $\text{Co}(\text{IO}_3)_2$ is similar to that of $\text{Zn}(\text{IO}_3)_2$; however, its unit-cell is doubled. Consequently, the vibrational spectrum of $\text{Co}(\text{IO}_3)_2$ is more complex than that of $\text{Zn}(\text{IO}_3)_2$. Raman and infrared (IR) spectra of $\text{Co}(\text{IO}_3)_2$ under ambient conditions were reported by Pracht and Lutz¹⁸ and Kochuthresia et al.¹⁹

Using X-ray diffraction (XRD) and vibrational spectroscopy experiments combined with density functional theory (DFT) calculations, we report here two subtle pressure-induced phase transitions in $\text{Co}(\text{IO}_3)_2$ at 3 GPa and in the range 9.0–11.0 GPa, respectively. The evolution of the unit-cell parameters under pressure up to 27 GPa reveals a counterintuitive expansion along the *a* and *c* axes in both the lower pressure

Received: May 27, 2021

Revised: July 2, 2021

Published: July 29, 2021



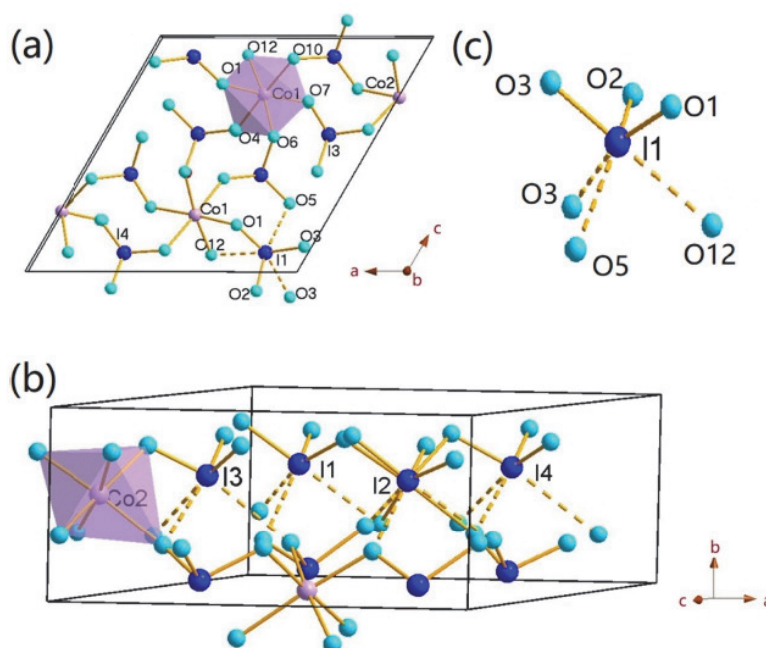


Figure 1. Crystal structure of $\text{Co}(\text{IO}_3)_2$ (a) along the b -axis and (b) perpendicular to the b -axis at ambient pressure. (c) Detail of the I1O_6 unit in (b). In the structure, the atoms are labeled. Solid yellow lines represent the bonds at ambient pressure. Dashed yellow lines, between iodine and the oxygen in the neighbor IO_3 units, represent the bonds that gradually form at high pressure. The detail of the iodine coordination change can be found in the article.

Table 1. $\text{Co}(\text{IO}_3)_2$ Lattice Parameters as Refined from Experimental Data and as Calculated by DFT

	a (Å)	b (Å)	c (Å)	β (deg)	V_0 (Å ³)
experiment	10.943(6)	5.078(1)	10.925(4)	119.814(3)	526.68(4)
calculation (PBEsol)	10.827	4.962	10.794	119.443	505.00
calculation (AM05)	10.761	5.171	10.796	119.095	525.00

phases (ambient-pressure and I1 phase) below 9–11 GPa, and the change found both in a and c axes were underpinned by the HP behavior of the LEP of the iodate ion. We show that increasing the I–O bond lengths in certain crystallographic directions becomes energetically favorable at HP in order to accommodate the formation of additional I–O bonds. The bond lengthening is confirmed by the Raman and IR spectroscopies as well as the DFT calculations. Birch–Murnaghan pressure–volume equations of state are presented along with the pressure dependence of the Raman- and infrared-active modes, their pressure coefficients, and the Grüneisen parameters at zero pressure. Also, symmetries are assigned to the optical modes. A critical comparison is made with other iodates.

METHODS

Sample Synthesis. Micron-sized needle-like crystals of $\text{Co}(\text{IO}_3)_2$ were synthesized from an aqueous solution of sodium iodate NaIO_3 (2 mmol, 98% purity, Fluka) and cobalt chloride CoCl_2 (1 mmol, 97% purity, Sigma-Aldrich) in de-ionized water, in which the following reaction took place: $2\text{NaIO}_3 + \text{CoCl}_2 \rightarrow \text{Co}(\text{IO}_3)_2 + 2\text{NaCl}$. The reaction mixtures were slowly evaporated at 60 °C for 4 days, leading to the precipitation of purple needle-like crystals, which were filtrated and washed with de-ionized water.

The particle size, morphology, and chemical composition of the samples were assessed using a scanning electron micro-

scope with a Peltier cooled XFlash™ silicon drift detector (model 410 M) for energy-dispersive X-ray (EDX) analysis. The analysis was performed using 20 keV primary electrons. SEM images of the $\text{Co}(\text{IO}_3)_2$ crystal morphology are shown in Figure S1 in the Supporting Information. The results from the EDX analysis are also shown in Figure S2 in the Supporting Information. Within the limits of experimental errors, only Co and I were detected. The weight percent and atomic percent of Co and I agree with the expected molar ratio of 1:2.

XRD at Ambient Pressure. Ambient-pressure powder XRD measurements were performed to identify the purity and the crystal structure of $\text{Co}(\text{IO}_3)_2$ using an X'Pert Pro diffractometer from Panalytical (Cu K_α radiation). The corresponding XRD data are shown in Figure S3 in the Supporting Information. The data were refined by the Rietveld method.²⁰ The structure information of $\text{Co}(\text{IO}_3)_2$ reported by Phanon et al.¹⁷ was used as a model for the refinement. The unit-cell parameters and volume obtained from our refinement are shown in Table 1 and are in good agreement with the values reported by Phanon et al.¹⁷ Moreover, the values reported here are close to the unit-cell parameters and volume obtained from our DFT calculations at 0 GPa (see Table 1). We refer the reader to the calculation details section to know more about the PBEsol and AM05 functionals. In the refinement, shown in Figure S3 in the Supporting Information, the positions of the observed and calculated reflections are well matched. The difference in observed and calculated intensities between 35° and 70° is caused by the partially preferred

direction of the needle-like crystals. The same issue has been previously detected for $\text{Zn}(\text{IO}_3)_2$ crystals synthesized by a similar chemistry method.¹⁶ No impurity or other phases were detected by XRD.

In Situ XRD at High Pressure. Angle-dispersive powder HP-XRD was performed at the BL04-MSPD beamline of ALBA synchrotron.²¹ An incident monochromatic X-ray beam with a wavelength of 0.4246 Å was focused down to a spot size of 20 μm × 20 μm. Diffraction data were recorded using a Rayonix SX165 CCD detector. The two-dimensional diffraction images were integrated into one-dimensional intensity versus 2θ patterns using Dioptas.²² The sample-to-detector distance along with detector orientation parameter were refined using diffraction data from a LaB_6 calibrant. The $\text{Co}(\text{IO}_3)_2$ sample was loaded into a membrane-driven diamond-anvil cell (DAC) with diamond culets of 400 μm using a T301 stainless-steel gasket, pre-indented to a thickness of 40 μm and with a sample chamber of 180 μm diameter in the center, drilled via spark erosion. A 16:3:1 methanol/ethanol/water mixture was used as the pressure-transmitting medium (PTM) and pressure was determined using the equation of state of gold.²³

High-Pressure Fourier Transform Infrared. FTIR measurements were conducted at ALBA synchrotron at the BL01-MIRAS beamline. $\text{Co}(\text{IO}_3)_2$ was loaded in a DAC designed for IR microspectroscopy equipped with IAC-diamonds (300 μm culet size). A stainless-steel gasket pre-indented to a thickness of 40 μm and with a 150 μm diameter hole in the center was used as a pressure chamber. Cesium iodide (CsI) was used as the PTM because it provides the widest IR transmission window amongst the possible PTMs.²⁴ The sample pressure was determined using the ruby scale.²⁵ The FTIR–microspectroscopy experiments were performed in transmission mode using a masking aperture size of 45 × 45 μm² and a beam current inside the synchrotron ring of 250 mA. More details on the experimental set-up of the MIRAS beamline can be found elsewhere.²⁶

Raman Spectroscopy. High-pressure Raman spectroscopy (HP-RS) measurements were carried out with a Horiba Jobin Yvon LabRAM HR UV microspectrometer using a 632.8 nm He/Ne laser light source. A thermoelectrically cooled multi-channel CCD detector was used to collect the signal and the spectral resolution was better than 2 cm⁻¹. The set-up was calibrated using He plasma lines before the HP-RS experiment. $\text{Co}(\text{IO}_3)_2$ crystals and ruby chips were loaded in a 250-μm hole of a pre-indented steel gasket (thickness of 45 μm) inside a membrane-driven DAC. The PTM used in HP-RS experiments was a 4:1 methanol/ethanol mixture, and the ruby fluorescence method was used for pressure calibration.²⁵

First-Principles Calculations. *Ab initio* calculations of the structural, electronic, dynamical, and elastic properties were performed in the framework of DFT.²⁷ We used the Vienna ab initio simulation package.^{28,29} The projector-augmented wave³⁰ pseudo-potentials method was used, with a 540 eV plane-wave cutoff to ensure high accurate convergence. The Brillouin zone *k*-point integration was carried out using a significant sampling of a 4 × 6 × 4 grid for the primitive unit cell. We employed the generalized-gradient approximation with both the Perdew, Burke, and Ernzerhof for solids (PBEsol)³¹ and the Armiento and Mattsson (AM05)³² prescription for the exchange–correlation energy. Additionally, we performed our simulations with the DFT + *U* scheme of Duradev et al.³³ to treat the strongly correlated states of the Co

atom through a single effective parameter, $U_{\text{eff}} = U - J$, where *U* and *J* are the screened Coulomb and exchange parameters, respectively. The selected value of U_{eff} was 3.32 eV for the Co atoms.³⁴ The antiferromagnetic configuration was found to be lowest in energy. The cell parameters and the atomic positions were relaxed to obtain the optimized configurations for a given volume, where the atomic forces were less than 0.004 eV/Å, and the stress tensor was diagonal to within an accuracy of more than 0.1 GPa. This procedure allowed us to obtain a set of volumes, energy, and pressure from our simulations, which were fitted with an equation of state to obtain the equilibrium volume, bulk modulus, and pressure derivative. To perform the lattice-dynamics calculations, we used the Phonopy package³⁵ to obtain the wavenumbers and the eigenvectors of the normal vibrational modes at the Γ point and its irreducible representations.

RESULTS AND DISCUSSION

HP-XRD Measurements. Selected HP-XRD patterns are presented in Figure 2. The Miller indices of the corresponding

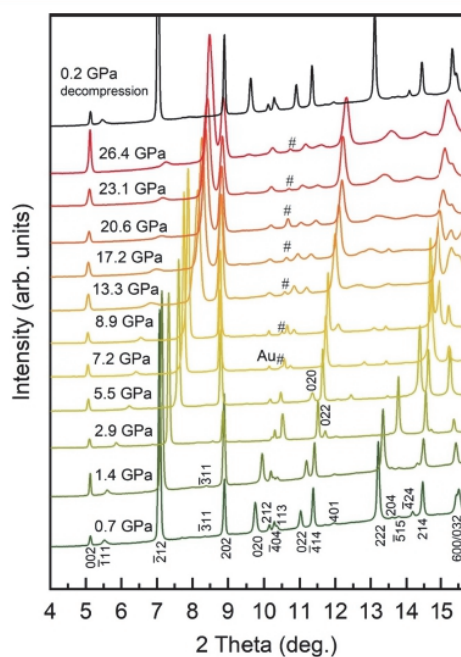


Figure 2. HP-XRD spectra of $\text{Co}(\text{IO}_3)_2$ at selected pressures. The top pattern was collected during the decompression process.

reflections are indicated. Under compression, most of the observed Bragg reflections shift to higher angles, indicating a pressure-induced decrease of the interplanar spacings. Some of the observed $\text{Co}(\text{IO}_3)_2$ reflections are more sensitive to pressure than others and therefore shift at different rates. For example, (020) is more sensitive to pressure than (414), resulting in a pressure-induced crossing of the reflections (Supporting Information, Figure S4a). Interestingly, some of the reflections shift to lower Bragg angles with increasing pressure, for example (202), thereby indicating a pressure-induced increase in the corresponding interplanar spacing. This strongly non-isotropic behavior results in the merging of some of the observed reflections at HP, most notably those above 14°. Pressure-induced reflection broadening occurs above 10 GPa, that is, beyond the hydrostatic limit of the

PTM.^{36,37} All these changes are reversible, as demonstrated by comparison of the top XRD pattern (acquired after sample decompression to 0.2 GPa) and the bottom XRD pattern (acquired upon commencing sample compression to 0.7 GPa). Over the entire pressure range of the experiments, no new reflections are observed, nor do any of them disappear. Therefore, all acquired XRD patterns can be indexed using the monoclinic $P2_1$ (SG no. 4) ambient-pressure structure and the Rietveld refinement of the XRD data at selected pressure can be found in the Supporting Information (Figure S5).

The pressure evolution of the unit-cell parameters (a , b , c , and β) was determined via the Le Bail method³⁸ and it is shown in Figure 3. The top panel of Figure 3 shows the

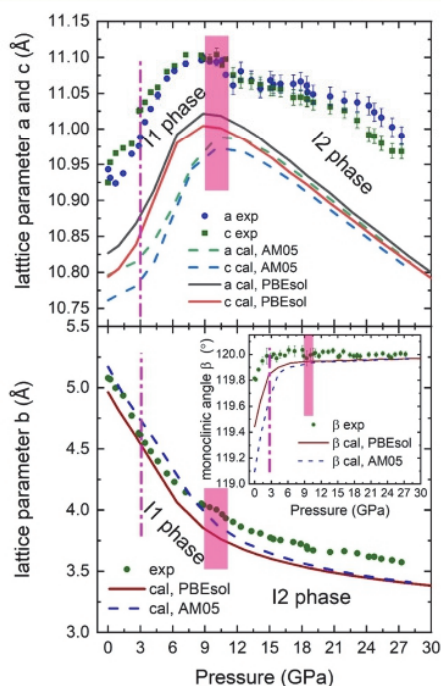


Figure 3. Pressure dependence of the unit-cell parameters. The inset is the pressure dependence of the monoclinic angle, β . The error of lattice parameter b is smaller than the symbol. Squares and circles correspond to experimental (exp) data while lines correspond to the calculated (cal) data (PBEsol-solid lines and AM05-dashed lines). The vertical pink dashed line and pink rectangle indicate the phase transition pressure or transition pressure region in the experiment and DFT calculation, respectively.

pressure dependence of the a - and c -axes. The values extracted from the experimental data are compared with those of DFT calculations performed using different exchange–correlation functionals: PBEsol and AM05. The experiments and calculations give similar results, whereby both a and c initially exhibit a slight increase upon compression from ambient pressure to 3.0 GPa, followed by a more abrupt increase in the pressure range of 3.0–9.0 GPa, and by a general decrease from 11.0 GPa to the highest pressure reached (27.0 GPa). This non-linear behavior of the unit-cell parameters is magnified in Figure S4b in the Supporting Information, where we report the pressure dependence of the d -spacing corresponding to peak (202). The non-linear behavior of the lattice parameters a and c is qualitatively similar to that observed in $\text{Zn}(\text{IO}_3)_2$.¹⁶ Notice that a different setting (unique axis) was used to describe

$\text{Zn}(\text{IO}_3)_2$ and $\text{Co}(\text{IO}_3)_2$ in the literature.^{16,17} For the sake of simplicity, we will here describe both structures with the same setting using the b -axis as the unique axis, as recommended by the International Union of Crystallography. The non-linear behavior of unit-cell parameters in $\text{Zn}(\text{IO}_3)_2$ ¹⁶ was identified as an evidence of the presence of symmetry-preserving phase transitions. For the sake of comparison, we have included in Figures S6–S10 in the Supporting Information the pressure evolution of the normalized lattice parameters and unit-cell volumes of $\text{Co}(\text{IO}_3)_2$ of this work and of $\text{Zn}(\text{IO}_3)_2$.¹⁶

Compressibility. In $\text{Co}(\text{IO}_3)_2$, a discontinuity in the compressibility of a and c lattice parameters and that of the b lattice parameter and unit-cell volume, as discussed later in the article, have been identified at 3.0 and in the 9.0–11.0 GPa range. The discontinuities are denoted by vertical dashed lines and the rectangles are shown in pink in Figure 3. The two HP phases are herein referred to as I1 and I2 (where “I” signifies that the phases are “isosymmetric”). The onset pressures of the two phase transitions in $\text{Co}(\text{IO}_3)_2$ are slightly higher than those observed in $\text{Fe}(\text{IO}_3)_3$ (in which similar transitions happen at 1.5–2.0 and 5.7–6.0 GPa)¹⁴ and they are similar to those observed in $\text{Zn}(\text{IO}_3)_2$ (in which they occur at 2.5–3.4 and 8.9 GPa).¹⁶ Qualitatively similar transitions have also been found in the iodate $\text{Na}_3\text{Bi}(\text{IO}_3)_6$.³⁹ Therefore, we suggest that symmetry-preserving transitions are a typical feature of metal iodates under compression.

Regarding the b lattice parameter, we found that its evolution under pressure is different from that of the a and c lattice parameters (see Figure 3). The b lattice parameter exhibits a conventional behavior in that it decreases under compression. Nonetheless, it is found to be very sensitive to pressure. The lattice parameter b shrinks drastically from 5.08 Å at ambient pressure to 3.57 Å at 27.2 GPa, thereby exhibiting a reduction of 29.7% in experiments (32.0% reduction in calculation using PBEsol and 34.1% reduction in calculation using AM05). Two discontinuities can be observed in the data, as shown in Figure 3, which correspond to the transition pressures discussed before in the context of the a and c lattice parameters. The relative change with pressure of the b -axis is dramatic compared with those of the a - and the c -axes, with both shrinking less than 2% in the same pressure range. Consequently, $\text{Co}(\text{IO}_3)_2$ exhibits significant anisotropic compressibility under pressure, with the b -axis exhibiting by far the largest zero-pressure compressibility of the three axes.

In order to explain the highly anisotropic compressibility of $\text{Co}(\text{IO}_3)_2$, it is necessary to recall that the LEPs of the $[\text{IO}_3]^-$ tetrahedra point along the b -axis direction (Figure 1b). At low pressures, the iodine atom only bonds with the three oxygen atoms on the top, leaving a layer of LEPs in the a - c plane. This “soft” layer of LEPs between the layers of $[\text{IO}_3]^-$ units is very sensitive to pressure, resulting in the higher compressibility of the b lattice parameter at low pressures. In contrast, the a and c axes consist of chains of CoO_6 octahedra and IO_3 polyhedra, which clearly leads to a lower compressibility along those directions. Notably, lattice parameters calculated using the PBEsol functional to describe the exchange–correlation energy show a better agreement with experimental data than those obtained using the AM05 functional.

For the monoclinic angle, β , we found that it increases from 119.82° at ambient pressure to around 120° at 3 GPa, when it becomes roughly constant within experimental accuracy above this pressure (see the inset in Figure 3). A similar behavior has also been found in the pressure dependence of the monoclinic

angle of $\text{Zn}(\text{IO}_3)_2$ ¹⁶ (see Supporting Information, Figure S9). Based on the negligible difference between a and c lattice parameters for $\text{Co}(\text{IO}_3)_2$ in the I2 phase (for instance, only 0.02 Å at the highest pressure) and on the 120° value of the β angle, we hypothesize that the symmetry of the I2 phase would follow a martensitic transformation from monoclinic to hexagonal under compression.

Coordination Change. In order to better understand the nature of the two observed phase transitions and the compressional anisotropy observed in the lattice parameters of $\text{Co}(\text{IO}_3)_2$, we now focus on the Co–O and I–O bond distances which underpin those observations. For that purpose, we have plotted in Figures 4 and 5 the theoretical pressure

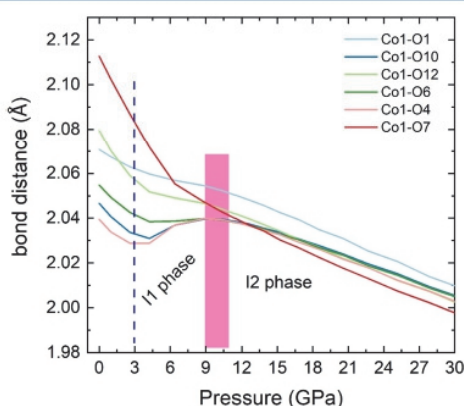


Figure 4. Theoretical (PBEsol) pressure dependence of the different Co1–O bond distances. The position of the atoms in this figure are shown in Figure 1. The vertical dashed line and rectangles indicate the isosymmetric phase transitions.

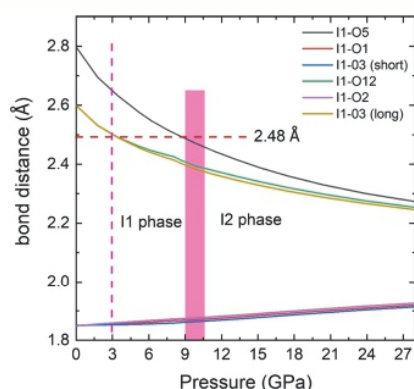


Figure 5. Theoretical (PBEsol) pressure dependence of the different I1–O bond distances. The atomic position atoms in this figure correspond to atoms labeled in Figure 1. The vertical dashed line and rectangles indicate the isosymmetric phase transitions.

dependence of Co1–O and I1–O bond distances as representative examples of the bond distances in all Co- and I-centered polyhedrals since the different Co coordination polyhedra within the $\text{Co}(\text{IO}_3)_2$ structure exhibit a very similar behavior (the same can be stated for the different I coordination polyhedra). Note that bond distances have been named using the nomenclature of Phanon et al.¹⁷

In Figure 4, all Co–O bond distances exhibit a similar pressure-induced behavior in that they all shorten under compression in both the ambient-pressure phase and in the I2

phase. Unusually, some of the bond distances increase with pressure in the I1 phase. Consequently, over the pressure range studied (0–28 GPa), some of the Co1–O bond distances show an s-like, non-linear behavior which supports the phase transitions observed in the lattice parameter evolution. The non-linear behavior also can be found in the distortion index change of CoIO_6 polyhedra (Supporting Information, Figure S11) calculated by VESTA.⁴⁰ The function used to calculate the distortion index can be found elsewhere.¹⁶ Under compression, the CoO_6 polyhedra gradually become more symmetric. The distortion index of CoO_6 decreases from 0.01 at 0 GPa to 0.003 at around 10 GPa and then further to 0.0009 at 29 GPa, thus becoming essentially a regular octahedron.

In order to study I-centered polyhedra, we have taken IO_6 units. We consider a 3 + 3 coordination of iodine because the original IO_3 polyhedron at ambient pressure (I atoms link to only three O atoms) changes at high pressure to link three additional O atoms from neighboring IO_3 units, thus forming two types of bonds (see Figure 5): the original shorter strong bonds and longer weak I–O bonds. These two types of bonds have lengths of around 1.8–1.9 and 2.6–3.0 Å, respectively (see Figure 1). In Figure 5, we show the pressure dependence of the I1–O bond distances inside the IO_6 polyhedron. The three first-neighboring oxygen atoms [I1–O2, I1–O3(short), and I1–O1] behave very differently from the three second-neighboring oxygen atoms [I1–O5, I1–O12, and I1–O3(long)]. The first-neighbor distances increase under compression, while the second neighbor distances rapidly decrease. If we consider 2.48 Å (a value 25% larger than the shortest I–O distance^{16,41}) as the maximum bonding distance or coordination distance, indicated by a horizontal pink dashed line in Figure 5, then there is a gradual increase in iodine coordination under compression. It can be observed that, as the IO_3 LEPs are pushed closer to the oxygen atoms in the next layer of IO_3 units at HP, they form new I–O bonds and the b -axis becomes shorter, thus decreasing the length of the new I–O bonds. In contrast, the bond distance between iodine and the original three first-neighbor oxygen atoms increases under compression to accommodate the additional oxygen atoms. It has been observed that the enlargement of the short I–O bonds induces the softening of high-wavenumber vibrational modes in $\text{Zn}(\text{IO}_3)_2$ and $\text{Fe}(\text{IO}_3)_3$ at HP.^{14,16} We will show in the next sections that the same phenomenon is observed in HP-RS experiments of $\text{Co}(\text{IO}_3)_2$. The subtle dynamic instability of the crystal lattice observed for $\text{Fe}(\text{IO}_3)_3$, indicated by the small negative frequency near the Γ -point in the theoretical calculated phonon dispersion curves, caused by the gradual increase of iodine coordination and the enlargement of the short I–O bonds, is likely also the reason triggering the two isostructural phase transitions in $\text{Co}(\text{IO}_3)_2$. The gradual increase of iodine coordination is related to the decrease of the stereoactivity of the LEP at HP as found in many compounds with strong LEP stereoactivity.^{11,39} This conclusion is based on the fact that we detect the two phase-transitions according to the behavior of the lattice parameters simultaneously with the increase of the coordination of iodine. Unlike the non-linear distortion index curve of the CoO_6 units under pressure (Supporting Information, Figure S11), the distortion index of IO_6 units decreases continuously from 0.18 at 0 GPa to 0.08 at 29 GPa, whereby the IO_6 polyhedron becomes more symmetrical with pressure.

Equation of State. The unit-cell volume of $\text{Co}(\text{IO}_3)_2$ is shown as a function of pressure in Figure 6. Third-order

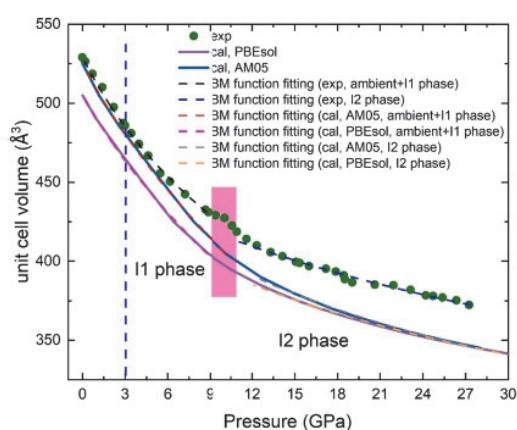


Figure 6. Isothermal equation of state of $\text{Co}(\text{IO}_3)_2$ at room temperature. The solid green circle and the solid line are the experimental and calculated volumes, respectively. The error of unit-cell volume is smaller than the symbol. Dashed color lines were used for the Birch–Murnaghan^{42,43} function fitting on the experimental data and calculated data, respectively. The vertical dashed line and rectangle are the indication of the phase transition.

Birch–Murnaghan (BM) equations of state^{42,43} were used to fit the volume of different phases separately using EoSFit7c.⁴⁴ Notice that it is impossible to fit the data over the whole pressure range with only one equation of state, which also supports the existence of isostructural phase transitions. Considering that no noticeable discontinuity is observed between the ambient-pressure and I1 phases and that there are no sufficient data for the ambient-pressure phase to fit the BM equation, we fit those two phases together with only one equation of state, where the zero-pressure volume was fixed. On the other hand, the zero-pressure volume was left as a free parameter during the fitting procedure for the I2 phase. The obtained zero-pressure volume (V_0), bulk modulus (B_0), and its pressure derivative (B_0') of those two regions (experiment and calculations) are summarized in Table 2. The close agreement between the experimental and calculated bulk modulus with the PBEsol functional for the different phases reflects the reasonable description of the equation of state by *ab initio* calculations. In contrast, with the previously reported metal iodates, the experimental bulk modulus of the ambient-pressure + I1 phase (29.8 GPa) is a little higher than that of the ambient-pressure phase of KIO_3 (24.3 GPa)¹² and $\text{Zn}(\text{IO}_3)_2$ (21.6 GPa).¹⁶ On the contrary, the I2 phase of $\text{Co}(\text{IO}_3)_2$ is one of the least compressible metal iodates observed to date according to the values in the literature (70.8(3.6) GPa).

Interestingly, the experimental bulk modulus of the low pressure phase of $\text{Co}(\text{IO}_3)_2$ is lower than that of $\text{Fe}(\text{IO}_3)_3$ (55 GPa),¹⁵ LiIO_3 (34 GPa),⁴⁵ and $\text{LiZn}(\text{IO}_3)_3$ (55 GPa).⁴⁶ Additionally, fitting a third-order BM equation of state to the calculated CoIO_6 and IIO_6 polyhedra in the ambient and I1

phases gives us polyhedral bulk moduli of $B_0 = 102(14)$ GPa and 22(1) GPa, respectively. Thus, it is clear that the bulk modulus of $\text{Co}(\text{IO}_3)_2$ is dominated by the higher compressibility of IO_6 polyhedra rather than by the harder CoO_6 octahedra. The same behavior has also been observed in the theoretical data of iron and zinc iodates under pressure,^{15,16} whose bulk moduli have also been shown to be dominated by the compressibility of the IO_6 polyhedra (where we assume a similar 3 + 3 coordination of iodine) rather than that of the AO_6 polyhedra where A represents a metal atom. The drastic increase of the bulk modulus after the transition to the HP I2 phase observed in this work on $\text{Co}(\text{IO}_3)_2$ is a consequence of the decrease of the compressibility of the coordination polyhedron of iodine.

Raman Study. In Figure 7, we present the Raman spectrum of $\text{Co}(\text{IO}_3)_2$ measured under ambient conditions.

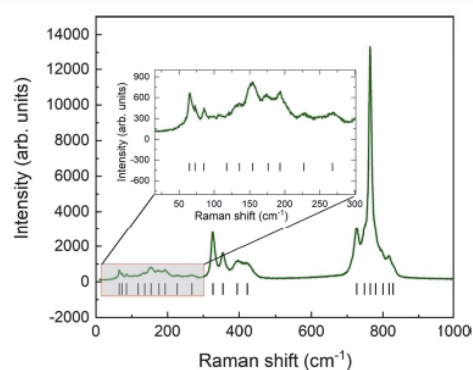


Figure 7. Raman spectrum of $\text{Co}(\text{IO}_3)_2$ at ambient pressure. Short vertical bars at the bottom of the spectra are an indication of the determined peak position. The insert spectrum is a zoom of the wavenumber range 0–300 cm^{-1} .

The determined Raman peaks are indicated with vertical bars, and the zero-pressure wavenumbers are listed in Table 3 along with their pressure coefficients and Grüneisen parameters. The zero-pressure wavenumbers are also compared with the data reported in the literature.^{18,19} A tentative assignment of the symmetries of the modes' symmetries is provided in Table 3 based on a comparison of the calculated and experimental ambient pressure wavenumbers (ω_0) and pressure coefficients ($d\omega_0/dP$), which were determined via linear fit to the data for pressures smaller than 3 GPa.

Here, we only focus on the calculations performed with the PBEsol functional because of the better agreement with experimental data in the structural part of the work. The agreement between calculations and experiments is similar to that found in $\text{Fe}(\text{IO}_3)_3$ and $\text{Zn}(\text{IO}_3)_2$.^{14,16} As in previous metal iodates calculations, our simulations underestimate the measured wavenumbers, especially of the high-wavenumber modes (wavenumber offset is around 70 cm^{-1} in the high-wavenumber range), thus underestimating the phonon gap

Table 2. Equation of State of $\text{Co}(\text{IO}_3)_2$ as Determined by Experiments and by Theoretical Calculations

data source	ambient + I1 phase			I2 phase		
	V_0 (\AA^3)	B_0 (GPa)	B_0'	V_0 (\AA^3)	B_0 (GPa)	B_0'
experiment	529	29.8(1)	3.5(0.3)	462.9(5.6)	70.8(3.6)	5.2(0.6)
calculation (PBEsol)	505	32.1(1.1)	2.3(0.3)	451.1(2.6)	50.7(1.6)	5.5(0.3)
calculation (AM05)	525	30.7(0.6)	2.2(0.1)	473.7(4.9)	38.3(1.9)	5.4(0.4)

Table 3. Theoretical and Experimental Raman- and IR-Active Zero-Pressure Wavenumbers (ω) for $\text{Co}(\text{IO}_3)_2$ (the Lowest Pressure in the Infrared Spectroscopy Experiment Is 0.2 GPa) and Pressure Coefficients ($d\omega/dP$)^a

modes	theory ($B_0 = 32.1$ GPa)			experiment, Raman ($B_0 = 29.8$ GPa)			experiment, IR ($B_0 = 29.8$ GPa)					
	ω (cm^{-1})	$d\omega/dP$ ($\text{cm}^{-1}/\text{GPa}$)	γ	ω (cm^{-1}), this work	$d\omega/dP$ ($\text{cm}^{-1}/\text{GPa}$)	γ	ω (cm^{-1}) ¹⁸	ω (cm^{-1}) ¹⁹	ω (cm^{-1}), This work	$d\omega/dP$ ($\text{cm}^{-1}/\text{GPa}$)	γ	ω (cm^{-1}) ¹⁹
B	62.3	0.3	0.16	65								
A	71.9	4.3	1.91	73	5.4	2.21						
A	91.70	4.0	1.39	85	6.8	2.39	84	85				
A	117.9	2.5	0.68	118	11.0	2.79		115				
B	136.3	4.5	1.05	136	9.7	2.13	135	135				
A	161.38	3.9	0.78	154	11.1	2.15	153	154				
A	155.5	5.0	1.03						162	9.8	1.80	161
B	173.7	6.9	1.27	176	8.1	1.37	172	167	172	9.6	1.66	171
B	184.4	6.2	1.07						186	12.3	1.97	
A	196.8	5.6	0.91	193	6.2	0.96	191	192				
A	221.2	5.6	0.81	227	9.9	1.29	224	231	231	6.7	0.86	227
A	246.5	6.6	0.86						268	4.2	0.47	267
A	251.0	8.5	1.09	268	7.8	0.87	265	266				
B	311.2	4.8	0.49	327	6.5	0.59	327	327				
B	333.6	2.4	0.23						331	1.4	0.13	327
A	344.5	6.6	0.62	354	7.4	0.62	353	353				
B	358.5	6.0	0.53						357	1.8	0.15	355
B	385.2	3.7	0.31						397	4.1	0.31	399
A	387.8	5.3	0.44	395	5.0	0.37	394	392				
A	412.6	7.3	0.57	421	4.8	0.34	409	429				
B	429.8	4.9	0.36						427	5.7	0.40	421
A	670.2	-3.8	-0.18	727	-4.0	-0.16	727	727				
B	677.1	-3.4	-0.16	748	-3.8	-0.15	750					
A	720.1	-1.7	-0.08	765	-1.2	-0.05	763	763				
A	724.6	-2.4	-0.11	779	0.8	0.03						
B	748.4	-2.3	-0.10	800	1.0	0.04	798	800				
B	749.4	-0.6	-0.03	817	1.1	0.04						
B	756.0	1.1	0.05	828	-1.5	-0.05						

^aData were obtained by fitting the wavenumbers up to 3 GPa. The corresponding Grüneisen parameters (γ) were calculated by the function $\gamma = (B_0/\omega_0) \cdot (d\omega/dP)$ using $B_0 = 29.8$ GPa obtained from the HP-XRD data. For the sake of simplicity, here we only provide the calculated vibrational modes, which have been tentatively attributed to the experimentally observed Raman- and IR-active modes. The total number of calculated vibrational modes (108) can be found in the Supporting Information (Table S1).

between the modes below 500 cm^{-1} and the part of the spectrum above 700 cm^{-1} . In this work, we have detected 21 Raman-active modes in $\text{Co}(\text{IO}_3)_2$ in contrast to previous studies reporting only 15 modes.^{18,19} The agreement between different experiments is good. According to group theory, all 18 independent atoms in $\text{Co}(\text{IO}_3)_2$ are located in $2a$ Wyckoff sites, resulting in 108 vibrational modes ($54A + 54B$). Since both are polar modes, all of them are both Raman- and IR-active; therefore, up to 216 modes could be observed in the IR spectra due to the TO–LO (transverse optical–longitudinal optical) splitting.

Experimentally, the strongest mode is found at 765 cm^{-1} in $\text{Co}(\text{IO}_3)_2$, a wavenumber almost identical to 763 cm^{-1} reported in the literature^{18,19} and very close to that of the strongest mode in $\text{Zn}(\text{IO}_3)_2$ (782 cm^{-1}) and in $\text{Fe}(\text{IO}_3)_3$ (790 cm^{-1}).^{14,16} The similar wavenumber of the strongest mode in metal iodates is reasonable since this mode can be related to an internal I–O stretching vibration of the IO_3 molecule, according to the vibrational modes of the pyramidal IO_3^- free ion.^{47–50}

The comparison of the Raman spectra of iron, zinc, and cobalt iodates at ambient pressure with our DFT calculations^{14,19} enables us to analyze the vibrations which produce the spectrum. The high-wavenumber part of $\text{Co}(\text{IO}_3)_2$ (wavenumber above 700 cm^{-1}) is likely associated with symmetric and asymmetric stretching I–O vibrations of the IO_3 molecule. According to a previous vibrational study of $\text{Co}(\text{IO}_3)_2$,¹⁹ the most intense band near 762 cm^{-1} and the bands near 781 and 800 cm^{-1} are assigned to symmetric I–O stretching modes of the IO_6 molecule, whereas the 727 cm^{-1} mode was assigned to the asymmetric I–O stretching mode of the IO_6 molecule. This assignment is different from previous authors who attributed these modes to stretching modes of the pyramidal IO_3^- molecule.^{47–50} Shen et al. attributed the modes of iodates between 779 and 826 cm^{-1} to the symmetric (ν_1) and asymmetric (ν_3) I–O stretching modes of the IO_3 molecule.⁴⁷ A similar assignment was performed by Dasent and Waddington.⁴⁸ In contrast, the modes at 775 and 805 cm^{-1} were assigned to the asymmetric (ν_3) and symmetric (ν_1) I–O stretching modes of the IO_3^- molecule by Gardiner et al.^{49,50} Consequently, which of the symmetric or asymmetric stretching modes has the highest wavenumber seems to be controversial. In two recent studies, we have clarified that the strongest mode of metal iodates corresponds to the symmetric I–O stretching mode and that the asymmetric I–O stretching modes have a lower wavenumber than the symmetric I–O stretching modes.^{14,16} Additionally, it must be clarified that the vibrational modes of the monoclinic $P2_1$ structure are not gerade and ungerade, as suggested in ref 19, and in fact they have the same number of A and B modes. Based on our DFT calculations (see Supporting Information, Figure S12), we have observed a mode at 727 cm^{-1} that can be assigned to an asymmetric stretching I–O vibration and the modes at 765 , 779 (strongest mode), and 800 cm^{-1} can be assigned to a symmetric stretching I–O vibration in the IO_3 molecule, which is exactly the same as the assignment given in ref 19.

The bending modes of iodates are observed in the region from 300 to 500 cm^{-1} . In ref 19, the modes at 327 , 353 , and 392 cm^{-1} were assigned to a threefold degenerate symmetric bending mode and the 429 cm^{-1} mode to the asymmetric bending mode of the IO_6 molecule. Again, these assignments contrast with previous studies that attributed them to the pyramidal IO_3^- molecules. Modes at 330 and 390 cm^{-1} were

attributed by Shen et al. to the asymmetric (ν_4) and symmetric (ν_2) bending modes of the IO_3^- molecule, respectively.⁴⁷ Similarly, modes above 400 cm^{-1} were also attributed to symmetric (ν_2) bending modes of the IO_3^- molecule.⁴⁸ Modes at 320 and 358 cm^{-1} were assigned to the asymmetric (ν_4) and symmetric (ν_2) bending modes of the IO_3^- molecule, respectively.⁴⁹ Therefore, it is clear that symmetric bending modes have higher wavenumbers than asymmetric bending modes in iodates as they occur in chlorates and bromates.⁵⁰ In our experiments, the bending modes of $\text{Co}(\text{IO}_3)_2$ are observed at 327 , 354 , 395 , and 421 cm^{-1} , respectively. Based on the vibration symmetry of the corresponding calculated modes (see Supporting Information, Figure S13), the three modes with the lowest wavenumbers can be assigned to symmetric (ν_2) bending modes of the IO_3^- molecule, and the modes around 421 cm^{-1} can be assigned to the asymmetric (ν_4) bending modes of the IO_3^- molecule, again in agreement with the assignment in ref 19. Finally, the modes below 300 cm^{-1} have been associated with the translational and rotational motions of the iodate as a rigid unit.

Results of HP-RS experiments on $\text{Co}(\text{IO}_3)_2$ at selected pressures up to 23.4 GPa are shown in Figure 8. The spectra

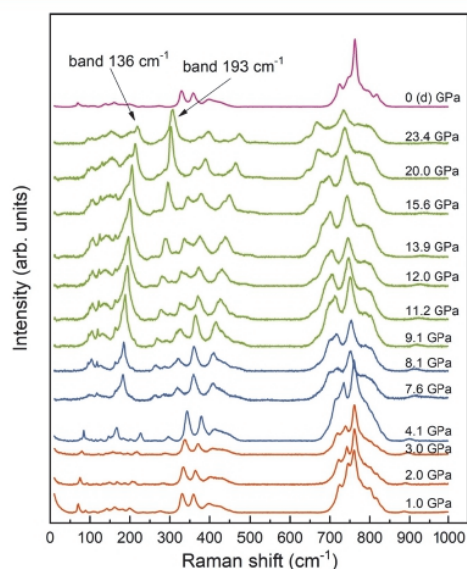


Figure 8. HP-RS spectra of $\text{Co}(\text{IO}_3)_2$ at selected pressures. The “d” in the top pattern means that it is collected during the decompression process. Here, the Raman spectra of different phases are shown in different colors (ambient-pressure phase–orange, I1 phase–blue, and I2 phase–green). The bands at 136 and 193 cm^{-1} determined at room pressure are also marked in the figure.

can be separated into two parts: wavenumber above 700 cm^{-1} and wavenumber below 500 cm^{-1} , with a phonon gap of more than 200 cm^{-1} at ambient pressure. Up to the highest pressure, there is no evidence of the occurrence of a first-order phase transition. Moreover, the Raman spectrum collected at ambient pressure after decompression (top spectrum in Figure 8) is like that obtained before the compression process (Figure 7), thus suggesting that pressure-induced structural changes up to 23 GPa are fully reversible. Apparently, there is a significant intensity increase of phonons at 136 and 193 cm^{-1} at ambient pressure, which shift to 220 and 307 cm^{-1} at 23.4 GPa . The intensity of the peak at 136 cm^{-1} (labeled in Figure 8)

increases to its highest level at 13.9 GPa and then decreases with further compression, whereas the intensity of the peak at 193 cm^{-1} increases continuously to the highest pressure and even surpasses the most intense band 762 cm^{-1} at the highest pressure. We plot the relative intensity ratio between the modes at 136 and 193 cm^{-1} in Figure 9. An evident change can

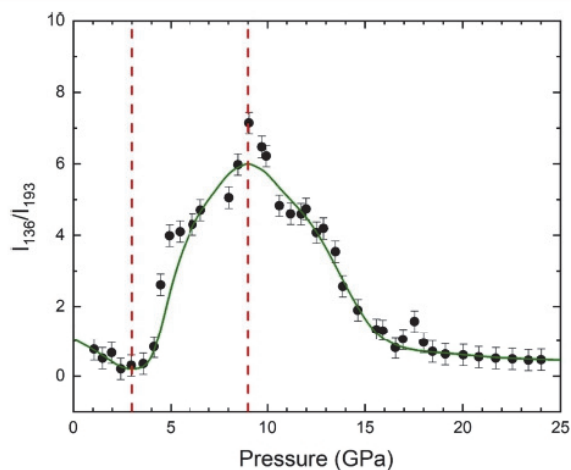


Figure 9. Relative Raman intensity ratio of the modes at 136 and 193 cm^{-1} as a function of pressure. The solid circles are the experimental data, while the green line is a guide for the eye. The orange dashed line marks the pressure of the phase transition.

be found at around 3 GPa , from a negative or even zero slope to a positive one, and at 9 GPa from a positive to negative slope, respectively. In general, the Raman spectrum can suffer a change of the peak intensity under pressure due to a change in the Raman scattering cross section of the different modes. Pressure can also affect the intensity of first-order Raman phonons, which mainly depend on the Hamiltonian matrix elements of electron–photon and electron–phonon interactions responsible for the Raman effect.^{51,52} In this context, pressure-induced changes of Raman intensities usually are

related to changes in the high-order susceptibility tensor of the material, which can be typical of certain Raman modes. In particular, structural changes leading to first-, second-, or higher-order pressure-induced phase transitions can alter the Raman intensity. Moreover, the presence of precursor effects of pressure-induced phase transitions or pressure-induced amorphization can also modify the Raman intensities. Additionally, the loss of perfect hydrostatic conditions with the emergence of pressure gradients, the change of the absorption coefficient under compression, and the presence of resonant Raman scattering can also affect the intensity of Raman peaks. In our case, we think the intensity change of bands at 136 and 193 cm^{-1} is induced by the two isostructural phase transitions identified by HP-XRD measurements. These two transitions also lead to changes in the pressure dependence of the Raman wavenumbers as we will discuss in the next paragraph.

The theoretical and experimental Raman-active modes of $\text{Co}(\text{IO}_3)_2$ as a function of pressure are shown in Figure 10 (and in Supporting Information, Figures S15–S17). The most notable features are as follows: (i) the pressure-induced reduction of the phonon gap (ca. between 450 and 700 cm^{-1} at room pressure) both in experiments and DFT calculations. The closing of the phonon gap is a result of the blue shift of the modes below 450 cm^{-1} and the red shift (softening) of the modes above 700 cm^{-1} . Usually, phonon softening is a sign of dynamic instability and may induce a crystalline–crystalline phase transition or an amorphization.⁵³ (ii) Some modes of the high-wavenumber region, which correspond to I–O stretching modes of IO_3^- units, show a soft behavior in the low-pressure and I1 phase, as occurs with other metal iodates.^{14,16,39} In order to accommodate the three additional oxyanions, the bond distance between iodine and the three original oxyanions will slightly increase under compression, and under a harmonic approximation, there is a linear relationship between the $\omega^{-2/3}$, where ω represented the soft modes, and the calculated average I–O bond length, which has been proven in $\text{Fe}(\text{IO}_3)_3$ and $\text{Zn}(\text{IO}_3)_2$.^{14,16} Therefore, the softening of several high-wavenumber modes in $\text{Co}(\text{IO}_3)_2$ under pressure is due to the

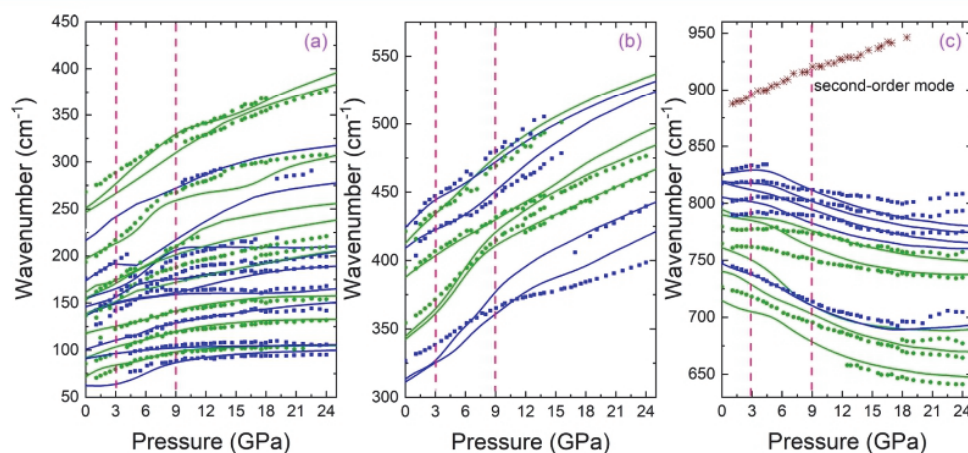


Figure 10. Pressure dependence of the Raman-active wavenumbers in $\text{Co}(\text{IO}_3)_2$. Different panels show different wavelength regions. Experiments are shown with symbols and calculations with lines. A- and B-symmetry modes are shown in green and blue, respectively. For the sake of clarity, here we show the theoretical modes tentatively attributed to the experimentally observed modes. In the Supporting Information, we include figures with all calculated modes. Vertical pink dashed lines indicate the suggested transition pressures corresponding to the two isostructural phase transitions we found in HP-XRD. In the highest wavenumber region, we apply the offset of 70 cm^{-1} to calculate wavenumbers to match experimental wavenumbers as described in the text.

slight enlargement of the shorter I–O bond distances under compression. (iii) Slope coefficient changes are found in almost every vibrational mode near 3 and 9 GPa. From the experimental side, this can be clearly recognized in the modes at 118, 193, and 327 cm^{-1} that exhibit a non-linear behavior. Qualitatively similar pressure dependence of the Raman modes has also been found in $\text{Fe}(\text{IO}_3)_3$ ¹⁴ and $\text{Zn}(\text{IO}_3)_2$,¹⁶ and other materials containing LEPs, such as $\beta\text{-Bi}_2\text{O}_3$,^{54,55} Sb_2S_3 ,⁵⁶ $\alpha\text{-As}_2\text{Te}_3$,⁵⁷ SbPO_4 ,⁵⁸ and As_2S_3 ,⁵⁹ and alkali-metal bismuth iodate $\text{Na}_3\text{Bi}(\text{IO}_3)_6$.³⁹ The observed non-linear behavior of the Raman modes gives further evidence of the two isostructural phase transitions we found in HP-XRD data. (iv) There are several low-wavenumber modes in both experimental and calculated modes with very high Grüneisen parameters, even exceeding the value of 2 (see Table 3). These high values indicate that many vibrational modes have a very high anharmonic contribution that is uncommon in covalent and ionic compounds.

Infrared Study. High-pressure Fourier transform infrared (HP-FTIR) spectra between 200 and 600 cm^{-1} on $\text{Co}(\text{IO}_3)_2$ are shown in Figure 11 at selected pressures up to 18.6 GPa.

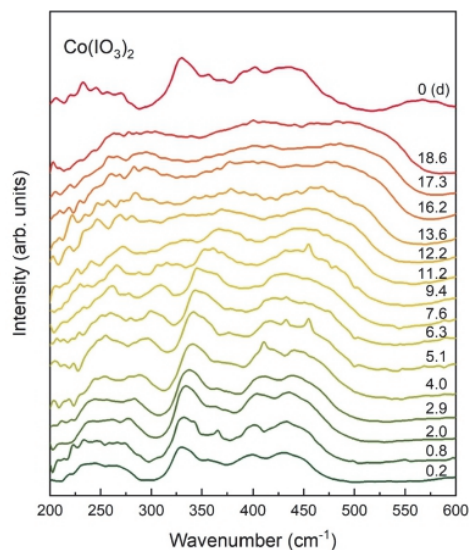


Figure 11. HP-FTIR spectra of $\text{Co}(\text{IO}_3)_2$ at selected pressures. The “d” in the top spectrum means that it is collected during the decompression process. The pressure of each pattern is shown on the right in “GPa”.

Nine modes have been detected at the lowest pressure (0.2 GPa). They are summarized in Table 3 and compared with previously reported IR data, together with a tentative mode assignment based on the theoretical calculated modes symmetries. The pressure coefficients are also shown in Table 3. They were obtained via a linear fit to data in the 0–3 GPa range. The detected IR-active modes are consistent with the values reported in ref 19; however, two modes near 208 and 250 cm^{-1} reported in ref 19 are missing in our experiment. The possible reason could be the merging with neighboring peaks at HP. Notably, the peaks become significantly broader at HP (above around 12 GPa), likely due to the loss of the hydrostatic conditions in the solid PTM (Cesium iodide, CsI).⁶⁰ For this reason, we have only followed the center of the absorption bands that contain more than one phonon. From the FTIR data collected at 0 GPa after

downstroke (see the top spectrum of Figure 11), we can confirm that the structural changes of $\text{Co}(\text{IO}_3)_2$ up to the highest pressure in our experiment (22.3 GPa) are fully reversible, in agreement with HP-XRD and HP-RS measurements.

Some theoretically predicted vibrational modes that have not been detected in the Raman spectra can be found in the IR spectra (see Table 3), a fact that confirms the complementarity of these two techniques. IR-active modes at 327, 355, and 399 cm^{-1} were previously attributed to the triply degenerate symmetric bending mode of IO_6 , whereas the mode at 421 cm^{-1} was attributed to the asymmetric bending of IO_6 .¹⁹ We have measured modes at 331, 357, and 397 cm^{-1} that have been assigned to the symmetric (ν_2) bending modes of the IO_3^- molecule, whereas the mode at 427 cm^{-1} has been attributed to the asymmetric (ν_4) bending mode of the IO_3^- molecule, thus in a good agreement with the previous study. Additionally, modes below 300 cm^{-1} can be associated with the translation and rotational motions.

The pressure dependence of the theoretical and experimental IR-active mode wavenumbers in $\text{Co}(\text{IO}_3)_2$ are plotted together in Figure 12. All modes harden under pressure and a

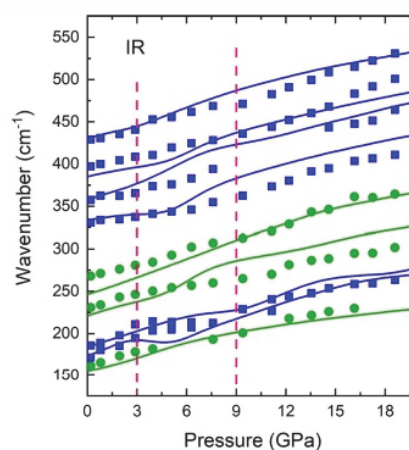


Figure 12. Pressure dependence of the IR-active wavenumbers in $\text{Co}(\text{IO}_3)_2$. Symbols correspond to experimental data while lines correspond to theoretically calculated data. A- and B-symmetries are represented by green and blue colors, respectively. Vertical pink dashed lines indicate suggested transition pressures. For the whole calculated IR-active modes in that region, the reader can find it in the Supporting Information, Figure S14.

change in the pressure coefficients of all modes can be observed at 3.0 and 9.0 GPa. The change is clearer in the three experimental modes with the lowest wavenumbers. The non-linear pressure dependence exhibited by the wavenumbers of the IR modes is like that of the Raman-active modes, thus providing further evidence of the two subtle symmetry-preserving phase transitions we have previously described. It can be also mentioned that the non-linear pressure dependence of the IR-active modes has also been reported for $\text{Zn}(\text{IO}_3)_2$ as evidence of the presence of isostructural phase transitions.⁶¹

To conclude, we must emphasize two aspects of this work. The first point is that isostructural phase transitions seem to be a common feature of a number of compounds featuring strong stereoactive cation or anion LEPs since they have been recently characterized in group-15 oxides and chalcogenides such as $\beta\text{-Bi}_2\text{O}_3$,^{54,55} As_2S_3 ,⁵⁹ and SbPO_4 ⁵⁸ and in several

iodates, as discussed here. In fact, many of these isostructural phase transitions seem to be of second-order or even of higher-order according to Ehrenfest's classification, and they can even appear as hidden or internal isostructural phase transitions, as recently reported for β - Sb_2O_3 .⁶²

The second point is that the short I–O bond distances increase in length under compression, the long I–O bond distances decrease in length in order to form a highly symmetric structure with very similar I–O bond distances and higher coordination at high pressure, and the presence of very high Grüneisen parameters and the softening of many high-wavenumber modes leading to phonon gap closing [as observed in the three metal iodates, $\text{Co}(\text{IO}_3)_2$, $\text{Zn}(\text{IO}_3)_2$, and $\text{Fe}(\text{IO}_3)_3$] are features similar to those recently reported in an HP study of As_2S_3 , a compound featuring a strong stereoactive cation LEP with threefold coordination for As at room pressure.⁵⁹ These features have been related to the novel phenomenon of “metavalent” bonding; that is, the observation of a new type of an intermediate chemical bonding between covalent and metallic bonding, which is characterized by bonds with less than two electrons per bond.^{63–65} It has been proved that metavalent bonding at room pressure is found in binary and ternary compounds of IV–VI and V₂–VI₃ families with 5 and 6 cation coordination (GeTe, SnTe, PbS, PbSe, PbTe, β - As_2Te_3 , Sb_2Te_3 , Bi_2Se_3 , Bi_2Te_3 , and rhombohedral GeSb_2Te_4 , rhombohedral SnSb_2Te_4 ^{65,66} and by extension in rhombohedral GeBi_2Te_4 and rhombohedral SnBi_2Te_4). Additionally, it has been proven that this kind of bonding develops at HP in compounds of IV–VI and V₂–VI₃ families with a smaller coordination at room pressure (GeSe ,⁶⁷ As_2S_3 ,⁵⁹ and related compounds). Recently, it has been suggested that metavalent bonding also occurs in halide perovskites,⁶⁸ thus opening the door to explore metavalent bonding in halide-related compounds such as metal iodates. However, in order to fully prove the presence of metavalent bonding in iodates at HP, calculations of the electronic density of I–O bonds, Born effective charges of I atoms, and optical dielectric constants under pressure will be required. Such calculations are beyond the scope of this work even if they are already planned for a more comprehensive study on this topic.

CONCLUSIONS

We have reported a joint experimental and theoretical study of the structural and vibrational properties of $\text{Co}(\text{IO}_3)_2$ under compression. We have observed compelling evidence of two reversible pressure-induced isosymmetric phase transitions at 3.0 GPa and in the pressure range of 9.0–11.0 GPa by means of HP-XRD, HP-RS, and HP-FTIR measurements and DFT calculations.

The unit cell of $\text{Co}(\text{IO}_3)_2$ shows a huge anisotropic compressibility, with the *b*-axis being the most compressible axis and largely determining the bulk moduli of 29.8 and 70.8 GPa in experiments (32.1 and 50.7 GPa in theoretical calculation) for the ambient + I1 and I2 phases, respectively. Moreover, the bulk modulus of the ambient pressure phase of $\text{Co}(\text{IO}_3)_2$ has been proven to be dominated by the large compressibility of the IO_6 polyhedra rather than that of the CoO_6 units.

A non-linear pressure dependence of Raman- and IR-active mode wavenumbers of $\text{Co}(\text{IO}_3)_2$ has been measured with soft high-wavenumber Raman modes, leading to a closing of the phonon gap under compression. The vibrational properties of $\text{Co}(\text{IO}_3)_2$ under compression are qualitatively similar to those

of $\text{Fe}(\text{IO}_3)_3$ and $\text{Zn}(\text{IO}_3)_2$, suggesting that these features are common to metal iodates with IO_3^- units.

The unit-cell parameters and volume deduced from the refinements of the HP-XRD data, as well as the Raman- and IR-active mode wavenumbers, exhibit a non-linear pressure dependence, indicating the presence of two symmetry-preserving phase transitions at 3.0 GPa and in the pressure range of 9.0–11.0 GPa. The theoretically calculated pressure dependence of the I–O and Co–O bond distances in $\text{Co}(\text{IO}_3)_2$ and its comparison with the bond distances previously reported for $\text{Fe}(\text{IO}_3)_3$ and $\text{Zn}(\text{IO}_3)_2$ allow us to conclude that the mechanism driving the two isostructural phase transitions is the lattice instability caused by the gradual coordination increase of iodine that in turn is related to the decrease of the stereoactivity of the LEP at HP. The decrease of three long I–O bond distances forces an increase of the three short I–O bond distances to accommodate the additional bonds, leading to the observed phase transitions. Because of the increase of the short I–O bonds, there is a softening of all the I–O stretching modes of the IO_3^- molecule. Additional support for the two transitions comes from the dramatic change of phonons' relative intensity ratio between 136 and 193 cm^{-1} in Raman spectra. Therefore, this work shows once again that isostructural phase transitions are common to compounds featuring strong LEPs.

The softening of the stretching modes and the large pressure coefficients of the bending modes, the concurrent increase of the short I–O bonds, and decrease of the long I–O bond distances leading to a high symmetry of the I2 HP phase (like the huge decrease on the distortion index of IO_6 polyhedra) suggest that these changes are probably related to the formation of pressure-induced metavalent bonding in metal iodates.

ASSOCIATED CONTENT

Supporting Information

The Supporting Information is available free of charge at <https://pubs.acs.org/doi/10.1021/acs.jpcc.1c04659>.

Microscopic image of the sample, Rietveld refinement of the XRD data collected at ambient pressure and high pressure, pressure dependence of the *d*-spacing, comparison of the lattice parameter and volume between $\text{Zn}(\text{IO}_3)_2$ and $\text{Co}(\text{IO}_3)_2$, atomic movement of some Raman modes, all the experimental and calculated pressure dependences of the Raman and infrared modes, and all the experiment- and calculation-determined modes and related information at ambient pressure (PDF)

AUTHOR INFORMATION

Corresponding Author

A. Liang – Departamento de Física Aplicada-ICMUV-MALTA Consolider Team, Universitat de Valencia, 46100 Burjassot (Valencia), Spain; orcid.org/0000-0002-0515-0484; Email: Akun2.Liang@uv.es

Authors

C. Popescu – CELLS-ALBA Synchrotron Light Facility, 08290 Barcelona, Spain
F. J. Manjon – Instituto de Diseño para la Fabricación y Producción Automatizada, MALTA Consolider Team,

Universitat Politècnica de València, 46022 València, Spain;

● orcid.org/0000-0002-3926-1705

R. Turnbull – Departamento de Física Aplicada-ICMUV-MALTA Consolider Team, Universitat de València, 46100 Burjassot (Valencia), Spain

E. Bandiello – Departamento de Física Aplicada-ICMUV-MALTA Consolider Team, Universitat de València, 46100 Burjassot (Valencia), Spain; ● orcid.org/0000-0003-0956-3195

P. Rodríguez-Hernandez – Departamento de Física and Instituto de Materiales y Nanotecnología, MALTA Consolider Team, Universidad de La Laguna, 38206 La Laguna, Spain

A. Muñoz – Departamento de Física and Instituto de Materiales y Nanotecnología, MALTA Consolider Team, Universidad de La Laguna, 38206 La Laguna, Spain; ● orcid.org/0000-0003-3347-6518

I. Yousef – CELLS-ALBA Synchrotron Light Facility, 08290 Barcelona, Spain; ● orcid.org/0000-0001-7818-8611

Z. Hebboul – Laboratoire Physico-Chimie des Matériaux (LPCM), University Amar Telidji of Laghouat, Laghouat 03000, Algeria

D. Errandonea – Departamento de Física Aplicada-ICMUV-MALTA Consolider Team, Universitat de València, 46100 Burjassot (Valencia), Spain; ● orcid.org/0000-0003-0189-4221

Complete contact information is available at:
<https://pubs.acs.org/10.1021/acs.jpcc.1c04659>

Notes

The authors declare no competing financial interest.

ACKNOWLEDGMENTS

This work was supported by the Generalitat Valenciana under Project PROMETEO 2018/123-EFIMAT and by the Spanish Ministerio de Ciencia, Universidades, e Investigación under Projects PID2019-106383GB-41/42/43, as well as through MALTA Consolider Team research network (RED2018-102612-T). A.M. and P.R.-H. acknowledge computing time provided by Red Española de Supercomputación (RES) and the MALTA Consolider Team cluster. D.E. acknowledges the resources and technical assistance provided by the Informatics Service of Universitat de València through the Tirant III cluster. A.L. and D.E. would like to thank the Generalitat Valenciana for the Ph.D. Fellowship no. GRISOLIAP/2019/025. R.T. acknowledges funding from the Spanish Ministerio de Economía y Competitividad (MINECO) via the Juan de la Cierva Formación fellowship (FJC2018-036185-I). C.P. is thankful for the financial support of the Spanish Mineco Project no. FIS2017-83295-P. E.B. would like to thank the University of Valencia for his “Attracció de Talent” postdoctoral contract (UV-INV_POSTDOC19-1026935). The authors thank Sandrine Beauquis from Symme, Université Savoie Mont Blanc (France), for her technical assistance concerning the SEM and ADX analyses. PXRD experiments were performed at the MSPD beamline of ALBA Synchrotron (experiment no. 2019083663). IR experiments were performed at the MIRAS beamline of ALBA Synchrotron (experiment no. 2020024118).

REFERENCES

- (1) Bergman, J. G.; Boyd, G. D.; Ashkin, A.; Kurtz, S. K. New Nonlinear Optical Materials: Metal Oxides with Nonbonded Electrons. *J. Appl. Phys.* **1969**, *40*, 2860–2863.
- (2) Ok, K. M.; Chi, E. O.; Halasyamani, P. S. Bulk Characterization Methods for Non-Centrosymmetric Materials: Second-Harmonic Generation, Piezoelectricity, Pyroelectricity, and Ferroelectricity. *Chem. Soc. Rev.* **2006**, *35*, 710–717.
- (3) Wang, C.; Zhang, T.; Lin, W. Rational Synthesis of Non-centrosymmetric Metal-Organic Frameworks for Second-Order Nonlinear Optics. *Chem. Rev.* **2012**, *112*, 1084–1104.
- (4) Phanon, D.; Gautier-Luneau, I. Promising Material for Infrared Nonlinear Optics: NaI₃O₈ Salt Containing an Octaoxotriiodate(V) Anion Formed from Condensation of [IO₃]⁻ Ions. *Angew. Chem., Int. Ed.* **2007**, *46*, 8488–8491.
- (5) Phanon, D.; Mosset, A.; Gautier-Luneau, I. New Materials for Infrared Non-Linear Optics. Syntheses, Structural Characterisations, Second Harmonic Generation and Optical Transparency of M(IO₃)₃ Metallic Iodates. *J. Mater. Chem.* **2007**, *17*, 1123–1130.
- (6) Kang, M. O.; Halasyamani, P. S. New Metal Iodates: Syntheses, Structures, and Characterizations of Noncentrosymmetric La(IO₃)₃ and NaY₄O₁₂ and Centrosymmetric β-Cs₂I₄O₁₁ and Rb₂I₆O₁₅(OH) 2·H₂O. *Inorg. Chem.* **2005**, *44*, 9353–9359.
- (7) Dmitriev, V. G.; Gurzadyan, G. G.; Nikogosyan, D. N. *Handbook of Nonlinear Optical Crystals*, 3rd ed.; Springer, 2013.
- (8) Bentría, B.; Benbental, D.; Bagieu-Beucher, M.; Mosset, A.; Zaccaro, J. Crystal Engineering Strategy for Quadratic Nonlinear Optics. Part II: Hg(IO₃)₂. *Solid State Sci.* **2003**, *5*, 359–365.
- (9) Huang, Y.; Meng, X.; Gong, P.; Yang, L.; Lin, Z.; Chen, X.; Qin, J. A₂Bi₅O₁₅ (A = K⁺ or Rb⁺): Two New Promising Nonlinear Optical Materials Containing [I₃O₉]₃⁻ Bridging Anionic Groups. *J. Mater. Chem. C* **2014**, *2*, 4057–4062.
- (10) Xu, X.; Hu, C.-L.; Li, B.-X.; Yang, B.-P.; Mao, J.-G. A-AgI₃O₈ and B-AgI₃O₈ with Large SHG Responses: Polymerization of IO₃ Groups into the I₃O₈ Polyiodate Anion. *Chem. Mater.* **2014**, *26*, 3219–3230.
- (11) Bu, K.; Luo, H.; Guo, S.; Li, M.; Wang, D.; Dong, H.; Ding, Y.; Yang, W.; Lü, X. Pressure-Regulated Dynamic Stereochemical Role of Lone-Pair Electrons in Layered Bi₂O₂S. *J. Phys. Chem. Lett.* **2020**, *11*, 9702–9707.
- (12) Bayarjargal, L.; Wiehl, L.; Friedrich, A.; Winkler, B.; Juárez-Arellano, E. A.; Morgenroth, W.; Haussühl, E. Phase Transitions in KIO₃. *J. Phys.: Condens. Matter* **2012**, *24*, 325401.
- (13) Suffren, Y.; Gautier-Luneau, I.; Darie, C.; Goujon, C.; Legendre, M.; Leynaud, O. First Evidence of a Phase Transition in a High-Pressure Metal Iodate: Structural and Thermal Studies of AgIO₃ Polymorphs. *Eur. J. Inorg. Chem.* **2013**, *2013*, 3526–3532.
- (14) Liang, A.; Rahman, S.; Rodríguez-Hernandez, P.; Muñoz, A.; Manjón, F. J.; Nenert, G.; Errandonea, D. High-Pressure Raman Study of Fe(IO₃)₃: Soft-Mode Behavior Driven by Coordination Changes of Iodine Atoms. *J. Phys. Chem. C* **2020**, *124*, 21329–21337.
- (15) Liang, A.; Rahman, S.; Saqib, H.; Rodríguez-Hernandez, P.; Muñoz, A.; Nenert, G.; Yousef, I.; Popescu, C.; Errandonea, D. First-Order Isostructural Phase Transition Induced by High-Pressure in Fe(IO₃)₃. *J. Phys. Chem. C* **2020**, *124*, 8669–8679.
- (16) Liang, A.; Popescu, C.; Manjón, F. J.; Muñoz, A.; Hebboul, Z.; Errandonea, D. Structural and Vibrational Study of Zn(IO₃)₂ Combining High-Pressure Experiments and Density-Functional Theory. *Phys. Rev. B* **2021**, *103*, 054102.
- (17) Phanon, D.; Bentría, B.; Jeanneau, E.; Benbental, D.; Mosset, A.; Gautier-Luneau, I. Crystal Structure of M(IO₃)₂ Metal Iodates, Twinned by Pseudo-Merohedry, with MII: MgII, MnII, CoII, NiII and ZnII. *Z. Kristallogr.* **2006**, *221*, 635–642.
- (18) Pracht, G.; Lutz, H. D. Phase Relationships in Cobalt Iodate Hydrates - Thermal Analyses, X-Ray, IR, and Raman Spectroscopic Studies. *Thermochim. Acta* **2000**, *354*, 153–160.
- (19) Kochuthresia, T. C.; Gautier-Luneau, I.; Vaidyan, V. K.; Bushiri, M. J. Raman and Ftir Spectral Investigations of Twinned

- M(IO₃)₂ (M = Mn, Ni, Co, AND Zn) Crystals. *J. Appl. Spectrosc.* **2016**, *82*, 941–946.
- (20) Rietveld, H. M. A Profile Refinement Method for Nuclear and Magnetic Structures. *J. Appl. Crystallogr.* **1969**, *2*, 65–71.
- (21) Fauth, F.; Peral, I.; Popescu, C.; Knapp, M. The New Material Science Powder Diffraction Beamline at ALBA Synchrotron. *Powder Diffr.* **2013**, *28*, S360–S370.
- (22) Prescher, C.; Prakapenka, V. B. DIOPTAS: A Program for Reduction of Two-Dimensional X-Ray Diffraction Data and Data Exploration. *High Pressure Res.* **2015**, *35*, 223–230.
- (23) Dewaele, A.; Loubeyre, P.; Mezouar, M. Equations of State of Six Metals above 94 GPa. *Phys. Rev. B: Condens. Matter Mater. Phys.* **2004**, *70*, 094112.
- (24) Palik, E. D. *Handbook of Optical Constants of Solid*; Academic Press: Maryland, 1997.
- (25) Mao, H. K.; Xu, J.; Bell, P. M. Calibration of the Ruby Pressure Gauge to 800 Kbar under Quasi-Hydrostatic Conditions. *J. Geophys. Res.: Solid Earth* **1986**, *91*, 4673–4676.
- (26) Yousef, I.; Ribó, L.; Crisol, A.; Sics, I.; Ellis, G.; Ducic, T.; Kreuzer, M.; Benseny-Cases, N.; Quispe, M.; Dumas, P.; et al. MIRAS: The Infrared Synchrotron Radiation Beamline at ALBA. *Synchrotron Radiat. News* **2017**, *30*, 4–6.
- (27) Hohenberg, P.; Kohn, W. Inhomogeneous Electron Gas. *Phys. Rev.* **1964**, *136*, B864–B871.
- (28) Kresse, G.; Furthmüller, J. Efficiency of Ab-Initio Total Energy Calculations for Metals and Semiconductors Using a Plane-Wave Basis Set. *Comput. Mater. Sci.* **1996**, *6*, 15–50.
- (29) Kresse, G.; Hafner, J. Ab Initio Molecular Dynamics for Liquid Metals. *Phys. Rev. B: Condens. Matter Mater. Phys.* **1993**, *47*, 558–561.
- (30) Blöchl, P. E. Projector Augmented-Wave Method. *Phys. Rev. B: Condens. Matter Mater. Phys.* **1994**, *50*, 17953–17979.
- (31) Perdew, J. P.; Ruzsinszky, A.; Csonka, G. I.; Vydrov, O. A.; Scuseria, G. E.; Constantin, L. A.; Zhou, X.; Burke, K. Restoring the Density-Gradient Expansion for Exchange in Solids and Surfaces. *Phys. Rev. Lett.* **2008**, *100*, 136406.
- (32) Mattsson, A. E.; Armiento, R. Implementing and Testing the AM05 Spin Density Functional. *Phys. Rev. B: Condens. Matter Mater. Phys.* **2009**, *79*, 155101.
- (33) Dudarev, S. L.; Botton, G. A.; Savrasov, S. Y.; Humphreys, C. J.; Sutton, A. P. Electron-Energy-Loss Spectra and the Structural Stability of Nickel Oxide: An LSDA+U Study. *Phys. Rev. B: Condens. Matter Mater. Phys.* **1998**, *57*, 1505–1509.
- (34) Jain, A.; Ong, S. P.; Hautier, G.; Chen, W.; Richards, W. D.; Dacek, S.; Cholia, S.; Gunter, D.; Skinner, D.; Ceder, G.; et al. Commentary: The Materials Project: A Materials Genome Approach to Accelerating Materials Innovation. *APL Mater.* **2013**, *1*, 011002.
- (35) Togo, A.; Tanaka, I. First Principles Phonon Calculations in Materials Science. *Scr. Mater.* **2015**, *108*, 1–5.
- (36) Klotz, S.; Chervin, J.-C.; Munsch, P.; Le Marchand, G. Hydrostatic Limits of 11 Pressure Transmitting Media. *J. Phys. D: Appl. Phys.* **2009**, *42*, 075413.
- (37) Errandonea, D.; Meng, Y.; Somayazulu, M.; Häusermann, D. Pressure-Induced ω Transition in Titanium Metal: A Systematic Study of the Effects of Uniaxial Stress. *Phys. B* **2005**, *355*, 116–125.
- (38) Le Bail, A. Whole Powder Pattern Decomposition Methods and Applications: A Retrospection. *Powder Diffr.* **2005**, *20*, 316–326.
- (39) Song, H.; Jiang, D.; Wang, N.; Xing, W.; Guo, R.; Lin, Z.; Yao, J.; Wang, Y.; Tu, H.; Zhang, G. Na₃Bi(IO₃)₆: An Alkali-Metal Bismuth Iodate with Intriguing One-Dimensional [BiI₆O₁₈] Chains and Pressure-Induced Structural Transition. *Inorg. Chem.* **2021**, *60*, 2893–2898.
- (40) Momma, K.; Izumi, F. VESTA 3 for Three-Dimensional Visualization of Crystal, Volumetric and Morphology Data. *J. Appl. Crystallogr.* **2011**, *44*, 1272–1276.
- (41) Krapp, A.; Bickelhaupt, F. M.; Frenking, G. Orbital Overlap and Chemical Bonding. *Chem. - Eur. J.* **2006**, *12*, 9196–9216.
- (42) Murnaghan, F. D. The Compressibility of Media under Extreme Pressures. *Proc. Natl. Acad. Sci. U.S.A.* **1944**, *30*, 244–247.
- (43) Birch, F. Finite Elastic Strain of Cubic Crystals. *Phys. Rev.* **1947**, *71*, 809–824.
- (44) Angel, R. J.; Alvaro, M.; Gonzalez-Platas, J. EosFit7c and a Fortran Module (Library) for Equation of State Calculations. *Z. Kristallogr. - Cryst. Mater.* **2014**, *229*, 405–419.
- (45) Zhang, W. W.; Cui, Q. L.; Pan, Y. W.; Dong, S. S.; Liu, J.; Zou, G. T. High-Pressure x-Ray Diffraction Study of LiIO₃ to 75 GPa. *J. Phys.: Condens. Matter* **2002**, *14*, 10579–10582.
- (46) Hebboul, Z.; Galez, C.; Benbertal, D.; Beauquis, S.; Mugnier, Y.; Benmakhlouf, A.; Bouchenafa, M.; Errandonea, D. Synthesis, Characterization, and Crystal Structure Determination of a New Lithium Zinc Iodate Polymorph LiZn(IO₃)₃. *Crystals* **2019**, *9*, 464.
- (47) Shen, S. T.; Yao, Y. T.; Wu, T.-Y. Depolarization of Raman Lines and Structure of Chlorate, Bromate and Iodate Ions. *Phys. Rev.* **1937**, *51*, 235.
- (48) Dasent, W. E.; Waddington, T. C. 491. Iodine-Oxygen Compounds. Part I. Infrared Spectra and Structure of Iodates. *J. Chem. Soc.* **1960**, *491*, 2429–2432.
- (49) Gardiner, D. J.; Girling, R. B.; Hester, R. E. Vibrational Spectra and Force Constants of Chlorate, Bromate and Iodate Ions in Aqueous Solution. *J. Mol. Struct.* **1972**, *13*, 105–114.
- (50) Nakamoto, K. Infrared and Raman Spectra of Inorganic and Coordination Compounds. *Handbook of Vibrational Spectroscopy*; American Cancer Society, 2006; p 115.
- (51) Debernardi, A.; Ulrich, C.; Syassen, K.; Cardona, M. Raman Linewidths of Optical Phonons in 3c-Sic under Pressure: First-Principles Calculations and Experimental Results. *Phys. Rev. B: Condens. Matter Mater. Phys.* **1999**, *59*, 6774–6783.
- (52) Lucazeau, G. Effect of Pressure and Temperature on Raman Spectra of Solids: Anharmonicity. *J. Raman Spectrosc.* **2003**, *34*, 478–496.
- (53) Manjón, F. J.; Rodríguez-Hernández, P.; Muñoz, A.; Romero, A. H.; Errandonea, D.; Syassen, K. Lattice Dynamics of YVO₄ at High Pressures. *Phys. Rev. B: Condens. Matter Mater. Phys.* **2010**, *81*, 075202.
- (54) Pereira, A. L. J.; Sans, J. A.; Vilaplana, R.; Gomis, O.; Manjón, F. J.; Rodríguez-Hernández, P.; Muñoz, A.; Popescu, C.; Beltrán, A. Isostructural Second-Order Phase Transition of β -Bi₂O₃ at High Pressures: An Experimental and Theoretical Study. *J. Phys. Chem. C* **2014**, *118*, 23189–23201.
- (55) Pereira, A. L. J.; Errandonea, D.; Beltrán, A.; Gracia, L.; Gomis, O.; Sans, J. A.; García-Domene, B.; Miquel-Veyrat, A.; Manjón, F. J.; Muñoz, A.; et al. Structural Study of α -Bi₂O₃ under Pressure. *J. Phys.: Condens. Matter* **2013**, *25*, 475402.
- (56) Ibáñez, J.; Sans, J. A.; Popescu, C.; López-Vidrier, J.; Elvira-Betanzos, J. J.; Cuenca-Gotor, V. P.; Gomis, O.; Manjón, F. J.; Rodríguez-Hernández, P.; Muñoz, A. Structural, Vibrational, and Electronic Study of Sb₂S₃ at High Pressure. *J. Phys. Chem. C* **2016**, *120*, 10547–10558.
- (57) Cuenca-Gotor, V. P.; Sans, J. A.; Ibáñez, J.; Popescu, C.; Gomis, O.; Vilaplana, R.; Manjón, F. J.; Leonardo, A.; Sagasta, E.; Suárez-Alcubilla, A.; et al. Structural, Vibrational, and Electronic Study of α -As₂Te₃ under Compression. *J. Phys. Chem. C* **2016**, *120*, 19340–19352.
- (58) Pereira, A. L. D. J.; Santamaría-Pérez, D.; Vilaplana, R.; Errandonea, D.; Popescu, C.; Da Silva, E. L.; Sans, J. A.; Rodríguez-Carvajal, J.; Muñoz, A.; Rodríguez-Hernández, P.; et al. Experimental and Theoretical Study of SbPO₄ under Compression. *Inorg. Chem.* **2020**, *59*, 287–307.
- (59) Cuenca-Gotor, V. P.; Sans, J. A.; Gomis, O.; Mujica, A.; Radescu, S.; Muñoz, A.; Rodríguez-Hernández, P.; Da Silva, E. L.; Popescu, C.; Ibáñez, J.; et al. Orpiment under Compression: Metavalent Bonding at High Pressure. *Phys. Chem. Chem. Phys.* **2020**, *22*, 3352–3369.
- (60) Celeste, A.; Borondics, F.; Capitani, F. Hydrostaticity of Pressure-Transmitting Media for High Pressure Infrared Spectroscopy. *High Pressure Res.* **2019**, *39*, 608–618.
- (61) Liang, A.; Turnbull, R.; Bandiello, E.; Yousef, I.; Popescu, C.; Hebboul, Z.; Errandonea, D. High-Pressure Spectroscopy Study of

Zn(IO₃)₂ Using Far-Infrared Synchrotron Radiation. *Crystals* **2021**, *11*, 34.

(62) Sans, J. A.; Manjón, F. J.; Pereira, A. L. d. J.; Ruiz-Fuertes, J.; Popescu, C.; Muñoz, A.; Rodríguez-Hernández, P.; Pellicer-Porres, J.; Cuenca-Gotor, V. P.; Contreras-García, J.; et al. Unveiling the Role of the Lone Electron Pair in Sesquioxides at High Pressure: Compressibility of β -Sb₂O₃. *Dalton Trans.* **2021**, *50*, 5493–5505.

(63) Wuttig, M.; Deringer, V. L.; Gonze, X.; Bichara, C.; Raty, J.-Y. Incipient Metals: Functional Materials with a Unique Bonding Mechanism. *Adv. Mater.* **2018**, *30*, 1803777.

(64) Raty, J. Y.; Schumacher, M.; Golub, P.; Deringer, V. L.; Gatti, C.; Wuttig, M. A Quantum-Mechanical Map for Bonding and Properties in Solids. *Adv. Mater.* **2019**, *31*, 1806280.

(65) Cheng, Y.; Wahl, S.; Wuttig, M. Metavalent Bonding in Solids: Characteristic Representatives, Their Properties, and Design Options. *Phys. Status Solidi RRL* **2021**, *15*, 2000482.

(66) Sans, J. A.; Vilaplana, R.; Da Silva, E. L.; Popescu, C.; Cuenca-Gotor, V. P.; Andrada-Chacón, A.; Sánchez-Benitez, J.; Gomis, O.; Pereira, A. L. J.; Rodríguez-Hernández, P.; et al. Characterization and Decomposition of the Natural van Der Waals SnSb₂Te₄ under Compression. *Inorg. Chem.* **2020**, *59*, 9900–9918.

(67) Xu, M.; Jakobs, S.; Mazzarello, R.; Cho, J.-Y.; Yang, Z.; Hollermann, H.; Shang, D.; Miao, X.; Yu, Z.; Wang, L.; et al. Impact of Pressure on the Resonant Bonding in Chalcogenides. *J. Phys. Chem. C* **2017**, *121*, 25447–25454.

(68) Wuttig, M.; Schön, C. F.; Schumacher, M.; Robertson, J.; Golub, P.; Bousquet, E.; Raty, J. Y. Halide Perovskites: Third Generation Photovoltaic Materials Empowered by Metavalent Bonding. **2020**, arXiv:2012.03794 (cond-mat), p 03794.

High-pressure tuning of $d-d$ crystal-field electronic transitions and electronic band gap in $\text{Co}(\text{IO}_3)_2$ A. Liang¹, F. Rodríguez², P. Rodríguez-Hernandez³, A. Muñoz³, R. Turnbull¹ and D. Errandonea¹¹*Departamento de Física Aplicada—ICMUV, Universitat de València, MALTA Consolider Team, Edificio de Investigación, c/ Dr. Moliner 50, 46100 Burjassot, Valencia, Spain*²*DCITIMAC, MALTA Consolider Team, Facultad de Ciencias, Universidad de Cantabria, 39005 Santander, Spain*³*Departamento de Física and Instituto de Materiales y Nanotecnología, MALTA Consolider Team, Universidad de La Laguna, 38206 La Laguna, Tenerife, Spain*

(Received 21 December 2021; revised 11 February 2022; accepted 10 March 2022; published 25 March 2022)

High-pressure optical-absorption measurements performed on polycrystalline $\text{Co}(\text{IO}_3)_2$ samples were used to characterize the influence of pressure on the electronic $d-d$ transitions associated with Co^{2+} and the fundamental band gap of $\text{Co}(\text{IO}_3)_2$. The results shed light on the electron-lattice coupling and show that $\text{Co}(\text{IO}_3)_2$ exhibits an unusual behavior because the compression of Co–O bond distances is not coupled to pressure-induced changes induced in the unit-cell volume. Experimental results on the internal $d-d$ transitions of Co^{2+} have been explained based on changes in the constituent CoO_6 octahedral units using the semiempirical Tanabe-Sugano diagram. Our findings support that the high-spin ground state (4T_1) is very stable in $\text{Co}(\text{IO}_3)_2$. We have also determined the band-gap energy of $\text{Co}(\text{IO}_3)_2$ and its pressure dependence which is highly nonlinear. According to density-functional theory band-structure calculations, this nonlinearity occurs because the bottom of the conduction band is dominated by I- $5p$ orbitals and the top of the valence band by Co- $3d$ and O- $2p$ orbitals, and because the Co–O and I–O bond lengths exhibit different pressure dependences.

DOI: [10.1103/PhysRevB.105.115204](https://doi.org/10.1103/PhysRevB.105.115204)**I. INTRODUCTION**

The accurate characterization of the band-gap energy of semiconductors is fundamental for the development of electronic and optical applications. The study of the influence of pressure on the band-gap energy has gained interest over recent decades [1–3]. One of the reasons for the increasing interest is that high pressure (HP) has been shown to be an excellent tool to study the fundamental electronic properties of semiconductors [4,5]. In the case of cobalt iodate, $\text{Co}(\text{IO}_3)_2$, there is an interest in its band structure and band-gap energy. This is primarily motivated by its potential applications as a high-performance nonlinear-optical material [6]. The structural and vibrational properties of $\text{Co}(\text{IO}_3)_2$ have been characterized under HP [7], but as of yet there is no information on the band-gap energy or its pressure dependence. In addition to the optical absorptions associated with the fundamental band gap, there is an additional interest in $\text{Co}(\text{IO}_3)_2$. This interest is associated with the existence of internal intraconfigurational transitions within the $3d^7$ electron configuration of Co^{2+} and with the $3d$ orbitals splitting caused by the octahedral crystal field [8]. These transitions are known as internal $d-d$ transitions and are present in compounds with transition metals with partially occupied d shells (like Mn^{2+} , Cu^{2+} , and Co^{2+}). Such internal $d-d$ transitions between localized states produce a weaker absorption (which is connected to the crystal field) compared to the fundamental absorption between the valence and conduction bands [9]. In particular, the pressure dependence of the $d-d$ transitions is different from that of the fundamental band gap because they are governed by different physical mechanisms [10].

A compound like $\text{Co}(\text{IO}_3)_2$ can facilitate the experimental study of relevant electron-lattice couplings, like the Jahn-Teller (JT) effect, which involve orbital-degenerate electrons and lattice distortions or vibrations [9]. This electron-lattice coupling is responsible for a diverse range of phenomena, including colossal magnetoresistance, insulator-to-metal transitions, or spin transitions [11–14]. A deep understanding of electron-lattice coupling can be obtained from HP studies; therefore, the study of electron-lattice coupling under HP has become a key topic [3,5–7]. Octahedral Co^{2+} oxides are particularly useful compounds for studying the influence of pressure on the electron-lattice coupling. In these compounds, the combined action of a weak JT effect ($T \otimes e$) and crystal anisotropy favors a low-symmetry distortion around the transition metal resulting in noncentrosymmetric octahedra. In addition, in octahedral Co^{2+} oxides, $d-d$ transitions result in weak optical-absorption bands with energies smaller than the band-gap energy. The energy of these bands is correlated to the crystal-field splitting of the $\text{Co}^{2+} 3d^7$ orbital in CoO_6 octahedral units, which is affected by the low-symmetry distortions. Therefore, optical-absorption (OA) spectroscopy under HP can provide important information to understand not only the HP behavior of the band gap, but also the pressure-induced changes in octahedral distortion, crystal-field strength, and spin configuration. Amongst the octahedral Co^{2+} oxides, cobalt iodate, $\text{Co}(\text{IO}_3)_2$, is a particularly interesting compound which enables the experimental study of electron-lattice coupling under HP. This compound, with a monoclinic crystal structure at ambient conditions (space group $P2_1$) is extremely compressible (it

has a bulk modulus of 30 GPa) due to the lone electron pair of the I^{5+} [7]. The crystal structure of $\text{Co}(\text{IO}_3)_2$ also shows a large anisotropic response to pressure [7]. Furthermore, the coordination polyhedra of Co^{2+} and I^{5+} are very sensitive to HP [8]. Due to these aspects of $\text{Co}(\text{IO}_3)_2$ outlined above, the application of low pressures (< 20 GPa) leads to important changes in the electron-lattice coupling and crystal field, making $\text{Co}(\text{IO}_3)_2$ an ideal prototype for studying correlations between electronic and crystal structures under compression.

Here, we report a combination of OA studies and density-functional theory (DFT) calculations on $\text{Co}(\text{IO}_3)_2$ under HP conditions. We show that changes in the fundamental band gap and internal $d-d$ absorption bands are intimately related to structural changes, thereby yielding an enhancement of the symmetry of CoO_6 octahedra under HP. The enhanced symmetry has a strong influence in the OA spectra due to the different electron-phonon couplings involved. The pressure evolution of the internal $d-d$ transitions and the fundamental band gap is explained by analyzing the crystal field and using DFT calculations.

II. METHODS

A. High-pressure optical-absorption experiments

HP optical-absorption experiments were carried out on a 3- μm -thin platelet of polycrystalline $\text{Co}(\text{IO}_3)_2$ which exhibited the $P2_1$ monoclinic structure [7]. The powder samples used in the present work were the same as those used for our previous study of the pressure-induced isostructural phase transition in $\text{Co}(\text{IO}_3)_2$. The crystal structure and sample purity of the $\text{Co}(\text{IO}_3)_2$ samples were reported in our previous work [7]. The optical-absorption measurements were performed in a diamond-anvil cell equipped with IIA-type diamonds with culet diameters of 480 μm . The sample was loaded in a 200- μm -diameter hole drilled in a stainless-steel gasket preindented to a thickness of 40 μm . Potassium bromide (KBr) was used as a pressure-transmitting medium (PTM) [15]. This medium is not fully hydrostatic above 2 GPa [15], but non-hydrostatic stresses do not substantially affect the behavior of $\text{Co}(\text{IO}_3)_2$ in the pressure range of our study, as shown in previous infrared studies [7]. In addition, KBr has the advantage of transparency in the energy range of optical-absorption experiments. The sample pressure was determined using the ruby scale [16]. The sample-in, sample-out method was used to acquire OA spectra using a bespoke optical setup [17]. The absorbance of the sample was obtained by normalizing the intensity of the light transmitted through the sample [$I(\omega)$] with the intensity of the light transmitted through the PTM [$I_0(\omega)$]. Further details regarding the optical-absorption setup can be found elsewhere [18]. Due to the difference in the intensity of the absorption of the band gap and internal $d-d$ transitions, the OA measurements were performed using two different light sources to separately investigate the visible and ultraviolet regions of the electromagnetic spectrum. The lower-energy region, 1.5 to 2.9 eV, allows an accurate measurement of the weak internal $d-d$ transitions of Co^{2+} . The higher-energy region, >2.6 eV, allows for measurement of the band-gap energy.

B. First-principles calculations

The electronic properties of $\text{Co}(\text{IO}_3)_2$ were modeled within the framework of DFT [19] using the Vienna *Ab initio* Simulation Package (VASP). We used the generalized gradient approximation with the Armiento and Mattsson (AM05) prescription [20] for the exchange–correlation energy. Pseudopotentials were generated with the projector-augmented wave method [21] using a 540-eV plane-wave cutoff to ensure high accurate convergence. The Brillouin-zone k -point integration was carried out using a significant sampling of a $4 \times 6 \times 4$ grid for the primitive unit cell. The DFT + U scheme [22] was used to treat the strongly correlated $3d$ states of Co atoms. In our calculations, we used an effective Hubbard parameter $U_{\text{eff}} = 3.32$ eV [7]. This parameter was optimized at ambient conditions and (as is common practice) assumed to be pressure independent [23,24]. This approach was shown to properly describe the changes induced by pressure in the crystal structure and phonons of $\text{Co}(\text{IO}_3)_2$ [7].

III. RESULTS AND DISCUSSION

Figure 1 shows the absorbance spectra determined from a selection of OA spectra summarizing the pressure evolution of both the internal $d-d$ transitions [Fig. 1(a)] and the fundamental band gap [Fig. 1(b)]. In Fig. 1(a) we observe a change in the pressure evolution of absorptions associated with $d-d$ transitions at 7.3 GPa. In particular, the highest-energy band blueshifts with increasing pressure from ambient pressure to the highest pressure with a slope change at 7.3 GPa. This pressure of 7.3 GPa is close to the transition pressure of a previously reported isostructural phase transition [7]. This phase transition involves the enhancement of the symmetry of the CoO_6 octahedra and a change in the pressure dependence of Co–O bond distances. As we show, this fact is consistent with the observations of the present work. From the OA experiment data, we have obtained the pressure dependence of the $d-d$ transition energies by fitting Gaussian profiles to the absorption bands. The results are given in Fig. 2(c). In Fig. 1(b) it can be seen that the fundamental band gap redshifts as pressure increases. We later show that there are also changes in the pressure dependence of the band-gap energy near 7.3 GPa.

The data analysis indicates that changes in the optical properties are directly correlated to changes in the crystal structure, in particular, to local changes of the CoO_6 octahedra. In the crystal structure of $\text{Co}(\text{IO}_3)_2$ there are two Co atoms occupying nonequivalent crystallographic positions. However, their coordination octahedra are nearly identical [7]. A representation of the CoO_6 octahedra is provided in Fig. 2(a). From ambient pressure to 7.3 GPa the CoO_6 octahedra are noncentrosymmetric. At ambient conditions they have an average Co–O bond length of $r_0 = 2.067$ Å with a distortion index [$\sigma = (\sum_{i=1}^6 (r_i - r_0)^2)^{1/2}$, and $r_0 = \frac{\sum_{i=1}^6 r_i}{6}$] of $\sigma = 0.06$ Å according to DFT calculations [25]. The pressure dependence of σ is represented in Fig. 2(d). The oxygen-metal (Co and Zn) bond distances used to calculate the distortion index were obtained from previously reported DFT calculations [7,26]. The distortion index of the CoO_6 octahedra initially decreases very rapidly with pressure. At 7.3 GPa, $r_0 = 2.046$ Å and $\sigma = 0.02$ Å. After the phase transition at 7.3 GPa, the

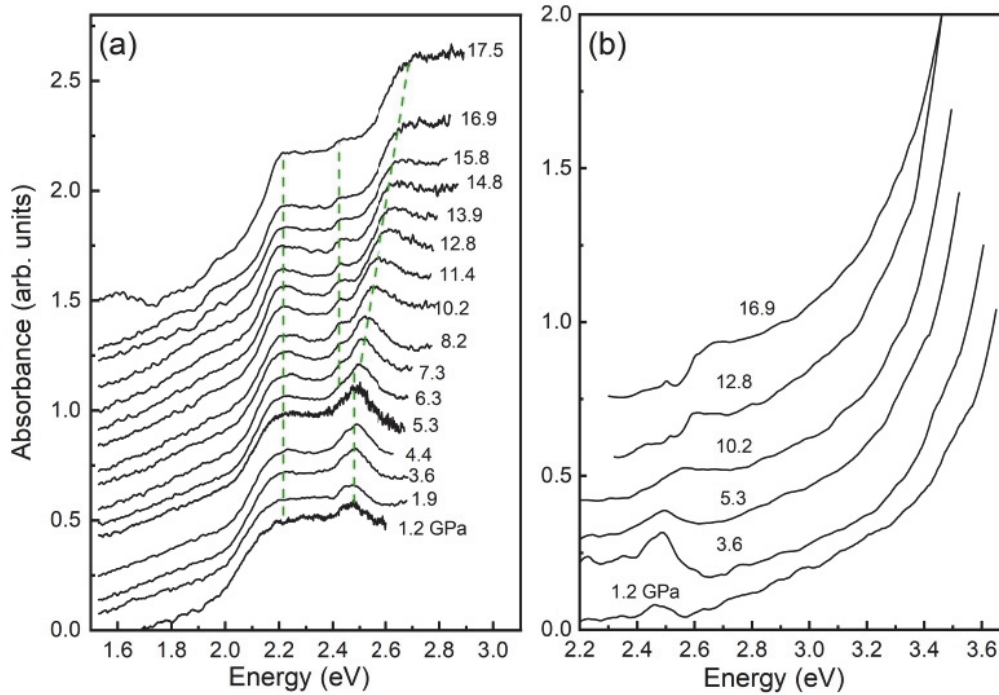


FIG. 1. High-pressure optical-absorption spectra of $\text{Co}(\text{IO}_3)_2$. (a) The lower-energy region, 1.5 to 3.1 eV, selected to highlight the weak internal $d-d$ absorption bands. (b) The higher-energy region, 2.2 to 3.7 eV, selected to show the fundamental band-gap absorption. Pressures in GPa are indicated in the figures. Different light sources were used in (a) and (b) corresponding to the different energy regions. In (a), the green lines show the pressure evolution of Co^{2+} $d-d$ bands. The absorbance was obtained by the function $A = \log_{10} \frac{I(\omega)}{I_0(\omega)}$, where A is absorbance, and $I(\omega)$ and $I_0(\omega)$ are, respectively, the light transmitted through the sample and the PTM.

rate of change of distortion index with increasing pressure is much lower, despite the fact that the Co–O bond lengths continue to decrease, eventually reaching values of $r_0 = 2.029 \text{ \AA}$ and $\sigma = 0.01 \text{ \AA}$ at 17.5 GPa. Therefore, the CoO_6 octahedra become more symmetric with increasing pressure, eventually becoming quasicosymmetrical beyond 7.3 GPa. As shown in Fig. 2(d), the two inequivalent CoO_6 octahedra exhibit the same pressure dependence of the distortion index σ . This means that, to a first approximation, we can analyze the OA spectra with a model including only one effective CoO_6 octahedron.

The octahedral distortion in $\text{Co}(\text{IO}_3)_2$ probably arises from structural modifications induced by the crystal anisotropy and the weak Jahn-Teller effect ($T \otimes e$) associated with the t_{2g} orbitals [the ${}^4T_{1g}(F)$ ground state] [27–29]. Thus, the octahedral distortion affects the crystal-field splitting of the Co^{2+} ($3d^7$) orbitals in CoO_6 under HP as we show in the one-electron energy-level diagram given in Fig. 2(b). The splitting of the parent octahedral $t_{2g}(\Delta_t)$ and $e_g(\Delta_e)$ orbitals was estimated through correlations between the low-symmetry local structure and both Δ_e and Δ_t established elsewhere for halides and oxides [9,27–29]. For an octahedral distortion of $\sigma = 0.06 \text{ \AA}$, we estimate Δ_e of about 0.2–0.3 eV and Δ_t of about 0.05 eV at ambient conditions, both of which decrease by a factor of 6 by 17.5 GPa. As discussed later in the present work, the reduction of the crystal-field splitting with increasing pressure yields a narrowing of the $d-d$ absorption band at 2.15 eV [see Fig. 1(a)]. The Co^{2+} cation in $\text{Co}(\text{IO}_3)_2$ has a $3d^7$ electronic configuration wherein the seven $3d$ electrons occupy the d_{xy} , d_{xz} , d_{yz} , $d_{x^2-y^2}$, and d_{z^2} orbitals with five electrons in triply degenerate t_{2g} level and two spin-up electrons in the doubly

degenerate e_g level, both of which are split by Δ_t and Δ_e , respectively, in the O_h -distorted CoO_6 octahedron.

In sixfold-coordinated Co^{2+} , in nearly octahedral coordination, the absorption bands originating from $d-d$ transitions can be well described using the Tanabe-Sugano (TS) diagram for octahedral Co^{2+} ($3d^7$) [30]. This diagram is shown in Fig. 3. The TS diagram is based on a semiempirical model that describes the internal $d-d$ transitions using the crystal-field splitting energy, Δ , and the interelectronic repulsion interactions through the Racah parameters B and C [31]. The energies of all possible transitions from the ground state can be precisely described through these three parameters and they are represented through the Tanabe-Sugano diagram [32]. In the high-spin state of Co^{2+} , the only spin-allowed transitions are: ${}^4T_{1g}(F) \rightarrow {}^4T_{2g}(F)$, ${}^4T_{1g}(F) \rightarrow {}^4A_{2g}(F)$, ${}^4T_{1g}(F) \rightarrow {}^4T_{1g}(P)$. Amongst them, the ${}^4T_{1g}(F) \rightarrow {}^4T_{1g}(P)$ transition shows the maximum oscillator strength and a relatively narrow full width at half maximum (FWHM). The ${}^4T_{1g}(F) \rightarrow {}^4T_{2g}(F)$ transition energy, which is proportional to the crystal-field splitting Δ , is below the explored spectral range (at about 0.7 eV). Furthermore, the energy of the ${}^4T_{1g}(F) \rightarrow {}^4A_{2g}(F)$ transition, involving two electrons jumping from t_{2g} to e_g , is proportional to 2Δ , giving rise to strong electron-phonon couplings, yielding a band broadening and thus being difficult to detect at ambient conditions. Examples of this behavior can be found in KCoF_3 , CoF_2 [33], and CoCl_2 [34]. Therefore, the ${}^4T_{1g}(F) \rightarrow {}^4T_{1g}(P)$ transition is the major feature of the OA spectra of these compounds, and it is responsible for their characteristic red color. Therefore, the band placed at 2.13 eV at 1.2 GPa in $\text{Co}(\text{IO}_3)_2$ [see Fig. 1(a)] can be assigned to the spin-allowed ${}^4T_{1g}(F) \rightarrow {}^4T_{1g}(P)$ transition. Additionally,

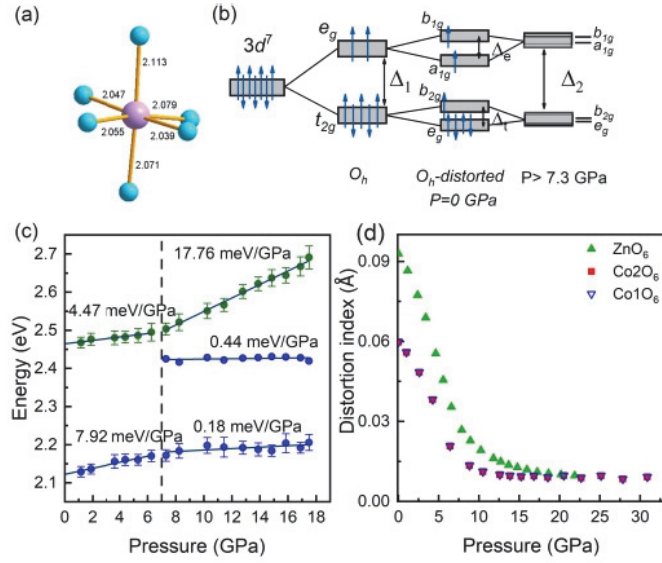


FIG. 2. (a) Representation of the CoO_6 octahedron. (b) Diagram of Co^{2+} d levels in $\text{Co}(\text{IO}_3)_2$ for $P < 7.3$ GPa and $P > 7.3$ GPa. (c) Pressure dependence of the $d-d$ transition energies. The solid lines are linear fits. The vertical dashed line indicates the phase transition pressure. Where not visible the error bars are smaller than symbols. (d) Distortion index of Co1O_6 and Co2O_6 in $\text{Co}(\text{IO}_3)_2$ compared to that of ZnO_6 in $\text{Zn}(\text{IO}_3)_2$. The bond distance between the metal (Co and Zn) and iodine used to calculate the distortion index was obtained from DFT calculations [7].

the weaker absorption band at 2.47 eV is associated with the ${}^4T_{1g}(F) \rightarrow {}^2A_{1g}(G)$ transition. Although this transition is initially spin forbidden by the electric dipole (ED) mechanism, the spin-orbit interaction and the proximity of charge-transfer states make it ED allowed. The pressure coefficients of these bands [Fig. 2(c)] support the present assignment. Other bands are difficult to identify in the absorption spectra due to their broad FWHM, especially at lower pressures ($P < 7.3$ GPa).

An important feature in the pressure evolution of the absorption spectra is the progressive band narrowing experienced by the absorption bands above 7.3 GPa. This narrowing allows us to clearly resolve the narrow spin-fliplike ${}^4T_{1g}(F) \rightarrow {}^2T_{1g}(H)$ transition at 2.43 eV, and the oscillator-strength enhanced ${}^4T_{1g}(F) \rightarrow {}^2A_{1g}(G)$ transition that blueshifts with pressure from 2.52 to 2.63 eV when increasing pressure from 7.5 to 17.5 GPa. This pressure-induced narrowing of all $d-d$ absorption bands correlates with the symmetrization of the CoO_6 octahedra with pressure, as indicated by the progressive decrease of the octahedral distortion index, σ , from 0.06 at ambient pressure, to 0.01 Å at 17.5 GPa; see Fig. 2(d). The homogeneous band narrowing is associated with the reduction of the FWHM due to the e_g splitting Δ_e . The energy-level splitting is represented in Fig. 2(b). The band energies and their variation with pressure can be described based on the TS diagram given in Fig. 3. According to the transition assignment in the TS diagram, the energy ratio between the two $d-d$ transition bands observed in experiments at 1.2 GPa is $2.47 \text{ eV} / 2.13 \text{ eV} = 1.16$. The same ratio between states ${}^2A_{1g}(G)$ and ${}^4T_{1g}(P)$ in the TS diagram corresponds to $\Delta/B = 9.08$ (x axis) and $E/B = 21.7$ (y axis), when $E = 2.13 \text{ eV}$. Thus, the Racah parameters $B =$

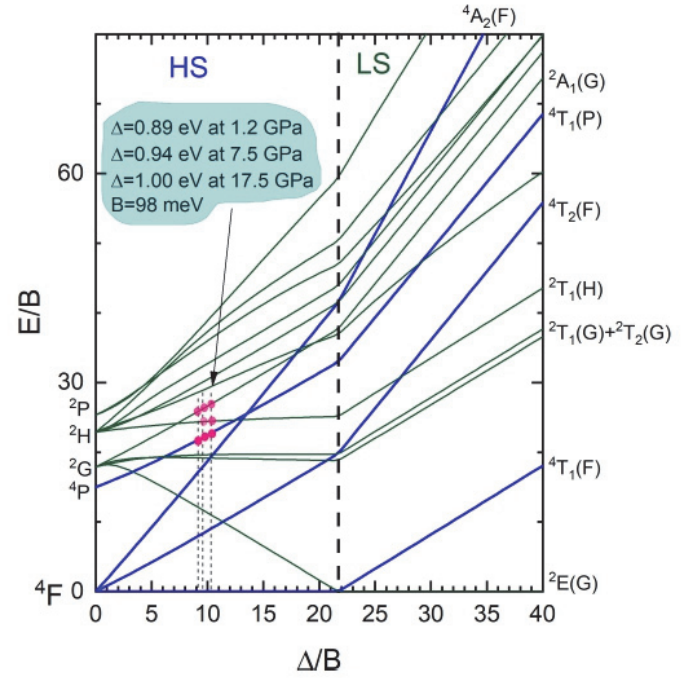


FIG. 3. TS diagram for $3d^7$ ions calculated for $C/B = 4.62$. The state energy is a function of the crystal-field energy Δ in terms of the Racah parameter B . For clarity, only relevant energy states are plotted. Blue (green) lines represent states where the transition is spin allowed (forbidden). Red dots correspond to selected spectroscopic data at different pressures. The vertical dashed line shows the high-spin (HS, $S = 3/2$) to low-spin (LS, $S = 1/2$) crossover at $\Delta/B = 22$.

0.098 eV, $C = 0.453 \text{ eV}$, and the crystal-field splitting $\Delta = 0.89 \text{ eV}$ at 1.2 GPa are consistent with the nephelauxetic series [35]. In particular, B is similar to the parameters obtained at ambient pressure in KCoF_3 (Co^{2+}), $B = 0.105 \text{ eV}$ ($\Delta = 0.95 \text{ eV}$) [33], in CoCl_2 (Co^{2+}), $B = 0.097 \text{ eV}$ ($\Delta = 0.87 \text{ eV}$) [34], in CoO (Co^{2+}), $B = 0.105 \text{ eV}$ ($\Delta = 1.15 \text{ eV}$) [35], and in the hexa-aquo $\text{Co}(\text{OH}_2)_6$ complex, which has Co^{2+} octahedrally surrounded oxygen atoms, $B = 0.073 \text{ eV}$ ($\Delta = 1.12 \text{ eV}$) [35], and it is higher than that found in MnWO_4 (Mn^{2+}O_6), $B = 0.077 \text{ eV}$ ($\Delta = 0.94 \text{ eV}$) [36], which is reasonable as Mn^{2+} has a d^5 configuration.

It is worth noting that the pressure-induced band narrowing of the $d-d$ bands observed in the optical spectra above 7.3 GPa is a sign of the suppression of the low-symmetry distortion of the CoO_6 octahedra due, in part, to the Jahn-Teller effect associated with the ${}^4T_{1g}(F)$ ground state. The symmetry enhancement of the divalent metal coordination octahedra is not a feature unique to HP $\text{Co}(\text{IO}_3)_2$. It also happens in other metal iodates such as $\text{Fe}(\text{IO}_3)_3$ [37] and $\text{Zn}(\text{IO}_3)_2$ [26], as can be seen in Fig. 2(d), where the distortion index of ZnO_6 is compared with that of CoO_6 . However, the $d-d$ absorption bands of other metal iodates are typically not observable in their OA spectra. Therefore, $\text{Co}(\text{IO}_3)_2$ provides a unique way to investigate the pressure evolution of metal oxygen complexes in metal iodates.

From the data shown in Fig. 2(c) it can be deduced that the crystal-field splitting in the CoO_6 octahedra is enhanced under pressure. This phenomenon is a direct consequence of the volume reduction upon compression of the crystal structure of

$\text{Co}(\text{IO}_3)_2$ which yields a reduction in the Co–O bond distance. We have found a variation of Δ from 0.89 at 1.2 GPa, to 1.00 eV at 17.5 GPa; see Fig. 3. Interestingly, this fact is consistent with expectations of the crystal- (or ligand-) field theory (CFT). According to CFT, $\Delta/\Delta_0 = (r_0/r)^n$ with the n exponent close to 5 [29]. This relationship is usually employed with $(V_0/V)^{n/3}$ since the volumes can be more easily obtained by, for example, the equation of state determined by x-ray diffraction [7]. The corresponding bond distances $r(P)$, on the other hand, often require single-crystal x-ray diffraction (XRD) measurements. The approach utilizing $(V_0/V)^{n/3}$ is correct provided that the bond distances scale proportionally to the crystal volume with pressure [29]. The results obtained from $\text{Co}(\text{IO}_3)_2$ in the present work provide a primary example of how the Co–O bond distances and unit-cells volumes can scale disproportionately; therefore, in the present case of $\text{Co}(\text{IO}_3)_2$, the approximation $\Delta/\Delta_0 = (V_0/V)^{n/3}$ is no longer valid. Considering the variations of Δ , V , and r we obtain exponents of $n = 3(1)$ and $6(1)$ using $(V_0/V)^{n/3}$ and $(r_0/r)^n$, respectively, the latter being compatible with crystal-field theory expectations of $n = 5$. The large difference between the exponents acquired using different assumption reveals that the reduction in the average volume per atom in the crystal structure upon compression is mainly accounted for by the iodine coordination polyhedra (which are more compressible due to the presence of a lone electron pair on the I^{5+} cation,) rather than the CoO_6 octahedra. This also reveals that the I–O bonds are more compressible than the Co–O bonds.

Another interesting feature to explore from our results is the possible occurrence of a spin transition in $\text{Co}(\text{IO}_3)_2$. Using the TS diagram, the critical pressure for the high-spin to low-spin crossover can be estimated. According to Fig. 3, this is expected to happen at $\Delta/B = 22$ ($\Delta = 2.2$ eV). Based on these results, the corresponding volume reduction needed to reach $\Delta = 2.2$ eV would be about 60%, which would be equivalent to a pressure of about 110 GPa, according to results from XRD studies [7]. This pressure is much higher than the spin-crossover transition pressure found in CoCl_2 (near 70 GPa) [34]. This result indicates that the high-spin state is very stable in $\text{Co}(\text{IO}_3)_2$.

To conclude, we discuss the pressure dependence of the band gap. According to our band-structure calculations, $\text{Co}(\text{IO}_3)_2$ has an indirect band gap, as is observed in other metal iodates [38]. Based on the assumption of an indirect band gap, we have determined the pressure dependence of the band-gap energy from the OA spectra measured in the high-energy range. The values of the indirect band-gap energy were determined using a Tauc plot analysis [39], wherein the linear fit of the high-energy part of the $(\alpha h\nu)^{1/2}$ vs $h\nu$ plot was extrapolated to $(\alpha h\nu)^{1/2} = 0$, where α is the absorption coefficient, h is Plank's constant, and ν is the photon's frequency. The value of the band-gap energy was thereby estimated to be 3.5(1) eV at 1.2 GPa, which is similar to that of the structurally related metal iodate $\text{Zn}(\text{IO}_3)_2$ [40]. The pressure dependence of the band-gap energy is shown in Fig. 4, where the experimental results are compared with those derived from our DFT calculations. The DFT calculations underestimate the band-gap energy at ambient pressure, giving a value of 2.26 eV; however, they provide a good description of the pressure dependence of the band-gap energy. The difference between

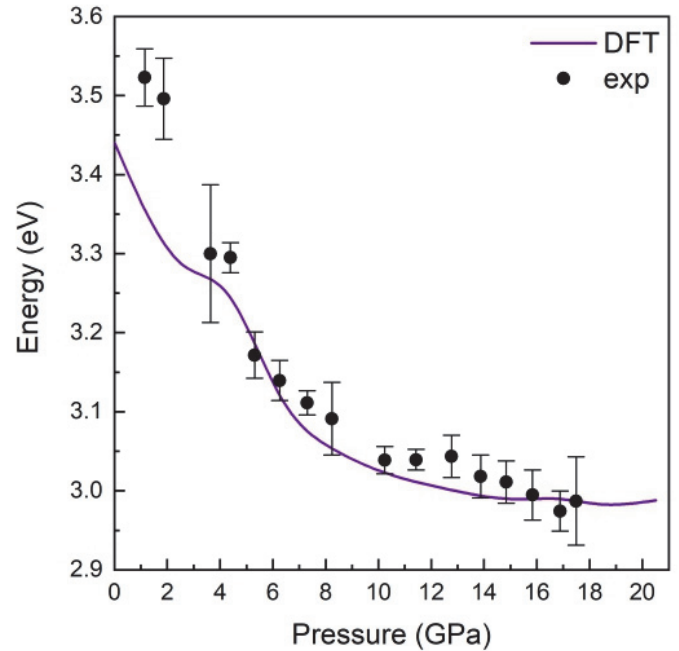


FIG. 4. Pressure dependence of the band gap of $\text{Co}(\text{IO}_3)_2$. Data from experiments and DFT calculations are, respectively, shown with symbols and with a solid line. The calculated band gap has been offset by 1.2 eV to facilitate comparison as discussed in the main text.

measured and calculated band gaps at ambient pressure is typical of DFT calculations and it is related to the approximations used to describe the exchange and correlation energies. However, the underestimation of the absolute value of the band gap does not affect the calculated relative changes induced by pressure [41,42], as is shown by the good agreement between experiment and theory in Fig. 4, where the calculated band gap has been offset by 1.2 eV to facilitate comparison. In the figure it can be seen that the band-gap energy decreases rapidly from 3.5 eV at ambient pressure to 3.1 eV at 8 GPa. Above 8 GPa, the band-gap energy decreases much more slowly, eventually reaching a value of 3 eV at 18 GPa.

In Fig. 5 we present the electronic density of states (DOS) and projected density of states (PDOS) at ambient pressure. The pressure dependence of the atomic character in the valence-band maximum (VBM) and conduction-band minimum (CBM) are shown in Fig. 6, where we can observe that the VBM is dominated by the Co-3d and O-2p orbitals, and the CBM is dominated by the I-5p orbitals, with some contribution from the O-2p orbitals. Thus, the band-gap energy will be strongly affected by changes in the Co–O and I–O bond distances. As we have reported previously [7], the Co–O bond distances decrease from ambient pressure (2.067 Å) to around 7 GPa (2.046 Å), after which pressure the distance continues to decrease but more slowly. On the other hand, the length of the I–O bonds in the original IO_3 polyhedron (a trigonal pyramid) continuously increases under compression, in order to accommodate the three second-nearest neighboring oxygen atoms, thereby gradually transforming the original IO_3 polyhedron into an IO_6 distorted octahedron. Consequently, there are two competing effects affecting the states near the Fermi level under compression. The decrease of the Co–O bond

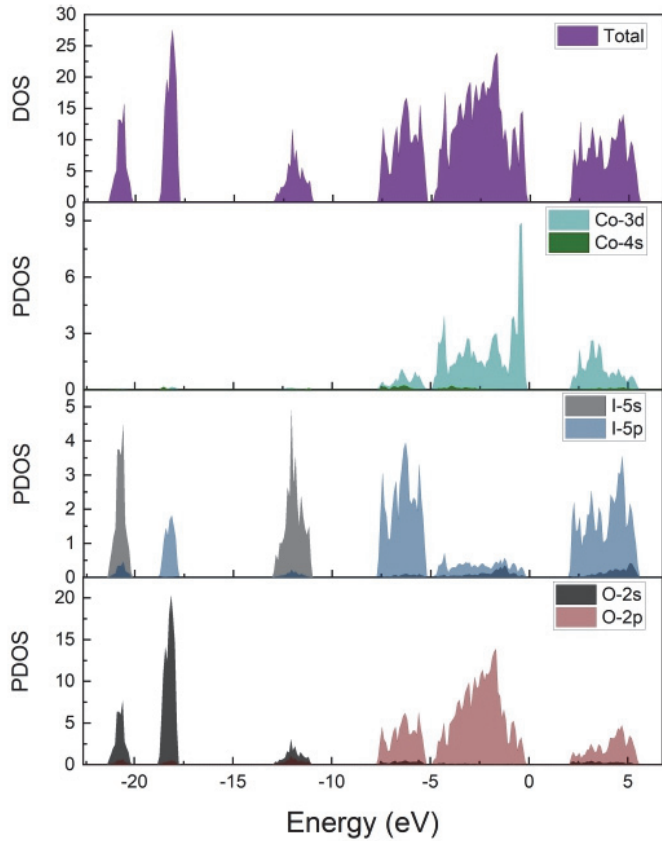


FIG. 5. Calculated total electronic DOS and PDOS for $\text{Co}(\text{IO}_3)_2$ at ambient pressure.

distances enhances the overlap between Co and O orbitals, favoring the narrowing of the band-gap energy. In contrast, the increase of the three I–O bond distances reduces the hybridization between iodine and oxygen, which favors the opening of the band gap. At lower pressures, the large contribution of Co states to the VBM dominates the change of the band-gap energy, so the band gap decreases with pressure, up to around 8 GPa. Beyond this pressure, the two effects neutralize each other, and the band gap of $\text{Co}(\text{IO}_3)_2$ almost remains unchanged under increasing pressure. A consequence of the competition between the two mechanisms described above is a small shoulder in the pressure dependence of the band gap predicted by calculations around 4 GPa. This shoulder is not observed in experiments, probably due to the associated experimental error.

IV. CONCLUSIONS

In conclusion, optical-absorption measurements of $\text{Co}(\text{IO}_3)_2$ provide useful information regarding the electron-lattice coupling of this Co^{2+} compound. In particular, we have been able to determine that the pressure evolution of

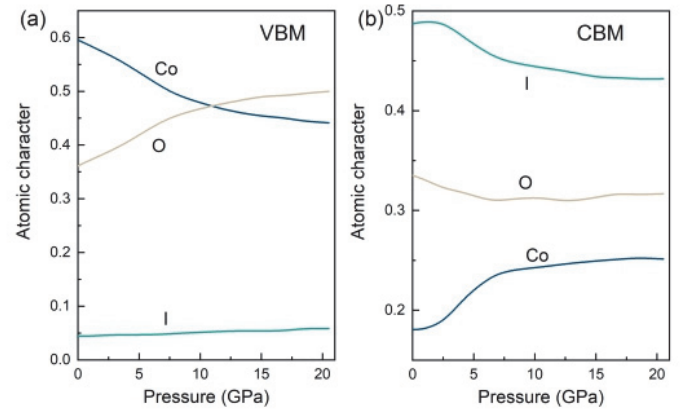


FIG. 6. Calculated pressure dependence of the normalized atomic character in (a) the VBM and (b) CBM of the electronic band structure in $\text{Co}(\text{IO}_3)_2$.

the $d-d$ transitions in $\text{Co}(\text{IO}_3)_2$ is distinct from that observed in other Co^{2+} compounds, and that, therefore, $\text{Co}(\text{IO}_3)_2$ provides a primary example of how the pressure dependencies of volume and Co–O bond distances can be decoupled. We have correlated the large broadening of $d-d$ bands at ambient conditions with the low-symmetry octahedral distortion of CoO_6 that additionally splits the e_g and t_{2g} Co^{2+} orbitals. The pressure-induced band narrowing is thus associated with the symmetrization of the CoO_6 octahedra, that in turn unveils the existence of a structural phase transition at 7.3 GPa. Additionally, we have found that changes in the $d-d$ transition energies also support the existence of such a phase transition. Using the Tanabe-Sugano diagram we have provided a rational explanation for all observed results. Based on this analysis, we concluded that the high-spin state is very stable in $\text{Co}(\text{IO}_3)_2$, and the high-spin to low-spin transition could be expected in the 110-GPa range. Finally, it was determined that the band-gap energy follows a strong nonlinear pressure dependence, with a change in slope near the transition pressure. An explanation for this behavior is provided based upon DFT band-structure calculations.

ACKNOWLEDGMENTS

This work was supported by the Generalitat Valenciana under Project No. PROMETEO 2018/123-EFIMAT and by the Spanish Research Agency (AEI) and Spanish Ministry of Science and Investigation (MCIN) under Projects No. PID2019106383GB-C41/C43 (DOI: 10.13039/501100011033) cofinanced by EU FEDER funds, No. PGC2018-101464-B-I00, and No. RED2018-102612-T. A.L. and D.E. thank the Generalitat Valenciana for the Ph.D. Fellowship No. GRISOLIAP/2019/025. R.T. acknowledges funding from the Spanish MINECO via the Juan de la Cierva Formación program (Grant No. FJC2018-036185-I).

[1] J. Ibáñez, A. Segura, B. García-Domene, R. Oliva, F. J. Manjón, T. Yamaguchi, Y. Nanishi, and L. Artús, *Phys. Rev. B* **86**, 035210 (2012).

[2] R. Lacomba-Perales, D. Errandonea, A. Segura, J. Ruiz-Fuertes, P. Rodríguez-Hernández, S. Radescu, J. López-Solano, A. Mujica, and A. Muñoz, *J. Appl. Phys.* **110**, 043703 (2011).

- [3] E. Bandiello, J. Sánchez-Martín, D. Errandonea, and M. Bettinelli, *Crystals* **9**, 237 (2019).
- [4] P. Botella, D. Errandonea, A. B. Garg, P. Rodriguez-Hernandez, A. Muñoz, S. N. Achary, and A. Vomiero, *SN Appl. Sci.* **1**, 389 (2019).
- [5] F. J. Manjón, D. Errandonea, A. Segura, A. Muñoz, G. Tobías, P. Ordejón, and E. Canadell, *Phys. Rev. B* **63**, 125330 (2001).
- [6] C. L. Hu and J. G. Mao, *Coord. Chem. Rev.* **288**, 1 (2015).
- [7] A. Liang, C. Popescu, F. J. Manjon, R. Turnbull, E. Bandiello, P. Rodriguez-Hernandez, A. Muñoz, I. Yousef, Z. Hebboul, and D. Errandonea, *J. Phys. Chem. C* **125**, 17448 (2021).
- [8] F. Rodríguez, D. Hernández, J. Garcia-Jaca, H. Ehrenberg, and H. Weitzel, *Phys. Rev. B* **61**, 16497 (2000).
- [9] J. Ruiz-Fuertes, A. Segura, F. Rodríguez, D. Errandonea, and M. N. Sanz-Ortiz, *Phys. Rev. Lett.* **108**, 166402 (2012).
- [10] E. Jara, J. A. Barreda-Argüeso, J. González, R. Valiente, and F. Rodríguez, *Pap. Phys.* **11**, 110004 (2019).
- [11] M. R. Otto, J. H. Pöhls, L. P. René de Cotret, M. J. Stern, M. Sutton, and B. J. Siwick, *Sci. Adv.* **7**, edbf2810 (2021).
- [12] I. Loa, P. Adler, A. Grzechnik, K. Syassen, U. Schwarz, M. Hanfland, G. Kh. Rozenberg, P. Gorodetsky, and M. P. Pasternak, *Phys. Rev. Lett.* **87**, 125501 (2001).
- [13] M. Baldini, V. V. Struzhkin, A. F. Goncharov, P. Postorino, and W. L. Mao, *Phys. Rev. Lett.* **106**, 066402 (2011).
- [14] K. Liu, C. Li, T. Wen, D. Jiang, Z. Jiang, Y. Ma, and Y. Wang, *Chem. Asian J.* **16**, 3437 (2021).
- [15] J. Zhao and N. L. Ross, *J. Phys.: Condens. Matter* **27**, 185402 (2015).
- [16] H. K. Mao, J. Xu, and P. M. Bell, *J. Geophys. Res.* **91**, 4673 (1986).
- [17] A. Segura, J. A. Sans, D. Errandonea, D. Martínez-García, and V. Fages, *Appl. Phys. Lett.* **88**, 011910 (2006).
- [18] D. Errandonea, C. Popescu, A. B. Garg, P. Botella, D. Martínez-García, J. Pellicer-Porres, P. Rodríguez-Hernández, A. Muñoz, V. Cuenca-Gotor, and J. A. Sans, *Phys. Rev. B* **93**, 035204 (2016).
- [19] P. Hohenberg and W. Kohn, *Phys. Rev.* **136**, B864 (1964).
- [20] A. E. Mattsson and R. Armiento, *Phys. Rev. B* **79**, 155101 (2009).
- [21] P. E. Blöchl, *Phys. Rev. B* **50**, 17953 (1994).
- [22] S. L. Dudarev, G. A. Botton, S. Y. Savrasov, C. J. Humphreys, and A. P. Sutton, *Phys. Rev. B* **57**, 1505 (1998).
- [23] O. Bengone, M. Alouani, P. Blöchl, and J. Hugel, *Phys. Rev. B* **62**, 16392 (2000).
- [24] S. A. Tolba, K. M. Gameel, B. A. Ali, H. A. Almossalami, and N. K. Allam, in *Density Functional Calculations: Recent Progresses of Theory and Application*, The DFT+U: Approaches, Accuracy, and Applications, edited by G. Yang (IntechOpen, London, 2018), pp. 3–30.
- [25] A. Y. Ramos, H. C. N. Tolentino, N. M. Souza-Neto, J. P. Itié, L. Morales, and A. Caneiro, *Phys. Rev. B* **75**, 052103 (2007).
- [26] A. Liang, C. Popescu, F. J. Manjon, P. Rodriguez-Hernandez, A. Muñoz, Z. Hebboul, and D. Errandonea, *Phys. Rev. B* **103**, 054102 (2021).
- [27] F. Aguado, F. Rodríguez, and P. Núñez, *Phys. Rev. B* **67**, 205101 (2003).
- [28] F. Aguado, F. Rodríguez, and P. Núñez, *Phys. Rev. B* **76**, 094417 (2007).
- [29] M. N. Sanz-Ortiz and F. Rodríguez, *J. Chem. Phys.* **131**, 124512 (2009).
- [30] Y. Tanabe and S. Sugano, *J. Phys. Soc. Jpn.* **9**, 753 (1954).
- [31] M. Atanasov, D. Ganyushin, K. Sivalingam, and F. Neese, in *Molecular Electronic Structures of Transition Metal Complexes II*, A Modern First-Principles View on Ligand Field Theory through the Eyes of Correlated Multireference Wavefunctions, edited by D. M. P. Mingos, P. Day, and J. P. Dahl (Springer Science & Business Media, Berlin, 2012), pp. 149–220.
- [32] L. Nataf, F. Rodríguez, and R. Valiente, *Phys. Rev. B* **86**, 125123 (2012).
- [33] J. A. Barreda-Argüeso, F. Aguado, J. González, R. Valiente, L. Nataf, M. N. Sanz-Ortiz, and F. Rodríguez, *J. Phys. Chem. C* **120**, 18788 (2016).
- [34] J. A. Barreda-Argüeso, L. Nataf, F. Aguado, I. Hernández, J. González, A. Otero-de-la-Roza, V. Luaña, Y. Jia, C. Jin, B. Kim, K. Kim, B. I. Min, W. Heribert, A. P. Jephcoat, and F. Rodríguez, *Sci. Rep.* **9**, 5448 (2019).
- [35] R. G. Burns, *Mineralogical Applications of Crystal Field Theory* (Cambridge University Press, Cambridge, 1993).
- [36] J. Ruiz-Fuertes, S. López-Moreno, J. López-Solano, D. Errandonea, A. Segura, R. Lacomba-Perales, A. Muñoz, S. Radescu, P. Rodríguez-Hernández, M. Gospodinov, L. L. Nagornaya, and C. Y. Tu, *Phys. Rev. B* **86**, 125202 (2012).
- [37] A. Liang, S. Rahman, H. Saqib, P. Rodriguez-Hernandez, A. Munoz, G. Nenert, I. Yousef, C. Popescu, and D. Errandonea, *J. Phys. Chem. C* **124**, 8669 (2020).
- [38] A. Liang, P. Rodríguez-Hernandez, A. Munoz, S. Raman, A. Segura, and D. Errandonea, *Inorg. Chem. Front.* **8**, 4780 (2021).
- [39] J. Tauc, *Mater. Res. Bull.* **3**, 37 (1968).
- [40] A. Benghia, Z. Hebboul, R. Chikhaoui, I. Khaldoun Lefkaier, A. Chouireb, and S. Goumri-Said, *Vacuum* **181**, 109660 (2020).
- [41] A. Liang, L. T. Shi, S. Gallego-Parra, O. Gomis, D. Errandonea, and I. M. Tiginyanu, *J. Alloys Compd.* **886**, 161226 (2021).
- [42] A. Mujica, A. Rubio, A. Muñoz, and R. J. Needs, *Rev. Mod. Phys.* **75**, 863 (2003).

5. Crystal structure and atomic vibration of $\text{Zn}(\text{IO}_3)_2$ under pressure

As the partial filled $3d$ orbital of transition metal will contribute to the band structure near to the Fermi level and narrow the bandgap of metal iodates, which is contrary to our goal of synthesizing wide-bandgap metal iodates, now we move our study to the closed-shell transition metal iodate, $\text{Zn}(\text{IO}_3)_2$. In this chapter we only present the study on the crystal structure and atomic vibrations under pressure. The electronic band structure of this sample will be presented in the next chapter together with that of another non-transition metal iodate, $\text{Mg}(\text{IO}_3)_2$. In this chapter, the high-pressure behavior of $\text{Zn}(\text{IO}_3)_2$ was characterized by the combination of high-pressure X-ray diffraction (HPXRD), high pressure Raman scattering (HPRS), High-pressure synchrotron based Fourier transform infrared microspectroscopy (HPFTIR), and first-principles calculations. Under pressure, $\text{Zn}(\text{IO}_3)_2$ undergoes two subtle isostructural phase transitions (IPTs) at 2.5-3.4 GPa and 8-9 GPa pressure intervals. The two IPTs were driven by the oxygen coordination increase from 3-fold to 6-fold in iodine. The coordination increase in turn is a consequence of the existence of the lone electrons pairs (LEP) in iodine and the pressure-induced shortening of the bond distance between the iodine and the oxygen in the neighboring IO_3 layer. In order to accommodate to the additional oxygen, the bond distance between the iodine and the three inlayer oxygen atoms slightly expanded under compression, and caused most of the Raman-active modes in the high-frequency region to soften under pressure. Both the Raman- and Infrared- active modes show a nonlinear pressure dependence under pressure, which supports the two IPTs we found in HPXRD. Finally, the equation of state obtained from experiments and calculations, frequency of Raman and infrared modes at ambient and high pressure, and their symmetry assignment were reported.

5.1 Introduction

At ambient conditions, $\text{Zn}(\text{IO}_3)_2$ crystallizes in a monoclinic structure (space group: $P2_1$, No. 4) which is shown in **Figure 30** [147]. The crystal structure of $\text{Zn}(\text{IO}_3)_2$ is similar to that of $\text{Co}(\text{IO}_3)_2$ but half in length in the b -axis. When view along the c -axis,

the Zn atom is surrounded by six IO_3 pyramid by sharing one oxygen, and each iodine atom is bonded with three oxygen. In the IO_3 pyramid, the pentavalent iodine will form three covalent bond with oxygen by sharing its p electrons, leaving the two s electrons free as LEPs and orient toward the opposite direction of the bottom of pyramid. When view perpendicular to the c -axis, it is a layered structure formed by IO_3 units. The same layered structure also has been observed in the structure of Fe and Co iodates.

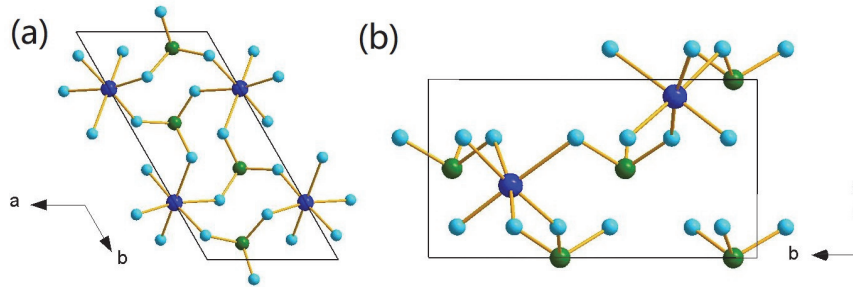


Figure 30. Crystal structure of $\text{Zn}(\text{IO}_3)_2$ at ambient pressure [147]. (a) Crystal structure projected onto ab plane and (b) Perpendicular to c axis. Blue, green and cyan-blue ball represent Zn, I and O atoms, respectively.

This chapter includes two published papers [141,148], the first one published in February 2021 [141]. In this paper we reported the HPXRD, HPRS, and first-principle study on the crystal structural and atomic vibrations of $\text{Zn}(\text{IO}_3)_2$. Two symmetry preserving phase transitions have been evidenced by the nonlinear behavior of the lattice parameters and the Raman-active modes under pressure. The driven mechanism of the pressure-induced two IPTs have been explained by the coordination changes in iodine.

The second paper for this chapter was published in December 2020 [148]. This paper reported the HPFTIR study of $\text{Zn}(\text{IO}_3)_2$. The nonlinear behavior of the infrared-active modes under pressures provides further evidence of those two IPTs we found in other diagnostics.

5.2 Experiment and calculation details

5.2.1 Sample preparation

Needle-like $\text{Zn}(\text{IO}_3)_2$ crystals were synthesized by mixing the Potassium iodate KIO_3 (2 mmol, 99.5% purity, Fluka) and zinc chloride ZnCl_2 (1 mmol, 98% purity, Riedel-deHeän) in deionized water. The mixture follows the following reaction: $2\text{KIO}_3 + \text{ZnCl}_2 \rightarrow \text{Zn}(\text{IO}_3)_2 + 2\text{KCl}$. The mixtures were slowly evaporated and maintained at 60 °C for 4 days, after that the white precipitations were obtained. Finally, the crystals were filtered and washed with deionized water.

XRD at ambient pressure was performed by using an XPERT Pro diffractometer from Panalytical employing monochromatic $\text{Cu K}\alpha_1$ radiation, to confirm the crystal structure and the purity of the sample we synthesized. The Rietveld refinement was used to refine the XRD pattern with the monoclinic crystal structure reported in the literature [147]. The quality factors of Rietveld refinement are $R_p = 7.22\%$ and $R_{wp} = 9.91\%$. The lattice parameters and atomic positions obtained from the Rietveld refinement, together with the calculated lattice parameters and the value reported in the literature, are shown in the ref. [141]. The lattice parameter from the three different sources show an excellent agreement. No XRD detectable impurity was found.

5.2.2 HPXRD

High-pressure angle-dispersive polycrystalline X-ray diffraction was conducted at BL04-MSPD beamline station of ALBA synchrotron [133]. A membrane type DAC with a diamond culet of 400 μm was used to generate the high pressure environment. A stainless-steel was firstly pre-indented to a thickness of 40 μm , and a 180- μm -hole was drilled in the center which was used as the sample chamber. A mixture of methanol: ethanol: water (MEW) at a ratio of 16:4:1 was used as the PTM. The equation of state of gold was used as the pressure gauge [92]. More information about the set-up in the beamline can be found in **Chapter 4.2.2** in this thesis.

5.2.3 HPRS

A membrane type DAC with the diamond culet of 300 μm was used to generate the high pressure environment. The sample was loaded together with Ruby gauge [93] and MEW in a 150 μm hole, drilled in the center of the pre-indented stainless-steel. More information about the Raman set-up can be found in **Chapter 3.2.4** in this thesis.

5.3.3 HPFTIR

HPFTIR was conducted at MIRAS beamline of the ALBA synchrotron [105]. A membrane type DAC designed for IR spectroscopy (IIAC-diamonds) with the diamond culet of 300 μm was used to generate the high pressure environment. Stainless-steel gasket was pre-indented to a thickness of 40 μm and drilled with a 150 μm hole in the center. CsI was used as the PTM, pressure was determined by using the ruby scale [93]. More detail of the set-up in MIRAS beamline can be found in **Chapter 3.2.3** in this thesis.

5.3.4 Overview of the Calculations

VASP within the density functional theory (DFT) framework and projector-augmented wave pseudopotential method was used to do the theoretical calculation [107–109,111–113]. The cutoff of the plane-wave energy is 540 eV, the exchange-correlation energy was described by generalized gradient approximation (GGA) with the Perdew–Burke–Ernzerhof (PBE) for solids prescription (PBEsol) [114]. The Monkhorst-Pack scheme [117] was employed to discretize the Brillouin-zone (BZ) integrations with a $4 \times 8 \times 4$ mesh to ensure accuracy. All the structure was fully relaxed and the lattice parameters were obtained at selected volumes, the lattice parameter obtained from the calculation show a good agreement with that from the HPXRD not only at ambient pressure, but also at high pressure [141], indicating a proper description of the material by calculations. The calculation on the phonons was performed at the zone center (Γ point) of the BZ by using the direct method [149], as well as the symmetry and eigenvectors of the phonons at the Γ point.

5.3 Results and Discussion

The collected XRD patterns of $\text{Zn}(\text{IO}_3)_2$ at selected pressures are shown in **Figure 31**, and the miler index of the observed diffraction peak are indexed in the XRD profile collected at 0.2 GPa. Similar to the XRD of $\text{Fe}(\text{IO}_3)_3$ and $\text{Co}(\text{IO}_3)_2$, the peaks shift in a different rate under pressure. The peak (100) moves slowly or even almost invariably under pressure, whereas the peak (101) is very sensitive to pressure. It shifts from 7 degrees at 0.2 GPa to around 9 degrees at 27.8 GPa. This behavior indicates that the crystal structure is anisotropic.

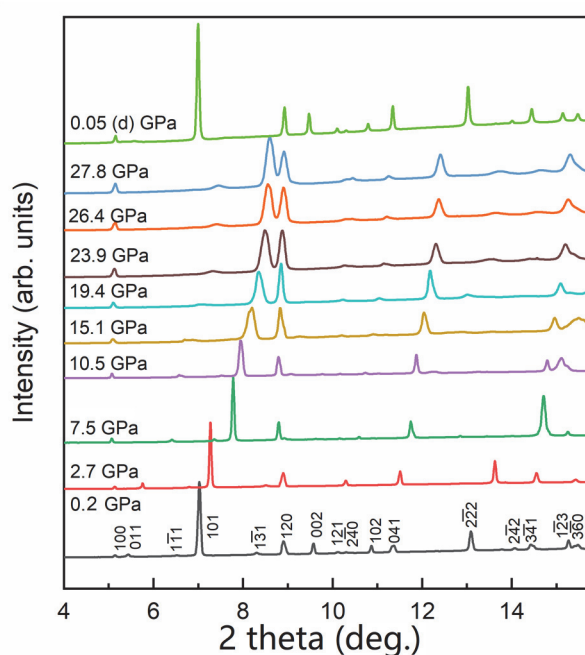


Figure 31. XRD spectra of $\text{Zn}(\text{IO}_3)_2$ at selected pressure, miler index was shown in the spectra of 0.2 GPa, the topmost spectra were collected after release the pressure and “d” means “decompression”.

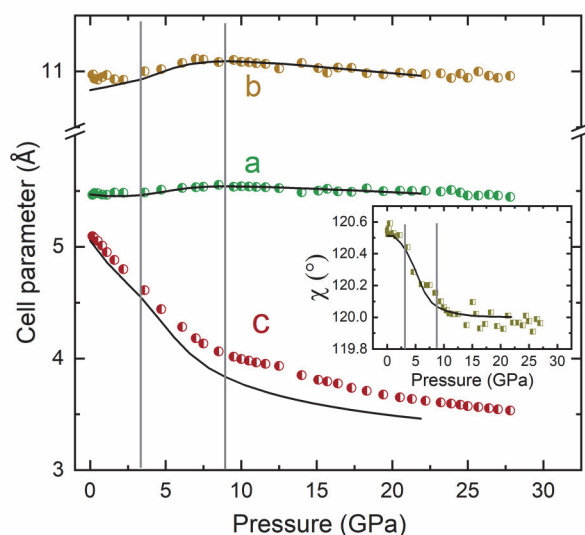


Figure 32. Experiment (dots) and calculation (solid lines) determined lattice parameter of $\text{Zn}(\text{IO}_3)_2$ as a function of pressure. The vertical dash line indicate the pressure coefficient change of the lattice parameter.

No new peaks appear, disappear or split throughout the pressure range, indicating that no first-order phase transition has taken place within the studied pressure. As the Rietveld refinement of the XRD at lowest and highest pressure shown (see ref. [141]), all the observed peaks can be assigned to the monoclinic structure we described in the **Introduction**. The changes in the XRD spectra is reversible as the topmost spectra in **Figure 31** shown.

The lattice parameters determined from experiments and calculations are shown in **Figure 32**. There is an excellent agreement between them. (i) Both of them show a discontinuity at around 3.4 and 8.9 GPa in the pressure coefficient. Lattice parameter a and c show a similar behavior. They exhibit a pressure independent behavior at pressure lower than 3.4 GPa, then slight expand with the increasing pressure at the pressure interval of 3.4 -8.9 GPa, after that there is little change with increasing pressure. (ii) Lattice parameter c decreases with increasing pressure, but also show a discontinuity at 8.9 GPa, c -axis is the most compressible axis. The anisotropic behavior of the crystal structure is related to the layered structure along the c -axis, a common feature of the studied metal iodates studied in this thesis. (iii) The monoclinic angle, γ , shows a nonlinear reduction under pressure, and fluctuates back and forth at around 120 degrees at the pressure higher than 8.9 GPa. The nonlinear pressure dependence of the lattice parameter, as well as the unit-cell volume [141], has been attributed to two IPTs

happening at 3.4 and 8.9 GPa.

A third-order BM EOS was adopted to fit the unit-cell volume obtained from experiments and calculations. The bulk modulus is 21.6 GPa and 18.4 GPa, respectively. The bulk modulus of $\text{Zn}(\text{IO}_3)_2$ is close to that of $\text{Co}(\text{IO}_3)_2$ (29.8 GPa for ambient+I1 phase in experiment). Here we use only one EOS to fit the unit-cell volume instead of two as in the study of $\text{Co}(\text{IO}_3)_2$. As ref. [141] showed, the fitting is not good, especially in the calculated unit-cell volume, which is a sign of the existence of those two IPTs. By adopting a third-order BM EOS to fit the theoretically determined volume of ZnO_6 , IO_6 and I_2O_6 polyhedra, the bulk modulus of them are 66 ± 2 GPa, 21 ± 2 GPa, and 20 ± 2 GPa, respectively. It is clear that the bulk modulus of $\text{Zn}(\text{IO}_3)_2$ is mainly determined by the compressible of IO_6 units, rather than ZnO_6 octahedra. The same relationship as observed in $\text{Fe}(\text{IO}_3)_3$ and $\text{Co}(\text{IO}_3)_2$.

Based on the fact that the calculations properly described the changes in the crystal structure under pressure, it is reasonable to analyze the pressure dependence of the Zn-O and I-O bond distances from calculation results. The same as what we observed in $\text{Co}(\text{IO}_3)_2$, all the six Zn-O bond distances show a nonlinear reduction under pressure, the slope changed at 3.8 and 8.9 GPa. These facts support the IPT we found in the changes of lattice parameter. The bond distance between iodine and inlayer oxygen become slightly longer with pressure. In contrast, the bond distance between iodine and interlayer oxygen become shorter with pressure. If we chose 2.48 \AA as the maximum distance for bonding between iodine and oxygen (25% larger than the shortest I-O bond [121]) then there is a gradually increase of the oxygen coordination in iodine. The same behavior was found also in $\text{Fe}(\text{IO}_3)_3$ and $\text{Co}(\text{IO}_3)_2$.

The Raman spectra of $\text{Zn}(\text{IO}_3)_2$ at selected pressures are shown in **Figure 33**. The spectra are similar to those of $\text{Fe}(\text{IO}_3)_3$ and $\text{Co}(\text{IO}_3)_2$. The spectra can be divided into three regions: high-frequency region with a wavenumber range from 600 to 900 cm^{-1} , contribute by the stretching of I-O bond. Mid-frequency region located in the wavenumber range from 300 to 500 cm^{-1} , and linked to the I-O bending. The low-frequency region below 200 cm^{-1} . The strongest peak is located in the high-frequency region at 782 cm^{-1} . The equivalent modes in $\text{Fe}(\text{IO}_3)_3$ is at 790 cm^{-1} and in $\text{Co}(\text{IO}_3)_2$ is at 765 cm^{-1} . It is reasonable that the strongest modes of the above studied metal iodates located at the similar frequency, since the I-O bond distance is very similar in them.

According to group theory, $\text{Zn}(\text{IO}_3)_2$ should have $27A+27B$ in total 54 vibration

modes, three of them are acoustic modes, and all the rest are both Raman- and infrared-active. At ambient pressure, 22 Raman-active modes have been detected, the results and the modes reported previously work have been summarized in ref. [141]. The symmetry of the Raman modes observed in experiments has been assigned (see Table II in ref. [141]) based on the comparison of the frequency at ambient pressure and the pressure coefficient at high pressure with that obtained from calculation. There is a phonon gap closing in the Raman spectra. This is as a consequence of the hardening of the modes in mid- and low-frequency regions and softening of the modes in the high-frequency region. Most of the modes at the high-frequency region soften under compression, which is a results of the enlargement of the I-O (inlayer oxygen) bond distances under compression.

Under a harmonic approximation, the force constant, k , of the I-O bond is a function of the negative cubic of the average I-O bond distance, $(d_{I-O})^{-3}$. Meanwhile, the frequency of the stretching mode, ω , can be written as $\omega=(k/\mu)^{1/2}$, where μ is the reduced mass. So if this approximation is correct and the modes at high-frequency region soften is related to the enlargement of the I-O (inlayer oxygen) bond distance. Then there is a linear relationship between I-O average bond distance and $\omega^{-2/3}$. Just as expected, there is a linear relationship between them as shown in **Figure 34**. Notice, the bond distance and the modes frequency are obtained from calculations.

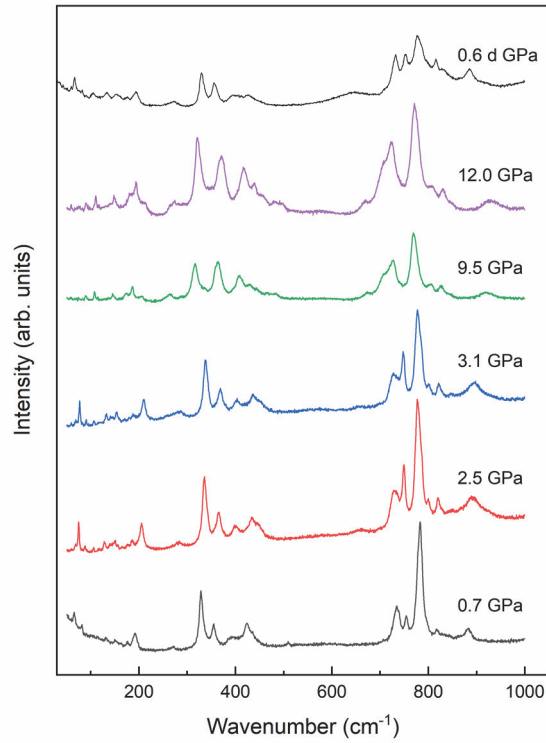


Figure 33. Raman spectra of $\text{Zn}(\text{IO}_3)_2$ at selected pressure, the topmost spectra was collected after release the pressure, “d” means “decompression”.

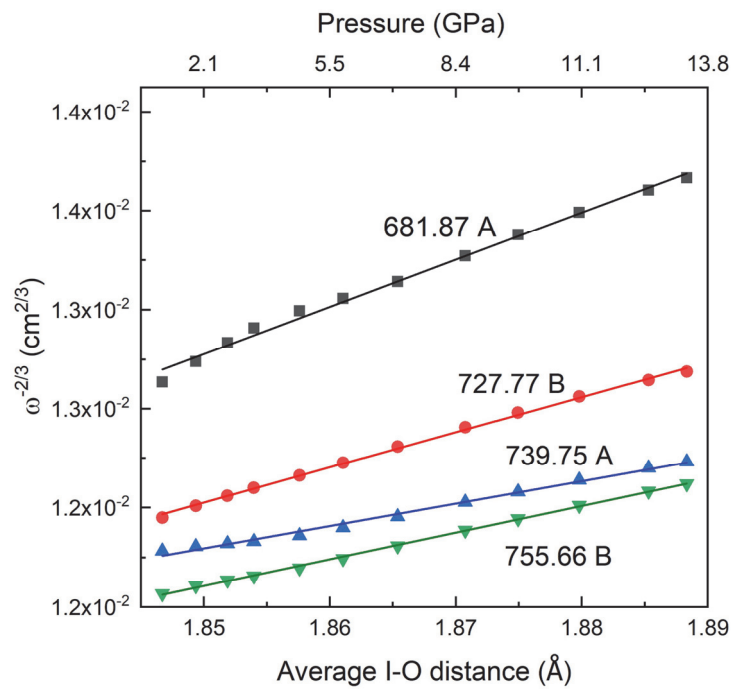


Figure 34. Relationship between the calculated average I-O bond distance and the $\omega^{-2/3}$, where ω is the calculated frequency of some modes in the high-frequency region and show a soft behavior under compression. The pressure of the bond distance was indicated in the upper axis.

The far-infrared spectra of $\text{Zn}(\text{IO}_3)_2$ at selected pressures are shown in **Figure 35**. This part of the infrared spectra corresponds to the mid-frequency and part of the low-frequency region in the Raman spectrum. As we discussed before, all the modes are both Raman and infrared-active, so in principle, the infrared and Raman modes will show similar behavior under pressure. A comparison of the frequency determined from Raman and infrared spectra was summarized in the Table 1 in ref. [148], as expected, some modes detected in Raman spectra were also observed in infrared spectra at the lowest pressure. Those modes found in infrared spectra but not in Raman spectra can complete the investigation on the vibration modes of $\text{Zn}(\text{IO}_3)_2$. In the HPFTIR spectra in **Figure 35**, all the modes shift to the higher frequency, in consistence with the modes in Raman spectra in the same frequency region. Some peaks changed in intensity at 3.6 and 8.8 GPa. They are marked by asterisks. Furthermore, the infrared-active modes show a nonlinear behavior under pressure and the slop changed at 3.6 and 8.8 GPa, such as modes 425 cm^{-1} and 440 cm^{-1} in mid-frequency region (**Figure 36b**), 158 cm^{-1} and 208 cm^{-1} in the low-frequency region (**Figure 36a**). All those changes observed in the infrared spectra are qualitatively similar to those changes found in $\text{Fe}(\text{IO}_3)_3$ and $\text{Co}(\text{IO}_3)_2$, providing further evidence of the two IPTs found in other diagnostics. It is worth noting that there is a sign change in the pressure dependence of infrared modes at around 12 GPa. These changes have not been found in any other diagnostics. They could be related to the occurrence of non-hydrostatic stresses at 12 GPa and higher pressures because the peaks become significant broad at the pressure higher than 12.1 GPa. In the hydrostaticity study on the PTM broadly used for infrared spectroscopy, the hydrostaticity of CsI is perfect at the pressure lower than 2 GPa but become worse at a pressure higher than about 16 GPa [91].

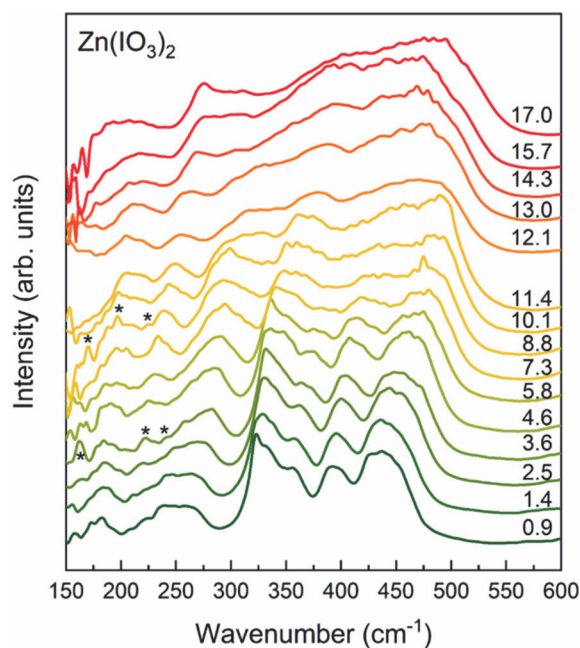


Figure 35. Infrared spectra of $\text{Zn}(\text{IO}_3)_2$ at selected pressure, the pressure of each spectrum are indicated in the right in the units of “GPa”. The asterisks are indication of the peaks intensity change.

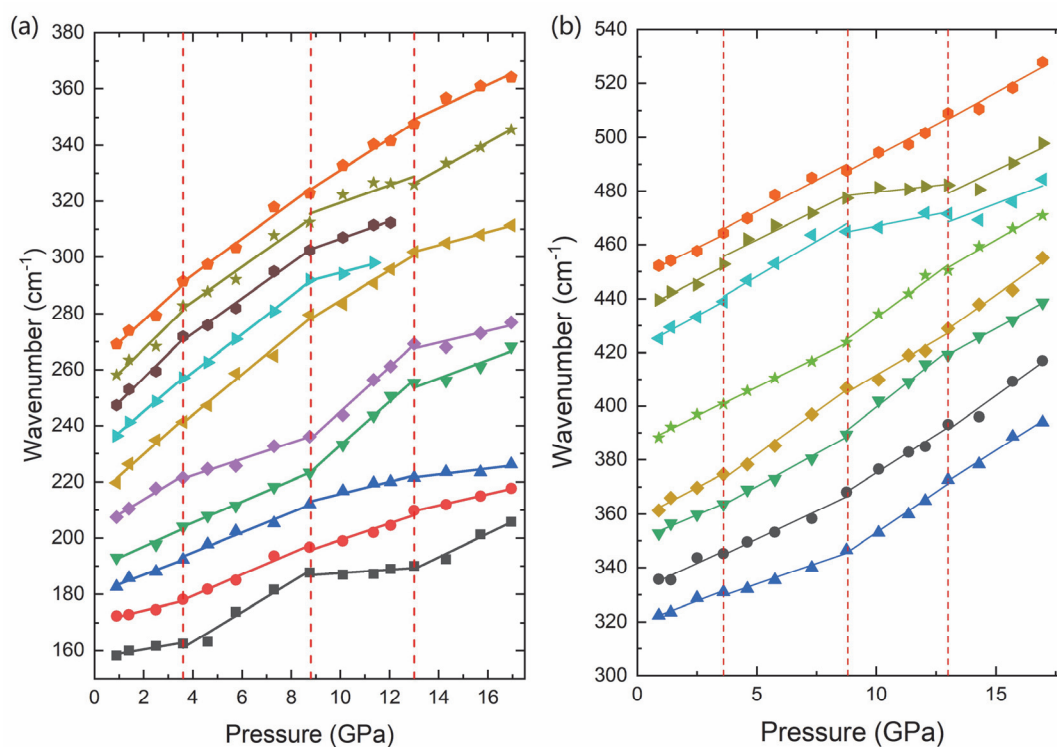


Figure 36. Pressure dependence of the Infrared modes at (a) low-frequency region, which related to the lattice modes and (b) mid-frequency region where contribute by the I-O internal bending modes. The vertical dash lines indicate the sign change of the modes under pressure.

5.4 Conclusions

- (1). $\text{Zn}(\text{IO}_3)_2$ undergoes two IPTs at the pressure range of 2.5-3.4 GPa and 8-9 GPa. The two IPTs were evidenced by the nonlinear behavior determined from experiments and calculations for the lattice parameters, unit-cell volume, and Raman and infrared-active modes under pressure.
- (2). The crystal structural behavior of $\text{Zn}(\text{IO}_3)_2$ is anisotropic, c -axis is the most compressible axis, which is caused by the layer structure formed by IO_3 units in this direction.
- (3). The bulk modulus of $\text{Zn}(\text{IO}_3)_2$ is 21.6 GPa and 18.4 GPa determined from experiments and calculations, a third-order BM EOS was adopted to fit the unit-cell volume in the whole pressure range. The bulk modulus of $\text{Zn}(\text{IO}_3)_2$ is mainly determined from the compressibility of IO_6 units.
- (4). According to the calculations, the Zn-O bond distances show a nonlinear shortening under pressure, and the slope changes at the same pressure of IPTs. The bond distances of iodine and inlayer oxygen atoms slightly increase under pressure, while the bond distances between iodine and interlayer decrease under pressure.
- (5). The oxygen coordination of iodine gradually increases from 3 to 6-fold, if we chose the 2.48 Å as the maximum bond distance between iodine and oxygen.
- (6). The Raman spectra of $\text{Zn}(\text{IO}_3)_2$ can be divided into three regions, the high-frequency region (600-900 cm^{-1}) is related to the stretching of I-O bond, the strongest mode is located at 782 cm^{-1} at ambient pressure. The mid-frequency (300-500 cm^{-1}) is related to the bending of I-O bonds, and the low-frequency region is the modes lower than 200 cm^{-1} .
- (7). Most of the modes in the high-frequency region show a soft behavior under pressure, while all the modes in the mid and low-frequency region harden under pressure, causing a phonon gap closing under pressure.
- (8). Under a harmonic approximation, the mode softening under pressure is a reason of the enlargement of the bond distance between iodine and inlayer oxygen.
- (9). The infrared-active modes also show a nonlinear behavior under pressure, the sign changes were located at 3.6 and 8.8 GPa, provide further evidence of the two IPTs found in other diagnostics.
- (10). The changes found in HPXRD, HPRS and HPFTIR are reversible.

5.5 Author contribution

The author of this doctoral thesis is the first author of the two published papers, which are the main content of this chapter. HPRS were conducted by the author. HPFTIR were conducted by the author, Robin Turnbull and Enrico Bandiello. HPXRD was conducted by Catalin Popescu. The theoretical calculations were conducted by Placida Rodriguez-Hernandez and Alfonso Muñoz. Francisco Javier Manjón provides help in the HPRS experiments and the discussion on the results. The sample used in these studies was synthesized by Zoulikha Hebboul. Ibraheem Yousef helped in the HPFTIR experiment. Daniel Errandonea supervised the project. All the data were analyzed by author, the author and Daniel Errandonea wrote the first draft of those two papers, the two papers were revised by all authors.

A. Liang, C. Popescu, F. J. Manjon, A. Muñoz, Z. Hebboul, and D. Errandonea, Structural and Vibrational Study of $\text{Zn}(\text{IO}_3)_2$ Combining High-Pressure Experiments and Density-Functional Theory, *Phys. Rev. B* **103**, 054102 (2021).

A. Liang, R. Turnbull, E. Bandiello, I. Yousef, C. Popescu, Z. Hebboul, and D. Errandonea, High-Pressure Spectroscopy Study of $\text{Zn}(\text{IO}_3)_2$ Using Far-Infrared Synchrotron Radiation, *Crystals* **11**, 34 (2021).

Structural and vibrational study of $\text{Zn}(\text{IO}_3)_2$ combining high-pressure experiments and density-functional theory

A. Liang¹, C. Popescu², F. J. Manjon³, P. Rodriguez-Hernandez⁴, A. Muñoz⁴, Z. Hebboul⁵, and D. Errandonea¹

¹*Departamento de Física Aplicada-ICMUV-MALTA Consolider Team, Universitat de València, c/Dr. Moliner 50, 46100 Burjassot (Valencia), Spain*

²*CELLS-ALBA Synchrotron Light Facility, Cerdanyola del Vallès, 08290 Barcelona, Spain*

³*Instituto de Diseño para la Fabricación y Producción Automatizada, MALTA Consolider Team, Universitat Politècnica de València, Camí de Vera s/n, 46022 València, Spain*

⁴*Departamento de Física and Instituto de Materiales y Nanotecnología, MALTA Consolider Team, Universidad de La Laguna, 38206 La Laguna, Tenerife, Spain*

⁵*Laboratoire Physico-Chimie des Matériaux (LPCM), University Amar Telidji of Laghouat, BP 37G, Ghardaïa Road, Laghouat 03000, Algeria*



(Received 16 November 2020; revised 24 January 2021; accepted 26 January 2021; published 2 February 2021)

We report a characterization of the high-pressure behavior of zinc iodate, $\text{Zn}(\text{IO}_3)_2$. By the combination of x-ray diffraction, Raman spectroscopy, and first-principles calculations we have found evidence of two subtle isosymmetric structural phase transitions. We present arguments relating these transitions to a nonlinear behavior of phonons and changes induced by pressure on the coordination sphere of the iodine atoms. This fact is explained as a consequence of the formation of multivalent bonding at high pressure which is favored by the lone-electron pairs of iodine. In addition, the pressure dependence of unit-cell parameters, volume, and bond distances is reported. An equation of state to describe the pressure dependence of the volume is presented, indicating that $\text{Zn}(\text{IO}_3)_2$ is the most compressible iodate among those studied up to now. Finally, phonon frequencies are reported together with their symmetry assignment and pressure dependence.

DOI: [10.1103/PhysRevB.103.054102](https://doi.org/10.1103/PhysRevB.103.054102)

I. INTRODUCTION

Metal iodates form a group of materials that have been intensively studied as promising nonlinear optics (NLO) materials [1–3] in the visible-, near-, and midinfrared (IR) ranges of the electromagnetic spectrum. Moreover, recent density-functional theory (DFT) calculations reveal that metal iodates exhibit large or even giant elastocaloric (EC) effect, which made them promising materials for developing solid-state cooling technologies [4,5]. These materials are of interest also for fundamental research owing to the presence of stereochemically active lone electron pairs (LEPs) on iodine atoms.

Of special interest are the studies of the crystal structure and vibration behavior of metal iodates at high pressure (HP). Recently, we have reported a comprehensive crystal structure and vibration study of $\text{Fe}(\text{IO}_3)_3$ under compression employing x-ray diffraction, IR spectroscopy, Raman scattering (RS) measurements, and first-principles DFT calculations [6,7]. Three isostructural phase transitions (IPTs) were found at 1.5, 5.7, and 22 GPa, respectively. The first two transitions do not involve detectable discontinuities in the unit-cell volume, but the third transition has associated a large volume collapse, being a first-order transition. The sequence of transformations is accompanied by a gradual increase of iodine (I) coordination from three to six [6]. The rich phase transition sequence and coordination change is mostly due to changes associated

with the LEPs of I atoms [7]. As we have demonstrated in the previous HP-study of $\text{Fe}(\text{IO}_3)_3$, iodates seem to exhibit many unusual and interesting properties and changes at HP [6,7]. However, until now, except for $\text{Fe}(\text{IO}_3)_3$, only the behavior of the crystal structure of LiIO_3 [8–10], KIO_3 [11], and AgIO_3 [12] has been studied at HP. This does not include other properties, such as lattice vibrations, electronic density of states, and electronic band structure. For $\text{Zn}(\text{IO}_3)_2$, its crystal structure [13–15], Raman and IR spectrum [16,17] have been well studied at ambient conditions, but research at HP is not available.

Here we extend the HP study on another metal iodate, $\text{Zn}(\text{IO}_3)_2$. At ambient conditions, $\text{Zn}(\text{IO}_3)_2$ crystallizes in a monoclinic structure (space group: $P2_1$, $Z = 4$) [15], which is shown in Fig. 1. In this structure ZnO_6 octahedral units are bridged by IO_3 triangular pyramids (see Fig. 1). In the IO_3^- anion, iodine, with a valence configuration $5s^25p^5$, is pentavalent and forms three covalent bonds with oxygen by sharing its p electrons, leaving the $5s$ electrons free to orient along the c axis, showing an IO_3E configuration, E being the LEP. This characteristic of the IO_3^- anion triggers an interesting and unusual behavior in $\text{Fe}(\text{IO}_3)_3$ at HP [6,7,11,12]. Apart from that, the LEP-induced anharmonicity can provide an efficient way to minimize the lattice thermal conductivity [18,19]. These characteristics are shared by the crystal structures of $\text{Zn}(\text{IO}_3)_2$ and $\text{Fe}(\text{IO}_3)_3$, which suggests that $\text{Zn}(\text{IO}_3)_3$ could potentially have a quite interesting EC effect at HP.

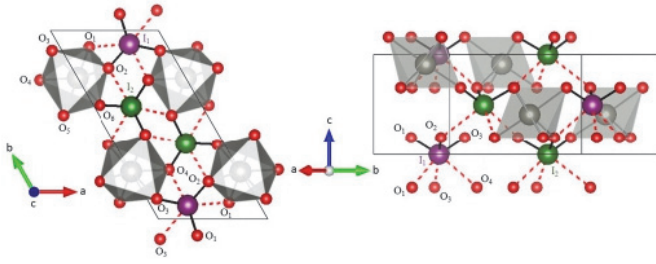


FIG. 1. Crystal structure of $\text{Zn}(\text{IO}_3)_2$ at ambient conditions. (a) Schematic crystal structure projected onto ab plane and (b) in a perspective where all iodine atoms in the unit cell can be seen. I atoms are shown in purple (I_1) and green (I_2) color. The Zn coordination octahedral units are shown in gray. O atoms are shown in red and have been labeled. First-neighbor I-O bonds are shown with solid black lines and second-neighbor I-O bonds are shown with red dashed lines. First-neighbor O atoms of Zn have been labeled in one octahedron. First and second neighbors of I_1 have also been labeled for the I_1 atom in the bottom part of the structure.

In this paper, HP x-ray diffraction (HP-XRD), HP Raman scattering (HP-RS), and DFT calculations have been used to investigate the HP behavior of $\text{Zn}(\text{IO}_3)_2$. Two symmetry-preserving phase transitions have been found. Their existence has been related to changes found in the iodine atom coordination. We have also observed the existence of soft-phonon modes, which have been found in the high-frequency range in HP-RS studies. These vibrations have been associated with the vibration behavior of I-O bonds. All of the experimental data will be compared with DFT simulations, giving a deep insight into the structural and vibrational behavior of $\text{Zn}(\text{IO}_3)_2$ under pressure.

II. METHODS

A. Sample preparation

For the study of $\text{Zn}(\text{IO}_3)_2$, micrometer-sized needlelike crystals were synthesized from an aqueous solution [20]. $\text{Zn}(\text{IO}_3)_2$ was prepared by mixture of potassium iodate KIO_3 (2 mmol, 99.5% purity) and zinc chloride ZnCl_2 (1 mmol, 98% purity) in deionized water: $2\text{KIO}_3 + \text{ZnCl}_2 \rightarrow \text{Zn}(\text{IO}_3)_2 + 2\text{KCl}$. The reagents were purchased from Fluka (KIO_3) and Riedel-deHeñ (ZnCl_2). The reaction mixtures were slowly evaporated and maintained at 60°C for 4 d, leading to the formation of white precipitations. We filtrated and washed the crystals with deionized water.

To confirm the purity and crystal structure of $\text{Zn}(\text{IO}_3)_2$, we performed powder XRD measurements at room conditions (see Fig. 2) using an XPERT Pro diffractometer from Panalytical in a reflection Bragg-Brentano geometry and employing monochromatic $\text{Cu } K_{\alpha 1}$ radiation. The Rietveld refinement method [21] was adopted to analyze the phase and lattice parameter information. The structural information of $\text{Zn}(\text{IO}_3)_2$ reported by Liang *et al.* [15] (space group $P2_1$) was used as a starting point to do the refinement. We have found in the refinement that all the peak positions match very well and that the intensity of most peaks agrees with those already reported except for some peaks between 30° – 50° due to the partially preferred direction of the needle-shaped sample. The

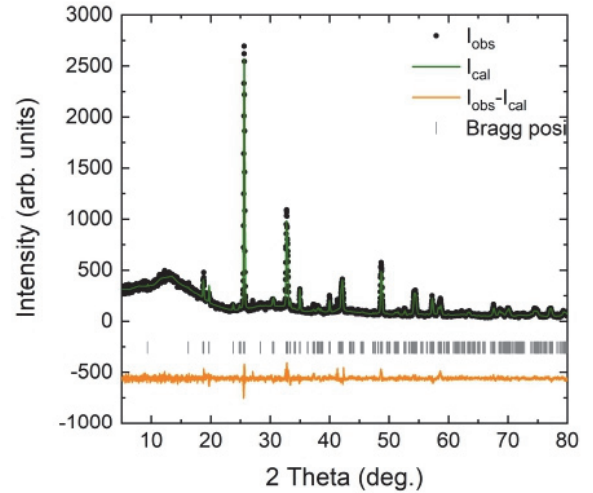


FIG. 2. XRD pattern measured at ambient pressure (circles). The green line is the Rietveld refinement. The quality factors of Rietveld refinement are $R_p = 7.22\%$ and $R_{wp} = 9.91\%$. Residuals are shown in orange.

lattice parameters obtained from our refinements and DFT calculations are listed in Table I and compared with the values reported in the literature [15]. The atomic positions are given in the Supplemental Material (Table S1) [22]. The agreement regarding unit-cell parameters is good, differences between experiments and calculations being within 1%.

B. High-pressure experiment details

Angle-dispersive powder HP-XRD experiments were performed at room temperature up to 27.8 GPa employing a membrane diamond-anvil cell (DAC), with diamond culets of $400\ \mu\text{m}$. For these experiments the $\text{Zn}(\text{IO}_3)_2$ sample was grinded to obtain a micrometer-size powder which was loaded in a $180\text{-}\mu\text{m}$ -diameter hole drilled on a stainless-steel gasket preindented to a thickness of $40\ \mu\text{m}$. We paid special attention to occupy with the sample a small fraction of the gasket hole to prevent the sample bridging between the diamond culets because of the thinning of the gasket under compression. Pressure was measured using the equation of state of gold [23] and a 16:3:1 methanol:ethanol-water mixture was used as the pressure-transmitting medium (PTM) [24]. Experiments were performed at the BL04-MSPD of ALBA synchrotron [25]

TABLE I. Summary of the lattice parameters and volume, V_0 , of $\text{Zn}(\text{IO}_3)_2$ at ambient pressure from calculations (DFT) and experiments (Exp.). Previous experimental data from Ref. [15] are also included for comparison.

	DFT ^a	Exp. ^a	Exp. [15]
a (Å)	5.469	5.465(4)	5.469
b (Å)	10.832	10.952(8)	10.938
c (Å)	5.054	5.129(4)	5.1158
γ ($^\circ$)	120.514	120.37(8)	120.000
V_0 (Å ³)	258.00	264.8(4)	265.03

^aThis work,

with a monochromatic x-ray beam ($\lambda = 0.4246 \text{ \AA}$) focused to a $20\text{-}\mu\text{m} \times 20\text{-}\mu\text{m}$ full with at half maximum spot.

HP-RS measurements were performed in $\text{Zn}(\text{IO}_3)_2$ needle-shaped crystals also with a DAC, where sample and ruby chips were loaded in the $150\text{-}\mu\text{m}$ -diameter hole of a preindented steel gasket. Based upon the results of HP XRD studies (which showed that phase transitions occur below 10 GPa as we will discuss in the next section) Raman studies were limited to 12 GPa. Again a 16:3:1 mixture was used as PTM [24]. Pressure was determined using the ruby fluorescence scale [26]. We paid special attention during sample loading to avoid the hydration of the metal iodates [27]. We also made a careful loading avoiding sample bridging between diamond anvils [28]. Measurements were performed in a backscattering geometry employing a HeNe laser (632.8 nm) with a 10-mW power and a HORIBA Jobin Yvon LabRAM HR UV microspectrometer with a spectral resolution better than 2 cm^{-1} .

C. *Ab initio* simulations

Calculations of the total energy as a function of pressure for $\text{Zn}(\text{IO}_3)_2$ were performed using the Vienna *Ab initio* simulations package (VASP) [29–32] within the framework of the density functional theory [33] and the projector-augmented wave pseudopotential method [34,35]. A high plane-wave energy cutoff of 540 eV was used to obtain accurate results. The exchange-correlation energy was described within the generalized gradient approximation (GGA) with the Perdew–Burke–Ernzerhof (PBE) for solids prescription (PBESOL) [36]. The Monkhorst–Pack scheme [37] was employed to discretize the Brillouin-zone (BZ) integrations with a $4 \times 8 \times 4$ mesh to ensure accuracy. We tested that this mesh is sufficient to avoid all nonsystematic discretization errors.

With this procedure, very high convergences of 1 meV per formula unit in the total energy are achieved and in the optimized configurations, the forces are lower than 2 meV/\AA per atom and the deviation of the stress tensor from a diagonal hydrostatic form is less than 0.1 GPa. All the structural parameters were obtained at selected optimized volumes. The agreement of the calculations with experiments regarding the crystal structure (within 1%, see Table II), supports that our DFT calculations properly describe $\text{Zn}(\text{IO}_3)_2$.

After optimizing the crystal structure at different pressures, a study of the phonons was performed at the zone center (Γ point) of the BZ using the direct method [38]. These calculations also allow identifying the symmetry and eigenvectors of the phonon modes at the Γ point.

III. RESULTS AND DISCUSSION

A. Structural study

Figure 3 shows HP-XRD patterns of $\text{Zn}(\text{IO}_3)_2$ at selected pressures. At the lowest pressure, all of the peaks can be assigned to the monoclinic structure we described above. Some peaks, like (120) and (041) peaks, show a relative intensity change with increasing pressure. This is due to preferred orientations related to the needle-shaped sample. We must note that preferred orientations were present at ambient pressure and become more obvious as pressure increases. From ambient to the highest pressure, all the XRD patterns can be

identified in the same space group. Since Fig. 3 shows only a selection of pressures, in the Supplemental Material [22] we include a figure (Fig. S1) with multiple XRD patterns to illustrate in more detail the gradual evolution of XRD patterns with no qualitative changes in the whole pressure range covered by experiments. However, as we will discuss below we will show that subtle changes observed in the pressure evolution of lattice parameters suggest the existence of isosymmetric structural phase transitions. The changes induced by pressure in XRD patterns are reversible as can be seen in Fig. 3 in the XRD pattern measured at ambient pressure after the decompression process.

Under compression, most diffraction peaks shift to higher angles, as expected [39]. However, some peaks, like (100), (120), and $(3\bar{4}1)$, have a different behavior. In particular, the d -spacing (see Fig. S2 in Supplemental Material [22]) of the above-mentioned peaks first increases with pressure and then remain almost unchanged or reduce to a very small extent. Moreover, it must be noticed that d -spacings of $(hk0)$ peaks change much less than the (hkl) peaks with $l \neq 0$. Lattice planes like (001), $(1\bar{1}1)$, (101), (002), and (102) have a high-pressure dependence comparable to other lattice planes. Therefore, we can ascribe the different shift rates of the XRD peaks, and even the opposite shifts of some peaks, to the anisotropic compressibility of $\text{Zn}(\text{IO}_3)_2$ which we will discuss in detail later. Another consequence of the anisotropic compression of $\text{Zn}(\text{IO}_3)_2$ is the merging and crossing of several XRD peaks (or d -spacings).

Before discussing the pressure dependence of unit-cell parameters and volume in detail, we would like to comment on the peak broadening observed in XRD peaks beyond 10 GPa. This can be seen in Figs. 3 and S1, in particular for peaks (100), (120), and $(3\bar{4}1)$. This peak broadening is caused by the nonisotropic compression of $\text{Zn}(\text{IO}_3)_2$ which we have described above. The peaks we labeled as (101), (120), and (041) are in fact multiples corresponding to $(021)/(101)$, $(1\bar{4}0)/(2\bar{2}0)/(120)$, and $(201)/(2\bar{4}1)/(041)$, respectively. Due to the anisotropic compression of $\text{Zn}(\text{IO}_3)_2$ the degeneracy of these multiples is broken around 10 GPa with the consequent peak broadening. We are aware that this phenomenon happens near the pressure where methanol-ethanol-water become a hard glass [24], and thus part of the broadening could be related to nonhydrostatic effects. However, since the conclusions we will report are supported by computer simulations (done under hydrostatic conditions) we consider that the phase transition we will report near 10 GPa is genuine, and not triggered by nonhydrostatic effects (or sample bridging).

Figure 4 shows the experimental and theoretical pressure dependence of the unit-cell volume of $\text{Zn}(\text{IO}_3)_2$. A continuous change of the experimental unit-cell volume of the monoclinic structure is found along the whole pressure range up to 28 GPa with no appreciable jump in volume at any pressure. A third-order Birch–Murnaghan (BM) [40,41] equation of state (EOS) was adopted to fit the volume within the whole pressure range. The bulk modulus is 21.6(0.7) and 18.4(1.5) GPa according to experiments and calculations and the corresponding pressure derivative is 7.0(0.3) and 6.7(0.7), respectively. Experiment and calculation describe a similar high-compressibility behavior of $\text{Zn}(\text{IO}_3)_2$ at low pressures and the minor difference between them is within a reasonable error [42]. However,

TABLE II. Calculated and measured zero-pressure frequencies (ω), pressure coefficients, and Grüneisen parameters of the Raman-active modes of $\text{Zn}(\text{IO}_3)_2$. Bulk moduli used to calculate Grüneisen parameters were obtained from our DFT-calculated and HP-XRD data. Results are compared with previous experiments [16,17].

Mode	Theory ($B_0 = 18.4$ GPa)			Experiment ($B_0 = 21.6$ GPa)				
	ω (cm^{-1})	$d\omega/dP$ ($\text{cm}^{-1}/\text{GPa}$)	γ	ω (cm^{-1})	$d\omega/dP$ ($\text{cm}^{-1}/\text{GPa}$)	γ	ω [17]	ω [16]
A	65.11	6.53	1.84	62	6.62	2.31	61	
B	68.35	1.06	0.28	67				
A	79.19	3.66	0.85	80	3.63	0.99	80	80
B	82.56	2.49	0.55					
A	101.30	2.07	0.38					
B	110.08	2.30	0.38	101	2.85	0.61	100	
A	117.58	11.84	1.85	111	8.60	1.67	111	113
B	130.82	6.62	0.93					
A	136.49	3.64	0.49	128	11.73	1.99	130	132
A	142.00	5.96	0.77	149			148	
B	148.24	2.43	0.30					
A	155.14	6.44	0.76					
B	165.41	8.50	0.95	156	3.71	0.51	155	152
A	171.85	6.49	0.70	173	7.28	0.91	173	173
B	173.82	5.64	0.60					
A	177.56	8.20	0.85					
B	178.19	6.34	0.65					
A	185.36	3.07	0.30					
B	193.47	6.39	0.61	187	7.54	0.87	187	189
A	196.60	10.48	0.98					
B	212.11	3.76	0.33					
A	212.35	0.96	0.08					
B	224.42	9.35	0.77					
B	237.16	9.88	0.77					
A	239.73	7.41	0.57					
B	243.07	8.52	0.64					
A	262.65	5.34	0.37	264	5.77	0.47	265	267
A	307.48	3.41	0.20					
B	309.88	4.45	0.26					
B	325.39	1.54	0.09	327	3.80	0.25	327	327
A	332.93	5.28	0.29					
A	337.63	4.90	0.27					
B	344.67	5.82	0.31	351	5.77	0.35	351	354
A	374.06	5.22	0.26					
B	375.29	3.13	0.15					
A	395.74	5.60	0.26	391	2.36	0.13	387	391
A	405.78	7.23	0.33	422	6.96	0.36	422	424
B	411.42	6.35	0.28					
B	428.70	5.74	0.25	432	10.06	0.50		
B	627.57	-6.90	-0.20	713			728	
A	656.22	-3.85	-0.11					
B	661.86	-9.36	-0.26					
A	666.36	-3.84	-0.11					
B	673.73	-6.06	-0.17	734	-2.93	-0.09	733	735
A	681.87	-5.62	-0.15					
A	688.54	-0.72	-0.02	757	-2.75	-0.08	756	760
A	715.60	-8.74	-0.22	782	-1.29	-0.04	781	782
B	727.77	-3.09	-0.08				796	
A	739.75	-0.85	-0.02					
B	755.66	-2.08	-0.05	817	-0.22	-0.01	815	815
B	767.03	2.02	0.05	840	7.79	0.20	838	836

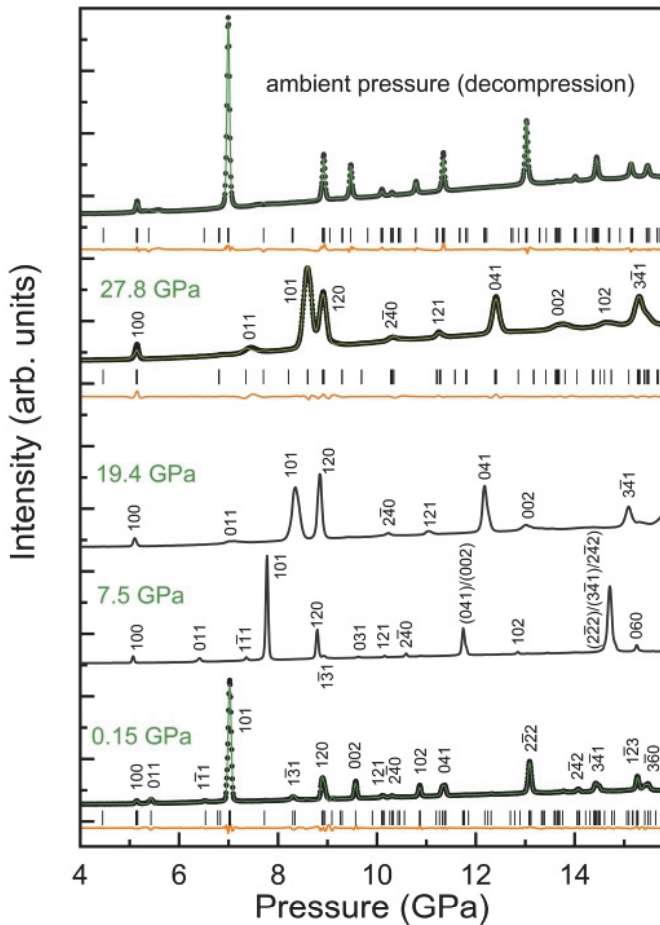


FIG. 3. Selected XRD patterns of $\text{Zn}(\text{IO}_3)_2$ under pressure. Bottom and top patterns show the refinement at the lowest pressures of the compression and decompression processes. Experimental data, refinement data, and residuals are plotted with dots, green and orange lines, respectively. The Bragg peak positions (black vertical lines) are also shown. A figure including more patterns can be found in the Supplemental Material (Fig. S1) [22].

the difference between experimental and calculated volumes becomes more pronounced as the pressure is increased, in opposition to the general systematic followed by oxides [42]. This could be a consequence of the formation of new I-O bonds under HP (as we will discuss later) which enhances localization of electronic states (in opposition to the electron delocalization induced by pressure in oxides). In this context, we must note that while our experimental data can be reasonably fitted to a single third-order EOS, our theoretical data do not fit nicely to a third-order EOS along the whole pressure range, especially between 3 and 10 GPa. This fact could be related to the occurrence of isosymmetric phase transitions in $\text{Zn}(\text{IO}_3)_2$, which will be discussed in the following paragraphs.

In our previous study [7], we summarized the bulk modulus of some metal iodates, including $\text{Fe}(\text{IO}_3)_3$ [7], LiIO_3 [9,10], KIO_3 [11], and $\text{LiZn}(\text{IO}_3)_3$ [43]. The bulk modulus of $\text{Zn}(\text{IO}_3)_2$ is equivalent to that of the ambient-pressure phase of KIO_3 [11], about two-thirds of that of LiIO_3 reported by our calculations [7] and Hu *et al.* [9], and two-fifths of that of the low-pressure phase of $\text{Fe}(\text{IO}_3)_3$ [7] and $\text{LiZn}(\text{IO}_3)_3$ [43].

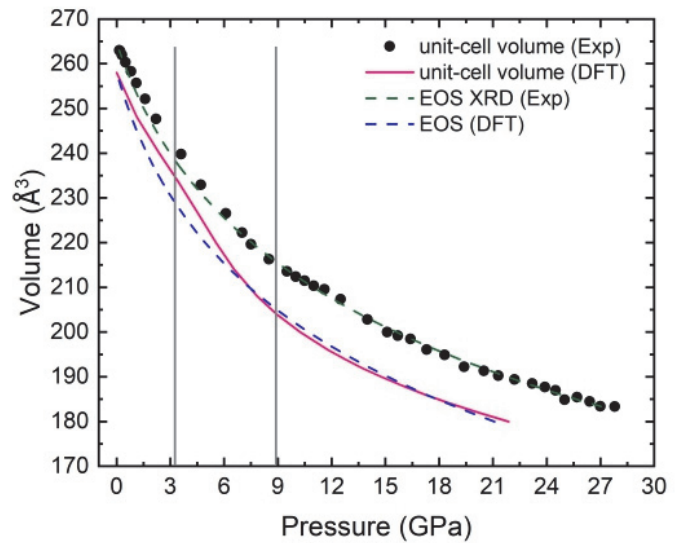


FIG. 4. Pressure dependence of the unit-cell volume. The black circles are the results of experiments and the magenta solid lines the results of calculations. The equations of state described in the text are shown with dashed lines. The vertical lines indicate the transition pressures.

Thus $\text{Zn}(\text{IO}_3)_2$ is one of the most compressible iodates, being as compressible as metal-organic frameworks [44] and group-XV oxides containing cationic LEPS [45,46], and having a bulk modulus only 30% larger than argon [47].

In order to further characterize volume changes, we have used a third-order BM EOS to describe the pressure dependence of the ZnO_6 , IO_6 , and I_2O_6 octahedral volumes (here we assume a 3+3 coordination of I). In this scenario, we obtain zero-pressure bulk moduli of 66(2), 21(2), and 20(2) GPa, with corresponding pressure derivatives of 4.2(0.5), 5.3(0.5), and 5.3(0.5), respectively. Since we already know that the bulk modulus of bulk $\text{Zn}(\text{IO}_3)_2$ is 21.6 GPa in the experiment and 18.4 GPa in the calculations, it is clear that the bulk modulus of the crystal is mainly determined by the compression of IO_6 units, rather than the compression of the ZnO_6 unit. This result is similar to what has been found in $\text{Fe}(\text{IO}_3)_3$ [7].

From Rietveld refinement of HP-XRD patterns, we have studied the evolution of unit-cell parameters of $\text{Zn}(\text{IO}_3)_2$ under pressure. To illustrate the quality of refinements we show them at 0.15 GPa, 27.8 GPa, and ambient pressure after decompression. The quality factors of Rietveld refinement are $R_p = 5.32\%$ and $R_{wp} = 7.19\%$ (0.15 GPa), $R_p = 5.86\%$ and $R_{wp} = 7.58\%$ (27.8 GPa), and $R_p = 5.48\%$ and $R_{wp} = 7.32\%$ (ambient pressure after decompression). Experimental results are compared with the results of DFT calculations in Fig. 5. There is an excellent agreement between experimental and theoretical results. Thus, we conclude that our calculations describe properly the crystal behavior under compression. As can be seen in Fig. 5, the behavior is strongly anisotropic. In addition, distinctive behaviors are observed for pressure ranges separated by vertical lines in Fig. 5 ($P < 3.4$ GPa, 3.4 GPa $< P < 8.9$ GPa, $P > 8.9$ GPa). In the low-pressure range, the linear compressibilities of a - and b axes are similar and very small. In the medium-pressure range, they are even negative. Finally, in the high-pressure range, both unit-cell

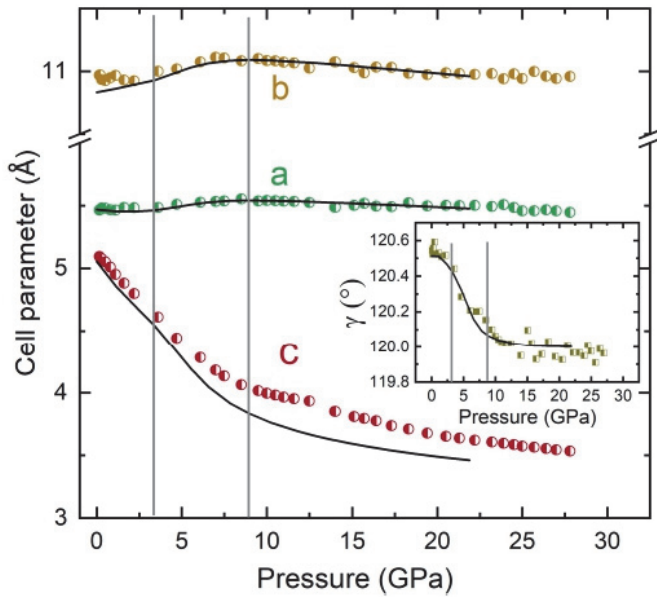


FIG. 5. Pressure dependence of the unit-cell parameters of $\text{Zn}(\text{IO}_3)_2$. The inset shows the evolution of the monoclinic angle γ . Half-filled circles or squares are the experimental data while DFT calculation results are shown in black solid lines.

parameters show a similar slow decrease with pressure. In contrast, the behavior of the c axis is very different, being much more compressible than the other two axes, at least in the two first pressure ranges, and showing a strong decrease of the compressibility in the third pressure range. The much higher compressibility of the c axis at low pressures is a consequence of the quasilayered structure formed by IO_3 polyhedra and connected by ZnO_6 octahedron along this direction (see Fig. 1). Note that the structure is not strictly layered because ZnO_6 octahedra connect alternate IO_3 layers; however, IO_3E units lead to considerable empty spaces in the structure along the c axis where the iodine LEs are located. The collapse of the space between IO_3 layers contributes to the high compressibility of the c axis and favors the formation of three additional I-O bonds. In contrast, the alternate arrangement of the ZnO_6 octahedron and IO_3 tetrahedron along a - and b axes strengthen the force and resist compression along those directions.

To highlight the different behavior of the axes in $\text{Zn}(\text{IO}_3)_2$, we plot in Fig. S3 the ratio between lattice parameters as a function of pressure. It can be seen that the b/a ratio is almost insensitive to pressure, but b/c and a/c have a subtle slope change at 3.4 and a more drastic slope change at 8.9 GPa that agree with those observed in the lattice parameters and the monoclinic gamma angle, as commented below. These changes are more evident in experiments than in calculations, but are detected by both methods.

We will comment now on the pressure dependence of the monoclinic γ angle (inset of Fig. 5). Before doing that, we would like to mention that at the lowest pressure (0.15 GPa) we got an experimental γ angle of $120.5(1)^\circ$, which is slightly higher than the ambient pressure value [$120.37(8)^\circ$] but comparable within error bars. Upon compression, we have found both an experimental and theoretical S -like nonlinear

pressure dependence of the monoclinic angle γ that is related to the symmetry increase of ZnO_6 and IO_6 polyhedra under pressure, with changes of slope near 3.4 and 8.9 GPa, in good agreement with the changes observed in the lattice parameters.

Based upon the good agreement between calculations and experiments regarding the pressure dependence of structural parameters and the difficulty to obtain reliable atomic positions from our HP-XRD measurements due to the influence of preferred orientations, we have performed a more detailed analysis of the theoretical data to investigate the behavior of the monoclinic structure near 3.4 and 8.9 GPa. In particular, we have used those data to calculate the pressure dependence of the theoretical distortion index $D = \frac{1}{n} \sum \frac{|l_i - l_{av}|}{l_{av}}$ (where n is the number of bonds, l_i is the distance from the central atom to the i th coordinating atom, and l_{av} is the average bond length) [48] of both polyhedra as calculated by using VESTA [49] (see Fig. S4 in the Supplemental Material [22]). The decrease of the distortion index of both polyhedra upon compression suggests a symmetry increase of both polyhedra under pressure. An almost linear decrease of the distortion index of IO_6 units is observed. Additionally, an S -like nonlinear decrease of the distortion index of ZnO_6 units with changes in slopes near 3.8 and 8.9 GPa are observed. The sum of the pressure effect on both polyhedra causes the nonlinear change of γ under pressure. Moreover, the changes observed in both polyhedra lead to: (i) a symmetrization of the ZnO_6 octahedron, and (ii) the gradual formation of IO_6 octahedra; i.e., an increase of I coordination due to the rapid decrease of the second-nearest neighbor I-O distances (represented in dashed lines in Fig. 1). These are evidence of the anisotropic compression of $\text{Zn}(\text{IO}_3)_2$. We will comment more on this unusual behavior below when talking about the behavior of Zn-O and I-O distances.

We think the structural changes observed at 3.4 and 8.9 GPa are caused by two subtle isostructural phase transitions [50,51] (understood as transitions between two phases having the same space group, involving subtle changes in cell dimensions and changes in polyhedral coordination). More evidence of the existence of the two IPTs is shown in Figs. S5–S13 in the Supplemental Material [22], where the pressure dependence of the theoretical atomic coordinates of Zn, I, and O atoms are presented. Just as an example, we will comment on the calculated y atomic coordinate of Zn (see Fig. S5). Its initial value 0.7460 decreases sharply to 0.7452 at 2.5 GPa, and then increases to 0.7482 at 8.9 GPa; above this pressure, there is a sudden slope change, increasing slowly to 0.7488 at 21.9 GPa. The whole picture of the evolution is nonlinear having an S -like shape. A similar S -like evolution of the atomic positions can be seen also in other atoms, thus supporting the two IPTs already commented.

More evidence for the two IPTs can be found in the theoretical pressure dependence of the Zn-O and I-O distances and, more importantly, in the experimental and calculated Raman-mode evolution under pressure to be discussed in the next section. Regarding the pressure dependence of the Zn-O distances (see Fig. 6), one can notice an unusual S -like behavior for most Zn-O bond distances, except for Zn– O_3 . The behavior of the three short Zn-O bonds is consistent with the proposed IPTs at 3.4 and 8.9 GPa, with a decrease of the bond distances up to 3.8 GPa, an increase above this pressure

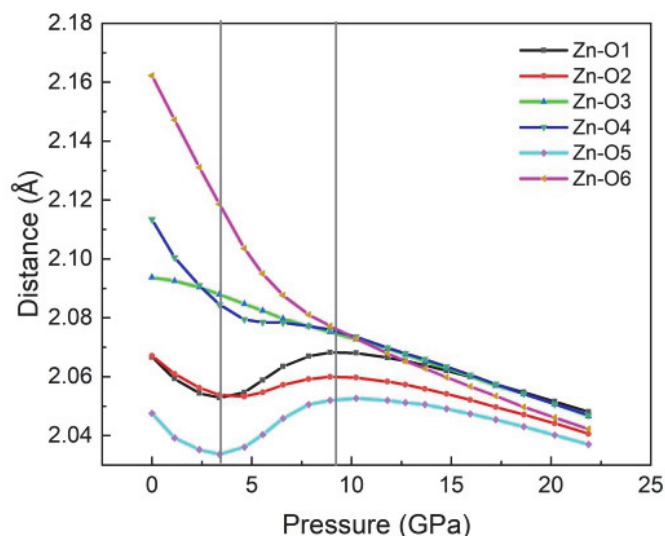


FIG. 6. Pressure dependence of the theoretical Zn-O bond distances.

and up to 8.9 GPa followed by a new decrease above this pressure. We can observe a considerable decrease of the three longest Zn-O bond distances to achieve an almost regular ZnO₆ polyhedron above 9.8 GPa, as already pointed out by the polyhedral distortion (Fig. S4).

As regards the pressure dependence of the I-O distances, we must recall that there are two different atomic positions for iodine, I₁, and I₂ (see Fig. 1 and Table S1 in Supplemental Material [22]). Each type of iodine atom is shown with a different color in Fig. 1. However, both coordination polyhedra are extremely similar. For instance, I₁-O distances are 1.8474, 1.8466, and 1.8462 Å at ambient pressure and I₂-O distances are 1.8475, 1.8452, and 1.8447 Å, behaving both polyhedra similarly under compression; indeed, their compressibility is very similar as commented before. Thus for the sake of brevity, here we will focus on the change of I₁-O bond distances with pressure (Fig. 7). As observed, for the I₁ atom there are three short I-O distances (I₁-O₁, I₁-O₂, and I₁-O₃) and three large distances above 2.5 Å at room pressure (I₁-O'₁, I₁-O'₃, and I₁-O'₄, which correspond to second neighbors; primes are used to identify second neighbors). In the IO₆ polyhedron, these three second-neighbor O atoms show distances above 2.5 Å and are not forming a bond with I at low pressure. As pressure increases, these long distances show a strong decrease and gradually form new bonds. We can find a gradual I coordination change if we choose 2.48 Å as the maximum bonding distance (a value 25% larger than the shortest I-O distance). [52]. In this way, with increasing pressure, O'₁, O'₃, and O'₄, which is on the side of the iodine LEPs, approaches I₁, first forming new I-O bonds with iodine at around 2.5 GPa, and then the I atom becomes sixfold coordinated above around 8 GPa due to the decrease of the I-O'₃ distance. On the other hand, at ambient pressure, the ZnO₆ octahedron is more symmetrical than the IO₆ octahedron, and compared with the change in the bond distance between Zn and O under pressure (the largest change is the change in the bond distance between the Zn and O₆ atoms, from 2.16 to 2.04 Å, 5.6% reduction), the change

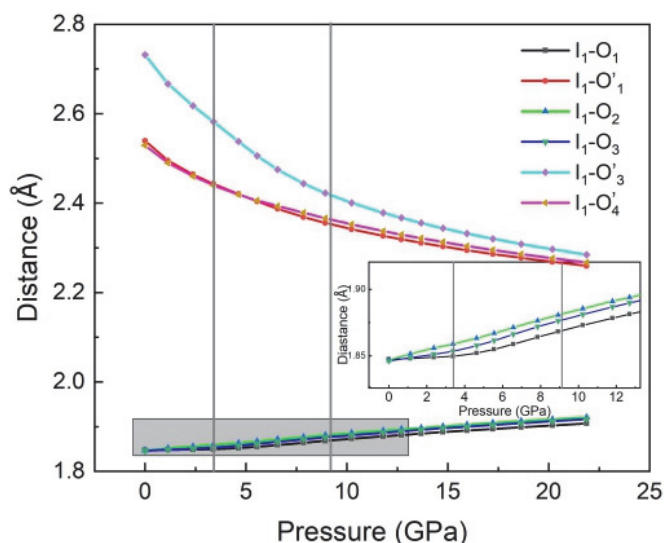


FIG. 7. Pressure dependence of the theoretical I-O bond distances. The inset shows a zoom of the I-O₁, I-O₂, and I-O₃ distances below 13 GPa. O' is used for second-neighbor oxygen atoms.

of the bond distance between I and O is in a larger range; the biggest change is the bond distance change between I and O₃ atom, shortened from 2.73 to 2.28 Å, a decrease of 16.5%. The great compressibility of the three longest I₁-O bond distances compared to the Zn-O bonds and the three shortest I-O bonds (Fig. 7) make the IO₆ octahedron to have a much larger compressibility than the ZnO₆ octahedron, as already commented.

The strong distortion of the IO₆ polyhedra at low pressures is due to the large stereoactivity of the iodine LEP. This stereoactivity decreases in strength with pressure and ultimately disappears in order to establish the three new bonds above around 8 GPa, thus leading to a more regular IO₆ polyhedron as already commented. The pressure-induced reduction of the cation LEP stereoactivity can be found in some other materials, like Fe(IO₃)₃ [6,7], SbPO₄ [53], and As₂S₃ [54]. On the other hand, we must say that the I₁-O₁ bond distance clearly shows a different pressure dependence before and after 3.4 GPa, thus supporting also the existence of an IPT around that pressure (see inset of Fig. 7).

Finally, we must note that there is an increase of the three shortest I-O distances that is in contrast to the decrease in the three largest I-O distances. The increase of the three shortest I-O distances will lead to the soft behavior of some Raman-active modes at HP that we will show in the next section. In this context, it must be stressed that an increase of the three shorter Zn-O bond distances with increasing pressure have also been observed between 3.8 and 8.9 GPa. The S-like behavior of the Zn-O bond distances with pressure is not normal. In particular, the increment of the cation-anion bond distance and the equalization of the different bond distances has been recently observed for As-S bonds in orpiment (As₂S₃) under compression [54]. In that case, it was ascribed to the formation of a new type of bond, named metavalent bonding, and ascribed to the sharing of electrons of two covalent As-S bonds (with 2 electrons per bond) in order to form 5 metavalent bonds (with 1 electron per bond). Therefore, we

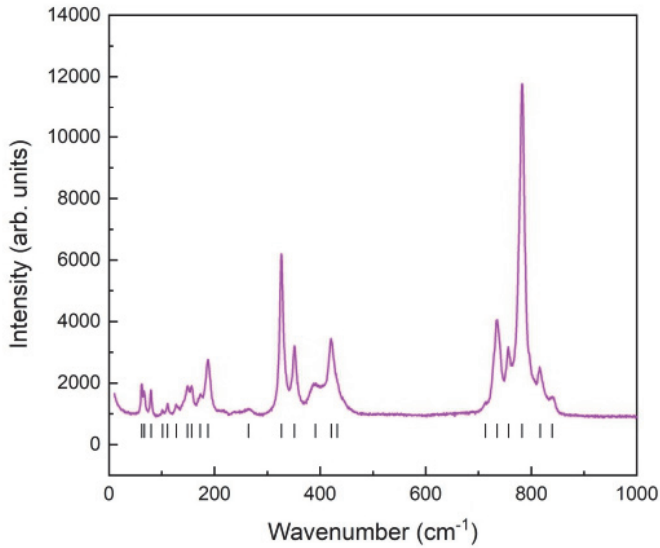


FIG. 8. Raman spectra of $\text{Zn}(\text{IO}_3)_2$ at ambient conditions. The determined peak position is indicated by ticks.

tentatively ascribe the *S*-like behavior of Zn-O bond distances to the competition of two effects that should be investigated in further works.

B. Raman study

First, we will start discussing the Raman spectra of $\text{Zn}(\text{IO}_3)_2$ at ambient pressure (see Fig. 8). The RS spectrum at ambient pressure is very similar to those reported in the literature [16,17]. It can also be mentioned that the Raman spectrum of $\text{Zn}(\text{IO}_3)_2$ bears some resemblance to that of $\text{Fe}(\text{IO}_3)_3$ [6], despite the different crystal structures of the two compounds. In particular, all of them have Raman-active modes distributed in two isolated regions separated by a phonon gap, one high-frequency region for wave numbers larger than 700 cm^{-1} and the other one for wave numbers smaller than 450 cm^{-1} . In fact, the lowest region can be subdivided into two regions, a low-frequency region below 200 cm^{-1} and a medium-frequency region between 200 and 450 cm^{-1} . The strongest mode is always in the high-frequency region. In this paper, we will show that the high-frequency modes can be linked to internal I-O vibrations (stretching and bending) inside the IO_6 polyhedra. In particular, the strongest mode is related to a symmetric stretching I-O vibration.

According to group theory, $\text{Zn}(\text{IO}_3)_2$ should have 54 vibrational modes with 3 acoustic modes ($A + 2B$) and 51 Raman-active and IR modes ($26A + 25B$). We have observed 22 Raman-active modes out of 51. In previous studies, 21 and 16 modes have been reported [16,17]. Our results and those of previous works show a nice agreement (see Table II). The calculated frequencies for all these modes together with a tentative mode assignment are also provided in Table II. We must note that the experimental mode assignment in Table II is based on comparing the experimental frequencies at ambient pressure and their pressure coefficients at different pressure ranges with those obtained from DFT calculations. The agreement between experiments and calculations is similar to that found in $\text{Fe}(\text{IO}_3)_3$ [6]. The strongest Raman modes

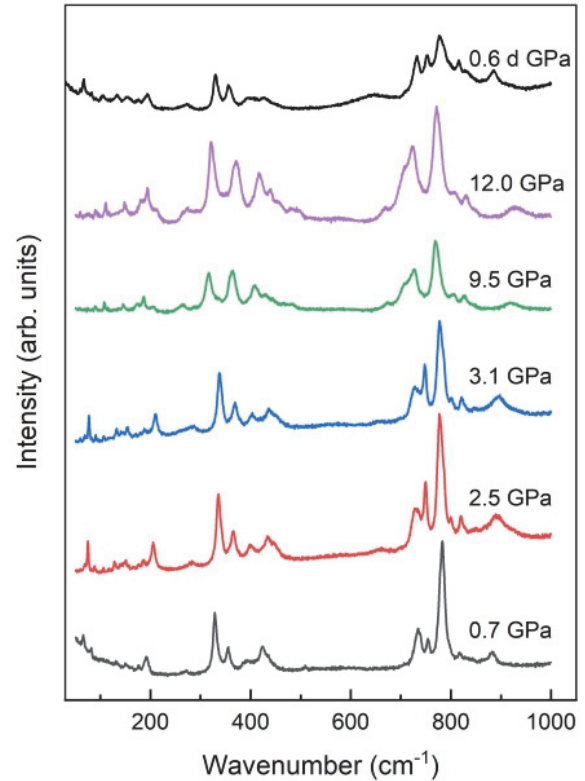


FIG. 9. Selected Raman spectra of $\text{Zn}(\text{IO}_3)_2$ under pressure. Pressure are indicated and “d” means decompression.

in $\text{Zn}(\text{IO}_3)_2$ and $\text{Fe}(\text{IO}_3)_3$ are at 782 and 790 cm^{-1} , respectively [6]. Indeed, this mode has been attributed to an *A* mode corresponding to the symmetric I-O stretching mode inside IO_3 units. Since I-O distances are very similar in both iodates, it is expected that both modes should have a similar frequency.

Now we focus on the HP behavior of the RS spectra in $\text{Zn}(\text{IO}_3)_2$ to continue our discussion (see Fig. 9). A change in the intensity of some modes is observed as pressure increases. For instance, the peak around 200 cm^{-1} at 0.7 GPa is barely followed above 9 GPa . In addition, some peaks merge into one broad peak, like what happened to the soft mode of the high-frequency region around 720 cm^{-1} at 0.7 GPa . In addition, we can observe two features in the RS spectra of $\text{Zn}(\text{IO}_3)_2$ under pressure that are similar to those reported in $\text{Fe}(\text{IO}_3)_3$ [6]: (i) A reversible change of the HP-RS spectra, and (ii) a closing of the phonon gap between the medium- and high-frequency regions.

The pressure evolution of the Raman-mode frequencies and the closing phonon gap can be better seen in Fig. 10. In the medium- and low-frequency regions, there is a close agreement between experimental and theoretical results. Under compression, there are some crossings and anticrossings of modes but all vibrational modes correspond to a monoclinic crystal structure described by space group $P2_1$ up to 12 GPa . In the high-frequency region ([Fig. 10 (c)], the behavior of the experimental modes can be described closely by calculations if we consider that theoretical calculations underestimate the experimental frequencies by ca. 70 cm^{-1} . This is a typical feature of DFT-GGA calculations [53], which tend to underestimate the restoring forces of internal modes. All the phonons

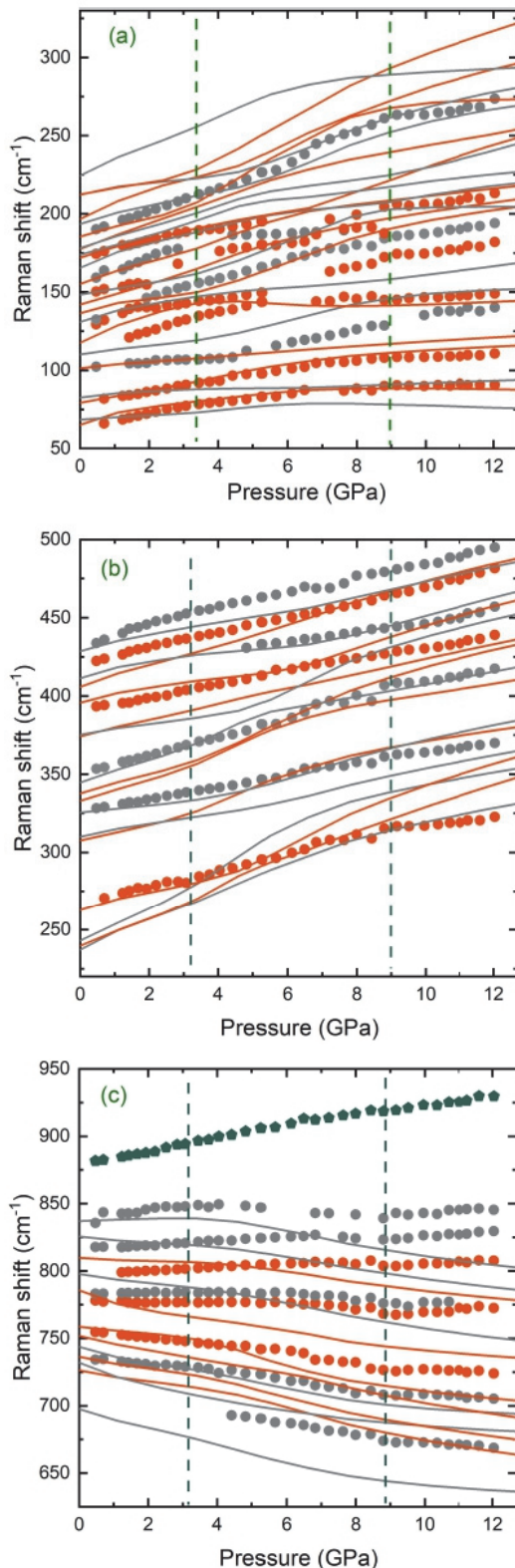


FIG. 10. Pressure dependence of experimental (symbols) and theoretical (lines) Raman-active modes of $\text{Zn}(\text{IO}_3)_2$. (a)–(c) show different wave-number regions. A tentative mode assignment of the experimental data is shown with different colors: Red and gray colors are used for *A* and *B* modes, respectively. In (c), we shifted all calculated modes by $+70 \text{ cm}^{-1}$, in order to facilitate the comparison with experiments.

were fitted by a quadratic equation using the data below 3 GPa due to the *S*-like behavior of the mode evolution curve and the zero-pressure coefficients and Grüneisen parameters can be found in Table II. The nonlinear *S*-like curve, which can be found in the evolution of almost all the experimental and calculated modes (see Fig. 10 and Fig. S14 in Supplemental Material for a selection of modes highlighting the phenomenon), is a result of the two symmetry-preserving IPTs. The vertical dashed green line indicated the phase transition pressure in HP-RS measurements, which is in excellent agreement with what we found in HP-XRD measurements. The nonlinear pressure dependence of the Raman-active mode frequencies, related to IPTs, can also be found in $\text{Fe}(\text{IO}_3)_3$ [6].

Now we focus on the high-frequency region of the Raman spectrum [see Fig. 10(c)]. First, we would like to mention that the experimental mode of highest frequency is a second-order Raman mode that is likely a combination of modes observed near $400\text{--}450 \text{ cm}^{-1}$ (all of them showing positive pressure coefficient). Second, we would like to comment on the observed phonon softening upon compression of many high-frequency modes. This is a common feature of all the calculated phonons and most experimental phonons of $\text{Zn}(\text{IO}_3)_2$. Based on our DFT calculation, we are capable of seeing the related atomic movements of all phonons by using J-ICE [55] and in particular, those corresponding to the high-frequency soft phonons (see Fig. S15 in the Supplemental Material [22]). The soft phonons in our experimental data are mostly related to the stretch of the short I-O bonds, and the cause of the soft behavior of those phonons is the decrease of the force of these bonds as pressure increases due to the increase of the short I-O distances as pressure increases (see Fig. 7) as suggested by our DFT calculations.

To verify the hypothesis of the softening of the high-frequency phonons due to the increase of the short I-O bonds, we have assumed under a harmonic approximation that the force constant, k , of the I-O bond is a function of negative cubic of the average I-O bond distance, $(d_{\text{I-O}})^{-3}$. Since the frequency of the stretching mode, ω , can be written as $\omega = (k/\mu)^{1/2}$, where μ is the reduced mass, if the assumption is right and the mode softening is caused by the increase of the bond distance, then we can find a linear relationship between $\omega^{-2/3}$ and the bond distance. By using the calculated data, we plotted the theoretical frequencies of the soft modes with the average I-O bond distance in IO_3 units (see Fig. 11). We do see a clear linear relationship between the frequency and average I-O bond distance; thus, the occurrence of the soft mode at the high-frequency region is induced by the increase of the three shortest I-O bond distances, which, as we explained before, is needed to accommodate the additional O atoms around iodine as pressure increases. The same HP behavior of the IO_3 units has been found in $\text{Fe}(\text{IO}_3)_3$ so it seems to be a common feature of compounds with iodine LEPs. We have to note that the softening of phonons related to the increase of short bonds with pressure has been also recently found in mineral orpiment (As_2S_3) and explained in the context of the formation of multivalent bonding at HP in compounds with stereoactive LEPs [54]. To explore this hypothesis in $\text{Zn}(\text{IO}_3)_2$ new studies are needed.

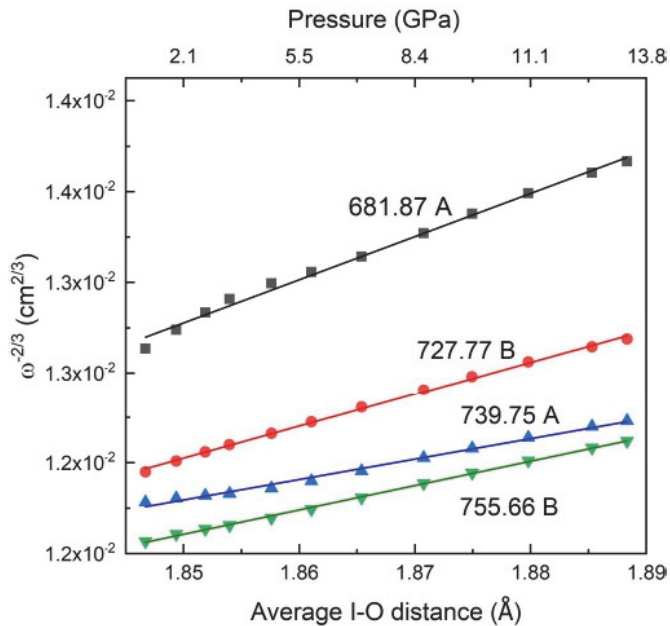


FIG. 11. Relationship between average I-O bonds and the theoretical $\omega^{-2/3}$ for some soft Raman-active modes of $\text{Zn}(\text{IO}_3)_2$. The corresponding atomic movement of each mode can be found in Fig. S15 [22]. In the upper axis the pressure of each average bond is indicated.

IV. CONCLUSIONS

HP-XRD and HP-RS measurements were used to study the HP behavior of $\text{Zn}(\text{IO}_3)_2$ along with DFT theoretical calculations. The monoclinic crystal structure shows a high anisotropy and the most compressible axis is the c axis. With a bulk modulus $B_0 = 21.6$ GPa, $\text{Zn}(\text{IO}_3)_2$ is the most compressible one among the whole reported metal iodine family. The compressibility of $\text{Zn}(\text{IO}_3)_2$ is governed by the compressibility of the IO_6 units. The symmetry of the

experimental Raman-active modes was tentatively assigned and the softened phonons found at the high-frequency region were related to the increase of the shortest I-O bonds under pressure.

Two reversible symmetry-preserving IPTs were found and located around 2.5–3.4 and 8–9 GPa, without change of the space-group symmetry or crystal volume collapse. The two IPTs are associated with a gradual change from threefold to sixfold of the I coordination under pressure, despite the fact that most notable changes at the two pressure ranges are found for the y atomic coordinate of the Zn atom. The presence of the two IPTs leads to a nonlinear S -like pressure dependence of the unit-cell lattice parameters and Raman-active modes upon compression in both experiments and theoretical calculations, as well as in the calculated Zn–O and I–O bond distances. The gradual increase of I coordination with pressure due to the decrease of the large I–O bonds followed by an increase of the short I–O distances could be indicative of the formation of metavalent bonding at HP in compounds with stereoactive LEPs, as recently suggested for orpiment. To explore this hypothesis further studies are needed.

ACKNOWLEDGMENTS

This work was supported by the Spanish Ministry of Science, Innovation and Universities under Grants No. PID2019-106383GB-C41/42/43 and No. RED2018-102612-T (MALTA Consolider-Team Network) and by Generalitat Valenciana under Grant No. Prometeo/2018/123 (EFIMAT). A.L. and D.E. would like to thank the Generalitat Valenciana for the Ph.D. Fellowship No. GRISOLIAP/2019/025). C.P. is thankful for the financial support of the Spanish Mineco Project No. FIS2017-83295-P. Powder x-ray diffraction-experiments were performed at the Materials Science and Powder Diffraction beamline of ALBA Synchrotron (Alba Experiment No. 2019083663). Z.H. sincerely thanks Professor I. K. Lefkaier – Laboratoire Physique des Matériaux (LPM) University of Laghouat Algeria – for the support and fruitful discussions.

- [1] J. G. Bergman, G. D. Boyd, A. Ashkin, and S. K. Kurtz, New nonlinear optical materials: Metal oxides with nonbonded electrons, *J. Appl. Phys.* **40**, 2860 (1969).
- [2] C. Wang, T. Zhang, and W. Lin, Rational synthesis of non-centrosymmetric metal-organic frameworks for second-order nonlinear optics, *Chem. Rev.* **112**, 1084 (2012).
- [3] K. M. Ok, E. O. Chi, and P. S. Halasyamani, Bulk characterization methods for non-centrosymmetric materials: Second-harmonic generation, piezoelectricity, pyroelectricity, and ferroelectricity, *Chem. Soc. Rev.* **35**, 710 (2006).
- [4] A. K. Sagotra, D. Errandonea, and C. Cazorla, Mechanocaloric effects in superionic thin films from atomistic simulations, *Nat. Commun.* **8**, 963 (2017).
- [5] C. Cazorla, Novel mechanocaloric materials for solid-state cooling applications, *Appl. Phys. Rev.* **6**, 041316 (2019).
- [6] A. Liang, S. Rahman, P. Rodriguez-Hernandez, A. Muñoz, F. J. Manjón, G. Nenert, and D. Errandonea, High-pressure Raman study of $\text{Fe}(\text{IO}_3)_3$: Soft-mode behavior driven by coordination changes of iodine atoms, *J. Phys. Chem. C* **124**, 21329 (2020).
- [7] A. Liang, S. Rahman, H. Saqib, P. Rodriguez-Hernandez, A. Muñoz, G. Nenert, I. Yousef, C. Popescu, and D. Errandonea, First-order isostructural phase transition induced by high-pressure in $\text{Fe}(\text{IO}_3)_3$, *J. Phys. Chem. C* **124**, 8669 (2020).
- [8] J. Liu, Z. Shen, Y. Zhang, X. Yin, and S. He, The P-T phase diagram of lithium iodate (LiIO_3) up to 40 Kbars, *Acta Phys. Sin.* **32**, 118 (1983).
- [9] J. Hu, L. Chen, L. Wang, R. Tang, and R. Che, Isothermal compression of α - LiIO_3 and its phase transition under high pressure and high temperature, *Acta Phys. Sin.* **36**, 1099 (1987).
- [10] W. W. Zhang, Q. L. Cui, Y. W. Pan, S. S. Dong, J. Liu, and G. T. Zou, High-pressure x-ray diffraction study of LiIO_3 to 75 GPa, *J. Phys.: Condens. Matter* **14**, 10579 (2002).
- [11] L. Bayarjargal, L. Wiehl, A. Friedrich, B. Winkler, E. A. Juarez-Arellano, W. Morgenroth, and E. Haussühl, Phase transitions in KIO_3 , *J. Phys.: Condens. Matter* **24**, 325401 (2012).
- [12] Y. Suffren, I. Gautier-Luneau, C. Darie, C. Goujon, M. Legendre, and O. Leynaud, First evidence of a phase transition

- in a high-pressure metal iodate: Structural and thermal studies of AgIO_3 polymorphs, *Eur. J. Inorg. Chem.* **2013**, 3526 (2013).
- [13] G. J. Shanmuga Sundar, S. M. R. Kumar, M. Packiyaraj, and S. Selvakumar, Synthesis, growth, optical, mechanical and dielectric studies on NLO active monometallic zinc iodate [$\text{Zn}(\text{IO}_3)_2$] crystal for frequency conversion, *Mater. Res. Bull.* **112**, 22 (2019).
- [14] D. Phanon, B. Bentría, E. Jeanneau, D. Benbental, A. Mosset, and I. Gautier-Luneau, Crystal structure of $\text{M}(\text{IO}_3)_2$ metal iodates, twinned by pseudo-merohedry, with MII: MgII, MnII, CoII, NiII and ZnII, *Z. Kristallogr.* **221**, 635 (2006).
- [15] J. K. Liang and C. G. Wang, The structure of $\text{Zn}(\text{IO}_3)_2$ crystal, *Acta Chim. Sin.* **40**, 985 (1982).
- [16] T. C. Kochuthresia, I. Gautier-Luneau, V. K. Vaidyan, and M. J. Bushiri, Raman and FTIR spectral investigations of twinned $\text{M}(\text{IO}_3)_2$ ($\text{M} = \text{Mn}, \text{Ni}, \text{Co}, \text{AND Zn}$) crystals, *J. Appl. Spectrosc.* **82**, 941 (2016).
- [17] S. Peter, G. Pracht, N. Lange, and H. D. Lutz, Zinkiodate-schwingungsspektren (IR, Raman) und kristallstruktur von $\text{Zn}(\text{IO}_3)_2 \cdot 2\text{H}_2\text{O}$, *Z. Anorg. Allg. Chem.* **626**, 208 (2000).
- [18] E. J. Skoug and D. T. Morelli, Role of Lone-Pair Electrons in Producing Minimum Thermal Conductivity in Nitrogen-Group Chalcogenide Compounds, *Phys. Rev. Lett.* **107**, 235901 (2011).
- [19] M. D. Nielsen, V. Ozolins, and J. P. Heremans, Lone pair electrons minimize lattice thermal conductivity, *Energy Environ. Sci.* **6**, 570 (2013).
- [20] A. Benghia, Z. Hebboul, R. Chikhaoui, I. khaldoun Lefkaier, A. Chouireb, and S. Goumri-Said, Effect of iodic acid concentration in preparation of zinc iodate: Experimental characterization of $\text{Zn}(\text{IO}_3)_2$, and its physical properties from density functional theory, *Vacuum* **181**, 109660 (2020).
- [21] H. M. Rietveld, A profile refinement method for nuclear and magnetic structures, *J. Appl. Crystallogr.* **2**, 65 (1969).
- [22] See Supplemental Material at <http://link.aps.org/supplemental/10.1103/PhysRevB.103.054102> for structural information, additional x-ray diffraction patterns, additional information on structural analysis and Raman experiments results, a description of atomic movements associated to phonons, and results from density-functional theory calculations.
- [23] A. Dewaele, P. Loubeyre, and M. Mezouar, Equations of state of six metals above 94 GPa, *Phys. Rev. B* **70**, 094112 (2004).
- [24] S. Klotz, J. C. Chervin, P. Munsch, and G. Le Marchand, Hydrostatic limits of 11 pressure transmitting media, *J. Phys. D: Appl. Phys.* **42**, 075413 (2009).
- [25] F. Fauth, I. Peral, C. Popescu, and M. Knapp, The new material science powder diffraction beamline at ALBA synchrotron, *Powder Diffraction* **28**, S360 (2013).
- [26] H. K. Mao, J. Xu, and P. M. Bell, Calibration of the ruby pressure gauge to 800 Kbar under quasi-hydrostatic conditions, *J. Geophys. Res.* **91**, 4673 (1986).
- [27] K. Nassau, J. W. Shiever, and B. E. Prescott, Transition metal iodates. I. Preparation and characterization of the 3d iodates, *J. Solid State Chem.* **7**, 186 (1973).
- [28] D. Errandonea, A. Muñoz, and J. Gonzalez-Platas, Comment on "High-pressure x-ray diffraction study of $\text{YBO}_3/\text{Eu}^{3+}$, GdBO_3 , and EuBO_3 : Pressure-induced amorphization in GdBO_3 " [*J. Appl. Phys.* **115**, 043507 (2014)], *J. Appl. Phys.* **115**, 216101 (2014).
- [29] G. Kresse and J. Hafner, Ab initio molecular dynamics for liquid metals, *Phys. Rev. B* **47**, 558 (1993).
- [30] G. Kresse and J. Hafner, Ab initio molecular-dynamics simulation of the liquid-metalamorphous- semiconductor transition in germanium, *Phys. Rev. B* **49**, 14251 (1994).
- [31] G. Kresse and J. Furthmüller, Efficiency of ab-initio total energy calculations for metals and semiconductors using a plane-wave basis set, *Comput. Mater. Sci.* **6**, 15 (1996).
- [32] G. Kresse and J. Furthmüller, Efficient iterative schemes for ab initio total-energy calculations using a plane-wave basis set, *Phys. Rev. B* **54**, 11169 (1996).
- [33] P. Hohenberg and W. Kohn, Inhomogeneous electron gas, *Phys. Rev.* **136**, B864 (1964).
- [34] P. E. Blöchl, Projector augmented-wave method, *Phys. Rev. B* **50**, 17953 (1994).
- [35] G. Kresse and D. Joubert, From ultrasoft pseudopotentials to the projector augmented-wave method, *Phys. Rev. B* **59**, 1758 (1999).
- [36] J. P. Perdew, A. Ruzsinszky, G. I. Csonka, O. A. Vydrov, G. E. Scuseria, L. A. Constantin, X. Zhou, and K. Burke, Restoring the Density-Gradient Expansion for Exchange in Solids and Surfaces, *Phys. Rev. Lett.* **100**, 136406 (2008).
- [37] H. J. Monkhorst and J. D. Pack, Special points for Brillouin-zone integrations, *Phys. Rev. B* **13**, 5188 (1976).
- [38] A. Togo, F. Oba, and I. Tanaka, First-principles calculations of the ferroelastic transition between rutile-type and CaCl_2 -Type SiO_2 at high pressures, *Phys. Rev. B: Condens. Matter Mater. Phys.* **78**, 134106 (2008).
- [39] D. Díaz-Anichtchenko, D. Santamaria-Perez, T. Marqueño, J. Pellicer-Porres, J. Ruiz-Fuertes, R. Ribes, J. Ibañez, S. N. Achary, C. Popescu, and D. Errandonea, Comparative study of the high-pressure behavior of ZnV_2O_6 , $\text{Zn}_2\text{V}_2\text{O}_7$, and $\text{Zn}_3\text{V}_2\text{O}_8$, *J. Alloys Compd.* **837**, 155505 (2020).
- [40] F. D. Murnaghan, The compressibility of media under extreme pressures, *Proc. Natl. Acad. Sci. U.S.A.* **30**, 244 (1944).
- [41] F. Birch, Finite elastic strain of cubic crystals, *Phys. Rev.* **71**, 809 (1947).
- [42] B. Winkler and V. Milman, Density functional theory based calculations for high pressure research, *Z. Kristallogr.* **229**, 112 (2014).
- [43] Z. Hebboul, C. Galez, D. Benbental, S. Beauquis, Y. Mugnier, A. Benmakhlouf, M. Bouchenafa, and D. Errandonea, Synthesis, characterization, and crystal structure determination of a new lithium zinc iodate polymorph $\text{LiZn}(\text{IO}_3)_3$, *Crystals* **9**, 464 (2019).
- [44] J. Navarro-Sánchez, I. Mullor-Ruiz, C. Popescu, D. Santamaría-Pérez, A. Segura, D. Errandonea, J. González-Platas, and C. Martí-Gastaldo, Peptide metal-organic frameworks under pressure: Flexible linkers for cooperative compression, *Dalton Trans.* **47**, 10654 (2018).
- [45] A. L. J. Pereira, L. Gracia, D. Santamaría-Pérez, R. Vilaplana, F. J. Manjón, D. Errandonea, M. Nalin, and A. Beltrán, Structural and vibrational study of cubic Sb_2O_3 under high pressure, *Phys. Rev. B* **85**, 174108 (2012).
- [46] A. L. J. Pereira, D. Errandonea, A. Beltrán, L. Gracia, O. Gomis, J. A. Sans, B. García-Domene, A. Miquel-Veyrat, F. J. Manjón, A. Muñoz, and C. Popescu, Structural study of α - Bi_2O_3 under pressure, *J. Phys.: Condens. Matter* **25**, 475402 (2013).

- [47] D. Errandonea, R. Boehler, S. Japel, M. Mezouar, and L. R. Benedetti, Structural transformation of compressed solid Ar: An x-ray diffraction study to 114 GPa, *Phys. Rev. B* **73**, 092106 (2006).
- [48] W. H. Baur, The geometry of polyhedral distortions. Predictive relationships for the phosphate group, *Acta Crystallogr. B* **30**, 1195 (1974).
- [49] K. Momma and F. Izumi, VESTA 3 for three-dimensional visualization of crystal, volumetric and morphology data, *J. Appl. Crystallogr.* **44**, 1272 (2011).
- [50] N. Boccara, Second-order phase transitions characterized by a deformation of the unit cell, *Ann. Phys. (N. Y.)* **47**, 40 (1968).
- [51] M. T. Dove, Theory of displacive phase transitions in minerals, *Am. Mineral.* **82**, 213 (1997).
- [52] A. Krapp, F. M. Bickelhaupt, and G. Frenking, Orbital overlap and chemical bonding, *Chem. - Eur. J.* **12**, 9196 (2006).
- [53] A. L. D. J. Pereira, D. Santamariá-Pérez, R. Vilaplana, D. Errandonea, C. Popescu, E. L. Da Silva, J. A. Sans, J. Rodríguez-Carvajal, A. Muñoz, P. Rodríguez-Hernández, A. Mujica, S. E. Radescu, A. Beltrán, A. Otero-De-La-Roza, M. Nalin, M. Mollar, and F. J. Manjón, Experimental and theoretical study of SbPO₄ under Compression, *Inorg. Chem.* **59**, 287 (2020).
- [54] V. P. Cuenca-Gotor, J. Á. Sans, O. Gomis, A. Mujica, S. Radescu, A. Muñoz, P. Rodríguez-Hernández, E. L. Da Silva, C. Popescu, J. Ibañez, R. Vilaplana, and F. J. Manjón, Orpiment under compression: metavalent bonding at high pressure, *Phys. Chem. Chem. Phys.* **22**, 3352 (2020).
- [55] P. Canepa, R. M. Hanson, P. Ugliengo, and M. Alfredsson, J-ICE: A new Jmol interface for handling and visualizing crystallographic and electronic properties, *J. Appl. Crystallogr.* **44**, 225 (2011).

Article

High-Pressure Spectroscopy Study of $\text{Zn}(\text{IO}_3)_2$ Using Far-Infrared Synchrotron Radiation

Akun Liang ¹, Robin Turnbull ¹, Enrico Bandiello ¹, Ibraheem Yousef ², Catalin Popescu ², Zoulikha Hebboul ³ and Daniel Errandonea ^{1,*}

¹ Departamento de Física Aplicada-ICMUV, Universitat de València, Dr. Moliner 50, 46100 Burjassot, Spain; akun2.liang@uv.es (A.L.); robin.turnbull@uv.es (R.T.); enrico.bandiello@uv.es (E.B.)

² CELLS-ALBA Synchrotron Light Facility, 08290 Barcelona, Spain; iyousef@cells.es (I.Y.); cpopescu@cells.es (C.P.)

³ Laboratoire Physico-Chimie des Matériaux (LPCM), Université Amar Telidji de Laghouat, BP 37G, Laghouat 03000, Algeria; z.hebboul@lagh-univ.dz

* Correspondence: daniel.errandonea@uv.es

Abstract: We report the first high-pressure spectroscopy study on $\text{Zn}(\text{IO}_3)_2$ using synchrotron far-infrared radiation. Spectroscopy was conducted up to pressures of 17 GPa at room temperature. Twenty-five phonons were identified below 600 cm^{-1} for the initial monoclinic low-pressure polymorph of $\text{Zn}(\text{IO}_3)_2$. The pressure response of the modes with wavenumbers above 150 cm^{-1} has been characterized, with modes exhibiting non-linear responses and frequency discontinuities that have been proposed to be related to the existence of phase transitions. Analysis of the high-pressure spectra acquired on compression indicates that $\text{Zn}(\text{IO}_3)_2$ undergoes subtle phase transitions around 3 and 8 GPa, followed by a more drastic transition around 13 GPa.

Keywords: iodate; infrared spectroscopy; high pressure; phase transitions



Citation: Liang, A.; Turnbull, R.; Bandiello, E.; Yousef, I.; Popescu, C.; Hebboul, Z.; Errandonea, D. High-Pressure Spectroscopy Study of $\text{Zn}(\text{IO}_3)_2$ Using Far-Infrared Synchrotron Radiation. *Crystals* **2021**, *11*, 34. <https://doi.org/10.3390/cryst11010034>

Received: 17 December 2020

Accepted: 28 December 2020

Published: 30 December 2020

Publisher's Note: MDPI stays neutral with regard to jurisdictional claims in published maps and institutional affiliations.



Copyright: © 2021 by the authors. Licensee MDPI, Basel, Switzerland. This article is an open access article distributed under the terms and conditions of the Creative Commons Attribution (CC BY) license (<https://creativecommons.org/licenses/by/4.0/>).

1. Introduction

Metal iodates $[\text{M}(\text{IO}_3)_x]$ receive great attention because of their non-linear optical properties. In particular, they are promising materials for second-harmonic generation (SHG) [1–4]. They have been also proposed for applications as dielectric materials, in non-linear optics, and for desalination and water treatment [1–4]. Amongst the iodates, the quasi-two-dimensional zinc iodate, $\text{Zn}(\text{IO}_3)_2$, has recently been studied by several research groups [5–8]. The crystal structure, thermal stability, and other physical properties of this compound have been characterized at ambient pressure [9–11]. However, nothing is known of its structural and vibrational behavior under high-pressure (HP) conditions. At ambient conditions, $\text{Zn}(\text{IO}_3)_2$ crystallizes into a monoclinic structure, which is represented in Figure 1. The monoclinic structure consists of ZnO_6 octahedral units connected by IO_3 triangular pyramidal units. In these units, the pentavalent iodine atom forms three covalent bonds with oxygen atoms, leaving two 5s electrons free to act as lone electron pairs (LEP). The presence of the LEP has been shown to induce an interesting HP behavior in iodates related to $\text{Zn}(\text{IO}_3)_2$ like $\text{Fe}(\text{IO}_3)_3$ [12,13], with two isostructural phase transitions taking place at pressures below 10 GPa in this compound. These transitions have been detected from changes in the pressure dependences of phonon frequencies, which show a nonlinear behavior, as well as kinks and slope changes in the frequency-versus-pressure plot at the identified transition pressures [12,13]. Such unusual behavior of phonons has been proposed to be connected with gradual modifications of the iodine coordination, which is favored by the LEP of iodine and has been connected with the isostructural phase transitions discovered in $\text{Fe}(\text{IO}_3)_3$ [12,13]. Since the LEP of iodine is a typical feature of many $\text{M}(\text{IO}_3)_x$ iodates, it would be interesting to explore if low-pressure phase transitions are a typical feature of this family of compounds. Given the structural similarities between

$\text{Fe}(\text{IO}_3)_3$ and $\text{Zn}(\text{IO}_3)_2$ (both structures consist of MO_6 octahedral units connected by iodine atoms coordinated by three oxygen atoms with non-bonding LEP orbitals), the possibility of isostructural phase transitions at low pressures in the unexplored $\text{Zn}(\text{IO}_3)_2$ motivated the present work, in which we studied the pressure dependence of phonons by means of HP infrared (IR) spectroscopy. This is a technique useful for understanding the changes induced by compression in the physical–chemical properties of iodates. Additionally, the discovery of the existence of phase transition in $\text{Zn}(\text{IO}_3)_2$ could be very useful for the development of solid-state cooling technologies, which take advantage of the pressure-induced barocaloric effect [14].

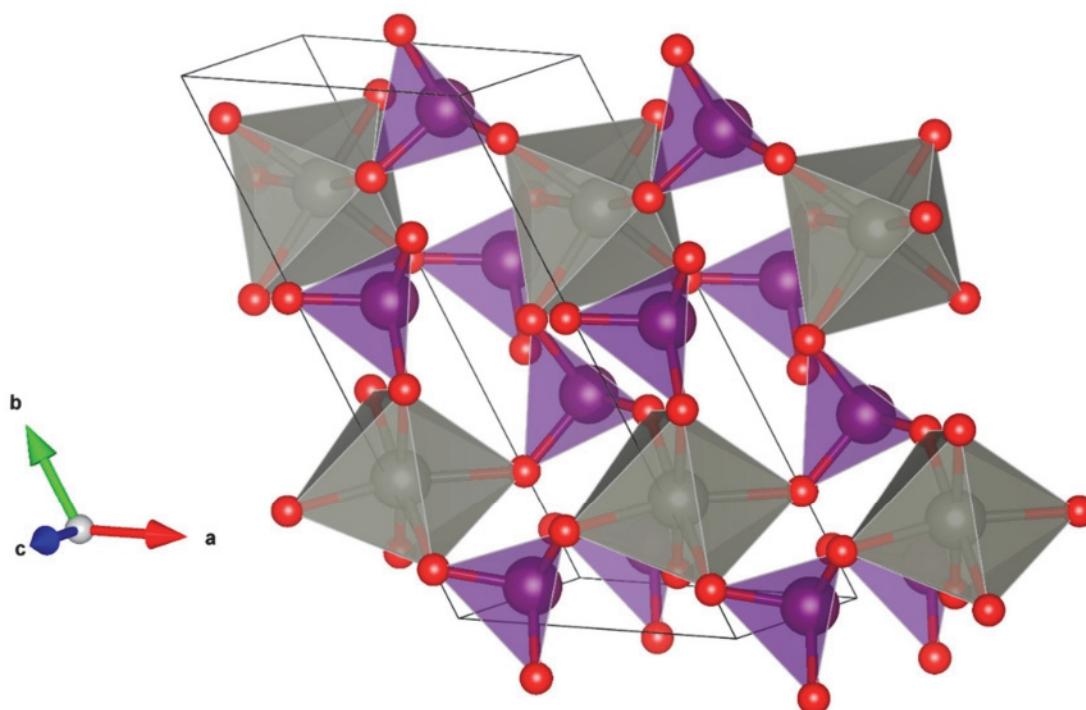


Figure 1. Crystal structure of $\text{Zn}(\text{IO}_3)_2$. ZnO_6 octahedral units are shown in grey and IO_3 trigonal pyramidal units are shown in purple. Small red circles are oxygen atoms. The monoclinic unit cell is shown with black solid lines.

Infrared spectroscopy has been shown to be an effective diagnostic for the detection of pressure-induced phase transitions in solids [15]. In the present work, IR spectroscopy provides information on the vibrational properties of $\text{Zn}(\text{IO}_3)_2$, which, until the present work, have remained relatively underexplored. In fact, less than one-third of the 51 phonons predicted by group theory analysis have been reported experimentally for $\text{Zn}(\text{IO}_3)_2$ [5–9,16]. Therefore, the present far-infrared spectroscopy study of $\text{Zn}(\text{IO}_3)_2$ under high-pressure conditions makes a timely and valuable contribution. $\text{Zn}(\text{IO}_3)_2$ has not previously been studied under high-pressure conditions. The information obtained from this study is relevant not only to improve the knowledge on the aforementioned issues but also to provide an accurate determination of the phonon frequencies, which are needed to properly model other physical properties such as heat capacity and thermal expansion. The use of high-brilliance infrared synchrotron radiation facilitated the measurement of tiny samples loaded in diamond-anvil cells (DACs) with a very good signal-to-noise ratio. Using this methodology, we have been able to identify 25 phonons between 98 and 600 cm^{-1} . We then follow the pressure-induced evolution of these phonons up to 17 GPa. The analysis of the results leads us to propose the existence of three phase transitions, as will be discussed in the manuscript.

2. Materials and Methods

Experiments were performed on $\text{Zn}(\text{IO}_3)_2$ powders synthesized from aqueous solution according to the synthesis method and sample characterization found in Ref. [6]. The crystal structure was confirmed by powder XRD measurements (X'Pert Pro diffractometer, Panalytical, Almelo, The Netherlands) using $\text{Cu K}\alpha_1$ radiation, which corroborated the crystal structure reported by Liang et al. [10] (space group $P2_1$) with unit-cell parameters: $a = 5.465(4)$, $b = 10.952(8)$, $c = 5.129(4)$ Å, and $\gamma = 120.37(8)^\circ$. HP Fourier transform infrared (FTIR) measurements (Vertex 70 spectrometer, Bruker Optik GmbH, Ettlingen, Germany) were conducted at MIRAS beamline of the ALBA synchrotron. $\text{Zn}(\text{IO}_3)_2$ samples were loaded in a DACs designed for IR spectroscopy, using IIAC-diamonds with culets of 300 μm . Stainless-steel gaskets were pre-indented to a thickness of 40 μm and drilled with a hole in the center of 150 μm in diameter. Cesium iodide (CsI) was used as the pressure-transmitting medium (PTM) [17]. The CsI PTM is not quasi-hydrostatic beyond 3 GPa; however, radial pressure gradients were smaller than 1 GPa in the pressure range of this study [18]. CsI was chosen because it has the widest IR transmission window amongst the possible PTMs [18]. Pressure was determined using the ruby scale [19]. Synchrotron-based FTIR-micro-spectroscopy experiments were performed in the transmission mode of operation. We used a masking aperture size of $50 \times 50 \mu\text{m}^2$ and a beam current inside the synchrotron ring of 250 mA. The measurements were performed by employing a 3000 Hyperion microscope coupled to a Vertex 70 spectrometer (Bruker Optik GmbH, Ettlingen, Germany). The microscope was equipped with a helium-cooled bolometer detector optimized for operation in the range covering the far-infrared spectral region. A Mylar beam splitter was used in the spectrometer. Spectra were measured using a $15\times$ Schwarzschild magnification objective (NA = 0.52) coupled to a $15\times$ Schwarzschild magnification condenser. Measurements at selected pressures were collected using the OPUS 8.2 software (Bruker Optik GmbH, Ettlingen, Germany) in the $90\text{--}600 \text{ cm}^{-1}$ range with a spectral resolution of 4 cm^{-1} and 256 co-added scans per spectrum. The analysis of FTIR results was carried using the Multiple Peak Fit Tool of the OriginPro software (OriginLab Corporation, Northampton, MA, United States) and employing Gaussian functions to model the peaks.

3. Results and Discussion

The results at the lowest measured pressure (0.9 GPa) are shown in Figure 2 together with the multiple-peak fit used to identify phonons. We have identified 25 modes, as can be seen in the figure, thereby greatly extending the number of modes previously observed in zinc iodate. The frequencies of all 25 of these modes are summarized in Table 1 and compared with those reported in the literature. $\text{Zn}(\text{IO}_3)_2$ exhibits 51 modes (26A + 25B) according to group theory. All of these 51 modes are both Raman-active and IR-active. They can be described as internal vibrations of the of the IO_3 units and external vibrations (commonly known as lattice modes) involving the relative movements of IO_3 (behaving as rigid units) and Zn, which are observed in the low-frequency region [7,20]. Symmetric (ν_1) and asymmetric (ν_3) stretching vibrations of the pyramidal IO_3 units are in the $780\text{--}630 \text{ cm}^{-1}$ and $820\text{--}730 \text{ cm}^{-1}$ wavenumber regions, respectively [7,21,22]. The symmetric (ν_2) and asymmetric bending vibrations (ν_4) are in the $400\text{--}320 \text{ cm}^{-1}$ wavenumber region and around $450\text{--}400 \text{ cm}^{-1}$, respectively [7,21,22]. In our experiments, we detected four ν_4 modes. The frequencies of the modes we found at 425, 440, and 452 cm^{-1} are less than 9 cm^{-1} larger than those measured in previous ambient-pressure Raman and IR experiments [6,7,16]. This is consistent with the fact that our experiment was performed at a pressure of 0.9 GPa. The expected phonon hardening [23], or increase in the phonon frequency, is due to the shortening bond distance caused by increasing pressure in our experiment. The mode reported at 405 cm^{-1} in Ref. [5] was not detected in previous works from the literature, but in our case could be probably assigned to a shoulder of the peak with wavenumber 388 cm^{-1} , which can be identified at 402 cm^{-1} . Additionally, the mode previously reported at 524 cm^{-1} in Ref. [8] is not consistent either with the present

or previous experiments [5–7,16]. Indeed, there are no phonons in $\text{Zn}(\text{IO}_3)_2$, or in any divalent metal iodate [7], in the $600\text{--}500\text{ cm}^{-1}$ range. The origin of such a phonon could be related with twinning of the crystal structure when large single crystals are grown [9], being a possible overtone, since 524 cm^{-1} is approximately double of the frequency of the lattice modes.

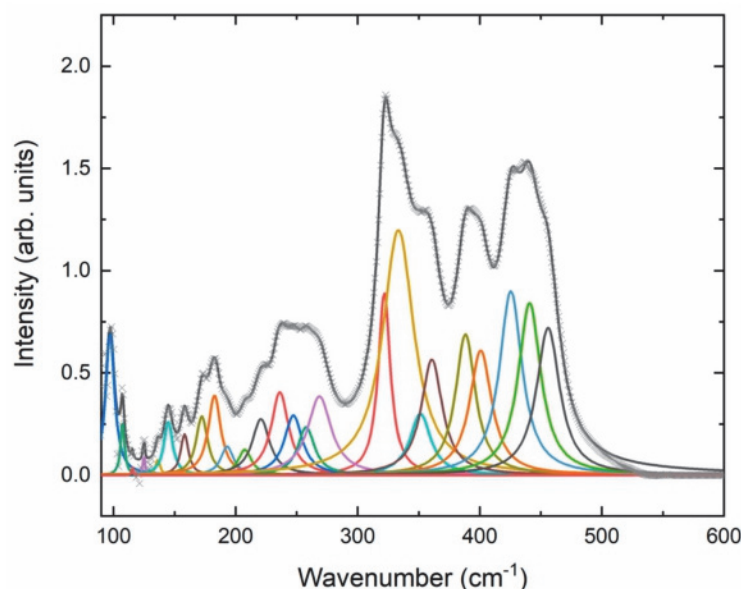


Figure 2. Far-IR spectrum of $\text{Zn}(\text{IO}_3)_2$ measured at 0.9 GPa and room temperature. The Gaussians used for the multiple peak fit are also shown in different colors. Each of them corresponds to the phonons summarized in Table 1.

Table 1. A comparison of the phonon frequencies determined by IR- and Raman-spectroscopy from this work (at 0.9 GPa) and from previous studies (ambient pressure). For the present study, frequencies are given with errors. The horizontal dashed line indicates the cut-off of the IR set-up, below which it was not possible to detect signal due to experimental constraints.

Assignment	$\omega\text{ (cm}^{-1}\text{)}$ This Work IR	$\omega\text{ (cm}^{-1}\text{)}$ [5] IR	$\omega\text{ (cm}^{-1}\text{)}$ [6] IR	$\omega\text{ (cm}^{-1}\text{)}$ [7] IR	$\omega\text{ (cm}^{-1}\text{)}$ [7] Raman	$\omega\text{ (cm}^{-1}\text{)}$ [8] IR>	$\omega\text{ (cm}^{-1}\text{)}$ [16] Raman
							61
							67
				73			80
	98(2)				80		80
	107(2)			101			100
	116(2)				113		111
	125(2)						
	135(2)				132		139
Lattice modes	145(2)			141			148
	158(2)				152		155
	172(2)				173		173
	183(2)			180			
	193(2)				189		187
	208(2)						
	220(2)						
	236(2)						
	247(2)						
	258(2)			255			
	269(2)				267		265

Table 1. Cont.

Assignment	ω (cm ⁻¹) This Work IR	ω (cm ⁻¹) [5] IR	ω (cm ⁻¹) [6] IR	ω (cm ⁻¹) [7] IR	ω (cm ⁻¹) [7] Raman	ω (cm ⁻¹) [8] IR>	ω (cm ⁻¹) [16] Raman
ν_2	322(2)				327		327
	336(2)						
	348(2)						
	353(2)				354		351
	388(2)		366			391	
ν_4	402(2)	405					
	425(2)		418	418	424		422
	440(2)						432
	452(2)		444				
						524	

Regarding the other bending vibrations, five ν_2 modes were detected in our experiments. The frequencies of three of them agree well with previous studies [6,7,16], with ours observed at 3–5 cm⁻¹ higher frequencies due to the higher pressure (0.9 GPa) in the sample. The brilliance and resolution of the experimental set-up enabled the identification of two modes that were previously undetected. Additionally, the mode reported at 366 cm⁻¹ in Ref. [5] was not observed in our measurements, and it was not reported in the rest of the works in the literature [6–8,16]. We note that the frequency of this mode is approximately double the frequency of the 183 cm⁻¹ mode detected in the present work and elsewhere in the literature [6–8,16] and that it is therefore likely to be an overtone.

Regarding the lattice modes, sixteen in total were observed. Ten of these modes have been detected in previous studies [7,16], thereby providing good agreement with the results of the present work (especially considering the frequency increase due to the 0.9 GPa experimental sample pressure). In the literature, four modes have been detected by Raman and IR spectroscopy [7,8,16], which could be detected in our experiment because it is below the cut-off frequency of our setup. Lattice modes are mainly related to translation and libration movements of IO₃, and the coupling of these movements with movements of Zn atoms. In particular, the 145 cm⁻¹ phonon has been assigned to a O–Zn–O deformation of the ZnO₆ octahedron [8]. This is consistent with the fact that a mode involving the same deformation of ZnO₆ has the same frequency in ZnWO₄ [24] and ZnMoO₄ [25]. Additionally, the modes below 120 cm⁻¹ are likely to be due to pure translational or librational movements of IO₃, because of the large mass of the iodine atom. This hypothesis is consistent with the observation that these modes have nearly the same frequency in Mn(IO₃)₂, Ni(IO₃)₂, Co(IO₃)₂, and Zn(IO₃)₂ [8] as well as in Fe(IO₃)₃ [10].

We will now comment on the data acquired at higher pressures. For the sake of accuracy, we will concentrate on wavenumbers higher than 150 cm⁻¹ because the signals at lower energy became noisy with increasing pressure. Figure 3 displays IR spectra measured at different pressures (indicated in the figure). It is clear in Figure 3 that there are qualitative changes in the spectra at 3.6 GPa, in particular for wavelengths smaller than 300 cm⁻¹. In particular, three modes (marked by asterisks) increase in intensity. The transition pressure is close to the loss hydrostaticity of the pressure medium (3 GPa) [18]. The influence of non-hydrostaticity in phase transitions induced by pressure in Zn(IO₃)₂ is beyond the scope of this study. Additional changes occur in the IR spectra at 8.8 GPa. In particular, several modes broaden, and three low-frequency modes (also marked with asterisks) become enhanced. Finally, there is a considerable broadening of phonon bands at 13 GPa and higher pressures. Similar changes have been assigned to phase transitions in the case of Fe(IO₃)₃ [12,13]. Thus, phase transitions could be the cause of the changes observed in the IR spectra. Further evidence supporting the existence of phase transitions

in $\text{Zn}(\text{IO}_3)_2$ is obtained via the analysis of the pressure dependence of the mode frequencies described immediately below.

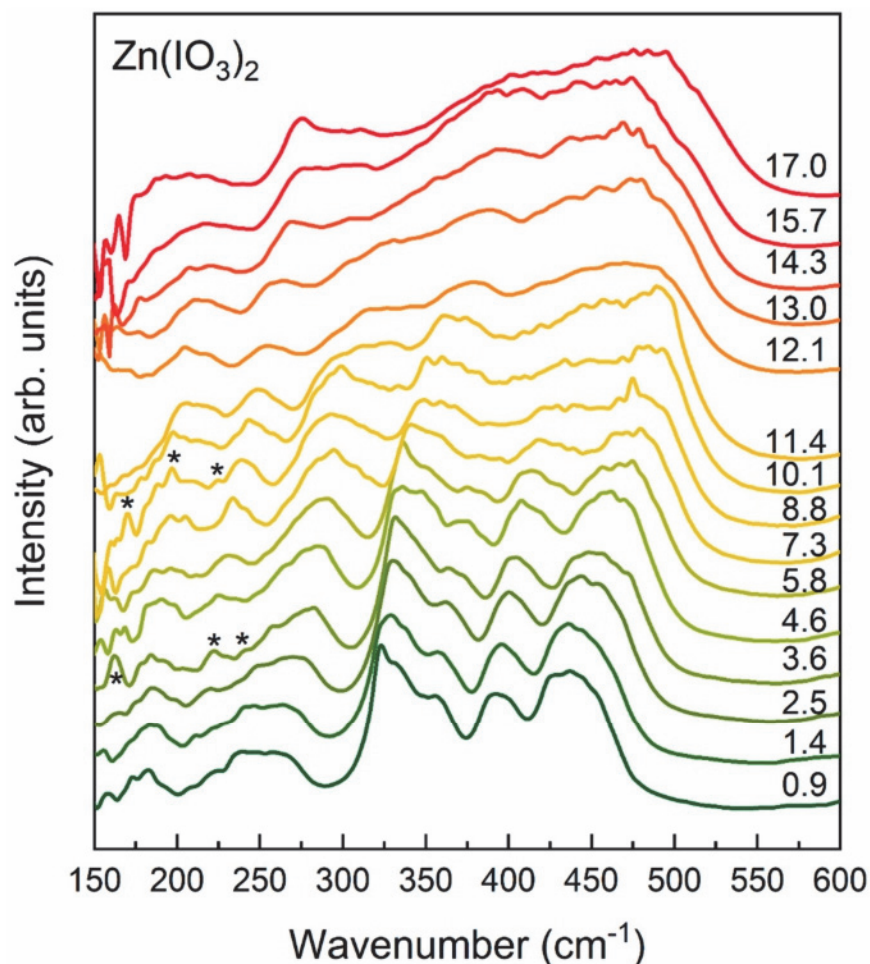


Figure 3. IR spectra acquired at increasing pressures (indicated in GPa in the figure). The asterisks indicate changes in the phonons described in the text.

From the analysis of the HP experiments, we determined the pressure dependence of eight internal bending modes and ten lattice modes. The results are shown in Figures 4 and 5. In Figure 4, it can be clearly seen that there are changes, at 3.6 and 8.8 GPa, in the pressure dependence of several modes; in particular, the bending modes with frequencies of 360 and 440 cm^{-1} among others. There are also clear changes in the modes with frequency 353 and 425 cm^{-1} at 8.8 GPa. On top of this, at 13 GPa, there are noticeable changes in the eight bending modes shown in Figure 4. In particular, there are discontinuities in at least two of the frequencies, indicating the occurrence of more important structural changes in the third phase transition than in the other two transitions.

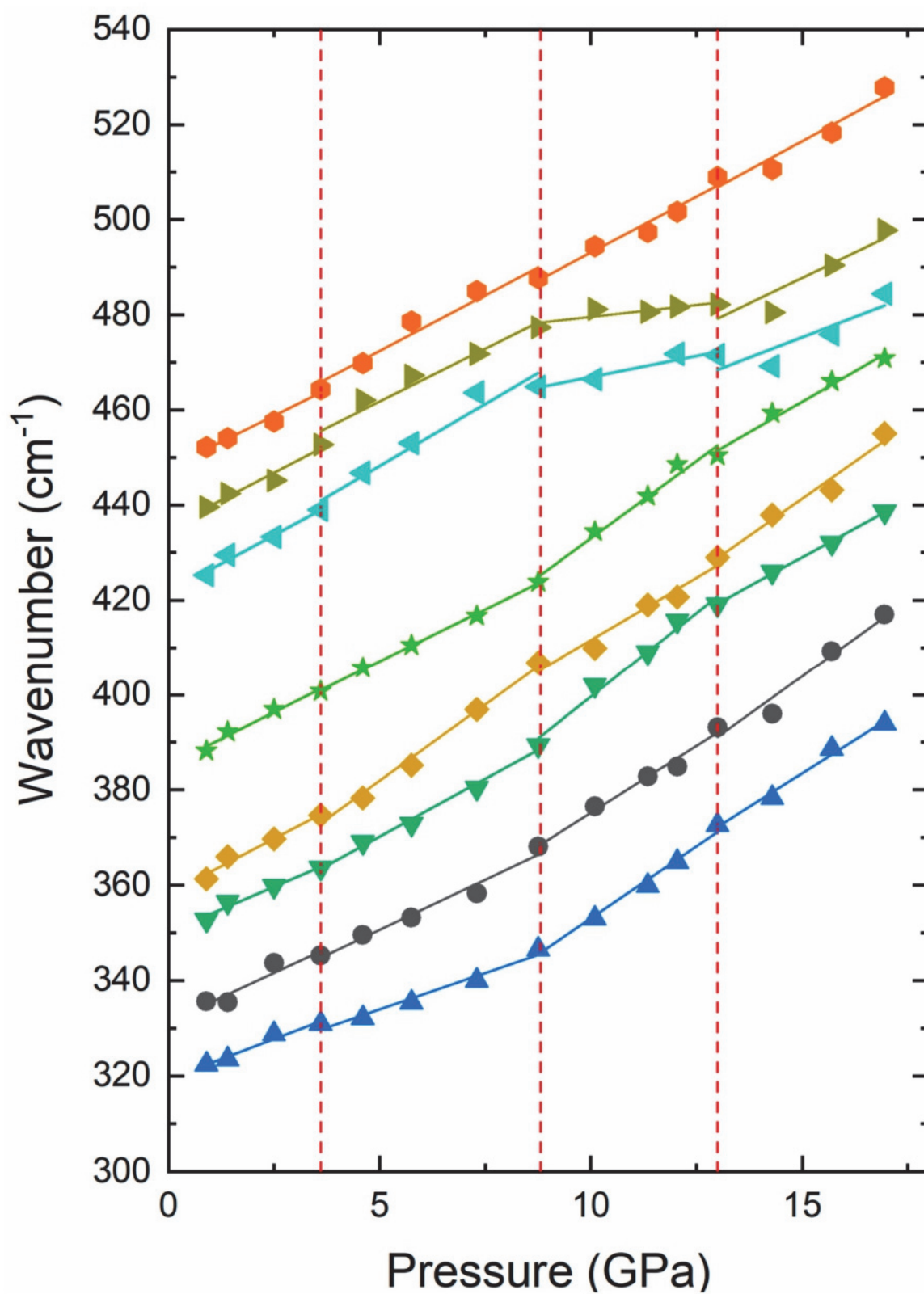


Figure 4. Pressure dependence of IR modes obtained from experiments. Only IO_3 internal bending modes are shown. Vertical lines indicate suggested transition pressures.

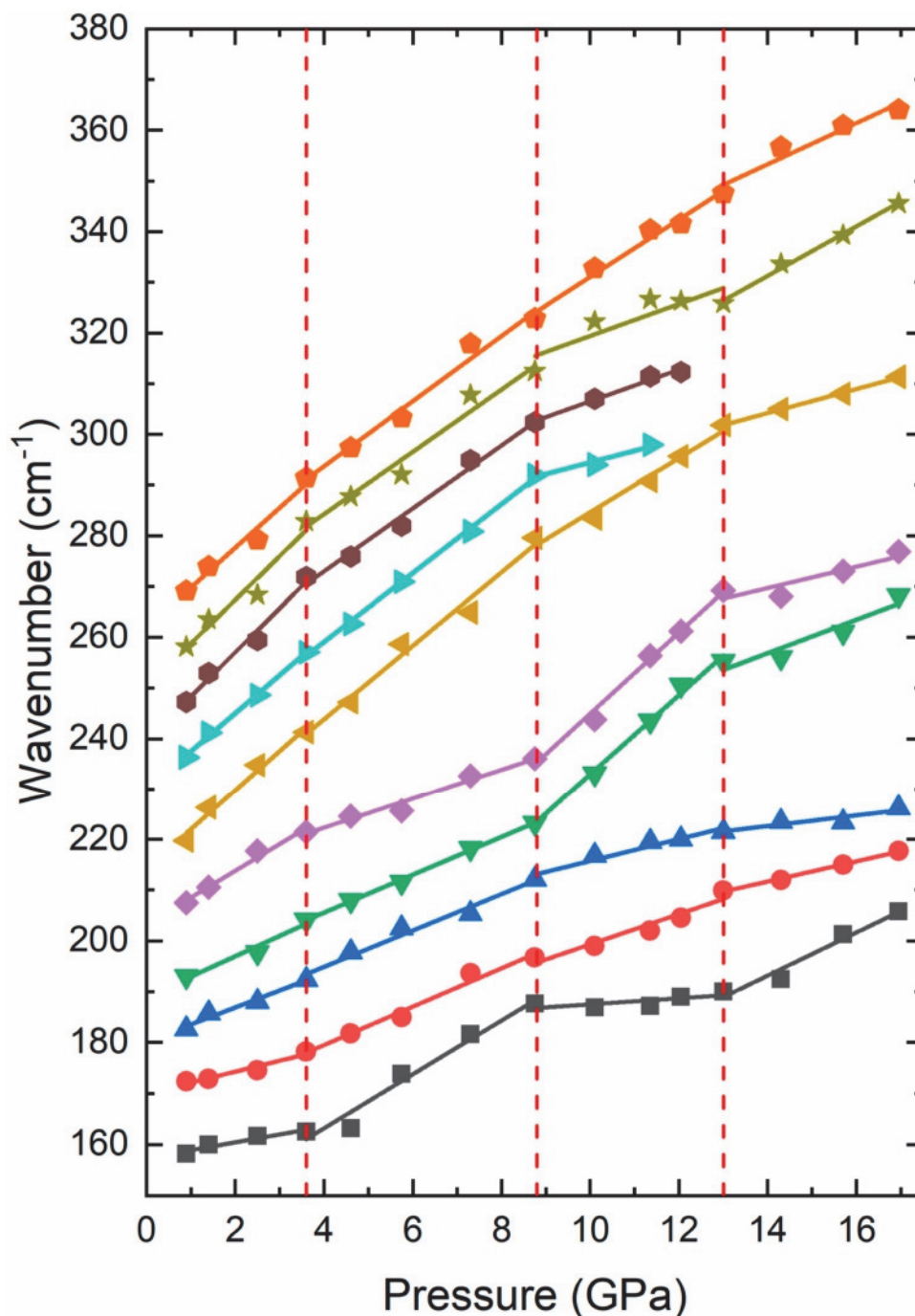


Figure 5. Pressure dependence of IR modes obtained from experiments. Only lattice modes are shown. Vertical lines indicate suggested transition pressures.

We will comment now on the pressure dependence of the ten lattice modes that were observed under sample compression. For these modes, the changes in the frequency pressure dependence, at phase transitions, are more evident than in the bending modes, as can be seen in Figure 5. In particular, slope changes can be seen at the transition pressures (3.6, 8.8, and 13 GPa), which are represented by vertical lines in the figure. Such changes are very noticeable in the lowest-frequency mode shown in Figure 5. They are also quite evident for the mode at 208 cm⁻¹ at 0.9 GPa. As happened in the bending modes, the changes at 13 GPa are more noticeable than changes at the other transitions. In particular, there are discontinuities in the frequencies of at least two modes. The changes in the frequency pressure dependences at the phase transitions detected at 3.6 and 8.8 GPa, and

the strongly non-linear pressure dependences, are qualitatively similar to those observed for phonons in $\text{Fe}(\text{IO}_3)_3$ at 2 and 6 GPa [12,13]. In $\text{Fe}(\text{IO}_3)_3$, these changes have been related to isostructural phase transitions occurring in Ref. [12,13], which are themselves related to gradual pressure-induced changes in the coordination sphere of iodine, which are affected by the presence of lone electron pairs. The similarities between $\text{Zn}(\text{IO}_3)_2$ and $\text{Fe}(\text{IO}_3)_3$ therefore provide further support to the observation of phase transitions in the $\text{Zn}(\text{IO}_3)_2$ investigated here. Future studies using other characterization techniques, including X-ray diffraction and Raman spectroscopy should be performed to confirm the present interpretation of results and to determine if the transitions at 3.6 and 8.8 GPa are isostructural or not. We hope our work will trigger such studies as well as computer simulation studies.

Before concluding, we would like to add a comment on the transition at 13 GPa. The changes observed around 13 GPa are more apparent than those observed around 3.6 and 8.8 GPa. This suggests that the changes around 13 GPa can be linked to the occurrence of a first-order structural transition. The fact that the changes are accompanied by a marked broadening of phonon bands suggests a disorder of the crystal structure [26], which could be related to the presence of non-hydrostatic stresses at 13 GPa and higher pressures [27].

To conclude, we note that all observed modes harden under compression. In the pressure range up to 3.6 GPa (before the first phase transition), the pressure coefficients are all within the range of $1\text{--}9\text{ cm}^{-1}/\text{GPa}$. This can be seen in Table 2, where we represent phonons frequencies (ω) and pressure coefficients ($d\omega/dP$) for different modes in the different phases. We have named the phases as follows: phase I (low-pressure phase), II, III, and IV (successive HP phases). Table 2 shows clearly the change in the pressure dependences at 3.6 GPa and 8.8 GPa as well as the changes in frequencies and pressure dependencies at 13 GPa, supporting the existence of the proposed transitions. The pressure coefficients in the low-pressure phase are comparable to pressure coefficients in $\text{Fe}(\text{IO}_3)_3$ [13], LiIO_3 [28], and KIO_3 [29] in the same frequency region, indicating that $\text{Zn}(\text{IO}_3)_2$ is extremely compressible, similar to these other iodates. Additionally, the pressure coefficients for the different HP phases are of the same order of magnitude as in the low-pressure phase, suggesting that the changes in the coordination polyhedra are not drastic and that the transition is probably related to gradual changes in cation coordination number [30].

Table 2. Phonon frequencies (ω) of the modes observed under compression for phases I (at 0.9 GPa), II (at 3.6 GPa), III (at 8.8 GPa, and IV (at 13 GPa). The pressure coefficients ($d\omega/dP$) obtained from linear fits are also given.

ω (cm^{-1}) Phase I 0.9 GP	$d\omega/dP$ ($\text{cm}^{-1}/\text{GPa}$)	ω (cm^{-1}) Phase II 3.6 GPa	$d\omega/dP$ ($\text{cm}^{-1}/\text{GPa}$)	ω (cm^{-1}) Phase III 8.8 GPa	$d\omega/dP$ ($\text{cm}^{-1}/\text{GPa}$)	ω (cm^{-1}) Phase IV 13 GPa	$d\omega/dP$ ($\text{cm}^{-1}/\text{GPa}$)
158(2)	1.5(1)	163(2)	5.3(1)	188(2)	0.6(1)	190(2)	4.2(1)
172(2)	2.1(1)	178(2)	3.8(1)	197(2)	3.0(1)	210(2)	2.0(1)
183(2)	3.3(1)	192(2)	3.6(1)	212(2)	2.2(1)	222(2)	1.1(1)
193(2)	4.0(1)	204(2)	3.7(1)	223(2)	7.8(1)	255(2)	3.3(1)
207(2)	5.3(1)	221(2)	2.9(1)	236(2)	8.0(1)	269(2)	2.1(1)
220(2)	7.8(1)	241(2)	7.2(1)	280(2)	5.3(1)	302(2)	2.4(1)
236(2)	7.5(1)	257(2)	6.8(1)	292(2)	2.3(1)	–	–
247(2)	8.7(1)	272(2)	6.2(1)	302(2)	3.1(1)	–	–
258(2)	8.6(1)	283(2)	6.1(1)	312(2)	3.2(1)	326(2)	4.9(1)
269(2)	7.9(1)	291(2)	6.4(1)	323(2)	5.7(1)	348(2)	4.1(1)
322(2)	4.1(1)	331(2)	4.2(1)	347(2)	5.6(1)	373(2)	6.4(1)
336(2)	3.4(1)	345(2)	3.1(1)	368(2)	6.0(1)	393(2)	5.6(1)
353(2)	3.8(1)	364(2)	4.9(1)	389(2)	7.1(1)	419(2)	4.9(1)
361(2)	4.6(1)	375(2)	6.4(1)	407(2)	5.2(1)	429(2)	6.3(1)
388(2)	4.8(1)	401(2)	5.2(1)	424(2)	1.8(1)	450(2)	3.4(1)
425(2)	4.6(1)	439(2)	4.4(1)	465(2)	0.5(1)	471(2)	4.3(1)
440(2)	4.4(1)	453(2)	4.7(1)	477(2)	0.7(1)	482(2)	4.8(1)
452(2)	4.5(1)	464(2)	4.4(1)	488(2)	6.5(1)	509(2)	5.1(1)

4. Conclusions

Synchrotron far-infrared spectroscopy measurements have allowed us to determine that $\text{Zn}(\text{IO}_3)_2$ undergoes three phase transitions at 3.6, 8.8, and 13 GPa. The phase transitions are identified from changes in the infrared spectra. The first two transitions resemble those previously observed in $\text{Fe}(\text{IO}_3)_3$ at similar pressures and are probably isostructural transitions favored by the presence of lone electron pairs in $\text{Zn}(\text{IO}_3)_2$. The third phase transition appears to be a first-order transition that is connected to the occurrence of more important structural changes. Assignment of phonon modes has been discussed and their pressure dependence reported. We found that the lattice modes are more sensitive than the bending modes of IO_3 to pressure-induced structural changes.

Author Contributions: Conceptualization, D.E.; IR experiments, A.L., R.T., E.B., I.Y., and C.P.; formal analysis, A.L. and D.E.; sample preparation, Z.H.; writing, review, and editing, all the authors. All authors have read and agreed to the published version of the manuscript.

Funding: This work was supported by the Spanish Ministry of Science, Innovation, and Universities under grants PID2019-106383GB-C41 and RED2018-102612-T (MALTA Consolider-Team Network) and by Generalitat Valenciana under grant Prometeo/2018/123 (EFIMAT). R.T. acknowledges funding from the Spanish MINECO via the Juan de la Cierva Formación program (FJC2018-036185-I). A.L. and D.E. would like to thank the Generalitat Valenciana for the Ph.D. fellowship GRISO-LIAP/2019/025.

Institutional Review Board Statement: Not applicable.

Informed Consent Statement: Not applicable.

Data Availability Statement: Data is contained within the article.

Acknowledgments: The authors thank ALBA synchrotron for providing beamtime at MIRAS beamline for performing synchrotron far-infrared experiments.

Conflicts of Interest: The authors declare no conflict of interest.

References

1. Bonacina, L.; Mugnier, Y.; Courvoisier, F.; Le Dantec, R.; Extermann, J.; Lambert, Y.; Boutou, V.; Galez, C.; Wolf, J.P. Polar $\text{Fe}(\text{IO}_3)_3$ nanocrystals as local probes for nonlinear microscopy. *Appl. Phys. B Lasers Opt.* **2007**, *87*, 399–403. [[CrossRef](#)]
2. Hebboul, Z.; Galez, C.; Benbental, D.; Beauquis, S.; Mugnier, Y.; Benmakhlouf, A.; Bouchenafa, M.; Errandonea, D. Synthesis, characterization, and crystal structure determination of a new lithium zinc iodate polymorph $\text{LiZn}(\text{IO}_3)_3$. *Crystals* **2019**, *9*, 464. [[CrossRef](#)]
3. Jia, Y.J.; Chen, Y.G.; Guo, Y.; Guan, X.F.; Li, C.; Li, B.; Liu, M.M.; Zhang, X.M. $\text{LiM}_{\text{II}}(\text{IO}_3)_3$ ($\text{M}_{\text{II}} = \text{Zn}$ and Cd): Two Promising Nonlinear Optical Crystals Derived from a Tunable Structure Model of $\alpha\text{-LiIO}_3$. *Angew. Chemie Int. Ed.* **2019**, *58*, 17194–17198. [[CrossRef](#)] [[PubMed](#)]
4. Hebboul, Z.; Ghozlane, A.; Turnbull, R.; Benghia, A.; Allaoui, S. Simple new method for the preparation of $\text{La}(\text{IO}_3)_3$ nanoparticles. *Nanomaterials* **2020**, *10*, 2400. [[CrossRef](#)] [[PubMed](#)]
5. Patil, A.B. FTIR study of second group iodate crystals grown by gel method. *Int. J. Grid Nad. Distrib. Comput.* **2020**, *13*, 227–235.
6. Benghia, A.; Hebboul, Z.; Chikhaoui, R.; Khaldoun Lefkaier, I.; Chouireb, A.; Goumri-Said, S. Effect of iodic acid concentration in preparation of zinc iodate: Experimental characterization of $\text{Zn}(\text{IO}_3)_2$, and its physical properties from density functional theory. *Vacuum* **2020**, *181*, 109660. [[CrossRef](#)]
7. Kochuthresia, T.C.; Gautier-Luneau, I.; Vaidyan, V.K.; Bushiri, M.J. Raman and Ftir Spectral Investigations of Twinned $\text{M}(\text{IO}_3)_2$ ($\text{M} = \text{Mn}, \text{Ni}, \text{Co}, \text{AND Zn}$) Crystals. *J. Appl. Spectrosc.* **2016**, *82*, 941–946. [[CrossRef](#)]
8. Shanmuga Sundar, G.J.; Kumar, S.M.R.; Packiya raj, M.; Selvakumar, S. Synthesis, growth, optical, mechanical and dielectric studies on NLO active monometallic zinc iodate $[\text{Zn}(\text{IO}_3)_2]$ crystal for frequency conversion. *Mater. Res. Bull.* **2019**, *112*, 22–27. [[CrossRef](#)]
9. Phanon, D.; Bentría, B.; Jeanneau, E.; Benbental, D.; Mosset, A.; Gautier-Luneau, I. Crystal structure of $\text{M}(\text{IO}_3)_2$ metal iodates, twinned by pseudo-merohedry, with M_{II} : Mg_{II} , Mn_{II} , Co_{II} , Ni_{II} and Zn_{II} . *Z. Krist.* **2006**, *221*, 635–642.
10. Liang, J.K.; Wang, C.G. The structure of $\text{Zn}(\text{IO}_3)_2$ Crystal. *Acta Chim. Sin.* **1982**, *40*, 985–993.
11. Mougél, F.; Kahn-Harari, A.; Aka, G.; Pelenc, D. Structural and thermal stability of Czochralski grown GdCOB oxoborate single crystals. *J. Mater. Chem.* **1998**, *8*, 1619–1623. [[CrossRef](#)]
12. Liang, A.; Rahman, S.; Saqib, H.; Rodriguez-Hernandez, P.; Munoz, A.; Nenert, G.; Yousef, I.; Popescu, C.; Errandonea, D. First-Order Isostructural Phase Transition Induced by High-Pressure in $\text{Fe}(\text{IO}_3)_3$. *J. Phys. Chem. C* **2020**, *124*, 8669–8679. [[CrossRef](#)]

13. Liang, A.; Rahman, S.; Rodriguez-Hernandez, P.; Muñoz, A.; Manjón, F.J.; Nenert, G.; Errandonea, D. High-pressure Raman study of Fe(IO₃)₃: Soft-mode behavior driven by coordination changes of iodine atoms. *J. Phys. Chem. C* **2020**, *124*, 21329–21337. [[CrossRef](#)]
14. Sagotra, A.K.; Errandonea, D.; Cazorla, C. Mechanocaloric effects in superionic thin films from atomistic simulations. *Nat. Commun.* **2017**, *8*, 963. [[CrossRef](#)] [[PubMed](#)]
15. Ross, N.L.; Detrie, T.A.; Liu, Z. High-pressure raman and infrared spectroscopic study of prehnite. *Minerals* **2020**, *10*, 312. [[CrossRef](#)]
16. Peter, S.; Pracht, G.; Lange, N.; Lutz, H.D. Zinkiodate ± Schwingungsspektren (IR, Raman) und Kristallstruktur von Zn(IO₃)₂·2H₂O Zinc Iodates ± Infrared and Raman Spectra, Crystal Structure. *Z. Anorg. Allg. Chem.* **2000**, *626*, 208–215. [[CrossRef](#)]
17. Asami, K.; Kondo, Y. Effect of very high pressure on the optical absorption spectra in CsI. *Solid State Commun.* **1981**, *40*, 715–718. [[CrossRef](#)]
18. Celeste, A.; Borondics, F.; Capitani, F. Hydrostaticity of pressure-transmitting media for high pressure infrared spectroscopy. *High Press. Res.* **2019**, *39*, 608–618. [[CrossRef](#)]
19. Mao, H.K.; Xu, J.; Bell, P.M. Calibration of the ruby pressure gauge to 800 kbar under quasi-hydrostatic conditions. *J. Geophys. Res.* **1986**, *91*, 4673–4676. [[CrossRef](#)]
20. Bushiri, M.J.; Kochuthresia, T.C.; Vaidyan, V.K.; Gautier-Luneau, I. Raman scattering structural studies of nonlinear optical M(IO₃)₃ (M = Fe, Ga, and In) and linear optical β-In(IO₃)₃. *J. Nonlinear Opt. Phys. Mater.* **2014**, *23*, 1450039. [[CrossRef](#)]
21. Crettez, J.M.; Gard, R.; Remoissenet, M. Near and far infrared investigations from α and β lithium iodate crystals. *Solid State Commun.* **1972**, *11*, 951–954. [[CrossRef](#)]
22. Pimenta, M.A.; Oliveira, M.A.S.; Bourson, P.; Crettez, J.M. Raman study of Li_{1-x}H_xIO₃ crystals. *J. Phys. Condens. Matter* **1997**, *9*, 7903–7912. [[CrossRef](#)]
23. Errandonea, D.; Muñoz, A.; Rodríguez-Hernández, P.; Gomis, O.; Achary, S.N.; Popescu, C.; Patwe, S.J.; Tyagi, A.K. High-Pressure Crystal Structure, Lattice Vibrations, and Band Structure of BiSbO. *Inorg. Chem.* **2016**, *55*, 4958–4969. [[CrossRef](#)] [[PubMed](#)]
24. Errandonea, D.; Manjón, F.J.; Garro, N.; Rodríguez-Hernández, P.; Radescu, S.; Mujica, A.; Muñoz, A.; Tu, C.Y. Combined Raman scattering and ab initio investigation of pressure-induced structural phase transitions in the scintillator ZnWO₄. *Phys. Rev. B Condens. Matter Mater. Phys.* **2008**, *78*, 054116. [[CrossRef](#)]
25. Cavalcante, L.S.; Moraes, E.; Almeida, M.A.P.; Dalmaschio, C.J.; Batista, N.C.; Varela, J.A.; Longo, E.; Siu Li, M.; Andrés, J.; Beltrán, A. A combined theoretical and experimental study of electronic structure and optical properties of β-ZnMoO₄ microcrystals. *Polyhedron* **2013**, *54*, 13–25. [[CrossRef](#)]
26. Tschauer, O.; Errandonea, D.; Serghiou, G. Possible superlattice formation in high-temperature treated carbonaceous MgB₂ at elevated pressure. *Physica B* **2006**, *371*, 88–94. [[CrossRef](#)]
27. Errandonea, D.; Meng, Y.; Somayazulu, M.; Häusermann, D. Pressure-induced → ω transition in titanium metal: A systematic study of the effects of uniaxial stress. *Physica B* **2005**, *355*, 116–125. [[CrossRef](#)]
28. Mendes Filho, J.; Lemos, V.; Cerdeira, F.; Katiyar, R.S. Raman and x-ray studies of a high-pressure phase transition in β-LiIO₃ and the study of anharmonic effects. *Phys. Rev. B* **1984**, *30*, 7212–7218. [[CrossRef](#)]
29. Shen, Z.X.; Wang, X.B.; Tang, S.H.; Li, H.P.; Zhou, F. High pressure raman study and phase transitions of KIO₃ non-linear optical single crystals. *Rev. High Press. Sci. Technol. No Kagaku To Gijutsu* **1998**, *7*, 751–753. [[CrossRef](#)]
30. Sans, J.A.; Vilaplana, R.; Lora da Silva, E.; Popescu, C.; Cuenca-Gotor, V.P.; Andrada-Chacoón, A.; Muñoz, A.; Sánchez-Benitez, J.; Gomis, O.; Pereira, A.L.J.; et al. Characterization and decomposition of the natural van der Waals SnSb₂Te₄ under compression. *Inorg. Chem.* **2020**, *59*, 9900–9918. [[CrossRef](#)]

6. Crystal structure and atomic vibrations of $\text{Mg}(\text{IO}_3)_2$, electronic band structure of $\text{Mg}(\text{IO}_3)_2$ and $\text{Zn}(\text{IO}_3)_2$ under pressure

There are two parts in this chapter, the first part reports the structural and vibrational behavior of $\text{Mg}(\text{IO}_3)_2$ under pressure, which were studied by means of HPXRD, HPRS, HPFTIR, and first-principle calculations. We revealed that $\text{Mg}(\text{IO}_3)_2$ undergoes a phase transition at the pressure interval of 7.5-9.7 GPa from a monoclinic (LP phase, space group: $P2_1$) to a trigonal (HP phase, space group: $P3$) structure. The phase transition was evidenced by the Rietveld refinement of XRD, as well as the new peaks appearing in Raman and infrared spectra at 7.7 GPa and 9.6 GPa, respectively. The phase transition did not involve a collapse in the unit-cell volume. However, the unit-cell volume shows a different pressure coefficient before and after the phase transition. The oxygen coordination of iodine increased from 3 to 6 fold, as a consequence of (i). The shortening of the bond distance between iodine and the oxygen in the neighboring IO_3 layer, and (ii). The existence of the stereochemically active LEP in iodine. The softening behavior of several Raman modes, which is related to the stretching of the I-O bonds, have been observed under pressure. Furthermore, systematic studies of the crystal structure, EOS, and the symmetry assignment of the Raman- and infrared-modes of both phases were reported.

The second part of this chapter includes the electronic band structure studies on $\text{Mg}(\text{IO}_3)_2$ and $\text{Zn}(\text{IO}_3)_2$, as representatives of the non-transition and closed-shelled metal iodates. The pressure-induced changes in the bandgap have been investigated and correlated to the changes in the I-O bond distance. The bandgap of the two metal iodates shows a nonlinear narrowing under pressure caused by the competition of two effects. The enlargement of the bond distance between iodine and inlayer oxygen favors the narrowing the bandgap energy, while the reductions of the bond distance between iodine and interlayer oxygen favors the opening of the bandgap energy. The negative relationship between the bandgap energy and bond distance between iodine and inlayer oxygen have been confirmed by correlating the bandgap energy and corresponding average I-O bond distance of 71 different metal iodates reported in the literature. For

this purpose, only non-transition and closed-shelled metal iodates are included. Finally, the second instruction for designing wide-bandgap metal iodates is given in this chapter.

6.1 Introduction

At ambient pressure, $\text{Mg}(\text{IO}_3)_2$ crystallizes in a monoclinic structure (space group: $P2_1$, No. 4), the crystal structure of the low-pressure (LP) phase and high-pressure (HP) phase are shown in **Figure 37**. It is worth mentioning that there are two crystal structures for the LP phase reported in the literature [129,150], the hexagonal structure reported by Liang *et al* [150] have been ruled out as it failed to describe all the diffraction peak of the XRD at ambient pressure. Instead, the monoclinic structure reported by Phanon *et al* [151] can describe all the diffraction peaks in the XRD collected at ambient pressure (see Supplementary Information of ref. [151]). In the LP phase, when view along to b -axis, each iodine atom is bonded with three oxygen atoms, forming a IO_3 pyramid. Each Mg atom is surrounded by six IO_3 pyramid by sharing one oxygen atom. Mg occupies in two different Wyckoff positions and iodine occupies in four different Wyckoff positions (the atomic position of the LP phase have been summarized in Table I of ref. [151]). When view perpendicular to b -axis, there is a layered structure formed by IO_3 polyhedra, and the IO_3 layer is connected by MgO_6 octahedra.

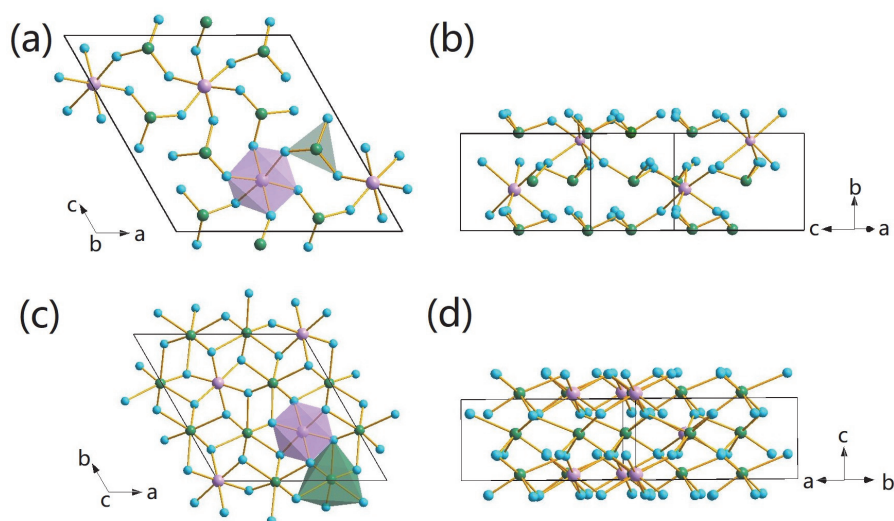


Figure 37. Crystal structure of Mg(IO₃)₂. (a) LP phase, along *b* axis. (b) LP phase, perpendicular to *b* axis. (c) HP phase, along to *c* axis. (d) HP phase, perpendicular to *c* axis. In the figure, Mg, I and O atoms are shown in purple, green and cyan-blue ball, respectively. Bonds are shown in solid yellow lines and the represented polyhedral are shown in (a) and (c).

This chapter contains two published papers [36,151]. The first paper was published in February 2022 [151], where the results of HPXRD, HPRS, HPFTIR, and first-principle calculations for Mg(IO₃)₂ were reported. The monoclinic to trigonal phase transition was characterized by all the diagnostics. The crystal structure and atomic vibration of the LP and HP phase were investigated.

The second paper was published in April 2022. The bandgap change of Mg and Zn iodates was reported. By utilizing the theoretically calculated DOS, PDOS and crystal orbital overlap population (COOP) for those two materials, the molecular orbital (MO) diagrams for them was established, and used to explain the pressure-induced bandgap change using the I-O bond distance change. Furthermore, the relationship between bandgap energy for Mg and Zn iodates and I-O bond distance was confirmed by collating the related data of 71 different metal iodates reported in the literature. The second rule for designing wide-bandgap energy metal iodates were given in this paper.

6.2 Experiment and calculation details

6.2.1 Sample preparation

Needle-like polycrystalline $\text{Mg}(\text{IO}_3)_2$ was synthesized from an aqueous solution with a mixture of 2 mmol of KIO_3 (99.5% purity, Sigma Aldrich) and 1 mmol of anhydrous MgCl_2 ($\geq 98\%$ purity, Sigma Aldrich). The mixture was thoroughly stirred and then the solvents were left to slowly evaporate for a few days at 60 °C. The polycrystalline sample was used to measure the HPXRD, HPRS, HPFTIR, and HPOA of $\text{Mg}(\text{IO}_3)_2$.

Single crystal $\text{Zn}(\text{IO}_3)_2$ was synthesized by single-diffusion gel technique at room temperature and hydrosilica gel was used as the medium. The gel was prepared by dissolving sodium meta silicate ($\text{Na}_2\text{SiO}_3 \cdot 9\text{H}_2\text{O}$, CDH) in bi-distilled water, and then the amount of potassium iodate (99%, Merck) corresponding to 0.5 M was dissolved in the SMS gel. The mixture of the gel was acidified with glacial acetic acid in a PH range of 4-7. The resulting solution was transferred into the sides of the test tubes (2.5 cm in diameter and 20 cm in length) to avoid air bubbles in the gel medium and to keep the medium undisturbed for gelation. An aqueous solution of zinc chloride was poured slowly over the set gel to prevent gel breakage. The zinc ions slowly diffuse through the narrow pores of the hydrosilica gel and react with the iodate ions present in the gel, leading to the formation of high-quality, white $\text{Zn}(\text{IO}_3)_2$ single crystals over a time period of 3 weeks. The single-crystal sample was used to measure the HPOA of $\text{Zn}(\text{IO}_3)_2$.

6.2.2 HPXRD

High-pressure angle-dispersion X-ray diffraction was conducted at BL04-MSPD beamline at ALBA synchrotron [133]. A membrane type of DAC with the diamond culet of 400 μm was used to generate the high pressure environment. A 180- μm hole was drilled in the center of the stainless-steel gasket, which have been pre-indented to a thickness of 40 μm , to serve as the sample chamber. The sample, together with copper and PTM was loaded in the sample chamber, the EOS of copper [92] was used to determine the pressure and a mixture of methanol: ethanol; water at a ratio of 16:3:1

(MEW) was used as the PTM. More information about the set-up in MSPD beamline can be found in 4.2.2, with the slight difference that the wavelength of X-ray has been changed to 0.4642 Å.

6.2.3 HPRS

A membrane-type DAC with the diamond culet of 500 µm was used to generate the high pressure environment, a stainless-steel gasket was first pre-indented to a thickness of 40 µm, and then a 250-µm hole was drilled in the center of the gasket as the sample chamber. The sample, together with Ruby and PTM, were loaded in the sample chamber. The pressure was measured by using the ruby fluorescence method [93] and the PTM is MEW. More information about the experiment set-up can be found in **Chapter 3.2.3** of this thesis.

6.2.4 HPFTIR

HPFTIR was conducted in MIRAS beamline at ALBA synchrotron [105]. A membrane-type DAC equipped with IIAC diamond with a culet of 300 µm was used to generate the high pressure environment. A stainless-steel was first pre-indented to a thickness of 40 µm and a hole with a diameter of 150 µm was drilled in the center and served as the sample chamber. The polycrystalline sample was first pressed into a 10-µm-thick platelets and then loaded into the sample chamber with the ruby and PTM, the ruby fluorescence method was used to measure the pressure [93] and CsI was used as the PTM. More detail about the experiment set-up for the HPFTIR can be found in **Chapter 3.2.3** of this thesis.

6.2.5 HPOA

For the experiments of Mg(IO₃)₂, a membrane-type of DAC was used to generate the high pressure environment, a stainless-steel gasket was first pre-indented to a thickness of 45 µm and then a 200-µm hole was drilled in the center as the sample chamber. The polycrystalline sample was first pressed into a compact 20-µm-thick platelets, and then loaded in the sample chamber, together with ruby and PTM, the ruby fluorescence

method was used to determine the pressure and KBr was used as the PTM.

For the experiments of $\text{Zn}(\text{IO}_3)_2$, the same DAC and gasket was used to generate the high pressure environment, a piece of single-crystal sample with a thickness of 20 μm was selected. The PTM used in this experiment is MEW and the ruby fluorescence method was used to determine the pressure [93]. The completeness of the loading for those two samples can be found later. More information about the experiment set-up can be found in **Chapter 3.2.5** of this thesis.

6.2.6 Overview of calculations

For the calculation on the crystal structure and phonon of $\text{Mg}(\text{IO}_3)_2$. The first-principle simulations were performed in VASP within the framework of DFT with the projector augmented-wave pseudopotentials [107–109,113]. The plane-wave kinetic energy cutoff was chosen as 540 eV to ensure an accurate result. The generalized gradient approximation with Armiento and Mattsson AM05 prescription was used to describe the exchange-correlation energy [152,153]. The Monkhorst-Pack scheme was employed for the Brillouin zone (BZ) integrations with a $6 \times 4 \times 6$ and $6 \times 6 \times 4$ grid of k -space points for the LP and HP phase [117]. The lattice parameters and the atomic positions at selected volumes were obtained from the fully relaxed structure, this simulation provides a series of volume, energy, and pressure, a BM EOS was used to fit the results and obtain the theoretical equilibrium volume, the bulk modulus and the related pressure derivatives.

The calculation on the phonon modes were carried out at the zone center (Γ point) of the BZ with the direct force-constant approach. The frequency of the normal modes, as well as the symmetry and polarization vectors, can be obtained from this calculation. The crystal structure and phonon calculation of $\text{Zn}(\text{IO}_3)_2$ can be found in 5.3.4 of this thesis.

The electronic band structure calculation for Mg and Zn iodates was performed with the SEEK-PATH tool [154], and the band-structure analysis was carried out with SUMO package [155], The calculation on COOP was performed by using the LOBSTER software [156].

6.3 Results and Discussion

The XRD patterns of $\text{Mg}(\text{IO}_3)_2$ at selected pressures are shown in **Figure 38a**, XRD can be well indexed by the crystal structure reported by Phanon *et al* [129]. The representative Rietveld refinement on the XRD collected at 0.1 GPa is shown in **Figure 38b**. There are no peaks appearance or split throughout the experiment. However, the structure, $P2_1$, failed to describe all the peaks simultaneously of the XRD pattern collected at 10.5 GPa (as **Figure 38b** shown), the peak (-111) changed in pressure coefficient after 8.5 GPa. In additional, the peak (111) and (-311) disappear above this pressure. All the changes in XRD indicating a phase transition happened at 8.5 GPa, the crystal structure of $\text{Mg}(\text{IO}_3)_2$ may increase in symmetry.

We found that the trigonal structure with a space group $P3$ can refine the XRD at pressures higher than 8.5 GPa, the comprehensive Rietveld refinement of the XRD pattern collected at 10.5 GPa was shown in **Figure 38b**. The quality of the refinement is $R_p = 10.6\%$ and $R_{wp} = 10.1\%$, the detailed crystal structure information of the HP phase (at 10.5 GPa) have been summarized in Table I of ref. [151]. The crystal structure of the HP phase is shown in **Figure 37b** and **c**. When view along c -axis (which is equivalent to the b -axis of the LP phase), each iodine atoms bonded with six oxygen atoms, and each Mg atom was surround by six IO_6 units by sharing two oxygen atoms. When view perpendicular to c axis, it transferred from the layered structure of the LP phase to the 3-dimensional structure, iodine bonded with additional three oxygen atoms in the neighboring IO_3 layer. The change in the XRD is reversible as the topmost XRD pattern in **Figure 38a** shows.

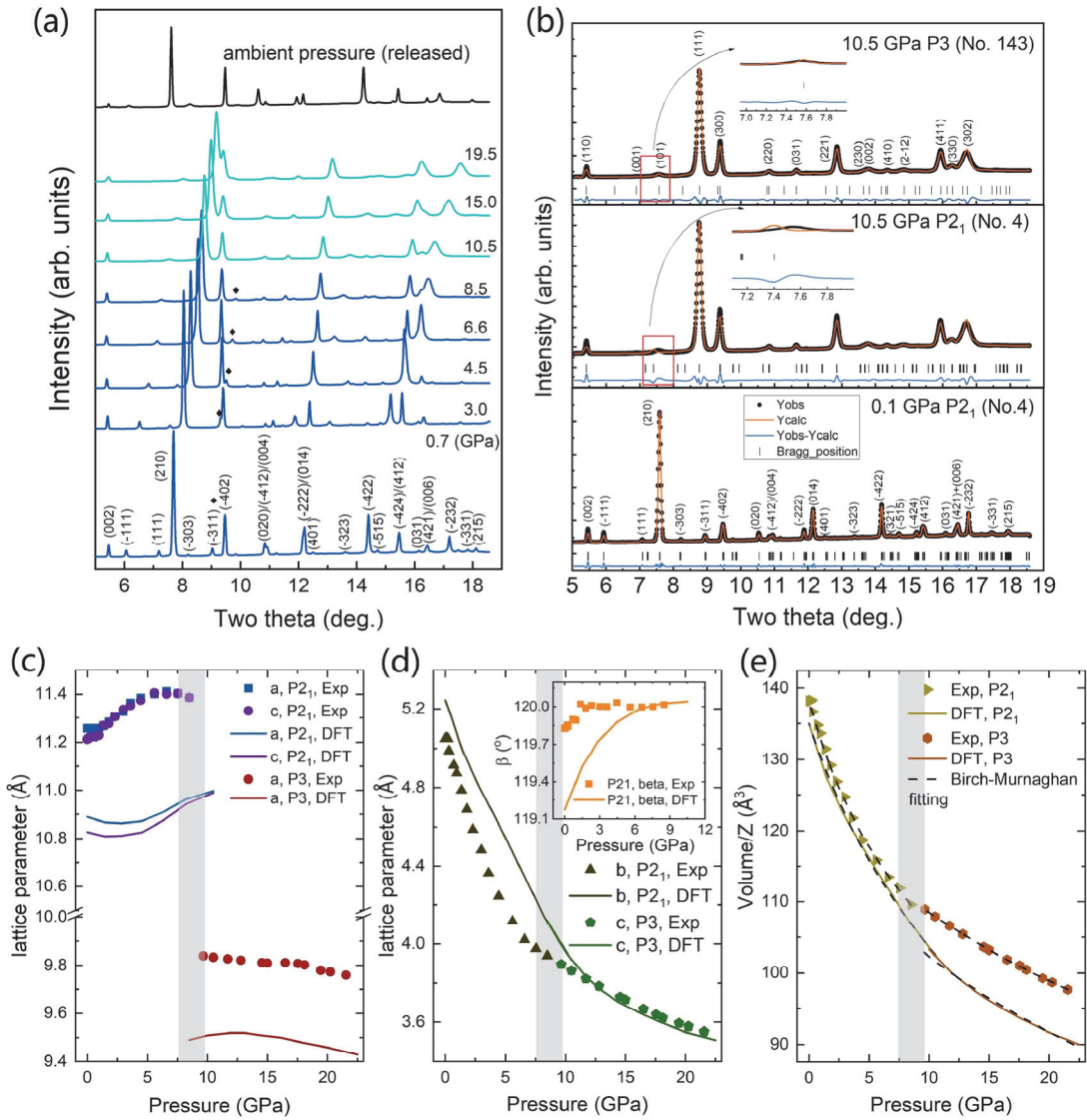


Figure 38. (a) XRD pattern of $\text{Mg}(\text{IO}_3)_2$ at selected pressure, the XRD pattern of the LP phase are shown in blue and that for HP phase are shown in cyan-blue. The pressure of each pattern are shown in the right in the units of “GPa”. The black diamond is a guide for the evolution of peak (-311) and the miller index of the XRD peaks are marked at the pressure of 0.7 GPa. (b) The representative Rietveld refinement at 0.1 and 10.5 GPa with the crystal structure of LP phase ($P2_1$), the Rietveld refinement at 10.5 GPa with the crystal structure of HP phase was shown in the top. Black dots show experimental data, orange lines are the refined patterns, ticks show the positions of diffraction peaks, and blue lines show the residuals. (c)-(d). Experiment (symbols) and calculation (solid lines) determined lattice parameter and unit-cell volume as a function of pressure. In (d) the dash line is the BM fitting.

The lattice parameters and unit-cell volume for both the LP and HP phase was obtained from the Rietveld refinement on the XRD patterns. They are shown in **Figure 38 c-d**. In the LP phase, the crystal structure favors the expansion of the *a* and *c* axis under compression, and show a large sharp decrease in the *b*-axis. The changes of lattice parameters in the LP phase are similar to that in Zn(IO₃)₂. The crystal structure in the LP phase shows a huge anisotropic response. The *b*–axis is the most compressible axis. This behavior is related to the layered structure of Mg(IO₃)₂ in the LP phase. In the HP phase, the lattice parameter *a* shows a slightly decrease under compression, and the lattice parameter *c* (equivalent to the *b* axis of the LP phase) shows a reduction under compression, but it is less sensitive to pressure than the *b*-axis in LP phase, as well as the unit-cell volume. The monoclinic angle in the LP phase increases from 119.1 degrees to 120 degrees at around 6 GPa. By adopting a 3rd-order BM EOS for the unit-cell volume in the LP and HP phase, the bulk modulus of the LP phase is 22.2 GPa (26.4 GPa) in experiments (calculations), the bulk modulus of LP phase obtained from experiments is close to that of Zn(IO₃)₂ (21.6 GPa), slightly smaller than that of the ambient+I1 phase of Co(IO₃)₂ (29.8 GPa), and much smaller than that of the LP phase of Fe(IO₃)₃ (55 GPa). The bulk modulus of the HP phase is 63.6 GPa in experiments and 44.4 GPa in calculations. The increase of the bulk modulus is related to the increase of the oxygen coordination of iodine after the phase transition. The coordination increase will be discussed later, the new bonds formed between the iodine and oxygen in the neighboring IO₃ layer resist the external compression.

Based on the fact that there is a good agreement between the experiment and calculations (**Figure 38 c-d**), it is reasonable to analyze the I-O and Mg-O bond distance change using calculation, as shown in **Figure 39**. In the LP phase, Mg is bonded with six oxygen atoms in six different Wyckoff positions, so there are six different Mg-O bond distances in the LP phase, and all of them shorten under compression. In the HP phase each Mg is bonded with six oxygen atoms located in two different Wyckoff positions. So there are only two different Mg-O bond distances after the phase transition, and both of them shorten under compression. The changes in the Mg-O bond distance indicate that the MgO octahedra become more symmetric as the **Figure 39c** shows. The two types of I-O bond distances in Mg(IO₃)₂ show a totally different behavior under compression. Both in the LP and HP phase, the bond between iodine and inlayer oxygen (distance between 1.8 and 1.9 Å at ambient pressure) become slightly longer under

pressure, and the bond distance between iodine and interlayer oxygen (bond distance range from 2.6 to 3.0 Å at ambient pressure) continuously shorten under pressure. As a consequence, the distortion index of IO₆ polyhedra decrease under compression as **Figure 39c** shows. If we chose 2.48 Å as the maximum bonding distance between iodine and oxygen, then there is a gradually increase of the oxygen coordination in iodine, and it becomes 6-fold in the HP phase. The driven force is the same as we discussed in the coordination increase of Fe, Co and Zn iodates in this thesis.

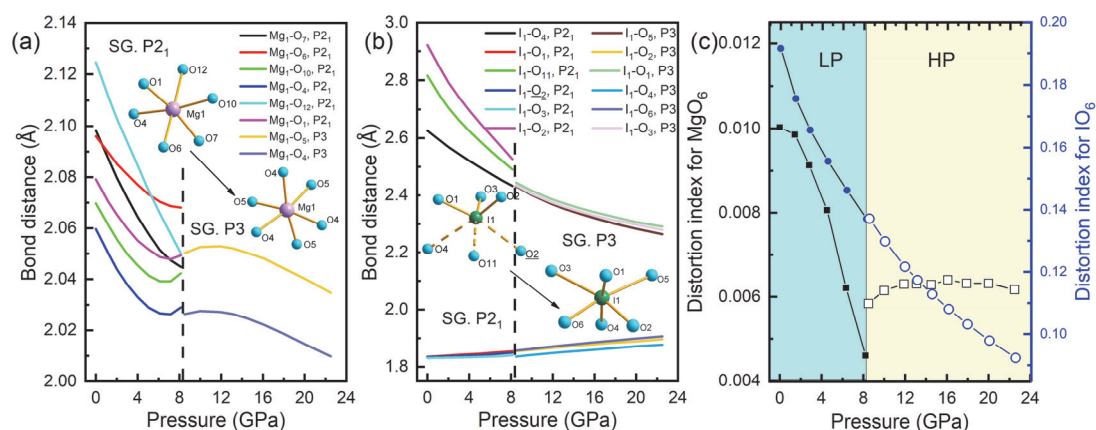


Figure 39. Calculation determined pressure dependence of the (a) Mg-O bond distance and (b) I-O bond distance. polyhedral coordination is shown in the figure. (c) calculation determined distortion index of MgO₆ and IO₆ polyhedral as a function of pressure.

According to group theory, the LP phase (space group: $P2_1$) is predicted to have 54A+54B in total 108 modes, including three acoustic vibrations (A+2B). The HP phase should have 27A+27E in total 54 modes, including two acoustic vibrations (A+E). The Raman spectra of Mg(IO₃)₂ are shown in **Figure 40** at the mid-frequency region (wavenumber range from 200 to 550 cm⁻¹) and high-frequency region (wavenumber range from 600 to 900 cm⁻¹), since those two regions provide the most vibrational information of IO₃ units. In the LP phase (pressure below 7.7 GPa in Raman), as the phonon and atomic movement calculation show (Supplementary Information of ref. [151]), the high-frequency region are contributed by the stretching of I-O bonds, while the mid-frequency region is mainly contributed by the bending of the I-O bonds. The mode symmetry assignment has been done by comparing the frequencies obtained from experiments and calculations at ambient pressure, as well as the pressure

coefficients. The vibration symmetry of the experimentally determined modes has been assigned and summarized in Table III of ref. [151], as well as the pressure coefficient and Grüneisen parameters obtained from experiment and calculation. The corresponding atomic movement of the experiment detected Raman peaks are shown in **Figure 40** for the spectra at 0.2 GPa. At 0.2 GPa, the strongest modes are located at 777 cm^{-1} in the high-frequency region, the atomic movement behind this mode is the symmetry stretching of I-O bonds (**Figure 40**).

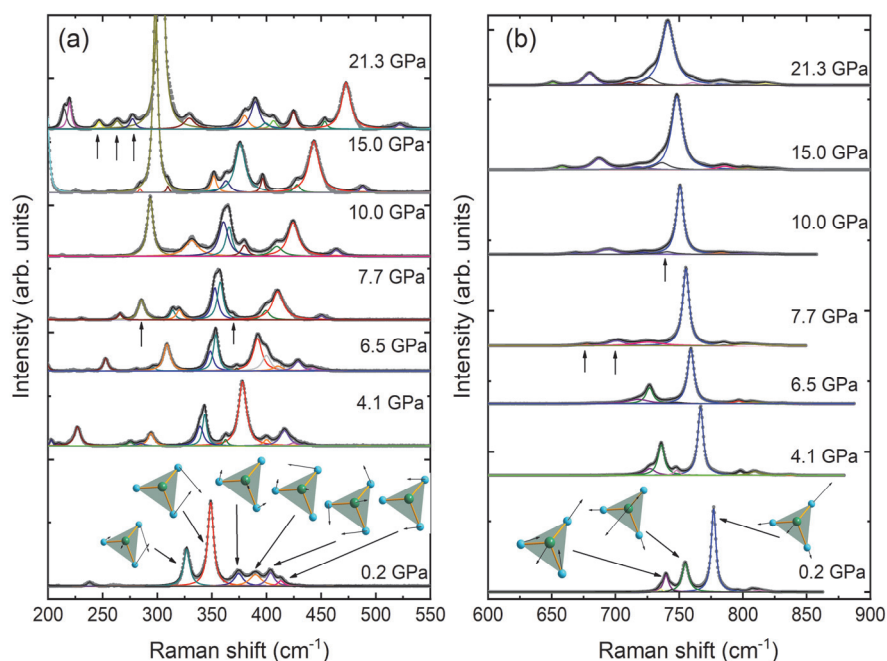


Figure 40. Selected Raman spectra of $\text{Mg}(\text{IO}_3)_2$ in (a). Mid-frequency region and (b). High-frequency region. Experimental results are shown in gray dots and the fitting of the Raman peaks with a Voigt profile are shown in solid lines. The intensity of the spectra in (a) have been multiplied by a factor of 10 compared to that in (b) to show the Raman spectra in this region clear.

There are some new Raman peaks that appeared at 7.7 GPa both in the mid- and high-frequency region (marked by the upward arrow in **Figure 40**). They are a sign of the onset of the phase transition found in HPXRD. By using the same method of the vibrational symmetry assignment as we made in the LP phase, the symmetry of the experiment determined modes at 7.7 GPa have been assigned and summarized in Table IV of ref. [151]. Both in the LP and HP phase, most of the modes in high-frequency region show a softening behavior under compression, like we have observed in the other

three metal iodates studied in this thesis. The reason is the enlargement of the bond distance between iodine and inlayer oxygen atoms in accommodate to the three additional interlayer oxygen atoms in the neighboring IO₃ layer. On the other hand, all the modes in the mid-frequency region hardening under pressure, resulting in the narrowing of the phonon gap between the two regions. The changes in the Raman spectra are reversible as the spectra collected from the released pressure shown (Supplementary Information of ref. [151]).

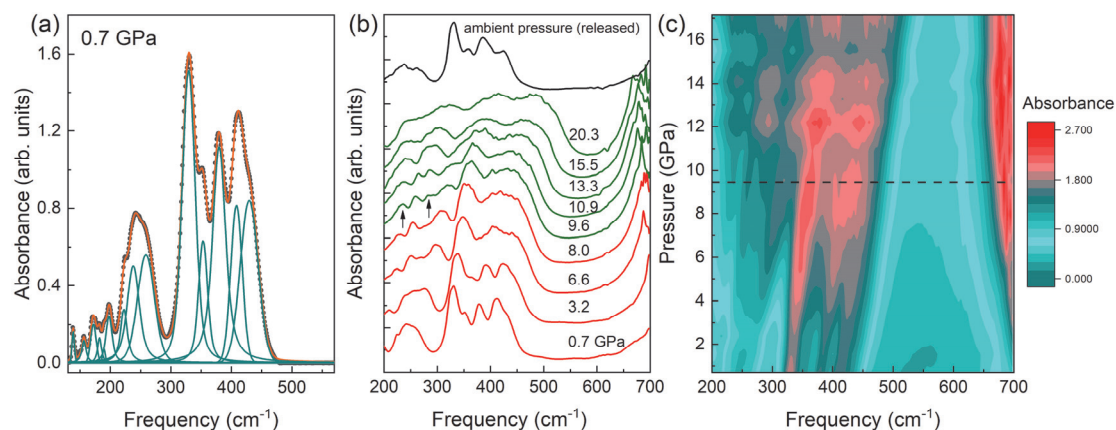


Figure 41. (a) Background-subtracted infrared spectra at the lowest pressure, the gray dots are experimental data, the spectra were fitted by a Voigt profile (yellow lines) and the peaks determined from the fitting are shown in light blue. (b). Infrared of Mg(IO₃)₂ at selected pressure, the LP and HP phase are shown in different color. (c). The contour plot of the same data in (b). Horizontal dash line indicates the onset of the phase transition found in Infrared spectra.

The infrared spectra at selected pressure are shown in **Figure 41**. The modes determined from the fitting of the spectra with Voigt profiles at 0.7 GPa and 9.6 GPa have been summarized in Table V in ref. [151]. In addition, Table V also includes the vibrational symmetry assignment of the observed modes, which has been done by the same method used in the Raman experiment. Pressure coefficients and Grüneisen parameters are reported as well. The infrared spectra we show corresponds to the mid-frequency region in the Raman spectra. As the modes are both Raman and infrared-active, some modes observed in Raman spectra also observed here. Some modes observed in infrared but not observed in Raman can complete the studies on the vibration behavior. At the pressure of 9.6 GPa and above, two new peaks appeared and are marked by the upward arrows in **Figure 41b**, supporting the phase transition found

in other diagnostics. Both in **Figure 41b** and **c**, there are some peaks that show up at the right edge of the figures and exhibits a soften behavior under compression. Those peaks are corresponding to the Raman peaks in the high-frequency region, the whole picture of the peaks in this region have not be investigated in infrared spectra, due to the cutoff of the experiment is around 700 cm^{-1} . As the infrared spectra collected from the released pressure shown, the changes in the infrared spectra is reversible.

Now we start looking at the bandgap behavior of Zn and Mg iodates. The optical absorption spectra of them are shown in ref. [36], as well as the representative Tauc plot for the absorption spectra. According to the calculated electronic band structure for Mg and Zn iodates (Supplementary Information of ref. [36]), the bandgap for them are indirect, the same as that for Fe and Co iodates. So the Tauc plot for indirect bandgap semiconductor have been adopted to analyze the optical absorption spectra of them, the experiment determined bandgap energy for those two metal iodates are shown in **Figure 42**, together with the bandgap energy determined by calculations.

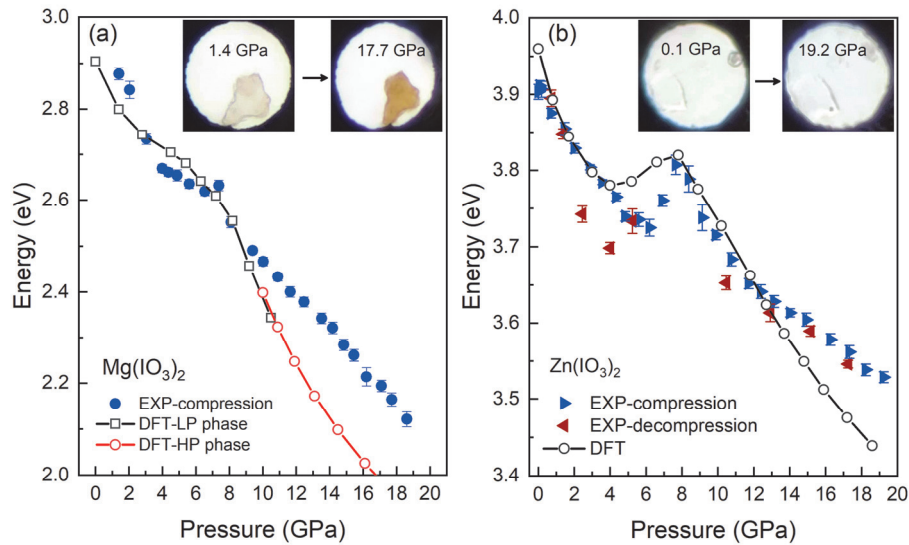


Figure 42. Experiment (symbols) and calculation (solid line and symbols) determined bandgap energy for (a) $\text{Mg}(\text{IO}_3)_2$ and (b) $\text{Zn}(\text{IO}_3)_2$ as a function of pressure. The calculated bandgap for $\text{Mg}(\text{IO}_3)_2$ and $\text{Zn}(\text{IO}_3)_2$ have been shifted by -0.5 eV and $+1.0\text{ eV}$ to better compare them with the experimental data. The insert optical images show the loading of the sample and the pressure-induced color change of them.

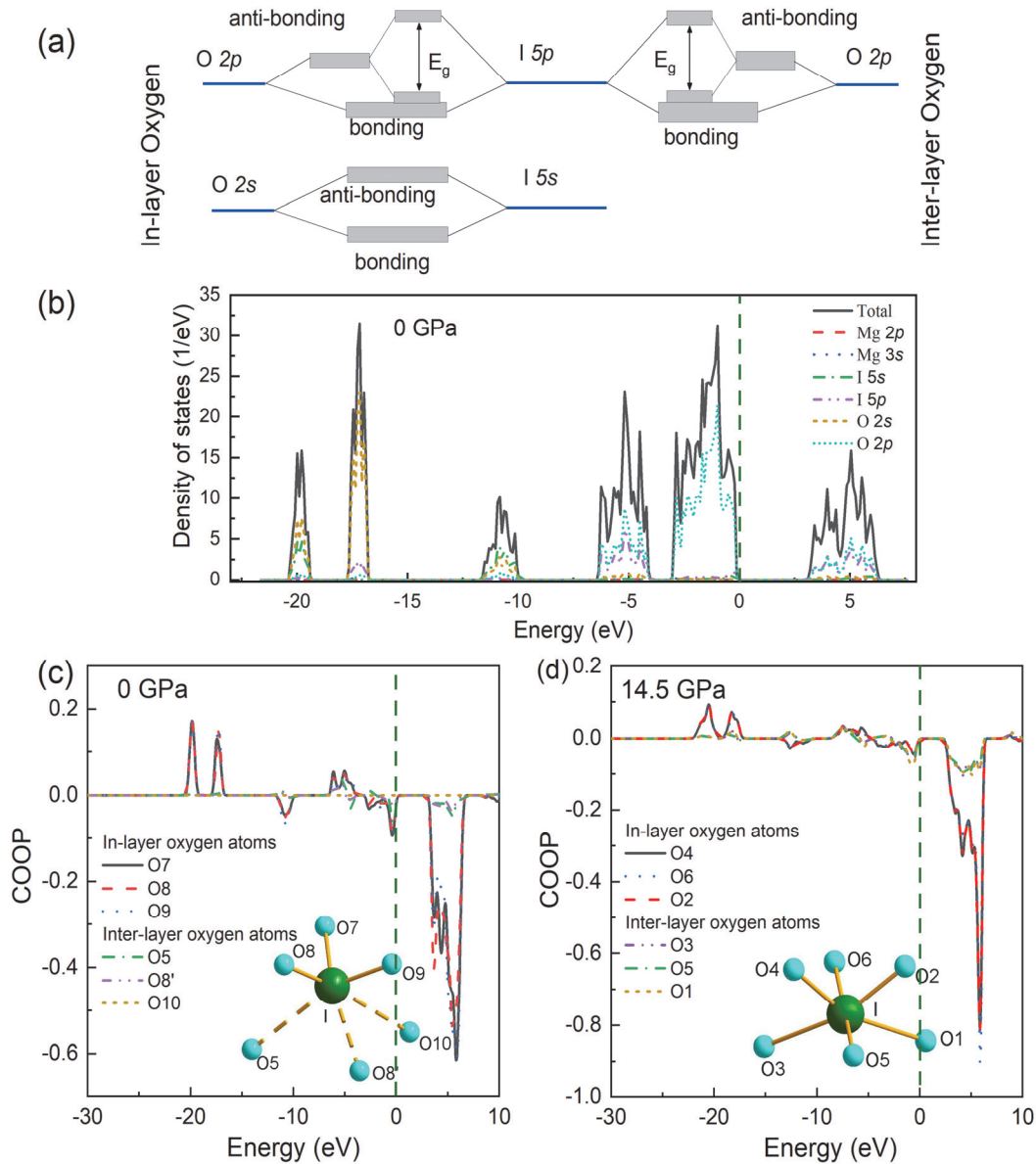


Figure 43. (a). Molecular orbital diagram for $\text{Mg}(\text{IO}_3)_2$ and $\text{Zn}(\text{IO}_3)_2$ at ambient pressure, E_g is bandgap. (b). Theoretically calculated DOS and PDOS for $\text{Mg}(\text{IO}_3)_2$. (c) and (d) theoretical calculation of COOP for $\text{Mg}(\text{IO}_3)_2$ at 0 and 14.5 GPa, respectively.

The bandgap energy for both Mg and Zn iodates exhibits a nonlinear narrowing under compression. For $\text{Mg}(\text{IO}_3)_2$, the slope changes at 3 and 8 GPa in experiments, there are no discontinuity around the phase transition pressure (**Figure 42a**). It is understandable as the phase transition we found in HPXRD is subtle and there is no collapse in the unit-cell volume. The nonlinear behavior of the bandgap for $\text{Zn}(\text{IO}_3)_2$ is more pronounced and the sign changed at 5.6 and 7.7 GPa in experiments. In the whole pressure range, the bandgap of $\text{Mg}(\text{IO}_3)_2$ shows a reduction of 29.3% and that for

Zn(IO₃)₂ is 9.5%. The color of Mg(IO₃)₂ changed from transparent with a slightly orange tone to completely orange, Zn(IO₃)₂ exhibits no detectable changes in color.

Since the bandgap of Mg and Zn iodates exhibits the similar behavior under pressure, here we choose Mg(IO₃)₂ as an example to explain the bandgap behavior for them. The MO diagram is useful to qualitatively explain the bandgap behavior of semiconductor [157]. Therefore, we have calculated the DOS, PDOS, and COOP in order to figure out the MO diagram for Mg(IO₃)₂. According to the calculated DOS and PDOS for Mg(IO₃)₂ at 0 GPa (**Figure 43b**), the VBM is dominated by the O-2*p* orbital, the CBM is dominated by the I-5*p* and O-2*p* states, this is a common feature of the non-transition or closed-shelled transition metal iodates as summarized in **Table 1** in **Chapter 1.3** of this thesis. The COOP calculated for Mg(IO₃)₂ at 0 and 14.5 GPa are the interaction between the iodine and two types of oxygen atoms: The inlayer oxygen which bonded with iodine at ambient pressure in a bond distance range from 1.8 to 1.9 Å (O7, O8 and O9 at 0 GPa, O4, O6, O2 at 14.5 GPa). The interlayer oxygen which bonded with iodine only at high pressure (O5, P8' and O10 at 0 GPa, O3 O5 and O1 at 14.5 GPa). From **Figure 43c**, there are no interaction between iodine and interlayer oxygen in the energy below -10 eV, that is minor in the upper part of the valence band and the whole conduction band, the COOP at 14.5 GPa show the same feature as that in 0 GPa, with a slightly change in the intensity.

The peaks at the energy range from -20 eV to -15 eV in **Figure 43b** is contributed by I-5*s* and O-2*s* orbital, it is positive in COOP (**Figure 43c**), so those peaks are the bonding state of the iodine 5*s* state and inlayer oxygen O-2*s* state. The corresponding anti-bonding state between them are the peak located at -10 eV in **Figure 43b**, since the peak also contributed by I-5*s* and O-2*s*, and it is negative in the COOP in **Figure 43c** (as shown in the bottom left part of **Figure 43a**). The peak located at around -5 eV in **Figure 43b** is dominated by O-2*p* and I-5*p* state, and it is positive in the COOP in **Figure 43c**, so this peak is the bonding state of *p-p* interaction between the iodine and inlayer or interlayer oxygen. The corresponding anti-bonding state is located in the conduction band, based on the fact that the peak in the conduction band in **Figure 43b** is also contributed by O-2*p* and I-5*p* and it is negative in the COOP in **Figure 43c** (as shown in the top of **Figure 43a**). The peak located in the upper part of the valence band in **Figure 43b** is only contributed by the O-2*p* state and it is negative in the COOP, so it is the non-bonding state. We suggest the MO diagram between the iodine and inlayer

oxygen as the left part of **Figure 43a**. The interaction between iodine and interlayer oxygen is weak and only have some intensity in the p - p interaction state, but indeed it show the same characterization as that between iodine and inlayer oxygen, so we suggest the same MO diagram for the p - p interaction between iodine and interlayer oxygen in the top right part of **Figure 43a**. The bandgap energy is the energy difference between the O- $2p$ non-bonding state and the antibonding state of the p - p interaction between iodine and oxygen. This MO diagram also applied to $\text{Zn}(\text{IO}_3)_2$, the calculated DOS, PDOS, COOP between iodine and oxygen can be found in the Supplementary Information of ref. [36].

It is clear that there are two effects affecting the bandgap energy of $\text{Mg}(\text{IO}_3)_2$ based on the MO diagram. The enlargement of the bond distance between the iodine and inlayer oxygen atoms favors the decrease of the overlap between the p state, thereby decreasing the energy difference between the bonding and anti-bonding state [158]. In that way, the pressure favors to reduce the bandgap energy (effect 1). Another effect is the shortening of the bond distance between iodine and interlayer oxygen, which enhances the overlap between the p state of them and increase the separation between the bonding and anti-bonding state. In that way, pressure favors the increase of the bandgap energy (effect 2).

The pressure dependence of the I-O bond distance both for inlayer and interlayer oxygen can be found in **Figure 39b**. In the case of $\text{Mg}(\text{IO}_3)_2$, the interaction between iodine and interlayer oxygen is weak at the pressure lower than 4 GPa due to the large distance between them, so the interaction between iodine and inlayer oxygen (effect 1) dominates the bandgap energy. At the pressure range from 4 to 8 GPa, as the pressure-induced shorten of the bond distance between iodine and interlayer oxygen, effect 2 starts to become stronger and counteracting the impact from the effect 1, but the effect is stronger as the bond distance between iodine and interlayer oxygen is more sensitive of pressure. After 8 GPa, the shortening of the iodine and interlayer oxygen start to slow down and the distance between iodine and inlayer oxygen continuously increases under pressure, so once again the effect 1 dominate the bandgap of $\text{Mg}(\text{IO}_3)_2$. The high-pressure bandgap behavior of $\text{Zn}(\text{IO}_3)_2$ also can be explained by following the same rationale and the MO diagram we suggested in **Figure 43a**.

From the high-pressure bandgap studies on $\text{Mg}(\text{IO}_3)_2$ and $\text{Zn}(\text{IO}_3)_2$, we observed that the bandgap energy for the two materials have a negative relationship with the bond

distance between iodine and inlayer oxygen atoms at ambient or low pressure, where the distance between iodine and interlayer oxygen is far and the overlap between them are weak. It is worth to examine the relation between the bandgap and I-O bond distance in other metal iodates reported in the literature, only at ambient pressure. The bandgap energy and the average I-O bond distance (only the bond distance shorter than 2.0 Å are chosen) of 71 non-transition or closed-shelled transition metal iodates are plotted in **Figure 44**. The cutoff value we chosen here is based on the fact that the interaction between iodine and oxygen is weak beyond than 2.0 Å (**Figure 43c**). Each point in **Figure 44** is one metal iodates and the detailed information for each point, including the corresponding chemical formula, average I-O bond distance, bandgap energy and reference can be found in the Supplementary Information of ref. [36]. Just as the expected, the bandgap energy of non-transition and closed-shelled transition metal iodates show a negative relationship with the average I-O bond distance. The shorter the I-O bond distance, the wider the bandgap energy of metal iodates (non-transition and closed-shelled transition metal), regardless of the crystal structure, metal species or chemical formula.

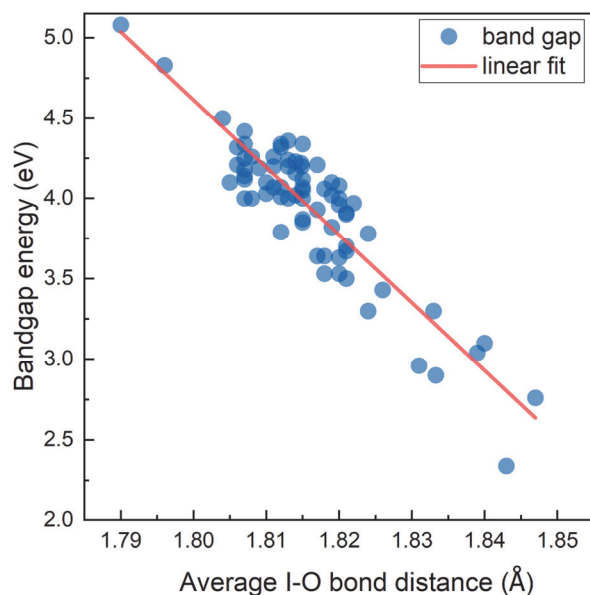


Figure 44. Collated bandgap energy and average I-O bond distance reported in the literature. Only the non-transition or closed shelled metal iodates are included here.

6.4 Conclusions

- (1). $\text{Mg}(\text{IO}_3)_2$ undergoes a monoclinic (space group: $P2_1$) to trigonal (space group: $P3$) phase transition at the pressure range of 7.5-9.7 GPa. The pressure-induced phase transition has been observed in the HPXRD, HPRS, HPFTIR, and first-principle calculations.
- (2). The phase transition was evidenced by the Rietveld refinement of XRD at high pressure, the appearance of new peaks in the Raman and Infrared spectra at high pressure. The phase transition is subtle and there is no collapse in the unit-cell volume.
- (3). The oxygen coordination of iodine increased from 3 to 6 under pressure, which is a consequence of (i). The pressure-induced shortening of the distance between iodine and the oxygen in the neighboring IO_3 layer, (ii). The existence of the LEP in iodine.
- (4). The bulk modulus of the low-pressure phase (LP) is 22.2 GPa in experiments and 26.4 GPa in calculations. That for the high-pressure phase (HP) is 63.6 GPa (44.4 GPa) in experiment (calculation).
- (5). Calculations revealed that the bond distance between iodine and inlayer oxygen atoms increase with increasing pressure, on the contract, the distance between iodine and the oxygen in the neighboring IO_3 layer shorten under compression.
- (6). The Raman spectra at LP phase can be divided into three regions. The modes in the mid-frequency region ($300\text{-}550\text{ cm}^{-1}$) are related to the bending of I-O bond, and the modes in the high-frequency region ($600\text{-}900\text{ cm}^{-1}$) are related to the stretching of I-O bond. The strongest mode is located in 770 cm^{-1} .
- (7). Both in the LP and HP phase, most of the modes in the high-frequency region soften under pressure. This is caused by the enlargement of the I-O bond distance under pressure, in order to accommodate to the additional three oxygen atoms in the neighboring IO_3 layer. All the modes in mid-frequency region hardening under compression, resulting in the closing of the phonon gap.
- (8). The bandgap of Mg and Zn iodates is indirect, the VBM is dominated by the O-2p state, and the CBM is dominated by the I-5p and O-2p state.
- (9). The bandgap of Mg and Zn iodates show a nonlinear narrowing under pressure, it shows an overall reduction of 29.3% for $\text{Mg}(\text{IO}_3)_2$, and 9.5% for $\text{Zn}(\text{IO}_3)_2$.
- (10). According to molecular orbital diagram established for Mg and Zn iodates in this chapter, the bandgap of them are determined by the non-bonding state of O-2p and the

antibonding state of the p - p interaction between iodine and oxygen.

(11). There are two effects affected the bandgap of Mg and Zn iodates. The pressure-induced enlargement of the bond distance between iodine and inlayer oxygen favors the narrowing of the bandgap, the pressure-induced shortening of the distance between iodine and interlayer oxygen favors the opening of the bandgap. The high pressure studies on the bandgap behavior of Mg and Zn iodates revealed that there is a negative relationship between the bandgap energy and the I-O bond distance.

(12). By collating the bandgap energy and average I-O bond distance of 71 different non-transition or closed shelled metal iodates reported in the literature, we found that there is a negative relationship between the bandgap energy and average I-O bond distance, where the I-O bond is shorter than 2.0 Å. For the iodates only include non-transition or closed-shell transition metal, the shorter the bond distance, the wider the bandgap energy.









(13). All the changes in the HPXRD, HPRS, HPFTIR, and HPOA are reversible.

6.5 Author contribution

The author of this doctoral thesis is the first author of all the two published papers, which are the main content of this chapter. HPXRD, HPRS were conducted by the author. HPFTIR were conducted by the author, Robin Turnbull, and Enrico Bandiello. Catalin Popescu helped the HPXRD experiment. The theoretical calculations were conducted by Placida Rodriguez-Hernandez, Alfonso Muñoz, and Lan-ting Shi. Francisco Javier Manjón provides help in the HPRS experiments and the discussion on the results. The polycrystalline sample used in those studies was synthesized by Zoulikha Hebboul. The single crystal of $\text{Zn}(\text{IO}_3)_2$ was synthesized by M. Jasmin. Ibraheem Yousef helped the HPFTIR experiment. Daniel Errandonea supervised the project. All the data were analyzed by the author, the author wrote the first draft of those two papers, the two papers were revised by all authors.

A. Liang, R. Turnbull, C. Popescu, F. J. Manjón, E. Bandiello, A. Muñoz, I. Yousef, Z. Hebboul, and D. Errandonea, Pressure-Induced Phase Transition and Increase of Oxygen-Iodine Coordination in Magnesium Iodate, *Phys. Rev. B* 105, 054105 (2022).

A. Liang, R. Turnbull, P. Rodríguez-herandez, A. Muñoz, M. Jasmin, L. Shi, and D. Errandonea, General Relationship between the Band-Gap Energy and Iodine-Oxygen Bond Distance in Metal Iodates, *Phys. Rev. Mater.* 6, 044603 (2022).

Pressure-induced phase transition and increase of oxygen-iodine coordination in magnesium iodateA. Liang ¹, R. Turnbull ¹, C. Popescu,² F. J. Manjón ³, E. Bandiello ¹, P. Rodriguez-Hernandez ⁴, A. Muñoz ⁴, I. Yousef,² Z. Hebboul ⁵ and D. Errandonea ^{1,*}¹*Departamento de Física Aplicada-ICMUV-MALTA Consolider Team, Universitat de València, c/Dr. Moliner 50, 46100 Burjassot, Valencia, Spain*²*CELLS-ALBA Synchrotron Light Facility, Cerdanyola, 08290 Barcelona, Spain*³*Instituto de Diseño para la Fabricación y Producción Automatizada, MALTA Consolider Team, Universitat Politècnica de València, Camí de Vera s/n, 46022 València, Spain*⁴*Departamento de Física and Instituto de Materiales y Nanotecnología, MALTA Consolider Team, Universidad de La Laguna, 38206 La Laguna, Tenerife, Spain*⁵*Laboratoire Physico-Chimie des Matériaux (LPCM), University Amar Telidji of Laghouat, BP 37G, Ghardaïa Road, Laghouat 03000, Algeria*

(Received 9 December 2021; revised 12 January 2022; accepted 8 February 2022; published 17 February 2022)

The structural and vibrational behavior of $\text{Mg}(\text{IO}_3)_2$ under compression has been investigated via a combination of high-pressure (HP) synchrotron x-ray diffraction (XRD), Raman scattering, and infrared spectroscopy experiments as well as first-principles *ab initio* calculations. In this paper, we reveal that $\text{Mg}(\text{IO}_3)_2$ undergoes a pressure-induced phase transition between 7.5 and 9.7 GPa at ambient temperature from a monoclinic (space group $P2_1$) to a trigonal (space group $P3$) structure. $\text{Mg}(\text{IO}_3)_2$ also exhibits the gradual formation of additional bonds between iodine and oxygen atoms in neighboring IO_3^- units with increasing pressure, thereby increasing the oxygen-iodine coordination from 3 to 6. The bond formation under compression is a consequence of the existence of lone electron pairs on the iodine cation. To accommodate the additional bonds, the I–O bonds within the original $[\text{IO}_3]^-$ trigonal pyramids increase in length under increasing compression. The appearance of additional Raman modes at 7.7 GPa and infrared modes at 9.6 GPa supports the phase transition observed in XRD experiments. Interestingly, the lengthening of I–O bonds causes a softening of several Raman modes under compression. We provide the crystal structure of the HP phase, the pressure-volume equations of state for both low- and HP phases, and the symmetry assignment of the Raman- and infrared-active modes of both phases.

DOI: [10.1103/PhysRevB.105.054105](https://doi.org/10.1103/PhysRevB.105.054105)**I. INTRODUCTION**

Metal iodates have recently attracted great interest in materials science, and they have been synthesized with a range of metal cation atoms, including alkali metals, alkaline-earth metals, transition metals, posttransition metals, and lanthanide elements. The properties of metal iodates, particularly their crystal structure, electronic structure, and second harmonic generation (SHG), have been well studied at ambient pressure [1–8]. Such research is significantly motivated by the search for a generation of high-performance nonlinear optical (NLO) materials and their potential application in photonic technologies. Due to the existence of a lone electron pair (LEP) on the I^{5+} cation, both the metal cation and the iodine cations are centered in asymmetric oxygen environments. The presence of such asymmetric units enhances the polarization effect in the noncentrosymmetric crystal structure of metal iodates, favoring a large SHG response [9,10]. By manipulating the direction of the polarization from the asymmetric coordination polyhedra, it is possible to produce polar materials with very large SHG responses. For instance, by introducing Nb^{5+} cations in metal iodates, Sun *et al.* [3] successfully

synthesized $\text{BaNbO}(\text{IO}_3)_5$, which has a SHG response 14 times larger than that of the currently widely used NLO materials, i.e., potassium dihydrogen phosphate (KH_2PO_4), usually known as KDP. Moreover, metal iodates usually exhibit transparency in a wide wavelength region [11,12], high optical-damage thresholds, and high thermal stability [5,6,13], which make them the choice for the next generation of NLO materials.

Since the crystal structure plays a significant role in the SHG performance and electronic structure of metal iodates [14], one important question about them is how stable they are under external stimuli, particularly under stress and compression. In this context, it is important to investigate the behavior of magnesium iodate under compression. Moreover, pressure is an ideal external parameter to modify the crystal and electronic structure of $\text{Mg}(\text{IO}_3)_2$. Pressure allows the shortening of interatomic distances and consequent modification of interatomic interactions. Therefore, high-pressure (HP) results will help to improve the understanding of the main physical properties of $\text{Mg}(\text{IO}_3)_2$ and other iodates. They will allow us to obtain a deeper understanding of the role played by bonding and iodine LEPs [15], which could lead to unusual behaviors at HP [14,16–19].

The crystal structure of $\text{Mg}(\text{IO}_3)_2$ at ambient conditions was reported by Liang *et al.* [20] based on powder x-ray

*daniel.errandonea@uv.es

diffraction (XRD). According to these results, it belongs to the hexagonal space group $P6_3$. The reported unit cell parameters are $a = 5.4777 \text{ \AA}$ and $c = 5.1282 \text{ \AA}$. This structure is isomorphic to that of $\alpha\text{-LiIO}_3$, but the Mg atoms are located at the $2a$ Wyckoff position in a 0.5 partial occupation. Recently, Phanon *et al.* [21] have reported that the crystal structure of $\text{Mg}(\text{IO}_3)_2$ is better described by a pseudo-hexagonal structure of monoclinic symmetry (space group $P2_1$) with similar lattice parameters: $a = 10.952 \text{ \AA}$, $b = 5.117 \text{ \AA}$, $c = 10.959 \text{ \AA}$, and $\beta = 120.01^\circ$. In this structure, all atomic positions are fully occupied. Despite this disagreement in the literature, it is clear that the crystal structure of $\text{Mg}(\text{IO}_3)_2$ is formed by asymmetric MgO_6 octahedral units, which are each connected to six trigonal IO_3 pyramids, via the oxygen atoms at the octahedral vertices. This structure is qualitatively like that of $\text{Zn}(\text{IO}_3)_2$, $\text{Co}(\text{IO}_3)_2$, and other metal iodates. The framework of interconnected octahedra and trigonal pyramids makes these iodates very anisotropic and compressible [16,17]. Additionally, HP Raman scattering (RS) and Fourier transform infrared (FTIR) spectroscopies have shown soft high-frequency phonons and phase transitions at relative low pressures (LPs; $P < 10 \text{ GPa}$) [16–18].

In this paper, we report a combined experimental and theoretical study of $\text{Mg}(\text{IO}_3)_2$ under compression. HP-XRD, HP-RS, and HP-FTIR measurements have been combined with density functional theory (DFT) calculations to systematically investigate the pressure-induced structural evolution, the stereochemically active LEP of I^{5+} , and the atomic vibrations of $\text{Mg}(\text{IO}_3)_2$. Here, we present evidence of a pressure-induced monoclinic-to-trigonal phase transition between 7.5 and 9.7 GPa, which has been confirmed by each of the four diagnostics used. The detailed crystal structural information and vibrational behavior for both the LP and HP phases are reported. We present evidence of a significant oxygen coordination increase in iodine at HP, which is explained by a shortening of the atomic distance between iodine, the oxygen in the second neighboring layer, and the decrease of the stereoactivity of the iodine LEP. We also show that this phenomenon causes the softening of several Raman modes and favors the occurrence of the phase transition.

II. METHODS

A. Sample preparation

Samples of $\text{Mg}(\text{IO}_3)_2$ were synthesized from an aqueous solution with a mixture of potassium iodate KIO_3 (99.5% purity, Sigma Aldrich) and anhydrous magnesium chloride MgCl_2 ($\geq 98\%$ purity, Sigma Aldrich). Potassium iodate was first dissolved into concentrated nitric acid (2 mmol of KIO_3 in 10 mL of 7N nitric acid) and then added to an anhydrous magnesium chloride solution (1 mmol in 10 mL of 7N nitric acid). After being stirred thoroughly, the reaction mixture was slowly evaporated and maintained at 60°C for a few days.

B. HP-XRD measurements

A membrane-type diamond anvil cell (DAC), with diamond culets of $400 \mu\text{m}$, was used to generate the HP conditions. A stainless-steel gasket was first pre-indented to

$40 \mu\text{m}$ in thickness, and a $180\text{-}\mu\text{m}$ -diameter hole was drilled to serve as the sample chamber. Pressure was measured using the equation of state (EOS) of copper [22] and a 16:3:1 methanol:ethanol:water mixture (MEW) was used as the pressure transmitting medium (PTM) [23].

In situ angle-dispersive powder HP-XRD data were collected at the BL04-MSPD beamline of synchrotron ALBA-CELLS [24]. The monochromatic x-ray beam with a wavelength of 0.4642 \AA was focused on a $20 \times 20 \mu\text{m}$ spot (full width at half maximum). The diffraction data were recorded with a Rayonix SX165 CCD image plate, high purity LaB_6 powder was used as the standard for sample-to-detector distance calibration, and the powder HP-XRD patterns were integrated by using the DIOPTAS program to obtain a two-dimensional (2D) XRD pattern [25]. The FULLPROF program was used to analyze (Rietveld refinement) the 2D XRD patterns [26].

C. HP-RS measurements

In the HP-RS experiment, a membrane-type DAC with the diamond culets of $500 \mu\text{m}$ was used to generate the HP conditions. A stainless-steel gasket was pre-indented to a thickness of $40 \mu\text{m}$, and a $250\text{-}\mu\text{m}$ -diameter hole was drilled in the gasket to be used as the sample chamber. The PTM used in HP-RS experiment is the same as what we used in HP-XRD (16:3:1 MEW), and a ruby sphere was loaded, together with the sample and PTM, to determine the pressure by using the ruby fluorescence method [27]. Measurements were carried out in a backscattering geometry employing a He/Ne laser (632.8 nm) light source and a HORIBA Jobin Yvon LabRAM HR UV microspectrometer. Signal was recorded with a thermoelectrically cooled multichannel CCD detector, and the spectral resolution is better than 2 cm^{-1} . Before the HP-RS experiment, the setup was calibrated by using the He plasma lines for pressure calibration and with the Si Raman-active mode for RS measurements.

D. HP-FTIR measurements

For HP-FTIR measurements, $\text{Mg}(\text{IO}_3)_2$ powder was pressed into compact $10\text{-}\mu\text{m}$ -thick platelets before being loaded in a DAC equipped with IIAC diamonds with culets of $300 \mu\text{m}$. Cesium iodide CsI was used as the solid PTM since it is transparent to a wide frequency range of IR light [28]. Notice that this PTM and MEW becomes nonhydrostatic in the pressure range of the experiments. However, we found a remarkable agreement between the three types of experiments and DFT simulations (which are done under fully hydrostatic conditions) suggesting that the influence of nonhydrostatic effect in the behavior of $\text{Mg}(\text{IO}_3)_2$ up to 24 GPa is not as relevant as in other materials [29]. A stainless-steel gasket, which was pre-indented to a thickness of $40 \mu\text{m}$ and drilled with a hole in the center of $150 \mu\text{m}$, was used as the sample chamber. The ruby fluorescence method was employed for the pressure calibration [27]. HP-FTIR microspectroscopy measurements in transmission mode were conducted at the MIRAS beamline of the ALBA-CELLS synchrotron [30]. The size of the masking aperture is $50 \times 50 \text{ cm}^2$, and the beam current was 250 mA. The measurement was performed

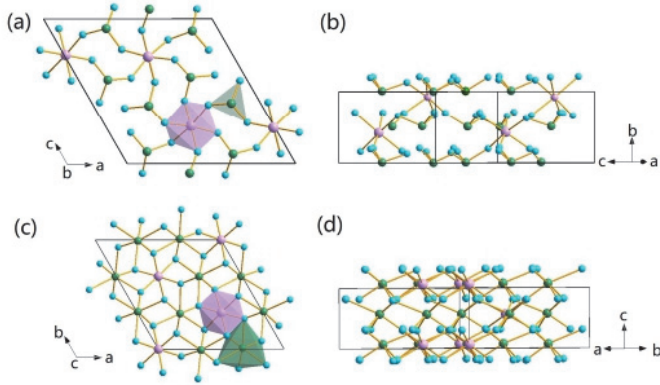


FIG. 1. Crystal structure of the low-pressure (LP) phase of $\text{Mg}(\text{IO}_3)_2$ (space group $P2_1$) (a) along the b axis and (b) perpendicular to the b axis. Crystal structure of the high-pressure (HP) phase of $\text{Mg}(\text{IO}_3)_2$ (space group $P3$): (c) along the c axis and (d) perpendicular to the c axis. Purple circles represent Mg atoms while green and sky-blue circles represent I and O atoms, respectively. Bonds between cations and oxygen are also shown. Polyhedral coordination is shown in (a) and (c).

in a Hyperion 3000 microscope coupled to a Vertex 70 spectrometer. The data were collected by a He-cooled bolometer detector, and the resolution of the spectra was 4 cm^{-1} . The used setup has a wave number cutoff of 700 cm^{-1} . More experimental details can be found in our previous works [17,31].

E. First-principles calculations

The *ab initio* simulations were performed within the framework of DFT [32] using the Vienna *Ab initio* Simulation Package [33] with the projector augmented-wave pseudopotentials [34,35]. Computer simulations were carried out using the primitive cell of the crystal structures. The plane-wave kinetic energy cutoff was large enough 530 eV to ensure highly converged results. Benchmark calculations showing the convergence of the simulation results with respect to the cutoff energy are provided in the Supplemental Material, Fig. S1 [36]. The Monkhorst-Pack scheme was employed for the Brillouin zone (BZ) integrations with a $6 \times 4 \times 6$ ($6 \times 6 \times 4$) grid of k -special points [37] for the LP (HP) phase. Exchange-correlation energy was described using the generalized gradient approximation with the Armiento and Mattsson AM05 [38,39] prescription.

The unit cell parameters and the atomic positions were fully optimized to obtain, at selected volumes, the relaxed structures requiring that the forces on the atoms were $<0.003 \text{ eV/\AA}$ and that the deviations of the stress tensors from a diagonal hydrostatic form $<0.1 \text{ GPa}$. The simulations provide a set of volume, energy, and pressure (from the stress tensor), which are fitted with a Birch-Murnaghan EOS to obtain the theoretical equilibrium volume, the bulk modulus, and its pressure derivatives.

Lattice-dynamic calculations of the phonon modes were carried out at the zone center (Γ point) of the BZ with the direct force-constant approach [40]. These calculations provide not only the frequency of the normal modes but also

TABLE I. Crystal structure information of the LP and HP phases obtained from the Rietveld refinement of the XRD respectively at ambient pressure and 10.5 GPa.

Atom	Wyckoff	x	y	z
Ambient pressure, space group $P2_1$, $a = 11.2563 \text{ \AA}$, $b = 5.0497 \text{ \AA}$, $c = 11.2128 \text{ \AA}$, $\beta = 119.8256^\circ$				
Mg_1	$2a$	0.508	0.426	0.319
Mg_2	$2a$	-0.008	0.920	0.402
I_1	$2a$	0.159	0.503	0.097
I_2	$2a$	0.327	0.008	0.401
I_3	$2a$	0.826	0.014	0.419
I_4	$2a$	0.661	0.510	0.066
O_1	$2a$	0.464	0.610	0.170
O_2	$2a$	-0.086	1.017	-0.212
O_3	$2a$	0.261	0.658	0.306
O_4	$2a$	0.390	0.122	0.211
O_5	$2a$	0.103	0.245	0.420
O_6	$2a$	0.415	0.188	0.554
O_7	$2a$	0.547	0.174	0.325
O_8	$2a$	1.240	-0.421	0.737
O_9	$2a$	1.047	0.178	0.239
O_{10}	$2a$	0.707	0.721	0.209
O_{11}	$2a$	0.894	0.745	0.132
O_{12}	$2a$	0.503	1.238	-0.213
$P = 10.5 \text{ GPa}$, space group $P3$, $a = 9.8336 \text{ \AA}$, $c = 3.8652 \text{ \AA}$				
Mg_1	$1b$	0.333	0.667	0.628
Mg_2	$1c$	0.667	0.333	0.128
Mg_3	$1a$	0.000	0.000	1.000
I_1	$3d$	0.334	0.977	0.095
I_2	$3d$	0.676	0.019	0.604
O_1	$3d$	0.984	0.053	0.680
O_2	$3d$	0.110	0.933	0.926
O_3	$3d$	0.577	0.127	0.224
O_4	$3d$	0.540	0.846	0.719
O_5	$3d$	0.197	0.720	0.301
O_6	$3d$	0.809	0.290	0.859

their symmetry and their polarization vectors. This allows us to identify the irreducible representations and the character of the phonon modes at the Γ point.

III. RESULTS AND DISCUSSION

A. HP-XRD measurements

1. Pressure-induced phase transition

Based upon Rietveld refinements of the XRD pattern of $\text{Mg}(\text{IO}_3)_2$ at ambient pressures (Supplemental Material, Fig. S2 [36]), we ruled out the hexagonal crystal structure proposed by Liang *et al.* [20], which fails to describe all of the diffraction peaks. Instead, we found that the XRD pattern of the LP phase corresponds to the monoclinic structure (space group $P2_1$) reported by Phanon *et al.* [21]. The crystal structure is shown in Figs. 1(a) and 1(b). Structural information on the crystal structure of the LP phase is given in Table I. When viewed along the b axis, the crystal structure consists of two asymmetric polyhedral units. One is the distorted MgO_6 octahedron with an off-centered Mg atom. The other is the IO_3 trigonal pyramid. This is a polar molecule, where the

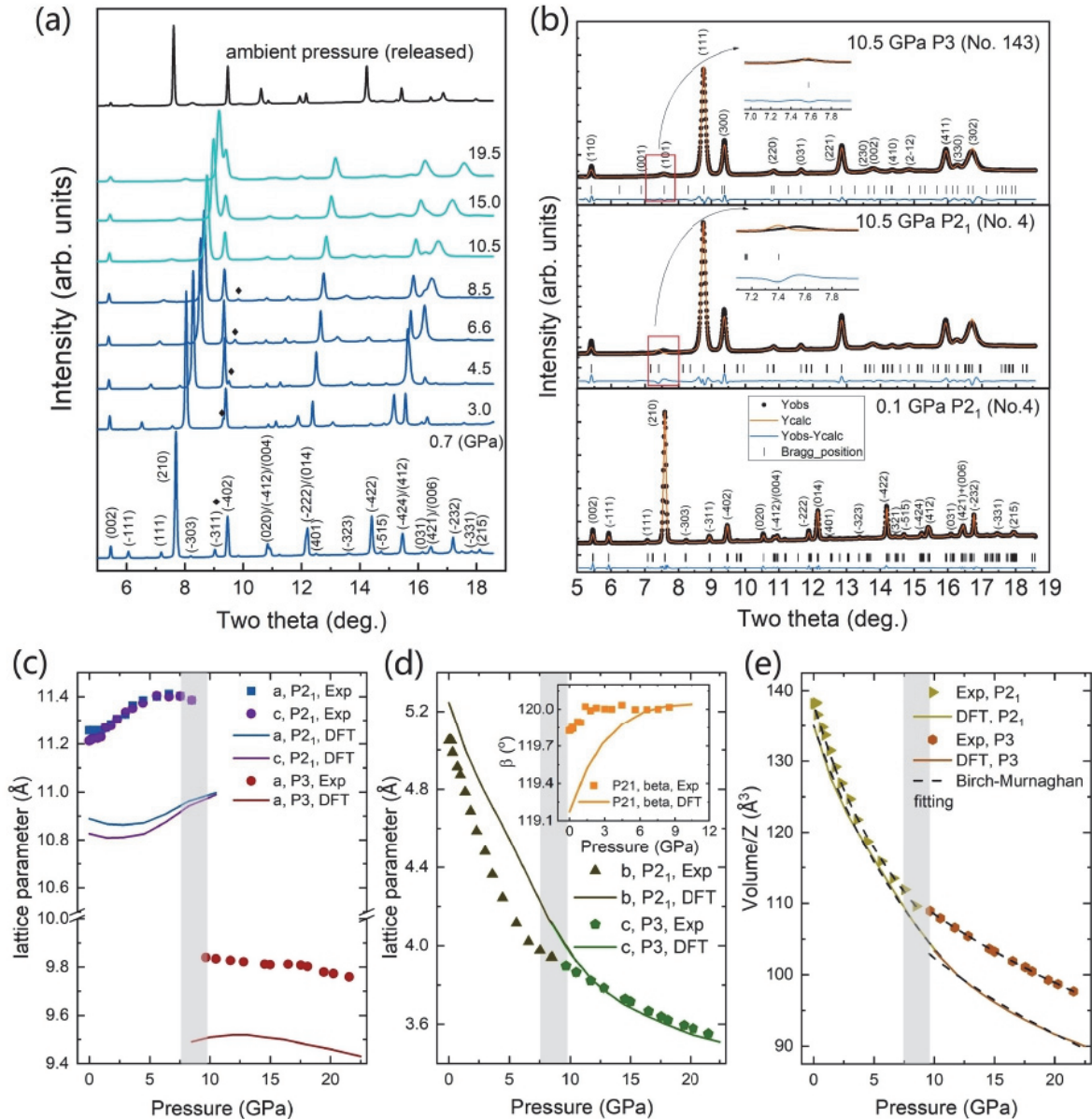


FIG. 2. Selections of high-pressure x-ray diffraction (HP-XRD) patterns. (a) Representative HP-XRD patterns of $\text{Mg}(\text{IO}_3)_2$. The XRD patterns of different phase are shown in different colors. Pressures are given in the right of each pattern in gigapascals. The black diamond shows the evolution of peak $(\bar{3}11)$ under compression. (b) Rietveld refinements at 0.1 and 10.5 GPa. For the HP phase, we show refinements with the low-pressure (LP) and HP crystal structures to support the assignment of the trigonal structure. Black dots show experimental data, orange lines are the refined patterns, ticks show the positions of diffraction peaks, and blue lines show the residuals. (c) and (d) Experimental and calculated pressure dependence of the different lattice parameters which are indicated in the figure. In (d), the inset is the pressure dependence of the monoclinic angle β . (e) Unit cell volume per formula unit as a function of pressure obtained from experiments and calculations. In (c)–(e), the phase transition region is marked as a grey rectangle.

three O atoms form the base of the pyramid, the I atom is located at the vertex, and the nonbonding LEP of the I^{5+} ion points in the opposite direction to the base of the pyramid. In Figs. 1(a) and 1(b), each MgO_6 octahedron is surrounded by six IO_3 pyramids due to the sharing of one O atom and every two MgO_6 octahedral units were bridged by two IO_3 units. When viewed perpendicular to the b axis, the structure of $\text{Mg}(\text{IO}_3)_2$ can be described as a 2D crystal structure, where layers of IO_3 pyramids are linked by MgO_6 octahedra.

Representative HP-XRD spectra of $\text{Mg}(\text{IO}_3)_2$ are shown in Fig. 2(a). Rietveld refinements of the XRD patterns collected at 0.1 and 10.5 GPa are shown in Fig. 2(b). At pressures up to 8.5 GPa, XRD patterns can be well refined by the ambient-pressure monoclinic crystal structure (space group $P2_1$) [21]. This is illustrated by the Rietveld refinement at 0.1 GPa which is shown in Fig. 2(b) ($R_p = 9.23\%$ and $R_{wp} = 8.85\%$). Under compression, most diffraction peaks shift to higher angles because of the unit cell contraction, but many diffraction peaks evolved in a different way, an indication of anisotropic

TABLE II. EOS of $\text{Mg}(\text{IO}_3)_2$ as determined by experiment and theoretical calculation for LP and HP phases, respectively.

Data source	LP phase ($Z = 4$)			HP phase ($Z = 3$)		
	V_0/Z (\AA^3)	B_0 (GPa)	B'_0	V_0/Z (\AA^3)	B_0 (GPa)	B'_0
Experiment	138.2	22.2 (0.8)	4.2 (0.4)	123.2 (0.1)	63.6 (0.4)	3.3 (0.1)
Calculation	135.0	26.4 (0.8)	2.9 (0.2)	121.3 (1.5)	44.4 (2.4)	3.6 (0.4)

behavior. For instance, the peak (002) almost remains unchanged at HP up to the highest pressure in our experiment, but the strongest peak (210) shifts continuously to higher angles, merging with peak (402) at HP. There is no obvious evidence of a structural phase transition up to 9.7 GPa. Above this pressure, peak (111) exhibits a sudden change in its shift rate under compression from 8.5 to 9.7 GPa (Supplemental Material, Fig. S3 [36]). On top of that, peaks (111) and (311) disappear. These and other subtle changes in the XRD pattern suggest an increase of symmetry of the crystal structure >9.7 GPa. In fact, the $P2_1$ space group predicts reflections that are not present in the XRD patterns beyond 8.5 GPa, as noted in the Rietveld refinement at 10.5 GPa in Fig. 2(b). These facts indicate the occurrence of a phase transition that has been further confirmed by the HP-RS and HP-FTIR measurements and DFT calculations discussed later.

Indexing the XRD pattern measured at 10.5 GPa leads to hexagonal or trigonal structures for the HP phase of $\text{Mg}(\text{IO}_3)_2$. After several attempts, we successfully refined the XRD pattern at 10.5 GPa by adopting the trigonal space group $P3$. The obtained refinement ($R_p = 10.6\%$ and $R_{wp} = 10.1\%$) is shown in Fig. 2(b). The refined crystal structure parameters of the HP phase at 10.5 GPa are given in Table I. The crystal structure of the HP phase is shown in Figs. 1(c) and 1(d). When viewed along the c axis (which is equivalent to the b axis of the monoclinic structure), the HP phase shows MgO_6 octahedra surrounded by six distorted IO_6 octahedra (two O atoms are shared between each octahedron). In this context, the oxygen coordination of I increases from threefold in the LP phase to sixfold in the HP phase (if we chose 2.48 \AA as the bonding limitation between iodine and oxygen atoms) [16,41]. When viewed perpendicular to the c axis, the HP phase of $\text{Mg}(\text{IO}_3)_2$ shows the transformation from the 2D layered structure of the LP phase to a three-dimensional structure. This is caused by the formation of extra bonds between iodine and oxygen atoms of the neighboring IO_3 layer. The I coordination change in the HP phase is discussed in detail later. We found that the pressure-induced structural phase transition in $\text{Mg}(\text{IO}_3)_2$ is reversible, as seen in the XRD collected after fully releasing pressure [top pattern in Fig. 2(a)]. More evidence of the reversibility can be found in the HP-RS and HP FTIR experiments later discussed.

2. Compressibility

From experiments and calculations, we determined the pressure dependence of the lattice parameters and unit cell volume of the LP and HP phases. Results are shown in Figs. 2(c) to 2(e). The agreement between the experimental and calculated lattice parameters reflects the reasonable description provided by *ab initio* calculations for the crystal

structure behavior under compression. In the LP phase, the crystal structure exhibits an unusual expansion of the a and c axes, which gradually become equivalent. In contrast, according to experiments (calculations), the lattice parameter b shows a dramatic shrinkage from 5.1 \AA (5.2 \AA) at ambient pressure to 4.0 \AA (4.4 \AA) at 6.6 GPa. This implies a 21.6% (15.4%) reduction that contrasts with the much smaller changes of the other two axes (1.4 and 1.7%, respectively, for a and c according to experiment). Thus, the behavior of the crystal structure of the LP phase of $\text{Mg}(\text{IO}_3)_2$ is highly anisotropic under compression. The large compressibility along the b axis is a consequence of the layered characteristic of the crystal structure, which consists of layers stacked along to the b axis [see Fig. 1(b)] with a relatively large empty space between each layer due to the alignment of the iodine LEP along the b axis. Regarding the monoclinic angle of the LP phase, it increases from 119.8° at ambient pressure to $\sim 120^\circ$ at 1.4 GPa in experiment, and after that, it becomes roughly constant within the experimental accuracy. Similar behavior is observed in the calculated monoclinic angle [see Fig. 2(d)]. Notice that, at 8.5 GPa, the unit cell parameters a and c are nearly identical, i.e., the crystal structure can be described as pseudohexagonal. Interestingly, >8.5 GPa, the phase transition to the trigonal phase takes place.

In the HP phase, both lattice parameters a and c are less sensitive to pressure than the unit cell parameters of the LP phase. For instance, the lattice parameter c of the HP phase, which corresponds to the b parameter of the LP phase, shows a reduction of 8.8% (11.4%) from 10 to 22 GPa according to experiments (calculations). This means that the compressibility of c in the HP phase is half that of the equivalent parameter of the LP phase. The fact that HP phase is less compressible than the LP phase also causes an increase of the bulk modulus, as can be seen in Table II, where we have summarized the zero-pressure volume (V_0), bulk modulus (B_0), and its pressure derivative (B'_0) for both phases. Parameters in Table II were obtained from fitting the P - V data for both phases using a third-order Birch-Murnaghan EOS [42,43] with the EOSFIT7C-GUI software [44]. To better compare both phases, we have used the volume per formula unit in both Fig. 2(e) and Table II. The bulk moduli for the LP phase obtained from experiments and calculations, 22.2 ± 0.8 and 26.4 ± 0.8 GPa, respectively, are in good agreement and are like those of the LP phase of KIO_3 (24.3 GPa) [45] and $\text{Zn}(\text{IO}_3)_2$ (21.6 GPa) [16], slightly smaller than that of the LP phase of $\text{Co}(\text{IO}_3)_2$ (29.8 GPa) [17] and α - LiIO_3 (34 GPa) [46], and much smaller than that of the LP phase of $\text{Fe}(\text{IO}_3)_3$ (55 GPa) [19]. The bulk modulus of the HP phase is almost three times larger than that of LP phase in experiment. In addition, the bulk modulus of the HP phase in $\text{Mg}(\text{IO}_3)_2$ is close to that of the HP phase of

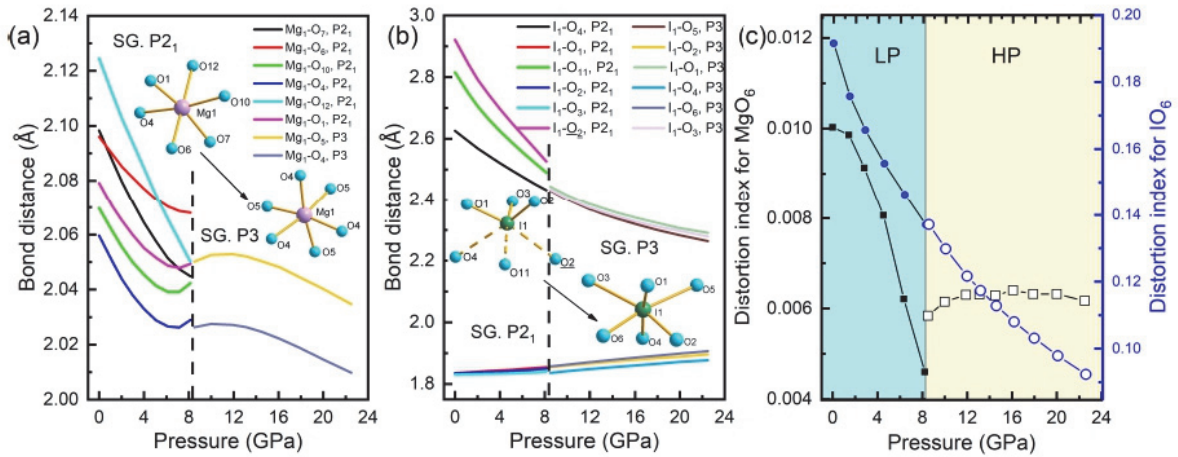


FIG. 3. Calculated pressure dependence of (a) Mg₁-O and (b) I₁-O bond distances. Polyhedral coordination is shown in the figure. The vertical dash line indicates the phase transition pressure. (c) Calculated distortion index of Mg₁O₆ (squares) and I₁O₆ (circles) octahedral extrapolated from the calculated structure by using the VESTA software program [50]. For a better comparison of the distortion index of the oxygen environment in iodine, we used the distortion index of IO₆ units for the whole pressure range.

Co(IO₃)₂ (70.8 GPa) [17] and the HP phase of Fe(IO₃)₃ (73 GPa) [19].

3. Oxygen coordination increase of iodine

In this section, we demonstrate the pressure-induced oxygen coordination increase of iodine. The calculated Mg-O and I-O bond distances as a function of pressure are shown in Figs. 3(a) and 3(b). In the LP phase, Mg atoms are bonded to six O atoms in six different Wyckoff positions. All six

Mg-O bond lengths are different from each other, resulting in a distorted MgO₆ octahedron. On the other hand, the iodine atoms are only bonded to three O atoms; however, for a better comprehension of changes in iodine coordination, we will consider in our analysis IO₆ units by including the distances between the iodine atom and the three second nearest neighboring O atoms, which in the case of I1 are O4, O11, and the second nearest neighboring O₂ [see the long I-O bonds in Fig. 3(b)]. Due to the large difference between the three short and the three long I-O bond distances, the distortion

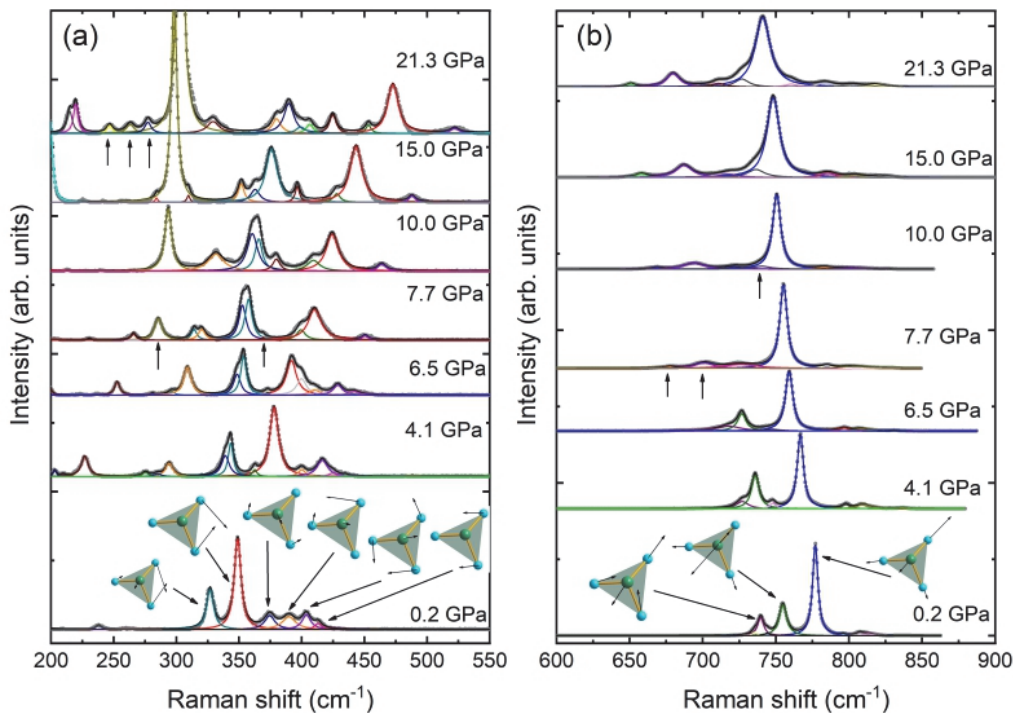


FIG. 4. Background-subtracted Raman spectra of Mg(IO₃)₂ at selected pressures in two different wave number ranges. Experimental results are shown in gray dots, and the fitting of Raman peaks via a Voigt profiles is shown with solid lines of different colors. The intensity axis of (a) is multiplied by a factor of 10 relative to (b) to show Raman-active peaks more clearly.

TABLE III. Frequency (ω), pressure coefficient ($d\omega/dP$), and Grüneisen parameters (γ) for different Raman-active modes of the LP phase. The pressure coefficients of each mode shown in this paper were extracted by fitting the Raman shift vs pressure plot in Fig. 5 with the quadratic function: $\omega = C + AP + BP^2$, where C , A , and B are constants, and P is pressure. The Grüneisen parameters were calculated by the expression $\gamma_0 = (B_0/\omega_0)(d\omega/dP)$, where B_0 is the bulk modulus we obtained from the HP-XRD data. For the sake of simplicity, we only listed the calculated modes that have been tentatively assigned to the modes observed in experiment. All calculated modes can be found in Table S1 in the Supplemental Material [36].

Modes	Theory (ambient pressure, $B_0 = 26.4$ GPa)			Experiment (0.2 GPa, $B_0 = 22.2$ GPa)		
	ω (cm ⁻¹)	$d\omega/dP$ (cm ⁻¹ /GPa)	γ	ω (cm ⁻¹)	$d\omega/dP$ (cm ⁻¹ /GPa)	γ
A	64.34	6.35	2.61	62	7.69	2.75
B	81.49	2.62	0.85	76	8.37	2.45
B	112.08	5.77	1.36	115	12.29	2.37
A	140.00	5.58	1.05	135	8.89	1.46
A	145.67	5.63	1.02	146	11.94	1.82
B	165.81	7.80	1.24	156	14.06	2.00
A	172.45	7.62	1.17	165	12.23	1.64
B	175.35	8.56	1.29	177	5.22	0.65
A	185.73	10.18	1.45	188	10.54	1.24
B	242.47	8.39	0.91	238	10.67	1.00
B	324.99	5.27	0.43	327	3.72	0.25
A	351.21	6.70	0.50	349	8.91	0.57
B	381.86	8.92	0.62	374	7.84	0.47
A	388.14	9.53	0.65	390	9.31	0.53
B	397.74	8.96	0.59	404	6.22	0.34
A	409.35	9.20	0.59	413	5.42	0.29
A	731.01	-3.78	-0.14	735	-3.85	-0.12
A	736.14	-4.92	-0.18	739	-2.80	-0.08
B	746.28	-3.84	-0.14	755	-5.78	-0.17
A	770.97	-3.58	-0.12	777	-2.21	-0.06
A	796.35	3.01	0.10	796	1.18	0.03
B	810.49	2.19	0.07	813	-1.27	-0.03

index of IO₆ units is ~ 0.19 at ambient pressure [see Fig. 3(c)]. Under compression, the distortion index of MgO₆ and IO₆ units decreases, thus indicating the increase of the symmetry of the structure at HP.

In the HP phase, Mg is in three different Wyckoff positions, and each of them is bonded with six oxygen atoms in two different Wyckoff positions. Then there are only two types of Mg-O bonds in each MgO₆ octahedron, and the distortion index of this unit almost remains unchanged after the phase transition. On the other hand, both the short and long I-O bonds show a continuous change under compression in the HP phase, and the distortion index of the IO₆ units continuously decreases up to ~ 24 GPa.

An interesting feature regarding the IO₆ units is the opposing evolution of the short and long I-O bond distances [see Fig. 3(b)]. The three short I-O bonds expand under compression in both the LP and HP phases, while the three long I-O bonds shrink. Moreover, if we choose 2.48 Å as the maxima bonding distance between I and O atoms [41,47], the iodine coordination gradually increases and becomes sixfold in the HP phase. Due to the existence of the iodine LEP, which will typically point out of the IO₃ layer [1,15], and the pressure-induced shortening of the long I-O bond distances, iodine will gradually bond with the oxygen in the neighboring IO₃ layer, which will be accompanied by the decrease of the stereoactivity of the LEP. Therefore, the three oxygen atoms in the trigonal IO₃ pyramid will be pushed away from

iodine to accommodate the additional three incoming oxygen atoms. A similar increase of the I coordination to O atoms has also been reported in other metal iodates, like Fe(IO₃)₃ [18,19], Zn(IO₃)₂ [16], Co(IO₃)₂ [17], KIO₃ [48], and in 2D bismuth-based materials, like Bi₂O₂S [15]. As the new I-O bonds are formed and the Mg-O bond distance also shortens, the repulsive interaction between atoms becomes significant and resists the external compression. Eventually, the crystal structure of the HP phase becomes less compressible, and the bulk modulus in experiment ($B_0 = 63.6 \pm 0.4$ GPa) becomes three times higher than that of the LP phase.

B. HP-RS measurements

According to group theory, the LP phase (space group $P2_1$) has 54A + 54B modes at the BZ center. One A and two B modes are acoustic vibrations. The remaining 105 modes are optical modes, which are both Raman- and IR-active modes. On the other hand, the HP phase (space group $P3$) should have 27A + 27E vibrational modes at the BZ center. In this case, one A and one E modes are acoustic modes. Again, the remaining 52 modes are both Raman- and IR-active modes. It must be noted that, since all modes in both phases are both Raman- and IR-active, they are polar and can show a transverse optical–longitudinal optical (TO-LO) splitting. Therefore, up to double the number of modes can be observed in the spectra.

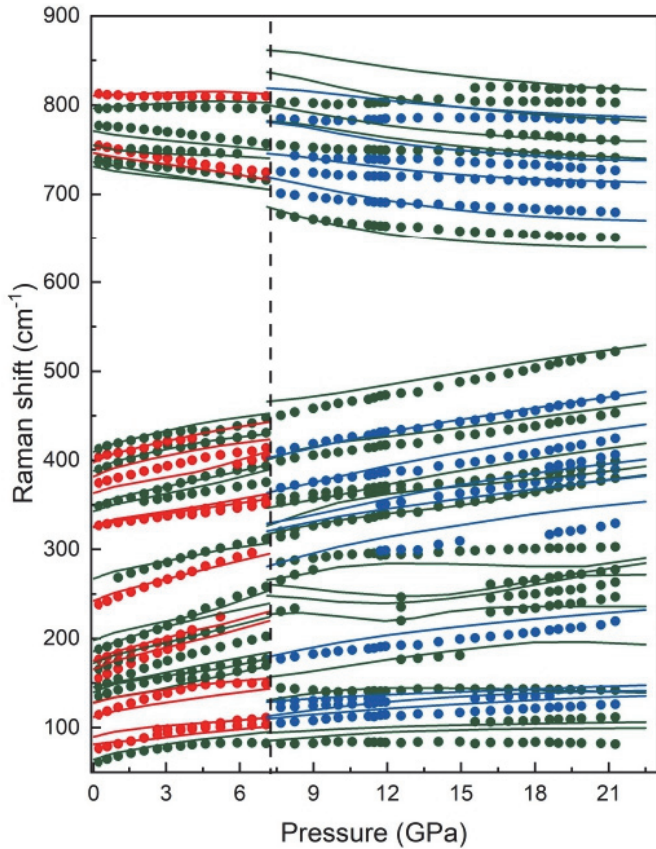


FIG. 5. Calculation (solid lines) and experiment (dots) determined pressure dependence of the Raman modes; the vertical dashed line indicates the phase transition pressure. For the low-pressure (LP) phase, A and B symmetry modes are shown in green and red, respectively. For the high-pressure (HP) phase, A and E symmetry modes are shown in green and blue, respectively. For the sake of simplicity, we only plotted the calculated modes which correlate to the experiment observed modes. The theoretical results of the HP phase at wave numbers $> 600 \text{ cm}^{-1}$ have been upshifted by 70 cm^{-1} to match with the experimental results.

Raman spectra of $\text{Mg}(\text{IO}_3)_2$ at selected pressures are shown in two ranges: from 200 to 550 cm^{-1} [Fig. 4(a)] and from 600 to 900 cm^{-1} [Fig. 4(b)]. The entire range of the Raman spectra (from 10 to 1000 cm^{-1}) at selected pressures can be found in the Supplemental Material, Fig. S4 and Table S1 [36]. We only present these two ranges in this paper because they provide the most interesting information regarding the HP behavior of $\text{Mg}(\text{IO}_3)_2$. The spectra are split into two different plots because of the intensity difference between the modes in the two ranges.

Near ambient pressure (0.2 GPa), a total of 22 Raman-active modes have been detected (see Table III). The symmetries of the different Raman-active modes have been assigned with the help of calculations because calculated frequencies show a rather good agreement with experimental ones. Moreover, the experimental pressure dependence of the frequencies of the Raman-active modes is well described by calculations (see Fig. 5). Seven modes are observed in the midfrequency range (200 to 550 cm^{-1}) and six in the high-frequency range (600 to 900 cm^{-1}).

Thanks to calculations, the atomic displacements associated with the observed Raman-active modes have been obtained. Raman-active modes of the midfrequency range are associated with the internal bending of $[\text{IO}_3]^-$ polyhedron, while modes of the high-frequency range are associated with the internal stretching of IO_3^- units. On the other hand, the modes $< 200 \text{ cm}^{-1}$ are associated with the translational and rotational motions of iodate as a rigid unit. This result is like those previously found in other metal iodates, such as KIO_3 [48], $\text{Mn}(\text{IO}_3)_2$ [49], $\text{Fe}(\text{IO}_3)_3$ [18], $\text{Zn}(\text{IO}_3)_2$ [16], and $\text{Co}(\text{IO}_3)_2$ [17].

In the midfrequency range [Fig. 4(a)], the strongest mode near ambient pressure is $\sim 349 \text{ cm}^{-1}$ and has been assigned to the I-O symmetric bending mode of the $[\text{IO}_3]^-$ unit. The modes at 374 , 390 , and 413 cm^{-1} are also assigned to the I-O symmetric bending modes, and the modes at 327 and 404 cm^{-1} are assigned to the I-O asymmetric bending modes of the $[\text{IO}_3]^-$ unit. All these modes of the midfrequency region stiffen under compression. Notably, the mode at 327 cm^{-1} splits beyond 4.1 GPa as a consequence of the different pressure dependence of two constituent modes which have almost the same frequency at 0.2 GPa (see Fig. 5).

Above 7.7 GPa , two additional Raman peaks appear [see arrows in Fig. 4(a)]. The intensity of these two peaks grows with increasing pressure. We consider these modes are an indication of the onset of a phase transition, which agrees with the results of HP-XRD. By using the same symmetry assignment provided by calculations, the Raman modes of the HP phase at 7.7 GPa and their vibration symmetry have been determined (see Tables IV and S2 in the Supplemental Material [36]). There are three Raman peaks that become more evident near 17 GPa at $\sim 250 \text{ cm}^{-1}$, but we interpret that these modes are not an indication of any structural change since we consider that these modes are predicted by calculations for the HP phase. We consider that these modes already exist $> 7.7 \text{ GPa}$, but unfortunately, they are too weak to be accurately determined, so they are not included in Fig. 4. According to calculations, these modes have a nonlinear pressure dependence (see Fig. 5), with a softening from 7.5 to 12 GPa and then a subsequent hardening.

In the high-frequency range [Fig. 4(b)], the strongest Raman peak, which also is the strongest Raman peak of the spectrum, is located at 777 cm^{-1} at 0.2 GPa in LP phase. The frequency of this mode is comparable with that of the strongest mode of $\text{Zn}(\text{IO}_3)_2$ (782 cm^{-1}) [16], $\text{Fe}(\text{IO}_3)_3$ (790 cm^{-1}) [18], $\text{Co}(\text{IO}_3)_2$ (765 cm^{-1}) [17], $\text{Mn}(\text{IO}_3)_2$ (774 cm^{-1}) [49], and KIO_3 (750 cm^{-1}) [48]. This is reasonable since, in all the above-mentioned compounds, the strongest mode corresponds to the same internal I-O stretching vibration of the $[\text{IO}_3]^-$ unit. Thanks to calculations, we have assigned the modes at 735 and 755 cm^{-1} to the asymmetric I-O stretching modes of $[\text{IO}_3]^-$ and the mode at 777 cm^{-1} to the symmetric I-O stretching mode of $[\text{IO}_3]^-$. It is worth noting that the three modes soften under compression. At 7.7 GPa , we found three extra Raman peaks. They are marked by arrows in Fig. 4(b). In addition, there is an intensity drop of the mode 755 cm^{-1} (at 0.2 GPa), and the modes at frequencies $> 777 \text{ cm}^{-1}$ disappear. The changes observed in the high-frequency range of the spectrum also support the occurrence of the phase transition we found in HP-XRD. Interestingly,

TABLE IV. Frequency (ω), pressure coefficient ($d\omega/dP$), and Grüneisen parameters (γ) for different Raman-active modes of the HP phase. More details can be found in the caption of Table III. All theoretical predicted modes at 8.5 GPa can found in Table S2 in Supplemental Material [36]. The miss of the pressure coefficient and Grüneisen parameters for the experimental mode at 231 cm^{-1} is due to insufficient data at HP.

Modes	Theory (8.5 GPa, $B_0 = 44.4$ GPa)			Experiment (7.7 GPa, $B_0 = 63.6$ GPa)		
	ω (cm^{-1})	$d\omega/dP$ ($\text{cm}^{-1}/\text{GPa}$)	γ	ω (cm^{-1})	$d\omega/dP$ ($\text{cm}^{-1}/\text{GPa}$)	γ
A	88.39	1.93	0.97	82	0.45	0.35
E	113.68	2.38	0.93	105	1.72	1.04
E	118.12	3.40	1.28	123	1.56	0.81
E	131.76	1.59	0.53	130	0.82	0.40
A	136.93	2.35	0.76	144	0.07	0.03
E	187.53	4.95	1.17	177	2.70	0.97
A	228.93	0.06	0.01	231	×	×
E	271.82	2.32	0.38	286	4.20	0.93
A	325.46	4.08	0.56	320	4.05	0.81
A	340.00	6.22	0.81	353	2.81	0.51
A	353.44	5.79	0.73	358	3.72	0.66
E	371.86	6.33	0.76	369	3.09	0.53
A	412.55	4.62	0.50	399	3.46	0.55
E	411.22	5.92	0.64	410	4.19	0.65
A	469.89	4.30	0.41	451	4.66	0.66
A	624.40	-6.21	-0.44	678	-3.20	-0.30
E	661.56	-5.81	-0.39	701	-2.16	-0.20
E	692.15	-3.77	-0.24	726	-0.98	-0.09
A	728.70	-4.30	-0.26	755	-0.62	-0.05
E	766.70	-3.26	-0.19	785	0.71	0.06
A	780.14	-6.10	-0.35	803	0.88	0.07

in both the LP and HP phases, several high-frequency modes show a soft behavior (see Fig. 5). As we have previously demonstrated in $\text{Zn}(\text{IO}_3)_2$ [16], for the internal I-O stretching modes of $[\text{IO}_3]^-$, $\omega^{-2/3}$ shows a linear relationship with the average I-O bond. Therefore, it is reasonable to conclude that

the soft behavior of the Raman modes in $\text{Mg}(\text{IO}_3)_2$ is caused by the enlargement of the three short I-O bonds under compression to accommodate the three additional oxygen atoms. This observation agrees with the results shown at the bottom of Fig. 3(b), and it is expected that the increase of the short I-O

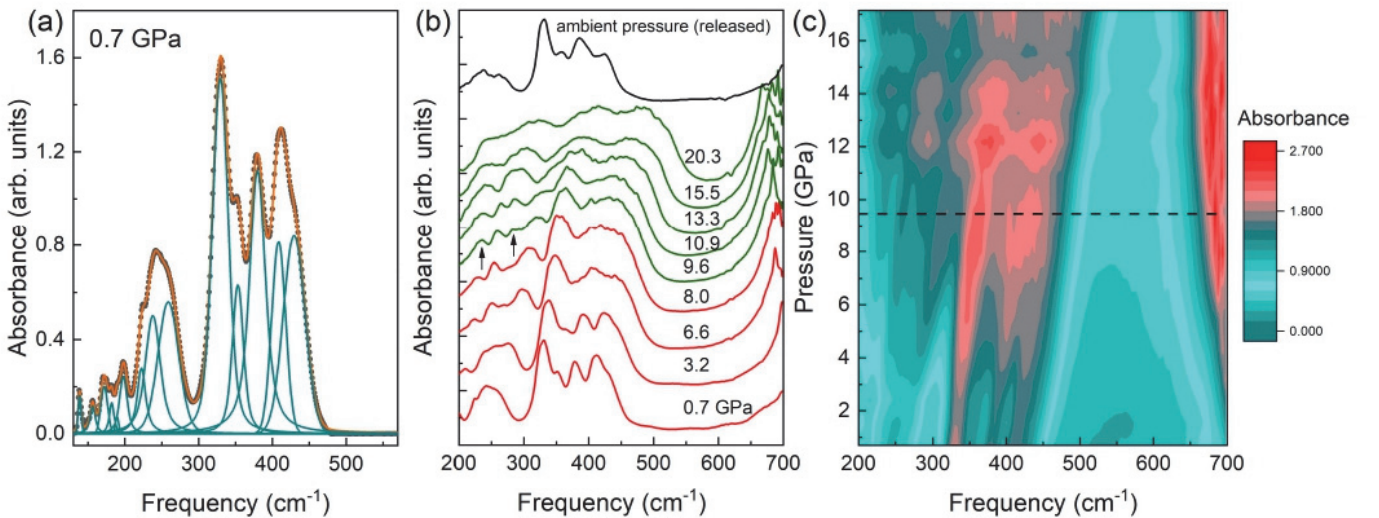


FIG. 6. Infrared (IR) spectra of $\text{Mg}(\text{IO}_3)_2$ at selected pressures. (a) Background-subtracted IR spectra at the lowest pressure in our experiment (0.7 GPa); experimental data are shown by gray dots, the fitting of the experimental data with Voigt profiles is shown by the orange line, and the individual Voigt peaks are shown in light blue. (b) Infrared spectra collected at selected pressures. Red (green) color indicates the low-pressure (LP) [high-pressure (HP)] phase. Pressures are indicated, the units for pressure are gigapascals, the up arrows at 9.6 GPa mark extra IR peaks, which are a sign of the phase transition. (c) Contour plot of the same data in (b); the horizontal dash line indicates the start of the phase transition.

TABLE V. Frequency (ω), pressure coefficient ($d\omega/dP$), and Grüneisen parameters (γ) for different IR-active modes of the LP (top) and HP (bottom) phase. More details can be found in the caption of Table III. The miss of the pressure coefficient and Grüneisen parameters for the experimental modes 156, 182, and 189 cm^{-1} is due to insufficient data at HP. The complete theoretical predicted modes for LP and HP phases can be found in Tables S1 and S3 in Supplemental Material [36].

Modes	Theory (at 0 GPa, $B_0 = 26.4$ GPa)			Experiment (at 0.7 GPa, $B_0 = 22.2$ GPa)		
	ω (cm^{-1})	$d\omega/dP$ ($\text{cm}^{-1}/\text{GPa}$)	γ	ω (cm^{-1})	$d\omega/dP$ ($\text{cm}^{-1}/\text{GPa}$)	γ
B	135.69	5.46	1.06	139	7.84	1.25
B	142.20	2.98	0.55	156	×	×
A	155.07	5.01	0.85	172	7.22	0.93
A	163.35	5.63	0.91	182	×	×
A	172.45	9.10	1.39	189	×	×
A	184.56	9.89	1.41	198	6.56	0.74
B	211.11	10.62	1.33	222	9.72	0.97
B	220.82	9.24	1.10	238	5.96	0.56
B	242.47	7.45	0.81	259	9.39	0.80
B	324.99	4.70	0.38	329	2.20	0.15
A	342.87	5.53	0.43	353	5.05	0.32
A	364.69	4.66	0.34	380	4.39	0.26
A	409.35	8.92	0.58	408	2.22	0.12
A	416.32	8.89	0.56	429	1.25	0.06
	Theory (at 10.0 GPa, $B_0 = 44.4$ GPa)			Experiment (at 9.6 GPa, $B_0 = 63.6$ GPa)		
A	199.40	2.97	0.66	204	4.96	1.55
A	224.96	2.34	0.46	236	0.97	0.26
E	259.91	6.91	1.18	259	8.21	2.02
E	281.96	7.02	1.10	279	5.92	1.35
E	320.46	3.32	0.46	321	0.82	0.16
E	360.82	5.99	0.74	355	5.49	0.98
E	411.78	6.68	0.72	396	9.72	1.56
A	430.23	8.63	0.89	423	9.57	1.44
E	477.20	6.03	0.56	463	8.78	1.21

bonds finishes when the IO_6 unit becomes more regular, i.e., with almost a single I-O bond distance at ~ 48 GPa by fitting the calculation data. From the Raman spectra collected after releasing pressure (Supplemental Material, Fig. S4 [36]), the phase transition is reversible, as found in HP-XRD.

C. HP-FTIR measurements

Figure 6(a) shows the FTIR spectra of $\text{Mg}(\text{IO}_3)_2$ at the lowest pressure (0.7 GPa) in the far-IR range (130–600 cm^{-1}). Table V summarizes the frequencies of the IR-active modes obtained from a peak fitting performed using Voigt profiles. The symmetry of the IR-active modes has been assigned based on calculations as done for the Raman-active modes. A total of 14 IR-active modes has been determined at 0.7 GPa. Since all optical modes of $\text{Mg}(\text{IO}_3)_2$ are both Raman and IR active, we will compare the results obtained from both techniques. However, it must be considered that usually strong modes in the Raman spectrum tend to be weak modes in the IR spectrum and vice versa. In the range of 300–500 cm^{-1} , where modes are related to I-O bending vibrations of $[\text{IO}_3]^-$ units, six Raman-active modes and five IR-active modes have been detected. Only two of them have been found at similar frequencies by both techniques. The Raman-active modes at 327 and 413 cm^{-1} were measured at 329 and 408 cm^{-1} in IR. The rest of the modes are not the same, so both techniques can complement to each other. Thanks to calculations, the

IR-active mode at 353 cm^{-1} can be assigned to an asymmetric I-O bending of IO_3^- units, while the IR-active modes at 380 and 429 cm^{-1} can be assigned to the symmetric I-O bending of IO_3^- units. In addition, we found three IR-active modes at 222, 238, and 259 cm^{-1} but only one Raman mode in the range of 200–300 cm^{-1} (the mode at 238 cm^{-1}). Unfortunately, the 259 cm^{-1} mode cannot be followed at HP.

Figure 6(b) displays the evolution of the IR spectrum of $\text{Mg}(\text{IO}_3)_2$ under compression. The experimental cutoff frequency was 700 cm^{-1} . In Fig. 6(c), we show a contour plot of the same data. It can be observed that there are IR peaks appearing at wave numbers > 600 cm^{-1} in Figs. 6(b) and 6(c) beyond 6.6 GPa. These are stretching modes originally at frequencies > 700 cm^{-1} which soften under compression, as discussed in the Raman section. Remember that all modes in $\text{Mg}(\text{IO}_3)_2$ are both Raman and IR active. All IR-active modes in the medium-frequency range harden in the pressure range of stability of the LP and HP phases as it was found in Raman measurements. On the other hand, the IR-active modes of the high-frequency range soften at HP as it was found in Raman measurements. The pressure dependence of the frequencies of the IR-active modes is shown in Fig. 7.

The splitting of the IR peak at 250 cm^{-1} is due to the presence of two modes with a different pressure coefficient. In addition, there is a significant broadening and merging of the peaks in the 300–500 cm^{-1} range. The appearance of two new peaks at 9.6 GPa (with wave numbers 236 and 279 cm^{-1})

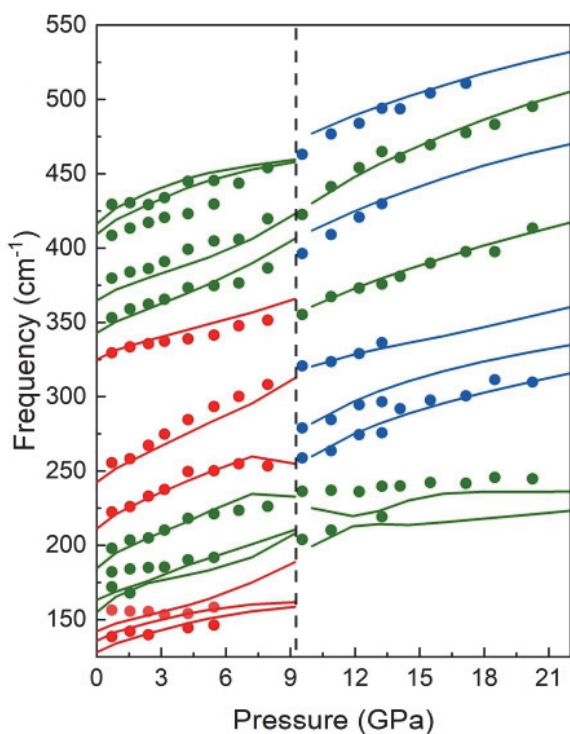


FIG. 7. Experimental (dots) and calculated (solid lines) determined infrared (IR) modes as a function of pressure. A, B, and E symmetry are shown in green, red, and blue, respectively. The symmetry of the experimentally observed IR modes has been assigned based on the same method used in the symmetry assignment of Raman modes; the vertical dashed line indicates the phase transition.

evidences the onset of the phase transition [see arrows in Fig. 6(b)]. The frequency of one of the extra peaks found in IR experiments is close to that of one of the extra peaks found in the Raman spectra at 9.4 GPa [which is shown in dark yellow in Fig. 4(a)]. A total of nine IR-active modes have been determined at 9.6 GPa. They are summarized in Table V (and Table S3 in the Supplemental Material [36]) together with the symmetry assignment. The nine modes will merge into four modes at pressures > 18 GPa. This result agrees with the expected merging of peaks at HP that will occur because of the equalization of the I-O bond distances in the IO_6 unit, i.e., upon the increase in symmetry of the IO_6 unit. All the pressure-induced changes in the IR spectra are reversible, as shown in Fig. 6(b).

IV. CONCLUSIONS

By combining the use of DACs, synchrotron-based angle dispersion powder XRD, RS, FTIR spectroscopy, and first-principle calculations, we discovered a pressure-induced phase transition and oxygen coordination increase (from 3 to 6) of iodine in metal iodate $\text{Mg}(\text{IO}_3)_2$. According to Rietveld refinements of HP-XRD data, $\text{Mg}(\text{IO}_3)_2$ transforms from the monoclinic LP phase (space $P2_1$) to a trigonal HP phase (space group $P3$) between 7.5 and 9.7 GPa. At the transition, the number of formula units per unit cell changes from 4 to

3: There is no obvious collapse in the volume per formula unit at the transition. The bulk modulus increases from 22.2 GPa (in the LP phase) to 63.6 GPa (in the HP phase) according to experiments. Additionally, the compressibility of the LP phase is highly anisotropy. The b axis is by far the most compressible. This is a result of the layered character of the crystal structure. Calculations revealed that pressure application leads to increase in the I-O bond length, which is accompanied by a shortening of the bond distance of iodine and second neighboring oxygen atoms. This favors a gradual increase of the oxygen coordination of iodine. This behavior is caused by the existence of LEP in iodine.

According to HP-RS and HP-FTIR experiments, the phase transition takes place between 7.7 and 9.6 GPa. The phase transition is evidenced by the appearance of extra peaks and the gradually enhancement of their intensity. The vibration symmetry of all experimentally observed Raman- and IR-active modes has been assigned by the comparison between experiments and calculations. In the LP phase, the vibrational modes in the midfrequency range (300–550 cm^{-1}) are related to I-O bending motions of $[\text{IO}_3]^-$ units, while those of the high-frequency range (600–900 cm^{-1}) are related to I-O stretching motions of $[\text{IO}_3]^-$ units. While the modes in the midfrequency range harden at HP, the modes at the high-frequency range soften at HP in both the LP and HP phases. This softening is caused by the increase of the I-O bond distances at HP and the charge transfer from short I-O bonds to large I-O bonds to form IO_6 units at HP. The phase transition found by the three experimental techniques was found to be reversible.

ACKNOWLEDGMENTS

This paper was supported by the Generalitat Valenciana under Project PROMETEO 2018/123-EFIMAT and by the Spanish Ministerio de Ciencia e Innovación and Agencia Estatal de Investigación (MCIN/AEI/10.13039/501100011033) and by the European Union under Grants PID2019-106383GB-41/42/43, and RED2018-102612-T (MALTA Consolider Team). A.M. and P.R.-H. acknowledge computing time provided by Red Española de Supercomputación (RES) and the MALTA Consolider Team cluster. D.E. acknowledges the resources and technical assistance provided by the Informatics Service of Universitat de Valencia through the Tirant III cluster. A.L. and D.E. would like to thank the Generalitat Valenciana for the Ph.D. Fellowship No. GRISOLIAP/2019/025. R.T. acknowledges funding from the Spanish Ministerio de Economía y Competitividad (MINECO) via the Juan de la Cierva Formación fellowship (FJC2018-036185-I). C.P. is thankful for the financial support of the Spanish MINECO Project No. FIS2017-83295-P. E.B. would like to thank the University of Valencia for his “Attracció de Talent” postdoctoral contract (UV-INV_POSTDOC19-1026935). Powder XRD experiments were performed at the MSPD beamline of ALBA Synchrotron (Experiment No. 2019083663). IR experiments were performed at the MIRAS beamline of ALBA Synchrotron (experiment No. 2020024118).

- [1] H. Y. Chang, S. H. Kim, M. O. Kang, and P. S. Halasyamani, Polar or nonpolar? $A+$ cation polarity control in $A_2Ti(IO_3)_6$ ($A = Li, Na, K, Rb, Cs, Tl$), *J. Am. Chem. Soc.* **131**, 6865 (2009).
- [2] H. Y. Chang, S. H. Kim, P. S. Halasyamani, and K. M. Ok, Alignment of lone pairs in a new polar material: synthesis, characterization, and functional properties of $Li_2Ti(IO_3)_6$, *J. Am. Chem. Soc.* **131**, 2426 (2009).
- [3] C. F. Sun, C. L. Hu, X. Xu, J. B. Ling, T. Hu, F. Kong, X. F. Long, and J. G. Mao, $BaNbO(IO_3)_5$: a new polar material with a very large SHG response, *J. Am. Chem. Soc.* **131**, 9486 (2009).
- [4] S. D. Nguyen, J. Yeon, S. H. Kim, and P. S. Halasyamani, $BiO(IO_3)$: a new polar iodate that exhibits an Aurivillius-type $(Bi_2O_2)^{2+}$ layer and a large SHG response, *J. Am. Chem. Soc.* **133**, 12422 (2011).
- [5] X. Xu, C. Hu, B. Li, B. Yang, and J. Mao, α - AgI_3O_8 and β - AgI_3O_8 with large SHG responses: polymerization of IO_3 groups into the I_3O_8 polyiodate anion, *Chem. Mater.* **26**, 3219 (2014).
- [6] Y. Huang, X. Meng, P. Gong, L. Yang, Z. Lin, X. Chen, and J. Qin, $A_2Bi_5O_{15}$ ($A = K^+$ or Rb^+): two new promising nonlinear optical materials containing $[I_3O_9]^{3-}$ bridging anionic groups, *J. Mater. Chem. C* **2**, 4057 (2014).
- [7] L. Xiao, Z. Cao, J. Yao, Z. Lin, and Z. Hu, A new cerium iodate infrared nonlinear optical material with a large second-harmonic generation response, *J. Mater. Chem. C* **5**, 2130 (2017).
- [8] F. F. Mao, C. L. Hu, J. Chen, B. L. Wu, and J. G. Mao, $HBa_{2.5}(IO_3)_6(I_2O_5)$ and $HBa(IO_3)(I_4O_{11})$: explorations of second-order nonlinear optical materials in the alkali-earth polyiodate system, *Inorg. Chem.* **58**, 3982 (2019).
- [9] C. Sun, B. Yang, and J. Mao, Structures and properties of functional metal iodates, *Sci. China Chem.* **54**, 911 (2011).
- [10] C. L. Hu and J. G. Mao, Recent advances on second-order NLO materials based on metal iodates, *Coord. Chem. Rev.* **288**, 1 (2015).
- [11] D. Phanon and I. Gautier-Luneau, Promising material for infrared nonlinear optics: NaI_3O_8 salt containing an octaoxotriiodate(V) anion formed from condensation of $[IO_3]^-$ ions, *Angew. Chem. Int. Ed.* **46**, 8488 (2007).
- [12] D. Phanon, A. Mosset, and I. Gautier-Luneau, New materials for infrared non-linear optics. Syntheses, structural characterisations, second harmonic generation and optical transparency of $M(IO_3)_3$ metallic iodates, *J. Mater. Chem.* **17**, 1123 (2007).
- [13] R. Chikhaoui, Z. Hebboul, M. A. Fadla, K. Bredillet, A. Liang, D. Errandonea, S. Beauquis, A. Benghia, J. C. Marty, R. Le Dantec, Y. Mugnier, and E. Bandiello, Synthesis and characterization of novel nanoparticles of lithium aluminum iodate $LiAl(IO_3)_4$, and DFT calculations of the crystal structure and physical properties, *Nanomaterials* **11**, 3289 (2021).
- [14] A. Liang, P. Rodríguez-Hernandez, A. Muñoz, S. Raman, A. Segura, and D. Errandonea, Pressure-dependent modifications in the optical and electronic properties of $Fe(IO_3)_3$: the role of $Fe\ 3d$ and $I\ 5p$ lone-pair electrons, *Inorg. Chem. Front.* **8**, 4780 (2021).
- [15] K. Bu, H. Luo, S. Guo, M. Li, D. Wang, H. Dong, Y. Ding, W. Yang, and X. Lü, Pressure-regulated dynamic stereochemical role of lone-pair electrons in layered Bi_2O_2S , *J. Phys. Chem. Lett.* **11**, 9702 (2020).
- [16] A. Liang, C. Popescu, F. J. Manjon, A. Muñoz, Z. Hebboul, and D. Errandonea, Structural and vibrational study of $Zn(IO_3)_2$ combining high-pressure experiments and density-functional theory, *Phys. Rev. B* **103**, 054102 (2021).
- [17] A. Liang, C. Popescu, F. J. Manjon, R. Turnbull, E. Bandiello, P. Rodríguez-Hernandez, A. Muñoz, I. Yousef, Z. Hebboul, and D. Errandonea, Pressure-driven symmetry-preserving phase transitions in $Co(IO_3)_2$, *J. Phys. Chem. C* **125**, 17448 (2021).
- [18] A. Liang, S. Rahman, P. Rodríguez-Hernandez, A. Muñoz, F. J. Manjón, G. Nenert, and D. Errandonea, High-pressure Raman study of $Fe(IO_3)_3$: soft-mode behavior driven by coordination changes of iodine atoms, *J. Phys. Chem. C* **124**, 21329 (2020).
- [19] A. Liang, S. Rahman, H. Saqib, P. Rodríguez-Hernandez, A. Muñoz, G. Nenert, I. Yousef, C. Popescu, and D. Errandonea, First-order isostructural phase transition induced by high-pressure in $Fe(IO_3)_3$, *J. Phys. Chem. C* **124**, 8669 (2020).
- [20] J.-K. Liang, Y.-D. Yu, and S.-L. Ding, The structure and phase transitions of magnesium iodate crystals, *Acta Phys. Sin.* **27**, 710 (1978).
- [21] D. Phanon, B. Bentría, E. Jeanneau, D. Benbental, A. Mosset, and I. Gautier-Luneau, Crystal structure of $M(IO_3)_2$ metal iodates, twinned by pseudo-merohedry, with M^{II} : Mg^{II} , Mn^{II} , Co^{II} , Ni^{II} and Zn^{II} , *Z. Kristallogr. Cryst. Mater.* **221**, 635 (2006).
- [22] A. Dewaele, P. Loubeyre, and M. Mezouar, Equations of state of six metals above 94 GPa, *Phys. Rev. B* **70**, 094112 (2004).
- [23] S. Klotz, J. C. Chervin, P. Munsch, and G. Le Marchand, Hydrostatic limits of 11 pressure transmitting media, *J. Phys. D: Appl. Phys.* **42**, 075413 (2009).
- [24] F. Fauth, I. Peral, C. Popescu, and M. Knapp, The new material science powder diffraction beamline at ALBA Synchrotron, *Powder Diffr.* **28**, 360 (2013).
- [25] C. Prescher and V. B. Prakapenka, DIOPTAS: a program for reduction of two-dimensional x-ray diffraction data and data exploration, *High Press. Res.* **35**, 223 (2015).
- [26] J. Rodríguez-Carvajal, Recent advances in magnetic structure determination by neutron powder diffraction, *Phys. B Condens. Matter* **192**, 55 (1993).
- [27] H. K. Mao, J. Xu, and P. M. Bell, Calibration of the ruby pressure gauge to 800 kbar under quasi-hydrostatic conditions, *J. Geophys. Res.* **91**, 4673 (1986).
- [28] E. D. Palik, *Handbook of Optical Constants of Solid* (Academic Press, Maryland, 1997).
- [29] D. Errandonea, A. Muñoz, and J. Gonzalez-Platas, Comment on “High-pressure x-ray diffraction study of YBO_3/Eu^{3+} , $GdBO_3$, and $EuBO_3$: Pressure-induced amorphization in $GdBO_3$ ” [*J. Appl. Phys.* **115**, 043507 (2014)], *J. Appl. Phys.* **115**, 216101 (2014).
- [30] I. Yousef, L. Ribó, A. Crisol, I. Šics, G. Ellis, T. Ducic, M. Kreuzer, N. Benseny-Cases, M. Quispe, P. Dumas, S. Lefrançois, T. Moreno, G. García, S. Ferrer, J. Nicolas, and M. A. G. Aranda, MIRAS: the infrared synchrotron radiation deamline at ALBA, *Synchrotron Radiat. News* **30**, 4 (2017).
- [31] A. Liang, R. Turnbull, E. Bandiello, I. Yousef, C. Popescu, Z. Hebboul, and D. Errandonea, High-pressure spectroscopy study of $Zn(IO_3)_2$ using far-infrared synchrotron radiation, *Crystals* **11**, 34 (2021).
- [32] P. Hohenberg and W. Kohn, Inhomogeneous electron gas, *Phys. Rev.* **136**, B864 (1964).

- [33] G. Kresse and J. Furthmüller, Efficient iterative schemes for *ab initio* total-energy calculations using a plane-wave basis set, *Phys. Rev. B* **54**, 11169 (1996).
- [34] P. E. Blöchl, Projector augmented-wave method, *Phys. Rev. B* **50**, 17953 (1994).
- [35] G. Kresse and D. Joubert, From ultrasoft pseudopotentials to the projector augmented-wave method, *Phys. Rev. B* **59**, 1758 (1999).
- [36] See Supplemental Material at <http://link.aps.org/supplemental/10.1103/PhysRevB.105.054105> for additional information on structural and vibrational analysis.
- [37] H. J. Monkhorst and J. D. Pack, Special points for Brillouin-zone integrations, *Phys. Rev. B* **13**, 5188 (1976).
- [38] R. Armiento and A. E. Mattsson, Functional designed to include surface effects in self-consistent density functional theory, *Phys. Rev. B* **72**, 085108 (2005).
- [39] A. E. Mattsson, R. Armiento, J. Paier, G. Kresse, J. M. Wills, and T. R. Mattsson, The AM05 density functional applied to solids, *J. Chem. Phys.* **128**, 084714 (2008).
- [40] A. Togo and I. Tanaka, First principles phonon calculations in materials science, *Scr. Mater.* **108**, 1 (2015).
- [41] A. Krapp, F. M. Bickelhaupt, and G. Frenking, Orbital overlap and chemical bonding, *Chem. Eur. J.* **12**, 9196 (2006).
- [42] F. D. Murnaghan, The compressibility of media under extreme pressures, *Proc. Natl. Acad. Sci. USA* **30**, 244 (1944).
- [43] F. Birch, Finite elastic strain of cubic crystals, *Phys. Rev.* **71**, 809 (1947).
- [44] R. J. Angel, J. Gonzalez-Platas, and M. Alvaro, EOSFIT7C and a Fortran module (library) for equation of state calculations, *Z. Kristallogr. Cryst. Mater.* **229**, 405 (2014).
- [45] L. Bayarjargal, L. Wiehl, A. Friedrich, B. Winkler, E. A. Juarez-Arellano, W. Morgenroth, and E. Haussühl, Phase transitions in KIO_3 , *J. Phys. Condens. Matter* **24**, 325401 (2012).
- [46] W. W. Zhang, Q. L. Cui, Y. W. Pan, S. S. Dong, J. Liu, and G. T. Zou, High-pressure x-ray diffraction study of LiIO_3 to 75 GPa, *J. Phys. Condens. Matter* **14**, 10579 (2002).
- [47] A. Lobato, M. A. Salvadó, J. M. Recio, M. Taravillo, and V. G. Baonza, Highs and lows of cond lengths: is there any limit? *Angew. Chem. Int. Ed.* **60**, 17028 (2021).
- [48] Z. X. Shen, X. B. Wang, S. H. Tang, H. P. Li, and F. Zhou, High pressure Raman study and phase transitions of KIO_3 non-linear optical single crystals, *Rev. High Press. Sci. Technol.* **7**, 751 (1998).
- [49] T. C. Kochuthresia, I. Gautier-Luneau, V. K. Vaidyan, and M. J. Bushiri, Raman and FTIR spectral investigations of twinned $M(\text{IO}_3)_2$ ($M = \text{Mn}, \text{Ni}, \text{Co}, \text{and D Zn}$) crystals, *J. Appl. Spectrosc.* **82**, 941 (2016).
- [50] K. Momma and F. Izumi, VESTA 3 for three-dimensional visualization of crystal, volumetric and morphology data, *J. Appl. Crystallogr.* **44**, 1272 (2011).

General relationship between the band-gap energy and iodine-oxygen bond distance in metal iodates

Akun Liang¹, Robin Turnbull¹, Placida Rodríguez-Hernandez², Alfonso Muñoz², M. Jasmin³, Lan-Ting Shi⁴, and Daniel Errandonea^{1,*}

¹*Departamento de Física Aplicada-ICMUV-MALTA Consolider Team, Universitat de València, c/Dr. Moliner 50, Burjassot (Valencia) 46100, Spain*

²*Departamento de Física and Instituto de Materiales y Nanotecnología, MALTA Consolider Team, Universidad de La Laguna, La Laguna 38206, Tenerife, Spain*

³*TKM College of Arts and Science, Kollam, Kerala 691005, India*

⁴*College of Physics, Sichuan University, Chengdu 610065, China*



(Received 10 March 2022; revised 9 April 2022; accepted 13 April 2022; published 28 April 2022)

A wide band gap is a fundamental requirement for an ideal nonlinear optical material. A two-step investigation has been implemented to determine the relationship between the band-gap energy and the iodine-oxygen bond distance in optically nonlinear metal iodate materials. Firstly, we utilized high-pressure conditions on Mg and Zn iodates to correlate the pressure-induced changes in band-gap energy with changes in the iodine-oxygen bond distances. On both cases, the band-gap energy shows a nonlinear decrease under compression. The nonlinear behavior is a consequence of the interplay between the pressure-induced increase of the first-nearest neighbor iodine-oxygen bonds, which favors a narrowing of the band gap, and the decrease of the second-nearest neighbor iodine-oxygen bonds, which favors an opening of the band gap. The inverse correlation between the band-gap energy and the iodine-oxygen bond distance is confirmed in the second part of the investigation by collating and comparing the band-gap energies and corresponding average iodine-oxygen bond distances of the metal iodates reported in the literature. In the comparison, only nontransition and closed-shelled transition metals were included, without regard for their chemical formula, crystal structure, or stoichiometry.

DOI: [10.1103/PhysRevMaterials.6.044603](https://doi.org/10.1103/PhysRevMaterials.6.044603)

I. INTRODUCTION

The search for the next-generation nonlinear optical (NLO) materials has driven the synthesis and characterization of numerous new metal iodates, wherein the metal element covers alkali metals [1,2], alkaline-earth metals [3,4], transition and post-transition metals [4,5] as well as lanthanide elements [6]. In these different compounds, the iodate molecules exhibit different configurational geometries, such as isolated $[\text{IO}_3]^-$ trigonal pyramids [7,8], $[\text{I}_2\text{O}_5]$ [3], $[\text{I}_3\text{O}_8]^-$ [5,9], and $[\text{I}_4\text{O}_{11}]^{2-}$ dimeric chains [3]. An ideal NLO crystal should have a high laser damage threshold (LDT), an excellent thermal stability, a wide transparency window which means a wide band-gap energy, and a large second-harmonic generation response (SHG) [10]. Notably, control of the band gap in the designed NLO materials is essential because the band gap directly determines the transparency. In addition, a large band gap may achieve a high LDT [11], and, typically, the band gap has a significant effect on the SHG response [12]. Therefore, it is important to understand which general factors affect the band-gap energy in the various metal iodates which have different chemical formula. Here, we use pressure to investigate the band-gap change of metal iodates because pressure is an efficient tool to manipulate the interaction between atoms and, therefore, to engineer the band gap in semiconductor

materials [13,14]. In a previous work we found that iron iodate, $\text{Fe}(\text{IO}_3)_3$, has the smallest band gap (2.1 eV) amongst the studied iodates reported in the literature [15]. We also explained the observed pressure-induced band-gap evolution in the same material [15]. By comparing the band gap of $\text{Fe}(\text{IO}_3)_3$ with that of other metal iodates reported in the literature, we have established that the main factor narrowing the band-gap width in transition-metal iodates is the contribution of partially filled d states from the transition metals to either the valence-band maxima (VBM) or conduction-band minima (CBM) [15]. In contrast, in nontransition or closed-shelled transition-metal iodates, the VBM and CBM are dominated by contributions from O-2*p* and I-5*p* orbitals and band-gap energies are generally larger.

Since the conclusions of our previous study [15] suggest that transition metals are best avoided if you wish to engineer a wide band gap, we have moved the focus of our research to the study of nontransition (Mg) and closed-shelled transition metal (Zn) iodates: $\text{Mg}(\text{IO}_3)_2$ and $\text{Zn}(\text{IO}_3)_2$. There are some advantages to choosing $\text{Mg}(\text{IO}_3)_2$ and $\text{Zn}(\text{IO}_3)_2$ as representative metal iodates: (i) Their high-pressure behaviors, including crystal structures, equations of state, pressure-induced phase transitions, and atomic vibrations have been well characterized and reported [16,17]. This enables us to analyze the pressure-induced band-gap changes of $\text{Mg}(\text{IO}_3)_2$ and $\text{Zn}(\text{IO}_3)_2$ from the perspective of the crystal structure, using available information on the iodine-oxygen bond distance. (ii) Their chemical formulas are simple and they are

*daniel.errandonea@uv.es

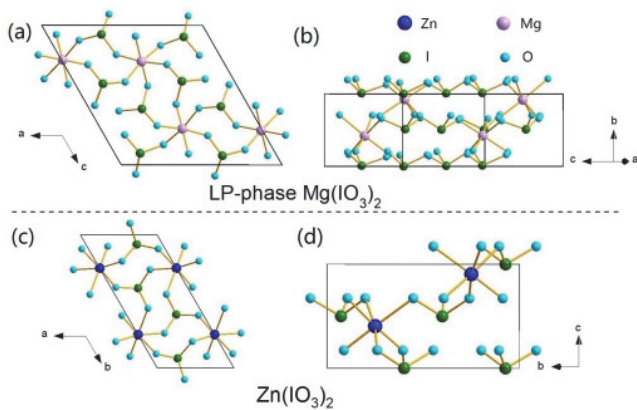


FIG. 1. The crystal structure of the low-pressure (LP) phase of $\text{Mg}(\text{IO}_3)_2$ projected (a) along the b axis and (b) along the ac plane, approximately along the a axis, to emphasize the layered structure. The crystal structure of the LP phase of $\text{Zn}(\text{IO}_3)_2$ projected (c) along the c axis and (d) along the a axis. Pink, dark blue, green, and light blue spheres represent Mg, Zn, I, and O atoms, respectively.

isostructural. Both compounds have related crystal structures, which facilitates comparison to find the factor which governs the band gap. (iii) Their bulk moduli are small, 22.2 GPa [17] and 21.6 GPa [16] for $\text{Mg}(\text{IO}_3)_2$ and $\text{Zn}(\text{IO}_3)_2$, respectively. Therefore, the application of pressures smaller than 20 GPa can cause significant changes in the crystal structure, resulting in observable changes in the band gap.

At ambient pressure, both $\text{Mg}(\text{IO}_3)_2$ and $\text{Zn}(\text{IO}_3)_2$ crystallize in monoclinic crystal structures (space group: $P2_1$). They are represented in Fig. 1. The main difference between the structures in Fig. 1 is the fact that the crystallographic a axis of $\text{Zn}(\text{IO}_3)_2$ doubles in length to become the same axis of $\text{Mg}(\text{IO}_3)_2$. In Figs. 1(a) and 1(c) it can be seen that Zn and Mg are each coordinated by six oxygen atoms forming an octahedron. Additionally, in both compounds, iodine is bonded to three oxygen atoms, forming a trigonal pyramid. The metal octahedra, MO_6 , and iodate units, $[\text{IO}_3]^-$, are connected to each other by corner-sharing oxygen atoms, and the metal octahedra are linked to each other by two $[\text{IO}_3]^-$ units. When viewed along the a axis, $\text{Mg}(\text{IO}_3)_2$ [Fig. 1(b)] and $\text{Zn}(\text{IO}_3)_2$ [Fig. 1(d)], can be described by structures formed by layered $[\text{IO}_3]^-$ units [the $\text{Mg}(\text{IO}_3)_2$ structure in Fig. 1(b) has been rotated slightly around the b axis to better show the layered structure]. Each of the $[\text{IO}_3]^-$ units has a lone electrons pair (LEP) from the iodine atom which points towards the opposite side of the base of the pyramid [8], i.e., towards the neighboring layer. This LEP orientation means that the interlayer distance is easily reduced under compression. Consequently, upon compression the distance between the iodine atoms and their second-nearest neighboring oxygen atoms is reduced, leading to a gradual increase in the coordination number of iodine and the suppression of the LEPs [16,17]. In order to accommodate the new I–O bonds, the length of the original in-layer iodine-oxygen bonds slightly increases under compression [16,17]. This behavior has been concluded as a common feature of the metal iodates under pressure [16–21], and it leads to the occurrence of subtle phase transitions, which do not exhibit volume discontinuities. As we

previously reported [17], $\text{Zn}(\text{IO}_3)_2$ remains monoclinic up to 27 GPa, but $\text{Mg}(\text{IO}_3)_2$ transforms from the monoclinic crystal structure (space group: $P2_1$, LP phase) to a trigonal structure (space group: $P3$, HP phase) in a pressure range from 7.5 to 9.7 GPa. The phase transition was characterized by the means of high-pressure synchrotron x-ray diffraction, Raman scattering, the infrared spectroscopy experiments, and first-principle calculations. The structures of both the LP and HP phases were obtained from the refinement of the polycrystalline x-ray diffraction data collected at ambient pressure and high pressures, respectively. As we show later in the present work, the band gaps of these metal iodates change continuously under compression even across the phase transitions.

In this paper we report a two-step investigation into the high-pressure behavior of the electronic band gap of non-transition and closed-shelled transition-metal iodates. In the first step, we determine the band-gap energies of $\text{Mg}(\text{IO}_3)_2$ and $\text{Zn}(\text{IO}_3)_2$ under compression up to 18 GPa via optical absorption experiments. The results are compared with results we obtained from first-principle calculations. An analysis of the change of iodine-oxygen bond distances has been used to explain the observed band-gap changes under compression. In the second step, we collate and compare the band-gap energies and corresponding average iodine-oxygen bond distances of the metal iodates reported in the literature. In the comparison, only nontransition and closed-shelled transition metals were included, without regard for their chemical formula, crystal structure, or stoichiometry. The validation of our conclusions provides a rational criterion for designing metal iodates with band-gap energies tailored for applications.

II. EXPERIMENT AND CALCULATION DETAILS

A. Sample synthesis

Zinc chloride (99.9%, CDH), potassium iodate (99%, Merck), and sodium meta silicate nanohydrate ($\text{Na}_2\text{SiO}_3 \cdot 9\text{H}_2\text{O}$, CDH) were used as the starting materials for synthesizing zinc iodate crystals. High-quality single crystals of zinc iodate were grown by single-diffusion gel technique at room temperature and hydrosilica gel was used as the medium of crystal growth. Gel of predetermined specific gravity 1.03–1.05 g/cc was prepared by dissolving the required amount of sodium meta silicate (SMS) in bidistilled water. The amount of potassium iodate corresponding to 0.5 M was dissolved in the SMS. The resulting gel was acidified with glacial acetic acid to obtain a pH in the range 4–7. The resulting solution was transferred into the sides of test tubes with internal diameter 2.5 cm and length 20 cm to avoid air bubbles in the gel medium and to keep the medium undisturbed for gelation. An aqueous solution of zinc chloride was poured slowly over the set gel to prevent gel breakage. The zinc ions slowly diffuse through the narrow pores of the hydrosilica gel and react with the iodate ions present in the gel leading to the formation of high-quality, white zinc iodate single crystals over a time period of 3 weeks.

The polycrystalline $\text{Mg}(\text{IO}_3)_2$ used in the present work is the same as used in our previous work [17]. While the synthesis method is summarized here, sample purity and crystal structure information can be found in Ref. [17].

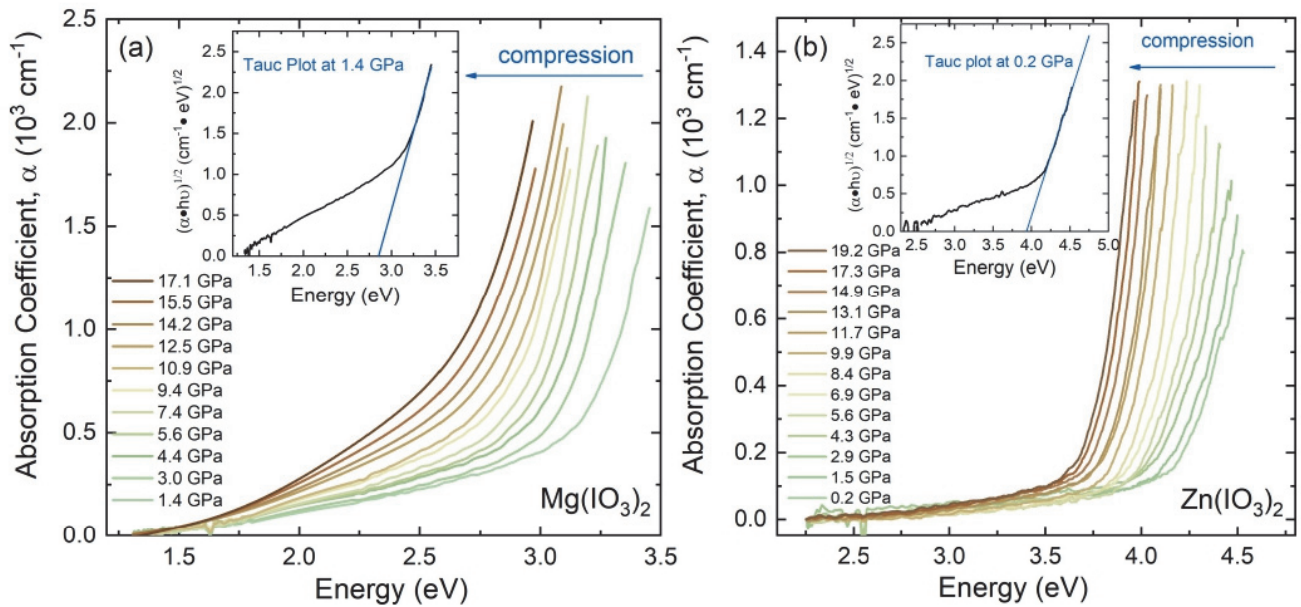


FIG. 2. Optical absorption spectra of (a) $\text{Mg}(\text{IO}_3)_2$ and (b) $\text{Zn}(\text{IO}_3)_2$ at selected pressures. The insets are the Tauc plots at the lowest pressure.

Polycrystalline $\text{Mg}(\text{IO}_3)_2$ was synthesized by adding potassium iodate (99.5% purity, Sigma-Aldrich) dissolved into concentrated nitric acid (2 mmol of KIO_3 in 10 mL of 7N nitric acid) to anhydrous magnesium chloride (98% purity, Sigma-Aldrich) dissolved in concentrated nitric acid (1 mmol in 10 mL of 7N nitric acid). The mixture was thoroughly stirred and then the solvents were left to slowly evaporate for a few days at 60 °C.

B. Optical absorption experiments under high pressure

Membrane-type diamond-anvil cells have been used to generate the high-pressure sample environment. The polycrystalline $\text{Mg}(\text{IO}_3)_2$ sample was first pressed into compact transparent 20- μm -thick platelets, and for the single crystal $\text{Zn}(\text{IO}_3)_2$, a piece of sample with a thickness around 20 μm was selected. In two separate experiments, the sample was loaded in 200- μm -diameter holes drilled in a stainless-steel gasket which has been precompressed to a thickness of 45 μm . A mixture of methanol, ethanol, and water in a ratio of 16:3:1 was used as the pressure transition medium (PTM) in the experiment of $\text{Zn}(\text{IO}_3)_2$. For $\text{Mg}(\text{IO}_3)_2$, the solid potassium bromide (KBr) was used as PTM in the high-pressure optical absorption experiment, as it can provide quasi-hydrostatic environment up to 11 GPa [22] and it is transparent in a wide range from 0.23 to 23 μm [23]. In all the experiments, the ruby fluorescence method was employed for pressure calibration [24]. [See the completeness of the loading for those two samples found in the inserted optical micrographs in Figs. 3(a) and 3(b).]

The sample-in and sample-out method was used to acquire the optical absorption spectra at each pressure, in which the intensity of the light transmitted through the sample $[I(\omega)]$ was normalized against the intensity of the light transmitted through the PTM $[I_0(\omega)]$. The experiment was conducted on a bespoke optical setup consisting of a tungsten lamp, fused

silica lenses, reflecting optics objectives, and a visible near-IR spectrometer (Ocean Optics Maya2000 Pro). More details can be found in earlier works [13,25].

C. Calculation details

Ab initio simulations were carried out within the framework of density-functional theory (DFT) [26], with the Vienna *Ab initio* Simulation Package (VASP) [27]. The projector augmented-wave and pseudopotentials were employed and the plane-wave kinetic cutoff was extended up to 540 eV to ensure highly converged results. The exchange-correlation energy was described within the generalized gradient approximation (GGA) with the Perdew-Burke-Ernzerhof (PBE) for solids prescription (PBEsol) [28]. The integrations over the Brillouin zone (BZ) were carried out with a dense k -point grid as described in Ref. [16] for $\text{Zn}(\text{IO}_3)_2$. For $\text{Mg}(\text{IO}_3)_2$, the integrations over the BZ were performed with a $6 \times 4 \times 6$ sampling of k -special points. At selected volumes, the structures we adopted for Mg and Zn iodates were fully relaxed to their optimized configuration through the calculation of the force and the stress tensor. Not only the calculated equilibrium lattice parameter at ambient condition, but also the pressure dependence of the lattice parameter and equation of state show good agreement with that obtained from experiment both for $\text{Mg}(\text{IO}_3)_2$ [17] and $\text{Zn}(\text{IO}_3)_2$ [16]. The electronic band-structure calculations were performed using the k path chosen with the SEEK-PATH tool [29], and the band-structure analysis was carried out with the SUMO package [30]. The crystal orbital overlap population (COOP) calculations were performed using the LOBSTER software [31].

III. RESULTS AND DISCUSSION

A. Band-gap energy under compression

Absorption spectra of $\text{Mg}(\text{IO}_3)_2$ and $\text{Zn}(\text{IO}_3)_2$ at selected pressures are shown in Figs. 2(a) and 2(b), respectively. Their

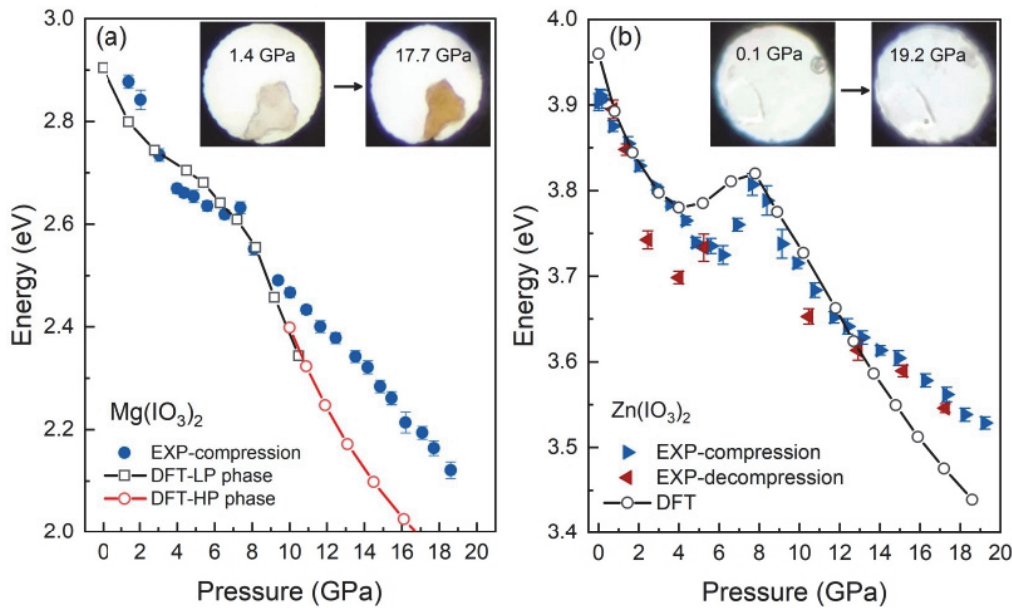


FIG. 3. Pressure dependence of the band-gap energy of (a) $\text{Mg}(\text{IO}_3)_2$ and (b) $\text{Zn}(\text{IO}_3)_2$. The experimental results (EXP) are shown with symbols only. The calculated results (DFT) are shown with solid lines and symbols. The insets include optical micrographs showing the sample loaded in the diamond-anvil cell at the indicated pressures. In (a) the theoretical calculated band gap of $\text{Mg}(\text{IO}_3)_2$ has been shifted by -0.5 eV. In (b) the theoretical calculated band gap of $\text{Zn}(\text{IO}_3)_2$ has been shifted by $+1.0$ eV.

absorption edges exhibit a gradual redshift with increasing pressure. According to the calculated electronic band structures (Supplemental Material, Fig. S1 [32]) $\text{Mg}(\text{IO}_3)_2$ and $\text{Zn}(\text{IO}_3)_2$ are indirect band-gap semiconductors. A Tauc plot analysis for indirect band-gap materials has been used here to obtain the band-gap energy at each pressure by extrapolating the linear fit of the high-energy part of the $(\alpha h\nu)^{1/2}$ vs $h\nu$ plot to zero [33], where α is the absorption coefficient, h is the Planck constant, and ν is the photon frequency. Examples of the Tauc fits are given in the insets of Figs. 2(a) and 2(b).

At ambient pressure the band gap of $\text{Zn}(\text{IO}_3)_2$ is 3.90(1) eV (2.96 eV) according to experiments (calculations). This value is higher than the previously reported [34] value of 3.53 eV (2.59 eV) according to experiments (DFT calculations). The difference in observed band-gap energy could be related to (i) different sample thicknesses used for optical absorption experiments [35]. For example, a 20- μm -thick sample was used in the present work, the sample thickness used in the previous study is unknown [34]. It is known that the use of very thick samples can lead to an underestimation of the band-gap energy due to misidentification of Urbach tails as fundamental band-gap absorptions. (ii) According to the calculated electronic band structure, from both this work and Ref. [34], $\text{Zn}(\text{IO}_3)_2$ has an indirect band gap. However, in Ref. [34], a Tauc plot for direct band-gap materials [25,33] was used.

For $\text{Mg}(\text{IO}_3)_2$, due to the polycrystalline sample used in our experiments, we could not measure its optical absorption spectra at ambient pressure. However, using the band gap of $\text{Mg}(\text{IO}_3)_2$ determined at low pressures [see Fig. 3(a)] it is possible to estimate the ambient-pressure band gap by adopting a linear fit to data obtained from 1.4 to 4.4 GPa. The estimated ambient-pressure band gap of $\text{Mg}(\text{IO}_3)_2$ is 3.00(5) eV. This value is slightly lower than the band-gap value of

3.4 eV obtained from calculations. The underestimation of the calculated band gap in $\text{Zn}(\text{IO}_3)_2$ and overestimation of the calculated band gap in $\text{Mg}(\text{IO}_3)_2$ deserves a comment. The discrepancy in $\text{Zn}(\text{IO}_3)_2$ is typical of DFT calculations and it is related to the GGA-PBESol approximations used to describe the exchange and correlation energies [36,37]. The underestimation of the band-gap energy is more notorious when transition metals (like Zn) are present in the compound and is mostly explained in the literature in terms of the effects of self-interaction and particularly of the derivative discontinuity of the exchange-correlation energy [38]. However, there are indeed more than a few examples where the band gap is overestimated by DFT [39,40]. $\text{Mg}(\text{IO}_3)_2$ seems to be within these cases. The reasons for band-gap overestimations are still under debate [41] and they are beyond the scope of this work. It should be noted here that in spite of the discrepancies regarding the absolute value of the band gap at zero pressure, calculations closely reproduce the experimental pressure dependence of the band gap of materials including cobalt iodates [42]. This is also the case of $\text{Zn}(\text{IO}_3)_2$ and $\text{Mg}(\text{IO}_3)_2$ as we show in the next section.

The experimental and calculated band-gap energies of $\text{Mg}(\text{IO}_3)_2$ and $\text{Zn}(\text{IO}_3)_2$ are shown in Figs. 3(a) and 3(b) as functions of pressure. For a better comparison of the experimental and calculated band-gap energy, we have downshifted the calculated band gap of $\text{Mg}(\text{IO}_3)_2$ by 0.5 eV and upshifted the calculated band gap of $\text{Zn}(\text{IO}_3)_2$ by 1.0 eV. The band gaps of both compounds decrease under compression and exhibit a nonlinear pressure dependence. For $\text{Mg}(\text{IO}_3)_2$, there are slope changes around 3 and 8 GPa. We also noticed that the band gap does not show a discontinuity at the structural phase transition pressure 9 GPa. This fact is consistent with the gradual changes associated with the transition. Under pressure, the band-gap energy exhibits a reduction of 29.3%, from 3.00 eV

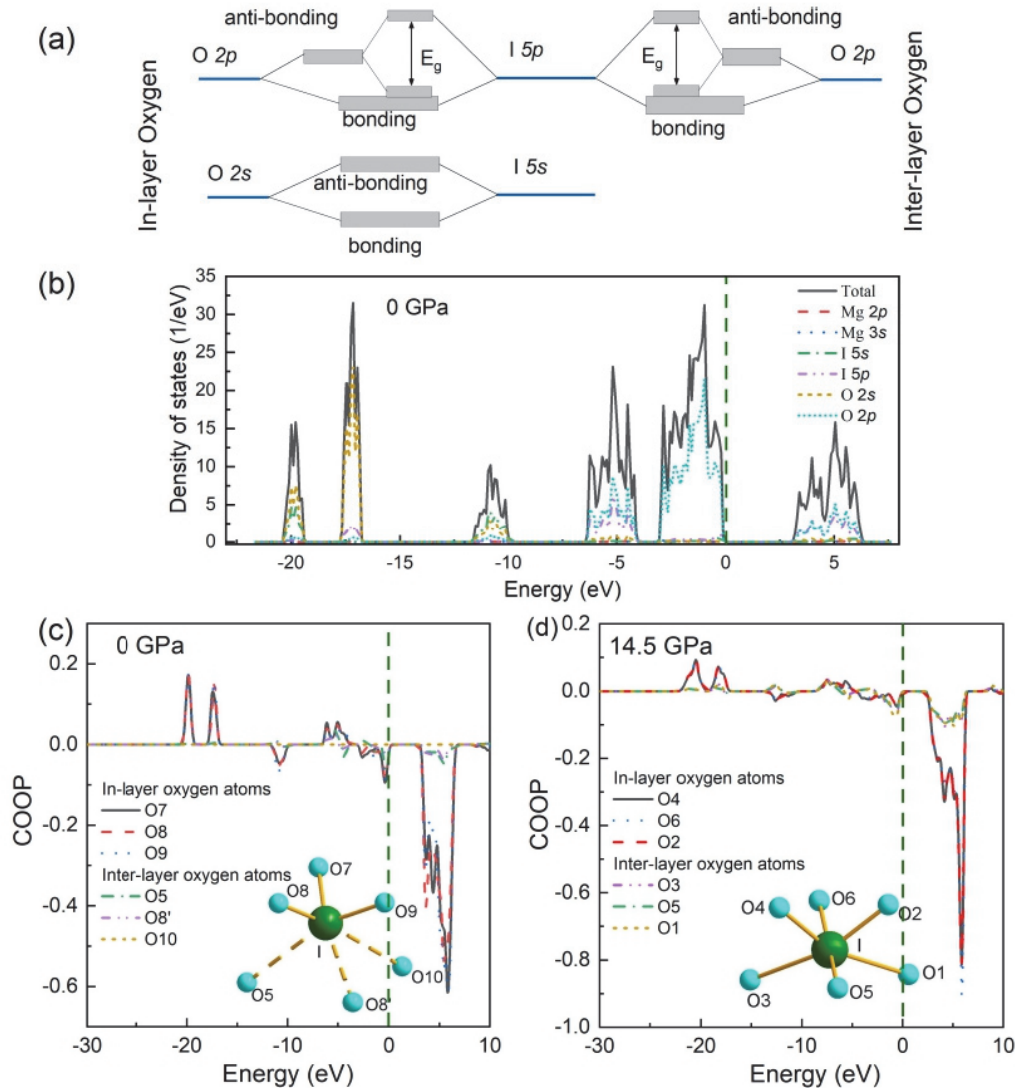


FIG. 4. (a) Molecular orbital diagrams for $\text{Mg}(\text{IO}_3)_2$ and $\text{Zn}(\text{IO}_3)_2$ at ambient pressure; here, E_g represents band-gap energy. (b) Calculated DOS and PDOS for $\text{Mg}(\text{IO}_3)_2$. (c) Calculated COOP for $\text{Mg}(\text{IO}_3)_2$ at 0 GPa and (d) at 14.5 GPa. The vertical dashed line shows the Fermi level.

at ambient pressure, to 2.12 eV at 18.6 GPa. As shown in the inset in Fig. 3(a), the color of the $\text{Mg}(\text{IO}_3)_2$ crystal changed from transparent, with a slightly orange tone, to completely orange. Regarding $\text{Zn}(\text{IO}_3)_2$, the band-gap behavior is similar, showing a decrease in energy from 3.90 eV at ambient pressure to 3.74 eV at 5.6 GPa according to experiments. In our calculations, the band-gap energy decreases from 2.96 eV at 0 GPa to 2.78 eV at 4 GPa. Upon further compression, band-gap narrowing is followed by a slight broadening of the band gap up to 7.7 GPa. Beyond 7.7 GPa, the band gap shows a continuous narrowing up to the highest pressure covered in this study. The total reduction of the band gap is 9.5% in the experiment. In $\text{Zn}(\text{IO}_3)_2$ we did not detect any observable color change in the experiments.

B. Molecular orbital diagram

Due to the fact that both $\text{Mg}(\text{IO}_3)_2$ and $\text{Zn}(\text{IO}_3)_2$ show qualitatively similar high-pressure behavior of the band-gap

energy, we shall use $\text{Mg}(\text{IO}_3)_2$ as the example in point to discuss the pressure evolution of the band-gap energy in both materials. The calculated density of states (DOS) and projected density of states (PDOS) are provided in Fig. 4(b). The VBM is dominated by O-2p orbitals and the CBM by contributions from O-2p and I-5p orbitals. In this regard, the PDOS is qualitatively similar to those reported for other nontransition-metal iodates [15]. The common feature of dominant contributions from O-2p and I-5p orbitals indicates that the band-gap energy in metal iodates is strongly affected by the I-O interaction. In Figs. 4(c) and 4(d), we show the calculated COOP of $\text{Mg}(\text{IO}_3)_2$ between iodine and the six nearest oxygen atoms at 0 and 14.5 GPa, respectively. Notably, there are two types of I-O interaction. The first type of I-O interaction is the bonding between iodine and the in-layer oxygen atoms; O8, O7, and O9 in Fig. 4(c). (For clarity, we follow the same labeling convention as provided in the crystallographic information file (CIF) provided by Phanon *et al.* [43]). These I-O bonds are relatively short, typically

from 1.75 to 1.86 Å. The second type of I-O interaction is between iodine and the oxygen atoms in the neighboring $[\text{IO}_3]^-$ layer. These interlayer oxygen atoms are O5, O8', and O10 in Fig. 4(c). These types of bonding are weak or do not exist at low pressure. The distance between the iodine and the interlayer oxygen atoms is from 2.6 to 3.1 Å.

The combination of the PDOS and COOP enables us to determine the molecular orbital (MO) diagram of $\text{Mg}(\text{IO}_3)_2$ [Fig. 4(a)]. In the -20 to -17 eV energy region, the DOS and PDOS of $\text{Mg}(\text{IO}_3)_2$ [Fig. 4(b)] are dominated by I-5s and O-2s states. Both of them are positive in COOP [Fig. 4(c)] for the in-layer oxygen atoms, and both are almost zero for the interlayer oxygen. The energy region around -10 eV in PDOS is contributed to mainly by I-5s and O-2s states. The contribution to the COOP is negative for in-layer oxygen atoms and zero for interlayer oxygen atoms. These two energy regions correspond to the bonding and antibonding states between I-5s and O-2s [as illustrated in the bottom left part of Fig. 4(a)]. There are also two broad bands located between -7 eV and the top of the valence band. The lower-energy band is dominated by O-2p and I-5p orbitals and the corresponding contribution to the COOP is positive, which means these orbitals belong to the bonding state of the p - p interaction between iodine and oxygen [see the left-hand part of Fig. 4(a)]. The antibonding state of these p orbitals is at the bottom of the conduction band, which is primarily contributed to by the O-2p and I-5p states and shows a negative COOP. Based on this description, and the fact that the top of the valence band is also dominated by nonbonding O-2p states, we construct the MO diagram (for the -8 to 6 eV energy region) provided in Fig. 4(a). In this energy range, the COOP indicates only a minor interaction but the same characteristics between iodine and the interlayer oxygen atoms. Therefore, we suggest the same MO diagram for the p - p interaction between iodine and the interlayer oxygen atoms [the top right part in Fig. 4(a)]. The band-gap energy is given by the energy between the oxygen nonbonding state and the p - p antibonding state between iodine and oxygen. At high pressures, taking 14.5 GPa as an arbitrary example above the phase transition pressure (9 GPa [17]), the interaction between iodine and interlayer oxygen atoms is enhanced at the conduction band and the upper part of the valence band due to the compression of the interlayer distance. The COOPs at 0 and at 14.5 GPa share very similar characteristics [Figs. 4(c) and 4(d)] and can be used to determine essentially similar MO diagrams. Only minor differences are observed: for example, at 14.5 GPa the iodine and the interlayer oxygen atoms have small amount of contribution to the lower-energy region; however, the overall characterization is the same.

In Fig. 5 we have plotted the calculated pressure dependence of the bond distances between iodine and in-layer/interlayer oxygen atoms [17]. These I-O distances are taken from our DFT calculations, which show good agreement with our experimental results regarding crystallographic lattice parameters (determined from powder x-ray diffraction) and their pressure evolution (via the P/V equation of state). The distance between iodine and interlayer oxygen atoms (O5, O8', and O10 in the LP phase) shortens under compression. In contrast, the bond distance between iodine and the in-layer oxygen atoms (O7, O8, and O9) slightly

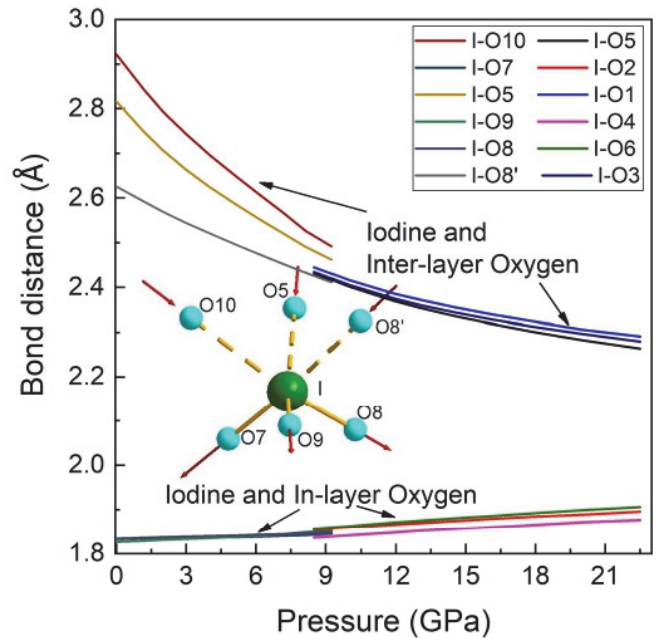


FIG. 5. Calculated pressure dependence of the bond distance between iodine and the in-layer/interlayer oxygen atoms in $\text{Mg}(\text{IO}_3)_2$. The slight discontinuity at around 9 GPa is due to a phase transition.

enlarges under compression. Due to the stereoactive LEP on iodine, and the shortening of the distance between iodine and interlayer oxygen atoms, new I-O bonds form between them on compression. Consequently, the in-layer oxygen atoms are pushed away from iodine. This is a typical behavior observed in metal iodates under compression [16–18,21] as discussed in the Introduction. Therefore, there are two competing effects which determine the pressure evolution of the band-gap energy of $\text{Mg}(\text{IO}_3)_2$. The first effect (effect 1) is the enlargement of the I-O bond distance between iodine and in-layer oxygen atoms which results in a decrease of the hybridization between their orbitals, thereby decreasing the energy difference between their bonding and antibonding states. As a consequence, the band-gap energy will tend to decrease with increasing pressure. The second effect (effect 2) is the shortening of the distance between iodine and the interlayer oxygen atoms which increases the hybridization between their states and increase the separation between bonding and antibonding states, thereby favoring an increase in the band-gap energy.

In the case of $\text{Mg}(\text{IO}_3)_2$, below 4 GPa the interaction between iodine and the interlayer oxygen atoms is weak due to the large interlayer distance. Therefore, the interaction between iodine and the closer in-layer oxygen atoms dominates the band gap. Since the in-layer I-O distances increase with increasing pressure, the band-gap energy consequently decreases with increasing pressure. In other words, effect 1 is dominant below 4 GPa. From 4 to 8 GPa the distance between iodine and the interlayer oxygen atoms quickly gets shorter, thereby enhancing their mutual interaction and counteracting the narrowing of the band gap. In other words, there is competition between effects 1 and 2 between 4 and 8 GPa, but effect 2 dominates because the interlayer I-O bond distance is more sensitive to pressure. Above 8 GPa, the shortening

of the interlayer I-O bond distance becomes less sensitive to pressure (see Fig. 5). Therefore, the increasing in-layer I-O distance (effect 1) once again dominates the pressure dependence of the band-gap energy, which continues to decrease above 8 GPa up to the maximum pressure studied in the present work. The high-pressure band-gap behavior of $\text{Zn}(\text{IO}_3)_2$ can also be explained following the same rationale and by the same MO diagram. (The $\text{Zn}(\text{IO}_3)_2$ DOS, PDOS, and pressure dependence of the distance between iodine and in-layer/interlayer oxygen atoms can be found in Figs. S2 and S3 in the Supplemental Material [32], respectively.) Notice that both compounds exhibit a qualitatively similar pressure dependence for the band-gap energy. The differences in the pressure dependence of the band-gap energy (see Fig. 3) are a consequence of the difference in the pressure evolution of both crystal structures (which are similar but not identical) under compression, as we have shown in our previous works [16,17]. Our conclusions indicate that wide band-gap metal iodates can be designed based on crystal structures which contain iodate molecules with short iodine-oxygen bond distances.

It is worth mentioning here that the MO model we suggested can only qualitatively explain the band-gap behavior of nontransition or closed-shell transition-metal iodates. Indeed, the band-gap energies for different metal iodates exhibit different sensitivities to the I-O bond distance, although the trend is the same, i.e., the band-gap energy decreases as the average I-O distance increases. According to the theoretical calculated band-gap energy and I-O bond distance for Zn and Mg iodates at the pressure range from 0 to 18 GPa, the band-gap energy decreases with the I-O bond distance by 8 and 31 eV/Å, respectively, thereby exhibiting different pressure dependences which are not explained by our model. The corresponding value for all the data shown in Fig. 6, where we summarized the band-gap energy and average I-O bond distance for 71 different metal iodates at ambient condition, is -42 eV/Å.

C. Metal iodate band gaps at ambient pressure

It is worth examining the relationship between the iodine-oxygen bond distances and the band-gap energies we found in Mg and Zn iodates by making comparison with other metal iodates. In Fig. 6 we have plotted the band-gap energy vs the average I-O bond distance of the metal iodates measured in this work and reported in the literature [1–3,10–12,16,43–82] (see Figs. S4 and S5 in the Supplemental Material [32]). In the comparison, only nontransition and closed-shelled transition metal iodates were included, without regard for their chemical formula, crystal structure, or stoichiometry. Partial-filled transition-metal iodates were not included because in those iodates the $3d$ electrons also contribute to the electronic states near the Fermi level [15]. The average I-O bond was calculated by considering bond distances shorter than the cutoff value of 2.0 Å. The choice of the cutoff value is based on the fact that the interaction between iodine and oxygen is weak when the oxygen is further than 2.0 Å away from iodine (see Fig. 5). The band-gap energy of the metal iodates ranges from 2.34 eV in $\text{K}_8\text{Ce}_2\text{I}_{18}\text{O}_{53}$ [44] to 5.08 eV in $\text{Rb}_3(\text{IO}_3)_3(\text{I}_2\text{O}_5)(\text{HIO}_3)_4(\text{H}_2\text{O})$ [45], and the average I-O bonds varies from 1.79 to 1.84 Å. In Fig. 6 it can be seen that there is a negative correlation between the average

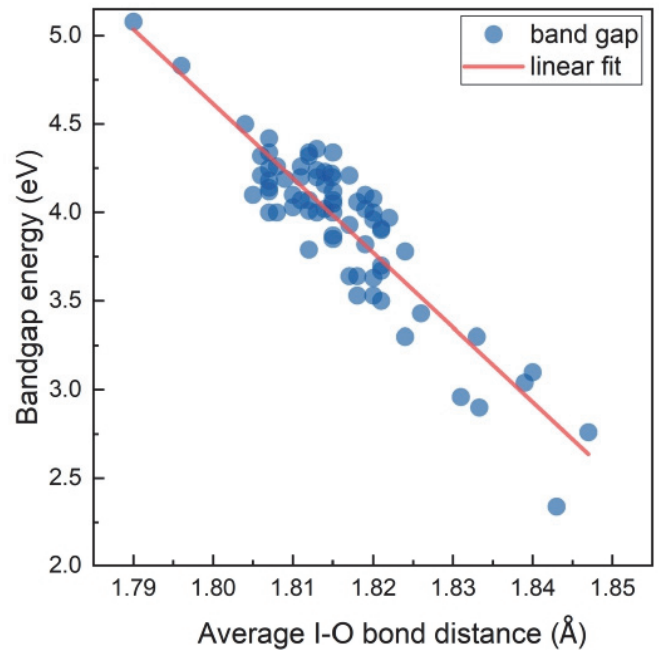


FIG. 6. Collated band-gap energy and average I-O bond distances as found in the literature. The detailed information for each point, including chemical formula, average I-O bond distance, and band-gap energy for the compounds, can be found in Fig. S5 and Table S1 in Supplemental Material [32].

iodine-oxygen bond distance and the band-gap energy of metal iodates. This is a reasonable result because the electronic structure of the metal iodates has a common characteristic near the Fermi level. That is, the VBM is dominated by the O- $2p$ orbital, while the CBM is contributed to by the O- $2p$ and I- $5p$ orbitals, which indicates that the band-gap energy is dominated by the interaction between the iodine and oxygen atoms, and that the metal species is not the dominant factor. According to the MO diagram we suggested for Mg and Zn iodates in the previous part, their band-gap energies decrease with increasing bond distance between iodine and the in-layer oxygen atoms. Therefore, the band gap of nontransition or closed-shelled metal iodates have a negative correlation with the bond distance, regardless of crystal structure, metal species, or chemical formula.

IV. CONCLUSIONS

The main conclusion from the first half of the present work is that the band-gap energy of the studied iodates [nontransition (Mg) and closed-shell transition-metal (Zn) iodates: $\text{Mg}(\text{IO}_3)_2$ and $\text{Zn}(\text{IO}_3)_2$] is strongly related to the distance between the iodine and in-layer/interlayer oxygen atoms. Through the analysis of the experimental band-gap energy as a function of pressure, combined with the help of calculated density of states, projected density of states, and calculated crystal orbital overlap populations between the iodine and oxygen atoms, we conclude that there are two competing effects regarding the I-O bond distances. Firstly, the pressure-induced enlargement of the bond distance between iodine and in-layer oxygen atoms reduces their mutual interaction

and thereby causes a narrowing of the band gap. Secondly, hybridization between iodine and interlayer oxygen atoms causes opening of the band gap. The competition between these two effects causes the nonlinear reduction of the band-gap energy with increasing pressure.

The main conclusion from the second half of the present work, in which we examine the band-gap energies and average I-O bond distances of 71 different nontransition or closed-shelled transition-metal iodates reported in the literature, is that we find the band-gap energy in iodate materials to have a negative correlation with the average I-O bond distance regardless of chemical formula, crystal structure, metal species, or iodine coordination number. This observation is consistent with the model proposed in the first half of the present work to explain the high-pressure behavior of the band-gap energy of Mg and Zn iodates. Combining our previous work [15] on the high-pressure band-gap studies on transition-metal iodates, $\text{Fe}(\text{IO}_3)_3$, we thereby find two useful rules for designing wide band-gap metal iodates: (i) do not use partially filled

transition-metal iodates because their $3d$ electrons contribute to the electronic states near the Fermi level [15], and, (ii) the shorter the bond distance between iodine and nearest oxygen, the wider the band gap of the metal iodate.

ACKNOWLEDGMENTS

This work was supported by the Generalitat Valenciana under Grant No. PROMETEO 2018/123-EFIMAT and by the Spanish Ministerio de Ciencia e Innovación and Agencia Estatal de Investigación (Grant No. MCIN/AEI/10.13039/501100011033) and the European Union under Grants No. PID2019-106383GB-41/43 and No. RED2018-102612-T (MALTA Consolider Team). A.L. and D.E. thank the Generalitat Valenciana for the Ph.D. Fellowship No. GRISOLIAP/2019/025. R.T. acknowledges funding from the Spanish MINECO via Juan de la Cierva Formación program (Grant No. FJC2018-036185-I).

- [1] H. Fan, G. Peng, C. Lin, K. Chen, S. Yang, and N. Ye, $\text{Ba}(\text{IO}_3)\text{F}$: An alkaline-earth-metal iodate fluoride crystal with large band gap and birefringence, *Inorg. Chem.* **59**, 7376 (2020).
- [2] H. Jo, H. G. Kim, H. R. Byun, J. I. Jang, and K. M. Ok, Synthesis, structure, and third-harmonic generation measurements of a mixed alkali metal iodate, $\text{KLi}_2(\text{IO}_3)_3$, *J. Solid State Chem.* **282**, 121120 (2020).
- [3] F. F. Mao, C. L. Hu, J. Chen, B. L. Wu, and J. G. Mao, $\text{HBA}_{2.5}(\text{IO}_3)_6(\text{I}_2\text{O}_5)$ and $\text{HBA}(\text{IO}_3)(\text{I}_4\text{O}_{11})$: Explorations of second-order nonlinear optical materials in the alkali-earth polyiodate system, *Inorg. Chem.* **58**, 3982 (2019).
- [4] H. Liu, X. Jiang, X. Wang, L. Yang, Z. Lin, Z. Hu, X. Meng, X. Chen, and J. Qin, Influence of A-site cations on germanium iodates as mid-IR nonlinear optical materials: $\text{A}_2\text{Ge}(\text{IO}_3)_6$ ($\text{A} = \text{Li}, \text{K}, \text{Rb}$ and Cs) and $\text{BaGe}(\text{IO}_3)_6 \cdot \text{H}_2\text{O}$, *J. Mater. Chem. C* **6**, 4698 (2018).
- [5] X. Xu, C. Hu, B. Li, B. Yang, and J. Mao, α - AgI_3O_8 and β - AgI_3O_8 with large SHG Responses: Polymerization of IO_3 groups into the I_3O_8 polyiodate anion, *Chem. Mater.* **26**, 3219 (2014).
- [6] L. Xiao, Z. Cao, J. Yao, Z. Lin, and Z. Hu, A new cerium iodate infrared nonlinear optical material with a large second-harmonic generation response, *J. Mater. Chem. C* **5**, 2130 (2017).
- [7] J. Yeon, S. H. Kim, and P. S. Halasyamani, New thallium iodates-synthesis, characterization, and calculations of $\text{Tl}(\text{IO}_3)_3$ and $\text{Tl}_4(\text{IO}_3)_6$, $[\text{Tl}^+{}_3\text{Tl}^{3+}(\text{IO}_3)_6]$, *J. Solid State Chem.* **182**, 3269 (2009).
- [8] H. Y. Chang, S. H. Kim, M. O. Kang, and P. S. Halasyamani, Polar or nonpolar? A^+ cation polarity control in $\text{A}_2\text{Ti}(\text{IO}_3)_6$ ($\text{A} = \text{Li}, \text{Na}, \text{K}, \text{Rb}, \text{Cs}, \text{Tl}$), *J. Am. Chem. Soc.* **131**, 6865 (2009).
- [9] T. Abudouwufu, M. Zhang, S. Cheng, H. Zeng, Z. Yang, and S. Pan, $\text{K}_2\text{Na}(\text{IO}_3)_2(\text{I}_3\text{O}_8)$ with strong second harmonic generation response activated by two types of isolated iodate anions, *Chem. Mater.* **32**, 3608 (2020).
- [10] F. F. Mao, C. L. Hu, J. Chen, and J. G. Mao, A series of mixed-metal germanium iodates as second-order nonlinear optical materials, *Chem. Mater.* **30**, 2443 (2018).
- [11] Q. Wu, H. Liu, F. Jiang, L. Kang, L. Yang, Z. Lin, Z. Hu, X. Chen, X. Meng, and J. Qin, RbIO_3 and RbIO_2F_2 : Two promising nonlinear optical materials in mid-IR region and influence of partially replacing oxygen with fluorine for improving laser damage threshold, *Chem. Mater.* **28**, 1413 (2016).
- [12] Q. M. Huang, C. L. Hu, B. P. Yang, Z. Fang, Y. Lin, J. Chen, B. X. Li, and J. G. Mao, $[\text{GaF}(\text{H}_2\text{O})][\text{IO}_3\text{F}]$: A promising NLO material obtained by anisotropic polycation substitution, *Chem. Sci.* **12**, 9333 (2021).
- [13] D. Errandonea, C. Popescu, A. B. Garg, P. Botella, D. Martínez-García, J. Pellicer-Porres, P. Rodríguez-Hernández, A. Muñoz, V. Cuenca-Gotor, and J. A. Sans, Pressure-induced phase transition and band-gap collapse in the wide-band-gap semiconductor InTaO_4 , *Phys. Rev. B* **93**, 035204 (2016).
- [14] E. Bandiello, D. Errandonea, D. Martínez-García, D. Santamaria-Perez, and F. J. Manjón, Effects of high-pressure on the structural, vibrational, and electronic properties of Monazite-type PbCrO_4 , *Phys. Rev. B* **85**, 024108 (2012).
- [15] A. Liang, P. Rodríguez-Hernandez, A. Muñoz, S. Raman, A. Segura, and D. Errandonea, Pressure-dependent modifications in the optical and electronic properties of $\text{Fe}(\text{IO}_3)_3$: The Role of Fe 3d and I 5p lone-pair electrons, *Inorg. Chem. Front.* **8**, 4780 (2021).
- [16] A. Liang, C. Popescu, F. J. Manjón, A. Muñoz, Z. Hebboul, and D. Errandonea, Structural and vibrational study of $\text{Zn}(\text{IO}_3)_2$ Combining high-pressure experiments and density-functional theory, *Phys. Rev. B* **103**, 054102 (2021).
- [17] A. Liang, R. Turnbull, C. Popescu, F. J. Manjón, E. Bandiello, A. Muñoz, I. Yousef, Z. Hebboul, and D. Errandonea, Pressure-induced phase transition and increase of oxygen-iodine coordination in magnesium iodate, *Phys. Rev. B* **105**, 054105 (2022).
- [18] A. Liang, C. Popescu, F. J. Manjón, R. Turnbull, E. Bandiello, P. Rodríguez-Hernandez, A. Muñoz, I. Yousef, Z. Hebboul, and

- D. Errandonea, Pressure-driven symmetry-preserving phase transitions in $\text{Co}(\text{IO}_3)_2$, *J. Phys. Chem. C* **125**, 17448 (2021).
- [19] D. Jiang, H. Song, T. Wen, Z. Jiang, C. Li, K. Liu, W. Yang, H. Huang, and Y. Wang, Pressure-driven two-step second-harmonic-generation switching in BiOIO_3 , *Angew. Chem. Int. Ed.* **61**, e202116656 (2022).
- [20] H. Song, D. Jiang, N. Wang, W. Xing, R. Guo, Z. Lin, J. Yao, Y. Wang, H. Tu, and G. Zhang, $\text{Na}_3\text{Bi}(\text{IO}_3)_6$: An alkali-metal bismuth iodate with intriguing one-dimensional $[\text{BiI}_6\text{O}_{18}]$ chains and pressure-induced structural transition, *Inorg. Chem.* **60**, 2893 (2021).
- [21] A. Liang, S. Rahman, H. Saqib, P. Rodriguez-Hernandez, A. Munoz, G. Nenert, I. Yousef, C. Popescu, and D. Errandonea, First-order isostructural phase transition induced by high pressure in $\text{Fe}(\text{IO}_3)_3$, *J. Phys. Chem. C* **124**, 8669 (2020).
- [22] A. Celeste, F. Borondics, and F. Capitani, Hydrostaticity of pressure-transmitting media for high pressure infrared spectroscopy, *High Press. Res.* **39**, 608 (2019).
- [23] E. D. Palik, *Handbook of Optical Constants of Solid* (Academic Press, Maryland, 1997).
- [24] H. K. Mao, J. Xu, and P. M. Bell, Calibration of the ruby pressure gauge to 800 Kbar under quasi-hydrostatic conditions, *J. Geophys. Res.* **91**, 4673 (1986).
- [25] O. Gomis, R. Vilaplana, F. J. Manjón, J. Ruiz-Fuertes, E. Pérez-González, J. López-Solano, E. Bandiello, D. Errandonea, A. Segura, P. Rodríguez-Hernández, A. Muñoz, V. V. Ursaki, and I. M. Tiginyanu, HgGa_2Se_4 under high pressure: An optical absorption study, *Phys. Status Solidi Basic Res.* **252**, 2043 (2015).
- [26] P. Hohenberg and W. Kohn, Inhomogeneous electron gas, *Phys. Rev.* **136**, B864 (1964).
- [27] G. Kresse and J. Furthmüller, Efficient iterative schemes for ab initio total-energy calculations using a plane-wave basis set, *Phys. Rev. B* **54**, 11169 (1996).
- [28] J. P. Perdew, A. Ruzsinszky, G. I. Csonka, O. A. Vydrov, G. E. Scuseria, L. A. Constantin, X. Zhou, and K. Burke, Restoring the Density-Gradient Expansion for Exchange in Solids and Surfaces, *Phys. Rev. Lett.* **100**, 136406 (2008).
- [29] Y. Hinuma, G. Pizzi, Y. Kumagai, F. Oba, and I. Tanaka, Band structure diagram paths based on crystallography, *Comput. Mater. Sci.* **128**, 140 (2017).
- [30] A. M. Ganose, A. J. Jackson, and D. O. Scanlon, Sumo: Command-line tools for plotting and analysis of periodic ab initio calculations, *J. Open Source Softw.* **3**, 717 (2018).
- [31] S. Maintz, V. L. Deringer, A. L. Tchougréeff, and R. Dronskowski, LOBSTER: A tool to extract chemical bonding from plane-wave based DFT, *J. Comput. Chem.* **37**, 1030 (2016).
- [32] See Supplemental Material at <http://link.aps.org/supplemental/10.1103/PhysRevMaterials.6.044603> for additional information on calculated electronic structure and literature search for the band gap of metal iodates analysis (n.d.).
- [33] J. Tauc, Optical properties and electronic structure of amorphous Ge and Si, *Mater. Res. Bull.* **3**, 37 (1968).
- [34] A. Benghia, Z. Hebboul, R. Chikhaoui, I. khaldoun Lefkaier, A. Chouireb, and S. Goumri-Said, Effect of iodic acid concentration in preparation of zinc iodate: Experimental characterization of $\text{Zn}(\text{IO}_3)_2$, and its physical properties from density functional theory, *Vacuum* **181**, 109660 (2020).
- [35] J. P. Enríquez and X. Mathew, Influence of the thickness on structural, optical and electrical properties of chemical bath deposited CdS thin films, *Sol. Energy Mater. Sol. Cells* **76**, 313 (2003).
- [36] M. K. Y. Chan and G. Ceder, Efficient Band Gap Prediction for Solids, *Phys. Rev. Lett.* **105**, 196403 (2010).
- [37] A. Liang, L. T. Shi, S. Gallego-parra, O. Gomis, D. Errandonea, and I. M. Tiginyanu, Pressure-induced band anticrossing in two adamantane ordered-vacancy compounds: CdGa_2S_4 and HgGa_2S_4 , *J. Alloys Compd.* **886**, 161226 (2021).
- [38] J. P. Perdew, W. Yang, K. Burke, Z. Yang, E. K. U. Gross, M. Scheffler, G. E. Scuseria, T. M. Henderson, I. Y. Zhang, A. Ruzsinszky, H. Peng, J. Sun, E. Trushin, and A. Görling, Understanding band gaps of solids in generalized Kohn-Sham theory, *Proc. Natl. Acad. Sci.* **114**, 2801 (2017).
- [39] J. M. Crowley, J. Tahir-Kheli, and W. A. Goddard, Resolution of the band gap prediction problem for materials design, *J. Phys. Chem. Lett.* **7**, 1198 (2016).
- [40] P. Botella, D. Errandonea, A. B. Garg, P. Rodriguez-Hernandez, A. Muñoz, S. N. Achary, and A. Vomiero, High-pressure characterization of the optical and electronic properties of InVO_4 , InNbO_4 , and InTaO_4 , *SN Appl. Sci.* **1**, 389 (2019).
- [41] P. Borlido, J. Schmidt, A. W. Huran, F. Tran, M. A. L. Marques, and S. Botti, Exchange-correlation functionals for band gaps of solids: Benchmark, reparametrization and machine learning, *Npj Comput. Mater.* **6**, 96 (2020).
- [42] A. Liang, F. Rodríguez, A. Muñoz, P. Rodríguez-Hernandez, R. Turnbull, and D. Errandonea, High-pressure tuning of d-d crystal-field electronic transitions and electronic band gap in $\text{Co}(\text{IO}_3)_2$, *Phys. Rev. B* **105**, 115204 (2022).
- [43] D. Phanon, B. Bentría, E. Jeanneau, D. Benbortal, A. Mosset, and I. Gautier-Luneau, Crystal structure of $\text{M}(\text{IO}_3)_2$ metal iodates, twinned by pseudo-merohedry, with M^{II} : Mg^{II} , Mn^{II} , Co^{II} , Ni^{II} , and Zn^{II} , *Z. Kristallogr.* **221**, 635 (2006).
- [44] R. Wu, X. Jiang, M. Xia, L. Liu, X. Wang, Z. Lin, and C. Chen, $\text{K}_8\text{Ce}_2\text{I}_{18}\text{O}_{53}$: A novel potassium cerium(IV) iodate with enhanced visible light driven photocatalytic activity resulting from polar zero dimensional $[\text{Ce}(\text{IO}_3)_8]^{4-}$ units, *Dalton Trans.* **46**, 4170 (2017).
- [45] X. Xu, B. Yang, C. Huang, and J. Mao, Explorations of new second-order nonlinear optical materials in the ternary rubidium iodate system: Noncentrosymmetric $\beta\text{-RbIO}_3(\text{HIO}_3)_2$ and centrosymmetric $\text{Rb}_3(\text{IO}_3)_3(\text{I}_2\text{O}_5)(\text{HIO}_3)_4(\text{H}_2\text{O})$, *Inorg. Chem.* **53**, 1756 (2014).
- [46] J. K. Liang and C. G. Wang, The structure of $\text{Zn}(\text{IO}_3)_2$ crystal, *Acta Chim. Sin.* **40**, 985 (1982).
- [47] V. Petříček, K. Malý, B. Kratochvíl, J. Podlahová, and J. Loub, Barium Diiodate, *Acta Crystallogr., Sect. B: Struct. Crystallogr. Cryst. Chem.* **B36**, 2130 (1980).
- [48] S. Ghose, C. Wan, and O. Wittke, The crystal structure of synthetic lautarite, $\text{Ca}(\text{IO}_3)_2$, *Acta Crystallogr., Sect. B* **B34**, 84 (1978).
- [49] M. Zhang, C. Hu, T. Abudouwufu, Z. Yang, and S. Pan, Functional materials design via structural regulation originated from ions introduction: A study case in cesium iodate system, *Chem. Mater.* **30**, 1136 (2018).
- [50] Y. J. Jia, Y. G. Chen, Y. Guo, X. F. Guan, C. Li, B. Li, M. M. Liu, and X. M. Zhang, $\text{LiM}^{\text{II}}(\text{IO}_3)_3$ ($\text{M}^{\text{II}} = \text{Zn}$ and Cd): Two promising nonlinear optical crystals derived from a tunable structure model of $\alpha\text{-LiIO}_3$, *Angew. Chemie - Int. Ed.* **58**, 17194 (2019).

- [51] M. Luo, F. Liang, X. Hao, D. Lin, B. Li, Z. Lin, and N. Ye, Rational design of the nonlinear optical response in a tin iodate fluoride $\text{Sn}(\text{IO}_3)_2\text{F}_2$, *Chem. Mater.* **32**, 2615 (2020).
- [52] D. Phanon and I. Gautier-Luneau, Promising material for infrared nonlinear optics: NaI_3O_8 Salt containing an octaoxotriiodate(V) anion formed from condensation of $[\text{IO}_3]^-$ ions, *Angew. Chemie - Int. Ed.* **46**, 8488 (2007).
- [53] Y. Huang, X. Meng, P. Gong, L. Yang, Z. Lin, X. Chen, and J. Qin, $\text{A}_2\text{BiI}_5\text{O}$ ($\text{A} = \text{K}^+$ or Rb^+): Two new promising nonlinear optical materials containing $[\text{I}_3\text{O}_9]^{3-}$ bridging anionic groups, *J. Mater. Chem. C* **2**, 4057 (2014).
- [54] S. D. Nguyen, J. Yeon, S. H. Kim, and P. S. Halasyamani, $\text{BiO}(\text{IO}_3)$: A new polar iodate that exhibits an Aurivillius-type $(\text{Bi}_2\text{O}_2)^{2+}$ layer and a large SHG response, *J. Am. Chem. Soc.* **133**, 12422 (2011).
- [55] F.-F. Mao, C.-L. Hu, X. Xu, D. Yan, B.-P. Yang, and J.-G. Mao, $\text{Bi}(\text{IO}_3)\text{F}_2$: The first metal iodate fluoride with a very strong second harmonic generation effect, *Angew. Chemie* **129**, 2183 (2017).
- [56] Z. Cao, Y. Yue, J. Yao, Z. Lin, R. He, and Z. Hu, $\text{Bi}_2(\text{IO}_4)(\text{IO}_3)_3$: A new potential infrared nonlinear optical material containing $[\text{IO}_4]^{3-}$ anion, *Inorg. Chem.* **50**, 12818 (2011).
- [57] M. Zhang, X. Su, M. Mutailipu, Z. Yang, and S. Pan, $\text{Bi}_3\text{OF}_3(\text{IO}_3)_4$: metal oxyiodate fluoride featuring a carbon-nanotube-like topological structure with large second harmonic generation response, *Chem. Mater.* **29**, 945 (2017).
- [58] T. Hu, L. Qin, F. Kong, Y. Zhou, and J. G. Mao, $\text{Ln}_3\text{Pb}_3(\text{IO}_3)_{13}(\mu^3-\text{O})$ ($\text{Ln} = \text{La}-\text{Nd}$): New types of second-order nonlinear optical materials containing two types of lone pair cations, *Inorg. Chem.* **48**, 2193 (2009).
- [59] J. Chen, C. L. Hu, F. F. Mao, B. P. Yang, X. H. Zhang, and J. G. Mao, $\text{REI}_5\text{O}_{14}$ ($\text{RE} = \text{Y}$ and Gd): Promising SHG materials featuring the semicircle-shaped $\text{I}_5\text{O}_{14}^{3-}$ polyiodate anion, *Angew. Chemie - Int. Ed.* **58**, 11666 (2019).
- [60] F. F. Mao, C. L. Hu, B. X. Li, and J. G. Mao, Acentric $\text{La}_3(\text{IO}_3)_8(\text{OH})$ and $\text{La}(\text{IO}_3)_2(\text{NO}_3)$: Partial substitution of iodate anions in $\text{La}(\text{IO}_3)_3$ by hydroxide or nitrate anion, *Inorg. Chem.* **56**, 14357 (2017).
- [61] B. P. Yang, C. F. Sun, C. L. Hu, and J. G. Mao, A series of new alkali metal indium iodates with isolated or extended anions, *Dalton Trans.* **40**, 1055 (2011).
- [62] L. Lin, L. Li, C. Wu, Z. Huang, M. G. Humphrey, and C. Zhang, Incorporating rare-earth cations with moderate electropositivity into iodates for the optimized second-order nonlinear optical performance, *Inorg. Chem. Front.* **7**, 2736 (2020).
- [63] J. Chen, C. L. Hu, F. F. Mao, X. H. Zhang, B. P. Yang, and J. G. Mao, $\text{LiMg}(\text{IO}_3)_3$: An excellent SHG material designed by single-site aliovalent substitution, *Chem. Sci.* **10**, 10870 (2019).
- [64] S. J. Oh, H. G. Kim, H. Jo, T. G. Lim, J. S. Yoo, and K. M. Ok, Photoconversion mechanisms and the origin of second-harmonic generation in metal iodates with wide transparency, $\text{NaLn}(\text{IO}_3)_4$ ($\text{Ln} = \text{La}, \text{Ce}, \text{Sm}, \text{and Eu}$) and $\text{NaLa}(\text{IO}_3)_4 : \text{Ln}^{3+}$ ($\text{Ln} = \text{Sm}$ and Eu), *Inorg. Chem.* **56**, 6973 (2017).
- [65] M. Gai, Y. Wang, T. Tong, Z. Yang, and S. Pan, ZnIO_3F : Zinc iodate fluoride with large birefringence and wide band gap, *Inorg. Chem.* **59**, 4172 (2020).
- [66] G. Peng, C. Lin, D. Zhao, L. Cao, H. Fan, K. Chen, and N. Ye, $\text{Sr}[\text{B}(\text{OH})_4](\text{IO}_3)$ and $\text{Li}_4\text{Sr}_5[\text{B}_{12}\text{O}_{22}(\text{OH})_4](\text{IO}_3)_2$: Two unprecedented metal borate-iodates showing a subtle balance of enlarged band gap and birefringence, *Chem. Commun.* **55**, 11139 (2019).
- [67] C. Sun, Y. Wu, D. Mei, and T. Doert, $\text{Bi}_2(\text{IO}_3)(\text{IO}_6)$: First combination of $[\text{IO}_3]^-$ and $[\text{IO}_6]^{5-}$ anions in three-dimensional framework, *Solid State Sci.* **77**, 37 (2018).
- [68] H. S. Ahn, D. W. Lee, and K. M. Ok, Dimensionality variations in new zirconium iodates: Hydrothermal syntheses, structural determination, and characterization of $\text{BaZr}(\text{IO}_3)_6$ and $\text{K}_2\text{Zr}(\text{IO}_3)_6$, *Dalton Trans.* **43**, 10456 (2014).
- [69] Y. An, Y. Zhong, T. Sun, H. Wang, Z. Hu, H. Liu, S. Liu, Y. Kong, and J. Xu, Synthesis, structure and characterization of $\text{M}(\text{IO}_3)_2(\text{HIO}_3)$ ($\text{M} = \text{Ca}, \text{Sr}$) as new anhydrous alkaline earth metal bis-iodate hydrogeniodate compounds, *Dalton Trans.* **48**, 13074 (2019).
- [70] G. X. He, Y. G. Chen, N. Yang, M. L. Xing, and X. M. Zhang, $\text{KSbI}_6\text{O}_{18}$: An antimony iodate semiconductor material with cyclic chiral S_6 -symmetric hexaiodate, *Inorg. Chem. Commun.* **65**, 13 (2016).
- [71] J. H. Zhang, Q. Wu, and W. Z. Lai, A study of composition effects on the bandgaps in a series of new alkali metal aluminum/gallium iodates, *Dalton Trans.* **49**, 2337 (2020).
- [72] F. F. Mao, J. Y. Hu, B. X. Li, and H. Wu, $\text{Bi}_4\text{O}(\text{I}_3\text{O}_{10})(\text{IO}_3)_3(\text{SeO}_4)$: Trimeric condensation of IO_4^{3-} monomers into the $\text{I}_3\text{O}_{10}^{5-}$ polymeric anion observed in a three-component mixed-anion NLO material, *Dalton Trans.* **49**, 15597 (2020).
- [73] C. K. Aslani, V. V. Klepov, M. A. A. Aslani, and H. C. Zur Loye, Hydrothermal synthesis of new iodates $\text{Ln}_2(\text{IO}_3)_3(\text{IO}_4)$ ($\text{Ln} = \text{La}, \text{Nd}, \text{Pr}$) containing the tetraoxoiodate(V) Anion: creation of luminescence properties by doping with Eu, Dy, and Tb, *Cryst. Growth Des.* **21**, 4707 (2021).
- [74] Y. Li, J. Huang, and H. Chen, Crystal growth, characterization and theoretical studies of the noncentrosymmetric compound $\text{Al}_3(\text{IO}_3)_9 \cdot (\text{HIO}_3)_6 \cdot 18\text{H}_2\text{O}$, *J. Alloys Compd.* **856**, 157852 (2021).
- [75] G. Peng, C. Lin, H. Fan, K. Chen, B. Li, G. Zhang, and N. Ye, $\text{Be}_2(\text{BO}_3)(\text{IO}_3)$: The first anion-mixed van der Waals member in the $\text{KBe}_2\text{BO}_3\text{F}$ family with a very strong second harmonic generation response, *Angew. Chemie - Int. Ed.* **60**, 17415 (2021).
- [76] M. Ding, H. Yu, Z. Hu, J. Wang, and Y. Wu, $\text{Na}_7(\text{IO}_3)(\text{SO}_4)_3$: The First noncentrosymmetric alkaline-metal iodate-sulfate with isolated $[\text{IO}_3]$ and $[\text{SO}_4]$ units, *Chem. Commun.* **57**, 9598 (2021).
- [77] T. Y. Chang, B. P. Yang, C. L. Hu, D. Yan, and J. G. Mao, $\text{M}(\text{IO}_3)(\text{HPO}_4)(\text{H}_2\text{O})$ ($\text{M} = \text{Sc}, \text{Fe}, \text{Ga}, \text{In}$): Introduction of Phosphate Anions into Metal Iodates, *Cryst. Growth Des.* **17**, 4984 (2017).
- [78] H. Song, N. Wang, Y. Li, W. Liu, Z. Lin, J. Yao, and G. Zhang, $\text{SrI}_3\text{O}_9\text{H}$: A new alkaline earth metal iodate with two different anionic units using mild aqua-solution method, *Solid State Sci.* **97**, 105982 (2019).
- [79] Y. Xu, C. Lin, D. Zhao, B. Li, L. Cao, N. Ye, and M. Luo, Chemical substitution-oriented design of a new polar PbFIO_3 achieving a balance between large second-harmonic generation response and wide band gap, *Scr. Mater.* **208**, 114347 (2022).
- [80] D. Wang, X. Jiang, P. Gong, X. Zhang, Z. Lin, Z. Hu, and Y. Wu, A new $\text{I}_3\text{O}_9^{3-}$ group constructed from IO_3^- and IO_5^{2-} anion units in $\text{Cs}_3[\text{Ga}_2\text{O}(\text{I}_3\text{O}_9)(\text{IO}_3)_4(\text{HIO}_3)]$, *CrystEngComm* **24**, 77 (2022).

- [81] M. Gai, T. Tong, Y. Wang, Z. Yang, and S. Pan, New alkaline-earth metal fluoriodates exhibiting large birefringence and short ultraviolet cutoff edge with highly polarizable $(\text{IO}_3\text{F})^{2-}$ units, *Chem. Mater.* **32**, 5723 (2020).
- [82] Y. H. Kim, T. T. Tran, P. S. Halasyamani, and K. M. Ok, Macroscopic polarity control with alkali metal cation size and coordination environment in a series of tin iodates, *Inorg. Chem. Front.* **2**, 361 (2015).

7. Conclusions

7.1 Crystal structure at ambient pressure

The ambient-pressure crystal structures of the four studied metal iodates are shown in **Figure 45**. The crystal data and structure refinement details of them are summarized in **Table 2**. Except for $\text{Fe}(\text{IO}_3)_3$, which crystallizes in a hexagonal structure described by space group $P6_3$ (No. 173), the rest of the metal iodates crystallize in a monoclinic structure, described by space group $P2_1$ (No. 4). The crystal structure of them consists of IO_3 and AO_6 (A =metal) polyhedral units and share some common features. When view along the c -axis of Fe and Zn iodates (equivalent to the b -axis of Co and Mg iodates), each iodine atom is bonded with three oxygen atoms and the bond distance range from 1.8 Å to 2.0 Å. Each metal cation is surrounded by six IO_3 pyramids by sharing one oxygen atom. When view perpendicular to the c -axis of Fe and Zn iodates (which is b -axis of Co and Mg iodates), the crystal structure of the four metal iodates shows a layered structure, formed by IO_3 layers which are connected by the AO_6 octahedra. According to the lattice parameters for Co, Zn and Mg iodates summarized in **Table 2**, the lattice parameter a and c of them are very close in value and the monoclinic angle is close to 120 degrees, so the crystal structure of these three metal iodates are pseudo-hexagonal. The unit-cell volume per formula unit of Co, Zn, and Mg iodates are similar (**Table 2**), around 1/3 of that for $\text{Fe}(\text{IO}_3)_3$. The lattice parameter a in $\text{Zn}(\text{IO}_3)_2$ is almost half of that in the structure of Co and Mg iodates.

Formula	Fe(IO ₃) ₃	Co(IO ₃) ₂	Zn(IO ₃) ₂	Mg(IO ₃) ₂
Crystal system	hexagonal	monoclinic	monoclinic	monoclinic
Space group	<i>P</i> 6 ₃	<i>P</i> 2 ₁	<i>P</i> 2 ₁	<i>P</i> 2 ₁
a (Å)	9.2476(4)	10.943(6)	5.465(4)	11.2563
b (Å)	9.2476(4)	5.078(1)	10.952(8)	5.0497
c (Å)	5.2326(2)	10.925(4)	5.129(4)	11.2128
β (°)	120	119.814(3)	120.37(8)	119.8256
Z	2	4	2	4
V(Å ³)/Z	193.00	131.67	132.4	138.23
Refinement method	Rietveld	Rietveld	Rietveld	Rietveld
<i>R</i> _p	3.83%	9.60%	7.22%	9.23%
<i>R</i> _{wp}	13.42%	13.30%	9.91%	8.85%

Table 2. Crystal structure data and structure refinement detail of the four metal iodates studied in this thesis. The lattice parameters are obtained from the Rietveld refinement of the XRD collected at ambient pressure. *R*_p and *R*_{wp} reflected the quality of the Rietveld refinement.

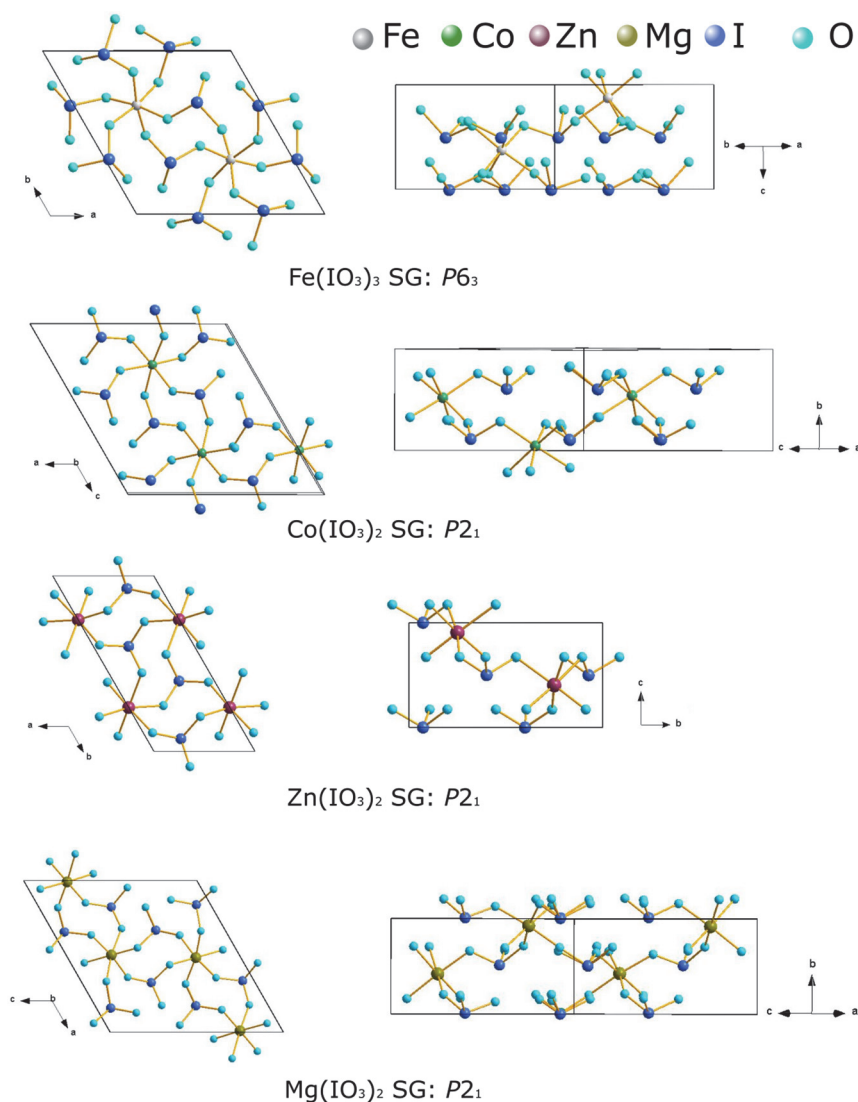


Figure 45. Crystal structure of $\text{Fe}(\text{IO}_3)_3$, $\text{Co}(\text{IO}_3)_2$, $\text{Zn}(\text{IO}_3)_2$ and $\text{Mg}(\text{IO}_3)_2$ at ambient pressure. the iron, cobalt, zinc, magnesium, iodine and oxygen atoms are shown in gray, green, brown, pale yellow, blue and cyan-blue, respectively. “SG” means space group.

7.2 Crystal structure and compressibility at high pressure

$\text{Fe}(\text{IO}_3)_3$ undergoes three isostructural phase transition (IPT) at 1.5-2.0 GPa, 5.7-6.0 GPa and 22.2 GPa (**Figure 46**). The first two IPTs were evidenced by the nonlinear pressure dependence of the Raman-active modes, the discontinuity of the calculated elastic constants, and the instability in the calculated phonon dispersion under high pressure. The third IPTs was evidenced by the appearance of new peaks in the XRD pattern at 22.2 GPa, and the crystal structure of the high pressure phase (HP) was solved

by the Rietveld method. The third IPT was accompanied by a 5% collapse on the unit-cell volume.

$\text{Co}(\text{IO}_3)_2$ undergoes two IPTs at 3 GPa and the pressure range of 9-11 GPa (**Figure 46**). The phase transitions were evidenced by the nonlinear behavior of the lattice parameter, calculated Co-O bond distance, relative intensity of two Raman modes, Raman- and infrared-active modes under pressure. No discontinuity was found in the unit-cell volume around the phase transition pressure.

$\text{Zn}(\text{IO}_3)_2$ undergoes two IPTs at the pressure range of 2.5-3.4 GPa and 8-9 GPa (**Figure 46**). The phase transition was evidenced by the nonlinear behavior of the pressure dependence of lattice parameter, calculated Zn-O bond distance and pressure dependence of the Raman- and infrared-active modes. No discontinuity was found in the unit-cell volume around the phase transition pressure.

$\text{Mg}(\text{IO}_3)_2$ undergoes one phase transition from monoclinic (space group: $P2_1$) to trigonal structure (space group: P_3) at the pressure range of 7.7-9.6 GPa (**Figure 46**). The phase transition was evidenced by the Rietveld refinement of XRD, and the appearance of new peaks in the Raman and infrared spectra under high pressure. No discontinuity was found in the unit-cell volume around the phase transition pressure. The IPTs found in other three metal iodates was not observed here.

The bulk modulus of the four metal iodates in different phases were summarized in **Table 3**. For the low pressure phase (ambient-pressure phase, I1 phase or I2 phase), the bulk modulus of $\text{Fe}(\text{IO}_3)_3$ is the highest one, and $\text{Zn}(\text{IO}_3)_2$ have the lowest bulk modulus. The bulk modulus will drastically increase at high pressure phase (I2 or HP phase). The reason is the gradually increase of the oxygen coordination of iodine, the new bonds formed between the iodine and the oxygen in the neighboring IO_3 layer strengthened the resistance to the external pressure. All of the four metal iodates show a huge anisotropic behavior, c -axis in $\text{Fe}(\text{IO}_3)_3$ and $\text{Zn}(\text{IO}_3)_2$ and b -axis in $\text{Co}(\text{IO}_3)_2$ and $\text{Mg}(\text{IO}_3)_2$ are the most compressible axis, due to the layered structure in those directions.

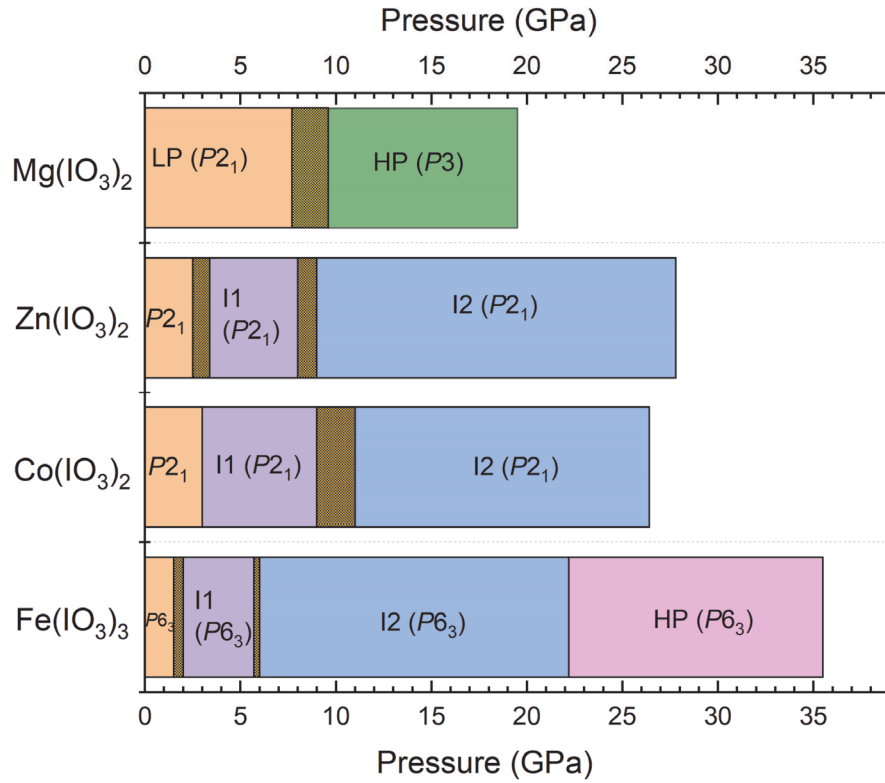


Figure 46. Summary of the crystal structure and space group adopted to the four metal iodates studied in this thesis as a function of pressure. The area filled with grid pattern indicated the pressure interval where the phase transition occurs.

Compounds	Phase	BM-EOS	V_0 (\AA^3)	B_0 (GPa)	B_0'
$\text{Fe}(\text{IO}_3)_3$	Ambient+I1+I2	3 rd -order	385	55(2)	4.3(0.3)
	HP	2 nd -order	353(9)	73(9)	4.0
$\text{Co}(\text{IO}_3)_2$	Ambient+I1	3 rd -order	529	29.8(1)	3.5(0.3)
	I2	3 rd -order	462.9(5.6)	70.8(3.6)	5.2(0.6)
$\text{Zn}(\text{IO}_3)_2$	Ambient+I1+I2	3 rd -order	264.8(4)	21.6(0.7)	7.0(0.3)
$\text{Mg}(\text{IO}_3)_2$	LP	3 rd -order	552.8	22.2(0.8)	4.2(0.4)
	HP	3 rd -order	369.6(0.3)	63.6(0.4)	3.3(0.1)

Table 3. Experimental determined volume, bulk modulus and the related pressure derivate for the four metal iodates in different phases. The hulk modulus was obtained from the fitting of the unit-cell volume by adopting the Birch-Murnaghan equation of state (BM-EOS)

7.3 Oxygen coordination increase of iodine

For all the studied metal iodates in this thesis, there are two types of I-O bonds, and they are different from each other on distance. The first type of I-O bonds (between iodine and inlayer oxygen atoms like O7, O8 and O9 in **Figure 47**) range from 1.8 to 2.0 Å, they exist at ambient pressure, the bond distance will slightly increase under pressure. Another type of I-O bonds with a distance range from 2.5 to 3.2 Å such as O10, O5 and O8' in **Figure 47**), are between iodine and the oxygen atoms in the neighboring IO₃ layer, this kind of bond only formed under high pressure, as a consequence of two effects; (i). The pressure-induced shortening of the bond distance and (ii). The existence of the LEP in iodine. The second type of I-O bonds shorten under pressure. The approach of the interlayer oxygen atoms to iodine pushed away the inlayer oxygen atoms and caused the enlargement of the first type of I-O bond distance.

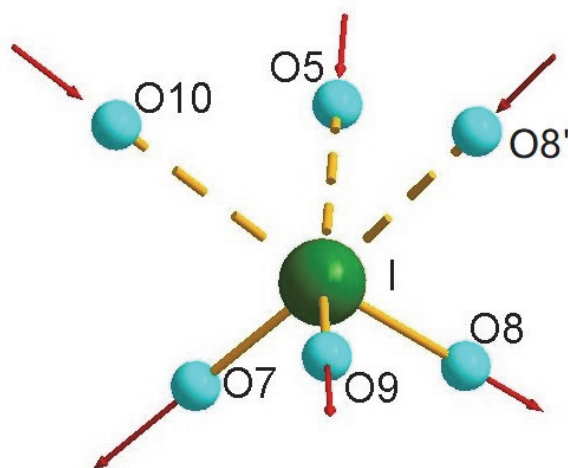


Figure 47. Illustration of the two types of I-O bond.

7.4 Raman spectra at ambient pressure

Figure 48 shows the Raman spectra of those four metal iodates at ambient condition. The Raman spectra can be divided into three regions: (i). The high-frequency region located in the wavenumber interval of 600-900 cm⁻¹, which is contributed by the stretching vibration of I-O bonds, the strongest modes are in this region and have been marked in **Figure 48**. (ii). The mid-frequency region is in the wavenumber interval of

300-500 cm^{-1} , this region contributed by the bending of I-O bonds. (iii). The low-frequency region is the modes lower than 300 cm^{-1} , which could be associated with the translational and rotational motions of the iodates as a rigid unit.

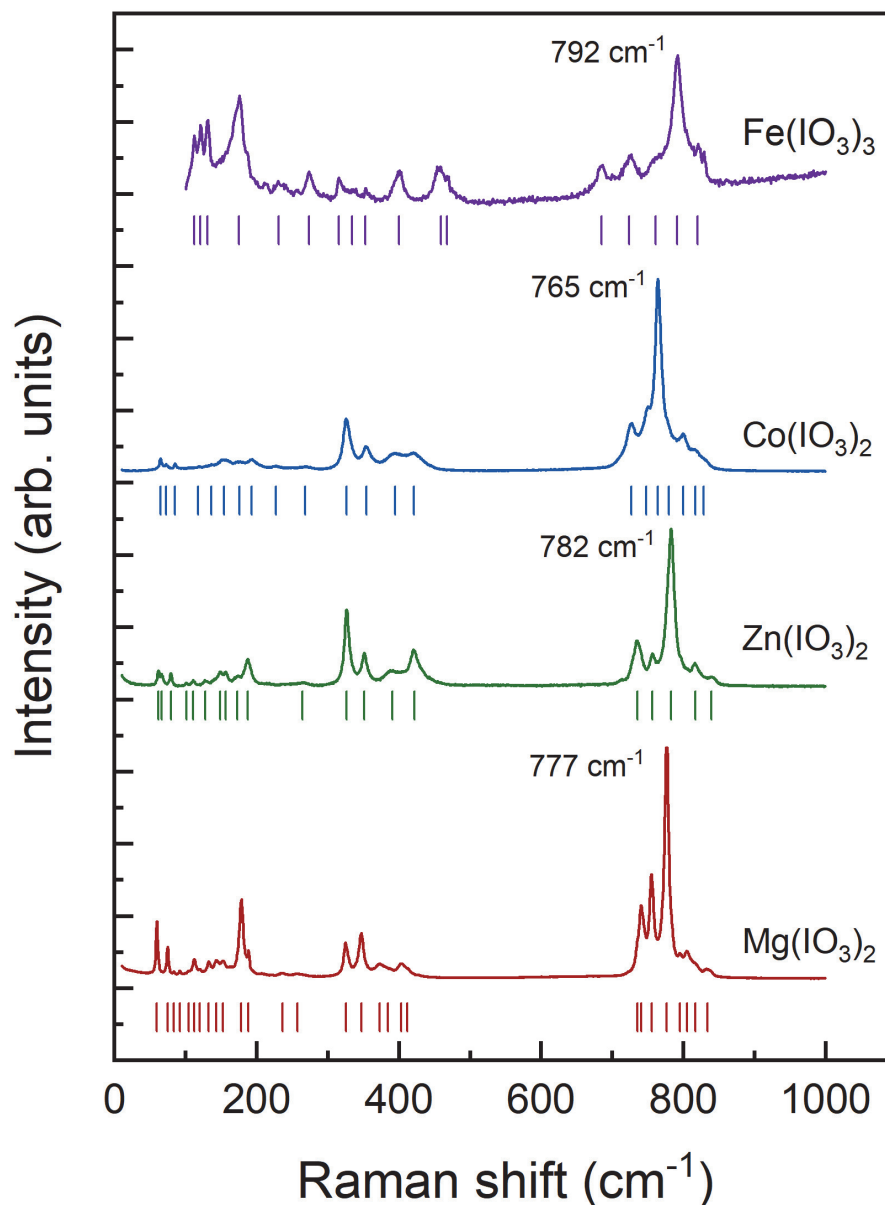


Figure 48. Raman spectra of those four metal iodates at ambient condition. The wavenumber of the strongest modes in each Raman spectra have been marked beside it. The short vertical bars below of each Raman spectra are an indication of the determined peak position.

7.5 Raman spectra at high pressure

Most of the Raman modes in the high-frequency region show a soft behavior under compression, which is a result of the pressure-induced enlargement of the I-O bond distance, all the modes in the mid- and low-frequency region harden under compression, the combination of both phenomena caused a reduction of the phonon gap between the mid- and high-frequency region. Furthermore, some Raman modes in Fe, Co, and Zn iodates show a nonlinear behavior under pressure, the slope change at the pressure where the IPTs occurred. There are some new peaks appeared at around 7.7 GPa in the Raman spectra of $\text{Mg}(\text{IO}_3)_2$, support the monoclinic-to-trigonal phase transition.

7.6 Infrared spectra

The infrared spectra were collected at the wavenumbers below 700 cm^{-1} . For $\text{Fe}(\text{IO}_3)_3$, 12 Infrared-active modes were detected at ambient pressure, 8 of them were followed under high pressure before the third IPT, there is a suddenly shift of the modes at 15.3 GPa, the changes in the infrared spectra have been assigned to the third IPT. Only five infrared-active modes have been followed under pressure in the HP phase.

A total of 9 infrared-active modes in $\text{Co}(\text{IO}_3)_2$ have been detected at the lowest pressure (0.2 GPa) and followed under high pressure, most of the modes show a nonlinear behavior under pressure and the sign changed at the pressure where the IPTs happened. No new peaks were observed under pressure.

A total of 25 infrared-active modes were detected in $\text{Zn}(\text{IO}_3)_2$ at the lowest pressure (0.9 GPa), and 18 of them have been followed under pressure. Most of the infrared-active modes show a nonlinear behavior under pressure, the sign changed at the pressure where the IPT happened, an unexpected change happened in the pressure coefficient at 13 GPa, maybe caused by a third phase transition but not observed at other diagnostics.

A total of 14 infrared-active modes have been detected in the LP phase and 9 were detected in the HP phase of $\text{Mg}(\text{IO}_3)_2$, two new peaks were observed at 9.6 GPa, a results of the pressure-induced monoclinic-to-trigonal phase transition.

7.7 Electronic band structure

According to the calculated electronic band structure, all the four metal iodates have an indirect gap. For $\text{Fe}(\text{IO}_3)_3$, the VBM in the electronic structure is dominated by the O-2*p* state, while the CBM is dominated by the Fe-3*d* and I-5*p*. The bandgap of $\text{Fe}(\text{IO}_3)_3$ shows a nonlinear behavior at the pressure before the third IPT, the nonlinear behavior can be explained by two effects competing under pressure, the pressure-induced shortening of the Fe-O bond distance increases the overlap between Fe and O orbital, this fact favors the narrowing of the bandgap. On the other hand, the slightly enlargement of the I-O bond distance reduces the hybridization between iodine and oxygen atoms, this fact favors the opening of the bandgap energy. There is a bandgap jump at 23.5 GPa, accompanied by an indirect-to-indirect transition in the electronic band structure, owing to the unit-cell volume collapse found in HPXRD. The resistivity exhibits a nonlinear behavior before the third IPT and the show a rapidly decrease after around 20 GPa, the changes is a results of the exponential increase of the intrinsic carrier concentration.

For $\text{Co}(\text{IO}_3)_2$, the bandgap shows a rapid decrease from the ambient pressure up to around 8 GPa, and then show a small pressure dependence. The VBM in the electronic band structure is dominated by O-2*p* and Co-3*d* state, and the CBM is dominated by the I-5*p* state, with small contribution from O-2*p* state. The behavior of the bandgap can be explained by the competition of two effects under pressure. The enhancement interaction between Co and O caused by the shortening of the Co-O bond distance, this fact favors the narrowing of the bandgap energy. On the other hand, the enlargement of the I-O bond distance under pressure decreases the hybridization between iodine and oxygen atoms, this fact favors the opening of the bandgap energy. In the optical absorption spectra, we also found the multi-absorption band caused by the *d-d* internal transition in Co^{2+} . Those three observed absorption bands have been assigned to the transition from the ground state ${}^4T_{1g}(F)$ to spin allowed ${}^4T_{1g}(P)$, spin forbidden ${}^2A_{1g}(G)$ and ${}^2T_{1g}(H)$ state. There is a pressure-induced narrowing of the absorption band, a results of the pressure-induced suppression of the Jahn-teller distortion. The high-spin to low-spin transition have been predicted at 110 GPa.

For $\text{Zn}(\text{IO}_3)_2$ and $\text{Mg}(\text{IO}_3)_2$, the VBM is dominated by the O-2*p* state, and the CBM is dominated by O-2*p* and I-5*p* state. The bandgap shows a nonlinear behavior

under pressure. According to the molecular diagram established for them by using the calculated DOS, PDOS, and COOP between iodine and oxygen, the bandgap for them are determined by the energy difference between (i). The anti-bonding state of the p - p interaction between oxygen and iodine (ii). The nonbonding state of O-2 p . There are two effects competing under pressure, the increasing of the bond distance between iodine and inlayer oxygen favors the reduction of the hybridization between them, and narrows the separation between bonding and anti-bonding state, thus narrowing the bandgap energy. The shortening of the bond distance between iodine and interlayer oxygen favors the increase of the interaction between them, and increases the separation between the bonding and anti-bonding states, thus opening the bandgap energy.

The partial filled 3 d state in transition metal contribute to either the VBM or CBM, thus narrowing the bandgap energy of metal iodates. Therefore, the first instruction for designing wide bandgap energy metal iodates is avoiding the use of partial filled transition metals. There is a negative relationship between the bandgap energy and the average bond distance between iodine and inlayer oxygen atoms in non-transition or closed-shelled transition metal iodates, the shorter the I-O bond distance, the wider the bandgap energy. Therefore, the second instruction for designing wide bandgap metal iodates is shortening the I-O bond distance.

Bibliography

- [1] C. F. Sun, C. L. Hu, X. Xu, J. B. Ling, T. Hu, F. Kong, X. F. Long, and J. G. Mao, BaNbO(IO₃)₅: A New Polar Material with a Very Large SHG Response, *J. Am. Chem. Soc.* **131**, 9486 (2009).
- [2] H. Y. Chang, S. H. Kim, P. S. Halasyamani, and K. M. Ok, Alignment of Lone Pairs in a New Polar Material: Synthesis, Characterization, and Functional Properties of Li₂Ti(IO₃)₆, *J. Am. Chem. Soc.* **131**, 2426 (2009).
- [3] S. D. Nguyen, J. Yeon, S. H. Kim, and P. S. Halasyamani, BiO(IO₃): A New Polar Iodate That Exhibits an Aurivillius-Type (Bi₂O₂)²⁺ Layer and a Large SHG Response, *J. Am. Chem. Soc.* **133**, 12422 (2011).
- [4] H. Liu, Q. Wu, X. Jiang, Z. Lin, X. Meng, X. Chen, and J. Qin, ABi₂(IO₃)₂F₅ (A=K, Rb, and Cs): A Combination of Halide and Oxide Anionic Units To Create a Large Second-Harmonic Generation Response with a Wide Bandgap, *Angew. Chemie-Int. Ed.* **56**, 9492 (2017).
- [5] J. Chen, C. L. Hu, F. F. Mao, B. P. Yang, X. H. Zhang, and J. G. Mao, REI₅O₁₄ (RE=Y and Gd): Promising SHG Materials Featuring the Semicircle-Shaped I₅O₁₄³⁻ Polyiodate Anion, *Angew. Chemie-Int. Ed.* **58**, 11666 (2019).
- [6] Y. J. Jia, Y. G. Chen, Y. Guo, X. F. Guan, C. Li, B. Li, M. M. Liu, and X. M. Zhang, LiM^{II}(IO₃)₃ (M^{II}=Zn and Cd): Two Promising Nonlinear Optical Crystals Derived from a Tunable Structure Model of α-LiIO₃, *Angew. Chemie-Int. Ed.* **58**, 17194 (2019).
- [7] G. Peng, C. Lin, H. Fan, K. Chen, B. Li, G. Zhang, and N. Ye, Be₂(BO₃)(IO₃): The First Anion-Mixed Van Der Waals Member in the KBe₂BO₃F₂ Family with a Very Strong Second Harmonic Generation Response, *Angew. Chemie-Int. Ed.* **60**, 17415 (2021).
- [8] F.-F. Mao, C.-L. Hu, X. Xu, D. Yan, B.-P. Yang, and J.-G. Mao, Bi(IO₃)F₂: The First Metal Iodate Fluoride with a Very Strong Second Harmonic Generation Effect, *Angew. Chemie* **129**, 2183 (2017).
- [9] J. Chen, C. L. Hu, F. F. Mao, X. H. Zhang, B. P. Yang, and J. G. Mao, LiMg(IO₃)₃: An Excellent SHG Material Designed by Single-Site Aliovalent Substitution, *Chem. Sci.* **10**, 10870 (2019).
- [10] L. Kang, M. Zhou, J. Yao, Z. Lin, Y. Wu, and C. Chen, Metal Thiophosphates with Good Mid-Infrared Nonlinear Optical Performances: A First-Principles Prediction and Analysis, *J. Am. Chem. Soc.* **137**, 13049 (2015).
- [11] T. T. Tran, H. Yu, J. M. Rondinelli, K. R. Poeppelmeier, and P. S. Halasyamani, Deep Ultraviolet Nonlinear Optical Materials, *Chem. Mater.* **28**, 5238 (2016).
- [12] F. Liang, L. Kang, Z. Lin, Y. Wu, and C. Chen, Analysis and Prediction of Mid-IR Nonlinear Optical Metal Sulfides with Diamond-like Structures,

- Coord. Chem. Rev. **333**, 57 (2017).
- [13] V. Petrov, Frequency Down-Conversion of Solid-State Laser Sources to the Mid-Infrared Spectral Range Using Non-Oxide Nonlinear Crystals, Prog. Quantum Electron. **42**, 1 (2015).
- [14] P. A. Franken, A. E. Hill, C. W. Peters, and G. Weinreich, Generation of Optical Harmonics, Phys. Rev. Lett. **7**, 118 (1961).
- [15] R. C. Miller, Optical Second Harmonic Generation in Piezoelectric Crystals, Appl. Phys. Lett. **5**, 17 (1964).
- [16] J. D. Bierlein and H. Vanherzeele, Potassium Titanyl Phosphate: Properties and New Applications, J. Opt. Soc. Am. B **6**, 622 (1989).
- [17] B. Wu, D. Tang, N. Ye, and C. Chen, Linear and Nonlinear Optical Properties of the $\text{KBe}_2\text{BO}_3\text{F}_2$ (KBBF) Crystal, Opt. Mater. **5**, 105 (1996).
- [18] C. Chen, B. Wu, A. Jiang, and G. You, A New-Type Ultraviolet SHG Crystal— β - BaB_2O_4 , Sci.Sin.Ser.B (Engl.Ed.) **28**, 235 (1985).
- [19] C. Chen, A. Jiang, B. Wu, G. You, S. Lin, and Y. Wu, New Nonlinear Optical Crystal LiB_3O_5 , J. Opt. Soc. Am. B **6**, 616 (1989).
- [20] G. D. Boyd, R. C. Miller, K. Nassau, W. L. Bond, and A. Savage, LiNbO_3 : An Efficient Phase Matchable Nonlinear Optical Material, Appl. Phys. Lett. **5**, 234 (1964).
- [21] H. Fan, G. Peng, C. Lin, K. Chen, S. Yang, and N. Ye, $\text{Ba}(\text{IO}_3)\text{F}$: An Alkaline-Earth-Metal Iodate Fluoride Crystal with Large Band Gap and Birefringence, Inorg. Chem. **59**, 7376 (2020).
- [22] H. Jo, H. G. Kim, H. R. Byun, J. I. Jang, and K. M. Ok, Synthesis, Structure, and Third-Harmonic Generation Measurements of a Mixed Alkali Metal Iodate, $\text{KLi}_2(\text{IO}_3)_3$, J. Solid State Chem. **282**, 121120 (2020).
- [23] F. F. Mao, J. Y. Hu, B. X. Li, and H. Wu, $\text{Bi}_4\text{O}(\text{I}_3\text{O}_{10})(\text{IO}_3)_3(\text{SeO}_4)$: Trimeric Condensation of IO_4^{3-} Monomers into the $\text{I}_3\text{O}_{10}^{5-}$ Polymeric Anion Observed in a Three-Component Mixed-Anion NLO Material, Dalt. Trans. **49**, 15597 (2020).
- [24] H. Liu, X. Jiang, X. Wang, L. Yang, Z. Lin, Z. Hu, X. Meng, X. Chen, and J. Qin, Influence of A-Site Cations on Germanium Iodates as Mid-IR Nonlinear Optical Materials: $\text{A}_2\text{Ge}(\text{IO}_3)_6$ (A=Li,K,Rb and Cs) and $\text{BaGe}(\text{IO}_3)_6 \cdot \text{H}_2\text{O}$, J. Mater. Chem. C **6**, 4698 (2018).
- [25] X. Xu, C. Hu, B. Li, B. Yang, and J. Mao, α - AgI_3O_8 and β - AgI_3O_8 with Large SHG Responses: Polymerization of IO_3 Groups into the I_3O_8 Polyiodate Anion, Chem. Mater. **26**, 3219 (2014).
- [26] K. Liu, J. Han, J. Huang, Z. Wei, Z. Yang, and S. Pan, $\text{SrTi}(\text{IO}_3)_6 \cdot 2\text{H}_2\text{O}$ and $\text{SrSn}(\text{IO}_3)_6$: Distinct Arrangements of Lone Pair Electrons Leading to Large Birefringences, RSC Adv. **11**, 10309 (2021).
- [27] L. Xiao, Z. Cao, J. Yao, Z. Lin, and Z. Hu, A New Cerium Iodate Infrared Nonlinear Optical Material with a Large Second-Harmonic Generation

- Response, *J. Mater. Chem. C* **5**, 2130 (2017).
- [28] J. Yeon, S. H. Kim, and P. S. Halasyamani, New Thallium Iodates–Synthesis, Characterization, and Calculations of $\text{Tl}(\text{IO}_3)_3$ and $\text{Tl}_4(\text{IO}_3)_6$, $[\text{Tl}^+{}_3\text{Ti}^{3+}(\text{IO}_3)_6]$, *J. Solid State Chem.* **182**, 3269 (2009).
- [29] H. Y. Chang, S. H. Kim, M. O. Kang, and P. S. Halasyamani, Polar or Nonpolar? A^+ Cation Polarity Control in $\text{A}_2\text{Ti}(\text{IO}_3)_6$ ($\text{A} = \text{Li}, \text{Na}, \text{K}, \text{Rb}, \text{Cs}, \text{Tl}$), *J. Am. Chem. Soc.* **131**, 6865 (2009).
- [30] F. F. Mao, C. L. Hu, J. Chen, B. L. Wu, and J. G. Mao, $\text{HBa}_{2.5}(\text{IO}_3)_6(\text{I}_2\text{O}_5)$ and $\text{HBa}(\text{IO}_3)(\text{I}_4\text{O}_{11})$: Explorations of Second-Order Nonlinear Optical Materials in the Alkali-Earth Polyiodate System, *Inorg. Chem.* **58**, 3982 (2019).
- [31] A. You, M. A. Y. Be, I. In, L. Nonlinear, O. Coefficient, P. M. Second, O. Nonlinear, S. Of, and L. Iodate, Optical Nonlinearities in LiIO_3 , *J. Appl. Phys.* **40**, 5201 (1969).
- [32] Q. Wu, H. Liu, F. Jiang, L. Kang, L. Yang, Z. Lin, Z. Hu, X. Chen, X. Meng, and J. Qin, RbIO_3 and RbIO_2F_2 : Two Promising Nonlinear Optical Materials in Mid-IR Region and Influence of Partially Replacing Oxygen with Fluorine for Improving Laser Damage Threshold, *Chem. Mater.* **28**, 1413 (2016).
- [33] Q. M. Huang, C. L. Hu, B. P. Yang, Z. Fang, Y. Lin, J. Chen, B. X. Li, and J. G. Mao, $[\text{GaF}(\text{H}_2\text{O})][\text{IO}_3\text{F}]$: A Promising NLO Material Obtained by Anisotropic Polycation Substitution, *Chem. Sci.* **12**, 9333 (2021).
- [34] A. Liang, P. Rodríguez-Hernandez, A. Munoz, S. Raman, A. Segura, and D. Errandonea, Pressure-Dependent Modifications in the Optical and Electronic Properties of $\text{Fe}(\text{IO}_3)_3$: The Role of Fe 3d and I 5p Lone-Pair Electrons, *Inorg. Chem. Front.* **8**, 4780 (2021).
- [35] X. Xu, B. Yang, C. Huang, and J. Mao, Explorations of New Second-Order Nonlinear Optical Materials in the Ternary Rubidium Iodate System: Noncentrosymmetric β - $\text{RbIO}_3(\text{HIO}_3)_2$ and Centrosymmetric $\text{Rb}_3(\text{IO}_3)_3(\text{I}_2\text{O}_5)(\text{HIO}_3)_4(\text{H}_2\text{O})$, *Inorg. Chem.* **53**, 1756 (2014).
- [36] A. Liang, R. Turnbull, P. Rodríguez-hernandez, A. Muñoz, M. Jasmin, L. Shi, and D. Errandonea, General Relationship between the Band-Gap Energy and Iodine-Oxygen Bond Distance in Metal Iodates, *Phys. Rev. Mater.* **6**, 044603 (2022).
- [37] A. Benghia, Z. Hebboul, R. Chikhaoui, I. khaldoun Lefkaier, A. Chouireb, and S. Goumri-Said, Effect of Iodic Acid Concentration in Preparation of Zinc Iodate: Experimental Characterization of $\text{Zn}(\text{IO}_3)_2$, and Its Physical Properties from Density Functional Theory, *Vacuum* **181**, 109660 (2020).
- [38] M. K. Y. Chan and G. Ceder, Efficient Band Gap Prediction for Solids, *Phys. Rev. Lett.* **105**, 196403 (2010).
- [39] P. Borlido, J. Schmidt, A. W. Huran, F. Tran, M. A. L. Marques, and S. Botti,

- Exchange-Correlation Functionals for Band Gaps of Solids: Benchmark, Reparametrization and Machine Learning, *Npj Comput. Mater.* **6**, 96 (2020).
- [40] C. Huang, C. L. Hu, X. Xu, B. P. Yang, and J. G. Mao, Explorations of a Series of Second Order Nonlinear Optical Materials Based on Monovalent Metal Gold(III) Iodates, *Inorg. Chem.* **52**, 11551 (2013).
- [41] Y. H. Kim, T. T. Tran, P. S. Halasyamani, and K. M. Ok, Macroscopic Polarity Control with Alkali Metal Cation Size and Coordination Environment in a Series of Tin Iodates, *Inorg. Chem. Front.* **2**, 361 (2015).
- [42] M. Zhang, C. Hu, T. Abudouwufu, Z. Yang, and S. Pan, Functional Materials Design via Structural Regulation Originated from Ions Introduction: A Study Case in Cesium Iodate System, *Chem. Mater.* **30**, 1136 (2018).
- [43] M. Luo, F. Liang, X. Hao, D. Lin, B. Li, Z. Lin, and N. Ye, Rational Design of the Nonlinear Optical Response in a Tin Iodate Fluoride $\text{Sn}(\text{IO}_3)_2\text{F}_2$, *Chem. Mater.* **32**, 2615 (2020).
- [44] D. N. Nikogosyan, *Rarely Used and Archive Crystals*, in *Nonlinear Optical Crystals: A Complete Survey* (Springer, New York, 2005), pp. 319–398.
- [45] G. Yao, Y. Chen, X. Y. An, Z. Q. Jiang, L. H. Cao, W. D. Wu, and Y. Zhao, First-Principles Study of the Structural, Electronic and Optical Properties of Hexagonal LiIO_3 , *Chinese Phys. Lett.* **30**, 067101 (2013).
- [46] H. Song, D. Jiang, N. Wang, W. Xing, R. Guo, Z. Lin, J. Yao, Y. Wang, H. Tu, and G. Zhang, $\text{Na}_3\text{Bi}(\text{IO}_3)_6$: An Alkali-Metal Bismuth Iodate with Intriguing One-Dimensional $[\text{Bi}_6\text{O}_{18}]$ Chains and Pressure-Induced Structural Transition, *Inorg. Chem.* **60**, 2893 (2021).
- [47] Y. J. Jia, Y. G. Chen, T. Wang, Y. Guo, X. F. Guan, and X. M. Zhang, $\text{KBi}(\text{IO}_3)_3(\text{OH})$ and $\text{NaBi}(\text{IO}_3)_4$: From the Centrosymmetric Chain to a Noncentrosymmetric Double Layer, *Dalt. Trans.* **48**, 10320 (2019).
- [48] Y. Huang, X. Meng, P. Gong, L. Yang, Z. Lin, X. Chen, and J. Qin, $\text{A}_2\text{Bi}_5\text{O}_{15}$ ($\text{A} = \text{K}^+$ or Rb^+): Two New Promising Nonlinear Optical Materials Containing $[\text{I}_3\text{O}_9]^{3-}$ Bridging Anionic Groups, *J. Mater. Chem. C* **2**, 4057 (2014).
- [49] R. Wu, X. Jiang, M. Xia, L. Liu, X. Wang, Z. Lin, and C. Chen, $\text{K}_8\text{Ce}_2\text{I}_{18}\text{O}_{53}$: A Novel Potassium Cerium(IV) Iodate with Enhanced Visible Light Driven Photocatalytic Activity Resulting from Polar Zero Dimensional $[\text{Ce}(\text{IO}_3)_8]^{4-}$ Units, *Dalt. Trans.* **46**, 4170 (2017).
- [50] F. F. Mao, C. L. Hu, J. Chen, and J. G. Mao, A Series of Mixed-Metal Germanium Iodates as Second-Order Nonlinear Optical Materials, *Chem. Mater.* **30**, 2443 (2018).
- [51] L. Xiao, F. You, P. Gong, Z. Hu, and Z. Lin, Synthesis and Structure of a New Mixed Metal Iodate $\text{Ba}_3\text{Ga}_2(\text{IO}_3)_{12}$, *CrystEngComm* **21**, 4981 (2019).
- [52] F. Mao, J. Liu, J. Hu, and H. Wu, From $\text{Ag}_2\text{Zr}(\text{IO}_3)_6$ to $\text{LaZr}(\text{IO}_3)_5\text{F}_2$: A Case of

- Constructing Wide-Band-Gap Birefringent Materials through Chemical Cosubstitution, *Chem.-An Asian J.* **15**, 3487 (2020).
- [53] B. P. Yang, C. L. Hu, X. Xu, C. Huang, and J. G. Mao, $Zn_2(VO_4)(IO_3)$: A Novel Polar Zinc(II) Vanadium(V) Iodate with a Large SHG Response, *Inorg. Chem.* **52**, 5378 (2013).
- [54] C. F. Sun, T. Hu, X. Xu, and J. G. Mao, Syntheses, Crystal Structures, and Properties of Three New Lanthanum(III) Vanadium Iodates, *Dalt. Trans.* **39**, 7960 (2010).
- [55] T. Palasyuk, I. Troyan, M. Eremets, V. Drozd, S. Medvedev, P. Zaleski-Ejgierd, E. Magos-Palasyuk, H. Wang, S. A. Bonev, D. Dudenko, and P. Naumov, Ammonia as a Case Study for the Spontaneous Ionization of a Simple Hydrogen-Bonded Compound, *Nat. Commun.* **5**, 3460 (2014).
- [56] S. Ninet, F. Datchi, P. Dumas, M. Mezouar, G. Garbarino, A. Mafety, C. J. Pickard, R. J. Needs, and A. M. Saitta, Experimental and Theoretical Evidence for an Ionic Crystal of Ammonia at High Pressure, *Phys. Rev. B* **89**, 174103 (2014).
- [57] A. Mujica, A. Rubio, A. Muñoz, and R. J. Needs, High-Pressure Phases of Group-IV, III-V, and II-VI Compounds, *Rev. Mod. Phys.* **75**, 863 (2003).
- [58] F. P. Bundy, Direct Conversion of Graphite to Diamond in Static Pressure Apparatus, *J. Chem. Phys.* **38**, 631 (1963).
- [59] Y. Tian, B. Xu, D. Yu, Y. Ma, Y. Wang, Y. Jiang, W. Hu, C. Tang, Y. Gao, K. Luo, Z. Zhao, L. M. Wang, B. Wen, J. He, and Z. Liu, Ultrahard Nanotwinned Cubic Boron Nitride, *Nature* **493**, 385 (2013).
- [60] M. I. Eremets, A. G. Gavriliuk, I. A. Trojan, D. A. Dzivenko, and R. Boehler, Single-Bonded Cubic Form of Nitrogen, *Nat. Mater.* **3**, 558 (2004).
- [61] P. Loubeyre, F. Occelli, and P. Dumas, Synchrotron Infrared Spectroscopic Evidence of the Probable Transition to Metal Hydrogen, *Nature* **577**, 631 (2020).
- [62] M. S. Miao, Caesium in High Oxidation States and as a P-Block Element, *Nat. Chem.* **5**, 846 (2013).
- [63] J. Botana, X. Wang, C. Hou, D. Yan, H. Lin, Y. Ma, and M. S. Miao, Mercury under Pressure Acts as a Transition Metal: Calculated from First Principles, *Angew. Chemie-Int. Ed.* **54**, 9280 (2015).
- [64] M. S. Miao, X. L. Wang, J. Brgoch, F. Spera, M. G. Jackson, G. Kresse, and H. Q. Lin, Anionic Chemistry of Noble Gases: Formation of Mg-NG (NG=Xe, Kr, Ar) Compounds under Pressure, *J. Am. Chem. Soc.* **137**, 14122 (2015).
- [65] K. Kuno, T. Matsuoka, T. Nakagawa, N. Hirao, Y. Ohishi, K. Shimizu, K. Takahama, K. Ohta, M. Sakata, Y. Nakamoto, T. Kume, and S. Sasaki, Heating of Li in Hydrogen: Possible Synthesis of LiH_x , *High Press. Res.* **35**, 16 (2015).
- [66] C. M. Pépin, A. Dewaele, G. Geneste, P. Loubeyre, and M. Mezouar, New

- Iron Hydrides under High Pressure, *Phys. Rev. Lett.* **113**, 265504 (2014).
- [67] B. Li, Y. Ding, D. Y. Kim, R. Ahuja, G. Zou, and H. K. Mao, Rhodium Dihydride (RhH_2) with High Volumetric Hydrogen Density, *Proc. Natl. Acad. Sci. U. S. A.* **108**, 18618 (2011).
- [68] T. Scheler, M. Marqués, Z. Konôpková, C. L. Guillaume, R. T. Howie, and E. Gregoryanz, High-Pressure Synthesis and Characterization of Iridium Trihydride, *Phys. Rev. Lett.* **111**, 215503 (2013).
- [69] W. Zhang, A. R. Oganov, A. F. Goncharov, Q. Zhu, S. E. Boulfelfel, A. O. Lyakhov, E. Stavrou, M. Somayazulu, V. B. Prakapenka, and Z. Konopková, Unexpected Stable Stoichiometries of Sodium Chlorides, *Science*. **342**, 1502 (2013).
- [70] N. W. Ashcroft, Metallic Hydrogen: A High-Temperature Superconductor?, *Phys. Rev. Lett.* **21**, 1748 (1968).
- [71] J. McMinis, R. C. Clay, D. Lee, and M. A. Morales, Molecular to Atomic Phase Transition in Hydrogen under High Pressure, *Phys. Rev. Lett.* **114**, 105305 (2015).
- [72] S. Azadi, B. Monserrat, W. M. C. Foulkes, and R. J. Needs, Dissociation of High-Pressure Solid Molecular Hydrogen: A Quantum Monte Carlo and Anharmonic Vibrational Study, *Phys. Rev. Lett.* **112**, 165501 (2014).
- [73] P. Loubeyre, F. Occelli, and R. LeToullec, Optical Studies of Solid Hydrogen to 320 GPa and Evidence for Black Hydrogen, *Nature* **416**, 613 (2002).
- [74] A. P. Drozdov, M. I. Eremets, I. A. Troyan, V. Ksenofontov, and S. I. Shylin, Conventional Superconductivity at 203 Kelvin at High Pressures in the Sulfur Hydride System, *Nature* **525**, 73 (2015).
- [75] A. P. Drozdov, P. P. Kong, V. S. Minkov, S. P. Besedin, M. A. Kuzovnikov, S. Mozaffari, L. Balicas, F. F. Balakirev, D. E. Graf, V. B. Prakapenka, E. Greenberg, D. A. Knyazev, M. Tkacz, and M. I. Eremets, Superconductivity at 250 K in Lanthanum Hydride under High Pressures, *Nature* **569**, 528 (2019).
- [76] P. Kong, V. S. Minkov, M. A. Kuzovnikov, A. P. Drozdov, S. P. Besedin, S. Mozaffari, L. Balicas, F. F. Balakirev, V. B. Prakapenka, S. Chariton, D. A. Knyazev, E. Greenberg, and M. I. Eremets, Superconductivity up to 243 K in the Yttrium-Hydrogen System under High Pressure, *Nat. Commun.* **12**, 5075 (2021).
- [77] A. Schilling, M. Cantoni, J. D. Guo, and H. R. Ott, Superconductivity above 130 K in the Hg-Ba-Ca-Cu-O System, *Nature* **363**, 56 (1993).
- [78] L. Gao, Y. Y. Xue, F. Chen, Q. Xiong, R. L. Meng, D. Ramirez, C. W. Chu, J. H. Eggert, and H. K. Mao, Superconductivity up to 164 K in $\text{HgBa}_2\text{Ca}_{m-1}\text{Cu}_m\text{O}_{2m+2+\delta}$ ($M=1, 2, \text{ and } 3$) under Quasihydrostatic Pressures, *Phys. Rev. B* **50**, 4260 (1994).
- [79] X. J. Chen, V. V. Struzhkin, Y. Song, A. F. Goncharov, M. Ahart, Z. Liu, H. K.

- Mao, and R. J. Hemley, Pressure-Induced Metallization of Silane, Proc. Natl. Acad. Sci. U. S. A. **105**, 20 (2008).
- [80] J. Hama, Y. Shiomi, and K. Suito, Equation of State and Metallization of Ice under Very High Pressure, J. Phys. Condens. Matter **2**, 8107 (1990).
- [81] S. F. Elatresh and S. A. Bonev, Stability and Metallization of Solid Oxygen at High Pressure, Phys. Chem. Chem. Phys. **22**, 12577 (2020).
- [82] M. R. Stewart, Phase Transformations and Metallization of Magnesium Oxide at High Pressure and Temperature, Science. **338**, 1330 (2012).
- [83] D. Zhou, Y. Zhou, C. Pu, X. Chen, P. Lu, X. Wang, C. An, Y. Zhou, F. Miao, C. H. Ho, J. Sun, Z. Yang, and D. Xing, Pressure-Induced Metallization and Superconducting Phase in ReS₂, Npj Quantum Mater. **2**, 19 (2017).
- [84] N. Li, B. Manoun, Y. Tamraoui, Q. Zhang, H. Dong, Y. Xiao, P. Chow, P. Lazor, X. Lü, Y. Wang, and W. Yang, Structural and Electronic Phase Transitions of CO₂TE₃O₈ Spiroffite under High Pressure, Phys. Rev. B **99**, 245125 (2019).
- [85] J. A. Barreda-Argüeso, L. Nataf, F. Aguado, I. Hernández, J. González, A. Otero-de-la-Roza, V. Luaña, Y. Jia, C. Jin, B. Kim, K. Kim, B. I. Min, W. Heribert, A. P. Jephcoat, and F. Rodríguez, Pressure-Induced Spin Transition and Site-Selective Metallization in CoCl₂, Sci. Rep. **9**, 5448 (2019).
- [86] N. Dubrovinskaia, L. Dubrovinsky, N. A. Solopova, A. Abakumov, S. Turner, M. Hanfland, E. Bykova, M. Bykov, C. Prescher, V. B. Prakapenka, S. Petitgirard, I. Chuvashova, B. Gasharova, Y. L. Mathis, P. Ershov, I. Snigireva, and A. Snigirev, Terapascal Static Pressure Generation with Ultrahigh Yield Strength Nanodiamond, Sci. Adv. **2**, e1600341 (2016).
- [87] D. Yamazaki, E. Ito, T. Yoshino, N. Tsujino, A. Yoneda, X. Guo, F. Xu, Y. Higo, and K. Funakoshi, Over 1 Mbar Generation in the Kawai-Type Multianvil Apparatus and Its Application to Compression of (Mg_{0.92}Fe_{0.08})SiO₃ Perovskite and Stishovite, Phys. Earth Planet. Inter. **228**, 262 (2014).
- [88] R. F. Smith, J. H. Eggert, R. Jeanloz, T. S. Duffy, D. G. Braun, J. R. Patterson, R. E. Rudd, J. Biener, A. E. Lazicki, A. V. Hamza, J. Wang, T. Braun, L. X. Benedict, P. M. Celliers, and G. W. Collins, Ramp Compression of Diamond to Five Terapascals, Nature **511**, 330 (2014).
- [89] S. Dub, P. Lytvyn, V. Strelchuk, A. Nikolenko, Y. Stubrov, I. Petrusha, T. Taniguchi, and S. Ivakhnenko, Vickers Hardness of Diamond and Cbn Single Crystals: AFM Approach, Crystals **7**, 1 (2017).
- [90] S. Klotz, J. C. Chervin, P. Munsch, and G. Le Marchand, Hydrostatic Limits of 11 Pressure Transmitting Media, J. Phys. D: Appl. Phys. **42**, 075413 (2009).
- [91] A. Celeste, F. Borondics, and F. Capitani, Hydrostaticity of Pressure-

- Transmitting Media for High Pressure Infrared Spectroscopy, High Press. Res. **39**, 608 (2019).
- [92] A. Dewaele, P. Loubeyre, and M. Mezouar, Equations of State of Six Metals above 94 GPa, Phys. Rev. B **70**, 094112 (2004).
- [93] H. K. Mao, J. Xu, and P. M. Bell, Calibration of the Ruby Pressure Gauge to 800 Kbar under Quasi-Hydrostatic Conditions, J. Geophys. Res. **91**, 4673 (1986).
- [94] D. Errandonea, C. Popescu, A. B. Garg, P. Botella, D. Martínez-García, J. Pellicer-Porres, P. Rodríguez-Hernández, A. Muñoz, V. Cuenca-Gotor, and J. A. Sans, Pressure-Induced Phase Transition and Band-Gap Collapse in the Wide-Band-Gap Semiconductor InTaO₄, Phys. Rev. B **93**, 035204 (2016).
- [95] J. Liu, Z. Shen, Y. Zhang, X. Yin, and S. He, The P-T Phase Diagram of Lithium Iodate (LiIO₃) up to 40 Kbars, Acta Phys. Sin **32**, 118 (1983).
- [96] J. Hu, L. Chen, L. Wang, R. Tang, and R. Che, Isothermal Compression of α -LiIO₃ and Its Phase Transition under High Pressure and High Temperature, Acta Phys. Sin **36**, 1099 (1987).
- [97] W. W. Zhang, Q. L. Cui, Y. W. Pan, S. S. Dong, J. Liu, and G. T. Zou, High-Pressure x-Ray Diffraction Study of LiIO₃ to 75 GPa, J. Phys. Condens. Matter **14**, 10579 (2002).
- [98] L. Bayarjargal, L. Wiehl, A. Friedrich, B. Winkler, E. A. Juárez-Arellano, W. Morgenroth, and E. Haussühl, Phase Transitions in KIO₃, J. Phys. Condens. Matter **24**, 325401 (2012).
- [99] Y. Suffren, I. Gautier-Luneau, C. Darie, C. Goujon, M. Legendre, and O. Leynaud, First Evidence of a Phase Transition in a High-Pressure Metal Iodate: Structural and Thermal Studies of AgIO₃ Polymorphs, Eur. J. Inorg. Chem. **2013**, 3526 (2013).
- [100] A. Liang, S. Rahman, H. Saqib, P. Rodríguez-Hernández, A. Muñoz, G. Nenert, I. Yousef, C. Popescu, and D. Errandonea, First-Order Isostructural Phase Transition Induced by High Pressure in Fe(IO₃)₃, J. Phys. Chem. C **124**, 8669 (2020).
- [101] A. Liang, S. Rahman, P. Rodríguez-Hernández, A. Muñoz, F. J. Manjón, G. Nenert, and D. Errandonea, High-Pressure Raman Study of Fe(IO₃)₃: Soft-Mode Behavior Driven by Coordination Changes of Iodine Atoms, J. Phys. Chem. C **124**, 21329 (2020).
- [102] C. Galez, Y. Mugnier, J. Bouillot, Y. Lambert, and R. Le Dantec, Synthesis and Characterisation of Fe(IO₃)₃ Nanosized Powder, J. Alloys Compd. **416**, 261 (2006).
- [103] J. Rodríguez-Carvajal, Recent Advances in Magnetic Structure Determination by Neutron Powder Diffraction, Phys. B Phys. Condens. Matter **192**, 55 (1993).

- [104] C. Prescher and V. B. Prakapenka, DIOPTAS: A Program for Reduction of Two-Dimensional X-Ray Diffraction Data and Data Exploration, High Press. Res. **35**, 223 (2015).
- [105] I. Yousef, L. Ribó, A. Crisol, I. Šics, G. Ellis, T. Ducic, M. Kreuzer, N. Benseny-Cases, M. Quispe, P. Dumas, S. Lefrançois, T. Moreno, G. García, S. Ferrer, J. Nicolas, and M. A. G. Aranda, MIRAS: The Infrared Synchrotron Radiation Beamline at ALBA, Synchrotron Radiat. News **30**, 4 (2017).
- [106] D. Errandonea, A. Segura, D. Martínez-García, and V. Muñoz-San Jose, Hall-Effect and Resistivity Measurements in CdTe and ZnTe at High Pressure: Electronic Structure of Impurities in the Zinc-Blende Phase and the Semimetallic or Metallic Character of the High-Pressure Phases, Phys. Rev. B. **79**, 125203 (2009).
- [107] P. Hohenberg and W. Kohn, Inhomogeneous Electron Gas, Phys. Rev. **136**, B864 (1964).
- [108] P. E. Blöchl, Projector Augmented-Wave Method, Phys. Rev. B **50**, 17953 (1994).
- [109] G. Kresse and D. Joubert, From Ultrasoft Pseudopotentials to the Projector Augmented-Wave Method, Phys. Rev. B **59**, 1758 (1999).
- [110] G. Kresse and J. Hafner, Ab Initio Molecular Dynamics for Liquid Metals, Phys. Rev. B **47**, 558 (1993).
- [111] G. Kresse and J. Hafner, Ab Initio Molecular-Dynamics Simulation of the Liquid-Metamorphous- Semiconductor Transition in Germanium, Phys. Rev. B **49**, 14251 (1994).
- [112] G. Kresse and J. Furthmüller, Efficiency of Ab-Initio Total Energy Calculations for Metals and Semiconductors Using a Plane-Wave Basis Set, Comput. Mater. Sci. **6**, 15 (1996).
- [113] G. Kresse and J. Furthmüller, Efficient Iterative Schemes for Ab Initio Total-Energy Calculations Using a Plane-Wave Basis Set, Phys. Rev. B **54**, 11169 (1996).
- [114] J. P. Perdew, A. Ruzsinszky, G. I. Csonka, O. A. Vydrov, G. E. Scuseria, L. A. Constantin, X. Zhou, and K. Burke, Restoring the Density-Gradient Expansion for Exchange in Solids and Surfaces, Phys. Rev. Lett. **100**, 136406 (2008).
- [115] S. Dudarev and G. Botton, Electron-Energy-Loss Spectra and the Structural Stability of Nickel Oxide: An LSDA+U Study, Phys. Rev. B. (1998).
- [116] K. Parlinski, *Computer Code PHONON*.
- [117] H. J. Monkhorst and J. D. Pack, Special Points for Brillouin-Zone Integrations, Phys. Rev. B **13**, 5188 (1976).
- [118] P. Canepa, R. M. Hanson, P. Ugliengo, and M. Alfredsson, J-ICE: A New Jmol Interface for Handling and Visualizing Crystallographic and Electronic Properties, J. Appl. Crystallogr. **44**, 225 (2011).

- [119] F. Birch, Finite Strain Isotherm and Velocities for Single-Crystal and Polycrystalline NaCl at High Pressures and 300 K, *J. Geophys. Res.* **83**, 1257 (1978).
- [120] Z. Hebboul, C. Galez, D. Benbortal, S. Beauquis, Y. Mugnier, A. Benmakhlouf, M. Bouchenafa, and D. Errandonea, Synthesis, Characterization, and Crystal Structure Determination of a New Lithium Zinc Iodate Polymorph $\text{LiZn}(\text{IO}_3)_3$, *Crystals* **9**, 464 (2019).
- [121] A. Krapp, F. M. Bickelhaupt, and G. Frenking, Orbital Overlap and Chemical Bonding, *Chem.-A Eur. J.* **12**, 9196 (2006).
- [122] D. Errandonea, Y. Meng, M. Somayazulu, and D. Häusermann, Pressure-Induced $\rightarrow \omega$ Transition in Titanium Metal: A Systematic Study of the Effects of Uniaxial Stress, *Phys. B Condens. Matter* **355**, 116 (2005).
- [123] D. Errandonea, A. Muñoz, and J. Gonzalez-Platas, Comment on "High-Pressure x-Ray Diffraction Study of $\text{YBO}_3/\text{Eu}^{3+}$, GdBO_3 , and EuBO_3 : Pressure-Induced Amorphization in GdBO_3 ", *J. Appl. Phys.* **115**, 216101 (2014).
- [124] J. Tauc, Optical Properties and Electronic Structure of Amorphous Ge and Si, *Mater. Res. Bull.* **3**, 37 (1968).
- [125] F. Urbach, The Long-Wavelength Edge of Photographic Sensitivity and of the Electronic Absorption of Solids, *Phys. Rev.* **92**, 1324 (1953).
- [126] D. Errandonea, D. Martínez-García, R. Lacomba-Perales, J. Ruiz-Fuertes, and A. Segura, Effects of High Pressure on the Optical Absorption Spectrum of Scintillating PbWO_4 Crystals, *Appl. Phys. Lett.* **89**, 091913 (2006).
- [127] D. Errandonea, E. Bandiello, A. Segura, J. J. Hamlin, M. B. Maple, P. Rodriguez-Hernandez, and A. Muñoz, Tuning the Band Gap of PbCrO_4 through High-Pressure: Evidence of Wide-to-Narrow Semiconductor Transitions, *J. Alloys Compd.* **587**, 14 (2014).
- [128] C. R. Rotundu, T. Čuk, R. L. Greene, Z. X. Shen, R. J. Hemley, and V. V. Struzhkin, High-Pressure Resistivity Technique for Quasi-Hydrostatic Compression Experiments, *Rev. Sci. Instrum.* **84**, 063903 (2013).
- [129] D. Phanon, B. Bentría, E. Jeanneau, D. Benbortal, A. Mosset, and I. Gautier-Luneau, Crystal Structure of $\text{M}(\text{IO}_3)_2$ Metal Iodates, Twinned by Pseudo-Merohedry, with M^{II} : Mg^{II} , Mn^{II} , Co^{II} , Ni^{II} and Zn^{II} , *Zeitschrift Fur Krist.* **221**, 635 (2006).
- [130] A. Liang, C. Popescu, F. J. Manjon, R. Turnbull, E. Bandiello, P. Rodriguez-Hernandez, A. Muñoz, I. Yousef, Z. Hebboul, and D. Errandonea, Pressure-Driven Symmetry-Preserving Phase Transitions in $\text{Co}(\text{IO}_3)_2$, *J. Phys. Chem. C* **125**, 17448 (2021).
- [131] A. Liang, F. Rodríguez, Rodríguez-Hernandez, P, A. Muñoz, R. Turnbull, and D. Errandonea, High-Pressure Tuning of d-d Crystal-Field Electronic

- Transitions and Electronic Band Gap in $\text{Co}(\text{IO}_3)_2$, *Phys. Rev. B* **105**, 115204 (2022).
- [132] H. M. Rietveld, A Profile Refinement Method for Nuclear and Magnetic Structures, *J. Appl. Crystallogr.* **2**, 65 (1969).
- [133] F. Fauth, I. Peral, C. Popescu, and M. Knapp, The New Material Science Powder Diffraction Beamline at ALBA Synchrotron, *Powder Diffr.* **28**, 360 (2013).
- [134] J. Zhao and N. L. Ross, Non-Hydrostatic Behavior of KBr as a Pressure Medium in Diamond Anvil Cells up to 5.63 GPa, *J. Phys. Condens. Matter* **27**, 185402 (2015).
- [135] A. E. Mattsson and R. Armiento, Implementing and Testing the AM05 Spin Density Functional, *Phys. Rev. B* **79**, 155101 (2009).
- [136] A. Jain, S. P. Ong, G. Hautier, W. Chen, W. D. Richards, S. Dacek, S. Cholia, D. Gunter, D. Skinner, G. Ceder, and K. A. Persson, Commentary: The Materials Project: A Materials Genome Approach to Accelerating Materials Innovation, *APL Mater.* **1**, 011002 (2013).
- [137] A. Togo and I. Tanaka, First Principles Phonon Calculations in Materials Science, *Scr. Mater.* **108**, 1 (2015).
- [138] A. Le Bail, Whole Powder Pattern Decomposition Methods and Applications: A Retrospection, *Powder Diffr.* **20**, 316 (2005).
- [139] F. D. Murnaghan, The Compressibility of Media under Extreme Pressures, *Proc. Natl. Acad. Sci.* **30**, 244 (1944).
- [140] F. Birch, Finite Elastic Strain of Cubic Crystals, *Phys. Rev.* **71**, 809 (1947).
- [141] A. Liang, C. Popescu, F. J. Manjon, A. Muñoz, Z. Hebboul, and D. Errandonea, Structural and Vibrational Study of $\text{Zn}(\text{IO}_3)_2$ Combining High-Pressure Experiments and Density-Functional Theory, *Phys. Rev. B* **103**, 054102 (2021).
- [142] F. Aguado, F. Rodríguez, and P. Núñez, Pressure-Induced Jahn-Teller Suppression and Simultaneous High-Spin to Low-Spin Transition in the Layered Perovskite CsMnF_4 , *Phys. Rev. B* **76**, 094417 (2007).
- [143] F. Rodríguez and F. Aguado, Correlations between Structure and Optical Properties in Jahn-Teller Mn^{3+} Fluorides: A Study of TlMnF_4 and NaMnF_4 under Pressure, *J. Chem. Phys.* **118**, 10867 (2003).
- [144] Y. Tanabe and S. Sugano, On the Absorption Spectra of Complex Ions. I, *J. Phys. Soc. Japan* **9**, 753 (1954).
- [145] J. A. Barrera-Argüeso, F. Aguado, J. González, R. Valiente, L. Nataf, M. N. Sanz-Ortiz, and F. Rodríguez, Crystal-Field Theory Validity Through Local (and Bulk) Compressibilities in CoF_2 and KCoF_3 , *J. Phys. Chem. C* **120**, 18788 (2016).
- [146] R. G. Burns, *Mineralogical Applications of Crystal Field Theory* (Cambridge University Press, Cambridge, 1993).

- [147] J. K. Liang and C. G. Wang, The Structure of $\text{Zn}(\text{IO}_3)_2$ Crystal, *Acta Chim. Sin.* **40**, 985 (1982).
- [148] A. Liang, R. Turnbull, E. Bandiello, I. Yousef, C. Popescu, Z. Hebboul, and D. Errandonea, High-Pressure Spectroscopy Study of $\text{Zn}(\text{IO}_3)_2$ Using Far-Infrared Synchrotron Radiation, *Crystals* **11**, 34 (2021).
- [149] A. Togo, F. Oba, and I. Tanaka, First-Principles Calculations of the Ferroelastic Transition between Rutile-Type and CaCl_2 -Type SiO_2 at High Pressures, *Phys. Rev. B.* **78**, 134106 (2008).
- [150] J.-K. Liang, Y.-D. Yu, and S.-L. Ding, The Structure and Phase Transitions of Magnesium Iodate Crystals, *Acta Phys. Sin.* **27**, 710 (1978).
- [151] A. Liang, R. Turnbull, C. Popescu, F. J. Manjón, E. Bandiello, A. Muñoz, I. Yousef, Z. Hebboul, and D. Errandonea, Pressure-Induced Phase Transition and Increase of Oxygen-Iodine Coordination in Magnesium Iodate, *Phys. Rev. B.* **105**, 054105 (2022).
- [152] R. Armiento and A. E. Mattsson, Functional Designed to Include Surface Effects in Self-Consistent Density Functional Theory, *Phys. Rev. B* **72**, 085108 (2005).
- [153] A. E. Mattsson, R. Armiento, J. Paier, G. Kresse, J. M. Wills, and T. R. Mattsson, The AM05 Density Functional Applied to Solids, *J. Chem. Phys.* **128**, 084714 (2008).
- [154] Y. Hinuma, G. Pizzi, Y. Kumagai, F. Oba, and I. Tanaka, Band Structure Diagram Paths Based on Crystallography, *Comput. Mater. Sci.* **128**, 140 (2017).
- [155] A. M Ganose, A. J Jackson, and D. O Scanlon, Sumo: Command-Line Tools for Plotting and Analysis of Periodic Ab Initio Calculations, *J. Open Source Softw.* **3**, 717 (2018).
- [156] S. Maintz, V. L. Deringer, A. L. Tchougréeff, and R. Dronskowski, LOBSTER: A Tool to Extract Chemical Bonding from Plane-Wave Based DFT, *J. Comput. Chem.* **37**, 1030 (2016).
- [157] W. Zhou and N. Umezawa, Band Gap Engineering of Bulk and Nanosheet SnO : An Insight into the Interlayer Sn-Sn Lone Pair Interactions, *Phys. Chem. Chem. Phys.* **17**, 17816 (2015).
- [158] Y. Y. Peter and M. Cardona, *Fundamentals of Semiconductors* (Springer, Berlin, 2005).